PIERS 2013 Taipei

Progress In Electromagnetics Research Symposium

Abstracts

March 25–28, 2013
TAIPEI

www.emacademy.org
www.piers.org

PIERS 2013 Taipei Abstracts

Published by

The Electromagnetics Academy
777 Concord Avenue, Suite 207
Cambridge, MA 02138

www.emacademy.org
www.piers.org

ISSN: 1559-9450
ISBN: 978-1-934142-23-3

Progress In Electromagnetics Research Symposium

March 25–28, 2013

TAIPEI

PIERS 2013 TAIPEI ORGANIZATION

PIERS Founding Chair

J. A. Kong, MIT, USA

PIERS Chair

L. Tsang, University of Washington, USA

PIERS 2013 Taipei Honorable Chair

D. C. Rau, Oriental Institute of Technology, TAIPEI

PIERS 2013 Taipei General Chair

D. C. Chang, Oriental Institute of Technology, TAIPEI

PIERS 2013 Taipei General Vice Chairs

H. T. Chuah, Universiti Tunku Abdul Rahman, Kuala Lumpur, MALAYSIA

K. Kobayashi, Chuo University, JAPAN

PIERS 2013 Taipei International Advisory Committee

Y. M. M. Antar
K.-S. Chen
V. Freilikher
W. J. R. Hoefer
A. Ishimaru
A. N. Lagarkov
Y.-A. Liou
P. Pampaloni
J. W. Ra
L. Shafai
D.-P. Tsai
J. Vrba
R.-S. Yahya
A. Zhukov
W.-M. Boerner
W. C. Chew
L. Gürel
P. Hsu
K. Ito
K. J. Langenberg
K. M. Luk
P. H. Pathak
M. Raugi
Y. V. Shestopalov
P. Ya. Ufimtsev
K.-L. Wong
T. Yamasaki
S. Zouhdi
A. Büyükaksoy
N. Engheta
T. M. Habashy
C.-W. Hsue
E. O. Kamenetskii
L.-W. Li
K. K.-H. Mei
S.-T. Peng
A. S. Samokhin
P. D. Smith
P. L. E. Uslenghi
R.-B. Wu
K. Yasumoto
C.-H. Chan
H. T. Ewe
M. Hallikainen
M. Idemen
A. Komiyama
I. V. Lindell
Y. Miyazaki
A. Priou
A. H. Serbest
M. Tateiba
P. M. van den Berg
J. Wu
W.-X. Zhang

PIERS 2013 Taipei Technical Program Committee

B.-W. Alireza
A. Altintas
Y. Ando
H. Arai
S. Barmada
J. Bredow
D. Caratelli
D. Censor
H.-C. Chang
T.-N. Chang
H. S. Chen
H.-T. Chen
W.-S. Chen
Y. K. Cho
H.-T. Chou
B.-K. Chung
H.-T. Ewe
T. Fukusako
G. N. Georgiev
J. Gonzalez
F. Günes
S. L. He
C.-Y. Hsu
C.-N. Hu
R.-B. Hwang
K. Iwatsuki
Q. Jiang
R. Kastner
J.-F. Kiang
S.-Y. Kim
V. F. Kravchenko
Y. A. Kravtsov
M. Kuroda
G. A. Kyriacou
Y.-C. Lan
C.-H. Lee
K. W. Leung
H.-N. Lin
J.-C. Liu
M. A. Lyalinov
G. Manara
F. Molinet
P. Nepa
Y. Okuno
A. V. Osipov
K. Ouchi
B. Polat
F. A. Raham
L. X. Ran
A. K. Sarychev
T. Sengör
R. Shavit
X.-Q. Sheng
B. Shishkov
A. Sihvola
Y. G. Smirnov
R. Talhi
O. A. Tretyakov
S. Tretyakov
J.-D. Tseng
S.-C. Tuan
A. A. Vertiy
B.-I. Wu
G. Q. Xie
V. V. Yakovlev
T.-S. Yeo
W. H. Yu

PIERS 2013 Taipei Organizing Committee

C.-H. Chan
L.-L. Chen
Y.-H. Chen
F.-Y. Chiang
S.-T. Hsieh
C.-N. Hu
K.-H. Hu
Y.-C. Huang
M.-C. Hwang
K.-T Jheng
C.-N. Lee
H.-C. Lee
H.-W. Pao
S.-C. Tuan
H.-H. Tung

PIERS 2013 TAIPEI SESSION ORGANIZERS

H. Arai
C. T. Chan
Y. K. Chan
D.-C. Chang
H.-W. Chang
S.-Y. Chen
S. W. Cheung
A. Chin
C.-K. Chou
M. M. da Silva
Y. Du
H. T. Ewe
D. Felbacq
T. Fukusako
G. N. Georgiev
M. N. Georgieva-Grosse
E. Gescheidtová
Z. H. Hang
M. Horibe
H.-L. Kao
K. Kobayashi
Y.-C. Lan
C.-N. Lee
C.-H. Lee
J.-F. Lee
R.-K. Lee
J. Lettl
K. W. Leung
J. H. Li
H.-B. Liang
Q. H. Liu
K. M. Luk
N. Nishimura
S. Ohnuki
T. B. A. Rahman
C. K. Seow
Y. Shao
Y. V. Shestopalov
R. Talhi
S. Y. Tan
M. Tanaka
M. S. Tong
D. P. Tsai
I. Tsukerman
J. Vrba
C.-J. Wu
G. Q. Xie
T.-J. Yang
A. M. Zagoskin

PIERS 2013 TAIPEI SPONSORS

- ☐ Communication Research Center, Oriental Institute of Technology
- ☐ Department of Electronic Engineering, Oriental Institute of Technology
- ☐ Department of Communication Engineering, Oriental Institute of Technology
- ☐ Department of Taipei Information and Tourism
- ☐ Bureau of Foreign Trade
- ☐ MEET TAIWAN
- ☐ Department of Marketing Management, Takming University of Science and Technology
- ☐ Research Center for Applied Sciences, Academia Sinica
- ☐ IEEE IMS Taipei Chapter
- ☐ National Science Council
- ☐ Ministry of Education
- ☐ Far Eastern Memorial Foundation
- ☐ Far Eastern Y. Z. Hsu Science and Technology Memorial Foundation
- ☐ The Electromagnetics Academy at Zhejiang University
- ☐ The Electromagnetics Academy

PIERS 2013 TAIPEI EXHIBITORS

- ☐ Victory Microwave Cooperation
- ☐ Wavepro Cooperation
- ☐ CST — Computer Simulation Technology
- ☐ Communication Research Center, OIT

PIERS 2013 SESSIONS

1A1 Nonlinear Propagation in Optical Systems 9
1A2 Extended/Unconventional Electromagnetic Theory, EHD(Electro-hydrodynamics)/EMHD(Electro-magneto-hydrodynamics), and Electro-biology 1 21
1A3a Wireless Network and Applications 33
1A3b MIMO Systems 41
1A4 Novel Mathematical Methods in Electromagnetics 51
1A5 Reconfigurable Antenna and Array Antenna 61
1P1 Quantum Metamaterials 71
1P2a Extended/Unconventional Electromagnetic Theory, EHD(Electro-hydrodynamics)/EMHD(Electro-magneto-hydrodynamics), and Electro-biology 2 83
1P2b Application of EM Field in Medicine and in Ecological Technologies 91
1P3a Near-field Engineering, Surface-enhanced Raman Scattering and Their Applications 99
1P3b Wireless Communication, Propagation Prediction 107
1P4 Advanced Numerical Techniques in Electromagnetics 117
1P5a Antennas for Wireless Communications 127
1P5b Small Size and Low-profile Antennas 135
2A1 Manipulating Wave with Metamaterials and Photonic Crystal 1 143
2A2 Biological Effects and Medical Applications of Electromagnetic Energy 1 155
2A3 Microwave Remote Sensing and Polarimetry, SAR, GPR 165
2A4 Multi-scale and Multi-physics Computational Techniques 175
2A5 Antenna Measurement 185
2A6 Passive Waveguide Devices Theory and Numerical Modeling 197
2A7 Resonators, Filters, Interconnects, Packaging, MMIC 209
2A8 Poster Session 1 219
2P1a Manipulating Wave with Metamaterials and Photonic Crystal 2 259
2P1b Electromagnetic Theory, Analysis and Simulation in Photonics 269
2P2a Biological Effects and Medical Applications of Electromagnetic Energy 2 277
2P2b Medical Electromagnetics, Medical Imaging, MRI 285
2P3a Earth Electromagnetic Environment and Radiowaves Propagation & Scattering: Modeling, Observation and Measurements 295
2P3b Present and Future of Terahertz Science & Technology, Including Applications in Radio-sciences 309
2P4 Advanced Mathematical and Computational Methods in Electromagnetic Theory and Their Applications 315
2P5 Wideband and Multi-band Antennas 331
2P6 Optics and Photonics, Fiber, Lasers, Gyrotrons 345
2P7 Electromagnetics of Gradient Nanostructures and Heterogeneous Media 361

2P8 Poster Session 2 . . . 363
3A1 Plasmonic Nanophotonics 1 - Experiment and Fabrication . . . 411
3A2 Power Electronics . . . 423
3A3 EM Scattering Models and Applications . . . 431
3A4 Design and Simulation of Electromagnetic and Optical Devices 1 . . . 441
3A5 Microstrip and Printed Antenna, Antenna Theory . . . 455
3A6 Electromagnetic Theory and Design on the Optical Dispersive Materials, Invisible Cloak and Photonic Crystals . . . 467
3A7 Microwave and Millimeter Wave Circuits and Devices, CAD . . . 477
3A8 Poster Session 3 . . . 493
3P1 Plasmonic Nanophotonics 2 - Analysis, Theory, Calculation and Simulation . . . 539
3P2a Intelligent Electronics . . . 553
3P2b RF, Microwave and Millimeter-wave Measurements . . . 559
3P3 SAR System and Signal Processing . . . 567
3P4a Design and Simulation of Electromagnetic and Optical Devices 2 . . . 579
3P4b Computational Electromagnetics . . . 585
3P5 Antenna and EMC . . . 595
3P6a Biomedical Electromagnetic Instruments, EM Condensed Materials and Imaging and Education 613
3P6b Electromagnetic Modeling, Inversion and Applications . . . 621
3P8 Poster Session 4 . . . 629
Author Index . . . 693

Session 1A1
Nonlinear Propagation in Optical Systems

Simulation of Quantum Mechanics in Optical Systems
Blas Manuel Rodriguez-Lara, ... 10

Barycenter Properties of Diffraction-free Light Beams
Chun-Fang Li, Shuang-Yan Yang, Zi-Hua Xin, ... 11

Giant Goos-Hänchen Shift in Evanescent Field and Near-field Applications
Xi Chen, ... 12

Optical Soliton Perturbation by Semi-inverse Variational Principle
Anjan Biswas, ... 14

Bragg Grating Solitons in Semilinear Couplers with Dispersive Reflectivity
S. A. M. S. Chowdhury, Javid Atai, ... 15

Few-cycle Optical Solitons
Yuan-Yao Lin, Mou-Ray Chen, I-Hong Chen, Ray-Kuang Lee, ... 16

Influence of Six-wave Interactions and Saturated Nonlinearity on the Statistics of Waves in the Framework of One-dimensional Generalized NLS Equation
Dmitry Agafontsev, ... 17

Spatial Optical Solitons and Their Interaction in Nonlocal Media with Competing Nonlinearities
Ming Shen, H. Zhao, L. Chen, Y.-Y. Lin, C. C. Jeng, R.-K. Lee, Wieslaw Krolikowski, ... 18

Second Harmonic Generation Due to Magnetic Field of Intense Light Field
Shouvik Mukherjee, Sourabh Mukhopadhyay, Biplab Kumar Datta, Prasanta Kumar Dutta, ... 19

Simulation of Quantum Mechanics in Optical Systems

B. M. Rodríguez-Lara
Instituto Nacional de Astrofísica, Óptica y Electrónica
Calle Luis Enrique Erro No. 1, Sta. Ma. Tonantzintla, Pue. CP 72840, Mexico

Abstract— Back in 1982, Feynman conjectured that quantum computers may be able to simulate other quantum systems in a more efficient way than classical computers [1]. This was the first difficult task posed for universal quantum computers. In 1996, Lloyd showed that such a thing is possible [2]. Frequently, a universal quantum computer is overkill for the problem at hand; e.g., one could be interested in simulating just a particular class of quantum systems. It is in these cases that classical and quantum simulators enter the picture. A simulator is a controllable system that can be used to mimic other systems and, in general, simulation is less demanding than universal computation; it has been said that a mere 40 qubits are enough to perform a quantum simulation of the Hubbard model that delivers the intricacies of this physical system [2].

In this talk, I will make use of electromagnetic field propagation through coupled single-mode waveguide lattices to report classical simulators of quantum walks [4], relativistic quantum mechanics [5], and quantum optics [6]. Such lattices are described by the coupled mode generalized paraxial equation in the tight binding regime [3]:

$$-i\partial_z \mathcal{E}_j = \gamma_j \mathcal{E}_j + \beta_j(\mathcal{E}_{j-1} + \mathcal{E}_{j+1}), \quad j = -\infty, \ldots, \infty, \tag{1}$$

in the case of infinite lattices and modified accordingly for semi-infinite and finite lattices. Quantum simulators exploit photon transport in the same or equivalent systems; e.g., coupled cavities, circular resonators or strip-line resonators described by Hamiltonians of the type

$$H = \sum_j \omega_j \hat{a}_j^\dagger \hat{a} + g_j \left(\hat{a}_j^\dagger \hat{a}_{j+1} + \hat{a}_j \hat{a}_{j+1}^\dagger \right), \tag{2}$$

with equations of motion given by

$$i\partial_t \hat{a}_j = \omega_j \hat{a}_j + g_j \left(\hat{a}_{j+1} + \hat{a}_{j-1} \right), \quad j = -\infty, \ldots, \infty. \tag{3}$$

For the case of a single photon, Eq. (1) and Eq. (3) are equivalent up to an overall phase and variable change $t \to z$. In matrix form, say $\partial_z \vec{\mathcal{E}} = \mathbf{M}\vec{\mathcal{E}}$ or $\partial_t \vec{a} = \mathbf{M}\vec{a}$, both differential sets are solvable, $\vec{\mathcal{E}}(t) = e^{i\mathbf{M}z}\vec{\mathcal{E}}(0)$ or $\vec{a}(t) = e^{-i\mathbf{M}t}\vec{a}(0)$, for any combination of variables as long as they are position/time independent, due to the tridiagonal form of $\mathbf{M}$ [4].

In particular, I will show how finite lattices can be used to produce quantum walks with sub-Poisson statistics [4], how semi-infinite binary lattices are curiously solved by Fibonacci polynomials [5] (these lattices are used to classically simulate relativistic quantum mechanics [7]) and, finally, how semi-infinite coupled waveguides can simulate nonlinear atom-field interactions that does not occur in nature, like a phase-driven two-level system [6].

REFERENCES

1. Feynman, R. P., "Simulating physics with computers," *Int. J. Theo. Phys.*, Vol. 21, 467–488, 1982.
2. Lloyd, S., "Universal quantum simulators," *Science*, Vol. 273, 1073–1078, 1996.
3. Jones, A. L., "Coupling of optical fibers and scattering in fibers," *J. Opt. Soc. Am.*, Vol. 55, 261–271, 1965.
4. Rodríguez-Lara, B. M., "Exact dynamics of finite Glauber-Fock photonic lattices," *Phys. Rev. A*, Vol. 84, 053845, 2011.
5. Rodríguez-Lara, B. M. and H. Moya-Cessa, "Photon transport in binary photonic lattices," *Phys. Scripta*, 2012 (accepted).
6. Rodríguez-Lara, B. M., A. Zárate Cárdenas, F. Soto-Eguibar, and H. Moya-Cessa, "A photonic realization of a phase driven two-level atom," arXiv: 1207.6552 [quant-ph], 2012.
7. Longhi, S., "Classical simulation of relativistic quantum mechanics in periodic optical structures," *Appl. Phys. B*, Vol. 104, 453–468, 2011.

Barycenter Properties of Diffraction-free Light Beams

Chun-Fang Li, Shuang-Yan Yang, and Zi-Hua Xin
Department of Physics, Shanghai University, China

Abstract— The so-called Jones wavefunction $\tilde{f}(\mathbf{k},t)$ of photon in momentum space is related with its three-component wavefunction $\mathbf{f}(\mathbf{k},t)$, called Maxwell wavefunction, through a quasi unitary matrix Π via

$$\mathbf{f}(\mathbf{k},t) = \Pi\tilde{f}(\mathbf{k},t). \tag{1}$$

The position operator of photon that acts on the Jones wavefunction splits into two parts, $\mathbf{x}_J = \boldsymbol{\Xi} + \xi$. The first part

$$\boldsymbol{\Xi} = i\Pi^{\dagger}\nabla\Pi \tag{2}$$

is interpreted as the barycenter of photon. The second part that takes on the form of gradient operator in the momentum space, $\xi = i\nabla$, is as the coordinate relative to the barycenter. Letting the propagation direction be along the z-axis, the Jones wavefunctions for the complete set of diffraction-free beams are given by

$$\tilde{f}_{\gamma,\omega_0,k_{z0},m}(\mathbf{k},t) = \sqrt{\frac{\omega_0}{2\pi}}\frac{\tilde{\alpha}_\gamma}{ck_{\rho 0}}\,\delta(k_\rho - k_{\rho 0})\delta(k_z - k_{z0})e^{im\varphi}e^{-i\omega_0 t}, \quad m = 0,\ \pm 1,\ \pm 2\ldots \tag{3}$$

which are characterized by a set of four quantum numbers γ, ω_0, k_{z0}, and m corresponding respectively to helicity, energy, the longitudinal components of momentum and orbital angular momentum about the barycenter. The matrix Π is characterized by an additional degree of freedom that originates from the constraint of transversality condition and takes on the form of a constant unit vector, $\mathbf{I}$. Letting the unit vector $\mathbf{I}$ be located in the plane xoz and make an angle Θ with the z-axis, the Cartesian coordinates of the barycenter for the diffraction-free beam (4) are given by

$$\begin{aligned}\langle\Xi_x\rangle &= \langle\Xi_z\rangle = 0,\\ \langle\Xi_y\rangle &= -\frac{\gamma}{k_0\tan\Theta} + \frac{\gamma}{2k_0\sin\Theta}\left(1 + \frac{\cos\Theta - \cos\vartheta_0}{|\cos\Theta - \cos\vartheta_0|}\right).\end{aligned}$$

Surprisingly, they show that the barycenter does not generally lie on the beam axis, the z-axis. (a) If $\mathbf{I}$ is outside the wavevector cone, $|\Theta| > \vartheta_0$, one gets

$$\langle\Xi_y\rangle = -\frac{\gamma}{k_0}\cot\Theta. \tag{4}$$

It vanishes only when $\mathbf{I}$ is perpendicular to the z-axis. (b) If $\mathbf{I}$ is inside the wavevector cone, $|\Theta| < \vartheta_0$, one finds

$$\langle\Xi_y\rangle = \frac{\gamma}{k_0}\tan\frac{\Theta}{2}. \tag{5}$$

It vanishes only when $\mathbf{I}$ is parallel to the propagation direction. The case in which $\mathbf{I}$ lies exactly on the wavevector cone, $|\Theta| = \vartheta_0$, is also considered.

Giant Goos-Hänchen Shift in Evanescent Field and Near-field Applications

Xi Chen
Department of Physics, Shanghai University, Shanghai 200444, China

Abstract— It is well known that Goos-Hänchen (GH) effect, suggested by Sir Isaac Newton, refers to the phenomenon that a light beam totally reflected from an interface of two substances is laterally displaced from the position predicted by pure geometric reflection [1–4]. In 1947, F. Goos and H. Hänchen demonstrated this surprising phenomenon for the first time in the microwave experiment [5, 6]. Since then, the GH shifts have been extended to various configurations, for instance, frustrated total internal reflection (FTIR) [7–9], attenuated total reflection [10, 11], and other areas of physics, such as acoustics, neutron physics, atom optics and graphene.

With the development of scanning near-field optical microscopy, the GH shift in the evanescent wave has attracted much attention [12–14]. Recently, M. Nieto-Vesperinas and J. R. Arias-Gonzalez have found that the GH shift induced by the total reflection has great effect on the distribution of forces [14]. On the other hand, evanescent fields, related to evanscent wave mirrors, are useful to manipulate atoms and molecules [15], or detect the cold trapped atoms [16]. More interestingly, the enhanced evanescent field can be obtained by adding the surface of the prism a highly conductive, nonmagnetic metal thin, which leads to the significant modification of atomic mirror potential [17].

Motivated by these progress, we will investigate the GH shift in the evanescent field, which is enhanced by coating a dielectric thin film onto the surface of the prim, as shown in Fig. 1. What we concentrate on is the GH shift in the transmitted evanescent region, instead of the reflected region. Similar to the enhancement of GH shift in the reflection due to the resonance in a single thin dielectric layer [18], the GH shift in the evanescent field can be also enhanced, which will change the near-field intensity distribution. With the giant GH shift in evanescent field, we will further calculate the forces exerted by the evanescent wave, to see how the forces can be modified by the GH shift produced by the enhanced evanescent wave in such configuration. We hope these GH-related phenomena could be useful in the near-field applications.

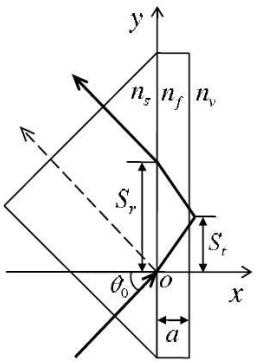

Figure 1: Scheme of the Goos-Hänchen S_t in transmitted evanescent region produced by the prim coated by a thin dielectric thin film.

ACKNOWLEDGMENT

This work was supported by the National Natural Science Foundation of China (Grant No. 61176118) and Shanghai Rising-Star Program (Grant No. 12QH1400800).

REFERENCES

1. Lotsch, H. K. V., *Optik*, Vol. 32, 116, Stuttgart, 1970.
2. Lotsch, H. K. V., *Optik*, Vol. 32, 189, Stuttgart, 1970.
3. Lotsch, H. K. V., *Optik*, Vol. 32, 299, Stuttgart, 1971.
4. Lotsch, H. K. V., *Optik*, Vol. 32, 553, Stuttgart, 1971.

5. Goos, F. and H. Hänchen, *Ann. Phys.*, Vol. 1, 333, 1947.
6. Goos, F. and H. Hänchen, *Ann. Phys.*, Vol. 5, 251, 1949.
7. Hsue, C. W. and T. Tamir, *J. Opt. Soc. Am. A*, Vol. 2, 978, 1985.
8. Haibel, A., G. Nimtz, and A. A. Stahlhofen, *Phys. Rev. E*, Vol. 63, 047601, 2001.
9. Chen, X., C. F. Li, R. R. Wei, and Y. Zhang, *Phys. Rev. A*, Vol. 80, 015803, 2009.
10. Yin, X., L. Hesselink, Z. Liu, N. Fang, and X. Zhang, *Appl. Phys. Lett.*, Vol. 85, 372, 2004.
11. Pillon, F., H. Gilles, S. Girard, M. Laroche, R. Kaiser, and A. Gazibegovic, *J. Opt. Soc. Am. B*, Vol. 22, 1290, 2005.
12. Baida, F. I., D. Van Labeke, and J.-M. Vigoureux, *J. Opt. Soc. Am. A*, Vol. 17, 858, 2000.
13. Zhang, Y., C.-F. Li, and X. Chen, "Nanophotonics, nanostructures, and nanometrology II," *Proc. SPIE*, Vol. 6831, 683103, 2008.
14. Nieto-Vesperinas, M. and J. R. Arias-Gonzalez, arXiv:1102.1613.
15. Kallush, S., B. Segev, and R. Côté, *Eur. Phys. J. D*, Vol. 35, 3, 2005.
16. Cornelussen, R. A., A. H. van Amerongen, B. T. Wolschrijn, R. J. C. Spreeuw, and H. B. van Linden van de Heuvell, *Eur. Phys. J. D*, Vol. 21, 347, 2002.
17. García-Segundo, C., H. Yan, and M. S. Zhan, *Phys. Rev. A*, Vol. 75, 030902(R), 2007.
18. Kaiser, R., Y. Levy, J. Fleming, S. Muniz, and V. S. Bagnato, *Pure Appl. Opt.*, Vol. 5, 891, 1996.

Optical Soliton Perturbation by Semi-inverse Variational Principle

Anjan Biswas
Department of Mathematical Sciences, Delaware State University, Dover, DE 19901-2277, USA

Abstract— The dynamics of the propagation of solitons through an optical fiber is studied in presence of higher order dispersions and other Hamiltonian perturbations with full nonlinearity. The semi-inverse variational principle is applied to solve the perturbed nonlinear Schrodinger's equation (NLSE) which is the governing equation. There are three types of nonlinearity that will be considered, namely the Kerr law, power law and log law nonlinearity. The soliton amplitude, width and its velocity will be determined. A couple of constraint conditions will fall out during the course of derivation of the soliton solution.

Bragg Grating Solitons in Semilinear Couplers with Dispersive Reflectivity

S. A. M. S. Chowdhury and Javid Atai
School of Electrical and Information Engineering, The University of Sydney, NSW 2006, Australia

Abstract— Fiber Bragg grating (FBG) is a periodic structure where the interplay of the counterpropagation and linear resonant coupling gives rise to strong effective dispersion and a gap in the linear spectrum. The equilibrium between the effective dispersion and nonlinearity in the FBG results in soliton-like states that are generally termed Bragg-grating (BG) solitons. The existence and stability of BG solitons in periodic media with Kerr nonlinearity have been the subject of much interest both theoretically and experimentally over the past two decades [1–4]. They have also been investigated in more complex systems such as semilinear couplers [5] and cubic-quintic nonlinearity [6].

In this paper, we investigate the existence and stability of Bragg grating (BG) solitons in a semilinear dual-core system with dispersive reflectivity where one of the cores has Kerr nonlinearity and is equipped with a grating and the other core is linear. The objective of the present work is to study the effects of dispersive reflectivity, which accounts for nonuniformity in Bragg grating, on the solitons. Following the approach described in Refs. [7, 8], the model of Ref. [5] can be modified to include dispersive reflectivity as follows:

$$iu_t + iu_x + \left[|v|^2 + (1/2)|u|^2\right] u + v + \kappa\phi + mv_{xx} = 0 \quad (1)$$

$$iv_t - iv_x + \left[|u|^2 + (1/2)|v|^2\right] v + u + \kappa\psi + mu_{xx} = 0 \quad (2)$$

$$i\phi_t + ic\phi_x + \kappa u = 0 \quad (3)$$

$$i\psi_t - ic\psi_x + \kappa v = 0 \quad (4)$$

where u and v denote the forward and backward propagating waves in the nonlinear core and ϕ and ψ are their counterparts in the linear core, respectively. κ is the linear coupling between the two cores, m represents the strength of the dispersive reflectivity and c is the relative group velocity in the linear core (group velocity in the nonlinear core has been set to 1).

Using a relaxation algorithm, we have found quiescent solitons in the system. The stability of these solitons have been analyzed by means of a systematic numerical stability analysis. It is found that the stability of solitons is greatly affected by c. Another interesting result is that the presence of dispersive reflectivity tends to stabilize the solitons. However, the degree of stabilization is dependent upon the value of the coupling coefficient.

REFERENCES

1. De Sterke, C. M. and J. E. Sipe, *Prog. Opt.*, Vol. 33, 203, 1994.
2. Aceves, A. B. and S. Wabnitz, *Phys. Lett. A*, Vol. 141, 37, 1989.
3. Eggleton, B. J., C. M. de Sterke, and R. E. Slusher, *J. Opt. Soc. Am. B*, Vol. 14, 2980, 1997.
4. Taverner, D., N. G. R. Broderick, D. T. Richardson, R. I. Laming, and M. Ibsen, *Opt. Lett.*, Vol. 23, 328, 1998.
5. Atai, J. and B. A. Malomed, *Phys. Rev. E*, Vol. 62, 8713, 2000.
6. Atai, J. and B. A. Malomed, *Phys. Lett. A*, Vol. 284, 247, 2001.
7. Atai, J. and B. A. Malomed, *Phys. Lett. A*, Vol. 342, 404, 2005.
8. Neill, D. R., J. Atai, and B. A. Malomed, *J. Opt. A: Pure Appl. Opt.*, Vol. 10, 085105, 2008.

Few-cycle Optical Solitons

Y. Y. Lin, **M.-R. Chen**, **I-H. Chen**, **and R.-K. Lee**
Institute of Photonics Technologies, National Tsing-Hua University
Hsinchu City 300, Taiwan

Abstract— To understand few cycle optical pulse propagation in nonlinear media in term of an efficient envelope function description, new model such as generalized few cycle envelope approximation (GFEA) [1] was proposed to work with a satisfactory accuracy beyond the slowly varying envelope approximation (SVEA) and to prevent the excess computation complexity in finite-difference-time domain (FDTD) approach. In GFEA, the few-cycle expansion in polarization is parameterized by the ratio of phase velocity over group velocity of an optical pulse. Under the scope of GFEA, we investigate the formation of few-cycle optical soliton in a kerr nonlinear media, which nevertheless,has never been revealed. We find soliton solutions with chirp which is essentially governed by the first correction term similar to the self-steepening effect [2]. When propagating few-cycle GFEA soliton with full vectorial model through FDTD method, we observed negligible distortion in the envelope function in great contrast to the SVEA soliton. By the same technique, we reveal the existence of an optical self-induced-transparency soliton family in a two-level absorbing system down to the few-cycle limit. Based on the GFEA, we introduce a systematical method of reducing the Maxwell-Bloch equations beyond the SVEA and characterize the parameter space to achieve slow and fast lights. Verified by direct numerical simulations with full vectorial Maxwell-Bloch equations, we also give the relationships for a number of optical cycles on area theory and pulse group velocity, which demonstrate possible coherent photon-matter interactions.

REFERENCES

1. Kinsler, P. and G. H. C. New, "Few-cycle soliton propagation," *Phys. Rev. A*, Vol. 69, 013805, 2004.
2. Biswas, A. and B. Aceves, "Dynamics of solitons in optical fibers," *J. Mod. Opt.*, Vol. 48, No. 7, 11351150, 2001.

Influence of Six-wave Interactions and Saturated Nonlinearity on the Statistics of Waves in the Framework of One-dimensional Generalized NLS Equation

D. Agafontsev
P. P. Shirshov Institute of Oceanology, Russian Academy of Sciences, Moscow, Russia

Abstract— We study the influence of six-wave interactions on the statistics of waves in the framework of one-dimensional generalized Nonlinear Schrodinger equations that take into account (1) the collapsing six-wave interactions term, dumping terms (linear dissipation, two- and three-photon absorption) and a pumping term,

$$i\Psi_t + (1-ia)\Psi_{xx} + (1+ib)|\Psi|^2\Psi + (1+ic)\alpha|\Psi|^4\Psi = ip\Psi, \quad \alpha > 0, \quad a,b,c,p \ll 1. \qquad (1)$$

and (2) saturated nonlinearity, dumping and pumping terms,

$$i\Psi_t + (1-ia)\Psi_{xx} + \frac{|\Psi|^2}{1+q|\Psi|^2}\Psi + ib|\Psi|^2\Psi + ic|\Psi|^4\Psi = ip\Psi, \quad q > 0, \quad a,b,c,p,q \ll 1. \qquad (2)$$

Saturated nonlinearity in the form $(1-\exp(-q|\Psi|^2))\Psi$ is also considered. We solve Eqs. (1)–(2) numerically in the box with periodically boundary conditions starting from the initial data $\Psi|_{t=0} = 1 + \epsilon(x)$ or $\Psi|_{t=0} = \epsilon(x)$ where $\epsilon(x)$ is a stochastic noise. Coefficients before the additional terms to the classical NLS equation were chosen small in order to make the dynamics of Eqs. (1)–(2) close to that of the classical NLS equation.

We measure evolution of spectra $I_k = \langle|\Psi_k|^2\rangle$, spacial correlation functions and the PDFs for wave amplitudes, concentrating special attention on the formation of "fat tails" on the PDFs. In case of the classical NLS equation integrable turbulence appearing as a result of modulation instability of the stationary monochromatic wave leads to an almost Rayleigh PDF. Addition of the collapsing six-wave interactions in Eq. (1) leads to appearance of non-Rayleigh tails on the PDFs when high waves appear more frequently. The corresponding non-Rayleigh addition completely vanishes in the absence of the six-wave interactions and increase with six-wave constant α. In case of the saturated nonlinearity Eq. (2) non-Rayleigh tails appear in the region of medium amplitudes that corresponds to condensation process, while at high amplitudes PDFs vanish according to Rayleigh law.

Spatial Optical Solitons and Their Interaction in Nonlocal Media with Competing Nonlinearities

M. Shen[1], **H. Zhao**[1], **L. Chen**[1], **Y.-Y. Lin**[2], **C.-C. Jeng**[3], **R.-K. Lee**[2], **and W. Krolikowski**[4]

[1]Department of Physics, Shanghai University, Shanghai 200444, China
[2]Institute of Photonics Technologies, National Tsing-Hua University, Hsinchu 300, Taiwan
[3]Department of Physics, National Chung-Hsing University, Taichung 402, Taiwan
[4]Laser Physics Center, Research School of Physics and Engineering
Australian National University, Canberra ACT 0200, Australia

Abstract— We theoretically investigate spatial optical solitons and their interaction in nonlocal media with competing focusing and defocusing nonlinearities. In particular, we describe the properties of vortex solitons and dark solitons in such nonlocal competing media. We employ a variational approach to analytically describe their propagation properties and interactions. We also study the propagation and interaction of solitons using the split-step fourier transform. The numerical simulations fully confirm the analytical results.

Second Harmonic Generation Due to Magnetic Field of Intense Light Field

Shouvik Mukherjee[1], **Sourabh Mukhopadhyay**[2], **Biplab Kumar Datta**[3], **and Prasanta Kumar Datta**[1]

[1]Department of Physics and Meteorology, Indian Institute of Technology Kharagpur-721 302, India
[2]Govt. College, Jhargram, WB, India
[3]Technology Control Cell, Development Consultant Pvt. Ltd Park Centre, 24 Park St, Kolkata-700017, India

Abstract— Recent high intensity experiments [1, 2] on transparent dielectric liquids have reported magnetic continuum generation over a wide range of frequencies and magnetic scattering at fundamental frequency. Interactions of light with matter at relatively low intensities assume the response of matter to be dominated by the electric field of light. It seems to be a good approximation, at low intensities, to completely neglect the force exerted by the magnetic field of light, however, the same viewpoint might not be upheld when we probe matter with light of high intensity. Though the charges are influenced much strongly by electric field as compared to magnetic field, it has been realized [3] that even a weak magnetic response can get enhanced due to parametric resonance at virtually any detuning of the incident field. In light of this information, the magnetic forces on charges can no longer be neglected. Lights electric field accelerates the charges along the direction of polarization of light whereas the magnetic field rotates the accelerated charges about its axis. The superposition of these two effects forces the charges to take up a complicated trajectory. The trajectories traced by the charges have displacement components along incident wave propagation direction. So the charge response (in an isotropic medium) can no longer be approximated only by induced dipoles in transverse plane (plane containing $\vec{E}$ and $\vec{B}$). There will be induced dipoles in longitudinal plane (plane containing $\vec{B}$ and $\vec{k}$) as well. Solving Lorentz oscillator model without neglecting the magnetic component of force enables us to visualize the bound charge motion under the influence of incident field. Under suitable approximations, explicit analysis of this field induced motion helps us to identify some interesting consequences originating from charge motion dynamics. Since the incident electric field is strong and comparable to few orders of interatomic electric field, so the electrons undergo greater displacement from their equilibrium position. This introduces anharmonic oscillation because the potential is no more symmetric about equilibrium position in the limits of extended displacement of charge. Classical calculation suggests dependence of the electric polarization on $(\vec{E} \times \vec{B})$. Higher order dependences on $(\vec{E} \times \vec{B})$ arise due to the consideration of anharmonic potential. We discuss the modification in electric polarization response by considering the lowest order $(\vec{E} \times \vec{B})$ term (second order) which is not a manifestation of any nonlinear interaction with the potential. To account for the response of material to pseudo vector under spatial inversion operation we introduce electro-magnetic susceptibility η_{ij}. It is found that nonlinear polarization due to $(\vec{E} \times \vec{B})$ transforms the same way as any first order linear polarization component under spatial inversion operation. This leads to the realization that with a suitable choice of anisotropic response to $(\vec{E} \times \vec{B})$, it is possible to generate a transverse polarization wave propagating at second harmonic frequency. The governing equations for wave propagation in a medium are given by,

$$\vec{\nabla} \times (\vec{\nabla} \times \vec{E}) + \frac{1}{c^2} \left(\bar{\bar{I}} + \bar{\bar{\chi}}^{(1)} \right) \frac{\partial^2}{\partial t^2} \vec{E} \; = \; -\mu_0 \frac{\partial^2}{\partial t^2} \vec{P}^{NL} \tag{1}$$

$$\vec{\nabla} \times (\vec{\nabla} \times \vec{B}) + \frac{1}{c^2} \left(\bar{\bar{I}} + \bar{\bar{\chi}}^{(1)} \right) \frac{\partial^2}{\partial t^2} \vec{B} \; = \; \mu_0 \frac{\partial}{\partial t} (\vec{\nabla} \times \vec{P}^{NL}) \tag{2}$$

with

$$P_i^{NL} = \varepsilon_0 \eta_{i\alpha} \epsilon_{\alpha jk} E_j B_k \tag{3}$$

where, $\bar{\bar{I}}$ and $\bar{\bar{\chi}}^{(1)}$ represents 3×3 identity and first order susceptibility matrix respectively. $\eta_{i\alpha}$ and $\epsilon_{\alpha jk}$ represents electro-magnetic susceptibility and three dimensional Levi-Civita symbol respectively. Writing Equation (2) was not required for cases when nonlinear polarization was not affected by the magnetic field of EM wave. It is evident that in this case the nonlinear polarization depends on both electric and magnetic field of incident EM wave. The generation and propagation of second harmonic wave is then discussed.

REFERENCES

1. Oliveira, S. L. and S. C. Rand, *Phys. Rev. Lett.*, Vol. 98, 093901, 2007.
2. Rand, S. C., W. M. Fisher, and S. L. Oliveira, *J. Opt. Soc. Am. B*, Vol. 25, No. 7, July 2008.
3. Fisher, W. M. and S. C. Rand, *Phys. Rev. A*, Vol. 82, 013802, 2010.

Session 1A2
Extended/Unconventional Electromagnetic Theory, EHD(Electro-hydrodynamics)/EMHD(Electro-magneto-hydrodynamics), and Electro-biology 1

Dynamic Frequency Response of Charged Chiral Rods
Kyongok Kang, Jan K. G. Dhont, ... 22
Segmentation of OPG Images in Studying Jawbone Diseases
Jan Mikulka, ... 23
An Improved Segmentation of Brain Tumor, Edema and Necrosis
Jan Mikulka, Eva Gescheidtová, ... 24
Bone Marrow Analysis in Multi-contrast MR Images
Petr Marcon, Karel Bartušek, ... 25
Stochastic Models of Electrodynamics and Numerical Models
Robert Urban, Pavel Fiala, Michael Hanzelka, Jan Mikulka, ... 26
Stochastic Description of Wireless Channel for Cognitive Radio
Robert Urban, Pavel Fiala, Tomáš Kříž, Jan Mikulka, ... 27
Statistical Evaluation of Diffusion-weighted Imaging of the Human Tissues
Petr Marcon, Jan Mikulka, Eva Gescheidtová, Karel Bartušek, Andrea Sprlakova, ... 28
Software for Partial Discharge and Localization
Martin Cap, Petr Drexler, Pavel Fiala, Radek Myška, ... 29
Automatic Detection and Segmentation of the Tumor Tissue
Martin Cap, Eva Gescheidtová, Petr Marcon, Karel Bartušek, ... 30
Study of the Influence of Magnetic Fields on Plants Tissues
Eliska Hutová, Karel Bartušek, Jan Mikulka, ... 31
Combined X-ray Diagnostics of Heterogeneous Biological Material
Pavel Fiala, Petr Koňas, Martin Friedl, P. Šmíra, Premysl Dohnal, Michael Hanzelka, A. Nasswettrová, ... 32

Dynamic Frequency Response of Charged Chiral Rods

K. Kang and J. K. G. Dhont
Forschungszentrum Juelich, ICS-3 (Soft Condensed Matter), Juelich, Germany

Abstract— Various phases and dynamical states are induced by an external AC electric field in concentrated suspensions of charged, fibrous viruses (fd), which are model systems for very long and thin, stiff colloidal rods [1, 2]. The observed phases and dynamical states are the result of chiral rod-rod interactions between polarized electric double layers, polarized layers of condensed ions and electro-osmotic flow. We use various experimental methods, not only for the characterization of the field-induced phases/states, but also for the determination of the divergence of a length- and time-scale on approach of a non-equilibrium critical point [3–5]. Theory is developed for the frequency-dependent charge distribution and electrokinetic potential for both the diffusive double layer of very weakly charged rods, and condensed ions in case of highly charged rods [6, 7].

REFERENCES

1. Kang, K. and J. K. G. Dhont, "Double-layer polarization induced transitions in suspensions of colloidal rods," *EPL*, Vol. 84, 14005, 2008.
2. Kang, K. and J. K. G. Dhont, "Electric-field induced transitions in suspensions of charged colloidal rods," *Soft Matter*, Vol. 6, 273, 2010.
3. Kang, K. and J. K. G. Dhont, "Criticality in a non-equilibrium, driven system: Charged colloidal rods (fd-viruses) in electric fields," *EPJE*, Vol. 30, 333, 2009.
4. Kang, K., "Charged fibrous viruses (fd) in external electric fields: Dynamics and orientational order," *NJP*, Vol. 12, 063017, 2010.
5. Kang, K., "Diffusivity in an electric-fieldCinduced homeotropic phase of charged colloidal rods," *EPL*, Vol. 92, 18002, 2010.
6. Dhont, J. K. G. and K. Kang, "Electric-field-induced polarization and interactions of uncharged colloids in salt solutions," *EPJE*, Vol. 33, 51, 2010.
7. Dhont, J. K. G. and K. Kang, "Electric-field-induced polarization of the layer of condensed ions on cylindrical colloids," *EPJE*, Vol. 34, 40, 2011.

Segmentation of OPG Images in Studying Jawbone Diseases

J. Mikulka
Department of Theoretical and Experimental Electrical Engineering
Brno University of Technology, Kolejní 4, Brno 612 00, Czech Republic

Abstract— Image processing in biomedical applications is strongly developing issue. Many methods and approaches for image preprocessing, segmentation and visualization were described. This paper describes OPG image processing. The aim of processing is to segment regions of jawbone cysts and evaluate their local descriptors. It is necessary to choose suitable segmentation method because of adverse parameters of regions. The regions of the cysts are of low contrast and the pixel intensity distribution is not homogenous. The level set, the watershed and the live-wire segmentation method were chosen to testing. The results are compared. The second step of processing is to evaluate local descriptors of segmented regions which correspond to cysts. Several parameters were chosen to describe these regions — region area, mean gray value of intensities, modal gray value of intensities, standard deviation of intensities, minimal and maximal gray value of intensities, integrated intensity, median of intensities and shape descriptors of region (perimeter, circularity, aspect ratio, roundness and solidity). Values of these parameters will be used in following development of semiautomatic processing method with regard to current assessment of cysts by doctors. The algorithm for classification of the type of cyst is presented.

An Improved Segmentation of Brain Tumor, Edema and Necrosis

J. Mikulka and E. Gescheidtová
Department of Theoretical and Experimental Electrical Engineering
Brno University of Technology, Kolejni 4, Brno 612 00, Czech Republic

Abstract— Image processing in biomedical applications is strongly developing issue. Many methods and approaches for image preprocessing, segmentation and visualization were described. This paper deals with image segmentation, especially brain tumor segmentation. The main problem in medical practice is to recognize the type of brain or other tumor. Many methods for tumor classification were described. One of them is perfusion analysis. Perfusion images are of very low contrast and devaluated by noise. The main idea is to identify the level of perfusion of contrast agent transported into the tissue. The level of perfusion may decide on the type of tumor. The perfusion has to be monitored in tumor region, edema around the tumor region and in the interface between brain tumor and edema. The goal described in this paper is to propose a segmentation method to recognize brain tumor, edema and necrosis in structural magnetic resonance images (T1, T2) and create a binary mask that allows measurement in perfusion weighted images.

Bone Marrow Analysis in Multi-contrast MR Images

P. Marcon[1] and K. Bartusek[2]

[1]Department of Theoretical and Experimental Electrical Engineering
Brno University of Technology, Czech Republic
[2]Institute of Scientific Instruments of the ASCR
v.v.i, Kralovopolska 147, Brno 61264, Czech Republic

Abstract— In the article a magnetic resonance multi-contrast data collection and analysis are described. The research of pathology of bone marrow is very interesting at present. MRI measurement is very interesting method of bone marrow imaging because this technique provides images with excellent soft tissue contrast. In adults the bone marrow is in general composed of fatty tissue, which appears hyperintense on T_1 and T_2 weighted images and occurs hypointense on MR-sequences with fat-saturation. In case of trauma, tumor or infection infiltration, replacement and depletion of fatty bone marrow takes place resulting in intermediate to hypointense signals on T_1-weighted images and T_2 weighted images with fat-saturation. These changes obscure the distinct appearance of fatty bone marrow and serve as early indicators of pathology, which makes this imaging technique a very sensitive diagnostic tool.

MRI imaging of small bones is problematic, because the measured are loaded with susceptibility artifacts and low signal to noise ratio. Therefore, we focus on the comparison between commonly used MRI contrast (Proton Density-PD, relaxation time T_1, relaxation time T_2, Diffusion Weighted Imaging — DWI and Susceptibility Weighted Imaging — SWI) and multi-contrast weighted imaging (T_1/T_2, DWI/SWI, DWI/T_1, SWI/T_1, DWI/PD, SWI/PD). Acquired images are classified in terms of signal to noise ratio, intensity difference and steepness of edges.

In this paper we focus on the calculation SWI images. These images allow us to see better difference in the intensity of the magnetic field, particularly where one tissue turns into other tissue. For the images calculation we used two methods. The first one is based on classical measurement gradient echo sequence and the second one is based on measuring of asymmetrical spin echo.

The experiment was accomplished on a MR tomograph at the Institute of Scientific Instruments, Academy of Sciences of the Czech Republic (ISI ASCR). The MR tomograph dispose of static field flux density $B_0 = 4.7\,\mathrm{T}$, $1\,\mathrm{H}$ nuclei resonance frequency is $200\,\mathrm{MHz}$. Method of measurement and processing was tested on the chicken wing, especially bone: ulna and radius.

The results in the paper will be very important for next study of the bone marrow pathologies.

Stochastic Models of Electrodynamics and Numerical Models

R. Urban, P. Fiala, M. Hanzelka, and J. Mikulka
Department of Theoretical and Experimental Electrical Engineering
Brno University of Technology, Czech Republic

Abstract— The article presents the transient task numerical modelling of the electrodynamic process in gas with a pulsed electric field. Within the numerical model, non-linear electric properties of gas are respected and, by the help of a non-deterministic stochastic model, the possibility of an electric charge generation is analyzed. The authors examine the problem of electric charge probability evaluation; on the basis of testing the tip-tip disposition, a comparison of individual instances of the probability function evaluation is provided.

ACKNOWLEDGMENT

This work was supported by the project CZ.1.07/2.3.00/30.0005 of Brno University of Technology.

REFERENCES

1. Fiala, P. and M. Friedl, "Stochastic models of electrodynamics," *PIERS Proceedings*, 91–94, Suzhou, China, Sep. 12–16, 2011.
2. Drexler, P. and P. Fiala, "Methods for high-power EM pulse measurement," *IEEE Sensors Journal*, Vol. 7, No. 7–8, 1006–1011, Jul.-Aug. 2007.
3. Stratton, J. A., *Teorie Elektromagnetického Pole*, STNL, Praha, 1961.
4. Polivka, J., P. Fiala, and J. Machac, "Microwave noise field behaves like white light," *Progress In Electromagnetics Research*, Vol. 111, 311–330, 2011.

Stochastic Description of Wireless Channel for Cognitive Radio

R. Urban, **P. Fiala**, **T. Kriz**, **and J. Mikulka**
Department of Theoretical and Experimental Electrical Engineering
Brno University of Technology, Kolejni 2906/4, Brno 612 00, Czech Republic

Abstract— Wireless propagation channel is normally described by attenuation for significant frequency [1], which is not appropriate parameter for modern communication systems using micro cells. It is more required to have information about utilization of the particular channels, because there is enough power in link budget for wireless transmission. This paper introduces innovative channel stochastic description mainly for cognitive radio application [2]. Cognitive radio is represented by the awareness features of cognitive nodes. Cognitive nodes sense other users of the shared frequency spectrum, which are called primary users. Based on the localization of the primary users in the frequency spectrum, cognitive note minimize interference between primary and cognitive users using dynamic spectrum technique. For correct working of the cognitive engine it is necessary to have correct and precise information about spectrum situation and also spectrum prediction. This information should be obtained from frequency sensing mechanism. Generally, it is not possible to perform sensitive wideband and real-time spectrum sensing. From this reason it is possible to create suitable model of spectrum occupancy for cognitive system. It seems that the statistical models provide satisfactory results. Based on stochastic method it is possible to prepare models for these cognitive radio systems. According to the typical utilization of the wireless channel it is possible to classify typical radio transmission according to several criteria and improve methods of the primary user detection [3]. The prepared algorithms are also tested within real spectrum data which were obtained during spectrum survey measurement campaign. Finally, the spectrum model for several environments is prepared for purpose of the cognitive radio.

REFERENCES

1. Fontan, F. P. and P. M. Espineira, *Modeling the WirelessPropagation Channel: A Simulation Approach with MATLAB*, Wiley-Interscience, 2008.
2. Mitola, J., *Cognitive Radio Architecture: The Engineering Foundations of Radio XML*, Wiley-Interscience, Hoboken, N.J., 2006.
3. Wang, X., A. Wong, and P.-H. Ho, "Stochastic channel prioritization for spectrum sensing in cooperative cognitive radio, *6th IEEE Consumer Communications and Networking Conference, 2009, CCNC 2009*, 1–6, 2009.

Statistical Evaluation of Diffusion-weighted Imaging of the Human Tissues

P. Marcon[1], **J. Mikulka**[1], **E. Gescheidtova**[1], **K. Bartusek**[2], **and A. Sprlakova**[3]

[1]Department of Theoretical and Experimental Electrical Engineering
Brno University of Technology, Kolejni 4, Brno 612 00, Czech Republic
[2]Institute of Scientific Instruments of the ASCR, v.v.i
Královopolská 147, Brno 612 64, Czech Republic
[3]Radiological Clinic, The University Hospital Brno
Jihlavská 20, Brno 625 00, Czech Republic

Abstract— The research of pathology of human tissues is currently very interesting. Development of the magnetic resonance imaging represent very significant step because this technique provides images with excellent soft tissues contrast. We used two methods for measurement T_1 weighted images and T_2 weighted images. The first one variable is the spin-lattice relaxation T_1 is the mechanism by which the z component of the magnetization vector comes into thermodynamic equilibrium with its surroundings. The second one variable is the spin-spin relaxation T_2 is the mechanism by which the transverse component of the magnetization vector exponentially decays towards its equilibrium value of zero. In our experiment we used a MR tomograph at the University Hospital Bohunice. The MR tomograph dispose of static field flux density $B_0 = 1.5\,\mathrm{T}$. Method of measurement and processing was tested on the healthy volunteers.

We defined the area of individual tissues in the measured images. We are interested in these tissues: gray matter, white matter, muscle, bone marrow and bone. The statistic analysis was made in these selected areas of the tissues. The value of maximum, minimum, means, standard deviation and also higher statistic orders such as skewness and kurtosis was obtained. With the knowledge of the individual tissues statistical quantities, the particular tissues can be automatically searched by using a special proposed algorithm.

The results in the paper will be very important for next study for the comparison between healthy and pathology tissues.

Software for Partial Discharge and Localization

M. Cap, P. Drexler, P. Fiala, and R. Myska
Department of Theoretical and Experimental Electrical Engineering
Brno University of Technology, Kolejni 2906/4, Brno 612 00, Czech Republic

Abstract— This article deals with possibilities of localization of the partial discharges (PD) in oil power transformers. Localization can be performed on the basis of measured UHF waveforms analysis during activity of the partial discharges. The time-shifts of the waveforms related to transient process occurrence in the signals are the main input parameters for localization methods. In order to estimate the position of the signal source in the 3D space a minimum of four antennas has to be used, since the time of the PD is unknown. Designed application uses a numerical method for detection of the discharge spatial location. Diagnosis of the partial discharge is split into four Gross. At first, time graphs of detected signal are displayed for its visual verification. Each group of displayed signals include time stamp of the actual trigger. This time stamp is used as a information for visualization of the position of the signal group in time range of the power voltage period. Third part is focused on the spatial detection of measured discharges in volume of the transformer. At least, statistical results are shown.

ACKNOWLEDGMENT

The research described in the paper was financially supported by project of the BUT Grant Agency FEKT-S-10-13, by research plan No. MSM 0021630513 ELCOM and the grant of Czech ministry of industry and trade No. FR-TI1/001.

REFERENCES

1. Tang, J. and Y. Xie, "Partial discharge location based on time difference of energy accumulation curve of multiple signals," *IET Electric Power Applications*, Vol. 5, No. 1, 175–180, 2011, ISSN: 1751-8660.
2. Markalous, S. M., S. Tenbohlen, and K. Feser, "Detection and location of partial discharges in power transformers using acoustic and electromagnetic signals," *IEEE Transactions on Dielectrics and Electrical Insulation*, Vol. 15, No. 6, 1576–1583, 2008, ISSN: 1070-9878.

Automatic Detection and Segmentation of the Tumor Tissue

M. Cap[1], **E. Gescheidtova**[1], **P. Marcon**[1], **and K. Bartusek**[2]

[1]Department of Theoretical and Experimental Electrical Engineering
Brno University of Technology, Kolejni 2906/4, Brno 612 00, Czech Republic
[2]Institute of Scientific Instruments, Academy of Sciences of the Czech Republic
Kralovopolska 147, Brno 612 64, Czech Republic

Abstract— MRI is a constantly developing region of medicine, which is suitable for the study of soft tissues. The current methodologies for obtaining images weighted by relaxation times give only an idea of the distribution of soft tissues. Differential diagnosis of a high-grade glioms and solitary metastases is in some cases inconclusive. Investigators in several studies have demonstrated that in perfusion MRI (magnetic resonance imaging) of high-grade glioms and solitary metastases are differences. Analysis of the peritumoral region could be more useful than the analysis of the tumor itself. Precise evaluation of mentioned differences in peritumoral region gives a hopeful chance for tumor diagnosis.

This article describes automated detection and segmentation of the tumor and tumor edema. Automated detection of the tumor tissue area is based on the human brain symmetry. Healthy brain has a strong sagittal symmetry. Assuming the tumor is not placed symmetrically in both hemispheres, it is possible to apply this method for its detection. Tumor area is evaluated from image which is obtained by summing partial results from all T2 weighted images. Segmentation and precise detection of the tumor in the area marked during the previous step is based on Chan-Vese algorithm. Segmentation is provided in T1 and T2 weighted images in order to achieve highest precision on the tumor border. Resulting masks are applied to the various perfusion maps.

Study of the Influence of Magnetic Fields on Plants Tissues

E. Hutova[1], **K. Bartusek**[2], **and J. Mikulka**[1]

[1]Department of Theoretical and Experimental Electrical Engineering
Brno University of Technology, Kolejni 2906/4, Brno 612 00, Czech Republic
[2]Institute of Scientific Instruments, Academy of Sciences of the Czech Republic
Kralovopolska 147, Brno 612 64, Czech Republic

Abstract— When the magnetic field may influence behavior and movement of electrically charged particle, can this field also affect cells in the living organisms. The aim of the study was to determine a dependence of the growth of the plant cultures in a stationary homogenous and gradient magnetic field. It was created nine magnetic fields of various sizes of magnetic inductions and defined configurations. The magnetic fields were created by ferrite magnets and neodymium magnets. The map of magnetic fields was simulated by the methods the finite element in the ANSYS and experimentally measured with a Hall probe. The plant cultures in this experiment were represented an early somatic embryos (ESEs) of *Picea abies* (/L./Karsten, clone 2.2/2) and *Pinus Engelman*. These plant cultures were derived at the Institute of Plant Biology at Mendel University in Brno. The clusters of early somatic embryos were placed to the Petri dishes when each dish contained one cluster of ESEs. The Petri dishes were placed to the magnetic fields and concurrently five dishes were used as a control group and were placed in the earth's magnetic field. Very important for the experiment were the ambient conditions. It has been demonstrated that the ambient conditions especially outdoor temperature and humidity has great influence on the growth of ESEs.

The speed of growth was evaluated from 2D images of clusters in Petri dishes and it was calculated the size of the area. For a better characterization of the quality of ESEs were taken a measurements more cuts of ESEs by magnetic-resonance displaying techniques with a few types of contrasts. As the contrast were used a spin density (SD), the relaxation times T_1, T_2 and the magnetic field B_0. This field characterizes the magnetic susceptibility of plants cultures. The multi-contrast analysis of 2D images shows the possibility of capture better distinction of the clusters and characterization of the plan cultures growth.

Combined X-ray Diagnostics of Heterogeneous Biological Material

P. Fiala[1], **P. Koňas**[1], **M. Friedl**[1], **P. Šmíra**[2], **P. Dohnal**[1], **M. Hanzelka**[1], **and A. Nasswettrová**[2]

[1]Department of Theoretical and Experimental Electrical Engineering
Brno University of Technology, Kolejni 2906/4, Brno 612 00, Czech Republic
[2]Thermo Sanace s.r.o., Chamrádova 475/23, Ostrava-Kunčičky 718 00, Czech Republic

Abstract— The problem of finding a suitable diagnostic procedure for the examination of structural elements has been closely analyzed in recent years. In this connection, the main material of interest is wood as a sort of heterogeneous matter, and the diagnostic procedure is directed towards enabling industrial application in the future. A new diagnostic method based on combine acoustic and X-ray imaging has been proposed and tested. The X-ray technique utilizes the reduction of imaging information into 2D planar projection. It allows us to image clearly the rate of material damage through displaying the weighted damage rate.

ACKNOWLEDGMENT

The research described in the paper was financially supported by a grant of the BUT Foundation Agency FEKT-S-11-5, and the Thermosanace Company Czech Republic. This paper also benefited from the use of the Insight Segmentation and Registration Toolkit (ITK), an open source software developed as an initiative of the U.S. National Library of Medicine.

REFERENCES

1. Prosser, V., *Experimentální Metody Biofyziky*, Academia Praha, 1989.
2. O'Halloran, M., M. Glavin, and E. Jones, "Channel-ranked beamformer for the early detection of breast cancer," *Progress In Electromagnetics Research*, Vol. 103, 153–168, 2010.
3. Yoo, T. S., *Insight into Images — Principles and Practice for Segmentation, Registration, and Image Analysis*, 393, A K Peters, Ltd., Wellesey, 2004.
4. Liao, P. S., T. S. Chen, and P. C. Chung, "A fast algorithm for multilevel thresholding," *Journal of Information Science and Engineering*, Vol. 17, No. 5, 713–728, Institute of Information Science Academia Sinica, 2001.
5. Ibáñez, L., W. Schroeder, L. Ng, and J. Cates, *The ITK Software Guide*, 2nd Edition, Updated for ITK Version 2.4, 804, Kitware, Inc., 2005, ISBN 1-930934-15-7.
6. Polivka, J., P. Fiala, and J. Machac, "Microwave noise field behaves like white light," *Progress In Electromagnetics Research*, Vol. 111, 311–330, 2011.
7. Bartusek, K., R. Kubasek, and P. Fiala, "Determination of pre-emphasis constants for eddy current reduction," *Measurement Science & Technology*, Vol. 21, No. 10, 105601, Oct. 2010.
8. Bartusek, K., P. Fiala, and J. Mikulka, "Numerical modeling of magnetic field deformation as related to susceptibility measured with an MR system," *Radioengineering*, Vol. 17, No. 4, 113–118, Dec. 2008.

Session 1A3a
Wireless Network and Applications

Miniature Planar Triple Passband Filter Using Embedded Resonators
Soon Pheng Lim, K. M. Lum, ... 34
Design of Planar Single-section and Cascaded Directional Filters
Yong Huat Choo, K. M. Lum, ... 35
Wideband Planar Filter Using Signal-interference Techniques
Weiwen Hong, K. M. Lum, ... 36
Planar Bandpass Filter Design Using Transversal Filtering
Kien Keng Oh, K. M. Lum, ... 37
Performance of MIMO RADAR Using Two-way MUSIC
Pasan De Silva, Chee Kiat Seow, ... 38
Study of Channel Measurement Parameter Estimation for Precise Mobile Localization Applications
Chee Kiat Seow, Soon Yim Tan, Kai Wen, ... 39

Miniature Planar Triple Passband Filter Using Embedded Resonators

S. P. Lim and K. M. Lum
School of Science and Technology, SIM University, Singapore

Abstract— A triple passband filter has been proposed using embedded resonators. The proposed filter consists of a main dual feeding structure that embeds four resonators. The topology of the four embedded stepped impedance resonators are designed to control and adjust the return loss and insertion loss of the three passband response characteristics. Two transmission zeros are realized for each passband and the selectivity of the filter is significantly improved. The proposed filter is prototyped using material FR4 substrate with dielectric constant of 4.06, thickness of 1.6 mm and loss tangent of 0.014, conductor thickness of 35 µm. The fabricated structure has a miniature dimensional about the size of 15 mm by 22 mm. The three passbands are observed at center frequency 1.8 GHz, 3.3 GHz and 5.2 GHz respectively with S_{11} value less than −10 dB. The corresponding passband insertion loss S_{21} is approximately −1 dB to −5 dB. Attenuation is greater than 20 dB for lower and upper stopband. Measurement and simulation results are discussed and presented.

Design of Planar Single-section and Cascaded Directional Filters

Y. H. Choo and K. M. Lum
School of Science and Technology, SIM University, Singapore

Abstract— In the proposed paper, a single-section and cascaded microstrip directional filters is designed for modern communication systems, such as mobile telephony, radiolocation and satellite links. The proposed filter takes on the structure of a Quadrature Hybrid coupler, where a parallel branch is capacitively coupled by two coupling resonators. It also has four ports which are completely match and exhibits a directional and filter-like frequency characteristics. This four-port device has a bandpass response between ports 1 and 4 (S_{41}), and its complementary reject-band response between ports 1 and 2 (S_{21}). No power is transmitted to port 3 (isolation), and none is reflected to port 1. By compensating the line length between the coupling resonators of the single-section directional filter, better performance can be achieved, notably in matching. Furthermore, cascading multiple single-section directional filters will lead to the generation of transmission zeros in the stopband and therefore will sharper the cut-off response characteristics. To validate the proposed directional filter configuration, related analysis, and design theory, a single-section and cascaded microstrip directional filters are designed and fabricated using FR-4 substrate with dielectric constant of 4.05, loss tangent of 0.014 and thickness of 1.6 mm. The overall dimension of the single-section and cascaded directional filter are 74.4 mm by 45 mm, and 122.2 mm by 50 mm respectively. For the single-section directional filter, the best matched measured return loss S_{11} is less than -20 dB around center frequency of 2.35 GHz. Good isolation S_{31} is obtained at values less than -25 dB. The filter response shows a bandstop characteristic with band elimination, S_{21} of -14.03 dB and a bandpass characteristic with coupling S_{41} of -3.64 dB. For the cascaded directional filter, the best matched measured return loss S_{11} is less than -25 dB. The measured S_{21} and S_{41}, are -20.43 dB and -2.74 dB respectively. Power at port 3 is well isolated with S_{31} values of less than -25 dB. The measured filter response showed good agreement with the simulation results. Both simulation and measurement data are presented and discussed.

Wideband Planar Filter Using Signal-interference Techniques

W. W. Hong and K. M. Lum
School of Science and Technology, SIM University, Singapore

Abstract— This paper presents a new wideband planar filter using signal-interference technique. The passband has a center frequency 1.5 GHz. The proposed filter topology has a 50 Ω input and output port respectively. The core design topology consists of a transversal signal-interference filtering section that embeds a miniature transversal filter. Thus, under signal-interaction principles, the filtering action comes about through the generation of multiple out-of-band power transmission zeros and constructive passband signal combinations. The proposed filter is prototyped using FR4 substrate with a dielectric constant of 4.4, thickness of 1.6 mm, loss tangent of 0.022 and conductor thickness of 35 µm. The fabricated structure has a dimensional size of 90 mm by 100 mm. The best matched measured return loss S_{11} is observed at 1.27 GHz with a value less than −42 dB. The corresponding passband insertion loss S_{21} is approximately −0.5 dB with a −10 dB bandwidth of 1.2 GHz. The lower and upper stopband attenuation is greater than 40 dB respectively. Both simulation and measurement result are presented and discussed.

Planar Bandpass Filter Design Using Transversal Filtering

K. K. Oh and K. M. Lum
School of Science and Technology, SIM University, Singapore

Abstract— A new microwave single-passband planar filter using transversal filtering is presented. The proposed filter consists of transversal filtering sections. Three identical transversal sections are cascaded between the 50 Ω input and output terminations and two addition stubs are implemented at the input and output transmission line. These stubs vividly reduce the insertion losses. The center frequency of the proposed bandpass filter is 2.6 GHz. It is prototyped on FR4 substrate with dielectric constant 4.05, loss tangent 0.014 and thickness 1600 µm. The overall dimensional size is 72 mm by 46 mm. Best measured matching return loss S_{11} is observed at 2.6 GHz with a value less than −15 dB. The passband insertion loss S_{21} is approximately −2.5 dB. Attenuation for the lower stopband and upper stopband is greater than 40 dB respectively. Both simulation and measurement results are presented and discussed.

Performance of MIMO RADAR Using Two-way MUSIC

Pasan De Silva[1, 2] **and Chee Kiat Seow**[1, 2]

[1]School of Science and Technology, SIM University, Singapore
[2]Nanyang Technological University, Singapore

Abstract— Multiple Input Multiple Output (MIMO) concept have been a prevalent technology in the wireless communication system (IEEE 802.11n and 4G), as it helps to increase transmit power and data throughput by array gain and diversity gain, while reducing multipath fading. In recent years, the concept of MIMO technology has been exploited for outdoor RADAR system for direction finding of targets besides using the conventional monostatic and bi-static radar system. Direction finding subspace algorithms such as MUSIC, ESPRIT have been often used to estimate the angle of arrival (AOA) of signal path that has been transmitted from the single element transmitter impinging on the antenna array at the receiver end and in turn deduce the direction of the target in the space.

In this paper, we explore using the MUSIC algorithm for direction finding of the target in the space for RADAR system equipped with antenna array at both transmitter and receiver. This algorithm is known as two way MUSIC for MIMO RADAR system. We will assess the performance of the two way MUSIC algorithm for MIMO RADAR such as the advantages and limitations in terms of maximum no of target elements that can be detected for given no of transmitters and receivers. We will also explore the minimum angle of resolution for different SNR values.

Study of Channel Measurement Parameter Estimation for Precise Mobile Localization Applications

Chee Kiat Seow, Soon Yim Tan, and Kai Wen
Nanyang Technological University, Singapore

Abstract— Recent year has seen the need for precise localization for both commercial and government applications. The underlying first building block that affects the performance of the localization algorithm is the performance of the estimation of position related parameters such as Time of Arrival (TOA) and Angle of Arrival (AOA). These parametric estimation methodologies are generally classified as deterministic or subspace methods. The accuracy and resolution of these parametric estimation algorithms are also usually a function of the channel parameters such as coherence bandwidth, which can either manifest as flat fading or frequency selective fading. In this paper, we will investigate the effect of channel parameters such as bandwidth on the performance of the parametric estimation algorithms in different Non-line-of-Sight (NLOS) multipath environment coupled with experimental channel measurement campaign. The purposes are two fold. In existing NLOS localization schemes, only the dominant NLOS paths are necessary to deduce the position related parameters and hence the estimated position of Mobile Device (MD). As such, we will investigate the accuracy of detecting the dominant multipaths position related parameters. Secondly, the finding of required signal bandwidth needed for precise localization is another motivator for the study especially with the advent of 802.11n implementation.

Session 1A3b
MIMO Systems

On Multi-antenna Systems for Wireless Transmission Mediums
Mario Marques da Silva, Rui Dinis, Américo Correia, ... 42
On the Multihop Relays with Multiple Antennas for LTE-A
Carlos Reis, Américo Correia, Nuno Souto, Mario Marques da Silva, ... 44
Channel Capacity Improvement Dependency of the Number of Receiving Antennas for Aeronautical MIMO Systems
Naoki Kanada, Yasuto Sumiya, Naruto Yonemoto, Shunichi Futatsumori, Akiko Kohmura, Eiju Isozaki, ... 46
MIMO SC-FDE Transmission Techniques with Channel Estimation and High-order Modulations
João Carlos Silva, Rui Dinis, Nuno Souto, Mario Marques da Silva, ... 47
Single-stream Communication Using Orthogonal Signal Division Multiplexing with Multiple Antennas
Tadashi Ebihara, ... 49

On Multi-antenna Systems for Wireless Transmission Mediums

Mário Marques da Silva[1, 2], **Rui Dinis**[1, 3], **and Américo Correia**[1, 4]

[1]Instituto de Telecomunicações, Portugal
[2]Universidade Autónoma de Lisboa, Portugal
[3]DEE-FCT-UNL, Portugal
[4]ISCTE-IUL, Portugal

Abstract— The current work performs a comparison between different multi-antenna techniques that can be employed to achieve the requirements of the Fourth Generation Cellular (4G) Systems. The comparison is performed in different multi-user, throughputs and propagation environments, at the link and system level using the capacity and BER as performances indexes.

Multi-antenna systems are used in order to push the performance or capacity/throughput limits as high as possible without an increase of the spectrum bandwidth, although at the cost of an obvious increase of complexity. The antenna spacing must be larger than the coherence distance to ensure independent fading across different antennas elements [1, 2]. Alternatively, different antennas should use orthogonal polarizations to ensure independent fading across different antennas.

The various multi-antenna configurations are referred to as Single Input Single Output (SISO), Multiple Input Single Output (MISO), Single Input Multiple Output (SIMO) or Multiple Input Multiple Output (MIMO). The SIMO and MISO architectures are forms of receive and transmit diversity schemes, respectively. MIMO architectures can be used for combined transmit and receive diversity, for the parallel transmission of data or for spatial multiplexing. When used for spatial multiplexing, MIMO technology promises high bit rates in a narrow bandwidth. In this case, MIMO system considers the transmission of different signals from each transmit antenna element so that the receiving antenna array receives a superposition of all transmitted signals.

The multiple-antenna techniques may present the following configurations: Space-time block coding (STBC); multi-layer Transmission; Space Division Multiple Access (SDMA); beamforming.

Although STBC is essentially a MISO system, the use of receive diversity makes it a MIMO, which corresponds to the most common configuration for this type of diversity. STBC based schemes focus on achieving a performance improvement through the exploitation of additional diversity, while keeping the symbol rate unchanged [2, 3].

On the other hand, multi-layer Transmission and SDMA belong to another group, entitled spatial multiplexing (SM), whose principles are similar but whose purposes are quite different. The goal of the MIMO based on multi-layer transmission scheme is to achieve higher data rates in a given bandwidth, whose increase rate corresponds to the number of transmit antennas [1]. The increase of symbol rate is achieved by "steering" the receive antennas to each one of the transmit antennas, in order to receive the corresponding data stream [4, 5]. This is achieved through the use of the nulling algorithm. Finally, the beamforming is an effective solution to maximize the Signal to Noise Ration (SNR), as it steers the transmit (or receive) beam towards the receiver (or transmitter) [6]. As a result, an improved performance or coverage can be achieved with beamforming.

Multi-user MIMO: The approach behind Multi-User-MIMO (MU-MIMO) is similar to SDMA. Nevertheless, while SDMA is typically employed in the uplink, the MU-MIMO can also be implemented in the downlink. This allows sending different data streams into different User Equipments (UE). In this case, instead of performing the nulling algorithm at the receiver side, the nulling algorithm is performed using a pre-coding approach at the transmitter side (Base Station [BS]). This is possible because the BS can accommodate a high number of transmit antennas. In the downlink of a MU-MIMO configuration, the number of transmit antennas must be higher than the number of multiple data streams that is sent to multiple users, at the same time and occupying the same frequency bands (the opposite of the SDMA approach). In this configuration, the nulling algorithm is implemented at the transmitter side using a pre-processing algorithm such as Zero Forcing, Minimum Mean Square Error, dirty paper coding, etc. [4]. Alternatively, instead of implementing the above described spatial multiplexing principle, the MU-MIMO can be performed using the beamforming algorithm. In any case, MU-MIMO requires accurate downlink Channel State Information (CSI) at the transmitter side. Obtaining CSI is trivial using Time Division Duplexing (TDD) mode, being more difficult to be achieved when Frequency Division Duplexing (FDD) is employed. In FDD mode, CSI is normally obtained using a feedback link in the opposite direction.

It is worth noting that users located at the cell edge, served by MU-MIMO, may experience a SNR degradation due to inter-cell interference, inter-user interference, additional path loss or due to limited BS transmit power (which results from the use of a pre-coding). A mechanism that can be implemented to mitigate such limitation is to employ a dynamic MIMO system, where MU-MIMO is employed everywhere, except at the cell edge. In this location, the BS switches into SU-MIMO, which translates in an improvement of performance [4]. Alternatively, base station cooperation is known as an effective mechanism which improves the performance at the cell edge, resulting in an more homogenous service quality, regardless the users' positions.

REFERENCES

1. Foschini, G. J., "Layered space-time architecture for wireless communication in a fading environment when using multiple antennas," *Bell Laboratories Technical Journal*, Vol. 1, No. 2, 41–59, Autumn, 1996.
2. Alamouti, S. M., "A simple transmitter diversity scheme for wireless communications," *IEEE JSAC*, 1451–1458, Oct. 1998.
3. Tarokh, V., et al., "Space-time block codes from orthogonal designs," *IEEE Trans. Inform. Theory*, 1456–1467, Jul. 1999.
4. Marques da Silva, M., et al., *Transmission Techniques for Emergent Multicast and Broadcast Systems*, 1st Edition, CRC Press, Boca Raton, USA, May 2010, ISBN: 9781439815939.
5. Marques da Silva, M., R. Dinis, and A. Correia, "A new V-BLAST detector approach for W-CDMA signals with frequency selective fading," *PIMRC 2005*, Berlin, Germany, Sep. 2005.
6. Marques da Silva, M., *Multimedia Communications and Networking*, 1st Edition, CRC Press, New York, USA, Mar. 2012, ISBN: 9781439874844.

On the Multihop Relays with Multiple Antennas for LTE-A

Carlos Reis[1,2], **Américo Correia**[1,2], **Nuno Souto**[1,2], **and Mário Marques da Silva**[1,3]

[1]Instituto de Telecomunicações, Portugal
[2]ISCTE-IUL, Portugal
[3]Universidade Autónoma de Lisboa, Portugal

Abstract— In this paper, we analyze cooperative communications for broadcast/multicast wireless communication systems based on the LTE-Advanced (LTE-A) standard. Multihop relays utilizing the same frequency bands as the base station are considered. These relays are equipped with multiples antennas (MIMO), at least the double of those employed at the base station side. The simulation results show that multihop relays achieve an improvement of power efficiency, while keeping the average coverage and the overall network throughput unchanged. This can be viewed as an energy-efficient wireless transmission technique, which contributes to the implementation of the green cell networks concept, as it allows a reduction in the carbon emission footprint.

Relay Nodes (RN) were introduced in 3GPP Release 9 as a special type of eNodeB that is not directly connected to the core network. A RN receives data which was forwarded by an eNodeB that is connected to the Evolved Packet Core (EPC). Upon receiving such data, the RN sends it to the User Equipments (UE) that are under its area of coverage. This is a very interesting option for operators, as usually RN present structures less expensive to deploy and to maintain, as compared to eNB.

In [1, 2] four relay architectures are proposed and studied. Those architectures differ from each other in terms of expected behaviour of the RN/DeNB and how the data is sent within the EPC until it reaches the UE. That study concludes that an architecture where RN acts as a proxy for S1/X2 has the most overall benefits, having been incorporated in 3GPP Release 10 (LTE-Advanced). Type 1 half-duplex in-band relay does not transmit any signal to UE when it is supposed to receive data from the DeNB. The relay then configures these sub-frames as Multicast/Broadcast Single Frequency Network (MBSFN) sub-frames when UEs are not supposed to expect any downlink transmission.

In this paper, we consider Type 1 RN with advanced Multiple Input Multiple Output (MIMO) schemes with support of 4 antennas for enhancement to relay backhaul. The objective is to achieve the DeNB throughput in spite of its in-band half duplex mode.

We first analyse Base Station cooperation with MIMO and next we replace some BSs by Fixed Relays assuring that the overall throughput of the network is kept the same, but with an improved power efficiency. The 3GPP Release 10 (LTE-Advanced) parameters will be taken as reference in our system level simulations.

Based on the comparison between the reference SNR at a Block Error Rate (BLER) of 1%, and the evaluated SNR, it is decided whether the block is or not correctly received. This is achieved for all the transmitted blocks, for all users, in all 57 sectors of the 19 cells, during 500 seconds.

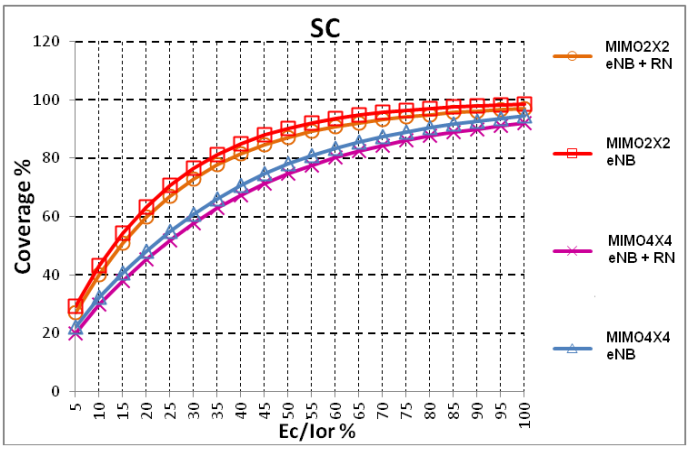

Figure 1: Coverage of SC scenario with and without relays.

Figure 1 presents the coverage as a function of the percentage of transmitted power from the base station (E_C/I_{0r}), for MIMO 2×2 and 4×4, coding rate 1/2 and SC scenario. This corresponds to a scenario where there is interference with different patterns due to different frequency reuse factors. We have chosen the frequency reuse of 1/3 in all simulations. All interfering sites transmit with the maximum power of 90%. The cell radius R is 2250 meters (inter-site-distance 3900 m), and for the reuse factor chosen the reference coverage of 95% is achieved by all the schemes. However, it should be noticed that coverage values of MIMO 4×4 are lower than those of MIMO 2×2 due to higher levels of spatial interference.

We have analyzed cooperative communications with fixed multihop relays, working in half-duplex mode and equipped with multiple antennas MIMO. A cellular network was considered, where some of the BSs have been replaced by fixed relay stations with much less transmitted power, while keeping the same global area. We have confirmed that, by using multihop relays, it is possible to keep the average coverage and the overall network throughput, while achieving an improvement of power efficiency. This can be viewed as an energy-efficient wireless transmission technique, which contributes to the implementation of the green cell networks concept, as it allow a reduction in the carbon emission footprint.

REFERENCES

1. 3GPP, "General aspects and principles for interfaces supporting multimedia broadcast multicast service (MBMS) within E-UTRAN," TS 36.440 v9.1.0, March 2010.
2. 3GPP, "Evolved universal terrestrial radio access (E-UTRA) and evolved universal terrestrial radio access network (E-UTRAN); Overall description," TS 36.300, 2008.
3. Tao, X., X. Xu, and Q. Cui, "An overview of cooperative communications," *IEEE Communications*, Vol. 50, No. 6, 65–71, June 2012.
4. Marques da Silva, M., A. Correia, R. Dinis, N. Souto, and J. Silva, *Transmission Techniques for Emergent Multicast and Broadcast Systems*, 1st Edition, CRC Press Auerbach Publications, Boca Raton, USA, June 2010, ISBN: 9781439815939.

Channel Capacity Improvement Dependency of the Number of Receiving Antennas for Aeronautical MIMO Systems

N. Kanada, Y. Sumiya, N. Yonemoto, S. Futatsumori, A. Kohmura, and E. Isozaki
Electronic Navigation Research Institute (ENRI), Tokyo 182-0012, Japan

Abstract— In this abstract, we discussed channel capacity improvement of Multiple-Input Multiple-Output (MIMO) antenna systems for new high-speed aeronautical digital communication technologies. It will be required to cope with increasing volumes of air traffic and airport surface congestion. We are studying design methods to optimize operational performances in Japanese airports. Performance analysis under worse conditions is important for safety communication such as air traffic control. Especially, the relationship between communication performance and the position of antennas around aircraft must be clarified due to the unknown effects of masking or reflection by aircraft components such as the fuselage, wings and empennage, and airport structures such as terminal buildings.

We experimentally evaluated channel capacities for communication performance analysis. Figure 1 illustrates a measurement configuration in Sendai Airport. We measured 12 transmission coefficients between 2 aircraft and 6 ground antennas. To investigate the relationship between the number of receive antennas and channel capacity, we calculate channel capacities of MIMO systems that two aircraft antennas transmit and from one to six ground antennas receive.

Table 1 shows a relationship between MIMO channel capacity and number of receiving antennas. Table 1 shows that minimum, average, and maximum of the MIMO channel capacitiesincrease with respect to the number of receiving antennas. Also standard deviation of the MIMO channel capacity decreases with respect to the number of receiving antennas on both MIMO conditions.

As the results, we experimentally show that introduction of MIMO systems contributeshigher speed aeronautical digital communications in an actual airport environment.

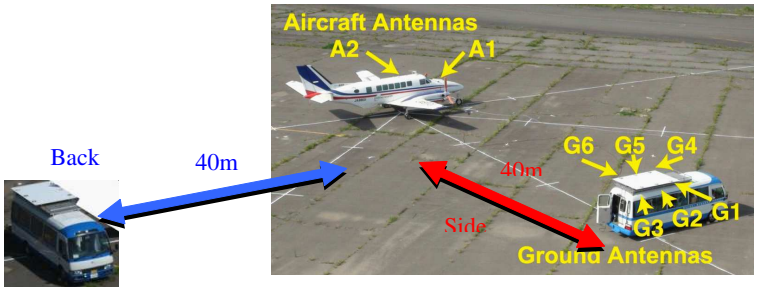

Figure 1: Measurement configuration.

Table 1: MIMO channel capacity improvement dependency of the number of receiving antennas.

	Side			Back		
# ANT	Min	Ave. ± Std. Dev.	Max	Min	Ave ± Std. Dev.	Max
1	19.543	19.880 ± 0.321	20.325	17.305	17.889 ± 0.390	18.228
2	37.611	38.623 ± 0.668	39.827	31.487	32.230 ± 0.383	32.784
3	38.946	39.715 ± 0.437	40.360	32.837	33.396 ± 0.234	33.728
4	39.7	40.309 ± 0.295	40.756	33.635	34.029 ± 0.149	34.245
5	40.46	40.757 ± 0.182	40.937	34.360	34.494 ± 0.095	34.614
6	41.084	41.084 ± 0	41.084	34.839	34.839 ± 0	34.839

MIMO SC-FDE Transmission Techniques with Channel Estimation and High-order Modulations

João Carlos Silva[1], **Rui Dinis**[2], **Nuno Souto**[1], **and Mário Marques da Silva**[3]

[1]ISCTE/Instituto de Telecomunicações, Lisboa, Portugal
[2]ISR/IST, Lisboa, Portugal
[3]UAL/Instituto de Telecomunicações, Lisboa, Portugal

Abstract— OFDM (Orthogonal Frequency Division Multiplexing) schemes are the choice modulation for broadband wireless broadcast and multicast systems. However, OFDM schemes have important limitations such as the high envelope fluctuations of the transmitted signals and its sensibility to carrier frequency errors. When these limitations bear critical we should consider SCFDE schemes (Single-Carrier Frequency Domain Equalization), which allow much higher power efficiency due to the lower envelope fluctuations. This can be further improved if the conventional linear FDE is replaced by an iterative FDE such as an IB-DFE (Iterative Block Decision Feedback Equalizer), adapted for use with hierarchical constellations.

In order to obtain good performance results, accurate channel estimates must be available at the receiver, especially if MIMO (Multiple Input, Multiple Output) is to be used. For this purpose, pilot symbols and/or training sequences are usually multiplexed with data symbols, which lead to spectral degradation. As an alternative, we can use implicit pilots (i.e., pilots superimposed to data).

In this paper, we consider SC-IB-FDE systems in MIMO broadband wireless broadcast and multicast systems where the channel estimation is based on either multiplexed (explicit) or implicit pilots, for comparison purposes. An iterative receiver with joint equalization, turbo decoding and channel estimation was employed in order to optimize the results, and to reduce the high interference levels between data and pilots (for the implicit pilots). The main differences between the different schemes are discussed and the performance results show that the proposed techniques for channel estimation yield excellent results.

Introduction: Block transmission techniques, with appropriate cyclic prefixes and employing FDE techniques (Frequency-Domain Equalization), have been shown to be suitable for high data rate transmission over severely time-dispersive channels [1, 2]. Two possible alternatives based on this principle are OFDM (Orthogonal Frequency Division Multiplexing) and Single Carrier (SC) modulation using FDE (or SC-FDE). Due to the lower envelope fluctuations of the transmitted signals (and, implicitly a lower PMEPR (Peak-to-Mean Envelope Power Ratio)), SC-FDE schemes are especially interesting for the uplink transmission (i.e., the transmission from the mobile terminal to the base station) [1, 2], being considered for use in the upcoming LTE (Long Term Evolution) cellular system. A promising IFDE (Iterative FDE) technique for SC-FDE, denoted IB-DFE (Iterative Block Decision Feedback Equalizer), was proposed in [3]. This technique was later extended to diversity scenarios [4] and layered space-time schemes [5]. These IFDE receivers can be regarded as iterative DFE receivers with the feed-forward and the feedback operations implemented in the frequency domain. Since the feedback loop takes into account not just the hard decisions for each block but also the overall block reliability, error propagation is reduced. Consequently, IFDE techniques offer much better performance than non-iterative methods [3–5]. Within these IFDE receivers the equalization and channel decoding procedures are performed separately (i.e., the feedback loop uses the equalizer outputs instead of the channel decoder outputs). However, it is known that higher performance gains can be achieved if these procedures are performed jointly. This can be done by employing turbo equalization schemes, where the equalization and decoding procedures are repeated in an iterative way [6], being essential in MIMO schemes. Although initially proposed for time-domain receivers, turbo equalizers also allow frequency-domain implementations [7, 8].

In order for the above schemes to operate correctly, good channel estimates are required at the receiver. Typically, these channel estimates are obtained with the help of pilot/training symbols that are multiplexed with the data symbols, either in the time domain or in the frequency domain [9–11].

REFERENCES

1. Gusmão, A., R. Dinis, J. Conceição, and N. Esteves, "Comparison of two modulation choices for broadband wireless communications," *Proc. IEEE*, 1300–1305, VTC Spring, May 2000.

2. Falconer, D., S. Ariyavisitakul, A. Benyamin-Seeyar, and B. Eidson, "Frequency domain equalization for single-carrier broadband wireless systems," *IEEE Comm. Mag.*, Vol. 4, No. 4, 58–66, April 2002.
3. Benvenuto, N. and S. Tomasin, "Block iterative DFE for single carrier modulation," *IEE Electronic Letters*, Vol. 39, No. 19, September 2002.
4. Dinis, R., A. Gusmão, and N. Esteves, "On broadband block transmission over strongly frequency-selective fading channels," *Wireless 2003*, Calgary, Canada, July 2003.
5. Dinis, R., R. Kalbasi, D. Falconer, and A. Banihashemi, "Iterative layered space-time receivers for single-carrier transmission over severe time-dispersive channels," *IEEE Comm. Letters*, Vol. 8, No. 9, 579–581, September 2004.
6. Tüchler, M., R. Koetter, and A. Singer, "Turbo equalization: Principles and new results," *IEEE Trans. on Comm.*, Vol. 50, May 2002.
7. Tüchler, M. and J. Hagenauer, "Turbo equalization using frequency domain equalizers," *Allerton Conf.*, October 2000.
8. Tüchler, M. and J. Hagenauer, "Linear time and frequency domain turbo equalization," *IEEE VTC'01-Fall*, October 2001.
9. Hoher, P., S. Kaiser, and P. Robertson, "Pilot-symbol-aided channel estimation in time and frequency," *IEEE Communication Theory Mini-conference (CTMC), IEEE GLOBECOM97*, 90–96, 1997.
10. Sanzi, F. and J. Speidel, "An adaptive two-dimensional channel estimator for wireless OFDM with application to mobile DVB-T," *IEEE Trans. on Broadcasting*, Vol. 46, 128–133, June 2000.
11. Deneire, L., B. Gyselinckx, and M. Engels, "Training sequence versus cyclic prefix — A new look on single carrier communications," *IEEE Comm. Letters*, Vol. 5, 292–294, September 2001.

Single-stream Communication Using Orthogonal Signal Division Multiplexing with Multiple Antennas

T. Ebihara
Faculty of Engineering, Information and Systems, University of Tsukuba, Tsukuba, Japan

Abstract— Orthogonal signal division multiplexing (OSDM) is a new information transmission method using the Kronecker product between the rows of IDFT matrix and the data sequences [1, 2]. This technique is designed to keep orthogonality among the data sequences over the frequencyselective fading channel. By sharing one data sequence as pilot between the transmitter and the receiver, the receiver can obtain the channel matrix from the pilot and can obtain the message by solving simultaneous equation. This technique has been extended to multi-stream communication with multiple antennas by the author [3, 4]. However, it is found that the simultaneous equation sometimes become ill-conditioned which results in loss in performance. This problem can be avoided with the increase in the number of antennas in the receiver. However, the increase in complexity cannot be avoided. In this paper, single-stream communication using OSDM with multiple antennas (2×2) is proposed. By designing the data sequences in the transmitter, the ill-condition problem can be avoided without increase in complexity. The simulation results suggest that the single-stream communication achieved far better bit-error rate performance to the multi-stream case.

REFERENCES

1. Suehiro, N., C. Han, and T. Imoto, "Very efficient wireless frequency usage based on pseudo-coherent addition of multipath signals using Kronecker product with rows of DFT matrix," *Proc. IEEE Proc. Int. Symp. Information Theory*, 385, Yokohama, Japan, July 2003.
2. Suehiro, N., R. Jin, C. Han, and T. Hashimoto, "Performance of very efficient wireless frequency usage system using Kronecker product with rows of DFT matrix," *Proc. IEEE Information Theory Workshop*, 526, Chengdu, China, Oct. 2006.
3. Ebihara, T. and N. Suehiro, "The orthogonal signal division multiplexing and its performance evaluation," *Denshi Joho Tsushin Gakkai Ronbunshi B*, Vol. 91-B, No. 9, 1086–1094, 2008.
4. Ebihara, T., "High-speed underwater acoustic communication using orthogonal signal division multiplexing: A MIMO approach," *Proc. Symp. Ultrasonic Electronics*, Chiba, Japan, Nov. 2012, in Press.

Session 1A4
Novel Mathematical Methods in Electromagnetics

General Ray Method for Solution of Dirichlet Boundary Value Problem for Helmholtz Equations
Alexandre Grebennikov, A. Lizbeth Cortés Cortés, ... 52
High Resolvability of Electrical Tomography Based on General Ray Method
Alexandre Grebennikov, ... 53
Fast Numerical Solution of Dirichlet Boundary Problem for Laplace Equation in 3D Domains with Complicated Geometry
Alexandre Grebennikov, ... 54
Electromagnetic Eigen-field Characteristics of Acousto-optic Waveguides with Transverse SAW
Yasumitsu Miyazaki, ... 55
Polynomial Modal Analysis of Slanted Lamellar Diffraction Gratings in Classical Mountings
Randriamihaja Manjakavola Honore, Karyl Raniriharinosy, Gérard Granet, ... 56
Diffraction by a Subwavelength Concaved Perfectly Conducting Wedge
Thierry E. Gilles, ... 57
Permittivity Determination of Multi-sectional Diaphragm with Metamaterial Layers in Rectangular Waveguide
Yury G. Smirnov, Yury V. Shestopalov, Ekaterina D. Derevyanchuk, ... 59

General Ray Method for Solution of Dirichlet Boundary Value Problem for Helmholtz Equations

Alexandre Grebennikov and A. Lizbeth Cortés Cortés
Facultad de Ciencias Físico Matemáticas, Benemérita Universidad Autónoma de Puebla
Av. San Claudio y Río verde, Ciudad Universitaria, Puebla, Pue., CP 72570, Mexico

Abstract— An approach for solution of the Dirichlet boundary value problems for Helmholtz equations on the base of the General Rays Principle is considered. The proposed approach to the problem under investigation consists in constructing for considering PDE an analogue as family of ODE describing the distribution of the electrical potential function $u(x, y)$ along of "General Rays", which are presented by a straight line l with some parameterization. We use the traditional Radon parameterization with a parameter t: $x = p\cos\varphi - t\sin\varphi$, $y = p\sin\varphi + t\cos\varphi$. Here $|p|$ is a length of the perpendicular from the centre of coordinates to the line l, $\varphi \in [0, \pi]$ is the angle between the axis x and this perpendicular.

We reduce PDE to the family of ODE applying the direct Radon transform PDE. This reduction leads to ODE with respect to variable p. But using the variable p makes it impossible to satisfy directly to the boundary conditions expressed in (x, y) variables. This p-version of the GR-method can be explained as the consequence of the next steps: 1) reduce the boundary value problem to homogeneous one; 2) describe the distribution of the potential function along the general ray (a straight line l) by its direct Radon transform $u_\varphi(p)$; 3) construct the family of ODE on the variable p with respect the function $u_\varphi(p)$; 4) solution of the constructed ODE with the zero boundary conditions; 5) calculate the inverse Radon transform of the obtained solution; 6) regress to the initial boundary conditions.

General Ray method present the solution of the considering problem by explicit analytical formulas that include the direct and inverse Radon transforms. The goal of this work is to investigate properties of this versions of the General Ray method for considering class of problems on the base of theoretical and numerical analysis.

High Resolvability of Electrical Tomography Based on General Ray Method

Alexandre Grebennikov
Facultad de Ciencias Físico Matemáticas, Benemérita Universidad Autónoma de Puebla
Av. San Claudio y Río verde, Ciudad Universitaria, Puebla, Pue., CP 72570, Mexico

Abstract— A computer simulation of a new special Electrical Tomography method of high resolvability is proposed. Its mathematical model and the measurement scheme of external data are constructed on the basis of General Ray Principle, proposed by the author for distribution of different, in particular electromagnetic, fields. Proposed model leads to the classic Radon transformation that appears as specific element in new General Ray Method, constructed by the author and realized as a simple linear fast numerical algorithm. Proposed measurement scheme and General Ray algorithms open possibility of high resolvability and fast computer recognition of compound structures. Developed scheme is realized as MATLAB software and justified by numerical experiments.

Fast Numerical Solution of Dirichlet Boundary Problem for Laplace Equation in 3D Domains with Complicated Geometry

Alexandre Grebennikov
Facultad de Ciencias Físico Matemáticas, Benemérita Universidad Autónoma de Puebla
Av. San Claudio y Río verde, Ciudad Universitaria, Puebla, Pue., CP 72570, Mexico

Abstract— We consider the Dirichlet boundary value problem for Laplace equation in 3D simply connected star domain Ω with continue boundary surface. The proposed approach to the numerical solution of the problem consists in the next scheme: 1) apply the two-dimensional p-version of the General Ray Method for some sufficient number slices of the domain; 2) construct 3D approximation of obtained results by explicit spline-approximation formulas for 3 variables. We suppose that in every slice the corresponding sub domain is also 2D simply connected star domain. Bought steps of the scheme can be realized by fast algorithms that guarantees rapidness of the calculation by scheme in general. Developed scheme is justified by theoretical aspects and numerical experiments realized on model examples, using constructed MATLAB software.

Electromagnetic Eigen-field Characteristics of Acousto-optic Waveguides with Transverse SAW

Yasumitsu Miyazaki
Faculty of Engineering, Aichi University of Technology
50-2 Manori, Nishihasama-cho, Gamagori 443-0047, Japan

Abstract— Integrated optics and optical devices consisting of active and passive waveguides have been developed recently. Among several optical devices, for optical switch using acoustoptic (A-O) effects, fundamental characteristics and application processing systems of collinear optical switching device have been studied about optical dielectric waveguides on $LiNbO_3$ crystal substrates. Conventional waveguide-type A-O devices use collinear interaction with mode coupling based on Bragg condition between optical waves and SAW both propagating in same directions. Collinear A-O devices of waveguide-type show sufficient performance for wavelength selective switching with narrow bandwidths. However, SAW propagation speed is very slow, comparing with optical wave speeds and in these collinear A-O devices, interaction time is several micro seconds for 10 mm waveguide device length.

In A-O devices of optical waveguides using transverse A-O interaction, where SAW propagates transversely and at right angles to optical wave propagation direction, SAW propagation lengths needed for complete A-O interaction may become 10 µm and interaction time may be several nano seconds. Ultra high speed switching can be accomplished, in A-O waveguide devices with transverse interaction of optical modes and SAW. In this paper, fundamental characteristics of transverse A-O interaction are studied as electromagnetic boundary value problem.

Refractive indexes in optical waveguides induced by A-O effects with SAW shown by sine functions derive wave equations with functional coefficients. Wave field characteristics in inhomogeneous media of periodic structures for transverse directions given by A-O effects due to SAW, are analyzed by analytic method of Hill's equations for transverse spectral functions. Electromagnetic fields in core and clad regions with periodic structures expressed by sine functions corresponding to SAW fields are shown by Mathieu functions with parameters a and q concerned with eigen values. By boundary conditions for electric and magnetic fields at boundaries between core and clad, eigen equations for eigen modes in transverse type A-O waveguides are derived. Dispersion characteristics of A-O eigen modes are studied for wavelengths of optical waves and SAW, with acousto-optic coefficients for stable pass and unstable forbidden bands. Based on these fundamental field characteristics of A-O waveguides, mode couplings and switchings in transverse A-O waveguide devices consisting of coupled several optical waveguides controlled by SAW may be shown.

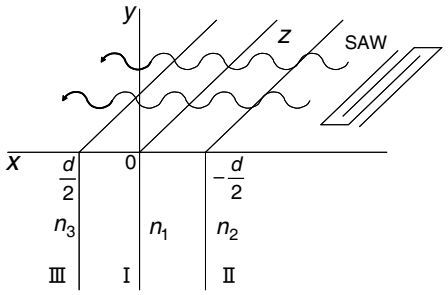

Figure 1: Transverse-type A-O waveguide device

REFERENCES

1. Kondo, T., Y. Miyazaki, and Y. Akao, *Jpn. Jour. Appl. Phys.*, Vol. 17, 1231, 1978.
2. Goto, N. and Y. Miyazaki, *Trans. IEICE*, Vol. E-70, 981, 1987.
3. Tsai, C. S., *IEEE Proc. 1975 Ultrason. Symp.*, 120, 1975.

Polynomial Modal Analysis of Slanted Lamellar Diffraction Gratings in Classical Mountings

Randriamihaja Manjakavola Honoré[1], **Karyl Raniriharinosy**[1], **and Gérard Granet**[2, 3]

[1]LAPAUF, BP 1264 CP 301, Faculté des Sciences, Université de Fianarantsoa, Madagascar
[2]Institut Pascal, Clermont Universités, Université Blaise Pascal
BP10448, F-63000 Clermont-Ferrand, France
[3]CNRS UMR 6602, Clermont Universités, Université Blaise Pascal
F-63177 Aubière, France

Abstract— When a structure is translation invariant along one axis, modal methods are well suited to characterize its electromagnetic behaviour. Lamellar gratings are the most simple structures that can be analyzed with a modal method. Since the dielectric constant depends only on one spatial coordinate it is possible to expand the electromagnetic field in the grating region in terms of the eigenfunctions of the Helmholtz equation. One of the main reason for difference in the convergence rate of the various numerical solution of the eigenvalue problem is the treatment of the discontinuities of the electromagnetic field at the interface between different dielectrics or metals. Using polynomials expansions within each domain of the lamellar gratings allow to express rigorously the different continuity relations that determine the eigenvalue problem and thus leads to exponential convergence for the eigenvalues and eigenvectors as was shown by Morf [1]. Recently, the polynomial modal method was revisited and Gegenbaueur polynomials were introduced [2, 3]. In this presentation, we show how the modal diffraction formulation may be generalized to deal with slanted lamellar gratings. For that purpose we introduce an inclined coordinate system (u, v, w) deduced from the Cartesian coordinate system (x, y, z) by $x = u - \tan(\phi)v$, $v = y$, $w = z$. In the new coordinate system the permittivity function depends on the only u variable and the structure is translation invariant along the v direction and we are thus lead to an eigenvalue problem in which the v dependence of the field components is of the form $\exp(i\beta v)$ where β is a sought eigenvalue. Numerically, we get a matrix eigenvalue equation by using the Galerkin Method with Legendre or Chebyshev polynomials. As an application, we will consider enhanced transmission through slanted small apertures in metallic films.

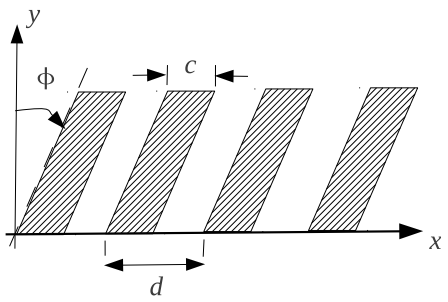

Figure 1: Geometry of the diffraction problem.

REFERENCES

1. Morf, R. H., "Exponentially convergent and numerically efficient solution of Maxwell's equations for lamellar gratings," Vol. 12, No. 5, 1043–1056, 1995.
2. Edee, K., "Modal method based on subsectional Gegenbauer polynomial expansion for lamellar gratings," *JOSA A*, Vol. 28, No. 10, 2006–2013, 2011.
3. Edee, K., I. Fenniche, G. Granet, and B. Guizal, "Modal method based on subsectional Gegenbauer polynomial expansion for lamellar gratings: Weighing function, convergence and stability," *Progress In Electromagnetics Research*, Vol. 133, 1735, 2012.

Diffraction by a Subwavelength Concaved Perfectly Conducting Wedge

Thierry Gilles
Ecole Royale Militaire, Laboratoire d'Electromagnétisme Appliqué (LEMA)
Avenue de la Renaissance 30, Bruxelles 1000, Belgium

Abstract— The fields and current densities behaviors in the vicinity of an isolated infinitely sharp edge or vertex are well known. Many analytic results are available to date for various diffraction problems. Just to name some of the most important ones, among others: Sommerfeld solved the half plane illuminated by a plane wave [1], Mac Donald generalized this result to the wedge [2]. Radlow [3] solved the the quarter plane sector case and Satterwhite and Kouyoumjian [4, 5] found the general solution for any sector and incident field source.

To ensure unicity of the solution in presence of an edge, it has been recognized that a condition was necessary: the so called "edge condition". It states that induced current densities must be integrable to produce finite scattered fields. The edge condition actually selects the solution having the lowest order of singularity at an edge, ruling out any singularities of order greater than $\rho^{-1/2}$, where ρ is the distance to the edge.

By expanding the fields as a power serie of ρ, Meixner characterized their behavior close to an edge surrounded by a combination of metal and dielectric sectors [6, 7]. After the pioneering work of Meixner, several authors analyzed the edge fields and current densities for several more complex configurations [8–10]. The general conclusion of all these works is that the singular fields grow like $\rho^{-\nu}$ very close to the edge, the exponent ν depending both on the geometry and the electromagnetic properties of the wedge-shaped sectors surrounding the edge. Two cases worth remembering are the metallic half plane ($\nu = -1/2$) and the metallic 90° wedge ($\nu = -1/3$) in free space.

More analytically challenging problems involving two or more edges have been tackled by various authors. Exact solutions have been obtained for an infinity [11, 12] or for only two [13] parallel stacked half planes. The so called "thick" half plane has been addressed first in an approximate way by Hanson [14], and later solved exactly by Jones [15] who obtained tractable expressions and numerical results for the far field only for subwavelength thicknesses.

In most of these examples it is found again, or simply assumed based on Meixner's work [16], that infinite current densities may arise in regions of the scattering surface where the local radius of curvature is zero, but much less effort is made to obtain the exact behavior of these current densities in the vicinity of the more or less coupled edges. The purpose of this work is to derive explicit laws for the growth to infinity of the current density for the case of a subwavelength perfectly conducting concaved wedge [17].

REFERENCES

1. Sommerfeld, A., *Math. Anal.*, No. 47, 317, 1896.
2. Macdonald, H. M., *Electric Waves*, 186–198, The University Press, Cambridge, England, 1902.
3. Radlow, J., "Diffraction by a quarter-plane," *Arch. Rational Mech. Anal.*, Vol. 8, No. 1, 139–158, 1961.
4. Satterwhite, R. and R. G. Kouyoumjian, *Electromagnetic Diffraction by a Perfectly Conducting Plane Angular Sector*, Tech. Rep. 2183-2, ElectroSci. Lab., Ohio State University, Columbus, 1970.
5. Satterwhite, R., "Diffraction by a quarter plane, the exact solution and some numerical results," *IEEE Transactions on Antennas and Propagation*, Vol. 22, No. 3, 500–503, May 1974.
6. Meixner, J., "Die kantenbedienung in der theorie der beugung electromagnetischer wellen an volkommen leitenden ebenen schirmen," *Ann. Phys.*, Vol. 6, 1–9, 1949.
7. Meixner, J., "The behavior of electromagnetic fields at edges," *IEEE Transactions on Antennas and Propagation*, Vol. 20, No. 4, 442–446, Jul. 1972.
8. Hurd, R. A., "The edge condition in electromagnetics," *IEEE Transactions on Antennas and Propagation*, Vol. 24, No. 1, 70–73, Jan. 1976.
9. Andersen, J. B., "Field behavior near a dielectric wedge," *IEEE Transactions on Antennas and Propagation*, Vol. 26, No. 4, 598–602, Jul. 1978.

10. Van Bladel, J., "Field singularities at metal-dielectric wedges," *IEEE Transactions on Antennas and Propagation*, Vol. 33, No. 4, 450–455, Apr. 1985.
11. Heins, A. E. and J. F. Carlson, "The reflection of an electromagnetic plane wave by an infinite set of plates, I," *Quart. Appl. Math.*, No. 4, 313–329, 1947.
12. Heins, A. E. and J. F. Carlson, "The reflection of an electromagnetic plane wave by an infinite set of plates, II," *Quart. Appl. Math.*, No. 5, 82–88, 1947.
13. Heins, A. E., "The radiation and transmission properties of a pair of semi infinite parallel plates I," *Quart. Appl. Math.*, No. 6, 157–166, 1948.
14. Hanson, E. T., "Diffraction," *Phil. Trans. R. Soc. Lond. A*, Vol. 229, 87–124, 1930.
15. Jones, D. S., "Diffraction by a thick semi infinite half plane," *Proc. Roy. Soc. Lond. A*, Vol. 217, 153–175, Apr. 1953.
16. Mei, K. K. and J. G. Van Bladel, "Scattering by perfectly-conducting rectangular cylinders," *IEEE Transactions on Antennas and Propagation*, Vol. 11, No. 2, 185–192, Mar. 1963.
17. Yu, J.-W. and N.-M. Myung, "TM scattering by a wedge with concaved edge," *IEEE Transactions on Antennas and Propagation*, Vol. 45, No. 8, 1315–1316, Aug. 1997.

Permittivity Determination of Multi-sectional Diaphragm with Metamaterial Layers in Rectangular Waveguide

Yu. G. Smirnov[1], **Yu. V. Shestopalov**[2], **and E. D. Derevyanchuk**[1]

[1]Penza State University, Russia
[2]Karlstad University, Sweden

Abstract— Determination of electromagnetic parameters of dielectric bodies that have complicated geometry or structure is an urgent problem as far as investigation of the properties and creation of nanocomposite materials are concerned. As a rule, these parameters cannot be directly measured which leads to the necessity of applying methods of mathematical modeling and numerical solution of the corresponding forward and inverse electromagnetic problems [1–3]. In [4] we proposed a numerical-analytical approach and determined in the closed form the permittivity of layered materials loaded in a waveguide. The aim of this work is the development of the proposed technique to the analysis of electromagnetic properties and solution to the inverse problem in the case of a multi-sectional diaphragm with metamaterial layers placed in a rectangular waveguide. Based on the developed recursive method of the solution to the inverse problem we perform a detailed analysis for a three-sectional diaphragm. We consider different fillings of the diaphragm sections and present the results of numerical modeling.

REFERENCES

1. Akleman, F., "Reconstruction of complex permittivity of a longitudinally inhomogeneous material loaded in a rectangular waveguide," *IEEE Microwave and Wireless Components Letters*, Vol. 18, No. 3, 158–160, 2008.
2. Baginski, M. E., D. L. Faircloth, and M. D. Deshpande, "Comparison of two optimization techniques for the estimation of complex complex permittivities of multilayered structures using waveguide measurements," *IEEE Trans. Microw. Theory Tech.*, Vol. 53, No. 10, 3251–3259, 2005.
3. Baker-Jarvis, J. and E. J. Vanzura, "Improved technique for determining complex permittivity with the transmission-reflection method," *IEEE Trans. Microw. Theory Tech.*, Vol. 38, No. 8, 1096–1103, 1990.
4. Shestopalov, Y. and Y. Smirnov, "Inverse scattering in guides," *J. Phys.: Conf. Ser.*, Vol. 346, 012019, 2012.

Session 1A5
Reconfigurable Antenna and Array Antenna

Multi Bands Reconfigurable Antenna for Mobile Phone Application
Dau-Chyrh Chang, Hsin-Chi Li, ... 62
Reconfigurable Antenna with Tri-polarization Capability
Dau-Chyrh Chang, Hsin-Chi Li, ... 63
Extension of Matrix Pencil Methods to the Synthesis of Sparse Linear Arrays with Multiple-patterns
Yanhui Liu, Qing Huo Liu, Zai-Ping Nie, Kun Liao, ... 64
Analysis of Phase Range Distribution of Different Reflectarray Elements on Polycrystalline Silicon Cell
Arshad Selamat, Norbahiah Misran, Mohammad Tariqul Islam, Mohd Fais Mansor, ... 65
Design a Patch Antenna Array to an Optimum Near Field Distribution in the Near-Zone for RFID Applications
Hsi-Tseng Chou, Kai-Te Wang, Shih-Chung Tuan, Chien-Te Yu, Kai-Hao Bai, Paolo Nepa, ... 66
Circularly Polarized Waveguide Slot Array
Ming Hui Chen, ... 67
Beam Steering of a Large Phased-array Antenna with Constant Major-lobe Width and Constrained Side-lobes
Song-Han Yang, Jean-Fu Kiang, ... 69

Multi Bands Reconfigurable Antenna for Mobile Phone Application

Dau-Chyrh Chang and Hsin-Chi Li
Institute of Information and Communication Engineering
Oriental Institute of Technology, New Taipei City, Taiwan

Abstract— The design of multi-band reconfigurable antenna with compact size and high efficiency is presented. Figure 1a shows the simulation model of the multi bands reconfigurable antenna. The antenna is composed of one main loop radiator, one monopole radiator, and coupling loop radiator. The size of the antenna is $50 \times 75 \times 0.8$ mm which is printed on FR4-exopy substrate with permittivity 4.4. There are four PIN diodes switch to control the antenna with multiple frequency capability. Bu adjusting the PIN diode switches, the antenna frequency can be switched for GSM850, GSM900, GSM1800, GSM1900, UMTS2100, and IEEE 802.11a/b/g as shown in Figure 1(b). The simulation result of return loss is larger than 6 dB and the overall efficiency is about 60% $\sim$ 80% for the desired bands. The operation theory, hardware implementation, and measurement results will be included at the full paper and oral presentation.

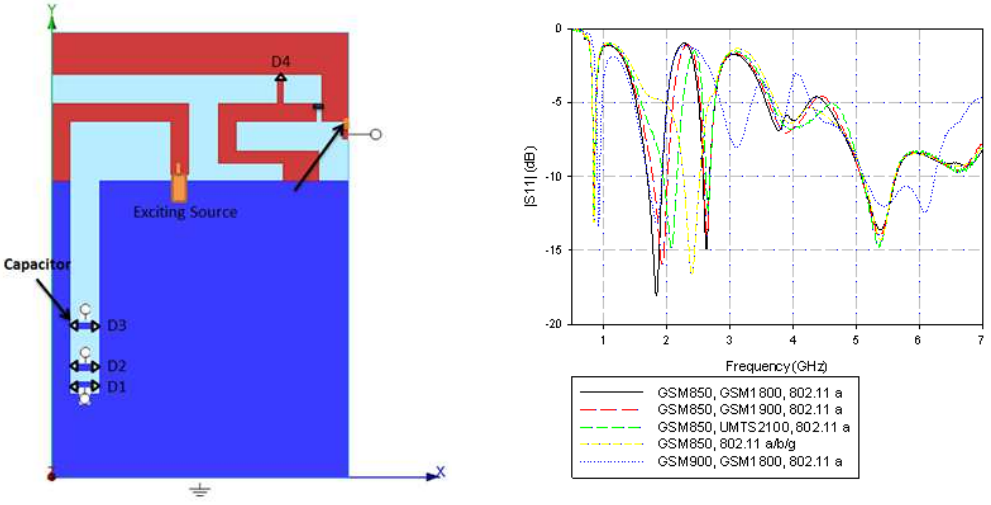

(a) (b)

Figure 1: (a) Configuration of the proposed antenna. (b) The S-parameter of the simulation result.

Reconfigurable Antenna with Tri-polarization Capability

Dau-Chyrh Chang and Hsin-Chi Li
Institute of Information and Communication Engineering
Oriental Institute of Technology, New Taipei City, Taiwan

Abstract— The design of the polarization reconfigurable antenna for tri-polarization diversity is presented. In order to satisfy the requirement of polarization diversity in the integrated communication systems we propose the concept of switching the polarization state of antennas by controlling high speed PIN diodes. In order to reduce the impact of antenna performance, the lumped elements, capacitor and inductor are used to isolate the direct current source and RF signal respectively. The antenna is illustrated in Figure 1(a). It is printed on a $50 \times 50 \times 0.8\,\mathrm{mm}^3$ FR4-epoxy substrate with relative permittivity 44. The CPW feeding line is used for the tri-polarization antenna. The tri-polarization antenna is composed of three meander radiators 1, 2, and 3 which will contribute the performance of vertical linear polarization (LP), left hand circular polarization (LHCP), and right hand circular polarization (RHCP). The distance between meander radiator 1 and meander radiators 2, 3 is quarter wavelength. The meander radiators 2 and 3 are controlled by the PIN diode switches. The main contribution of meander radiator 1 is for LP. The contributions of meander radiators 1 and 2 (3) are for RHCP (LHCP). When the two diodes near meander radiators 2 and 3 are off then most of the current will flow at radiator 1 which will cause LP radiation When one of the two diodes is off then will cause CP radiation. Figure 1(b) is the simulation results of axial ratio by using the GEMS for LP, RHCP and LHCP. Detail will be discussed in the full paper.

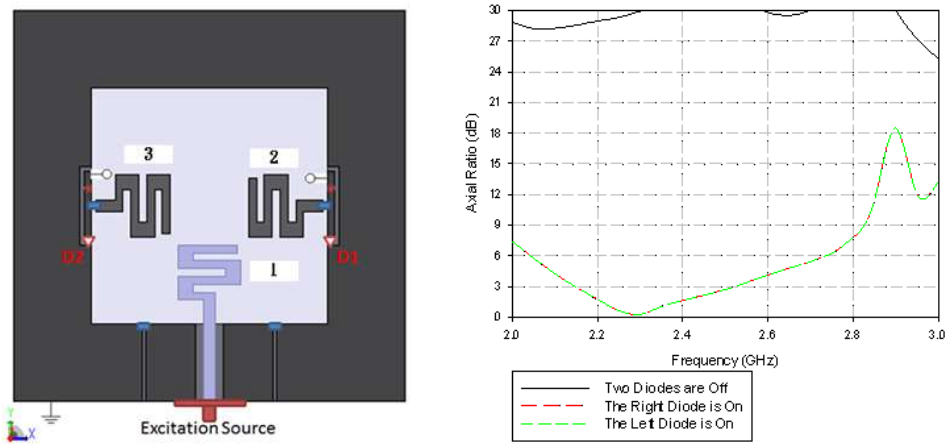

(a) (b)

Figure 1: (a) Configuration of the proposed antenna. (b) The axial ratio of tri-polarization.

Extension of Matrix Pencil Methods to the Synthesis of Sparse Linear Arrays with Multiple-patterns

Yanhui Liu[1], **Qing Huo Liu**[2], **Zaiping Nie**[3], **and Kun Liao**[1]

[1]Department of Electronic Science, Xiamen University, Fujian 361005, China
[2]Department of Electrical and Computer Engineering, Duke University, NC 27708, USA
[3]Department of Microwave Engineering, UEST of China, Sichuan 610054, China

Abstract— The reconfigurable array antennas capable of radiating dual or more patterns by varying only element excitations can reduce the number of antennas, and thereby the weight and the cost of whole hardware systems. The synthesis of such reconfigurable arrays has received increasing attention in the past thirty years. For most of existing synthesis techniques, multiple patterns are generated by controlling only excitation phases of a single array with prefixed or optimized common amplitudes. Such synthesis can simplify the design of feeding network, but in the meantime reduce the number of freedoms from the point of view of the pattern synthesis. In addition, most synthesis techniques deal only with uniformly spaced linear arrays and require a large number of elements to simultaneously meet all the requirements in the multiple-pattern synthesis.

To reduce the number of elements, the synthesis of a completely nonuniform array with the most control freedoms is usually required. For the multiple-pattern synthesis case, one needs to find the solution of many unknowns including the common element positions and multiple sets of complex excitations (amplitudes and phases) for the best approximation of all the desired patterns. This is a highly nonlinear inverse problem. For the synthesis of nonuniformly spaced arrays with single-patterns, many practical methods have been proposed. However, most of them cannot be easily extended to the synthesis of a sparse array with multiple-pattern since the best element positions usually change for different patterns.

Previously we presented a new synthesis technique based on the matrix pencil method (MPM) for the synthesis of linear arrays with pencil-beam patterns. This method was then recently extended to the synthesis of asymmetric or shaped patterns by using forward-backward matrix pencil method (FBMPM). However, when applied to the synthesis of reconfigurable arrays with multiple-patterns, the MPM and FBMPM-based synthesis methods also have the problem that the best element positions for different patterns may be different. Now we shall show that this problem can be solved by the extended MPM or FBMPM-based synthesis method which organizes the multiple pattern data into composite Hankel or composite Hankel-Toeplitz matrix. With the extended synthesis methods, the optimal solution of the common element positions can be found for the multiple-pattern. In particular, the extended FBMPM maintains the same constraint as the original FBMPM on the distribution of the common poles, which contributes to more accurate and robust synthesis of multiple-patterns. Numerical results are presented to show the effectiveness and advantages of the proposed synthesis methods.

Analysis of Phase Range Distribution of Different Reflectarray Elements on Polycrystalline Silicon Cell

A. Selamat[1], **N. Misran**[1, 2], **M. T. Islam**[1, 2], **and M. F. Mansor**[1]

[1]Department of Electrical, Electronic and System Engineering
Universiti Kebangsaan Malaysia, Bangi, Selangor 43600, Malaysia
[2]Institute of Space Science (ANGKASA), Universiti Kebangsaan Malaysia
Bangi, Selangor 43600, Malaysia

Abstract— The bandwidth behaviour of reflectarray elements are discussed in this paper to overcome the intrinsic limitation of narrow bandwidth it offers. This is done by analyzing the relationship between bandwidth and phasing distribution characteristics of the elements. Five shapes of elements i.e. ring, rectangular loop, triangular loop, square loop and ellipse loop have been investigated. Each element is designed on Kapton sheet positioned on top of a coverglass layer that protects the silicon layer. Rogers RT/Duroid 5880 dielectric substrate ($\varepsilon_r = 2.2$ and $\tan\delta = 0.0009$) is used to support the layers above. These elements are designed to operate at Ku-band frequency range using CST microwave studio. The elements dimension are varied thus modifies the surface current distribution that leads to variation of phase reflection from the elements. The relationship of bandwidth performance with the obtained reflection loss of each element is then investigated. It has been demonstrated from this work that triangular element can offer the highest static linear phase range about 263°, whereas the square element gives the lowest static linear phase range of 153°. The surface area of resonating element has significantly control the current distribution hence leads the triangular element with the lowest surface area to has steep phase variation. While square element with greater surface area is shown to exhibit smoother phase variation with broader bandwidth performance. Moreover, the CST simulation results also shown that triangular element can operate at two resonant frequencies within Ku-band at 12.22 GHz and 14.09 GHz which can be further exploited for satellite and communication applications.

Design a Patch Antenna Array to an Optimum Near Field Distribution in the Near-Zone for RFID Applications

Hsi-Tseng Chou[1], **Kai-Te Wang**[1], **Shih-Chung Tuan**[3], **Chien-Te Yu**[1], **Kai-Hao Bai**[1], **and Paolo Nepa**[2]

[1]Department of Communication Engineering, Yuan Ze University, Chung-Li 320, Taiwan
[2]Department of Information Engineering, University of Pisa, Pisa, Italy
[3]Department of Communication Engineering, Oriental Institute of Technology, Pan-Chiao, Taiwan

Abstract— The popularity of RFID in recent years has boomed a variety of potential applications in the commercial uses. Its successful applications rely strongly on the applicable scenario to implement the system, where the radiation from the antenna plays a key factor of successful operation. Good radiation characteristics may help to reduce the interferences from surrounding structures. A scenario of antenna design is thus developed, which makes the antenna to radiate fields with optimum field distributions in the near-zone of antenna. In particular, the design is based on the optimization of excitation weighting for phased array antennas. The antenna array is realized microstrip patch elements, which have advantages of easy implementation. This array will radiate electromagnetic fields that are relatively uniform in the near-zone of array aperture for RFID applications. To simplify the implementation cost, the array feeding network is simplified by using equal power dividers in one dimension. In another dimension, an open-end transmission line is used to create standing wave, which in conjunction with feeding microstrips allows one to control the phases and amplitudes of a row array. A prototype has been implemented to demonstrate the validity of this near-field focused array. This design allows one to define a target zone that can be used as detection area of RFID tags as interested in the department store management system. Antenna design, as well as the design procedure, is presented. Numerical simulations and experimental measurement are conducted and also presented to validate the concept.

Circularly Polarized Waveguide Slot Array

Ming Hui Chen
Victory Microwave Corporation, Xizhi District, New Taipei City, Taiwan

Abstract— It is well known that transmitting and receiving electromagnetic waves between base stations and end users with circularly polarized signals can reduce the multipath interference. This is because the reflection from the ground changes the polarization to the opposite sense. The interference signal interacts with the directly reflected signal and is thereby reduced. However, we have not found this scheme to be put into practice, possibly due to a lack of a circularly polarized base station antenna.

We have developed a circularly polarized slot array, which could be used for base station application. The radiating slots of the antenna are cut on the broad wall of a rectangular waveguide. The transverse and longitudinal slots fed by the magnetic fields inside the waveguide forms a pair of slots acting as a circularly polarized radiating element. This is shown in Fig. 1. The natural behavior of a 90 degree phase difference of transverse and longitudinal magnetic fields inside a rectangular waveguide is utilized for feeding the slots to meet the phase requirement for circularly polarized radiation.

A 4×4 slot array at 1.5 GHz was fabricated (shown in Fig. 2) to validate the theory. Slot pairs are spaced one guide wavelength apart along the waveguide to achieve in-phase radiation across all slot pairs. The neighboring waveguides are designed to have a 1/4 guide wavelength shift. This shift is compensated by a section of cable in the feed network so that all elements of the slot array radiate in phase. This arrangement will eliminate the grating lobe of the slot array. The

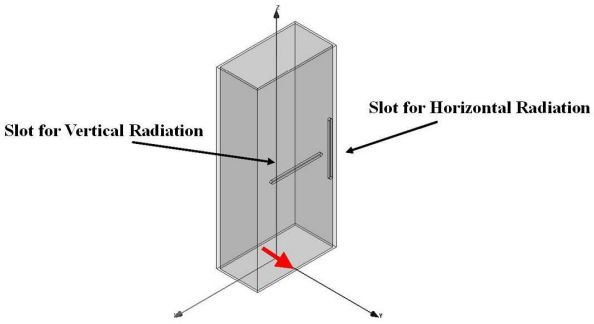

Figure 1: Circular polarized radiating element.

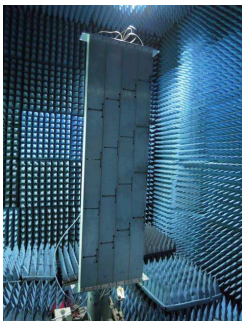

Figure 2: Photo of base station antenna.

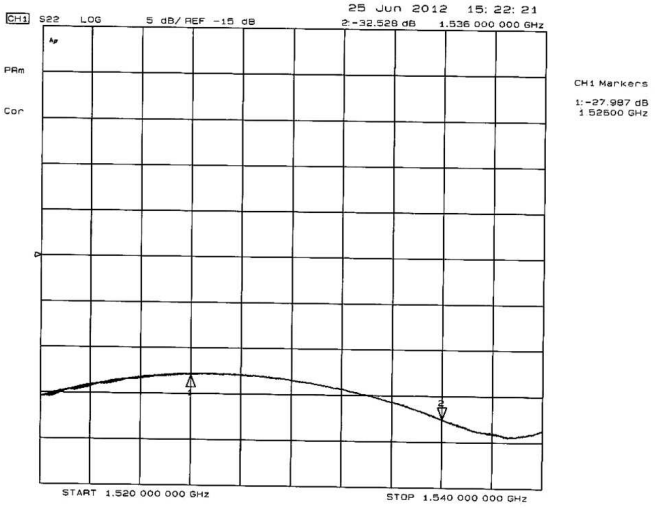

Figure 3: Measurement of return loss of prototype.

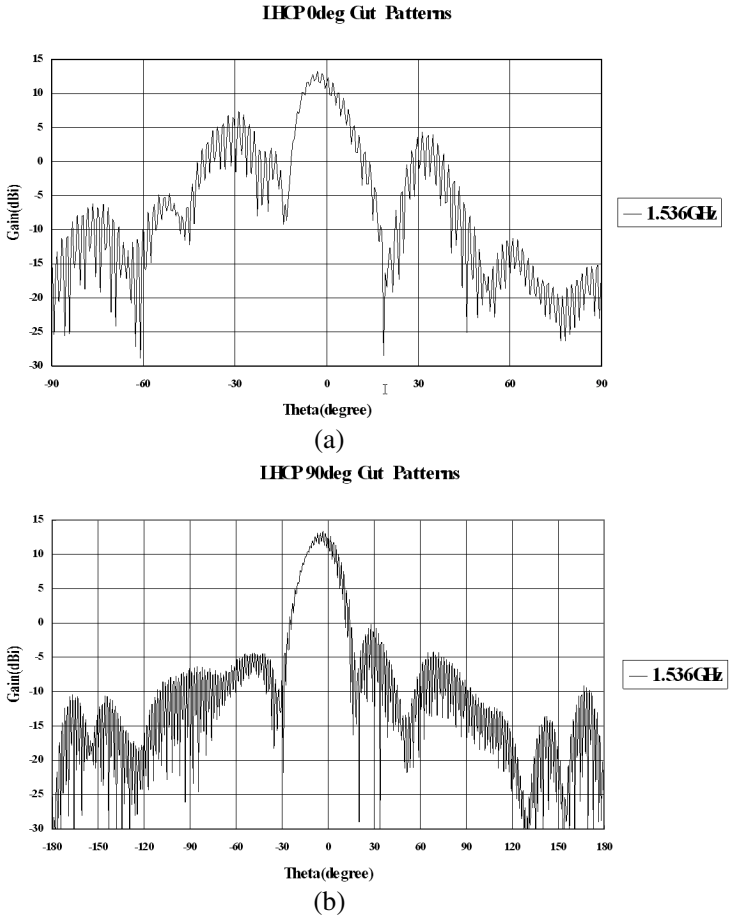

Figure 4: (a) Elevation pattern of prototype slot array. (b) Azimuth pattern of prototype slot array.

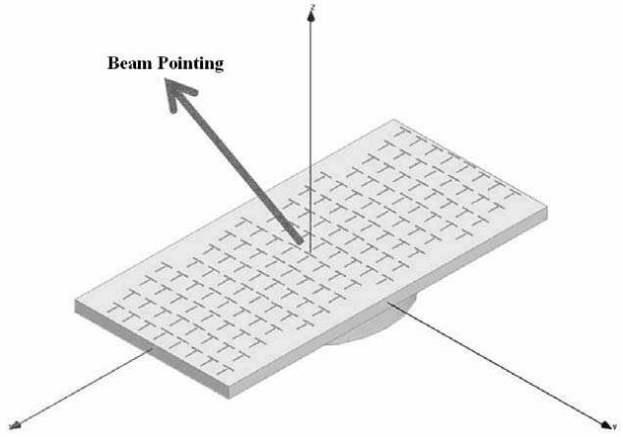

Figure 5: Flat plane slot array for mobile VSAT application.

measured return loss and radiation patterns are given in Fig. 3 and Fig. 4, and are satisfactory. This 4×4 slot array could be used as a sub array for a large slot array with more elements.

In addition, by adjusting the spacing of the slot elements, this slot array can make radiate at a designated angle instead of broadside. It can be considered as a leaky wave antenna and used for mobile VSAT. A conceptual design of a flat plate mobile VSAT antenna is shown in Fig. 5. The pointing angle toward the satellites at the synchronized orbit from a large local area on the earth is fixed and can be covered by the elevation beam (the forward beam). This type antenna needs to search only a single dimension (rotational) to find a satellite while on a vehicle.

Beam Steering of a Large Phased-array Antenna with Constant Major-lobe Width and Constrained Side-lobes

Song-Han Yang and Jean-Fu Kiang
Graduate Institute of Communication Engineering
National Taiwan University, Taipei, Taiwan

Abstract— Large phased-array antennas have been used for radar applications, for example, to track objects with beam-steering maneuvers. The major-lobe width grows bigger when it is steered away from the broadside direction, and the major-lobe size reduction is usually accompanied by side-lobe increase.

Several methods have been proposed to reduce sidelobe level of antenna arrays. A continuous genetic algorithm (GA) has been used to reduce sidelobe level of linear and circular arrays by adjusting complex excitations of all elements; the maximum sidelobe in the broadside can be reduced to −36 dB when applied to a 30-element linear array.

Comprehensive learning particle swarm optimization (CLPSO), GA, inertia weight PSO (IW-PSO), constriction factor PSO (CFPSO) algorithms have been proposed to optimize the spacings between elements of a linear array to minimize sidelobe level and control null locations; the maximum sidelobe level can be reduced by 19 dB, with no null control, when applied to a 10-element unequally-spaced linear array. A position mutated hierarchical PSO (PM-HPSO) has been presented to reduce sidelobe level of unequally spaced antenna arrays When applied to a 108 planar thinned array, the sidelobe reduction reaches about 20 dB.

In this work, a large phased-array antenna is studied for its beam-steering capability. A tapering technique is proposed to maintain a constant beamwidth of the major-lobe when it is steered to different directions, and a CLPSO algorithm is applied to adjust phases of all elements so that the side-lobe can be restrained to an acceptable level.

Session 1P1
Quantum Metamaterials

Quantum Measurement and Metamaterials
Mark J. Everitt, J. H. Samson, S. E. Savel'ev, T. P. Spiller, R. Wilson, Alexandre M. Zagoskin, . 72

Microwave Structures with Quantum Topological Effects Based on Magnetic-dipolar-mode Ferrite Particles
M. Berezin, Eugene O. Kamenetskii, Reuven Shavit, ... 73

A Quantum Phase-slip Junction Built from a Josephson Junction Crystal
Thomas Weissl, Gianluca Rastelli, Bruno Kung, Alexey K. Feofanov, Etienne Dumur, Vitaly N. Golovach, Olivier Buisson, Frank W. J. Hekking, Wiebke Guichard, ... 74

Superconducting Qubits for Quantum Optics and Quantum Metamaterials
Oleg Astafiev, ... 75

Quantum Metamaterials for Optical Elements and Detectors: New Possibilities
Alexandre M. Zagoskin, ... 76

Photon Generation from Quantum Vacuum Using a Josephson Metamaterial
Pasi Lähteenmäki, Gheorghe Sorin Paraoanu, J. Hassel, Pertti J. Hakonen, ... 77

Quantum-dot Metamaterials
M. Decker, I. Staude, I. Shishkin, K. B. Samusev, P. Parkinson, V. K. A. Sreenivasan, Alexander Minovich, Andrey E. Miroshnichenko, Andrei V. Zvyagin, C. Jagadish, Dragomir N. Neshev, Yuri S. Kivshar, ... 78

Low Threshold Confined Tamm Plasmon Laser
Joel Bellessa, Clementine Symonds, S. Aberra-Guebrou, A. Lemaitre, Pascale Senellart, ... 79

A Quantum Effect in the Classical Limit: Nonequilibrium Tunneling in the Quantum Duffing Oscillator
Alec Maassen Van Den Brink, ... 80

Surface Plasmon Interaction with a Gain Medium
Aurore Castanie, Brahim Guizal, Didier Felbacq, ... 81

Quantum Measurement and Metamaterials

M. J. Everitt[1], **J. H. Samson**[1], **S. E. Savelev**[1], **T. P. Spiller**[2], **R. Wilson**[1], **and A. M. Zagoskin**[1]

[1]Loughborough University, UK
[2]University of Leeds, Boston, USA

Abstract— In this paper, we consider a two-dimensional metamaterial comprising an array of qubits (two level quantum objects). Here we show that a two-dimensional quantum metamaterial may be controlled, e.g., via the application of a magnetic flux, so as to provide controllable refraction of an input signal. We investigate the role of measurement on the operation of the metamaterial. We note that the application of an external control parameter can be used to change the behaviour of the material. We note that quantum metamaterials as proposed here may be fabricated from a variety of current candidate technologies from superconducting qubits to quantum dots. Thus the ideas proposed in this work would be readily testable in existing state of the art laboratories.

Microwave Structures with Quantum Topological Effects Based on Magnetic-dipolar-mode Ferrite Particles

M. Berezin, E. O. Kamenetskii, and R. Shavit
Microwave Magnetic Laboratory
Department of Electrical and Computer Engineering
Ben Gurion University of the Negev, Beer Sheva, Israel

Abstract— Microwave ferrite structures with a reduced dimensionality brings into play new effects, which should be described based on the quantized picture and demonstrate the properties of artificial atomic structures. These effects can find unique applications in a view of a present strong interest in artificial structures that can control electromagnetic radiation by applying the rules of quantum mechanics [1, 2]. Magnetic-dipolar-mode (MDM) oscillations in a mesoscopic ferrite-disk particle are quantized oscillations, which are characterized by energy eigenstates, power-flow vortices and non-zero helicity [3–8]. For electromagnetic waves irradiating a quasi-2D MDM disk, this small ferrite sample appears as a singular subwavelength region with time and space symmetry breakings. With the observed helicity properties of the fields in a vacuum region abutting to a quasi-2D ferrite disk with the MDM oscillations, one becomes faced with fundamental aspects akin to the problems of axion electrodynamics. The near field originated from a MDM disk has local coupling between the time-varying electric and magnetic fields different from the electric-magnetic coupling in a free-space electromagnetic field. To distinguish such a field from a regular electromagnetic field, it was termed a magnetoelectric (ME) field [9]. A structure and conservation laws of a microwave ME field and its interaction with matter have been studied, for the first time, in Ref. [10]. In a recent paper [11], we analyzed twisted states of long-distant microwave fields scattered by MDM ferrite disks. We showed that in the long-distant fields scattered by MDM particles, one can clearly distinguish structures of rotating topological-phase dislocations. Specific long-distance topological properties of the fields are exhibited clearly in the effects of path-dependent interference with coupled MDM particles. Such double-twisted scattering is characterized by topologically originated split-resonance states. In the present paper, we study quantized topological-phase effects based on MDM ferrite particles in a view of novel applications for near- and far-field microwave structures.

REFERENCES

1. Rakhmanov, A. L., A. M. Zagoskin, S. Savel'ev, and F. Nori, *Phys. Rev. B*, Vol. 77, 144507, 2008.
2. Felbacq, D., *J. Nanophoton.*, Vol. 5, 050302, 2011.
3. Kamenetskii, E. O., M. Sigalov, and R. Shavit, *J. Phys.: Condens. Matter*, Vol. 17, 2211, 2005.
4. Kamenetskii, E. O., *J. Phys. A: Math. and Theor.*, Vol. 40, 6539, 2007.
5. Kamenetskii, E. O., *J. Phys.: Condens. Matter*, Vol. 22, 486005, 2010.
6. Sigalov, M., E. O. Kamenetskii, and R. Shavit, *J. Phys.: Condens. Matter*, Vol. 21, 016003, 2009.
7. Kamenetskii, E. O., M. Sigalov, and R. Shavit, *Phys. Rev. A*, Vol. 81, 053823, 2010.
8. Kamenetskii, E. O., R. Joffe, and R. Shavit, *Phys. Rev. A*, Vol. 84, 023836, 2011.
9. Kamenetskii, E. O., arXiv:1111.4359, 2011.
10. Kamenetskii, E. O., R. Joffe, R. Shavit, arXiv:1111.4361, 2011.
11. Berezin, M., E. O. Kamenetskii, and R. Shavit, *J. Opt.*, Vol. 14, 125602, 2012.

A Quantum Phase-slip Junction Built from a Josephson Junction Crystal

T. Weiβl[1], **G. Rastelli**[3], **B. Küng**[1], **A. K. Feofanov**[1], **E. Dumur**[1], **V. N. Golovach**[2], **O. Buisson**[1], **F. W. J. Hekking**[2], **and W. Guichard**[1]

[1]Institut Néel, CNRS, Université Joseph Fourier, 25 Rue des Martyrs, Grenoble 38042, France
[2]LPMMC, CNRS, Université Joseph Fourier, 25 Rue des Martyrs, Grenoble 38042, France
[3]Universität Konstanz, Fachbereich Physik, Konstanz 78457, Germany

Abstract— Superconductors have the remarkable property of showing quantum coherence of the superconducting phase on macroscopic length scales. In Josephson junctions (JJ's) the phase over the junction and the charge on the capacitor formed by the two electrodes are conjugate variables linked by the Heisenberg uncertainty relation. In a large JJ the phase undergoes very small quantum fluctuations whereas the charge fluctuates strongly. This phase precision of JJ's makes them an ideal system for metrology as voltage standards. Phase-slip junctions present dual dynamics to the one of Josephson junctions. Here the charge is fixed precisely while the phase is subject to strong fluctuations. The understanding of quantum phase-slips dynamics in Josephson junction circuits [1] will enable in the future the design of unique quantum meta-materials that may find applications in quantum metrology as their Josephson counterpart does currently for the voltage standard. In particular we pursue the realization of a quantum electrical current standard on a long term [2].

Small capacitance JJ's can act as phase slip junction provided they are decoupled from charge fluctuations in the environment by a large impedance. So far experiments have used large on-chip resistors to suppress fluctuations of the charge. These resistors however introduce dissipation in the system which makes these systems at present not suitable for metrology.

In our experiments we suppress the charge fluctuation by a large inductance in series with a squid which acts as a tunable quantum phase-slip element. As inductances of several μH are required we use a Josephson crystal, i.e., a one dimensional chain of JJ's. Like atomic crystals these Josephson meta-materials show internal electromagnetic, phonon-like modes. These modes represent the electromagnetic environment of the phase slip junction and can lead to decoherence. It is therefore essential to carefully design the mode structure of the Josephson crystal.

We present measurements of phase slip junctions showing the influence of the internal modes of Josephson crystals as well as direct measurements of these modes. We discuss solutions to engineer the band structure of the Josephson crystals.

REFERENCES

1. Pop, I. M., et al., "Measurement of the effect of quantum phase slips in a Josephson junction chain," *Nat. Phys.*, Vol. 6, 589–592, 2010.
2. Guichard, W. and F. W. J. Hekking, "Phase-charge duality in Josephson junction circuits: Role of inertia and effect of microwave irradiation," *Phys. Rev. B*, Vol. 81, 064508, 2010.

Superconducting Qubits for Quantum Optics and Quantum Metamaterials

Oleg Astafiev
NEC Smart Energy Research Laboratories, Tsukuba, Japan

Abstract— Superconducting circuits of nanometer-to-micron scale behave as quantum systems similarly to natural atoms and are using currently as quantum bits in experiments on quantum computing. Such systems are fully controllable, tunablile, strongly coupled to the environment and their properties can be designed in advance. The artificial atoms can be used for building devices of quantum electronics and artificial matters, particularly, quantum metamaterials. With the strong coupling, we study behavior of the single atoms in open 1D-space and demonstrate a series of fundamental phenomena from quantum optics: resonance fluorescence, electromagnetically induced transparency, quantum amplification. Controllable manipulation of the atom in open space demonstrates possibility to apply such a system for optical quantum computation with photons.

Quantum Metamaterials for Optical Elements and Detectors: New Possibilities

A. M. Zagoskin
Department of Physics, Loughborough University, Loughborough LE11 3TU, UK

Abstract— I review recent proposals concerning applications of quantum metamaterials towards imaging and detecting and evaluate the feasibility of their implementation.

Photon Generation from Quantum Vacuum Using a Josephson Metamaterial

P. Lähteenmäki[1], **G. S. Paraoanu**[1], **J. Hassel**[2], **and P. J. Hakonen**[1]

[1]Low Temperature Laboratory, Aalto University, P. O. Box 15100, FI-00076 AALTO, Finland
[2]VTT Technical Research Centre of Finland, P. O. BOX 1000, FI-02044 VTT, Finland

Abstract— The picture about vacuum that emerges from modern quantum field theory is very different from that offered by classical physics. In classical field theory, the vacuum is the zero-energy state of the field, defined by the absence of any excitation. In quantum field theory, the vacuum state has a finite zero-point energy associated with it, and the uncertainty principle indicates that fluctuations exist even in this state. Due to existence of fluctuations, under certain perturbations the quantum vacuum can become unstable, and the energy of the perturbation is converted into creation of real particles. For example, in the Schwinger effect a static intense electric field can create pairs of electrons and positrons. In very strong gravitational fields, at the event horizon of black holes, the vacuum becomes unstable and energy is radiated away (Hawking effect). By the equivalence principle, an accelerated observer in the Minkowski vacuum will detect a finite-temperature field (Unruh effect). Finally, the energy and the fluctuations of the electromagnetic vacuum confined in a cavity have real, measurable effects: they produce an attractive force between the walls of the cavity (static Casimir effect), and, if the boundary conditions or the index of refraction are changed, photons are created apparently out of nothing (dynamic Casimir effect). In this presentation, we report the observation of the dynamical Casimir effect using a flux-biased Josephson metamaterial embedded in a microwave cavity at 5.4 GHz [1]. A non-adiabatic change in the index of refraction of the cavity (or in the electrical length) is realized by modulating the flux at values close to double the resonant frequency of the cavity. We measure the frequency-correlated photons thus generated from the cavity at $T = 50$ mK, and we obtain a power spectrum displaying a bimodal, sparrow-tail distribution. The experimental results are in excellent agreement with the theoretical predictions.

The experiment demonstrates the potential of superconducting quantum circuits to serve as a platform for simulating effects from cosmology and quantum field theory. I will also briefly describe a few directions in which this type of experiments could be further developed.

REFERENCES

1. Lähteenmäki, P., G. S. Paraoanu, J. Hassel, and P. J. Hakonen, "Dynamical casimir effect in a josephson metamaterial," *Proc. Natl. Acad. Sci.*, Vol. 110, 4234, USA, 2013.

Quantum-dot Metamaterials

M. Decker[1], **I. Staude**[1], **I. Shishkin**[1, 2, 3], **K. Samusev**[1, 2, 3], **P. Parkinson**[4], **V. K. A. Sreenivasan**[5], **A. Minovich**[1], **A. E. Miroshnichenko**[1], **A. Zvyagin**[5], **C. Jagadish**[4], **D. N. Neshev**[1], **and Y. S. Kivshar**[1]

[1]Nonlinear Physics Centre, Research School of Physics & Engineering (RSPE)
The Australian National University, Canberra, Australia
[2]National Research University for Information Technology
Mechanics and Optics (ITMO), St. Petersburg 197101, Russia
[3]Ioffe Physics-Technical Institute of the Russian Academy of Science
St. Petersburg 194021, Russia
[4]Department of Electronic Materials Engineering, RSPE
Australian National University, Canberra, Australia
[5]MQ Photonics Centre, Macquarie University, Sydney, NSW, Australia

Abstract— Control of spontaneous emission is crucial for a broad range of applications such as single-photon sources, efficient lasers, displays, solar energy harvesting, and biological markers. The quantum dot (QD) emission can be efficiently controlled through coupling to photonic structures, such as microcavities, photonic crystals, and plasmonic particles. Nanostructured plasmonic materials can be superior for emission enhancement due to their high local-field enhancement and good coupling to free space. A special class of such materials are metamaterials that allow for simultaneous control over the *electric and the magnetic interaction of light with the emitters*. While control of spontaneous emission of light in metamaterial has be the subject of intense recent interest, only a single channel of this interaction has been explored. Importantly, the control of QD emission via simultaneous coupling to the magnetic and the electric modes of the metamaterials remains unexplored.

Here, report on the coupling of QD emission to simultaneously to both electric and magnetic resonances of magnetic metamaterials. We compare the emission enhancement for the zero-order electric and the first-order magnetic resonances (matched spectrally to the QD emission, with the same strength but orthogonal polarisations) and observe three-fold enhancement of the QD emission into the magnetic mode in comparison to the electric one.

The system investigated in our work is a planar magnetic metamaterial composed of split-ring resonators (SRRs) covered by a 200 nm-thick layer of polyvinyl alcohol (PVA) containing core-shell QDs emitting at 790 nm. In order to investigate how the QD PL is influenced by coupling to the different modes of the magnetic metamaterial we have performed QD micro-photoluminescence (PL) spectroscopy and micro-PL spatial mapping on the SRR metamaterial. In our experiments, we observe broadening of the QD PL spectrum for the electric resonance, while for the magnetic resonance a narrowing of the QD PL emission spectrum is observed. In addition, while the PL intensity does not change when coupling to the electric resonance, a three-fold enhancement can be observed in the magnetic resonance. Furthermore, we have measured lifetime of QD PL for both metamaterial resonances and have found that the decrease in lifetime (in comparison to the unstructured reference areas) is more pronounced in the case of the magnetic resonance. Thus, remarkably, the magnetic mode, which exhibits weaker coupling to the far-field (deducted from transmittance measurements) and can be considered as a darker mode, becomes the brighter mode in QD emission due to its higher Purcell enhancement.

Our experimental results are in good qualitative agreement with theoretical expectations, paving the way towards an ultimate control of emission by magnetic metamaterials.

Low Threshold Confined Tamm Plasmon Laser

J. Bellessa[1], **C. Symonds**[1], **S. Aberra-Guebrou**[1], **A. Lemaitre**[2], **and P. Senellart**[2]

[1]Laboratoire de Physique de la Matière Condensée et Nanostructures
Université Lyon 1, CNRS, UMR 5586, Domaine Scientifique de la Doua
Villeurbanne Cedex F-69622, France
[2]Laboratoire de Photonique et de Nanostructures
CNRS, Route de Nozay, Marcoussis F-91460, France

Abstract— The hybrid metal dielectric structures are very promising for the fabrication of compact efficient optical sources. Tamm plasmons which appear at the boundary between a photonic structure and a metallic layer, present both the advantages of surface plasmons and of microcavities photonic modes: the losses associated to these modes are relatively low and they can be spatially confined by structuring the metallic part of the system, thus reducing the size of the mode and allowing various geometries. Recently, laser effect has been demonstrated in non-confined Tamm structures [1]. It has also been demonstrated that high beta factor could be achieved for confined Tamm modes [2]. We will show that laser effect can be obtained in confined Tamm structures with a lateral dimension of the order of the micron, the confinement resulting in a reduced laser threshold.

For this purpose the lasing threshold will be studied as a function of the lateral dimension of the structure. The lateral confinement induces discret emission wavelengths.

Reducing the structure size increases the beta factor but at the same time decreases the quality factor of the structure. This reduction of the quality factor is due to the diffusion of the mode by the sides of the structured metal. These two opposites trends lead to an optimal size for the lasing threshold, obtained for a 4 µm diameter. We will also show that the angular emission distribution can be tailored by modifying the confined Tamm mode which emits. The experiments presented are performed under optical pumping but the Tamm structures are compatible with an electrical excitation, making these structures promising for new compact laser sources.

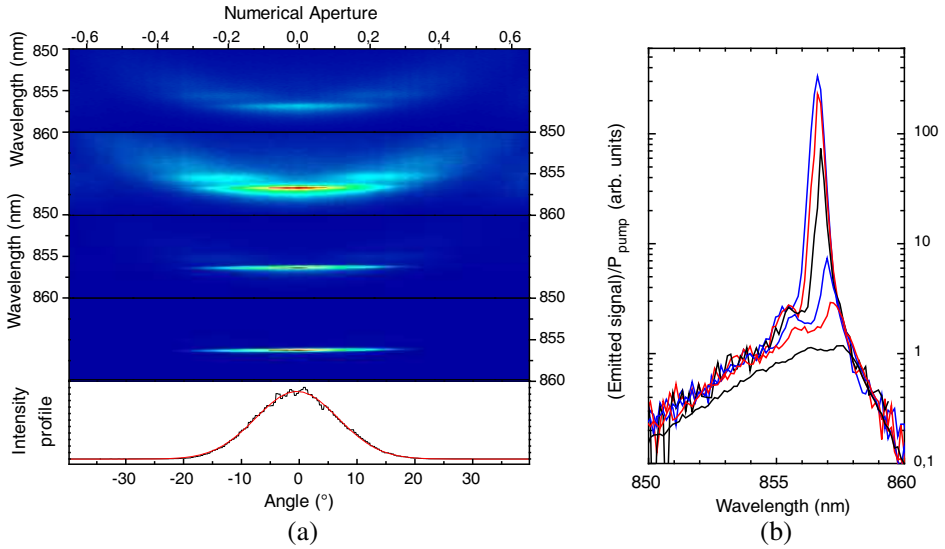

Figure 1: Emission as a function of the wavelength and the numerical aperture for (a) excitation power of 40 mW and (b) total emission.

REFERENCES

1. Symonds, C., A. Lemaître, P. Senellart, M. H. Jomaa, S. Aberra Guebrou, E. Homeyer, G. Brucoli, and J. Bellessa, *Appl. Phys. Lett.*, Vol. 100, 121122, 2012.
2. Gazzano, O., S. Michaelis de Vasconcellos, K. Gauthron, C. Symonds, J. Bloch, P. Voisin, J. Bellessa, A. Lemaître, and P. Senellart, *Phys Rev. Lett.*, Vol. 107, 247402, 2011.

A Quantum Effect in the Classical Limit: Nonequilibrium Tunneling in the Quantum Duffing Oscillator

Alec Maassen Van Den Brink
Research Center for Applied Sciences, Academia Sinica, Taipei, Taiwan

Abstract— The Duffing model is an oscillator with weak near-resonant driving, damping, and nonlinearity, which has often been studied in classical mechanics. For certain parameters, the stationary amplitude and phase of this system bifurcate depending on initial conditions, and vary widely from one stable branch to the other. Due to this sensitivity, the system can be used for constructing detection devices.

In recent years, an implementation using superconducting devices — the so-called Josephson bifurcation amplifier (JBA) — has been successfully used experimentally for superconducting qubit readout. In the experimental literature, the JBA is often taken as classical. However, for e.g., understanding how the stability of the stationary states is modified by tunneling, a proper quantum analysis is necessary. Such tunneling transitions would be an error process from the point of view of detector applications.

One thus has to study dissipative tunneling not between two potential wells, but between the limit cycles of a nonlinear dynamical system. Our numerical data, supported by semi-analytical asymptotic work, point at some intriguing aspects particular to the nonequilibrium setting, including noncommuting classical and low-temperature limits.

Surface Plasmon Interaction with a Gain Medium

A. Castanié, B. Guizal, and D. Felbacq
University of Montpellier 2, France

Abstract— In previous studies, we showed how to decrease the losses inherent to a surface plasmon mode by strongly coupling it to a guided mode. The resulting hybrid mode has a double propagation length. To go further, it is necessary to introduce some gain in the system. Thus, we began with the most naive approach consisting of using media with negative imaginary part of the dielectric constant. This concept has been found to be far from reality, although it gives some limited physical insight. In this work, we develop a more realistic approach, based on Maxwell-Bloch equations that take into account the interaction between light and matter at the quantum level. We used the finite-difference time-domain (FDTD) method, a full wave vector numerical technique that is efficient for directly solving the Maxwell-Bloch system in the time domain. The scheme for this semi-classical model is exposed. Then, several numerical simulations are performed and an analysis of the strong coupling in the structure under study is presented when the gain medium is added.

REFERENCES

1. Bidégaray, B., "Time discretizations for Maxwell-Bloch equations," *Numer. Methods Partial Differential Equations*, Vol. 19, No. 3, 284–300, 2003.
2. Ziolkowski, R. W., J. M. Arnold, and D. M. Gogny, "Ultrafast pulse interactions with two-level atoms," *Phys. Rev. A*, Vol. 52, No. 4, 3082–3094, 1995.
3. Taflove, A. and S. Hagness, *Computational Electrodynamics: The Finite-difference Time-domain Method*, Artech House Inc., Boston, MA, 2000.

Session 1P2a
Extended/Unconventional Electromagnetic Theory, EHD(Electro-hydrodynamics)/EMHD(Electro-magneto-hydrodynamics), and Electro-biology 2

Filtration Properties of a System for the Measurement of Air Ions
Zoltán Szabó, Zdeněk Roubal, Karel Bartušek, ... 84
Hierarchy of Discontinuous Solutions in Plasma Model of Two-fluids
Oleg V. Kravchenko, ... 85
A Comparison of the Dynamic Range of FDNR Building Blocks
Zoltán Szabó, Jirí Sedlácek, Martin Friedl, ... 87
Analysis of Leap-frog Filter in the Programme NAF
Lubomír Frohlich, Jirí Sedlácek, Martin Friedl, Martin Cap, ... 88
Application of the Level Set Method in MR-EIT Inverse Problems
Tomas Kriz, Jarmila Dědková, ... 89
Influence of Initial Conditions on Conductivity Calculation via the MR-EIT Inverse Problem
Tomas Kriz, Jarmila Dědková, ... 90

Filtration Properties of a System for the Measurement of Air Ions

Z. Szabó, **Z. Roubal**, **and K. Bartušek**
Department of Theoretical and Experimental Electrical Engineering
Brno University of Technology, Kolejni 2906/4, Brno 612 00, Czech Republic

Abstract— The measurement of air ion properties and concentration is a topical problem investigated by a large number of research institutes. Detailed medical analyses have proved that negative light ions exhibit a positive effect on human health; conversely, a deficiency of these ions is known to cause fatigue, health problems, and poor work performance.

A significant precondition for the evaluation of these effects consists in determining the concentration, polarity, and mobility spectrum of air ions in the given area.

The measurement of air ion concentration can be realized via a wide variety of methods, including the technique based on the application of an aspiration condenser (AC). This research study presents a methodology for the measurement of air ion concentration using an AC and comprises the formulation of systematic and random errors.

ACKNOWLEDGMENT

The research described in the paper was financially supported by a grant of Czech Ministry of Industry and Trade No. FR-TI1/368, project of the BUT Grant Agency FEKT-S-11-5/1012, and project CZ.1.07.2.3.00.20.0175, Elektro-výzkumník.

REFERENCES

1. Hörrak, U., "Air ion mobility spektrum at a rural area," *Dissertationes Geophysicales Universitatis Tartuensis*, Tartu, 2001.
2. Kondrashova, M. N., E. V. Grigigorreko, A. N. Tikhonov, T. V. Sirota, A. V. Temnov, I. G. Stavrovskaya, N. I. Kosyakova, N. V. Lange, and V. P. Tikonov, "The primary physicochemical mechanism for the beneficia biological/medical effects of negative air ions," *IEEE Trans. Plasma Sci.*, 230–237, 2000.

Hierarchy of Discontinuous Solutions in Plasma Model of Two-fluids

Oleg Kravchenko
Bauman Moscow State Technical University, Moscow, Russia

Abstract— In present work, we continue our earlier investigation and introduce a hierarchy of discontinuous solutions in plasma model of two-fluids both 1D and 2D cases. Such kind discontinuous solutions are related to the problem of generating a quasi-periodic structure of electron clusters [1] and so-called dusty plasma void [2]. Here we consider a system of nonlinear partial differential equations (PDE) in 2D also which is transformed into the one partial differential equation like 2D Burgers equation. Such kind of equation doesn't have an explicit solution that is why it is investigated numerically with help of wavelet Haar method (WHM).

Introduction: We consider the problems of charged jet flow in general form the mathematical point of view. But, the fluid equations are difficult to resolute because of their nonlinearity and mathematical complexity as a result. One of the approaches consists to study the influence of an electric field on a velocity field. Such approach allows to reduce a system of nonlinear PDEs into the one nonlinear Burgers type equation with constant source. Wavelet methods are successfully applied to the numerical investigation Burgers type equation.

Hierarchy of Models Related to Discontinuous Solutions: According to [3], we start from the first simple model

$$\begin{cases} en\vec{E} + \nabla p = 0, \\ \frac{\partial}{\partial t} n + \frac{\partial}{\partial x}(n\vec{v}_e) = 0, \\ \varepsilon_0 \nabla \vec{E} = -4\pi(n_e - n_i). \end{cases} \tag{1}$$

Here $\vec{v}_e = \vec{v}_e(t,x)$, $\vec{E} = \vec{E}(x,t)$ and $n_e = n_e(x,t)$ are unknown functions (characteristics of electron fluid). In the dimensionless variables the following nonlinear equation for the dimensionless electric field can be transformed into the one partial differential of Burgers type equation:

$$\frac{\partial y}{\partial \tau} = \frac{\partial^2 y}{\partial \xi^2} + y\frac{\partial y}{\partial \xi}, \tag{2}$$

where $y(\xi - \gamma\tau) = C_1 \tan(\xi - \gamma\tau) + C_2$ is a discontinuous wave solution of Eq. (2). Then we add $mn\nu(\vec{\nu}_e - \vec{\nu}_i)$ term and consider the following two-fluid model:

$$\begin{cases} en\vec{E} + \nabla p + mn\nu(\vec{\nu}_e - \vec{\nu}_i) = 0, \\ \frac{\partial}{\partial t} n + \frac{\partial}{\partial x}(n\vec{v}_e) = 0, \\ \varepsilon_0 \nabla \vec{E} = -4\pi(n_e - n_i). \end{cases} \tag{3}$$

In [1], was shown that system (3) have the following discontinuous wave solution:

$$y(\xi - \gamma\tau) = \frac{C_1 \mathrm{Ai}'(\xi - \gamma\tau) + C_2 \mathrm{Bi}'(\xi - \gamma\tau)}{C_1 \mathrm{Ai}(\xi - \gamma\tau) + C_2 \mathrm{Bi}(\xi - \gamma\tau)}. \tag{4}$$

Afterwards, we consider more complex model with $mn(\frac{d\vec{\nu}}{dt}) \equiv mn(\frac{d\vec{\nu}}{dt} + \vec{\nu}\frac{d\vec{\nu}}{dx})$ term

$$\begin{cases} mn\left(\frac{d\vec{\nu}}{dt} + \vec{\nu}\frac{d\vec{\nu}}{dx}\right) = en\vec{E} + \nabla p + mn\nu(\vec{\nu}_e - \vec{\nu}_i), \\ \frac{\partial}{\partial t} n + \frac{\partial}{\partial x}(n\vec{v}_e) = 0, \\ \varepsilon_0 \nabla \vec{E} = -4\pi(n_e - n_i), \end{cases} \tag{5}$$

with respect to the discontinuous solution. In general, system (5) does not resolute analytically, so we employ a Wavelet Haar Method [4] as a numerical tool of investigation of the partial differential equations.

REFERENCES

1. Pustovoit, V. I., "Mechanism of lightning discharge," *Journal of Communications Technology and Electronics*, Vol. 51, No. 8, 937–943, 2006.
2. Avinash, K., A. Bhattacharj, and S. Hu, "Nonlinear theory of void formation in colloidal plasma," *Phys. Rev. Lett.*, 2003.

3. Sapogin, V. G., "On compensation of coulomb Interaction of charges by beam's self-consistent field (model of isotermal equilibrium with homogeneous temperature)," *Proceedings 1st IEEE International Conference on Circuits and Systems for Communications*, 408–411, St. Petersburg, Russia, 2002.
4. Kravchenko, O. V. and D. V. Churikov, "Wavelet approximation of discontinuous solutions in EHD model of charged jet flow," *PIERS Proceedings*, 1228–1231, Moscow, Russia, Aug. 19–23, 2012.

A Comparison of the Dynamic Range of FDNR Building Blocks

Z. Szabó, J. Sedláček, and M. Friedl
Department of Theoretical and Experimental Electrical Engineering
Brno University of Technology, Kolejni 2906/4, Brno 612 00, Czech Republic

Abstract— A multitude of various active selective blocks are utilized for the design of active filters based on RLC prototypes. The design of low-pass filters is often realized by means of the Bruton transformation, in which the RLC prototype structure is transformed into an RCD structure. The basic building blocks applied within the latter structure are denoted as dual capacitors (FDNR). These active blocks, realized in various circuit configurations with different numbers of active circuit elements (operational amplifiers, OA), have recently been described by several authors [1, 2].

At present, it is possible to fabricate ARC filters for the frequency range within units of MHz, using simple and economical selective FDNR building blocks that work successfully with one active element (OA). The fabrication is enabled by modern active elements (such as voltage operational amplifiers working in the GBW of approximately 1 GHz or CFA amplifiers applicable up to higher frequencies) and by the synthesis method based on purposefully lossy RLC prototypes [3, 4].

This research report presents a comparison of the dynamic ranges of the most widely utilized lossy FDNR building blocks (types I and V), and the authors intend to employ the proposed comparative outline to help improve the practical exploitation of these capacitors in the process of optimizing active frequency filters.

ACKNOWLEDGMENT

The research described in the paper was financially supported by the grant of the Czech Ministry of Industry and Trade No. FR-TI1/368, project of the BUT Grant Agency FEKT-S-11-5/1012 and project CZ.1.07.2.3.00.20.0175, Elektro-vézkumnk.

REFERENCES

1. Sedláček, J. and Z. Szabó, "A simple economical building FDNR blocks with modern operational amplifiers," *PIERS Proceedings*, 1113–1117, Moscow, Russia, August 18–21, 2009.
2. Sedláček, J., Z. Szabó, and V. Michal, "A non cascade synthesis of optimized ARC filters," *TIEF 2007*, 1–7, UTEE, FEKT VUT v Brně, Paris, 2007, ISBN 978-80-214-3476-9.
3. Hájek, K. and J. Sedláček, "Lossy LC ladder prototypes and their use for arc filter optimization," *WSEAS Transactions on Electronics*, Vol. 2, No. 3, 94–99, July 2005, ISSN 1109-9445.
4. Martinek, P. and T. Daša, "Evolutionary algoritmes by ARC filter synthesis," *ECCTD 05*, 155–159, Cork, 2005.

Analysis of Leap-frog Filter in the Programme NAF

L. Fröhlich, J. Sedláček, M. Friedl, and M. Čáp
FEEC BUT, UTEE, Kolejní 2906/4, Brno 612 00, Czech Republic

Abstract— The method of design of ARC filters with the help of non-cascade realization Leap-Frog, which combines qualities of block realizations and realizations concerning ladder RLC filters, is considerably difficult. The programme for the complete synthesis of these ARC filters was created. This article describes the complete description of the programme NAF. It includes the correct depiction of the set values of RLC filters concerned with required user's parameters. The user's parameters can be for instance filters LP, HP, BP, BR, the type of approximation with or without zero transfers and the kind of filter configuration T or PI. From the following depiction of RLC filters the programme already realizes ARC depiction of Leap-Frog filter, even with certain values of individual elements.

However, the most important part for the design of this programme is the depiction of modular characteristics for already defined outputs of certain filters, with the regard to the following setting of dynamic ratios inside the filter including particular real OAs. With the help of depiction of module characteristics in individual filter outputs, it is not problematic to change norms of particular elements' values so that the individual transfers from the input to the output of the filter would be the same for their maximums.

The programme should serve mainly to bigger use of these circuits in practice, when a user can compare several ARC filter designs designed in different ways and he can judge which of the stated applications would be the most suitable.

ACKNOWLEDGMENT

The research described in the paper was financially supported by grant of Czech ministry of industry and trade no. FR-TI1/001 and projects GACR 102/09/0314, GACR 102/11/0318, and FEKT-S-11-15.

REFERENCES

1. Sedláček, J. and K. Hájek, "Kmitočtové filtry," Vol. 1. vydání, 535 s, BEN — Technická Literatura, Praha, 2002, ISBN 80-7300-023-7.
2. Sedra, A. and K. Martin, "Design of signal-flow graph (SFG) active filters," *IEEE Transactions on Circuits and Systems*, Vol. 25, No. 4, 185–195, 1978.
3. Biolek, D., "Řešíme elektronické obvody," Vol. 1. vydání, 520 s, BEN — Technická Literature, Praha, 2004, ISBN 80-7300-125-X.
4. Hájek, K., "Optimalizovaný návrh filtrů ARC s využitím počıtače," *Habilitační Práce*, Brno, VA, 1994.
5. Sedláček, J., "Optimalizace v syntéze filtrů RLC," *Habilitační Práce*, Brno, VA, 1994.

Application of the Level Set Method in MR-EIT Inverse Problems

T. Kříž and J. Dědková
Department of Theoretical and Experimental Electrical Engineering
Brno University of Technology, Kolejní 4, Brno 612 00, Czech Republic

Abstract— The authors describe the possibilities of utilizing the Level set method for conductivity reconstruction based on techniques used in electrical impedance tomography. Standard electrical tomography exploits voltages measured on the surface of the used samples, to which a current source is connected. Even though an EIT-based method is applied within this study, the authors utilize the values of components of the magnetic flux density measured in the vicinity of samples, to which a direct current source is connected. Conductivity reconstruction is an inverse, non-linear, and very illposed problem. Conductivity reconstructions realized by means of EIT-based deterministic methods are defined as the minimization of the suitably chosen objective function $\Psi(\sigma)$ related to σ. The objective function is most often minimized using the method of the least squares, which converges very quickly. Stability of the minimization process is ensured by means of regularization techniques such as the Tikhonov regularization method or a total variation method. The application of regularization methods consists in the introduction of a regularization term, which is added to the objective function. The objective function for the Tikhonov regularization method is expressed in the following formula:

$$\Psi(\sigma) = \frac{1}{2}\sum \|\mathbf{J}_{\mathrm{M}} - \mathbf{J}_{\mathrm{FEM}}(\sigma)\|^2 + \alpha \|\mathbf{R}\sigma\|^2, \tag{1}$$

where $\mathbf{J}_{\mathrm{M}}$ is the vector of current density obtained from the magnetic flux density components, $\mathbf{J}_{\mathrm{FEM}}$ is the vector of current density obtained via forward solution using the Finite element method, σ is the vector of conductivity on individual elements, and $\mathbf{R}$ is the regularization matrix connecting adjacent elements of different conductivities.

Moreover, the authors of the study analyze the possibilities of implementing the Level set method in the conductivity reconstruction process. The algorithm for computing the reconstruction can be divided into three parts (stages). At the first stage, a regularization method is applied for effecting an approximate distribution of conductivity to facilitate the detection of inhomogeneous regions. Within the second phase, the Level set method is exploited to allow the localization of these regions and their close vicinity, and then, at the third stage, another application of a regularization method is executed (now only for the selected region and in order to locate the resulting conductivity). The study presents the results of conductivity reconstruction for different distributions of inhomogeneities, and the described reconstruction technique is used for the testing of the accuracy and time duration of the solution.

Influence of Initial Conditions on Conductivity Calculation via the MR-EIT Inverse Problem

T. Kříž and J. Dědková
Department of Theoretical and Experimental Electrical Engineering
Brno University of Technology, Kolejní 4, Brno 612 00, Czech Republic

Abstract— The article describes the testing of an algorithm for conductivity reconstruction based on regularization techniques. For the calculation of conductivity in tested samples, the algorithm exploits the measured values of magnetic flux density **B** in the vicinity of these samples. Generally, problems based on electrical impedance tomography are non-linear and ill-posed. The reconstruction process is described as the minimization of the suitably chosen objective function $\Psi(\sigma)$ with respect to σ. The minimization of the objective function is very often realized using the method of least squares. Within standard methods based on electrical impedance tomography, regularization methods are exploited to ensure stability for the iteration process of the reconstruction. If a regularization method is used, the objective function has to be complemented with a regularization term to secure stability of the solution. Application of the Tikhonov regularization method provides the following form of the objective function:

$$\Psi(\sigma) = \frac{1}{2} \sum \|\mathbf{J}_{\mathrm{M}} - \mathbf{J}_{\mathrm{FEM}}(\sigma)\|^2 + \alpha \|\mathbf{R}\sigma\|^2, \tag{1}$$

where $\mathbf{J}_{\mathrm{M}}$ is the vector of current density obtained from the magnetic flux density components, $\mathbf{J}_{\mathrm{FEM}}$ is the vector of current density obtained via forward solution using the Finite element method, σ is the vector of conductivity on individual elements, and $\mathbf{R}$ is the regularization matrix connecting adjacent elements of different conductivities.

In the algorithm for the conductivity image reconstruction, we tested the values of initial conditions that exert significant influence on both the stability of the solution and the accuracy of the resulting conductivity image. The influence of the initial value of regularization parameter α was subject to testing; the initial value was changed within several orders. Moreover, we tested the magnitude of the change of regularization parameter $\Delta\alpha$ during the iteration process. The testing of the conductivity initial value was realized in such a manner that the initial value was selected within several intervals and as a random value on each element. In all the parameters tested, we evaluated the relative error, solution time, and stability of the reconstruction process. The conductivity reconstruction result, the accuracy, the time consumption, and the reconstruction time are presented in the article.

Session 1P2b
Application of EM Field in Medicine and in Ecological Technologies

Analytical Model of Resonant Dryer Textile
Jan Vrba, Marika Pourova, ... 92
Application of EM Field in Medicine
Jan Vrba, ... 93
EM Field and Biological Systems Interactions
Jan Vrba, ... 94
Electromagnetic Applicators for Deep Local Treatment
Jan Vrba, Jr., David Vrba, ... 95
EM Applicators: Apperture and Water Bolus Resonances
David Vrba, Jan Vrba, Jr., ... 96
Lens Applicator for EM Thermotherapy
David Vrba, Jan Vrba, Jr., ... 98

Analytical Model of Resonant Dryer Textile

Jan Vrba and Marika Pourová
Department of Electromagnetic Field, FEL, CTU, Czech Republic

Abstract— In cooperation with Research Institute of Textile Machines Liberec we developed applicator for microwave drying of textile in manufacturing, which is working on the open resonator principle at working frequency 2.45 GHz. In this contribution, we would like to describe our new analytic model of microwave applicator for drying textile. The purpose of the present work is to investigate influence of distribution of the electric field strength on the dielectric properties of textile materials. We have numerical simulation and the analyses of the electric field strength in the plate of textile.

Our new model is created by several cells. Every cell has own magnetron which is source of electromagnetic energy. Magnetron is situated in the waveguide which is ended with funnel. All the cells are placed on one reflective plate.

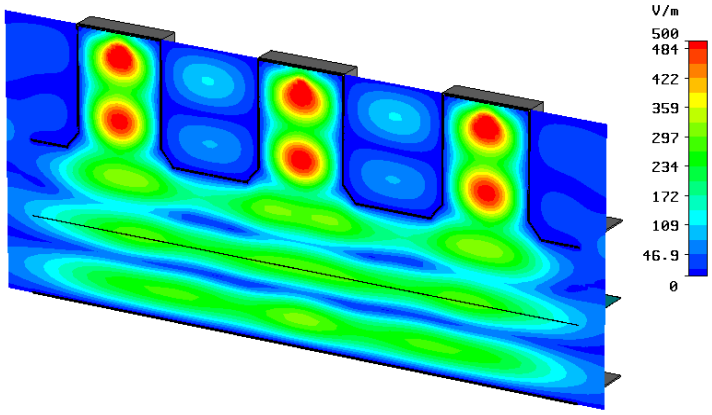

Figure 1: Distribution of electric field strength in applicator.

Conclusions: New results in optimization of microwave textile dryer based on analytical model are described in this paper. These results will enable us to increase efficiency of microwave drying machine.

Application of EM Field in Medicine

J. Vrba
Department of EM Field, Faculty of Electrical Engineering, Czech Technical University
Technická 2, Prague 16627, Czech Republic

Abstract— We would like to describe our new technical results dealing with microwave thermotherapy in the cancer treatment. Our research interest is to develop applicators for deep local heating and for intracavitary cancer treatment as well. Basic evaluation of clinical results is presented.

Deep Local and Regional Applicators: Microwave thermotherapy (hyperthermia) is being used for cancer treatment since early 80's in many countries around the world. Since 1981, we were interested in the local external applicators working at 434 MHz and 2450 MHz. These applicators were used here in Prague for the treatment of more then 500 patients with superficial or subcutaneous tumours (up to the depth of approximately 4 cm). Now, following new trends in this field, we continue our research in two important directions:

- deep local and regional applicators,
- intracavitary applicators.

For the deep local thermotherapy treatment we develop above all waveguide type applicators based on the principle of evanescent mode waveguide, which is our specific solution and original contribution to the theory of microwave hyperthermia applicators. This technology enable us:

- to design applicators with as small aperture as necessary also for the optimum frequency range for deep local and/or for regional thermotherapy treatment (the frequency band between 27 and 70 MHz).
- using our technology we need not to fill the applicator by dielectric (necessary for deep penetration into the biological tissue, i.e., up to 10 centimetres under the body surface).
- two to four of such applicators can be also used for regional treatment.

Waveguide type applicators are often used in the local external hyperthermia treatment of cancer and other modifications of microwave thermotherapy as they offer very advantageous properties, above all:

- depth of penetration of the EM energy approaching the ideal case of plane wave,
- low irradiation of the energy in the vicinity of the hyperthermia apparatus,
- very good impedance matching, i.e. perfect energy transfer to the biological tissue.

We have studied waveguide applicators heating pattern for the aperture excitation at above and at under the cut-off frequency. It has helped us to get analytical approximations of the electromagnetic field distribution in the treated area of the biological tissue. The most important results for the effective heating depth d can be characterised as follows:

- at high frequencies (above approx. 1000 MHz) the depth of effective heating d is above all a function of frequency f (skin effect),
- bellow approx. 100 MHz d is the dominantly function of the diameter D of applicator aperture ($d = 0.386D$).

Clinical Results: In the case of cancer treatment the long term statistics of clinical results can be described as follows:

Complete Response of Tumor ... 53%
Partial Response of the Tumor ... 31%
No Significant Response ... 16%

which corresponds to results obtained also by other groups in Europe.

ACKNOWLEDGMENT

This research is supported by Grant Agency of the Czech Republic, project: "Microwave Imaging for Biomedical Applications" (102/05/0959) and by the research program MSM6840770012 "Transdisciplinary Research in the Area of Biomedical Engineering II" of the CTU in Prague, sponsored by the Ministry of Education, Youth and Sports of the Czech Republic.

EM Field and Biological Systems Interactions

J. Vrba
Department of EM Field, Czech Technical University in Prague, Prague, Czech Republic

Abstract— Research of interactions between EM Field and biological systems is of growing interests elsewhere. Also here in Czech Republic there are several groups working in this field, often in international co-operations. We will describe here mainly basic technical equipment developed for 5 different research projects in the discussed area of interactions of EM field and biological systems.

Electromagnetic Applicators for Deep Local Treatment

Jan Vrba, Jr. and David Vrba
Department of Biomedical Devices, Faculty of Biomedical Engineering
Czech Technical University in Prague, Kladno, Czech Republic

Abstract— Paper deals with our new results in the field of external local applicators used for microwave thermotherapy, like, e.g., cancer treatment, physiotherap, etc..

Introduction: In our contribution we describe external local applicators working at 70, 434 and 2450 MHz see Refs. [1–6]. These applicators were used here in Prague for the treatment of more then 500 cancer patients with superficial or subcutaneous tumors (up to the depth of approximately 8 cm).

Local External Applicators: Waveguide type applicators and various types of horns are often used in the local external hyperthermia treatment of cancer and other modifications of microwave thermotherapy as they offer very advantageous properties, above all:

- depth of penetration of the EM energy approaching the ideal case of plane wave,
- low irradiation of the energy in the vicinity of the hyperthermia apparatus,
- very good impedance matching, i.e., perfect energy transfer to the biological tissue.

We have studied waveguide applicators heating pattern for the aperture excitation at above and at under the cut-off frequency. It has helped us to get analytical approximations of the electromagnetic field distribution in the treated area of the biological tissue. In the Fig. 1, there is one of very important result — diagram showing the theoretical depth of heating d as a function of the used frequency f and of the aperture diameter D of the applicator. The most important results for the effective heating depth d can be characterised as follows:

- at high frequencies (above approx. 1000 MHz) the depth of effective heating d is above all a function of frequency f (skin effect),
- bellow approx. 100 MHz d is the dominantly function of the diameter D of applicator aperture ($d = 0.386D$).

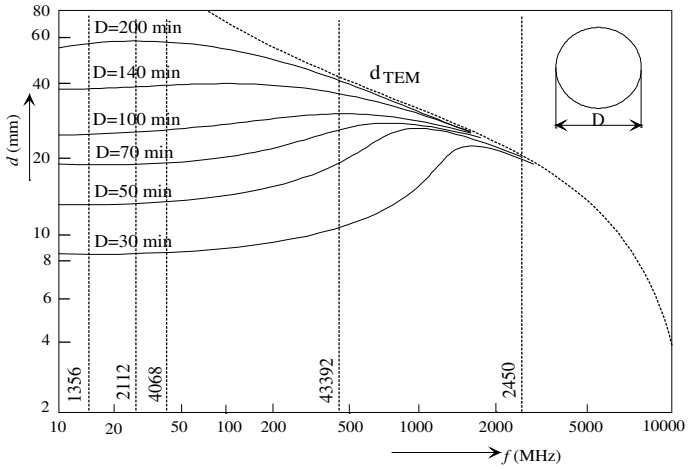

Figure 1: Effective depth of heating d for external applicator with respect to frequency f [MHz] and diameter of aperture D [mm].

Conclusions: Microwave thermotherapy is successfully applied in clinics in the Czech Republic. Technical support is at present from the Czech Technical University in Prague. Our goal for the next technical development is:

- improve the theory of the local and intracavitary applicator design and optimisation,
- innovate the system for the applicator evaluation (mathematical modelling and measurements),
- develop system for regional treatment.

EM Applicators: Apperture and Water Bolus Resonances

David Vrba and Jan Vrba, Jr.
Department of Biomedical Devices, Faculty of Biomedical Engineering
Czech Technical University in Prague, Kladno, Czech Republic

Abstract— Our research interests is to study what happens, when the frequency f of hyperthermia apparatus is either very different (much higher or much lower) from the cut-off frequency f_c of the used waveguide applicator or very near (even equal) to this cut-off frequency f_c. This happen when either the hyperthermia apparatus is tunable in broader frequency range or the cut-off frequency f_c of the applicator is changed by different dielectric parameters of various types of biological tissues near to heated locality.

Let us take into account the area of biological tissue surrounded by electric and magnetic walls. Then the hybrid waveguide mode HE_{11} (i.e., the lowest possible one) can be defined and excited in the biological tissue in front of applicator aperture (it is a linear superposition of the modes TE_{11} and TM_{11}). Higher order modes can be suppressed by the design of the applicator. Following 3 cases describe the change of the SAR in front of the applicator aperture as a function of working frequency f of the hyperthermia apparatus with respect to the f_c:

- if there is enough big difference between f and f_c, then homogeneous heating of the treated area can be expected — see Figs. 1(a) and (b).
- if the both frequencies are very near each to other (difference between f and f_c is going down), then overheating (hot-spots) out of the treated area can arise — see Fig. 2.

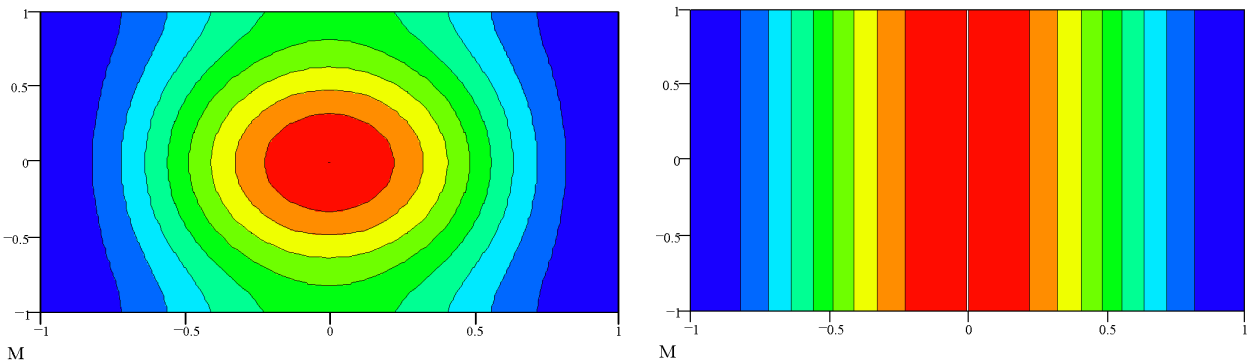

Figure 1: SAR in the aperture of applicator.

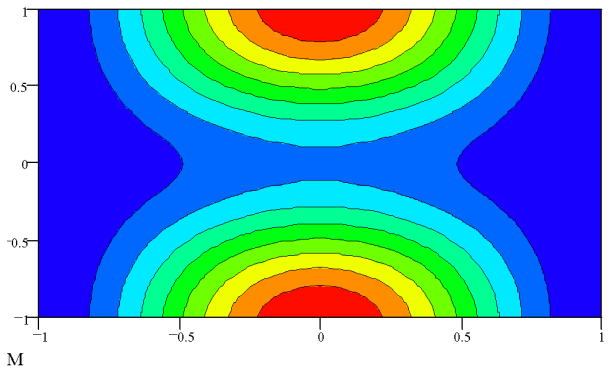

Figure 2: Calculated SAR in the waveguide aperture.

ACKNOWLEDGMENT

This research is supported by Czech Research Programme: "Transdisciplinary Research in the Area of Biomedical Engineering II" and by Grant Agency of the Czech Republic, project: "Microwave Imaging for Biomedical Applications" (102/05/0959).

REFERENCES

1. Franconi, C., J. Vrba, and F. Montecchia, "27 MHz Hybrid evanescent-mode applicator," *Int. J. Hyperthermia*, Vol. 9, No. 5, 655–674, 1993.
2. Vrba, J. and C. Franconi, "Evanescent-mode applicators for subcutaneous hyperthermia," *IEEE Trans. on BME*, Vol. 40, No. 5, 397–407, May 1993.

Lens Applicator for EM Thermotherapy

David Vrba and Jan Vrba, Jr.
Department of Biomedical Devices, Faculty of Biomedical Engineering
Czech Technical University in Prague, Kladno, Czech Republic

Abstract— In this contribution, we would like to describe our new results dealing with waveguide hyperthermia applicators, typically used for cancer treatment. We have designed and evaluated a water filled lens applicator (aperture of a the rectangular waveguide applicator is divided into 3 or 5 sectors with shifted excitation).

We would like to present theoretical model of this applicator, results of numerical modelling and experimetal evaluation as well. Focusing principle of the lens applicator enables to increase the depth of efficient heating in comparison with waveguide applicators.

The basic schematics of the discussed type applicator is shown in the Figure 1. The aperture of lens applicator is divided into 3 or 5 sectors with shifted excitation (i.e., different amplitude and phase). To achieve deep local treatment by aid of this applicator we can thus use a focusing principle.

In our contribution, we will discuss our results with the design of this type applicator and also some first experiments will be presented.

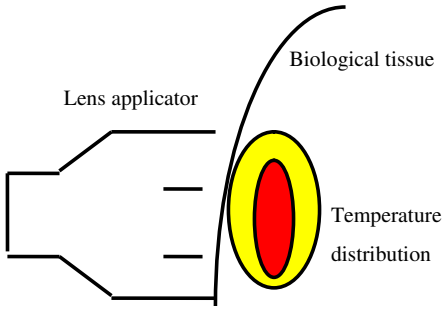

Figure 1.

ACKNOWLEDGMENT

This research is supported by the Grant Agency of the Czech Republic and by the Ministery of Education, Youth and Sport of the Czech Republic.

Session 1P3a
Near-field Engineering, Surface-enhanced Raman Scattering and Their Applications

A Nanotechnology Platform Based on Surface-enhanced Raman Spectroscopy for Rapid Detection of Microbes
Ting-Yu Liu, Huai-Hsien Wang, Kun-Tong Tsai, Yu Chen, Yu-Hsuan Chen, Yuan-Chun Chao, Hsuan-Hao Chang, Yin-Yi Han, Wei-Nan Lian, Chi-Hung Lin, Juen-Kai Wang, Yuh-Lin Wang, .. 100
Manipulating the Optical Properties of Metallic Thin Film with Nanoscale Holes
Jinfeng Zhu, Qing Huo Liu, ... 101
Barcoded Beads Based on Surface-enhanced Raman Scattering for Pathogen Detection
Lai-Kwan Chau, ... 102
Gain-assisted Hybrid-superlens Hyperlens for Nano Imaging
You Zhe Ho, Yao-Ting Wang, Bo Han Cheng, Yung-Chiang Lan, Pi-Gang Luan, Din Ping Tsai, . 103
Electromagnetic Modeling and Simulation for Interconnect Structures Based on Volume-surface Integral Equations
Y. Q. Zhang, M. H. Wei, Y. R. Cao, Y. Q. Wang, Mei Song Tong, ... 104
Fast Fabrication of Plasmonic Nanostructures on AgO_x Thin Film Using Femtosecond Laser-direct Writing
Ming Lun Tseng, Yueh-Hung Cheng, Yao-Wei Huang, Cheng Hung Chu, Chia Min Chang, Dingwei Huang, Hai-Pang Chiang, Greg Sun, Din Ping Tsai, Yu Lim Chen, ... 105
Refractive Index Profiling of Metal-diffused Planar Waveguides Using a Differential Near-field Optical Microscopy
Wan-Shao Tsai, Pei-Kuen Wei, ... 106

A Nanotechnology Platform Based on Surface-enhanced Raman Spectroscopy for Rapid Detection of Microbes

Ting-Yu Liu[1,2], **Huai-Hsien Wang**[1,3], **Kun-Tong Tsai**[1,4], **Yu Chen**[1,5], **Yu-Hsuan Chen**[1], **Yuan-Chun Chao**[1], **Hsuan-Hao Chang**[1], **Yin-Yi Han**[6], **Wei-Nan Lian**[7], **Chi-Hung Lin**[7], **Juen-Kai Wang**[1,8], **and Yuh-Lin Wang**[1,3]

[1]Institute of Atomic and Molecular Sciences, Academia Sinica, Taiwan
[2]Institute of Polymer Science and Engineering, National Taiwan University, Taiwan
[3]Department of Physics, National Taiwan University, Taiwan
[4]Institute of Photonics and Optoelectronics, National Taiwan University, Taiwan
[5]Institute of Clinical Medicine, National Yang-Ming University, Taiwan
[6]Department of Surgery, National Taiwan University Hospital, Taiwan
[7]Institute of Microbiology and Immunology, National Yang-Ming University, Taiwan
[8]Center for Condensed Matter Sciences, National Taiwan University, Taiwan

Abstract— Since the discovery of Raman scattering by Nobel laureate Chandrasekhara V. Raman in 1928, it has been used to measure vibratinal spectra of numerous molecules and to study the structures of molecules and compositions of materials. However, the weak signal of Raman scattering has limited the scope of its applications. We have used highly ordered arrays of closely packed metal (silver or gold) nanoparticles used to enhance the Raman spectral signals of the molecular adsorbed on the surface. This latest development in the so-called surface-enhanced Raman spectroscopy (SERS) greatly increased the possibility of its practical applications in the chemical and biological analysis because of the high reproducibility and uniformity of such SERS substrates. Furthermore, we also demonstrated a dual-function biochip that cannot only effectively capture bacteria in human blood but also enhances the Raman signals of the bacteria, allowing for their analysis by SERS. The core of the biochip is an array of Ag nanoparticles coated by vancomycin, on which bacteria are selectively captured while blood cells are excluded. Our results represent a critical step towards the creation of SERS-based multifunctional biochips for rapid culture- and label-free detection and drug-resistant testing of microorganisms in clinical samples.

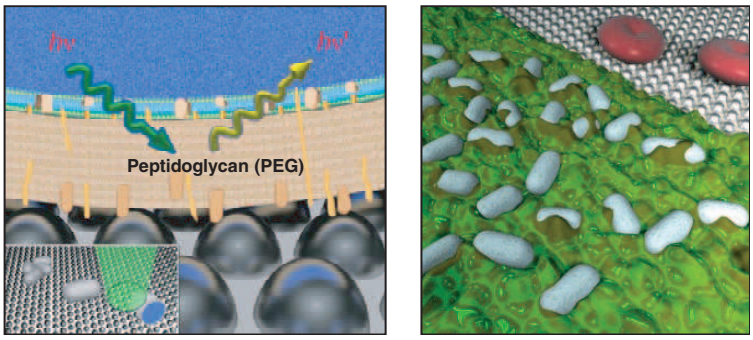

Figure 1: We have demonstrated a dual function biochip that can not only effectively capture bacteria in human blood but also enhances the Raman signals of the bacteria, allowing their analysis by surface enhanced Raman spectroscopy (SERS). The core of the biochip is an array of Ag nanoparticles (silver) coated by vancomycin (green), on which bacteria (white) are selectively captured while blood cells (red) are excluded.

REFERENCES

1. Wang, H. H., C. Y. Liu, S. B. Wu, et al., *Adv. Mater.*, Vol. 18, 491–95, 2006.
2. Liu, T. T., Y. H. Lin, C. S. Hung, et al., *PLOS ONE*, Vol. 4, e5470–79, 2009.
3. Liu, T. Y., K. T. Tsai, H. H. Wang, et al., *Nat. Commun.*, Vol. 2, 538, 2011, doi:10.1038/ncomms1546.
4. Liu, T. Y., Y. Chen, H. H. Wang, et al., *J. Nanosci. Nanotechno.*, Vol. 12, 5004–5008, 2012.
5. Liu, T. Y., H. H. Wang, K. T. Tsai, et al., *Formosan J. Med.*, Vol. 16, 271–83, 2012.

Manipulating the Optical Properties of Metallic Thin Film with Nanoscale Holes

Jinfeng Zhu[1] **and Qing Huo Liu**[2]

[1]Department of Electronic Science, Xiamen University
Xiamen 361005, China
[2]Department of Electrical and Computer Engineering
Duke University, Durham, North Carolina 27708, USA

Abstract— We develop a scalable method to fabricate a metallic thin film with arrayed periodic nanoscale holes by nanosphere lithography and metal evaporation. The optical near-field and far-field properties of the metallic film can be manipulated by tuning the film thickness, hole diameter, and periodicity. Electromagnetic modeling and simulation show that the influence of near-field distribution on optical transmission and reflection. This kind of metallic thin film has the potential as a promising plasmonic nanostructure for flexible and transparent components in optoelectronic devices.

Barcoded Beads Based on Surface-enhanced Raman Scattering for Pathogen Detection

Lai-Kwan Chau
Department of Chemistry and Biochemistry and Center for Nano Bio-Detection
National Chung Cheng University, Chiayi 62102, Taiwan

Abstract— Suspension arrays using barcoded beads have many advantages as compared to planar microarrays which identify each probe by positional encoding. Surface-enhanced Raman scattering (SERS) spectra of molecules adsorbed on noble metal nanoparticles have a great potential to be used as the barcodes for bead-based bioassays. The intensity of SERS can be made comparable to fluorescence. Therefore, the sharp SERS signatures serve as a promising alternative optical marker to replace the broad fluorescence signatures, particularly in multiplex detection, since it is difficult to excite multiple fluorophores with non-overlapping fluorescence bands by a single wavelength. For SERS to reach intensity comparable to fluorescence, strategies to create nanostructures that can generate high electromagnetic field enhancement are usually used. This research employed the following two nanostructures for Raman barcoding schemes: Raman reporter labeled nanoaggregate-embedded beads (NAEB) and Raman reporter labeled gold nanorod-embedded beads (GNREB). For NEAB, because of the incorporation of a "hot" nanoaggregate in each NAEB, SERS signal from a single NAEB can be detected. For GNREB, the longitudinal surface plasmon band of gold nanorod has been estimated to be able to generate at least an order of magnitude stronger localized electric field upon excitation than the isotropic plasmon band of nanospheres. By employing different Raman labeled beads in a sample, multiplex SERS analysis of pathogens is anticipated.

Gain-assisted Hybrid-superlens Hyperlens for Nano Imaging

You Zhe Ho[1], **Yao Ting Wang**[1], **Bo Han Cheng**[5], **Yung-Chiang Lan**[2], **Pi-Gang Luan**[3], **and Din Ping Tsai**[1, 4, 5]

[1]Department of Physics, National Taiwan University, Taipei 10617, Taiwan
[2]Department of Photonics, National Cheng Kung University, Tainan 70101, Taiwan
[3]Department of Optics and Photonics, National Central University, Jhungli 32095, Taiwan
[4]Graduate Institute of Applied Physics, National Taiwan University, Taipei 10617, Taiwan
[5]Research Center for Applied Sciences, Academia Sinica, Taipei 11574, Taiwan

Abstract— In the past ten years, superlens or hyperlens cannot be fabricated without using metallic materials. It always accompanies with significant energy loss when operating at terahertz frequency, even at optical frequency. This disadvantage results in that metamaterials are hardly utilized in practical manner since the throughput of the incident waves is extremely low. In this Letter, we propose an active device named gain-assisted hybrid-superlens hyperlens and demonstrate its super-resolution ability. The structure and material parameters of this device are based on our previous research of hybrid-superlens hyperlens [1]. By doping a dye molecule Coumarin 2 into PMMA, which is a gain medium with absorption wavelength at 365 nm [20–24], it can be made as a thin gain layer. Base on this concept, active hybrid-superlens hyperlens with gain can be designed. The gain medium is analyzed thoroughly using a generic four-level system model, and the permittivity of the gain medium is extracted from this analysis for simulating the imaging characteristics of the device. According to our simulation at wavelength of 365 nm, an excellent resolution power much better than the diffraction limit value can be achieved.

ACKNOWLEDGMENT

The authors acknowledge financial support from National Science Council, Taiwan, under grant numbers 100-2923-M-002-007-MY3, NSC 101-3113-P-002-021- and NSC101-2112-M-002-023-. We are also grateful to the National Center for Theoretical Sciences, Taipei Office, Molecular Imaging Center of National Taiwan University and National Center for High-Performance Computing, Taiwan and Research Center for Applied Sciences, Academia Sinica for their kind support.

REFERENCES

1. Cheng, B. H., Y. Z. Ho, Y. C. Lan, and D. P. Tsai, "Optical hybrid-superlens-hyperlens for superresolution imaging," *IEEE J. Sel. Top. Quantum Electron.*, in press.
2. Fang, A., Th. Koschny, M. Wegener, and C. M. Soukoulis, "Self-consistent calculation of metamaterials with gain," *Phys. Rev. B*, Vol. 79, 241104, 2009.
3. Wuestner, S., A. Pusch, K. L. Tsakmakidis, J. M. Hamm, and O. Hess, "Overcoming losses with gain in a negative refractive index metamaterial," *Phys. Rev. Lett.*, Vol. 105, 127401, 2010.
4. Duarte, F. J. and L. W. Hillman, "Dye laser principles with applications," 1990, See appendix.
5. Somasundaram, G. and A. Ramalingam, "Gain studies of Coumarin 1 dye-doped polymer laser," *J. Lumin.*, Vol. 90, 1, 2000.
6. Zimmerman, H. E., J. H. Penn, and C. W. Carpenter, "Evaluation of single-photon-couting measurements of excited-state lifetimes," *Proc. Natl. Acad. Sci.*, Vol. 79, 2128–2132, USA, 1982.

Electromagnetic Modeling and Simulation for Interconnect Structures Based on Volume-surface Integral Equations

Y. Q. Zhang, M. H. Wei, Y. R. Cao, Y. Q. Wang, and M. S. Tong
Department of Electronic Science and Technology, Tongji University
4800 Cao'an Road, Shanghai 201804, China

Abstract— Electromagnetic (EM) modeling and simulation are crucial for understanding the electrical performance of interconnect structures in microelectronic or nanoelectronic devices. The structures are usually small compared with the wavelength within a certain range of frequency, so extra care is required for achieving a good numerical accuracy. Also, the structures include multiscale features, namely, some dimensions are much smaller than others in geometries, leading to deteriorating the conditioning of system matrix. Moreover, the EM analysis usually requires covering a wide range of frequency with significant low-frequency components, resulting in a perplexity of low-frequency effects. These factors have caused much challenge in numerical implementation and thus choosing appropriate governing equations, robust numerical method, and wise implementation scheme has become essential. Traditionally, the EM modeling for interconnect structures is formulated with surface integral equations (SIEs) in integral equation approach and one has to assume the homogeneity of materials in the dielectric substrate. However, the inhomogeneity of materials could exist due to their impurity in some interconnect structures and the SIEs may not be appropriate for such a case.

In this work, we use the VIEs to replace the SIEs for the substrate and they are coupled with the SIEs for the conductors to form the volume-surface integral equations (VSIEs) for describing the EM features of the interconnect structures. The use of VIEs in the substrate allows the inhomogeneity of materials and may provide more flexibility in the analysis. The VSIEs are usually solved with the MoM in which the Rao-Wilton-Glisson (RWG) basis function is used to expand the surface current on the conductors with a triangular tessellation while the Schaubert-Wilton-Glisson (SWG) basis function is applied to represent the flux density in the substrate with a tetrahedral discretization. To facilitate the implementation, we suggest that the dyadic Green's function be kept in its original form without moving the gradient operator onto the basis and testing functions. We can avoid the inconvenience of conventional implementation in this way though requiring a good treatment for the hypersingularity in the dyadic Green's function. Numerical examples for analyzing typical inhomogeneous interconnect structures are presented to illustrate the approach and good results can be observed.

Fast Fabrication of Plasmonic Nanostructures on AgO_x Thin Film Using Femtosecond Laser-direct Writing

Ming Lun Tseng[1, 2, 3], **Yueh-Hung Cheng**[2], **Yao-Wei Huang**[1, 2], **Cheng Hung Chu**[2], **Chia Min Chang**[4], **Ding-Wei Huang**[4], **Hai-Pang Chiang**[5], **Greg Sun**[6], **Din Ping Tsai**[1, 2, 7], **and Yu Lim Chen**[2]

[1]Graduate Institute of Applied Physics, National Taiwan University, Taipei 106, Taiwan
[2]Department of Physics, National Taiwan University, Taipei 106, Taiwan
[3]Instrument Technology Research Center, National Applied Research Laboratories, Hsinchu 300, Taiwan
[4]Graduate Institute of Photonics and Optoelectronics, National Taiwan University, Taipei 106, Taiwan
[5]Institute of Optoelectronic Sciences, National Taiwan Ocean University, Keelung 202, Taiwan
[6]Department of Physics, University of Massachusetts Boston, MA 02125, USA
[7]Research Center for Applied Sciences, Academia Sinica, Taipei 115, Taiwan

Abstract— The plasmonic hotspots are very useful in various applications such as surface enhanced Raman spectroscopy, cancer therapy, and the photocatalyst. In this paper, we will demonstrate our recent results about using femtosecond laser direct writing technique to efficiently fabricate silver nanostructures as plasmonic substrates. Under focused femtosecond laser illumination, the Ag nanoparticles can be reduced on the sputtered silver oxide (AgO_x) thin film *in situ*. The laser-generated Ag nanostructures exhibit broadband optical absorption over visible light regime and function as SERS-active substrates. We find that the hotspots are uniformly distributed across the laser-fabricated silver nanostructures. Raman enhancements can also be optimized by varying the laser treatment condition. The reported technique is not only more efficient but also simpler than other reported methods (e.g., e-beam lithography and focus-ion beam lithography). This proposed technique has great potential for the fabrication of plasmon-active substrate with high throughput and efficiency.

ACKNOWLEDGMENT

The authors acknowledge financial support from National Science Council, Taiwan under grant numbers 100-2923-M-002-007-MY3, 100-2221-E-002-134, 101-2112-M-002-023-, 101-2911-I-002-107 and 101-3113-P-002-021- respectively. They are also grateful to National Center for Theoretical Sciences, Taipei Office, Molecular Imaging Center of National Taiwan University, National Center for High-Performance Computing, Taiwan, and Research Center for Applied Sciences, Academia Sinica, Taiwan for their support.

REFERENCES

1. Tseng, M. L., et al., "Fast fabrication of Ag nanostructure substrate using the femtosecond laser for broadband and tunable plasmonic enhancements," *ACS Nano*, Vol. 6, No. 6, 5190–5197, 2012.

Refractive Index Profiling of Metal-diffused Planar Waveguides Using a Differential Near-field Optical Microscopy

W.-S. Tsai[1] **and P. K. Wei**[2, 3]

[1]Department of Applied Materials and Optoelectronics Engineering
National Chi-Nan University, Taiwan
[2]Research Center for Applied Sciences, Academia Sinica, Taiwan
[3]Department of Optoelectronics, National Taiwan Ocean University, Taiwan

Abstract— Refractive index profiles of optical waveguides are crucial in determining optical characteristics of integrated optical waveguides, such as guiding mode behaviors, coupling condition, and so on. However, for the metal-diffused optical waveguides, the index profiles were mainly determined by the fabrication process. Therefore, several methods were proposed to determine accurate refractive index profiles of optical waveguides. Secondary ion mass spectrometry (SIMS) measures the concentration distribution of diffused metal ions and reconstructs index profiles indirectly and destructively. Prism coupling method measures the effective indexes of optical waveguides, and obtains index profiles using WKB approximation with measured effective indexes of multimode waveguides. For the nondestructive measurement of single-mode waveguide, guiding mode intensities were measured to relate index profiles with scalar wave equation. Previously, differential near-field optical microscopy (DNSOM) was proposed in measuring the symmetric index profile of an optical fiber, using differential inverse algorithm.

In this work, the DNSOM system was applied to reconstruct the asymmetric index profile of a metal-diffused planar waveguide. The index model of Ti:$LiNbO_3$ waveguides has been determined, however, exact index profile depends on the fabrication process. Therefore, we would like to apply DNSOM system on this waveguide, and compare the results with existing model. The Ti:$LiNbO_3$ planar waveguide was fabricated for single-mode operation at 632.8 nm. Using the differential inverse algorithm, the reconstructed index profile matches well with known index model of Ti:$LiNbO_3$ waveguides. Moreover, guiding mode profile calculated from fitted index model also shows good agreement with measured mode profile. Refractive index profiling of optical waveguides with unknown materials would be of great interests in the future.

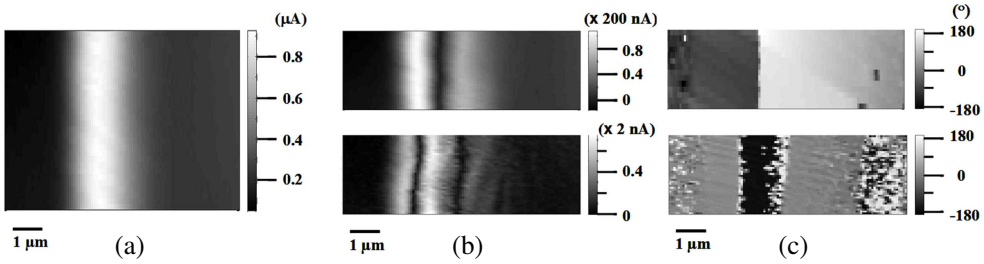

Figure 1: (a) Measured image of output field intensity, I. (b) Measured images of the first-, I', (upper part) and the second-derivative, I'', (lower part) of output field intensity. (c) The phase signals of (b).

Session 1P3b
Wireless Communication, Propagation Prediction

Evaluation of Path Visibility between Base and Mobile Stations in Cellular Communication Systems
Kazuya Iwasaki, Takehiko Kobayashi, ... 108
Interference Cancellation and DOA Estimation by Generalized Receiver Applying LMS and MUSIC Algorithms
Jingui Liu, Modar Safir Shbat, Vyacheslav Tuzlukov, ... 109
Rain Attenuation Prediction Using Frequency Scaling Technique at Tropical Region for Terrestrial Link
Ulaganathen Kesavan, Tharek Bin Abdul Rahman, Mohd Rafiqul Islam, ... 110
New Indoor Propagation Channel Model for Location Purposes
Alain Moretto, Elizabeth Colin, ... 111
Access Point Selection for WLAN Indoor Localization Systems Using RF Walk Test Data
Chamal Sapumohotti, Mohamad Yusoff Alias, Su Wei Tan, ... 112
Reducing the Calibration Effort in WLAN Indoor Localization Systems Using Cluster Analysis of RF Walk Test Data
Chamal Sapumohotti, Mohamad Yusoff Alias, Su Wei Tan, ... 114
Impact of Floor Attenuation Factor on Indoor Localization Accuracy for Multi-floor Environment
Abdulraqeeb Alhammadi, Mohamad Yusoff Alias, Su Wei Tan, ... 115

Evaluation of Path Visibility between Base and Mobile Stations in Cellular Communication Systems

Kazuya Iwasaki and Takehiko Kobayashi
Tokyo Denki University, Japan

Abstract— Radio propagation models for cellular mobile communication depend on line-of-sight (LOS) or non-line-of-sight (NLOS) states between base and mobile stations (BS and MS). An International Telecommunication Union-Radiocommunication Sector report [1] defined probability of LOS (path visibility) formulas in five scenarios — in home, urban micro-cell (UMi), urban macro-cell, suburban macro-cell (SMa), and rural macro-cell — for evaluating the systems proposed for IMT-Advanced. These formulas are the functions of only the distance between BS and MS.

The authors examined the path visibility with a ray tracing simulator and a building database in Japan and the United State. Fig. 1 presents 64 examples computed for a Tokyo metropolitan area (Shinjuku) overwritten against the distance. Wide variation is observed between the visibility curves. In addition, the average curve in Fig. 1 disagrees with the UMi formula given by [1]. While the visibility curves did not necessarily decrease monotonously with the distance, as shown in Fig. 1, these can be modeled by exponential functions ($\exp(d/d_0)$), where d is the distance between BS and MS. The ITU-R formulas also modeled the visibility by $\exp(d/36)$ ($d > 18\,\mathrm{m}$) and $\exp(-(d-10)/200)$ ($d > 10\,\mathrm{m}$) for UMi and SMa, respectively. The values of d_0 were calculated for Shinjuku and Yokosuka (a suburban-residential area near Tokyo), as shown in Fig. 2. The 95% confidence intervals of d_0 were $[110, 810]$ and $[120, 350]$ for Shinjuku and Yokosuka, respectively. These ranges depended on areas, location and height of BS, properties of buildings (area, height, and floor space ratio), and those of roads (width, length, and widings). A single curve, therefore, may fail to represent each scenario, and the ranges of d_0 and other factors affecting d_0 should be considered to predict the path visibility.

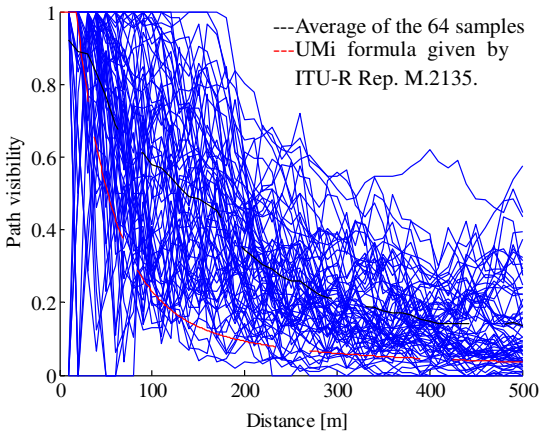

Figure 1: Illustration of 64 examples of path visibility in a metropolitan Tokyo area (Shinjuku).

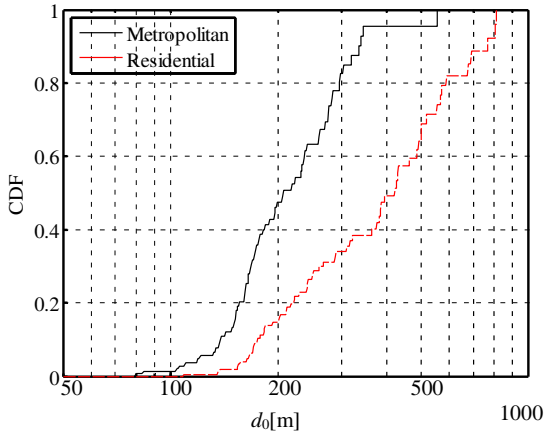

Figure 2: Cumulative distribution function of d_0 derived from a metropolitan and a residential area in Japan.

REFERENCES

1. ITU-R Rep. M.2135, "Guidelines for evaluation of radio interface technologies for IMT-Advanced," 2008.

Interference Cancellation and DOA Estimation by Generalized Receiver Applying LMS and MUSIC Algorithms

Jingui Liu, Modar Safir Shbat, and Vyacheslav Tuzlukov
College of IT Engineering, Kyungpook Natinal University, South Korea

Abstract— Under implementation of the generalized receiver (GR) constructed based on the generalized approach to signal processing (GASP) in noise, an interference cancellation method is to improve the GR performance in the presence of interfering signals. In this paper, an interference cancellation technique based on the non-blind beamfroming algorithm, namely, the least mean square (LMS) algorithm is employed by GR. The direction of arrival (DOA) estimation is also used by LMS algorithm to provide a priori knowledge about the desired signal in GR. The simulation results demonstrate superiority of GR performance and confirm the theoretical analysis.

Subspace algorithms are widely used for direction of arrival (DOA) estimation. For least mean square (LMS) beamforming employed by GR, the multiple signal classification (MUSIC) algorithm can be applied when the DOA of desired signal is unknown. DOA algorithm is applied after the preliminary filter (PF) of the GR to estimate the DOA of desired signal. The DOA information is supplied to the GR model signal generator (GR MSG). Preliminary simulation results for four cases when LMS algorithm is employed by Neyman-Pearson (NP) receiver and GR are presented in Fig. 1 in a form of relation between the input signal-to-noise ratio (SNR) and the output signal-to-interference-noise ratio (SINR) for both receivers. In all cases, the output SINR increases when the input SNR increases and the DOA estimation error decreases. When the input SNR is low, the NP receiver performance is better than GR performance. However, it is not practical case owing to low values of the probability of detection (less than 0.1). In practice, the GR overcomes NP by detection performance applying the LMS algorithm with and without DOA estimation.

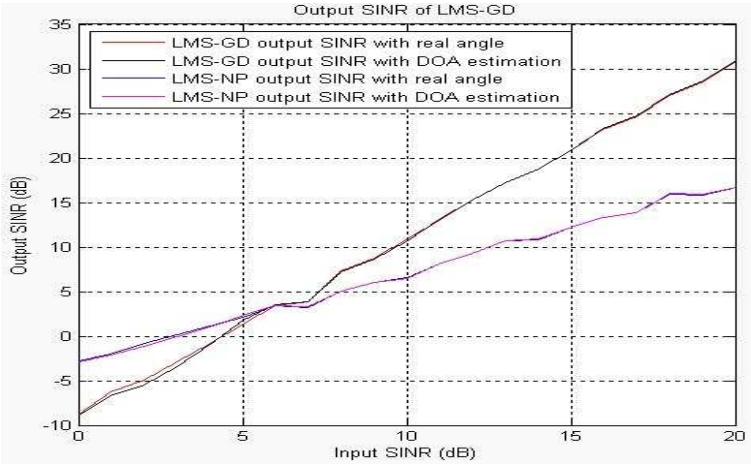

Figure 1.

REFERENCES

1. Tuzlukov, V., "A new approach to signal detection theory," *Digital Signal Processing*, Vol. 8, No. 3, 166–184, 1998.

Rain Attenuation Prediction Using Frequency Scaling Technique at Tropical Region for Terrestrial Link

Ulaganathen Kesavan[1, 2], **A. R. Tharek**[1], **and M. Rafiqul Islam**[3]

[1]Wireless Communication Centre, Fakulti Kejuruteraan Elektrik
Universiti Teknologi Malaysia, Skudai, Johor 81310, Malaysia
[2]Electrical Engineering Department
Sultan Haji Ahmad Shah Polytechnic of Malaysia, Malaysia
[3]Faculty of Engineering, International Islamic University, Malaysia

Abstract— The radio waves propagates through the earth atmosphere will be attenuated due to presence of the atmosphere particles such as water vapor, water drops and the ice particles. Meantime the atmospheric gases and rain will absorb the scatter the radio path consequently degrade the performance of the link. This paper presents studies on rain attenuation at 26 GHz, which is widely used for local multipoint distribution service deployment by using the measured and prediction methods for terrestrial microwave links point to point in tropical regions. Basically the models described in this paper include those of the ITU-R, revised Moupfouma and revised Silva Mello.el model. The objective of these studies is to show the most suitable rain attenuation prediction model for the Malaysian tropical region and comparison in term of attenuation on Ku band and Ka band. Various reduction factor models are also discussed for the particular models being considered. This paper will help provide useful information for researchers to make good considerations in rain attenuation predictions for a terrestrial link operating frequency at 26 GHz in a tropical region by using frequency scaling technique at operating frequency 15 GHz.

New Indoor Propagation Channel Model for Location Purposes

Alain Moretto and Elizabeth Colin
Allianstic, ESIGETEL, Villejuif, France

Abstract— In this paper, we propose a deterministic, close to indoor physical phenomena and hall orientated indoor propagation model for localization purposes. This multi-frequency, multi-path indoor channel model is based on geometrical optics (GO). The received electromagnetic power is given as a function of the carrier frequency, the distance between emitting and receiving antennas, the ceiling height and takes into account both building materials dielectric properties and radiation Rx/Tx antenna's pattern. Received power simulations are compared to measurements with an UHF RFID system using active tags at 868 MHz and 433 MHz in a 20 m long ground floor environment. A good match is noticed.

Access Point Selection for WLAN Indoor Localization Systems Using RF Walk Test Data

C. Sapumohotti, M. Y. Alias, and S. W. Tan
Multimedia University, Malaysia

Abstract— Recent proliferation of Wireless Local Area Network (WLAN) devices presents an opportunity to provide indoor localization by utilizing the unique WLAN beacon received signal strengths (RSS) corresponding to different locations in the map [1]. This method is referred to as location fingerprinting. Location fingerprinting utilizes periodic beacons broadcasted by WLAN Access Point (AP) to client devices. A typical location fingerprinting implementation consists of two phases which are referred to as online phase and offline phase [2]. In the offline phase which is also known as calibration phase, RSS data collected at predefined locations (referred to as calibration points) and the corresponding location information is stored in a database (referred to as radio map). The calibration points are distributed in a uniform grid such that the spacing between adjacent calibration points is constant. In the online phase, the beacon RSS measured in real-time by a client device is compared with the radio map to infer its location. The most costly operation associated with location fingerprinting systems is the offline calibration phase. This phase is non-trivial and requires significant amount of manual labour.

There are several challenges when deploying location fingerprinting systems. For example, there is no reliable method to identify the optimal locations to place APs prior to the calibration phase. Placing APs in non-optimal positions could result in high localization error in the online phase and cause the offline phase to be repeated. Another challenge is associated with the limited processing and communication resources in the client device. This is most significant when there are a large number of APs in the radio map as the computation power required by the localization algorithm increases with the number of AP. In addition, not all APs provide the same localization accuracy and filtering out APs which have a low impact on localization accuracy can reduce the computation and bandwidth requirement of the localization software. There is some work on filtering APs after the calibration phase. For example, *MaxMean* [3] metric and *InfoGain* [4] metric have been proposed for this purpose. However, understanding which APs provide the highest accuracy prior to calibration phase would be helpful in order to verify the long term availability of these APs.

This paper proposes a novel metric referred to as *LocationInfo* for the purpose of quantifying the localization efficacy of APs. First, *LocationInfo* computes an information theory based metric using walk test data. A walk test [5] as the name suggests involves walking through the corridors covered by the radio map while the device automatically collects RSS samples at a periodic scan interval which is in the range of 1 second. Typically this can be completed in a few minutes and is much more trivial compared to an offline calibration phase which takes a few hours. Second, the APs with the highest *LocationInfo* are included in the radio map. Compared to *InfoGain* which is also based on information theory, *LocationInfo* exploits the spatial relationship between adjacent walk test points and is able to include the discriminative ability of ambient APs. Furthermore, *LocationInfo* uses probability distributions to represent the RSS likelihood at each walk test point. The proposed metric is evaluated using simulations. The simulation results show that set of APs selected by *LocationInfo* provides higher localization accuracy compared to *InfoGain* and *MaxMean* metrics.

REFERENCES

1. Bahl, P. and V. N. Padmanabhan, "Radar: An in-building RF-based user location and tracking system," *Proc. IEEE Conf. Comput. Commun.*, 775–784, 2000.
2. Honkavirta, V., T. Perala, S. Ali-Loytty, and R. Piche, "A comparative survey of WLAN location fingerprinting methods," *6th Workshop on Positioning, Navigation and Communication, WPNC*, 243–251, Mar. 19, 2009.
3. Youssef, M. A., A. Agrawala, and A. Udaya Shankar, "WLAN location determination via clustering and probability distributions," *Proceedings of the First IEEE International Conference on Pervasive Computing and Communications, (PerCom)*, 143–150, Mar. 23–26, 2003.
4. Chen, Y., Q. Yang, J. Yin, and X. Chai, "Power-efficient access-point selection for indoor location estimation," *IEEE Transactions on Knowledge and Data Engineering*, Vol. 18, No. 7, 877–888, Jul. 2006.

5. Aragon-Zavala, A., B. Belloul, V. Nikolopoulos, and S. R. Saunders, "Accuracy evaluation analysis for indoor measurement-based radio-wave-propagation predictions," *IEE Proceedings — Microwaves, Antennas and Propagation*, Vol. 153, No. 1, 67–74, Feb. 6, 2006.

Reducing the Calibration Effort in WLAN Indoor Localization Systems Using Cluster Analysis of RF Walk Test Data

Chamal Sapumohotti, Mohamad Yusoff Alias, and Su Wei Tan
Faculty of Engineering, Multimedia University, Jalan Multimedia, Cyberjaya, Selangor 63100, Malaysia

Abstract— The Global Positioning System (GPS) [1] technology has become the de-facto standard for outdoor localization. GPS requires line-of-sight (LOS) between GPS satellites and client device for accurate localization. Unfortunately, GPS is impractical for indoor applications as the direct paths between satellites and the client are obstructed when the client device is located inside buildings. On the other hand, recent proliferation of Wireless Local Area Network (WLAN) devices presents an opportunity to utilize WLAN beacons which are periodically broadcasted by WLAN Access Point (AP) to client devices as a source of location information. This method is referred to as location fingerprinting [2, 3]. A typical location fingerprinting implementation consists of two phases which are referred to as online phase and offline phase [2, 3]. In the offline phase which is also known as calibration phase, RSS data collected at predefined locations (referred to as calibration points) and the corresponding location information is stored in a database (referred to as radio map). The calibration points are distributed in a uniform grid such that the spacing between adjacent calibration points is constant. In the online phase, beacon RSS measured in real-time by a client device is compared with the radio map to infer its location. The most costly operation associated with location fingerprinting systems is the offline calibration phase. This phase is non-trivial and requires significant amount of manual labour depending on the number of calibration points.

The set of AP RSS detected by a client device at any point can be considered as a vector space referred to as the signal space. However, the mapping between a point in physical space to a point in signal space is not entirely deterministic as several factors such as multipath noise, variations in body loss and measurement noise add random variations to the beacon RSS. Therefore, the signal space separation between calibration points is significant in discriminating them from each other. In other words, the inclusion of calibration points which are close to each other in signal space does not increase the localization accuracy of the indoor localization system. However, current approach of radio map construction [2, 3] relies on calibration points which are uniformly spread out in the area covered by the radio map without considering the signal space separation between calibration points. Hence, a significant amount of labour cost is wasted in the calibration phase.

This paper proposes the use of clustering algorithms on radio frequency (RF) walk test [4] data as a solution for identifying these unresolvable calibration points prior to calibration. However, a classical clustering algorithm such as *K-mean* clustering [5] is not appropriate for this purpose due to two reasons. Firstly, the number of clusters is unknown and secondly, the clustering has to take into account not only the signal space proximity, but also the physical space adjacency as well. Therefore, a novel clustering algorithm which is referred to as *Spatial aware Signal Space Clustering* (S3C algorithm) is proposed. This algorithm creates clusters between adjacent physical space points if the corresponding signal space separation is less than a constant referred to as cluster margin which represents the minimum signal space separation which is required to clearly resolve two calibration points. The simulation based study of the S3C algorithm shows that it is able to reduce the labour cost of location fingerprinting systems by removing these unresolvable calibration points while preserving the localization accuracy.

REFERENCES

1. Engee, P. K., "The global positioning system: Signals, measurements and performance," *Int. J. Wireless Inf. Netw.*, Vol. 1, No. 2, 83–105, 1994.
2. Bahl, P. and V. N. Padmanabhan, "RADAR: An in-building RF-based user location and tracking system," *Proc. IEEE Conf. Comput. Commun.*, 775–784, 2000.
3. Honkavirta, V., T. Perala, S. Ali-Loytty, and R. Piche, "A comparative survey of WLAN location fingerprinting methods," *6th Workshop on Positioning, Navigation and Communication, WPNC*, 243–251, Mar. 19, 2009.
4. Aragon-Zavala, A., B. Belloul, V. Nikolopoulos, and S. R. Saunders, "Accuracy evaluation analysis for indoor measurement-based radio-wave-propagation predictions," *IEE Proceedings — Microwaves, Antennas and Propagation*, Vol. 153, No. 1, 67–74, Feb. 6, 2006.
5. Marsland, S., *Machine Learning: An Algorithmic Perspective*, Chapman & Hall/CRC, 2009.

Impact of Floor Attenuation Factor on Indoor Localization Accuracy for Multi-floor Environment

Abdulraqeeb Alhammadi, Mohamad Yusoff Alias, and Tan Su Wei
Faculty of Engineering, Multimedia University, Malaysia

Abstract— Recently, indoor localization techniques that use wireless local area network (WLAN) beacon signals have gained much attention by the research communities [1]. Two important issues in indoor localization technology are high accuracy and reliability. In [2], it has been shown that signals in multi-floor environment could impact the system accuracy [2]. Two main factors that affect the accuracy in multi-floor localization are multipath effect and floor attenuation factor (FAF). Previous works mostly ignored the impact of FAF in location estimation [3].

In this paper, we introduced an experimental test bed in a typical multi-floor building. This experimental test bed consists of two parts. In the first part, FAF is measured at certain points between two floors by collecting received signal strength (RSS) from available access points. Second part, applying a fingerprinting-based localization algorithm which consists of two phases: offline phase and online phase. In the offline phase, calibration points are collected at certain places in both floors to build a radio map. In the online phase, K-Nearest Neighbor (KNN) algorithm is applied to get the correct estimated position of mobile device [4].

We present experimental results that show the impacts of FAF to the estimated position in multi-floor environment. Specifically, the fluctuation of FAF can result in high error rate to the estimated locations.

REFERENCES

1. Bahl, P. and V. N. Padmanabhan, "RADAR: An in-building RF-based user location and tracking system," *IEEE INFOCOM*, 775–784, Tel Aviv, March 26–30, 2000.
2. Pavel, P., K. Martin, and K. Miloš, "Indoor propagation modelling in multi-storey buildings in prague," *Millennium Conference on Antennas & Propagation*, Davos, April 9–14, 2000.
3. Huaiyi, J., G. Jian, and L. Hongqing, "The analysis and research of the radio propagation models in multifloored buildings," *3rd International Symposium on Electromagnetic Compatibility*, 2002.
4. Vahideh, M., D. Andrew, and L. Samsung, "Indoor localization using FM radio signals: A fingerprinting approach," *International Conference on Indoor Positioning and Indoor Navigation (IPIN)*, Sydney, Australia, September 21–23, 2011.

Session 1P4
Advanced Numerical Techniques in Electromagnetics

Electric Fields Radiated from an Electrostatic Discharge Suppressor Filled with Air, Argon, Helium, and Neon
Hsing-Yi Chen, Pei-Kuen Li, ... 118
Real-time Local Capacitance Extraction at Field-solver Accuracy Using Instantiable Basis Functions with Boundary Element Methods
Yu-Chung Hsiao, Luca Daniel, ... 119
An FMBEM for Periodic Transmission Problems Using Müller's Formulation and Nyström's Method
K. Niino, Naoshi Nishimura, ... 120
Analysis of Transient Electromagnetic Fields near Nano Objects by an Integral Equation Method with FILT
Seiya Kishimoto, Shinichiro Ohnuki, Yoshito Ashizawa, Katsuji Nakagawa, Shao Ying Huang, Weng Cho Chew, ... 121
Perturbation-based Electric Field Integral Equation for Low Frequency Capacitive Problems
Sheng Sun, Q. S. Liu, Weng Cho Chew, ... 122
Extension of the Spectral Acceleration Method to Absorptive Medium and Its Application to Electromagnetic Scattering from Rough Surfaces
Yinhui Wang, Yang Du, ... 123
Evaluation of Singular Potential Integrals with Linear Source Distribution
W. T. Sheng, Z. Y. Zhu, G. C. Wan, Mei Song Tong, ... 124
Direct Matrix Solutions of Linear Complexity for Rapid Electromagnetic Analysis of Large-scale Integrated Circuits
Dan Jiao, ... 125
SEM for Huge Enhancement of Second-harmonic Generation in Air-bridge Photonic Crystal Slabs
Ma Luo, Qing Huo Liu, ... 126

Electric Fields Radiated from an Electrostatic Discharge Suppressor Filled with Air, Argon, Helium, and Neon

Hsing-Yi Chen and Pei-Kuen Li
Department of Communications Engineering, Yuan Ze University
135, Yuan-Tung Road, Nei-Li, Chung-Li, Taoyuan Shian 32003, Taiwan

Abstract— An electrostatic discharge (ESD) event may result in a heavy current pulse with fast rise time and short duration time which can damage high sensitivity electronic circuits. In addition, it can also radiate the electromagnetic pulse (EMP) fields to destroy high sensitivity electronic circuits. In this paper, the finite-difference time-domain (FDTD) method was used to calculate the capacitance, ESD current, and radiated electric field for an electrostatic discharge (ESD) suppressor filled with air, argon, helium, and neon. The ESD suppressor contains two major structures of discharge electrodes, a substrate, an overcoat, two backside electrodes, two connect electrodes, and a solder layer. In order to check the validity of the FDTD method, the simulation result of capacitance of the ESD suppressor was validated by measurement data and time-domain moments method (TDMM). After checking the validity of the FDTD method, the FDTD method was used to further studies on the characteristics of the ESD suppressor filled with air, neon, argon, and helium. It is found that only a tiny variation of obtained capacitances for the ESD suppressor filled with air, neon, argon, and helium under the same conditions. But it is also found that the ESD suppressor filled with air has a much higher trigger and clamping voltage than the ESD suppressor filled with neon, argon, or helium. It is also found that the radiated electric field has a maximum value in the spark gap. Outside the spark gap, the maximum radiated electric field is below the breakdown strength, but the magnitude of the radiated electric field resulting from ESD events is still very large as the distance from the ESD suppressor is less than 2 mm.

Real-time Local Capacitance Extraction at Field-solver Accuracy Using Instantiable Basis Functions with Boundary Element Methods

Yu-Chung Hsiao and Luca Daniel
Massachusetts Institute of Technology, USA

Abstract— Traditional capacitance extraction for VLSI interconnects usually involves two steps: 2D scanning decomposition and then a table lookup or calculation through empirical formulas. The first step decomposes 3D geometries into 2D cross-sections, and the second step computes 2D capacitance on each cross-section. This two-step 2D approximation is fast and suitable for whole-chip extraction, but it cannot guarantee the capacitance accuracy to be within a 5% error. For common full 3D geometries, such as partially overlapping wires in two adjacent metal layers and comb capacitors, circuit designers oftentimes need to resort to 3D field solvers for 3D accuracy. Such 3D field solvers are usually several orders of magnitude slower than the aforementioned 2D approximation method. Widely used acceleration techniques, such as fast multipole expansion and pre-corrected FFT, have effectively made boundary element methods capable of handling hundreds of wires within minutes. But for the small-to-medium structures with tens of wires, which is the common size for local full 3D geometries, the extraction time of the accelerated boundary element methods still lies within the range of seconds to minutes. Ideally users would like to have instead sub-second "real-time" capacitance extraction updates when changing geometries and layouts by dragging wires with their mouse.

In this work, we proposed a complete automatic extraction flow from industry-standard GDS2 layout files to capacitance matrices that can meet the sub-second extraction performance within a 5% capacitance error. We utilized our previously proposed instantiable basis functions to replace piecewise constant basis functions as a more efficient charge distribution representation. Instantiable basis functions are the compound shapes of charge distribution that are directly extracted from primitive geometries for being reused in related capacitance extraction problems. By identifying and storing one essential arch shape, we can instantiate virtually all types of basis functions for Manhattan geometries. Using instantiable basis functions also facilitates parallel scalability. We demonstrated an almost linear relationship between parallel efficiency and number of processors in our examples. We achieved sub-second extraction time: 38 milliseconds for an invertor logic gate and 190 milliseconds for an NAND gate extraction, whereas the traditional fast multi-pole acceleration method requires one second and 2.5 seconds respectively to reach the same accuracy. The sub-second extraction performance of our proposed method enables real-time capacitance updates upon users' incremental geometry modification.

Our complete extraction toolkit consists of three parts: i) a series of geometric algorithms that can automatically transform layered polygon information from GDS2 files into instantiable basis functions, ii) a parallelized boundary element field solver implemented in Open MP and MPI that extract capacitance matrices given the generated instantiable basis functions, and iii) a graphical user interface equipped with 3D Open GL rendering of layout geometries. The overall C++ code will be released in the public domain.

An FMBEM for Periodic Transmission Problems Using Müller's Formulation and Nyström's Method

K. Niino and N. Nishimura
Kyoto University, Japan

Abstract— Solution of periodic boundary value problems for Maxwell's equation is of interest in view of various applications in optics, etc. In our previous studies we have developed a periodic Fast Multipole Method (FMM) as a fast solver of transmission problems in periodic domains using the PMCHWT formulation [1]. It has been found, however, that the convergence of the iterative solvers for linear equations slows down in large problems, particularly when the solutions show anomalies related to the periodicity of the problems. We were thus lead to the investigation of remedies using preconditioning schemes based on Calderon's formulae to accelerate convergence of iterative solvers in the periodic FMM for time harmonic wave problems. This approach allows the use of Gram matrix as a preconditioner with a proper ordering of equations, and turned out to be effective in the Helmholtz case [2], even near anomalies. Its extension to Maxwell using MoM [3] is possible with the use of dual basis, but its implementation has so far been not as easy as would be desirable.

In the present study, we investigate a Fast Multipole accelerated Boundary Element Method (FMBEM) using Müller's formulation for Maxwell's equations in periodic domains. This method is expected to reduce the iteration number of iterative solvers because the integral operators associated with Müller's formulation take the form of a sum of the identity operator and a compact operator. We use the Nyström method for the discretisation so that we do not need to use any basis. Through several numerical experiments we conclude that the proposed method is accurate and effective in reducing computational time.

REFERENCES

1. Otani, Y. and N. Nishimura, "A periodic FMM for Maxwell's equations in 3D and its applications to problems related to photonic crystals," *Journal of Computational Physics*, Vol. 227, 4630–4652, 2008.
2. Niino, K. and N. Nishimura, "Preconditioning based on Calderon's formulae for periodic fast multipole methods for Helmholtz' equation," *Journal of Computational Physics*, Vol. 231, 66–81, 2012.
3. Niino, K. and N. Nishimura, "Calderón preconditioning approaches for PMCHWT formulations for Maxwell's equations," *International Journal of Numerical Modelling: Electronic Networks, Devices and Fields*, Vol. 25, 558–572, 2012.

Analysis of Transient Electromagnetic Fields near Nano Objects by an Integral Equation Method with FILT

S. Kishimoto[1], **S. Ohnuki**[1], **Y. Ashizawa**[1], **K. Nakagawa**[1], **S. Y. Huang**[2], **and W. C. Chew**[3]

[1]College of Science and Technology, Nihon University, Japan
[2]Singapore University of Technology and Design, Singapore
[3]University of Illinois, USA

Abstract— For designing plasmonic devices, it is important to analyze electromagnetic problems for nano objects [1]. Using the finite difference time domain (FDTD) method or boundary integral equation method (BIEM), time domain responses of electromagnetic fields for nano particles have been analyzed [1–3]. In this talk, we investigate transient fields near nano objects by using the integral equation method with fast inverse Laplace transform (FILT). As the integral equation, the Poggio-Miller-Chang-Harrigton-Wu-Tsai (PMCHWT) formulation is considered and the formulation is extended in the complex frequency domain. We will show that our novel method has some advantages: (1) the computational error can be fully controlled, (2) arbitrary time increments can be selected, and (3) high parallel efficiency can be obtained.

The time domain response for a nano sphere is computed as shown in Figure 1. Our proposed method can perform a reliable simulation, compared with the exact solution.

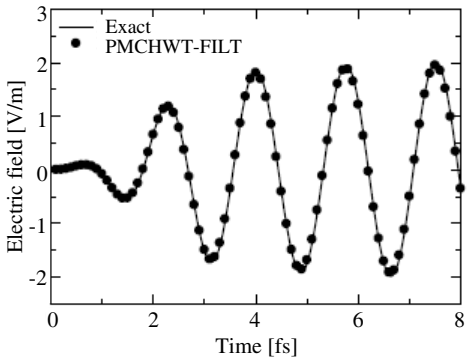

Figure 1: Time domain response for a nano sphere.

REFERENCES

1. Nakagawa, K., Y. Ashizawa, S. Ohnuki, A. Itoh, and A. Tsukamato, "Confined circularly polarized light generated by nano-size aperture for high density all-optical magnetic recording," *J. Appl. Phys.*, Vol. 109, No. 7, 07B735-1–07B735-3, 2011.
2. Mayergoyz, I. D., Z. Zhang, and G. Miano, "Analysis of dynamics of excitation and dephasing of plasmon resonance modes in nanoparticles," *Phys. Rev. Lett.*, Vol. 98, No. 14, 147401-1–147401-4, 2007.
3. Kishimoto, S., S. Ohnuki, Y. Ashizawa, K. Nakagawa, and W. C. Chew, "Time domain analysis of nanoscale electromagnetic problems by a boundary integral equation method with fast inverse laplace transform," *Journal of Electromagnetic Waves and Applications*, Vol. 26, Nos. 8–9, 997–1006, 2012.

Perturbation-based Electric Field Integral Equation for Low Frequency Capacitive Problems

S. Sun[1], **Q. S. Liu**[1], **and W. C. Chew**[1, 2]

[1]Department of Electrical and Electronic Engineering
The University of Hong Kong, Pokfulam Road, Hong Kong, China
[2]Department of Electrical and Computer Engineering
University of Illinois at Urbana-Champaign, Urbana, IL 61801, USA

Abstract— At low frequencies, the electric field integral equation (EFIE) usually breaks down when the Rao-Wilton-Glisson (RWG) basis function is employed. The physical reason is the decoupling between the electric field and magnetic field. In the integral representation of the EFIE, the electric field is decomposed into the vector potential part and the scalar potential part. When the frequency approaches zero, the vector potential part is much smaller than the scalar potential part and its contribution will be lost during the numerical process. Due to the divergence operator, the remaining scalar potential part has a null space, which makes the system matrix extremely ill-conditioned.

In this work, the perturbation method is directly applied on the EFIE. We can observe that the starting term of resultant current is on the order of ω^1. It means that the zeroth-order of the current has been lost during the numerical process in the original EFIE. This will lead to wrong results for plane wave scattering problems. However, for a circuit problem with capacitive surfaces, the leading term of the current is rightly aligned on the same order. Therefore, the low-frequency capacitive current at the first order of frequency can be accurately captured. Moreover, the nullspaces of the divergence operator are carefully studied, where the eigenvectors with small eigenvalue terms are not excited and the convergence of the iterative solution is ensured.

Extension of the Spectral Acceleration Method to Absorptive Medium and Its Application to Electromagnetic Scattering from Rough Surfaces

Yinhui Wang and Yang Du
Department of Information Science and Electronics Engineering
Zhejiang University, Hangzhou 310027, China

Abstract— Electromagnetic scattering from absorptive dielectric rough surfaces with underneath target carries rich information of the target and medium, which can be used for many important ends. The main concerns of conducting the analysis lie in the capability of the proposed numerical approach to be computationally efficient, robust, and able to handle large scale problems. Also since the popular spectral acceleration (SA) technique can deal with both time and storage complexity, it is desirable to extend its applicability to absorptive media as well.

The idea of the spectral acceleration technique is the following: in using the spectral representation of the Green's function which is the Hankel function for one dimensional case, the integration path can be appropriately chosen such that 1) the same path is used for all stationary points to ensure the formulation of the recursive relation critical to the reduction of computational complexity of the matrix-vector product from $O(N^2)$ to $O(N)$; 2) the integrand, — the so called I(phi) function, is well behaved along the integration path; and 3) integration interval and step size are well chosen to ensure accuracy and economy of computation. In the case of absorptive medium, the three requirements cannot be simultaneously fulfilled using the standard spectral acceleration technique.

In the current work we propose a method to identify 1) an appropriate set of integration paths, along each the I(phi) function is well behaved; 2) an proper integration interval which includes almost all the contribution of I(phi); and 3) an integration step size that balances accuracy and computation.

The proposed method has shown to be very accurate through comparison of its predictions of the Green's function against direct computation under different surface roughness conditions and dielectric constants. When applied to the electromagnetic scattering from randomly rough surfaces, the scattering coefficient predictions agrees almost perfectly with that of direct matrix inversion (DMI). The conservation of energy holds very well.

In conclusion, we have proposed a method to extend the spectral acceleration method to the case of absorptive medium, which when combined with highly efficient and robust numerical approaches, allows the analysis of scattering from rough surfaces under realistic settings, and bodes well for a number of important applications such as target detection.

Evaluation of Singular Potential Integrals with Linear Source Distribution

W. T. Sheng, Z. Y. Zhu, G. C. Wan, and M. S. Tong
Department of Electronic Science and Technology, Tongji University
4800 Cao'an Road, Shanghai 201804, China

Abstract— Integral equation method is widely used for solving electromagnetic (EM) problems due to its unique features compared to other approaches. The surface integral equations (SIEs) are preferred whenever available because they require less number of unknowns in the domain discretization. One fundamental problem in the integral equation method is the treatment of singularity or evaluation of singular potential integrals related to the Green's function. In the method of moments (MoM) with Rao-Wilton-Glisson (RWG) basis function for solving the electric field integral equation (EFIE), one needs to handle the $1/R$ weak singularity, where R is the distance between an observation point and a source point. This is because one can move the gradient operator of the integral kernel, which is the dyadic Green's function, onto the basis function and testing function and lower the degree of singularity to facilitate the evaluation.

The $1/R$ weak singularity has been widely studied and many efficient evaluation techniques have been developed. The well-known Duffy's method is the earliest work on this subject and it mainly uses a variable change to produce an extra zero in the Jacobian which can be used to cancel the singularity and regularize the integrand. The resultant integrals are regular and can be accurately evaluated with numerical quadrature rules.

However, the Duffy's method requires a two-fold numerical integration after regularizing the integral kernel and may be inconvenient in implementation. In this work, we develop a novel approach to evaluate the singular potential integrals with a linear source distribution by using a special polar coordinate system. The approach can automatically cancel the singularity without using a variable change or coordinate transform and reduce the integral to a one-fold numerical integration by deriving a closed-form expression for the integral over the polar coordinate. The one-fold numerical integration is for the angular coordinate and has a very simple integrand which can be easily evaluated. Numerical examples for EM scattering by conducting objects are presented to demonstrate the approach and good results can be observed.

Direct Matrix Solutions of Linear Complexity for Rapid Electromagnetic Analysis of Large-scale Integrated Circuits

Dan Jiao
School of Electrical and Computer Engineering, Purdue University
West Lafayette, IN 47907-2035, USA

Abstract— We have developed a linear-complexity inversion and LU factorization algorithm to directly solve the dense system of linear equations resulting from an integral-equation-based analysis of general 3-D circuit problems. The resultant direct integral equation solver outperforms state-of-the-art solvers for circuit extraction, be they direct or iterative solvers, with fast CPU time, modest memory consumption, and with prescribed accuracy satisfied, for both small and large number of unknowns. The inverse of a 2.68-million-unknown matrix arising from the full-wave extraction of a large-scale 3-D interconnect having 128 buses, which is a matrix solution for 2.68 million right-hand sides, was obtained in less than 1.5 GB memory and 1.3 hours on a single CPU running at 3 GHz.

We also develop a direct finite-element solver of linear complexity for solving general 3-D circuit problems. In this solver, we fully take advantage of the sparsity in the original matrix of size N and the reduced fill-ins due to nested dissection ordering. We also organize the overall factorization of a 3-D finite element matrix into a sequence of partial factorizations of dense smaller matrices by the multifrontal algorithm. We then develop fast $\mathcal{H}$-matrix based algorithms to accelerate the computation of all the intermediate dense matrices. The computational complexity of the proposed solver is theoretically analyzed and shown to be $O(N)$ in both time and storage for 3-D circuit analysis. The solvers controlled accuracy is also proved. A comparison with the state-of-the-art direct finite element solver that employs the most advanced sparse matrix solution has shown clear advantages of the proposed linear-complexity direct solver. A finite element matrix involving 4.87 million unknowns arising from a 3-D integrated circuit analysis is factorized in less than 1.7 hours on a single computer running at 3 GHz.

SEM for Huge Enhancement of Second-harmonic Generation in Air-bridge Photonic Crystal Slabs

Ma Luo and Qing Huo Liu
Department of Electrical and Computer Engineering
Duke University, Durham, North Carolina 27708, USA

Abstract— Nonlinear optical effects and the associated second harmonic generation (SHG) have widespread applications. However, as the nonlinear optical coefficients are usually small for most materials, the SHG effect is weak. Moreover, as optical materials are usually dispersive, there is a phase mismatch between the fundamental frequency and second harmonic fields, further weakening the SHG effect. Various design methods have been proposed to enhance the SHG effect, including the use of anisotropic crystal optical materials, some semiconductor materials with relatively large nonlinear optical coefficients, periodic structures to modify the dispersion relation, and microcavity resonant modes to increase the density of states.

In this work, the enhancement of second harmonic generation by a 2D air-bridge photonic crystal slab consisting of GaP is investigated with the three-dimensional spectral element method (SEM), a highly accurate and efficient numerical method for electromagnetic computation [1]. The in-plane band structure is calculated by the SEM, and is compared with the peaks of the second harmonic generation to reveal the mechanisms behind the SHG enhancement. The numerical results show that the scattered power of the second harmonic generation is enhanced for the eigenstates with large decay rates, while the stored energy of the second harmonic generation is enhanced for the eigenstates with a zero decay rate. The second harmonic generation in a photonic crystal slab is enhanced under two conditions, i.e., when there is phase matching and symmetry matching between the field pattern of the resonant eigenstate and the generated second harmonic polarization field. Compared with a uniform GaP slab, the designed air-bridge photonic crystal GaP slab can enhance the second harmonic generation by four orders of magnitude in a single layer. We have further investigated air-bridge multiple layers distributed Bragg reflector consisting of GaAs/AlAs with photonic crystal structure, and found that the SHG can be enhanced by six orders of magnitude. Such huge enhancement of SHG effects can be very useful in various nonlinear optics applications.

REFERENCES

1. Luo, M. and Q. H. Liu, "Enhancement of second harmonic generation in an air-bridge photonic crystal slab: Simulation by spectral element method," *JOSA B*, 2011.

Session 1P5a
Antennas for Wireless Communications

A Novel Square Ring Patch Antenna for GPS Signal Reception
Wen-Shan Chen, Yu-Ching Su, Ke-Ming Lin, Chien-Min Cheng, Yu-Zung Chiou, Chun-Kai Wang, 128
A Multi-arm Coupled-fed Monopole Antenna for WWAN Mobile Systems
Wen-Shan Chen, Bau-Yi Lee, Hung-Ying Lin, Chien-Min Cheng, Shih-Chiang Chiu, Jing-Yen Chen, 129
A Feeding Method for Broadband Microstrip Antenna Using Coaxial Structure
Sotaro Maruyama, Takeshi Fukusako, ... 130
Improving Wireless Power Transfer Efficiency by Using Coil Antenna Arrays for Charging Wireless Communication Devices
Shi Pu, Hon Tat Hui, ... 131
Design of Two-layer Hemispherical Dielectric Resonator Antenna
Xiao Sheng Fang, Kwok Wa Leung, ... 132
A Wideband Circularly Polarized Magneto-electric Dipole Antenna
Kwai Man Luk, Mingjian Li, ... 133

A Novel Square Ring Patch Antenna for GPS Signal Reception

Wen-Shan Chen, Yu-Ching Su, Ke-Ming Lin, Chien-Min Cheng, Yu-Zung Chiou, and Chun-Kai Wang
Southern Taiwan University of Science and Technology, Taiwan, R.O.C.

Abstract— Global satellite positioning system (GPS) coordinate positioning technology, which has advantages of high accuracy, fast, and convenient, is a widely used wireless communication technology for car navigation, navigation guidance, aircraft navigation, as well as military and commercial applications. To precisely indicate the coordinate in the global system, the antennas used in the GPS applications need to possess circularly polarized (CP) radiation patterns. In the paper, we proposed a square ring patch antenna operating the GPS L_1 band (1.57542 GHz). The proposed antenna having a dimensions 56 mm (length) $\times$ 56 mm (width) is fabricated on an FR4 substrate with a thickness of (1.6) mm, a relative permittivity of 4.4, and a loss tangent of 0.024. The square ring patch printed on the top side of the substrate occupies a size $40 \times 40\,\text{mm}^2$ ($L_1 \times W_1$) with a truncated slot of $13 \times 13\,\text{mm}^2$ ($L_2 \times W_2$). The corner feeding mechanism (feed point at diagonal line of the patch) resonate two orthogonal modes. By adding an inverted-L slot (horizontal slot of $L_3 \times W_3$, vertical slot of $L_4 \times W_4$) on ground plane, the CP feature is accomplished through two perturbed antenna currents that has a 90° phase difference. The measured bandwidth based on 10 dB return loss is 40 MHz (1.55 $\sim$ 1.59 GHz) and the simulated 3-dB AR bandwidth is 14 MHz (1.565 $\sim$ 1.579 GHz). With the compact size and good antenna performances, the proposed antenna is suitable for GPS applications. Other results of the proposed antenna will be presented and discussed on the conference.

ACKNOWLEDGMENT

This work was supported by the National Science Council of Taiwan under grant numbers of NSC 101-2632-E-218-001-MY3 and NSC 101-2221-E-218-032.

A Multi-arm Coupled-fed Monopole Antenna for WWAN Mobile Systems

Wen-Shan Chen[1], **Bau-Yi Lee**[2], **Hung-Ying Lin**[1], **Chien-Min Cheng**[1], **Shih-Chiang Chiu**[1], **and Jing-Yen Chen**[1]

[1]Department of Electronic Engineering
Southern Taiwan University of Science and Technology, Tainan City 710, Taiwan
[2]Department of Electrical Engineering
Tung Fang Design University, Kaohsiung City 82941, Taiwan

Abstract— This paper proposes a printed monopole antenna, which is fabricated on a 0.8 mm thick FR-4 substrate for WWAN 5-band application. On one side of the substrate, a monopole patch and a 50 Ω micro-strip feed-line with length of 25 mm are etched. The monopole patch is directed fed by the feed-line and operates a resonant mode at 2.66 GHz. On the other side of the substrate, a coupled-fed monopole with four arms (an L-shaped arm, a left arm, a right arm, and an F-shaped arm) and a ground plane are printed. The coupled-fed monopole is connected to the ground plane through one of the arms (the F-shaped arm). Beside, each arm of the monopole excites its own resonant mode, except one of the arms (the left arm) is used for improving the impedance matching. By adjusting the length of the four arms, the antenna's operating bandwidth based on the 6-dB return loss is from 0.72–1.15 GHz and 1.45–2.2 GHz for GSM 850/900, GSM 1800/1900, and UMTS applications. The overall dimension of the proposed antenna is $60 \times 110 \times 0.8\,\text{mm}^3$ that contains an antenna portion of $60 \times 15\,\text{mm}^2$ and a ground plane of $60 \times 95\,\text{mm}^2$. The proposed antenna having dual wide operating bandwidth and a small size with planar structure are suitable for smart phone handset. This article also provides the studies of measured radiation patterns, antenna gain, and radiation efficiency. Furthermore, the simulated results of antenna SAR obtained by SEMCAD-X are presented and discussed. Both the measured results and antenna SAR demonstrate the reliability of the proposed antenna.

ACKNOWLEDGMENT

This work was supported by the National Science Council of Taiwan under grant numbers of NSC 101-2632-E-218-001-MY3 and NSC 101-2221-E-218-032.

A Feeding Method for Broadband Microstrip Antenna Using Coaxial Structure

S. Maruyama and T. Fukusako
Department of Computer Science & Electrical Engineering, Kumamoto University, Japan

Abstract— A Bandwidth enhancement technique for microstrip antennas using coaxial structure is presented. The proposed method is to extend the outer conductor and inside dielectric substrate of a SMA connector, and a circular flange is mounted on top of the extended outer conductor. The proposed antenna has successfully achieved a simulated S_{11} bandwidth of 37%.

Introduction: Microstrip antenna has several advantages such as low profile and easiness to fabricate, etc., however, the characteristics of conventional microstrip antennas are very narrow. Various techniques to expand the bandwidth have been proposed for microstrip antennas [1, 2]. A new method is proposed in this paper, and it can achieve a simulated S_{11} bandwidth of 37% (4.75 GHz $\sim$ 6.90 GHz).

Antenna Structure: In the proposed feeding method, the outer conductor and the inside dielectric of a SMA connector are extended, and a circular flange is mounted on the top of the extended outer conductor. The propose antenna has a height of 4.8 mm and uses a RT/Duroid 5880 substrate with a permittivity of 2.2 and a dielectric loss of 0.001. The size of the radiate patch is 16.8×16.8 mm and the size of the ground plane is 40×40 mm. Impedance matching is determined by the following three values: the feeding point shifted by 3.0 mm from the center of the patch radiator, the outer conductor extended by 3.2 mm from the ground, and the radius of the mounted circular flange chosen as 4.0 mm.

Simulated Results: The propose antenna is simulated by Ansoft HFSS13.0. A simulated S_{11} bandwidth of 37% and a simulated boresight gain of 7.2 dBi are achieved. The broadband characteristics is occurred because a new resonance due to an inductance by the extended outer conductor and a capacitance between the radiate patch and the mounted flange.

Conclusion: A Bandwidth enhancement technique for microstrip antennas using coaxial structure has been presented. This method has been used in the broadband design of circularly polarized microstrip antenna using artificial ground structure [3], in which this study can also explain the mechanism of the feed structure.

REFERENCES

1. Luk, K. M., "Broadband microstrip patch antenna," *IET Journals & Magazines*, Vol. 34, No. 15, 1442–1443, 1989.
2. Yamashita, T. and M. Taguchi, "Ultra low profile inverted L antenna on a finite conducting plane," *2009 International Symposium on Antennas Propagation*, 361–364, Bangkok, Thailand, October 2009.
3. Nakamura, T. and T. Fukusako, "Broadband design of circularly polarized microstrip patch antenna using artificial ground structure with rectangular unit cells," *IEEE Trans. on Antennas and Propagation*, Vol. 59, No. 6, 3161–3164, Jun. 2011.

Improving Wireless Power Transfer Efficiency by Using Coil Antenna Arrays for Charging Wireless Communication Devices

Shi Pu and Hon Tat Hui
Department of Electrical and Computer Engineering, National University of Singapore, Singapore

Abstract— The conventional method of using cables for charging wireless communication devices such as mobile phones, iPADs, iPhones, laptops, etc., has always been an inconvenience for users, especially in such situations as charging these devices in airports or other stations. In this paper, we propose a method of wireless power transfer (WPT) for charging wireless communication devices efficiently. Different from the previous WPT methods, a new method of using coil antenna arrays in both the transmitter and receiver sides is introduced for wireless power transfer (WPT) employing the technique of mid-range strong magnetic resonant coupling. A two-coil antenna array is designed for the power transmission while another two-coil antenna array is designed for power reception. It is shown that a power transfer efficiency of well over 50% at a transmission separation of 50 cm can be achieved. This efficiency is much higher than the usual case of using only single coils at the transmitter and receiver sides. We will show in details of the design and characterization of the coil antenna arrays for this new method.

Design of Two-layer Hemispherical Dielectric Resonator Antenna

Xiaosheng Fang and Kwok Wa Leung

The State Key Laboratory of Millimeter Waves, Department of Electronic Engineering
City University of Hong Kong, Kowloon, Hong Kong, China

Abstract— The two-layer hemispherical dielectric resonator antenna (DRA) excited in the TE_{111} mode is studied. Its resonance frequency is found rigorously by solving the TE-mode characteristic equation. By using the covariance matrix adaptation evolutionary strategy (CMA-ES), results that determine the outer and inner radii of the two-layer hemispherical DRA are found for the first time. The results are compared with the exact solutions and good agreement is obtained.

A Wideband Circularly Polarized Magneto-electric Dipole Antenna

Kwai Man Luk and Mingjian Li
State Key Laboratory of Millimeter Waves, Department of Electronic Engineering
City University of Hong Kong, Kowloon, Hong Kong SAR, China

Abstract— A wideband circularly polarized antenna based on dual-polarized magneto-electric dipole antenna is proposed. The dual-polarized antenna consists of 4 identical metallic plates, 4 identical rectangular metallic posts and a box-shaped reflector. The plates operate as two pairs of electric dipoles and the posts together with the ground between them perform as two pairs of vertically quarter-wave shorted patch antennas. The combination can be represented by equivalent electric and magnetic currents excited simultaneously. This antenna is excited by two Γ-shaped probes orthogonal orientated in phase quadrature, which is realized by using a power divider and a broadband 90° phase shifter. The proposed antenna was fabricated and measured. It achieves a wide impedance bandwidth of 89.7% from 1.23–3.23 GHz with SWR ≤ 2 which covers the axial-ratio (AR) bandwidth of 81% from 1.28–3.05 GHz with AR $\leq$ 3 dB. In this operation frequency band, the proposed antenna has a broadside gain of larger than 3 dBi above 1.4 GHz. Considering the common overlapped bandwidth limited by the impedance, AR and gain, the proposed antenna exhibits an effective bandwidth of 74.1% from 1.4–3.05 GHz. Over the operating frequency band, the measured radiation pattern has broadside radiation, low cross-polarization and low back lobe.

Session 1P5b
Small Size and Low-profile Antennas

Use of Transparent Dielectric Resonator Antenna as a Light Cover
Xiao Sheng Fang, Kwok Wa Leung, ... 136
A Consideration of Grounded Helical Antenna for Coupled-resonant Wireless Power Transfer
Hiroshi Hirayama, Tomohiro Amano, Nobuyoshi Kikuma, Kunio Sakakibara, ... 137
A Compact Loop Antenna with Parasitic Split Ring for UHF RFID Application
Kittima Lertsakwimarn, Rattapong Suwalak, Chuwong Phongcharoenpanich, ... 138
Compact Size Antenna for Car FM Radio
Dau-Chyrh Chang, Fong-Yi Lin, Bing-Hao Zeng, Jay Chen, ... 139
Triple-band Circularly Polarized Small Microstrip Antenna with Crank Slits
Takafumi Fujimoto, Akinori Tanaka, ... 140
Gain Enhancement of Circularly Polarized Slender Antenna Using a Wider Helical Element
Ye Zhang, Takeshi Fukusako, ... 141
A New Method of Antenna Miniaturization
Li-Yuan Cheng, Fu-Chiarng Chen, ... 142

Use of Transparent Dielectric Resonator Antenna as a Light Cover

Xiaosheng Fang and Kwok Wa Leung
The State Key Laboratory of Millimeter Waves, Department of Electronic Engineering
City University of Hong Kong, Kowloon, Hong Kong, China

Abstract— Today, many modern buildings are equipped with antennas on their ceilings for indoor wireless communications. By using light-cover antenna, installations of the antenna and lighting systems can be done in one go, reducing the overall installation work and cost. Also, since the light-cover antenna simply appears as part of a lighting system, it is especially useful when invisible antennas are required to avoid psychological problems. This paper presents a dualband transparent hollow hemispherical dielectric resonator antenna (DRA) functioning as a light cover. K9 glass was employed to fabricate the DRA. The dualband DRA was simply excited by an aperture, which was fed by a coaxial cable. This feed network can largely reduce the production cost since only an aluminum plate is needed. It was found that the lower band of the antenna covers the IEEE 802.11b WLAN band (2.4–2.48 GHz), whereas its upper band covers the IEEE 802.11a WLAN band (5.15–5.35 GHz). Broadside radiation patterns were observed for both frequency bands, as desired for a dualband antenna. ANSYS HFSS was used to simulate the reflection coefficient, radiation pattern, and gain of the antenna. Measurements were carried out to verify the simulations and reasonable agreement between them is obtained. In studying the light-cover DRA, an LED is placed inside the hollow region of the DRA to serve as the light source. The light-cover DRA with LED was also measured. It was found that the LED has negligible effects on the antenna performance, and therefore it is needless to take it into account when designing the light-cover DRA.

A Consideration of Grounded Helical Antenna for Coupled-resonant Wireless Power Transfer

H. Hirayama, T. Amano, N. Kikuma, and K. Sakakibara
Department of Computer Science and Engineering, Nagoya Institute of Technology, Japan

Abstract— Basic characteristics of grounded helical antenna for coupled-resonant wireless power transfer (CR-WPT) [1] are investigated. Since the CR-WPT transfers power by near-field coupling between transmitting (TX) and receiving (RX) antennas, far-field radiation becomes transmission loss for the WPT system. Grounded helical antenna has an advantage of low radiation loss because it is electrically small antenna. Although the grounded helical antenna has been used for wireless communication systems, detailed investigation is necessary for an application of CR-WPT because it is used in the near-field region. Compared to the balanced helical antenna [2], grounded helical antenna has an advantage that 1) antenna size can be reduced, 2) unbalanced power supply can be directly connected, and 3) ground plane acts as a shield.

At first, we demonstrate transmission efficiency and far-field radiation of grounded helical antenna, whose diameter is 30 cm, height is 10 cm, and working around 10 MHz by using MoM simulation. Next, near electric- and magnetic-field distribution for 1 kW power transmission is investigated to comply with ICNIRP guideline to protect human body. Finally, effect of a ground size on transmission efficiency and radiation power is investigated. Experimental validation is also demonstrated.

ACKNOWLEDGMENT

This work was supported by JSPS KAKENHI Grant-in-Aid for Scientific Research (C) 24560453.

REFERENCES

1. Karalis, A., et al., "Efficient wireless non-radiative mid-range energy transfer," *Annals of Physics*, Vol. 323, 34–48, Apr. 2007.
2. Hirayama, H., et al., "A consideration of open- and short-end type helical antennas for magnetic-coupled resonant wireless power transfer," *Proc. of EuCAP*, Mar. 2012.

A Compact Loop Antenna with Parasitic Split Ring for UHF RFID Application

Kittima Lertsakwimarn, Rattapong Suwalak, and Chuwong Phongcharoenpanich
Faculty of Engineering, King Mongkut's Institute of Technology Ladkrabang
Bangkok 10520, Thailand

Abstract— This paper presents a compact loop antenna with parasitic split ring for the reader of the UHF RFID application. The proposed antenna is made up of the rectangular loop structure (feeding element) and the parasitic split ring to reduce the overall antenna dimension. It is found that the size can be decreased by 50% of the typical single loop antenna. The simulation is carried out by using CST Microwave Studio program based on the Finite Integral Technique (FIT). Furthermore, the antenna parameters are optimized using the Quasi Newton optimization method. The effect of the antenna parameters on the impedance bandwidth are investigated in this paper. The comparison between the simulation and experimental results are also discussed. From the results, the antenna has the $|S_{11}|$ less than -10 dB along the bandwidth of 12 MHz (1.6%). It can be operated in UHF RFID system in Thailand of the frequency band from 920 MHz to 925 MHz. The omnidirectional beam is obtained with the maximum gain of 1.5 dBi at the center frequency of 922.5 MHz. The antenna is designed on FR4-substrate. The overall size of the proposed antenna is $51\,\text{mm} \times 38\,\text{mm} \times 0.8\,\text{mm}$ ($0.15\lambda \times 0.11\lambda \times 0.02\lambda$). It is easily embedded inside handheld reader. Moreover, the proposed antenna is simple structure, low profile and easy fabrication. Therefore, the compact loop antenna with parasitic split ring can be employed with a handheld UHF RFID reader.

Compact Size Antenna for Car FM Radio

Dau-Chyrh Chang[1], **Fong-Yi Lin**[1], **Bing-Hao Zeng**[2], **and Jay Chen**[2]

[1]Oriental Institute of Technology, Taiwan
[2]Lorom Industrial Co. Ltd, Taiwan

Abstract— FM radio is almost required for any kinds of car. From the FCC regulation, the frequency band for FM radio is from 88 MHz to 105 MHz. That means the wavelength the FM car radio is around 3 meters. Due to the car environment, the size of antenna should be as small as possible to reduce the wind resistance when the car is moving. For the size of quarter wavelength monopole antenna for this band is about 75 cm. It is large in length for the car. In order to reduce the size of the monopole antenna, broadside mode helix antenna with height about 20 cm is used for the traditional FM car radio. This paper describes a meander line antenna, which is printed on FR4 with thickness 1.6 mm, is used for car FM radio. The geometry of the car antenna is shown in Figure 1. The part 7 with green color is the printed circuit board FM amplifier. During the simulation, it is the meter sheet and vertical mounted on the ground plane. Figure 2 is the simulation model with the antenna and amplifier mounted on roof of car. Figure 3 is the simulated efficiency of the antenna. Figure 4 is the environment of performance test for the antenna with amplifier and radio receiver mounted on the 1 meter by 1.5 meter ground. The test result shows that there are 38 radio base station are received with good audio quality.

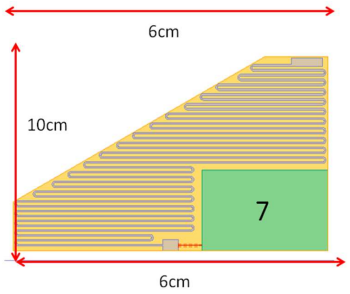

Figure 1: Geometry of meander antenna.

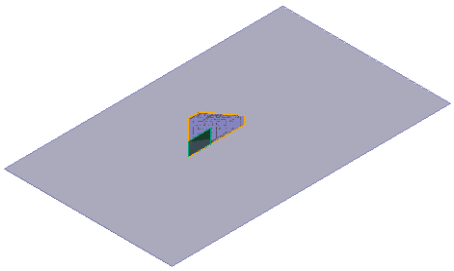

Figure 2: Simulation model with ground plane.

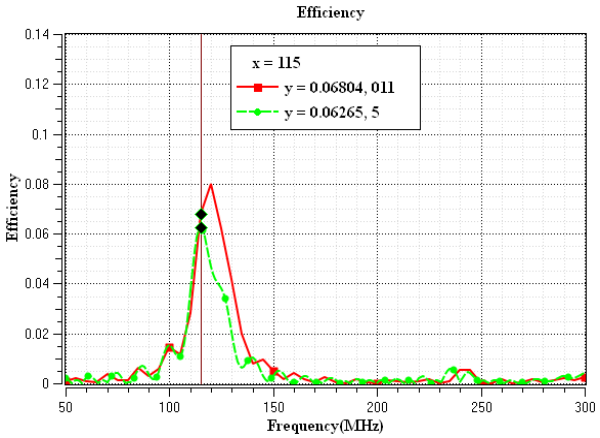

Figure 3: Efficiency of meander antenna.

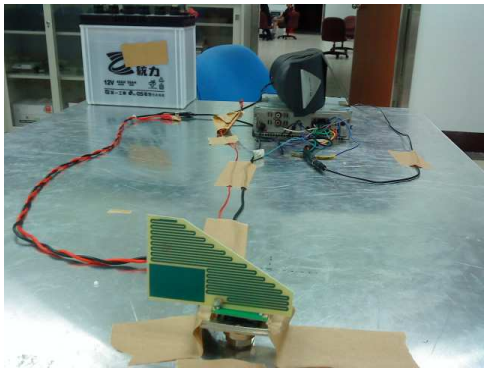

Figure 4: Field test of FM car radio.

Triple-band Circularly Polarized Small Microstrip Antenna with Crank Slits

Takafumi Fujimoto and Akinori Tanaka
Graduate School of Engineering, Nagasaki University, Japan

Abstract— Authors have proposed a triple band circularly polarized small square microstrip antenna (MSA) with two pair of L-shaped slits at each edge [1]. The antenna is excited at the patch conductor by a single coaxial feed through the dielectric substrate at point which lays around the diagonal. In order to radiate circularly polarized waves at the three frequency bands, the dimension and the location of the L-shaped slits along the x-axis are different from those along the y-axis. In [1], the operational principles of the antenna have been clarified by simulation. The simulated axial ratios at the triple band are less than 2.0 dB. The antenna has a good characteristic for circular polarization. However, the frequencies giving the minimum axial ratio cannot be controlled at the triple band. Moreover, the bandwidths of -10 dB return loss with 3 dB axial ratio are very small (less than 1.0 MHz) at the triple band.

In this paper, a novel triple band circularly polarized small square MSA is proposed. The antenna is fed by an L-probe coaxial feed for improvement for bandwidth. Moreover, the shape of L-slits installed at each edge in [1] is changed to a crank shape for enhancement for tunable frequency range. By parametric studies, the design procedure for tuning the frequencies giving the minimum axial ratio at the triple band is obtained. Moreover, the proposed antenna is designed using the design procedure for GPS ($L1$, $L2$, and $L5$ bands). The bandwidths of -10 dB return loss with 3 dB axial ratio at $L1$, $L2$ and $L5$ bands are 6 MHz, 4 MHz, and 4 MHz, respectively. The size of the patch conductor is $0.17\lambda_{L1}$, $0.13\lambda_{L2}$ and $0.11\lambda_{L5}$, respectively (λ_{La}: wavelength at La band). The bandwidth of the proposed antenna satisfies the specification of GPS and is very small in size.

REFERENCES

1. Fujimoto, T. and Y. Tagawa, "Triple band circularly polarized small microstrip antenna," *IEEE International Symposium on Antennas & Propagation*, July 2010, in CD-ROM.

Gain Enhancement of Circularly Polarized Slender Antenna Using a Wider Helical Element

Ye Zhang and Takeshi Fukusako
Department of Computer Science & Electrical Engineering, Kumamoto University, Japan

Abstract— This paper presents a gain enhancement of a small circularly polarized (CP), slender helical antenna with a wider helical line installed in a limited space. The gain of the helical antenna is increased to 0 dBic using a wider element width, which is higher by 6 dB than previous study. The antenna can generate circular polarization in the normal direction to the helical axis. A number of conventional circularly polarized antennas have roughly a square or circular shape for generating two orthogonal, linearly polarized modes of equal amplitude with a phase difference of 90°. The slender sharp antenna is novel and convenient for installation in some devices. The measured and simulated characteristics of the antenna are in good agreement. Furthermore, in order to apply the antenna to small handset devices, the antenna is installed on a large ground plane (60 mm × 40 mm) to discuss the effect of the ground, since the AR is affected by the radiation from both the antenna element and the large ground plane. Such planar and slender shaped antenna is useful to be installed in handsets or used as RFID tags.

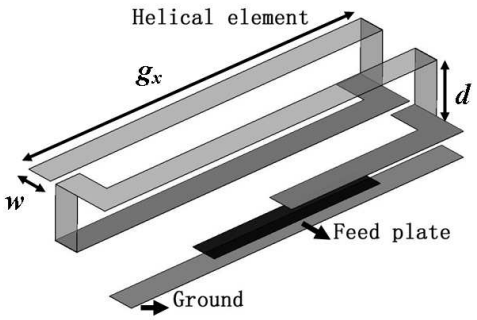

Figure 1: Geometry of the proposed antenna.

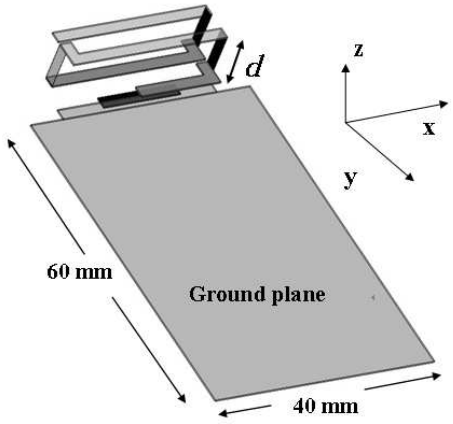

Figure 2: Geometry of the proposed antenna installed on a ground plane with a size of 60 mm × 40 mm.

A New Method of Antenna Miniaturization

Li-Yuan Cheng and Fu-Chiarng Chen
Department of Electrical Engineering, National Chiao Tung University
1001 Tahsueh Rd., Hsinchu 300, Taiwan

Abstract— This paper presents a new method of antenna miniaturization. By adding a properly sized symmetric annular parasitic conductor to a folded dipole, image current can be induced and total radiation length increased. In addition, the annular parasitic conductor with induced current works as a one-wavelength loop antenna and resonates to radiate. Inductive reactance is produced by the structure carrying the closed current loop to compensate for the capacitive dipole antenna at a lower frequency. A large reduction in resonant frequency is attained. A 1.4 GHz printed folded dipole antenna with a meandered side is used as the baseline antenna. This study integrates the baseline antenna with an annular parasitic conductor, achieving a reduction in resonant frequency from 1.4 to 0.87 GHz while maintaining good radiation properties. The study finally examines the effects of the annular parasitic conductor on printed folded dipole antennas and the physical mechanisms and principles that cause the resonant frequency drop.

Session 2A1
Manipulating Wave with Metamaterials and Photonic Crystal 1

Transformation Bending Device Emulated by Graded-index Waveguide
Y. Wang, C. Sheng, Hui Liu, Y. J. Zheng, Cong Zhu, S. M. Wang, S. N. Zhu, ... 144

Resonantly Confined Modes in Optical Fibers with Circularly Aligned High-index Rods
Yasuo Ohtera, Haruka Hirose, Hirohito Yamada, ... 146

Manipulating Electromagnetic Waves in Subwavelength Dimensions by Meta-atoms
Bo Hou, Sucheng Li, ... 147

Terahertz Metamaterial Absorbers for Sensing and Imaging
Patrick Kung, Seongsin Margaret Kim, ... 148

Anisotropic Guidance Correction on the Analytical Design Approach of Thin-film Photonic Lüneburg Lens
Hanhong Gao, Baile Zhang, George Barbastathis, ... 149

Operational Slow Line Underpinned by a 1D Metamaterial
Darell Dowlet, Thierry Ditchi, Emmanuel Geron, Jerome Lucas, ... 150

An Optimized Design of Cylindrical Acoustic Cloak with Two-phase Isotropic Layered Composites
Chung-Ning Weng, W. H. Chung, Tungyang Chen, ... 151

Energy Sinks in Optics of Metamaterials: Fundamentals and Applications
Vasily V. Klimov, ... 152

Engineering Transmission and Group Delay in Active Plasmonic Waveguide with Slightly Detuned Resonators
Jian-Wen Dong, Zi-Lan Deng, Jensen Li, ... 153

Flat Dispersion Eigenmode Drives Perfect Imaging in DNG Slab
Gilad Rosenblatt, G. Bartal, Meir Orenstein, ... 154

Transformation Bending Device Emulated by Graded-index Waveguide

Y. Wang, C. Sheng, H. Liu, Y. J. Zheng, C. Zhu, S. M. Wang, and S. N. Zhu
National Laboratory of Solid State Microstructures
Department of Physics, Nanjing University, Nanjing 210093, China

Abstract— We demonstrate that a transformation device can be emulated using a gradient-index waveguide. The effective index of the waveguide is spatially varied by tailoring a gradient thickness dielectric waveguide. Based on this technology, we demonstrate a transformation device guiding visible light around a sharp corner, with low scattering loss and reflection loss. The experimental results are in good agreement with the numerical results.

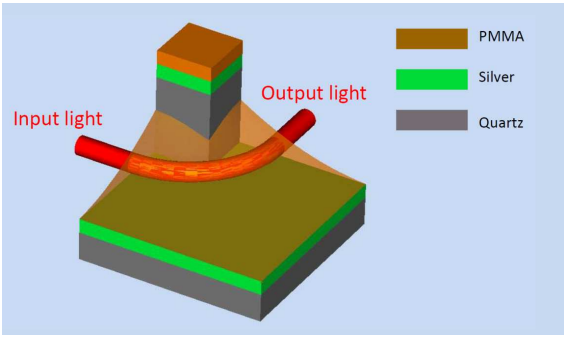

Figure 1: Schematic picture of graded-index waveguide around a right-angled corner.

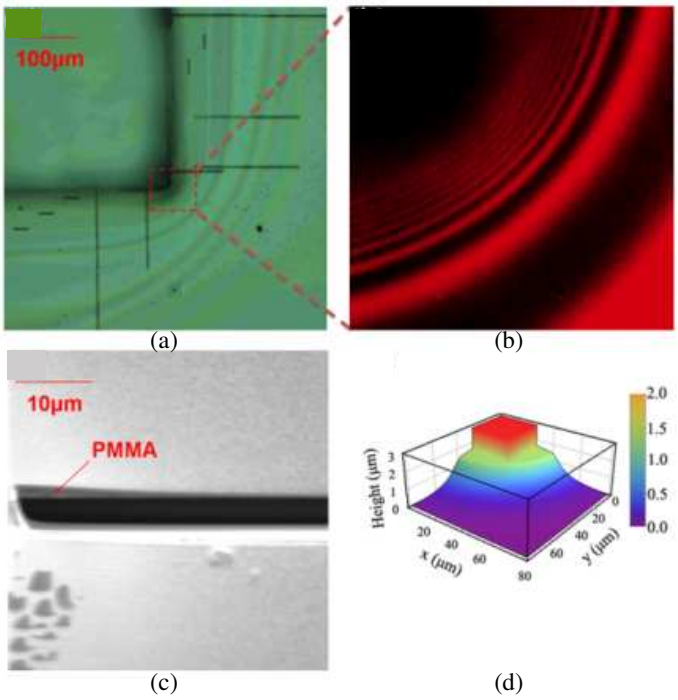

Figure 2: Microscopy interference pattern of the sample illuminated (a) by white light and (b) by a laser at 633 nm; (c) FIB image of a cross-section near the sharp corner; (d) thickness profile around the corner retrieved from (b) and (c).

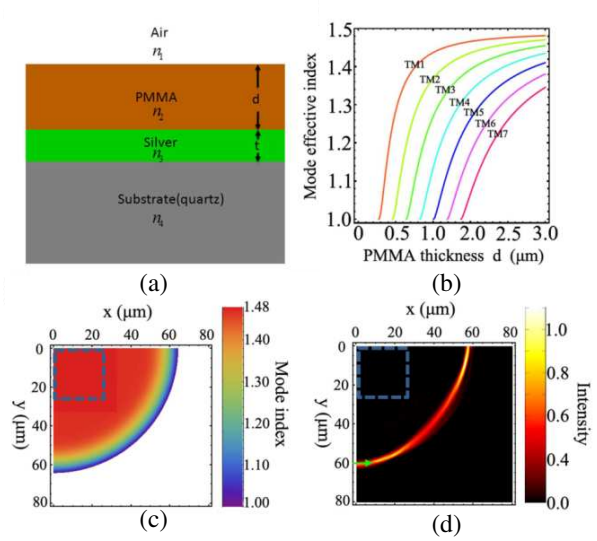

Figure 3: (a) Schematic picture of waveguide; (b) thickness dependence of effective mode index; (c) effective mode index profile of the structure; (d) numerical simulation results of light propagating around the corner.

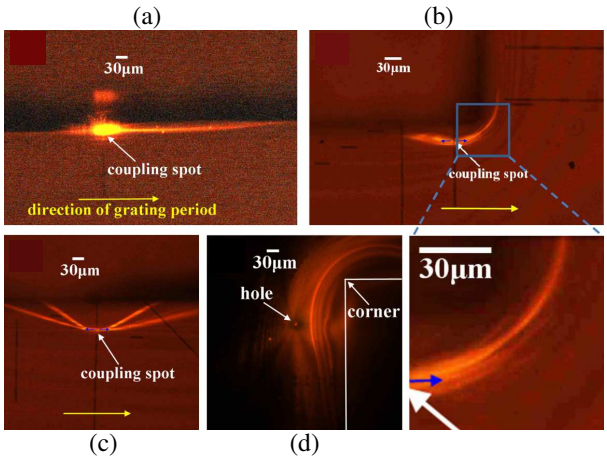

Figure 4: Fluorescence image of light propagation in the waveguide. (a) Light propagation along the boundary of waveguide; (b) light bending around the sharp corner; (c) mode splitting in thick waveguide; (d) radiation of a point source around the sharp corner; (e) magnified bending area taken from the frame in (b).

REFERENCES

1. Wang, Y., C. Sheng, H. Liu, Y. J. Zheng, C. Zhu, S. M. Wang, and S. N. Zhu, "Transformation bending device emulated by graded-index waveguide," *Optics Express*, Vol. 20, 13006, 2012.

Resonantly Confined Modes in Optical Fibers with Circularly Aligned High-index Rods

Yasuo Ohtera, Haruka Hirose, and Hirohito Yamada
Department of Communication Engineering, Graduate School of Engineering
Tohoku University, Japan

Abstract— Optical fiber-based sensing has become a key technology in a number of industrial fields due to its robustness to electromagnetic noise, low power consumption and multi-point detection capability. To improve the system's sensitivity it is straightforward to sharpen the wavelength dependence of the propagation characteristics (loss, etc.) of the fibers used. In this paper, we demonstrate that a class of optical fibers having an array of high-index rods can support highly wavelength dependent propagation modes. Fig. 1 shows a schematic view of the fiber structure. High index rods are circularly arranged with a constant azimuthal pitch. This rod array is a curved version of sub-wavelength grating [1], and exhibits guided-mode resonance (GMR [2]) for radial component of propagating wave in the fiber. Owing to the high reflectivity at GMR wavelength, fields are confined and guided along the center region of the fiber. As the resonance condition is highly wavelength dependent, the propagation loss rapidly changes along with the detuning from the resonance wavelength. Fig. 2 shows a dispersion relation and mode field profiles of a resonantly confined modes (RGM, marked by "A"), and ordinary index-guided mode (IGM, marked by B). All the calculation was carried out using compact 2-D FDTD method [3]. Field profiles clearly show the feature of GMR: azimuthal standing wave pattern is formed along the high-index rod array. According to the calculation of temporal decay rate of each mode, the RGMs were found to have loss minima at a specific wavelength whereas IGMs have no such characteristics. The existence of such minima implies the RGM's potential usefulness as a sensing probe, which detects environmental fluctuation via the change of propagation loss.

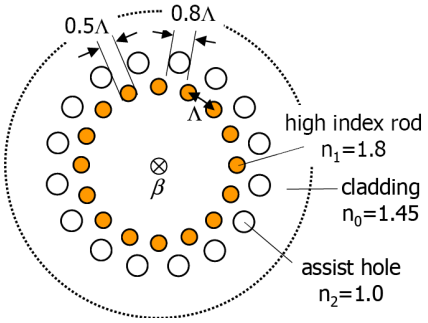

Figure 1: Index profile of the cross section.

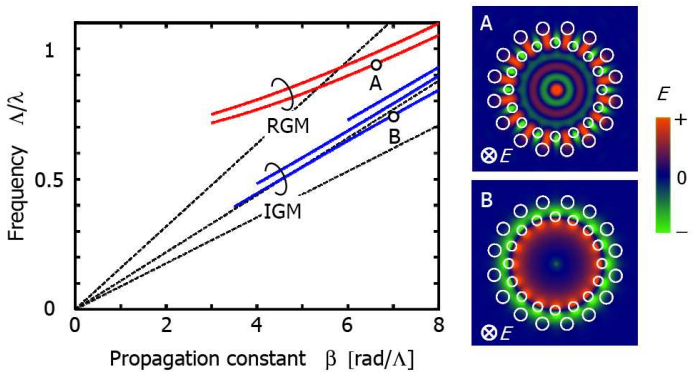

Figure 2: Dispersion relation and modal field profiles of typical Resonantly Guided Modes (RGMs) and Index Guided Modes (IGMs), respectively.

ACKNOWLEDGMENT

This work has been supported by JSPS KAKENHI Grant Number 24656041.

REFERENCES

1. Ohtera, Y., S. Iijima, and H. Yamada, *Micromachines*, Vol. 3, No. 1, 101–113, 2012.
2. Wang, S. S. and R. Magnusson, *Appl. Opt.*, Vol. 32, No. 14, 2606–2613, 1993.
3. Xiao, S. and R. Vahldieck, *IEEE Microwave Guided Wave Lett.*, Vol. 3, No. 5, 127–129, 1993.

Manipulating Electromagnetic Waves in Subwavelength Dimensions by Meta-atoms

Bo Hou and Sucheng Li
School of Physical Science and Technology, Soochow University
1 Shizi Street, Suzhou 215006, China

Abstract— In this study, we demonstrate a type of structured metallic units, three-dimensional H-fractals, in the microwave regime can behave like plasmonic spheres in optical frequencies. The underlying physics lies in these fractal units support the long wavelength electromagnetic resonances on their electrically small structure, which is revealed by our investigation on the scattering property of the single unit. By assembling them into a chain, we show that the microwave can be guided along the chain with the transverse confinement below the diffraction limit, and the low-loss propagation constant. Both longitudinal and transverse mode can be excited on the chain, respectively, via orienting these anisotropic meta-atoms. We conclude that these meta-atoms are able to mimic localized plasmons at low frequencies, and may pave a new way of manipulating electromagnetic waves in subwavelength dimensions.

Terahertz Metamaterial Absorbers for Sensing and Imaging

P. Kung and S. M. Kim
Department of Electrical and Computer Engineering, The University of Alabama, Tuscaloosa, USA

Abstract— The development of devices and structures with functionality in the terahertz (THz) portion of the electromagnetic spectrum is of great interest because of potential applications in sensing and imaging in the THz, including molecular spectroscopy and medical imaging. One of such devices is a THz absorber that has the ability to absorb THz radiation with specific characteristics, including polarization, bandwidth, or multiband capability.

In this work, we present the design, finite-element simulation and characterization of thin, tunable, polarization insensitive metamaterial THz absorbers and develop a corresponding electrical model for their absorption properties. We further propose a novel metamaterial structure with a broadened bandwidth of absorption in the THz and with a little concurrent decrease in absorption strength. This concept is based on multiple band absorption and is achieved by bringing absorption bands close enough to one another in a multi-layered pattern, which decreases the negative interaction between rings and corresponding resonances. Physically, the structure consists of multilayer concentric copper rings, interspaced with polyimide as the dielectric and a final copper plane to reflect selected frequencies back into the absorbing layered rings. These rings are tightly stacked in order to reduce their destructive interaction compared to when the rings are all placed on the same plane normal to the incident wave. The periodic absorber structures are fabricated using lift-off photolithography and their characteristics measured in a THz time domain spectrometer that provides a broad THz emission band. The absorption spectra obtained are shown to be in good agreement with the design and simulation results.

Anisotropic Guidance Correction on the Analytical Design Approach of Thin-film Photonic Lüneburg Lens

Hanhong Gao[1], **Baile Zhang**[2, 3], **and George Barbastathis**[3, 4]

[1]Department of Electrical Engineering and Computer Science
Massachusetts Institute of Technology, Cambridge, MA, USA
[2]Division of Physics and Applied Physics, School of Physical and Mathematical Sciences
Nanyang Technological University, Singapore
[3]Singapore-MIT Alliance for Research and Technology (SMART) Centre, Singapore
[4]Department of Mechanical Engineering, Massachusetts Institute of Technology, Cambridge, MA, USA

Abstract— GRadient INdex (GRIN) media such as the Lüneburg lens, provide rich opportunities for light manipulation. In our recent paper [1], an all-analytical method has been proposed to account for the thin-film effect existing in most nanostructured optical devices, and an aperiodic thin-film metamaterial Lüneburg lens has been designed accordingly. This approach calculates the effective refractive index of each unit cell from waveguide dispersion relation, assuming that the finiteCheight aperiodic lattice layer can be replaced by a certain continuum isotropic medium. This assumption is perfectly fine for transverse magnetic (TM) mode, where the electric field is always parallel to the interfaces of the effective waveguide; however, for transverse electric (TE) mode, the electric field is no longer fixed at the perpendicular direction, but instead varying when the light bounces back-and-forth between the two waveguide interfaces. Since electric field sees different structures (thus different effective permittivities) along parallel and perpendicular directions, this effective continuum medium should be anisotropic, at least for TE mode.

Here we developed an anisotropic guidance condition correction to improve the design of nanostructured GRIN lenses. Since the effective medium for thin-film nanostructure layer is now anisotropic, we first calculate analytically the effective permittivities parallel and perpendicular to the waveguide interfaces, noting that the optical axis of this effective birefringent layer is perpendicular to the interface. Then the guidance condition for anisotropic asymmetric waveguides was derived. We used it to calculate a new effective index of unit cell based on the corresponding anisotropic waveguide dispersion relation. Results show that the effective refractive index curves estimated with this anisotropic correction agree better with rigorous numerical results. Also, the performance of corrected Lüneburg lens has been compared with the original design, and verified with 3D finite-difference time-domain (FDTD) method.

ACKNOWLEDGMENT

This work is supported by Singapore's National Research Foundation through the Singapore-MIT Alliance for Research and Technology (SMART) Centre and the Air Force Office of Scientific Research MURI program on Nanomembranes under contract No. FA9550-08-1-0379. The authors thank Lei Tian for useful discussions and Justin W. Lee for setting up the computation server.

REFERENCES

1. *Opt. Express*, Vol. 20, 1617, 2012.

Operational Slow Line Underpinned by a 1D Metamaterial

D. Dowlett, **T. Ditchi**, **E. Géron**, **and J. Lucas**
Laboratoire de Physique et d'Étude des Matériaux, ESPCI-ParisTech
UPMC Univ. Paris 06, CNRS UMR8213, 10, Rue Vauquelin, Paris 75005, France

Abstract— Many hyper frequencies applications require slow lines. They can be used as delay lines, for data buffering, or to increase interactions between the electromagnetic wave and matter by increasing the interaction time as in electro-optic applications [1]. There are two ways to obtain a significant delay using a line. Whether a long line is used or it is possible to use shorter lines if the electromagnetic velocity is significantly smaller. In some radar applications, the required delays are very large. They imply such length that they are realized using optical fibers.

Without dispersion, the only way to obtain a slow velocity in a line or a material consists in using high dielectric constant material. Unfortunately only small velocity reduction can be obtained this way. It is possible though to obtain large velocity reduction by taking advantage of dispersion. Many applications are not wide band and can therefore withstand smaller bandwidth. It is possible to obtain a significant velocity reduction when the line or material is resonant over the considered bandwidth. Many works based on this effect have been carried out recently [2]. In this paper, we propose to use the properties of some metamaterial lines to obtain the same result.

In this work, we demonstrate how to calculate the required gain to obtain a given group velocity reduction using the Kramers-Kronig relations [3] and how it applies to 1D metamaterial lines. The design of the line is then checked using a circuit simulation software that only can take into account some internal propagation phenomena. At this point, the losses in both substrate and lumped components as well as impedance matching with the standard $50\,\Omega$ lines are taken into account.

Finally the results obtained with a prototype are presented. The usability of such a system to obtain large delays is verified and discussed focusing on ability to transmit data over such lines.

REFERENCES

1. *Optics Express*, Vol. 16, No. 6, 4177–4191, 2008.
2. *Nature Photonics*, Vol. 2, No. 8, 2008.
3. *AIP Advances*, Vol. 2, 032144-1, 2012.

An Optimized Design of Cylindrical Acoustic Cloak with Two-phase Isotropic Layered Composites

C. N. Weng, **W. H. Chung**, **and T. Chen**
Department of Civil Engineering, National Cheng Kung University, Tainan, Taiwan

Abstract— Acoustic cloaks designed by transformation techniques, as an analog of invisibility cloak, can hide objects form the detection of acoustic wave. Such cloak requires a material with inhomogeneous bulk modulus and anisotropic density to guide propagation direction of waves, and thus it is a challenging task from the fabrication viewpoint. In this work, we present an optimized design of cylindrical multilayered acoustic cloaks by adjusting the material parameter and layer thickness corresponding to a given incident frequency. Through the proposed optimization procedure, a simple cloak structure which consists of a multilayered composite made of only two isotropic materials is presented. In addition, with suitable constraints in calculations, the material parameters can be restricted within a certain range so that the constituent materials are close to nature materials. A selected example for underwater acoustic cloak comprised of the combination of a low density and a high density solid is demonstrated in our study. It is shown that the low density layer can be properly chosen as a conventional material, while the high density layer can be manufactured by composites or metamaterials. The thickness for each layer could be varying. Numerical simulation by finite element method is performed to verify the efficiency of cloaking effect and the field distributions are demonstrated. The presented optimized design can substantially reduce the total number of required materials. This means that it is more feasible in practice to fabricate an acoustic cloak.

Energy Sinks in Optics of Metamaterials: Fundamentals and Applications

Vasily Klimov
Lebedev Physical Institute, Russian Academy of Sciences, Russia

Abstract— Due to energy conservation law the energy emitted by one body (source) will be always absorbed by other bodies (sinks). Usually people do not worry about sinks because far fields are of primary interest. However in nano-optics and especially in nano-optics of metamaterials the role of sinks becomes very important. In fact even in usual media (vacuum) absorbing point dipole drastically disturbs the field distribution (Fig. 1) and can be neglected by no means (see Fig. 1).

In the case of closed cavities and metamaterials the situation becomes more complicated because in the stationary lossless regime strong spatial singularities arise there. From our point of view these singularities indicate that sinks (absorbers, detectors) should be explicitly incorporated in description of wave phenomena in metamaterial [1–3]. Our approach is not to try to avoid the appearance of new singularities by overdamping or changing geometry, but to include these singularities into wave propagation theory. So we suggest to put real sources and sinks (absorbers) in the places of possible singularities and to see what will happen. This expanded description results in new systems which turn out to be full of new physical sense. Moreover, such systems can serve as a base for a development of new applications of nano-optics. We have analyzed several negative refraction geometries (slab, sphere, wedge etc.) and closed elliptical cavities where singularities appear in formal solution of Maxwell equations. In all cases we found that it is possible to attribute real physical meaning to them. As an example of possible application of our paradigm the scheme of a perfect nano-absorber is shown in Fig. 2. It is proved by full scale simulations that this system can absorb 100% of wide angle incoming energy in deep subwavelength region. Other applications of our paradigm (e.g., preparation of entangled states of atoms for quantum computers) will be also discussed.

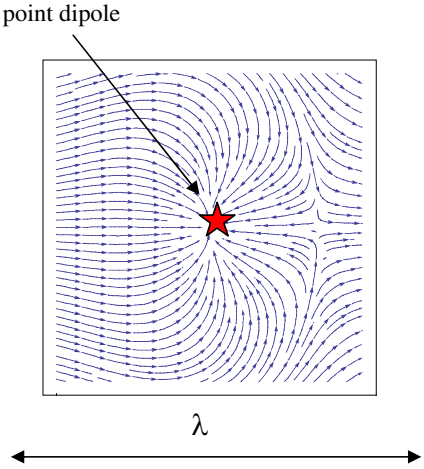

Figure 1: Resonant light absorption by point dipole.

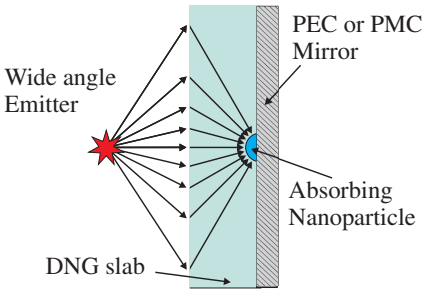

Figure 2: Schematic diagram of a perfect nanoabsorber based on our paradigm.

ACKNOWLEDGMENT

The author thanks the Russian Foundation for Basic Research (grants ## No. 11-02-91065, No. 11-02-92002, No. 11-02-01272 and No. 12-02-90014) for financial support of this work.

REFERENCES

1. Klimov, V., *JETP Lett.*, Vol. 89, 270, 2009.
2. Klimov, V., J. Baudon, and M. Ducloy, *Europhysics Lett.*, Vol. 94, 20006, 2011.
3. Klimov, V., S. Sun, and G.-Y. Guo, *Optics Express*, Vol. 20, A13071, 2012.

Engineering Transmission and Group Delay in Active Plasmonic Waveguide with Slightly Detuned Resonators

Jian-Wen Dong[1], **Zi-Lan Deng**[1], **and Jensen Li**[2]

[1]State Key Laboratory of Optoelectronic Materials and Technologies
Sun Yat-Sen (Zhongshan) University, Guangzhou 510275, China
[2]Department of Physics and Materials Science, City University of Hong Kong
Tat Chee Avenue, Kowloon Tong, Hong Kong, China

Abstract— An active plasmonic waveguide with a pair of slightly detuned resonators is investigated in the window of plasmon-induced transparency (PIT). The phenomenon is studied by a phase map of power transmittance for varying gain coefficients and frequency detunings. The gain coefficient for lasing oscillation condition is shown to vary quadratically with the frequency detuning of the two resonators, which is consistent with an analytical derivation based on coupled mode theory after considering gain contributions. In the amplification regime, the plasmonic wave will not only have large group delay compared to that in the bare structure without resonators, but also have high transmittance and narrow linewidth. This is in contrast to those in the loss-compensation regime and the passive case in which there always exists a tradeoff between the linewidth and the peak transmittance. All the results are demonstrated by finite element simulations.

Flat Dispersion Eigenmode Drives Perfect Imaging in DNG Slab

G. Rosenblatt, G. Bartal, and M. Orenstein
Department of Electrical Engineering, Technion, Israel

Abstract— First suggested by Pendry, perfect imaging using a slab made of a double-negative (DNG) medium, having both negative permittivity and permeability as envisioned by Veselago, has for some time now been in the forefront of much scientific research and debate. Surprisingly, the single DNG interface configuration was mainly sidelined in the process by its two-interfaced counterpart (slab) and given relatively little attention — it was nevertheless shown, by Ruppin and Kivshar's group, to support an either forward or backward surface wave eigen-mode in both polarizations.

Still, a unique quality of the single DNG interface has been overlooked, in between its forward and backward wave regimes: the possible formation of a completely flat dispersion band at both polarizations simultaneously — allowing all propagation constants β to be uniformly supported by the structure at a certain frequency.

Herein, we show that perfect imaging in a DNG slab stems from this flat-band single interface eigen-mode. The connection is made clearer by careful examination of the DNG slab's own eigenmodes: besides the usual symmetric and anti-symmetric modes an additional modal solution exists — a non-interacting combination of a confined and a virtual single-interface mode, resulting in a field distribution exponentially decreasing from one side of the slab while increasing from the other (Fig. 1). Retaining the single-interface dispersion relation, this mode allows uniform transmission via the DNG slab — establishing an association with Pendry's perfect lens, constituting our main theme.

This approach makes studying the DNG slab's efficacy as a perfect lens, under less ideal circumstances (the inclusion of losses for instance), straightforward. It is shown that these result in the flat band not being fully attained (Fig. 1 on the right) introducing a limitation on spatial resolution. These findings are shown to fit transmission based analysis.

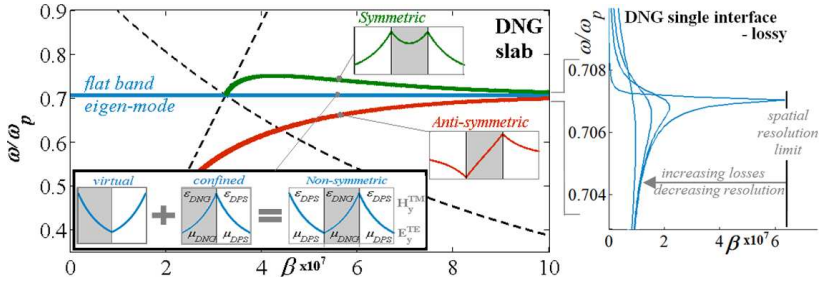

Figure 1: Dispersion curves for a lossless DNG slab (eigen-mode field distribution inset), and a zoomed section on the right showing the non-symmetric mode in multiple cases that include increasing losses. Drude form is used for both $\varepsilon_{\mathrm{DNG}}$ and μ_{DNG} with the same plasma frequency ω_p.

Session 2A2
Biological Effects and Medical Applications of Electromagnetic Energy 1

Topological Magnetoelectric Fields for Microwave Biosensing
Eugene O. Kamenetskii, Roman Joffe, Reuven Shavit, ... 156

Real-time Study of Sinusoidal Electromagnetic Fields Induced Intracellular $[Ca^{2+}]_i$ Responses in the Osteoblast Cells
Guixian Meng, Leiting Pan, Xiaoxu Wang, Taojie Bao, Haiying Sun, Renzhi (Imshik) Li (Lee), .. 157

Molecular Dynamics Simulations of Vesicles in Electric Fields
Xiaowei Zhao, Jianhua Zhang, Qing Huo Liu, ... 158

Do Microwaves Induce Free Radicals in Food or Tissues?
John Moses Osepchuk, Bob Schiffmann, Chung-Kwang Chou, ... 159

The Application of Electrochemotherapy in Medicine
Jing-Hong Li, Yu-Ling Xin, ... 160

Thermal Dosimetry and Thermodynamics of In Vitro RF Bioassays
Quirino Balzano, Asher R. Sheppard, Giorgi Bit-Babik, ... 161

Calculation of SAR and Temperature Increase in Human Bodies Due to on-body Communications at 900 MHz
Hsing-Yi Chen, Heng-Ming Lee, ... 162

Normalization of the Peak Spatial Absorption Rate for the Simulation of Wireless Communication Devices
Jafar Keshvari, Andreas Christ, ... 163

Evaluation on Electromagnetic Interference of Implanted Cardiac Pacemaker by Mobile Phone
Yuta Endo, Kazuyuki Saito, Soichi Watanabe, Masaharu Takahashi, Koichi Ito, ... 164

Topological Magnetoelectric Fields for Microwave Biosensing

E. O. Kamenetskii, R. Joffe, and R. Shavit
Microwave Magnetic Laboratory, Department of Electrical and Computer Engineering
Ben Gurion University of the Negev, Beer Sheva, Israel

Abstract— The rapid rate of adoption of mobile wireless communications has resulted in public concern about the health hazards of microwave fields emitted by such devices. Direct inspection of biological structures in microwave frequencies and understanding of the molecular mechanisms of microwave nonthermal effects is a problem of great importance [1]. Nowadays microwave biosensing lacks the spatial resolution to probe structural characteristics of chemical and biological objects [2, 3]. In contrast, optical biosensing has benefitted from in a large variety of such specialized tools. In particular, the resonant interactions between plasmon (or electrostatic) oscillations of metal nanoparticles and electromagnetric fields has become a powerful technique for chemical and biological sensing [4]. For biomedical diagnostics and pathogen detection, special plasmonic structures with left- and right-handed optical superchiral fields are effectively used [5]. Since resonance frequencies of plasmon oscillations in small particles are very far from microwave frequencies, the main ideas and results of the optical subwavelength photonics cannot be used for microwave biosensing. Nevertheless, there exists another type of subwavelength particles which show effective resonant interactions with microwave fields. There are small ferrite particles with magnetostatic (MS) (or MS-magnon) oscillations. The near fields of these particles are microwave superchiral fields with strong localization of energy [6–8]. The aim in this paper is to show unique properties of microwave devices with chiral probing fields to solve the problem of effective microwave characterization of chemical and biological objects.

REFERENCES

1. Belyaev, I. V., et al., "Microwaves from UMTS/GSM mobile phones induce long-lasting inhibition of 53BP1/g-H2AX DNA repair foci in human lymphocytes," *Bioelectromagnetics*, Vol. 30, 129, 2009.
2. Hayashi, Y., et al., "Dielectric spectroscopy study of specific glucose influence on human erythrocyte membranes," *J. Phys. D*, Vol. 36, 369, 2003.
3. Lee, H.-J., J.-H. Lee, and H.-I. Jung, "A symmetric metamaterial element-based RF biosensor for rapid and label-free detection," *Appl. Phys. Lett.*, Vol. 99, 163703, 2011.
4. Willets, K. A. and R. P. Van Duyne, "Localized surface plasmon resonance spectroscopy and sensing," *Annual Rev. Phys. Chem.*, Vol. 58, 267, 2007.
5. Hendry, E., et al., "Ultrasensitive detection and characterization of biomolecules using superchiral fields," *Nature Nanotechnol.*, Vol. 5, 783, 2010.
6. Kamenetskii, E. O., M. Sigalov, and R. Shavit, "Manipulating microwaves with magnetic-dipolar-mode vortices," *Phys. Rev. A*, Vol. 81, 053823, 2010.
7. Kamenetskii, E. O., R. Joffe, and R. Shavit, "Coupled states of electromagnetic fields with magnetic-dipolar-mode vortices: MDM-vortex polaritons," *Phys. Rev. A*, Vol. 84, 023836, 2011.
8. Kamenetskii, E. O., R. Joffe, and R. Shavit, "Microwave near-field helicity and its role in the matter-field interaction," *Phys. Rev. E*, arXiv:1111.4361, 2011 (Submitted).

Real-time Study of Sinusoidal Electromagnetic Fields Induced Intracellular $[Ca^{2+}]_i$ Responses in the Osteoblast Cells

Guixian Meng, **Leiting Pan**, **Xiaoxu Wang**, **Taojie Bao**, **Haiying Sun**, **and Imshik Lee**
The Key Laboratory of Weak-Light Nonlinear Photonics, Ministry of Education
School of Physics and TEDA Applied Physics School, Nankai University
Tianjin 300457, China

Abstract— The biological effects of electromagnetic fields (EMF) have been paid increasingly attention for a possible electromagnetic pollution. Although scientists have done extensive researches about extremely low frequencies (ELFs) EMF and its influence on tissues and cells, controversies of its effects still exist. Some studies reported intracellular calcium concentration ($[Ca^{2+}]_i$) changes induced by EMF, while some researches gave opposite or negative results, even under same conditions occasionally. In this paper, with osteoblast cells as targets, we did real time observations of $[Ca^{2+}]_i$ dynamics stimulated by ELFs sinusoidal EMF (SEMF). Osteoblast cells labeled via calcium fluorescent indicator Fluo-3 AM, were examined on inverted fluorescence microscope. Each group was carried in terms of the magnetic flux density and the frequencies, and SEMF of different conditions acted on cells for about 2 min. Here, we first observed remarkable calcium waves from nucleus to cytoplasm in osteoblast cells induced by SEMF at 1.1 mT, 100 Hz. The calcium waves from nucleus indicated that $[Ca^{2+}]_i$ responses to SEMF in osteoblast cells might be due to the signal paths associated with IP_3 and intracellular calcium stores, in spite of Ca^{2+} influx, which was also proposed in other investigations of osteoblast cells proliferation exposure in SEMF. Furthermore, there were the series of discrete frequency windows in a given intensity of 1.1 mT or 1.8 mT. These offered positive results for the window effect of EMF biological influence. In addition, in our previous work, $[Ca^{2+}]_i$ responses to Pulsed extremely low frequency (PELF) were founded at 0.8 mT, 50 Hz. Consequently, in osteoblast cells, $[Ca^{2+}]_i$ could respond to SEFM as well as to PELF.

Molecular Dynamics Simulations of Vesicles in Electric Fields

Xiaowei Zhao[1], **Jianhua Zhang**[1, 2], **and Qinghuo Liu**[3]

[1]Department of Electronic Science, Xiamen University, Xiamen, Fujian 361005, China
[2]State Key Laboratory for Physical Chemistry of Solid Surfaces, Department of Chemistry, China
[3]Department of Electrical and Computer Engineering, Duke University, NC 27708, USA

Abstract— We use coarse grained molecular dynamics (CGMD) simulations to study the effects of electric fields on vesicle, a cell-size membrane system. The initial structures of vesicles are prepared via the aggregation of various lipids in the simulations. The different processes of vesicles in the electric fields, such as electrodeformation, -poration and -fusion, are considered. The influences of the composition of vesicles and the nature of ions are also examined during the processes. Our simulations conform that the behaviors of vesicles are significant affected by the external electric field. The simulations describe the atomic details of the deformation of a vesicle from a sphere into an ellipsoid in electric fields. The shapes of vesicles in the electric fields are mainly depended on the different conductivity conditions and various field frequencies. The electrical breakdown of fluid lipid bilayers induced by strong electric pulse leads to formation of pores. The relaxation behavior of vesicles after the end of the pulse depends on whether the membrane was porated or not. In our simulations, the fusion of two vesicles is observed to proceed several stages: vesicles deformation, membrane proximity and contact, local perturbation of bilayer structure, formation of fusion pores or necks, and subsequent expansion of these necks. The nature of ions also play an important role in the fusion of vesicles. The results are in a good agreement with experimental observation and provide new insight into vesicle in electric field at atomic scale. The molecular dynamics studies of vesicles can help improve fundamental knowledge about the complex behaviors of cells and membranes in electric fields and can inspire novel practical applications.

Do Microwaves Induce Free Radicals in Food or Tissues?

John Osepchuk[1], **Robert Schiffmann**[2], **and Chung-Kwang Chou**[3]

[1]Full Spectrum Consulting, USA
[2]R. F. Schiffmann Associates, Inc., USA
[3]Motorola Solutions, Inc., USA

Abstract— Statements from a radiologist at a Taiwan Veterans Hospital have been frequently quoted as health advice in internet articles. He claims that "microwave ovens use electromagnetic waves with one less positive electron and the vibration of water to make the food hot. Thus, microwave-heated food can easily contain free radicals that can cause cancer." The doctor recommended "use of the microwave only once in a while for convenience, but preferably as little as possible." His statements are false claims and offer the wrong advice to the general public. This presentation is made to correct the misinformation.

Microwave ovens are now a universal item in the world with an estimated over 1 billion ovens. These appliances are designed to heat or cook foods and have been regulated by government authorities since the 1960's. The U. S. Government in 1968 officially determined that microwave energy was an alternative and safe method for heating, i.e., the effect is just heating. The government authorities, worldwide, continue to approve the microwave oven as a safe appliance for heating and cooking food. The FDA continues approval with oversight as in the "Food Code" and education of the consumer. This has been supplanted by the oversight of the U.S. Dept. of Agriculture (USDA), which is proactive on food safety and microwave ovens. In these government websites, there is no discernible or serious review of allegations of "free radicals" as a unique result of microwave heating or any other form of heating.

The claims of "free radicals" from microwave heating are widespread, especially on the Internet, but because these are rumors and not the results of science — either theory or experiment — the rebuttal of these claims is not formalized. Instead, there are numerous dismissals of the "free radical" claims by brief or anecdotal comments. Many dismiss the possibility of free radical formation under microwave heating on the basis of fundamental physics, i.e., the very small quantum energy of microwave photons is insufficient to alter the energy levels of electrons in atoms or molecules. This is the substance of many rebuttals, especially that by Dr. Lou Bloomfield of the University of Virginia, who maintains a popular website on "How things work" and is often cited at authoritative sites like those of the FDA or USDA. There is never enough microwave quantum energy delivered to a single molecule to shatter that molecule and form a free radical. While ultraviolet light carries enough quantum energy per photon (particle of light) to split a molecule and form a free radical, microwave radiation carries very little quantum energy per photon. That's why microwave photons can't do chemical damage the way ultraviolet photons can.

The case against the possibility of "free radical" generation is strengthened by much research on high-power effects in microwave processing of materials, where some suspected a "microwave" (nonthermal) effect along with strong heating. Most research, however, concludes that the effects are thermal and do not include a specific "microwave" effect. The burden of proof remains on those who claim other than heating as a mechanism such as free radicals for observed microwave bioeffects.

The Application of Electrochemotherapy in Medicine

Jing-Hong Li and Yu-Ling Xin
Department of Electrochemical Treatment
China-Japan Friendship Hospital, Beijing, China

Abstract—

Objective: To evaluate the efficacy and safety of electrochemotherapy in treating venous malformations.

Methods: Electrochemotherapy was applied to 665 patients with venous malformations of limbs and trunk, and 505 cases were followed up for half to 6 years. 228 male and 277 female patients, aged 2–59 years and 17.5 years old on average, were involved. The platinum electrodes were inserted into tumor through a trocar with plastic insulating cannula percutaneously and connected with the electrochemical therapeutic apparatus in anodes and cathodes separately. The treating voltage is 6–12 V and current 100–180 mA, the total electricity used is in general 80–100 coulombs per 1.0 square centimeter of tumors' area. The treating time was usually from several dozen minutes to over 2 hours depending on the size of the tumor. The severe cases which needed to be treated once again usually were operated after 6 months.

Results: The primary efficacy end point was defined as an improvement of patients' symptoms and a reduction in size of tumor 6 months after treatment. Effects were divided into 4 grades according to WHO guidelines for solid tumors. Grades 1, 2 and 3 are regarded as effective. The efficacy turned out that 30.1% (152/505) of patients was classified as grade 1; 46.3% (234/505) as grade 2; 19.0% (96/505) as grade 3 and 4.6% (23/505) as grade 4.

Conclusion: Electrochemotherapy shows special superiorities in treating venous malformations. It might bring a confirmed clinical efficacy with the advantages of less injury, quick recovery, simple operation and less complications.

Thermal Dosimetry and Thermodynamics of In Vitro RF Bioassays

Quirino Balzano[1], **Asher Sheppard**[2], **and Giorgi Bit-Babik**[3]

[1]University of Maryland, College Park, Maryland, USA
[2]Asher Sheppard Consulting, Santa Rosa, California, USA
[3]Motorola Solutions, Plantation, Florida, USA

Abstract— RF-exposed cell preparations require detailed analysis of the specific absorption rate (SAR) distribution and related thermally-driven dynamic effects in the medium. In comparison to the biological cells under test, the medium absorbs the bulk of the RF power transferred from the incident field. Whereas the sham-exposed preparation is in static equilibrium with the incubator environment, the exposed medium is in a dynamic equilibrium, with heat flow patterns created by nonuniform SAR distributions. However, dynamical effects of RF power transferred to the medium have not always received due attention. Consequently, diffusion-limited heat flow determines potential nonuniformities of temperature and fluid transport that may affect the nutrients available to cells. We focus on the important dosimetric implications of the liquid geometry in a Petri dish, test tube or flask, particularly if the meniscus has a significant fraction of the total liquid volume. For a given incident RF field, the geometry (volume and shape) of the medium and of the liquid meniscus are major influences on RF exposure of cell monolayers growing on the bottom surface of the exposure vessel. For shallow depths, the meniscus enhances SAR at the bottom surface, therefore heating the medium there more rapidly. The geometry of Petri dishes and flasks is unfavorable to convection phenomena because the least exposed liquid layer lies only a few mm above the bottom. Even if there is a peak SAR stratum at the bottom of the dish, its distance from the least exposed layer of liquid is only a few mm. Thus temperature diffusion prevents fluid mass buoyancy flow. However, test tubes with greater than 5 mm of liquid are much more favorable to convection because the medium with highest SAR occurs at a considerable vertical distance from the layer with least exposure. These observations are important because potential thermodynamic events in the medium may affect the validity of attempted replications of in vitro studies in cases where the exposure vessel shape and liquid volume have important influences. As a result, cells in the exposed medium do not experience temperatures and access to nutrients that are the same as for the sham-exposed control, despite identical incubator temperatures and good heat transfer from the exposure vessel.

Calculation of SAR and Temperature Increase in Human Bodies Due to on-body Communications at 900 MHz

Hsing-Yi Chen and Heng-Ming Lee
Department of Communications Engineering, Yuan Ze University
135, Yuan-Tung Road, Chung-Li, Taiwan 32003, Taiwan

Abstract— On-body communication systems have attracted much notice in industries and academic studies. However, the on-body communication system consists of numerous sensors placed in proximity to the human body. Public concern regarding potential health hazards due to the absorption of electromagnetic (EM) energy emitted from on-body transceivers has also been growing. Therefore, it is important to investigate the EM energy absorption in a human body due to the radio frequency (RF) EM fields emitted by the on-body transceivers. In this paper, the SAR and temperature increase in an inhomogeneous human model wearing clothes were studied by using the finite-difference time-domain (FDTD) method under the irradiation of a patch antenna located at different locations on the human body surface at 900 MHz. From simulation results it is found that the highest layer-averaged SARs are in the order of 10^{-4} to 10^{-3} W/kg for the patch antenna located on different locations on the human body surface, which is far below the ANSI/IEEE safety guideline of 1.6 W/kg for 1 g of tissue or 2 W/kg for 10 g of tissue in uncontrolled environments. It is also found that the maximum temperature increases of 1.2×10^{-3}°C and 6.3×10^{-4}°C occur in the left chest for 1 g of tissue and 10 g of tissue, respectively. The maximum temperature increase of 1.2×10^{-3}°C is also far below the threshold temperature increase of 4.5°C for neuron damage for more than 30 minutes and the temperature increase of 10°C for thermal damage in the skin.

Normalization of the Peak Spatial Absorption Rate for the Simulation of Wireless Communication Devices

Jafar Keshvari and Andreas Christ
Corporate Development Office, Nokia Corporation, Keilahdentie 2-4, Espoo 00240, Finland

Abstract— Mobile phone compliance testing is routinely performed through a very time consuming and expensive test procedure. Although the numerical modelling is theoretically easy and significantly faster and cheaper method to assess the compliance of the wireless communication device, but the accurate numerical modelling of commercial mobile devices is not an immediate task especially when considered with the head phantoms. One of the main challenges to deal with meaningful results is the question of how to normalize the simulated results.

The first approach is to calculate the source powers. This implies that the ratio of the simulated accepted power and the measured radiated power is equal to the ratio of the measured accepted power to the radiated power of the simulation. A more manifest approach could be based on the assumption that the ratio of the radiated power to the accepted power of measurement and simulation is equal. However the measurements and simulations of realistic mobile phoens have shown that this is not the case for the model used. As a consequence, the power dissipated in the dielectric materials (PCB, antenna support, case, etc.) of the numerical phone model is different from the actual situation. An alternative to normalization could be the adaptation of the dielectric losses in the phone such that this equation is fulfilled: $\frac{TRP_{sim}}{P_{acc\_sim}} = \frac{TRP_{meas}}{P_{acc\_meas}}$.

In this presentation, first different parameters which the results can be normalized to will be discussed, and then the relevance of each parameter as a normalization factor in the different scenarios will be analyzed.

Evaluation on Electromagnetic Interference of Implanted Cardiac Pacemaker by Mobile Phone

Yuta Endo[1], **Kazuyuki Saito**[1, 2], **Soichi Watanabe**[2], **Masaharu Takahashi**[1], **and Koichi Ito**[1]

[1]Chiba University, Japan
[2]National Institute of Information and Communications Technology, Japan

Abstract— In recent years, electromagnetic interference (EMI) on implanted cardiac pacemakers due to mobile phone has become a large concern. As a result of the previous studies, it was concluded that a connector between the pacemaker housing and the lead wire of the electrode plays a measure role for the EMI due to mobile phones. Moreover, in the study with a half-wavelength dipole antenna employed as a radiator of electromagnetic waves, EMI was more likely to occur when feeding point of the antenna faced the connector of the pacemaker. From these results, in the case of mobile phones, EMI possibly depends on the intensity of magnetic field around the connector. Here, in the previous studies, dipole antenna or monopole antenna loaded to a metallic case which simulates the PCB, battery and etc. were mainly employed as a mobile phone model. However, recent mobile phones are generally equipped with an embedded antenna. Furthermore recent mobile phone systems are operated at higher frequencies, i.e., 2 GHz while lower frequencies around 900 MHz have been assumed in the previous studies. In this study, the mobile phone with the embedded antenna was modeled with a planar inverted-F antenna (PIFA) mounted on a metallic case and the interference voltage induced at the pacemaker was calculated, in order to evaluate the characteristics of the EMI due to the mobile phones with existing system. It is consequently shown that the PIFA have different characteristics of the interference voltage from those of the half-wavelength dipole antenna and interference voltage strongly depends on the intensity of magnetic field around the connector.

Session 2A3
Microwave Remote Sensing and Polarimetry, SAR, GPR

Physical Models and Validation for L-band Radar Backscattering from Vegetated Surfaces
Tien-Hao Liao, Leung Tsang, Xiaolan Xu, Huanting Huang, Seung-Bum Kim, ... 166
Applicability of SSDC Method for SNR Evaluation on Hyperion and HJ-1A Hyperspectral Data
Xinhong Wang, Bo Zhu, Hongbing Niu, Lingli Tang, Guangzhou Ouyang, ... 167
3D Active Imaging Models and Systems to See through Adverse Conditions: Application to the Surveillance of an Aircraft Environment
Nicolas Riviere, Romain Ceolato, Erwan Bernard, Laurent Hespel, Mathieu Renaudat, ... 168
Time Series of Polarimetric Intensity and Coherence over Tropical Forest: Rainy and Dry Season
Alia Hamadi, Clément Albinet, Pierre Borderies, Thierry Koleck, Fabio Rocca, Stefano Tebaldini, Thuy Le Toan, L. Villard, ... 169
A Multi-scale SAR Segmentation Based on Hierarchical Merging
Xi Ye, Meng Liu, Hong Zhang, Chao Wang, ... 170
New SAW Odor and Gas Sensor for Sensor Network Installed in Smart House
Mitsutaka Hikita, Jun Hosaka, ... 171
Checking of Combustion Chamber of Liquid Rocket Using ECT with AMR Sensor
Dong Feng He, Mitsuharu Shiwa, S. Moriya, ... 172
Study of Earthquake Location Using Electromagnetic Precursors
Yi Wang, Qunsheng Cao, Xiao Yuan, Ya'nan Liu, ... 173
Prediction of Radar Reflectivity along Radio Link
Chrispin Tshikomb. Mulangu, Senzo Jerome Malinga, Thomas Joachim Odhiambo Afullo, ... 174

Physical Models and Validation for L-band Radar Backscattering from Vegetated Surfaces

Tien-Hao Liao[1], **Leung Tsang**[1], **Xiaolan Xu**[2], **Huanting Huang**[1], **and Seung-Bum Kim**[2]

[1]Department of Electrical Engineering, University of Washington, Seattle, WA 98195-2500, USA
[2]Jet Propulsion Laboratory, California Institute of Technology, Pasadena, CA 91109, USA

Abstract— In this paper, we present forward physical models of the microwave backscattering from a vegetated terrain at L-band. The physical models have applications in NASA SMAP (Soil Moisture Active and Passive) mission, Aquarius, PALSAR, UAVSAR, etc. In SMAP, the backscattering, VV, HH, and VH are pre-calculated as a function of three parameters, viz. rms heights (s), soil moisture (mv), and vegetation water content (VWC). These pre-calculated tables are known as data cubes. Pre-calculated data cubes from forward models are used to estimate the backscattering from vegetated surface and also are applied to retrieval algorithm. The vegetated surface model includes a layer of vegetation on top and the rough soil surface below.

For the scattering of waves by soil surfaces, the random rough surface is considered as a lossy dielectric medium and is characterized by Gaussian random process with exponential correlation functions. A hybrid UV/PBTG/SMCG method is developed to accelerate Method of Moment solution. Results are illustrated for bistatic scattering and backscattering. Lookup tables have been prepared for both co-polarization and cross-polarization of backscattering for a range of soil moisture, rms heights and correlation lengths. They are also validated with measurement data. We also calculated the Mueller matrix to study the full polarimetric signatures of backscattering from rough soil surfaces.

For volume scattering in vegetation, we have implemented body of revolution (BOR), discrete dipole approximation (DDA) as well as infinite cylinder approximation, and thin radius approximation for scatterers of simple shapes including cylinders, ellipsoids, and disks. These are used to model branches, stalks, and leaves in vegetation. By using the distorted Born approximation, the results of backscattering of vegetated surfaces are expressed in terms of volume scattering, surface scattering, and double bounce scattering. Data Cubes have been generated for a variety of crop types, including corn, soybean, wheat, as well as grassland. In this paper we show the validation of data cubes with SGP99, SMEX02, and SMAPVEX08 field measurements as well as with recent SMAPVEX12 data. The application and comparison with Aquarius data are also shown.

Applicability of SSDC Method for SNR Evaluation on Hyperion and HJ-1A Hyperspectral Data

Xinhong Wang, Bo Zhu, Hongbing Niu, Lingli Tang, and Guangzhou Ouyang
Academy of Opto-Electronics, Chinese Academy of Sciences, China

Abstract— The signal-to-noise ratio (SNR) is one of the most important indices to a sensor's performance, and it has significant influence on various remote sensing applications. Several typical SNR estimation algorithms have been developed based on different standpoints. The Spectral and Spatial Dimensional Correlation (SSDC) method developed by Roger et al. is said to be a reliable and automatic means to estimate the noises affecting the bands of a hyperspectral image. The method can be used for both reflectance and emissivity images. SSDC is also considered to be a fast and accurate method. With the development of remote sensing technology and the emergence of new types of sensors, hyperspectral imaging principles and methods are continuously modifying. So it is necessary to analyze the applicability, accuracy, and stability of the SSDC method with respect to different sensors, and in comparison with other SNR algorithms. In the end, a best method suitable for estimating the SNR on current conditions could be chosen and employed.

In this paper, two images, one from the "Hyperion" sensor aboard the EO-1 satellite and one from the "HSI" sensor aboard the HJ-1A satellite (Chinese first environment monitoring satellite), which were acquired at different time but in the same area, are used to calculate and estimate the SNR. The results derived by SSDC method were compared with those derived by the Local Standard Deviation (LSD) method of Gao. The imaging principle of the "Hyperion" data belongs to grating induced spectrometry, while the "HSI" employs the technology of interferometric spectrometry. By analyzing the calculated results of the two images, some key points were found:

Firstly, the calculated result by SSDC method is more accurate than the result by LSD method for the "Hyperion" image. Because land surface reflectance is usually smooth in spectral dimension, there are strong correlation among the signal values of several adjacent bands in a hyperspectral image. And according to the correlation, it is reasonable to estimate the signal value of current band by its adjacent bands. However, the result derived by LSD method, which depends on the size, the scene content and the complexity of surface features, is not stable enough. Moreover, the LSD method does not take into account the changes in signal values between bands, and this also affects the accuracy of the result by LSD method to some extent.

Secondly, when comparing the result by SSDC method with that by LSD method for the "Hyperion" image, the former is more reasonable and more stable. But in the case of "HSI" image, the SNR calculated by SSDC is far greater than that by LSD method and seems too high to be credible. It means that SSDC is not suitable to assess the SNR for the "HSI" image. This is mainly because the noise in the "HSI" image has certain correlation between adjacent bands, like the signal acts. When assessing the SNR for the "HSI" image data by SSDC method, the "residual" values (an estimate of noise level) are very small, so the estimated noise standard deviation will be very small, leading to a much greater final SNR results than any other methods. While according to the LSD method, there is no need to calculate the residuals. So the results by LSD method will not be affected by the spectrally correlated noise in the hyperspectral image.

Finally, the stability of SSDC method is superior to that of LSD method. On one hand, the limitations of LSD method lead to a less stable SNR. On the other hand, SSDC method can calculate on the whole image regardless of the sub-block size, homogeneity or the complexity of the surface features. In addition, the SSDC method takes into account the inter-band information, and the algorithm in fact is mainly based on the inter-band correlation. It means that the SSDC method is affected by spatial inhomogeneity less than others which mainly depend on spatial information.

In brief, the SSDC method is suitable for estimating the SNR for hyperspectral images observed by non-interferometric spectrometry, and under this circumstance, it behaves better than the LSD method. But it is worth noting that SSDC method is likely to yield abnormally high SNR estimations, when it is applied to an interferometrically imaging hyperspectral data like "HSI". While in this case, the LSD method will be a relatively better choice.

3D Active Imaging Models and Systems to See through Adverse Conditions: Application to the Surveillance of an Aircraft Environment

N. Riviere[1], R. Ceolato[1], E. Bernard[1], L. Hespel[1], and M. Renaudat[2]

[1]The French Aerospace Lab, Onera, Toulouse 31055, France
[2]Sagem Security and Defense, Massy 91344, France

Abstract— Onera, The French Aerospace Lab, develops and models 2D and 3D active imaging systems to understand the relevant physical phenomena impacting on their performances. As a consequence, efforts have been done both on the propagation of a pulse through the atmosphere (scintillation and turbulence effects) and, on target geometries and their surface properties (radiometric and speckle effects). But these imaging systems must operate at night in all ambient illuminations and weather conditions in order to perform the strategic surveillance of the environment for various worldwide operations or to perform the enhanced navigation of an aircraft. Onera has implemented codes for 3D laser imaging systems. As we aim to image a scene even in the presence of rain, snow, fog or haze, we introduce such meteorological effects in these numerical models and compares simulated images with measurements provided by commercial and home-made imaging systems.

Current vision systems are designed to perform in clear weather. In any outdoor application, there is no escape from "bad" weather. Weather conditions differ mainly in the types and sizes of the particles involved and their concentrations in space. Efforts have gone into evaluating the influence of particle size and concentrations for a variety of conditions. Given the small size of air molecules, relative to the wavelength of visible light, scattering due to air is rather minimal. We will refer to the event of pure air scattering as a clear day (or night). Larger particles (rain, snow, fog, haze, dust wind ...) produce a variety of weather conditions which we will describe in the full-paper.

Most critical bad weather conditions are linked to disruptive events introducing low visibilities and a disorientation of an aircraft on a taxiway. Snow could introduce a loss of the visibility. Moreover, light elements are dimmed, the surrounding is turned white and, in case of associated wind, pilot lost his bearings. Fog events with direct sunlight turn white or blurred the surrounding. A strong rain induces specular reflection and whiteout: this phenomenon is generally limited to less than 30 minutes but induces traffic delay on an airport. Sandstorm and smoke reduce the surrounding perception. Rain and snow could increase stopping distances and pilots need to anticipate. As a consequence, the pilot workload increases with such bad weather conditions.

We developed a complete end-to-end model to simulate images obtained with a 3D laser imaging system. The laser source and the propagation of the laser pulse through the atmosphere (including bad weather condition) would be described. The process of the pulse reflection on 3D objects would be explained as the optical properties of the materials are modified under bad weather condition. We also model real sensors adding noises to the signal. We will enhance the relevant physical phenomena impacting on the performances of active imaging systems under bad weather condition.

Time Series of Polarimetric Intensity and Coherence over Tropical Forest: Rainy and Dry Season

A. Hamadi[2], **C. Albinet**[3], **P. Borderies**[3], **T. Koleck**[1, 2], **F. Rocca**[4], **S. Tebaldini**[4], **T. Le Toan**[2], **and L. Villard**[2]

[1]CNES, Toulouse, France
[2]CESBIO, Toulouse, France
[3]ONERA, Toulouse, France
[4]POLIMI, Milan, Italy

Abstract— This abstract deals with ground experiments related to the future spaceborne BIOMASS mission for global forest biomass estimation.

Tropical forests present the major part of the world forest biomass and their changes in biomass by deforestation and/or by forest regeneration affect strongly the terrestrial carbon budget. To measure with accuracy tropical forest biomass and its temporal change is one of the objectives of the BIOMASS mission [1], a candidate for the European Space Agency 7th Earth Explorer Mission.

The possible retrieval algorithms currently developed for BIOMASS are based on the use of backscatter measurements derived from intensity, polarimetry and interferometry. However, these quantities are subject to evolution with the life cycle and the meteorological conditions at very different time scales, ranging from a few minutes to days, months... with the possibility that their changes may affect the inversion algorithms.

A ground experiment has been set up to follow systematically these evolutions. It has been installed over a temperate tree and also over a tropical forest in French Guiana. Based on the use of a Vector Network Analyzer and adequate antennas, it may deliver P band polarimetric, interferometric impulse responses and 2D (range/height) imaging.

In the presentation the impulse response acquired by the full system are analysed with several range filtering and averaging. Concerning the intensity, it appears that a single antenna couple exhibit diurnal cycles as well as long term evolution over 3 months depending on range (incidence and composition) and polarization, whereas with averaging on the 16 couples strongly attenuates the diurnal cycle, still preserving the long term evolution linked to soil moisture. Coherence is averaged through several derivations and exhibit long term behavior extrapolating satisfactorily the airborne measurements.

We have at our disposal data 3 months long of both the rainy season and also the dry one. Long term coherence is of the same order in both seasons, whereas it is very different at the scale of a few days. Influence of rain and water storage will be discussed.

REFERENCES

1. BIOMASS Phase 0 Report for Assessment, ref. SP1313/2, European Space Agency, Nov. 2008.

A Multi-scale SAR Segmentation Based on Hierarchical Merging

Xi Ye[1, 2], **Meng Liu**[1, 2], **Hong Zhang**[1], **and Chao Wang**[1]

[1]Center for Earth Observation and Digital Earth, CAS, Beijing 100094, China
[2]Graduate University of the Chinese Academy of Sciences, Beijing 100049, China

Abstract— With recent development of full polarimetric (FP) space synthetic aperture (SAR) configurations, the trade-offs among pulse repeated frequency, polarimetry, data amount and resolution have been drawn widespread attention. Herein, compact polarimetric (CP) SAR system, which transmits only one polarized wave while receives two orthogonal backscatter waves, has been proposed and become the currently researching hotspot, CP SAR data has opened a new path to promising application, i.e., in the field of land cover classification.

With regard to land cover classification, one of the most popular methods is based on the physical character of targets; several target decomposition (TD) algorithms for FP SAR data have been proposed and widely used. Two main ways of TD algorithms for CP SAR data have been preliminary investigated; one way is based on the reconstruction of pseudo FP covariance matrix C_3 from CP covariance matrix C_2, which depends on several assumptions. Once the assumptions are not met, the algorithm may fails. Another promising way is to extract useful information from CP data, mainly based on the 2×2 coherency matrix.

Raney derived the expression of Stokes parameters of two hybrid-Polarity SAR modes, namely CTLR (circular transmitted polarization and coherent dual linear receive polarizations) and DCP (circular transmitted polarization and dual circular receive polarization), and a decomposition strategy named $m - \delta$ algorithm was introduced. The parameter δ was the relative phase between the two linear vectors of the backscattered field, and the prime indicator of double-bounce backscatter based on the condition of circularly polarized illumination. Charbonneau et al. introduced a three-component algorithm for CTLR SAR data based on $m - \delta$ algorithm. S. R. Cloude et al. combined the $m - \delta$ algorithm and wave decomposition theorem together, and proposed a three-component compact decomposition algorithm, which had been successfully used in forest fire scar detection.

However, these compact decomposition algorithms cannot be used in DCP SAR data straightforwardly. In this paper, a three-component model-based target decomposition algorithm will be introduced. First, the 2×2 Jones coherency matrix will be derived, and a orientation angle of polarizer will be introduced to optimize the Jones matrix, the optimized matrix will reduce the number of pixels with negative power in following decomposition steps. Then, the H/α decomposition will be performed with DCP SAR data, the boundary of original H/α decomposition fails to determine the physical scattering mechanism of targets, a modified boundary will be introduced for DCP SAR data. By using the compact H/α decomposition, the PSM of targets can be discriminated into three basic scattering mechanisms, volume, surface and double-bounce scatter respectively. A new volume scattering coherency model given by An et al. will be used, the entropy of this model is one, and the scattering matrices of the other two scattering mechanisms and the Jones matrix will be derived in DCP mode, based on these models and the wave decomposition theorem, the decomposition equations can be established. However, the number of unknowns is larger the number of observables, to reduce the number of unknowns, the PSM obtained by compact H/α decomposition can be used to distinguish the dominant scattering mechanism between double-bounce and surface scatter, then the unknowns can be solved. The negative powers will be eliminated due to the employment of two power constraints.

The DCP data simulated from the RADARSAT-2 data are used to validate the proposed three-component algorithm. The experimental results show a good fit with physical character of targets, especially in ocean and forest. In urban area, the volume scattering power is overvalued, but the result still reflects the physical character accurately. In the future research, we will aim at decreasing the volume power in urban and improve the decomposition model.

New SAW Odor and Gas Sensor for Sensor Network Installed in Smart House

Mitsutaka Hikita and Jun Hosaka
Faculty of Global Engineering, Kogakuin University, Shinjuku-ku, Tokyo 163-8677, Japan

Abstract— "Sensor Network" has been proposed with the development of mobile communications systems such as cellular phones, wireless LANs. Sensed signals from many sensor nodes arranged in homes, offices and public places are gathered to center nodes by technology similar to that used in mobile communications. In this paper, we have proposed a new SAW (Surface Acoustic Wave) odor and gas sensor, which can be assembled in sensor nodes. Sensor network including these sensors will be very useful to monitor odors from patients or in sickroom and to sense hydrogen-gas leakage from future fuel-cell cars. They will also contribute to constructing the future smart house as well.

One of the most successful commercial SAW-gas sensors is a SAW GC (gas chromatography) provided by EST Corp. [1, 2]. However, it has a rather complicated structure using not only a SAW sensor but also a trap and a column tubes to separate gases according to their molecule weight. Due to the rather large size and the high power consumption, it can not be adopted in sensor network. Moreover, only Quartz crystal substrates with very good temperature characteristics have been used in these kinds of conventional SAW gas sensors. We have invented a new SAW sensor structure, which can remove such a limited selection for piezoelectric crystal substrates. The proposed sensor consists of three SAW delay lines, two ones of which are used to generate standard in-phase (I-) and quadrature-phase (Q-) signals. The third one is used for sensing of subtle-molecular particles. Phase shift for propagating SAW due to mass loading effect of sensing particles is measured based on the standard I- and Q-signals from the other two delay lines which are isolated from the sensing environment. The influence from temperature is same for the three delay lines, which provides self-temperature-compensated characteristics between phase of the sensing delay line and I-/Q-phases of the standard delay lines [3].

ZigBee has been regulated by IEEE 802.15.4 [4, 5] as a wireless-communications medium for the "Sensor Network". One of the most important features for ZigBee is the extremely low-power consumption, which provides several-year operation with a single battery. Our sensor is also designed to be combined with ZigBee. Sensing signals at several hundred MHz are generated by division and multiplication of the signals from a VCO (Voltage-Controlled Oscillator) in the RF circuit of sensor nodes. To overcome the large insertion losses of SAW sensors, we have invented not only the conventional transversal type sensor but also new lattice-circuit type sensor using SAW resonators, which consists of pairs of SAW reflectors arranged at both sides of the SAW transducer. This type can achieve smaller insertion losses as well as same self-temperature-compensation characteristics as previous one [3]. In the paper, ZigBee-based sensor network with SAW sensors will be illustrated combined with future smart house. Design procedures, simulation and experimental results for two types of new SAW-sensor structures will be presented.

REFERENCES

1. Electronic Sensor Technology HP, "Chemical sensor for the 21 century," http://www.estcal.com/.
2. Staples, E. J., "Odor chemistry of un-derivatized human body," http://www.estal.com/TechPapers/Odor_of_Blood.doc.
3. Hikita, M., "Surface acoustic wave gas sensor," Japanese Patent Pending, 2007-280020, Oct. 29, 2007.
4. IEEE Standard 802.15.4, "Wireless medium access control (MAC) and physical layer (PHY) Specifications for low rate wireless personal area networks (LR-WPANs)," 2003.
5. ZigBee Specification, Document 053474r17, Jan. 17, 2008.

Checking of Combustion Chamber of Liquid Rocket Using ECT with AMR Sensor

D. F. He[1], **M. Shiwa**[1], **and S. Moriya**[2]

[1]National Institute for Materials Science, Sengen 1-2-1, Tsukuba 305-0047, Japan
[2]Japan Aerospace Exploration Agency, Kakuda, Miyagi, Japan

Abstract— Using the eddy current testing (ECT) system with AMR sensor developed by us, we tested a liquid rocket combustion chamber specimen. The specimen was made of copper alloy; coolant channels and artificial defects were made in it as the real combustion chamber. Fig. 1(a) shows the scanning result by the ECT system. The artificial defects were successfully detected. However the coolant channels induced some signals which influenced the signal-to-noise ratio and limited the smallest defect that can be detected.

We developed an FFT (Fast Fourier Transform) method to reduce the influence of the coolant channel signals. We first made the FFT for the scanning result; and set the values of some frequencies and their harmonics to Zero (The frequencies are determined by the periodic channel signals); then made the inverse FFT (IFFT) of the spectrum. Fig. 1(b) shows the results after FFT and IFFT. We can see that the coolant channel signals were reduced and the signal-to-noise ratio was improved.

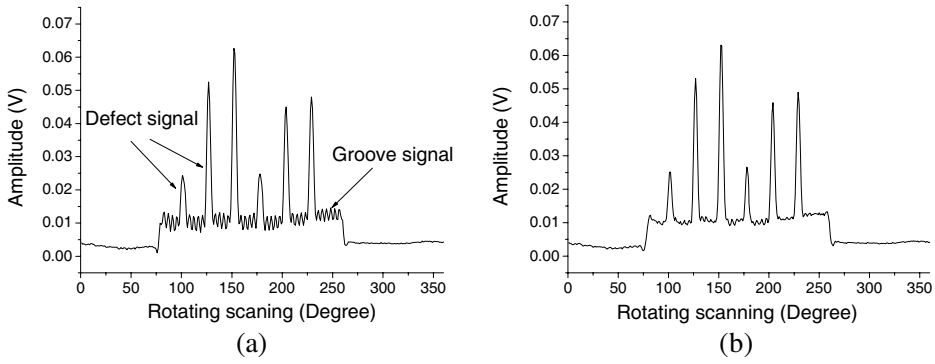

Figure 1.

Study of Earthquake Location Using Electromagnetic Precursors

Yi Wang, Qunsheng Cao, Xiao Yuan, and Ya'nan Liu
Nanjing University of Aeronautics and Astronautics, China

Abstract— Most present earthquake location techniques are based on recording phase arrival times in different stations, which is almost a real-time location technique that can detect earthquakes a few seconds in advance. Because anomalous electromagnetic (EM) phenomena are believed to arise during earthquake preparing process, establishing an early-warning (days or months) system for earthquakes is becoming possible.

In this work a technique to locate earthquake hypocenters using extremely low frequency (ELF) electromagnetic (EM) precursors is proposed. The technique relies on recording electromagnetic eruptions caused by physical mechanisms during the earthquake preparing process. Using the triangulation algorithm and the attenuation rate of EM waves in the Earth-ionosphere system, the source (usually the earthquake hypocenter) can be located. During the locating process, the attenuation rate of EM waves in local regions must be modified in order to improve accuracy of result.

Based on this technique, experiments are simulated using the geodesic finite difference time-domain (FDTD) method to test the efficiency of location. In the experiments, earthquakes with EM precursors is supposed to happen in (or not far from) a region surrounded by three EM observing stations. Once an EM eruption is detected in all the three stations, the technique is performed to locate the earthquake center. Results show that the locating error is within one cell of the FDTD method.

It is noted that only the simplest form of EM precursors is considered in the technique. Thus after the technique is described, possible difficulties of applying this technique to real earthquake predictions are discussed. Finally, further improvements and applications of the technique are suggested.

ACKNOWLEDGMENT

This work is supported by Natural Science Fundation under contract NFS61172024 and the Postdoctoral Foundation of Jiangsu Province under contract 1201006C.

Prediction of Radar Reflectivity along Radio Link

Chrispin T. Mulangu[1], **Senzo J. Malinga**[1], **and Thomas J. Afullo**[2]

[1]Department of Electrical Engineering, Mangosuthu University of Technology
Umlazi, KwaZulu-Natal 4031, South Africa
[2]School of Electrical, Electronic & Computer Engineering
University of KwaZulu-Natal, Durban 4041, South Africa

Abstract— Radiowave propagating through a rain zone, will be scattered, depolarized, absorbed and delayed in time. All these effects of rain on the wave propagation are related to the frequency at which the signal is transmitted and polarization of the wave as well as to the rain rate, which influences the form and size distribution of the raindrop. The average power received by the bistatic radar is proportional to the product of reflectivity and attenuation. These can be measured in practice but sometime there is need to determine them separately. In order to determine radar reflectivity, backscattering coefficient needs to be estimated. This study makes predictions about backscattering coefficient caused by hydrometers along terrestrial radio links, operated at wide bandwidth of 10–140 GHz frequencies. The scattering properties of the spherical raindrop are calculated for different sizes of raindrops. From the scattering properties, the back cross-sections for the spherical raindrops are determined and fitted to generate power-law models for different frequencies. These are integrated over different established raindrop-size distribution models to formulate radar reflectivity.

Session 2A4
Multi-scale and Multi-physics Computational Techniques

Time Domain Transient Analysis of Electromagnetic Field Radiation for Phased Periodic Array Antennas Applications
Shih-Chung Tuan, Hsi-Tseng Chou, ... 176
Effect of Random Medium on Wave Propagation in Evaporation Ducts above a Rough Sea Surface
Yung-Hsiang Chou, Jean-Fu Kiang, ... 177
Rigorous Conductor Modeling of Signal Integrity in ICs Using a Multi-solver Domain Decomposition Method
Yang Shao, Zhen Peng, Jin-Fa Lee, ... 178
Non-overlapping Integral Equation Domain Decomposition Method for Dielectric Problems
Ming Jiang, Jun Hu, Ran Zhao, Xiang Wei, Zai-Ping Nie, ... 179
Multiphysics Analysis for Electromagnetic Radiation by Elastic Media
M. H. Wei, Y. Q. Zhang, Y. Q. Wang, Mei Song Tong, ... 180
Multiphysics Modeling and Understanding for Plasmonic Organic Solar Cells
Wei E. I. Sha, Wallace C. H. Choy, Weng Cho Chew, ... 181
An Alternative Algorithm for Dynamic Recognition of Handwritten Signatures
Jimmy Alexander Cortes Osorio, David Esteban Ardila Nieto, Jairo Alberto Mendoza Vargas, ... 182
Homogenization and Applications of Ferromagnetic Nano-wires Based Metamaterials
Jue Wang, Zhen Peng, Jin-Fa Lee, ... 183

Time Domain Transient Analysis of Electromagnetic Field Radiation for Phased Periodic Array Antennas Applications

Shih-Chung Tuan[1] **and Hsi-Tseng Chou**[2]

[1]Department of Communications Engineering, Oriental Institute of Technology, Pan-Chiao, Taiwan
[2]Department of Communications Engineering, Yuan Ze University, Chung-Li, Taiwan

Abstract— The increasing interest in the time domain (TD) analysis of ultra wideband or short pulse target identification and remote sensing applications has resulted in the development of new TD techniques to analyze the antenna radiation, which provides more physically appealing interpretation of wave phenomena. Most recently the applications have been extended to treat the problems arising in the near zone of electrically large antennas such as the vital life-detection systems and noncontact microwave detection systems, where the objects under detection may locate in the near zone of antenna. The potential applications of near-field antennas continue to grow dramatically and desire more exploration in the near future. A TD analytic solution to predict the transient radiation from a phased periodic array of elemental antennas is thus developed. This paper presents an analytical transient analysis of electromagnetic field radiation from a phased and finite periodic array of antennas for the near- and far-field focused applications.

Effect of Random Medium on Wave Propagation in Evaporation Ducts above a Rough Sea Surface

Yung-Hsiang Chou and Jean-Fu Kiang
Graduate Institute of Communication Engineering
National Taiwan University, Taipei, Taiwan

Abstract— Evaporation duct is a surface duct appearing over water bodies, featuring rapid decrease of humidity with height. Evaporation ducts practically appear at lower latitudes. The worldwide mean of the evaporation duct height is about 10 m, sometimes reaches 30 m and exceptionally 40 m With the evaporation ducts so close to the sea surface, the latter has very strong effects on the signal propagating in the ducts.

Empirical evidence of duct height variation with wind speed indicates that large evaporation ducts can exist when the wind speed is relatively low, which can guide energy with little path loss over many kilometers The coastal areas are especially rich in super refractive layers and ducts that affect microwave propagation.

The CDF of duct height have been derived in three locations: the Western Pacific Ocean near the equator, the Coral Sea, and the littoral region around Lucinda, Queensland, respectively. The effect of wind speed on the duct height is analyzed. A series of evaporation-duct height measurements were made in July 1999 over a 100-minute period, by means of atmospheric sensors located near Lucinda, also related to the local wind speed.

Rough sea surface destroys the trapping property of the duct structure and changes the path-loss pattern. The shadowing effect will increase the destructive effect of the rough sea surface on the trapping capability of ducts, especially at long ranges.

Perturbation methods have been developed to analyze wave propagating through a random medium In this work, a numerical model is proposed to study wave propagation in evaporation ducts above a rough sea surface, including the random fluctuation of refractive index in the ducts. Simulation results are compared with measurement data in various scenarios, and the impact on communication links will also be analyzed.

Rigorous Conductor Modeling of Signal Integrity in ICs Using a Multi-solver Domain Decomposition Method

Yang Shao, Zhen Peng, and Jin-Fa Lee
ElectroScience Lab, The Ohio State University
1320 Kinnear Road, Columbus, OH 43212, USA

Abstract— The accurate simulation of large (with many degrees of freedom) and geometrically complicated electromagnetic (EM) problems is of vital importance in many engineering applications. We present herein a frequency-domain multi-region, multi-solver domain decomposition method (MS-DDM) [1], and apply it to accurately analyze signal integrity in multi-scale integrated circuits (ICs). In particular, we propose a novel formulation to rigorously account for the conductor loss due to finite conductivities in metals.

The fundamental strategy of the MS-DDM is to decompose the entire computational domain into many subregions based on the local material properties and geometrical features. For the IC application, it is natural to decompose the model into dielectric subregion and conductor subregion. Subsequently, we employ the most suitable computational electromagnetic (CEM) technique for each of the subregions. For the dielectric subregion, finite element (FE) based non-overlapping DDM method [2] is efficient to solve the complex multi-scale EM problem and account for the non-uniform material properties in this subregion. For the conductor region, the skin and proximity effects are significant at high frequencies and the FE method shall require considerable dense volume mesh for the high-density subregion. Thus, a DDM based surface integral equation method is desirable to solve the conductor sub-domains. Each local conductor sub-domain is enclosed by a closed surface and solved individually through the generalized combined field integral equation (GCFIE) with excitations that include radiations coming from all the other sub-domains. The continuities of tangential electric and magnetic fields on the interfaces between touching sub-domains are implicitly enforced via the optimized Robin type transmission conditions (TCs).

To further accelerate the performance of the GCFIE method, a hierarchical multi-level fast multipole method (H-MLFMM) [4] is adopted to accelerate the matrix vector-multiplication (MVP) and reduce memory consumption for the surface IE methods, especially for the low frequency and multi-scale problems. We shall present numerical results, IC package problems, and demonstrate the accuracy and exibility of the proposed MS-DDM.

REFERENCES

1. Shao, Y., Z. Peng, K. H. Lim and J.-F. Lee, "Non-conformal domain decomposition methods for time harmonic Maxwell equations," *Proc. R. Soc. A*, Vol. 468, No. 2145, 2433–2460, 2012.
2. Shao, Y., Z. Peng, and J.-F. Lee, "Full wave 3-D full package signal integrity analysis using non-conformal domain decomposition method," *IEEE Trans. Microw. Theory Techn.*, Vol. 59, No. 2, 230–241, 2012.
3. Peng, Z., K.-H. Lim, and J.-F. Lee, "Computations of electromagnetic wave scattering from penetrable composite targets using a surface integral equation method with multiple traces," *IEEE Trans. Antennas Propag.*, in press.
4. Wei, J., Z. Peng, and J.-F. Lee, "A hierarchical multi-level fast multipole algorithm for wideband multiscale electromagnetic problems," *IEEE Trans. Antennas Propag.*, accepted.

Non-overlapping Integral Equation Domain Decomposition Method for Dielectric Problems

Ming Jiang, Jun Hu, Ran Zhao, Xiang Wei, and Zaiping Nie
School of Electronic Engineering
University of Electronic Science and Technology of China, Chengdu, China

Abstract— In this paper, a hybrid algorithm based on non-overlapping domain decomposition method and surface Integral equation (IE-DDM) is presented for dealing with time-harmonic electromagnetic (EM) problems of dielectric object. It provides a flexible and efficient method to decompose the problem into easily solvable sub-domains. The decomposed problems will not have the same solution as the original entire domain problem unless proper boundary conditions are imposed for touching-face between neighboring sub-domains. Here a transmission condition is introduced to weakly enforce the field continuous across the touching-face, which is similar to the implantation of the Robin TCs proposed by Prof Jin-Fa lee and Peng. Moreover each sub-domain can be meshed independently without consideration of conformity to adjacent sub-domains. So each sub-domain can be totally independent in the sense of mesh preparation and solution. Here, the electric and magnetic current combined-field integral equation (JMCFIE) serves as a sub-domain solver for dielectric object. In fact, domain decomposition can be considered as a global preconditioning technique for the resulting linear system. Finally, some numerical examples are presented to demonstrate its validity and efficiency.

Multiphysics Analysis for Electromagnetic Radiation by Elastic Media

M. H. Wei, Y. Q. Zhang, Y. Q. Wang, and M. S. Tong
Department of Electronic Science and Technology, Tongji University
4800 Cao'an Road, Shanghai 201804, China

Abstract— Electromagnetic (EM) radiation is caused by electric oscillation in metallic devices like antennas. The fundamental mechanism of EM radiation is the acceleration or deceleration of free electric charges (electrons) when they move in metallic materials, therefore all devices with the acceleration or deceleration of free electric charges in movement will result in EM radiation through time-varying currents. EM radiation could also be produced by mechanical approaches through the mechanical-to-electrical converters, namely, piezoelectric or electrokinetic materials. Mechanical oscillation or vibration in such materials can yield a motion of electric charges with varying velocity and generate time-varying currents leading to EM radiation. The EM radiation from piezoactive rocks under the influence of elastic oscillations triggered by shots or mechanical impacts was first observed and studied by former Soviet scientists in 1950's and the related techniques were widely applied to geophysical exploration for many valuable minerals. To systematically study the EM radiation by mechanical approaches, one can exert controllable mechanical vibration on piezoelectric objects and measure radiated EM fields. The theoretical analysis and simulation for the phenomenon have been studied since 1950's based on coupled electrodynamic and elastodynamic equations. However, the investigations were only based on the original partial differential equation (PDE) form of the equations and the solutions for the equations were mostly obtained by analytical approaches with greatly simplified geometries.

In this work, we develop an integral equation method to study the EM radiation phenomenon from piezoelectric objects in controllable mechanical vibration. The coupled governing integral equations were developed from the PDE counterparts by using Huygens' equivalence principle and extinction theorem. In the derivation, it is recognized that the current is generated by the varying displacement vector through strain tensors in the Maxwell's equations. By the developed integral equations, all numerical methods for integral equation solvers, such as method of moments (MoM), boundary element method (BEM) or Nyström method can be used in the analysis and simulation, and the advantages of integral equation solvers can be exhibited. We use Nyström method to solve the coupled integral equations for EM radiation from 3D piezoelectric objects in vibration and some basic numerical results will be illustrated in the talk.

Multiphysics Modeling and Understanding for Plasmonic Organic Solar Cells

Wei E. I. Sha[1], **Wallace C. H. Choy**[1], **and Weng Cho Chew**[2]

[1]Department of Electrical and Electronic Engineering
The University of Hong Kong, Pokfulam Road, Hong Kong, China
[2]Department of Electrical and Computer Engineering
University of Illinois, Urbana-Champaign, Illinois, USA

Abstract— A multiphysics study carries out on bulk heterojunction organic solar cells (OSCs) by solving Maxwell's equations and semiconductor (Poisson, drift-diffusion, and continuity) equations simultaneously with unified finite difference framework. By introducing a metallic rectangular-grating as the anode, surface plasmon resonances are excited resulting in extremely nonuniform exciton generation. Meanwhile, the built-in potential and internal electrostatic field of the plasmonic OSC device are significantly modified due to the modulated anode boundary. From the theoretical model, we demonstrate that the plasmonic OSC structure improves 13% of short-circuit current but reduces 7% of fill factor compared to the standard one with a planar anode layer. The uneven photocarrier generation and transport induced by the metallic grating anode are the physical origins of the dropped fill factor. The spatially nonuniform exciton generation and internal electrostatic field distribution strongly depending respectively on the optical and electrical responses of the metallic grating should be taken into account for future designs of plasmonic OSCs. This work provides fundamental multiphysics modeling and understanding for plasmonic organic photovoltaics.

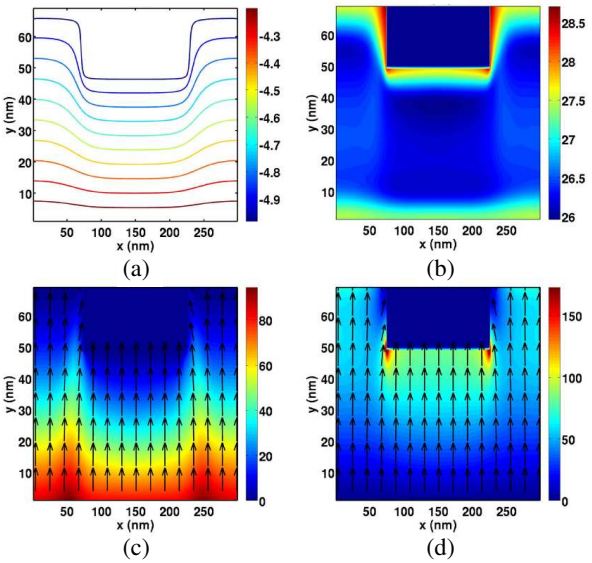

Figure 1: The electrical results of the plasmonic OSC at the short-circuit condition. (a) Equipotential lines (V); (b) recombination rate with the logarithmic scale ($m^{-3}s^{-1}$); (c), (d) electron and hole current densities (A/m^2). The color and arrow denote the amplitude and direction of the currents.

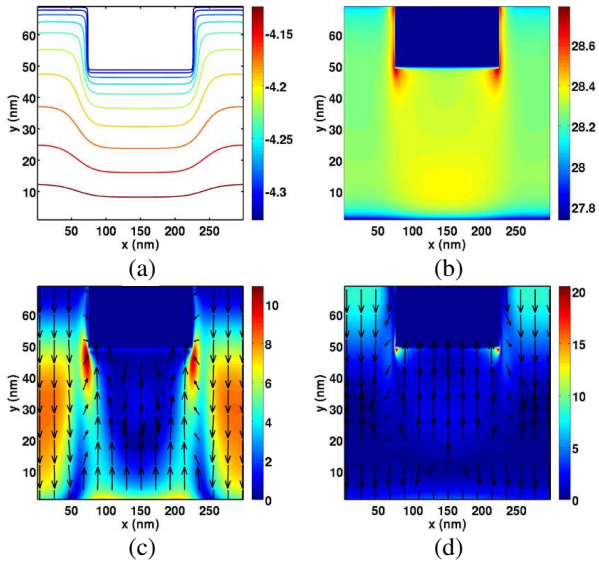

Figure 2: The electrical results of the plasmonic OSC at the open-circuit condition. (a) Equipotential lines (V); (b) recombination rate with the logarithmic scale ($m^{-3}s^{-1}$); (c), (d) electron and hole current densities (A/m^2). The color and arrow denote the amplitude and direction of the currents.

REFERENCES

1. Sha, W. E. I., W. C. H. Choy, and W. C. Chew, "The roles of metallic rectangular-grating and planar anodes in the photocarrier generation and transport of organic solar cells," *Applied Physics Letters*, AIP, Accepted for Publication.

An Alternative Algorithm for Dynamic Recognition of Handwritten Signatures

Jimy Alexander Cortés, David Esteban Ardila Nieto, and Jairo Alberto Mendoza Vargas
Universidad Tecnológica de Pereira, Colombia

Abstract— A signature is more than a simple drawing on a sheet of paper because each person has his own signing style which depends on the way the pen is used and the time is taken to do it. This paper research assesses and identifies the necessary characteristics and introduces an algorithm for dynamic recognition of handwritten signatures by using distinctive behavioural features of the signature such as position, velocity, acceleration, pressure and azimuth by means of pattern recognition precedure such as neuronal networks. This solution can be use to eliminate the huge flow of business stationery and its time consuming process by providing reliable remote agreements (such as transactions and contracts).

This paper evaluates the computational performance of the minimum requirements for the recognition of the handwritten signature and its implementation in an embedded system of modest computational performance. This development is intended to be set up on an embedded system which has to be able to recognize dynamic handwritten signatures from users.

There are important advances in the field of biometric research that have served to verify the person's identity in security systems around the world, but there is also much to develop in identifying the dynamic handwritten signature in Latin America where this kind of solution could help to improve the authentication at a lower cost where this is an important fact.

Homogenization and Applications of Ferromagnetic Nano-wires Based Metamaterials

Jue Wang, Zhen Peng, and Jin-Fa Lee
ElectroScience Lab, The Ohio State University
1330 Kinnear Road, Columbus, OH 43212, USA

Abstract— Metamaterials are broadly defined as artificial effective electromagnetic structures composed of electrically small units and achieving exotic responses that are not readily available in conventional materials. Extensive research conducted on metamaterials has led to many innovative theories and devices over the years [1, 2]. During the first decade of the new century, the development of artificially structural materials is at the stage where interdisciplinary interest is taking place, such as multiscale metamaterials, reconfigurable metamaterials and the combination with nanotechnology. While the potentials of metamaterials and their possible applications are appealing, it is often difficult to model them accurately due to inherently the very fine and complex structures involved. However, by observing that metamaterials usually consist of positioned inclusions (most often periodically) much smaller than the electromagnetic wavelength of interest, a homogenized description of the structure can be adopted as an accurate alternative.

We propose herein this paper numerical procedures to compute both the static and small signal magnetic field distributions within ferromagnetic material nanowires (FMNWs) based metameterial structures, extract macroscopic effective material properties through homogenization, and finally analyze the performance of microwave components/devices including such a macroscopic description of the FMNWs [3].

Instead of utilizing the usual analytical and crude approximate field averaging method [4, 5], this paper aims to pursue a homogenization process through 3-D full-wave electromagnetic computations in-conjunction with a suite of computational electromagnetic simulation tools developed previously at OSU [6, 7]. Particularly, we are interested in nanometer scale, the ferromagnetic wire array and exploit its magnetic properties as well as investigate its integrations with microwave/RF components. The use of ferromagnetic materials is not new, however, the marriage with metamaterial structure can potentially contribute significantly toward the reduction of size in microwave devices. This is mainly attributed to its tailored electromagnetic responses compared against traditionally bulky ferromagnets, which may lead to great interest practically in the future, aided by the constant progress achieved in fabrication of ferromagnetic material nanowires.

Numerical results of microwave devices integrated with FMNWs based metematerial structures show the accuracy and efficiency of the proposed homogenization method.

REFERENCES

1. Veselago, V. G., "The electrodynamics of substances with simultaneously negative values of ϵ and μ," *Sov. Phys. Usp.*, Vol. 10, 1968.
2. Smith, D. R., W. Padilla, D. C. Vier, S. C. Nemat-Nasser, and S. Schultz, "A composite medium with simultaneously negative permeability and permittivity," *Phys. Rev. Lett.*, Vol. 84, 2000.
3. Carignan, L.-P., A. Yelon, D. Menard, and C. Caloz, "Ferromagnetic nanowire metamaterials: Theory and applications," *IEEE Trans. on Microwave Theory and Techniques*, Vol. 59, 2011.
4. Boucher, V., L.-P. Carignan, T. Kodera, C. Caloz, A. Yelon, and D. Menard, "Effective permeability and double resonance of interacting bistable ferromagnetic nanowires," *Physical Review B*, Vol. 80, 2009.
5. Smith, D. R. and J. P. Pendry, "Homogenization of metamateirals by field averaging," *J. Opt. Soc. Am. B*, Vol. 23, 2006.
6. Seo, S. M. and J.-F. Lee, "A fast IE-FFT algorithm for solving PEC scattering problems," *IEEE Trans. on Magnetics*, Vol. 41, 2005.
7. Peng, Z., V. Rawat, and J.-F. Lee, "One way domain decomposition method with second order transmission conditions for solving electromagnetic wave problems," *J. Comp. Phys.*, 2010.

Session 2A5
Antenna Measurement

Input Impedance Measurement for Balanced Antenna by S-parameter Method
Takayuki Sasamori, Teruo Tobana, Yoji Isota, ... 186
Balanced and Unbalanced Mode Analysis in a Practical Balanced Dipole Antenna Using Mixed-mode $\boldsymbol{S}$-parameter
Nozomu Ishii, Junki Hayakawa, ... 187
Measurement Methods for Total Radiated Power from an Antenna
Hiroyuki Arai, Nozomu Ishii, ... 188
A New Transmission Formula to Extend Friis Formula
Masanobu Hirose, Michitaka Ameya, Satoru Kurokawa, ... 189
W-band Antenna Pattern Measurement System Using Photomixing Technique with UTC-PD
Michitaka Ameya, Masanobu Hirose, Satoru Kurokawa, ... 190
Near-field Magnetic Probe Method Predicting Far-field Measurements — Correlation of Dipole Boresight Measurements with Anechoic Range Model
Daniel Brooks, Stuart Nicol, Jesse Hones, John Lee, ... 191
Near-field Measurement System for Evaluation of Aperture Distribution, Radiation Pattern and Gain of Millimeter-wave Planar Array Antennas
Kunio Sakakibara, Hiroshi Hirayama, Nobuyoshi Kikuma, ... 192
Broadband and Simplified SAR Measurement Method Using Wave Absorber Phantom for Handset Antennas
Naobumi Michishita, Keita Ochiyama, Yoshihide Yamada, Hiroyuki Arai, Toshiyasu Tanaka, ... 193
A Planar PIM-generator for Antenna PIM Test Setup
Kohei Takada, Nobuhiro Kuga, ... 194

Input Impedance Measurement for Balanced Antenna by S-parameter Method

T. Sasamori, T. Tobana, and Y. Isota
Akita Prefectural University, Japan

Abstract— In recent years, many wireless telecommunication services have spread over the world. It is known that the characteristics of conventional antennas, such as monopole antennas, change considerably when the body of the handset is touched by the hand. This is caused by the variation of the current on the surface of the conducting box used for the handset due to human body influence. To decrease the influence of the human body, a balanced fed antenna is suggested. The input impedance of the balanced antenna is measured conventionally by using a balun that forces opposite currents into each part of the radiation element. Generally, due to the narrow available bandwidth, balun is not suitable for the measurement of the wideband balanced antenna. Recently, the S-parameter method is proposed to measure the balanced impedance of the antenna using a jig instead of the balun, and two ports of a vector network analyzer. We have examined the S-parameter method with calibration cables and a jig fabricated by semi-rigid cable.

In this presentation, measured results of the S-parameter method after the TRL calibration is performed are compared with the measured results after the OSLT calibration and the compensating method using $ABCD$-matrix is performed. A jig for measuring balanced loads is fabricated by the microstrip line on PCB to improve the fabrication accuracy and reproducibility. Three compensating methods using $ABCD$-matrix, called open-correction, short-correction, and open-short-correction are applied to eliminate the influence of the jig. The wideband input impedance of a dipole antenna, which is one of typical balanced fed antennas, is measured using our proposed methods, and are compared with a calculated results using the moment method.

Balanced and Unbalanced Mode Analysis in a Practical Balanced Dipole Antenna Using Mixed-mode *S*-parameter

Nozomu Ishii and Junki Hayakawa
Graduate School of Science and Technology, Niigata University, Japan

Abstract— The balanced antennas are often used in the radio communication devices. The unbalanced current on the antennas or devices is undesired and needed to be eliminated. Therefore, the input impedance/admittance for the balanced/unbalanced modes and the mode coupling should be accurately measured. The input impedance of the balanced antennas can be estimated by using not only 180 degree hybrid coupler/balun but also S-parameter method, where S parameters are measured between two ports attached to the symmetrical antennas. In this paper, first, S-parameter method can be derived by using the theory of the mixed-mode S parameter, where the normal S parameters are transformed into redefined S parameters for the balanced and unbalanced modes. Since the effect of the unbalanced mode in the practical balanced antennas, the input admittance for the unbalanced mode and CMRR (common-mode rejection ratio) can be also derived using the theory of the mixed-mode S parameter. By evaluating CRMM at the resonance of the balanced dipole antenna, we can find that the amount of the reflection for the balanced mode is reduced, CMRR is minimized, and the relatively large excitation for the unbalanced mode can be observed. Second, the validity of our derivation can be proven by some experiments using the 180 degree hybrid coupler. To correct the imperfect 180 degree hybrid coupler, we measure its S parameters and evaluate the input impedance or admittance for the balanced or unbalanced modes of the balanced antennas using the S parameters. In this paper, three ways of measuring the input impedance/admittance for the balanced/unbalanced mode of the balanced antennas are examined. To reduce the measurement time, one port reflection measurement with the other port matched or normal way of the balanced mode excitation using the 180 degree hybrid coupler is examined.

Measurement Methods for Total Radiated Power from an Antenna

Hiroyuki Arai[1] **and Nozomu Ishii**[2]

[1]Graduate School of Engineering, Yokohama National University, Japan
[2]Graduate School of Science and Technology, Niigata University, Japan

Abstract— Due to the diversification of operation forms of the wireless devices, the measurement of the radiated power from the devices in the operation status, that is, in all directions of the devices should be required. CTIA (Cellular Telecommunications and Internet Association) recommends the maximum division angle of 15 degree in azimuth and elevation angle, providing 264 sample points. In this paper, we present four methods for measuring total radiated power (TRP) using the pattern measurement in all direction, such as, ordinary equi-angle method, modified equi-angle method, generalized spiral method and partially spherical scanning method. The modified equi-angle method divides sampling interval to keep equal area between sampling points, which is almost equivalent to equi-area method. The generalized spiral method picks up each sample along a spiral line on the sphere. This method provides an easy and smooth probe scanning in the spherical coordinate. The partial scanning method uses a circular reflector base to hide the azimuth rotator to support heavy devices being tested. These methods are discussed to find the minimum number of sampling points by using radiation patterns of antennas built in notebook PC. Reference 3-D radiation patterns are given by the conical-cut method with angular spacing of 5 degree in elevation and 1 degree in azimuth angle. Numerical simulation using these 3-D data result in that the minimum total number of sampling points are 200 for modified equi-angle and generalized spiral methods, which reduces the measurement time with high accuracy. In addition to these measurements, this paper also presents a simple approximation method to reduce the measurement time.

A New Transmission Formula to Extend Friis Formula

Masanobu Hirose, **Michitaka Ameya**, **and Satoru Kurokawa**
AIST, Japan

Abstract— A new transmission formula has been proposed to extend the Friis transmission formula at the short distance between two antennas, which is a few times shorter than the far-field criterion. The new formula is expressed by the conventional phase centers of the antennas in addition to the pattern sharpness that is introduced newly. The validity of the new formula is demonstrated by numerical examples of a log-periodic antenna and a standard horn antenna.

W-band Antenna Pattern Measurement System Using Photomixing Technique with UTC-PD

Michitaka Ameya, Masanobu Hirose, and Satoru Kurokawa
AIST, Japan

Abstract— A number of wireless products using millimeter-wave (mm-wave) have been developed in recent years. The antenna of the wireless system is a key component and the evaluation of the antenna is high-priority issue for the wireless system. In the mm-wave region, rectangular waveguides are generally used as transmission lines. The mm-wave components, such as couplers and frequency multipliers are heavy and bulky because they are made with rectangular waveguides. Therefore, the antenna pattern measurement system consists of waveguide components has low flexibility and difficulty in rotating the antenna for pattern measurements. In addition, the measured results of antenna pattern are affected by waveguide components because they are electrically large.

To solve these problems, we propose the antenna pattern measurement system in W-band using photomixing technique with UTC-PD. Due to this system, we can use an optical fiber as the transmission line of mm-wave signal and miniaturize the mm-wave signal source. Accordingly, we can suppress the disturbance from the waveguide components and achieve precise pattern measurements.

In the presentation, we will show the measured antenna pattern of open ended waveguide probe and standard gain horn antenna in W-band by proposed system in comparison with a conventional system.

Near-field Magnetic Probe Method Predicting Far-field Measurements — Correlation of Dipole Boresight Measurements with Anechoic Range Model

Daniel Brooks, **Stuart Nicol**, **Jesse Hones**, **and John Lee**
Aprel Inc., Ottawa, Ontario, Canada

Abstract— Traditional methods for establishing EMC and field density can be predicted using a field approximation routine based on well documented principles. In the process of reducing spurious emissions or interference EMC engineers will use suppression techniques of shields, boxes and cages. These methods have been found to work in normal applications but as the frequency expands traditional methods of EMC suppression may not be as effective. The far field approximation technique presented in this paper allows an engineer to test a sub assembly in the near field and then have a value which can be extrapolated to the far field. Measurements taken using the broadband near field "magnetic probe method" used with an automated scanning system (EM-ISight) can be extrapolated to either a 3 m or 10 m range space. Such a technique can allow the design engineer to determine the effectiveness of their design prior to the final integration of an assembly thus understanding better the uncertainties of a previously developed reference design or suppression methods.

Near-field Measurement System for Evaluation of Aperture Distribution, Radiation Pattern and Gain of Millimeter-wave Planar Array Antennas

Kunio Sakakibara, Hiroshi Hirayama, and Nobuyoshi Kikuma
Nagoya Institute of Technology, Gokiso-cho, Showa-ku, Nagoya 466-8555, Japan

Abstract— Near-field measurement system was developed for evaluation of aperture distributions, radiation patterns, and gains of millimeter-wave planar array antennas. We have been in the development of various sizes of microstrip comb-line antennas and slotted waveguide antennas in the millimeter-wave band. Traveling-wave antennas are very attractive in low-loss property. However, high design accuracy is required in the assignment of the coupling factor to each radiating element for uniform distribution of high gain antenna and for Taylor distribution of low-sidelobe antenna. Aperture phase distribution inclines and beam direction shifts when frequency changes from the design frequency. Thus, the aperture distribution is a key feature to diagnose the design quality and the performance degradation from the design of the aperture array antennas. The near-field measurement systems are very useful to check the uniformity of the aperture amplitude and phase distributions of the planar array antennas. Radiation patterns can be obtained by Fourier Transform of the complex near-field data of the aperture distribution. Gain is also obtained by the sum of the gain of the standard horn antenna and the difference of the main beam levels in the radiation patterns of the antenna under test and the standard horn antenna. This paper summarizes the detail of the developed near-field measurement system which is capable of the measurement in the millimeter-wave band. Measurement results will be presented in the session for various measurement parameters, such as scan area, distance of the probe from the aperture, scan pitch, aperture size of the antenna under test, and so on.

Broadband and Simplified SAR Measurement Method Using Wave Absorber Phantom for Handset Antennas

Naobumi Michishita[1], **Keita Ochiyama**[1], **Yoshihide Yamada**[1], **Hiroyuki Arai**[2], **and Toshiyasu Tanaka**[3]

[1]National Defense Academy, Japan
[2]Yokohama National University, Japan
[3]Microwave Factory Co., Ltd., Japan

Abstract— To measure the specific absorption rate (SAR) of mobile devices used near the human body, the use of a liquid phantom is prescribed in the international specifications at each frequency. Electrical parameters of the liquid phantom vary due to evaporation or deposition. In addition, the standard SAR measurement is time consuming due to 3-D scanning. To overcome these problems, a lightweight phantom composed of a wave absorber and a broadband phantom composed of solid materials have been developed for simplification of the standard SAR measurement method. The proposed method using the wave absorber phantom has been verified at only 835 MHz and 1950 MHz. This paper focuses the measurement method using the wave absorber phantom to extend the measurement range from 700 MHz to 4 GHz for adapting to the recent cellular mobile communication systems. To reduce the measurement time in the simplified method, the internal electric field distribution in the liquid phantom is estimated by using the measured 2-D scanning data inside the wave absorber. Therefore, the attenuation characteristics in the liquid and the wave absorber phantoms will be clarified at several situations of the antenna under test. The antenna factor for obtaining the electric field intensity from the measured power at the probe will be also shown at each frequency.

A Planar PIM-generator for Antenna PIM Test Setup

Kohei Takada and Nobuhiro Kuga
Faculty of Engineering, Yokohama National University
Tokiwadai 79-5, Hodogaya-ku, Yokohama-shi 240-8501, Japan

Abstract— PIM is caused by non-linearity in passive circuits such as base-station antennas in mobile communication systems. In PIM measurements, level-known PIM generators are used to assess a measurement setup. For the purpose, the authors has proposed a new concept of variable PIM-level generator using antenna [1–3] while fixed-level generators using connectors has been used conventionally [4]. On the other hand, PIM measurements of antennas, the effect of external PIM sources have to be considered [5]. To carry out a basic examination as shown in Figure 1, the authors introduced an axial-lead diode with shunt loop shown as model-A in Figure 2, which was used as the external PIM source in Figure 1 [6]. The difference of the concept from [1, 3] is that a PIM source model is placed not in the near field but the far field of the antenna. PIM level generated from model-A is controlled by the polarization loss toward the left-side antenna. This polarization loss was a problem to be solved in that examination.

In this paper, a planar PIM-generator as an external PIM-generator is proposed. It consists of a holed cupper foil backed with a dielectric substrate, where a diode is mounted in on the hole. Compared to model-A, model-B can reduce the dependence on the polarization and improves the level-control ability because the PIM-level is determined by the mounting angle ϕ while the position of the rectangle mounting plate is remained. The proposed wide strip structure is effective to reduce the PIM caused by the copper foil itself.

Figure 3 shows the performance of a prototype, where the 3rd-order PIM at 1.90 GHz for the two-tone test with 2.05 GHz, 2.20 GHz is evaluated. It is the PIM level observed by the antenna as a function of the input power on the antenna. Although the absolute level of the PIM is lower than model-A with the axial-lead, good linearity for the input power is confirmed. It is also confirmed that the generated PIM level can be controlled by the mounting angle of the diode ϕ. The effect of the diode-mounting angle seems to be small in this result; however, it is due to the self-PIM of the antenna which can be improved.

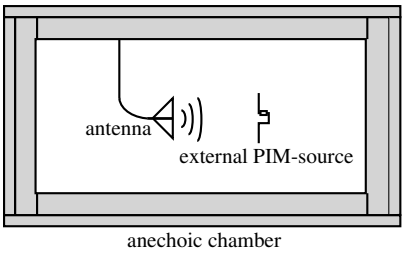

Figure 1: A simplified test setup for the effect of an external PIM source.

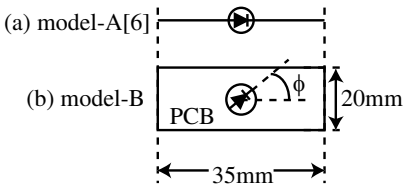

Figure 2: Configuration of the external PIM sources.

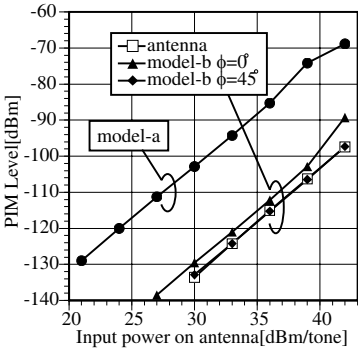

Figure 3: PIM level observed by the antenna as a function of the input power on the antenna.

ACKNOWLEDGMENT

We would like to thank Dr.Ihara with NTT Docomo for the support of experimental setup and fruitful discussion.

REFERENCES

1. Irie, K. and N. Kuga, "Patch antenna with diode as passive intermodulation source," *IEICE Trans. Commun.*, Vol. J93-B, No. 9, 1170–1176, Sep. 2010 (in Japanese).
2. Irie, K., N. Kuga, and K. Cho, "PIM-linearity improvement by the size of a diode mounting hole," *IEICE Electronics Express*, Vol. 8, No. 14, 1198–1203, Jul. 2011.

3. Irie, K. and N. Kuga, "Elliptical disk monopole antenna with diode for PIM measurement facility assessment," *IEICE Trans. Commun.*, Vol. J94-B, No. 9, 1146–1152, Sep. 2011 (in Japanese).
4. Henrie, J., A. Christian, and W. J. Chappel, "Engineered passive nonlinearities for broadband passive intermodulation distortion mitigation," *IEEE Microw. Wirel. Compon. Lett.*, Vol. 19, No. 10, 614–616, Oct. 2009.
5. Kim, J. T., L. K. Cho, M. Y. Jeong, and T. G. Choy, "Effects of external IM sources on antenna IM measurements," *ETRI Journal*, Vol. 24, No. 6, 435–442, Dec. 2002.
6. Takada, K., N. Kuga, and K. Cho, "An experimental consideration on the effect of antenna gain on the observed PIMs for an external PIM-source," *ISAP 2012*, Nov. 2012.

Session 2A6
Passive Waveguide Devices Theory and Numerical Modeling

Method of Connected Local Fields for the Helmholtz Equation
Hung-Wen Chang, Sin-Yuan Mu, ... 198
Dispersion Analysis of the 3D LFE-27 Formula for the Method of Connected Local Fields
Sin-Yuan Mu, Hung-Wen Chang, ... 199
FD-FD Analysis of SOI Based Micro-ring Cavities
Hung-Wen Chang, ... 200
Guided Modes of Photonic Crystal Fiber Coupler Using Vector Boundary Element Method
Jung-Sheng Chiang, Rui-Sheng Wang, Yu-Liang Chen, Nai-Hsiang Sun, ... 201
Grating-assisted Coupling between Contra-propagated Modes
Nai-Hsiang Sun, Chia-Ming Hu, Shou-Feng Tsai, Tsum-Yen He, Shih-Cing Lei, Jung-Sheng Chiang, 202
Analysis of Fiber Bragg Gratings with Multi-grating Sections
Nai-Hsiang Sun, Chia-Ming Hu, Kun-Jhe Li, Fang-Jui Chang, Jung-Sheng Chiang, ... 203
Analysis of Surface Plasmon Phenomenon of Multi-pair Array of Silver Nanocylinders and Design
Po-Jui Chiang, Fang-Chi Li, Nai-Hsiang Sun, Chia-Ming Hu, ... 204
Investigation of Frequency-domain Absorbing Boundary Conditions for the Helmholtz Equation
Hung-Wen Chang, ... 205
Comparison of Frequency-domain Absorbing Boundary Conditions for the Helmholtz Equation
Hung-Wen Chang, ... 206
Local Field Expansion Coefficients for Dielectric Media with Interfaces Based on the Method of Connected Local Fields
Hung-Wen Chang, Sin-Yuan Mu, ... 207

Method of Connected Local Fields for the Helmholtz Equation

Hung-Wen Chang and Sin-Yuan Mu
Department of Photonics, National Sun Yat-Sen University, Taiwan

Abstract— Over the past few years we been working on the method of connected local fields, CLF [1, 2] which is a semi-analytical solutions of the Helmholtz equation. In CLF the EM fields are expressed as collection of overlapping local fields called patches. We show that the local field in a given patch can be approximated by truncated Fourier-Bessel (F-B) series and the F-B coefficients are related to the control points on the surface of the given patch. Figure 1 illustrates a basic patch in a 2D/3D network of equally spaced points containing 8/26 points on the faces and a point inside the square/cube. The end result is that both the 2D LFE-9 and the 3D LFE-27 formulae behave just like the standard FD-FD methods with compact FD stencil. Under CLF, due to its semi-analytical nature, we are able to solve complex EM wave problems with a much reduced grid density.

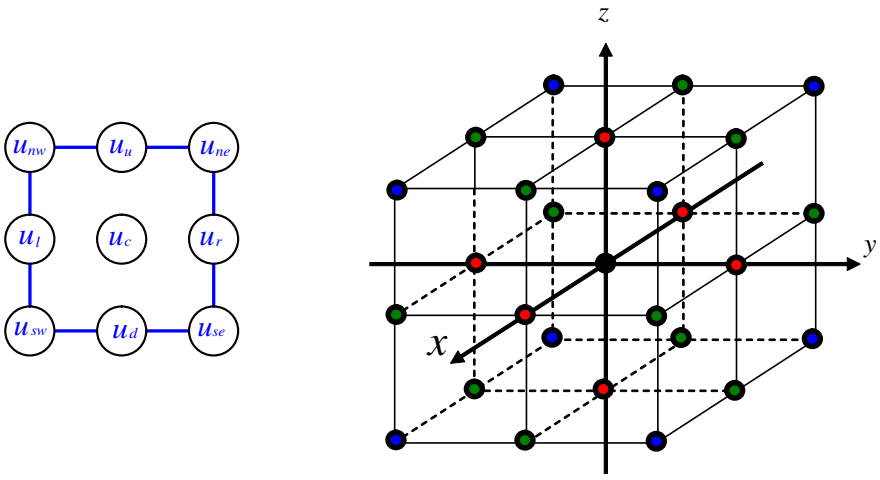

Figure 1: The unit square/cube and the 8/26 nodes for the 2D/3D theory of connected local fields.

ACKNOWLEDGMENT

We are grateful to the support of the National Science Council of the Republic of China under the contracts NSC 100-100-2221-E-110-065.

REFERENCES

1. Chang, H.-W. and S.-Y. Mu, "Semi-analytical solutions of Helmholtz equation by the method of connected local fields," *Progress In Electromagnetics Research*, Vol. 109, 399–424, 2010.
2. Mu, S.-Y. and H.-W. Chang, "Theoretical foundation for the method of connected local fields," *Progress In Electromagnetics Research*, Vol. 114, 67–88, 2011.

Dispersion Analysis of the 3D LFE-27 Formula for the Method of Connected Local Fields

Sin-Yuan Mu and Hung-Wen Chang
Department of Photonics, National Sun Yat-Sen University, Taiwan

Abstract— Following our previous work on the method of connected local fields [1, 2], we investigate the local field expansion (LFE) formulation, LFE-27, by means of rigorous dispersion analysis. Dispersion characteristic along various chosen directions are to be analyzed as shown in Figure 1. Both numerical phase velocity and numerical group velocity for LFE-27 are compared to other FD-like schemes. The classical FD formula (FD2-7) requires that the number of grid points per wavelength is more than fifteen to reduce the dispersion error (also phase velocity error) to less than 1% and to reduce the group-velocity error of to less than 2.5%. With LFE-27, when we use 2.7 grid points per wavelength, the corresponding error of the phase velocity is about 0.1% and the error of the group velocity is about 1%. LFE-27 exhibits high accuracy even if it is inspected by the harsher error evaluation, relative error of group velocity. In addition we will apply LFE-27 formulation to compute numerical Green's function for 3D Helmholtz equation in free space. Together with the plane wave analysis, we have numerically verified the validity of the newly-derived formula for the theory of connected local fields.

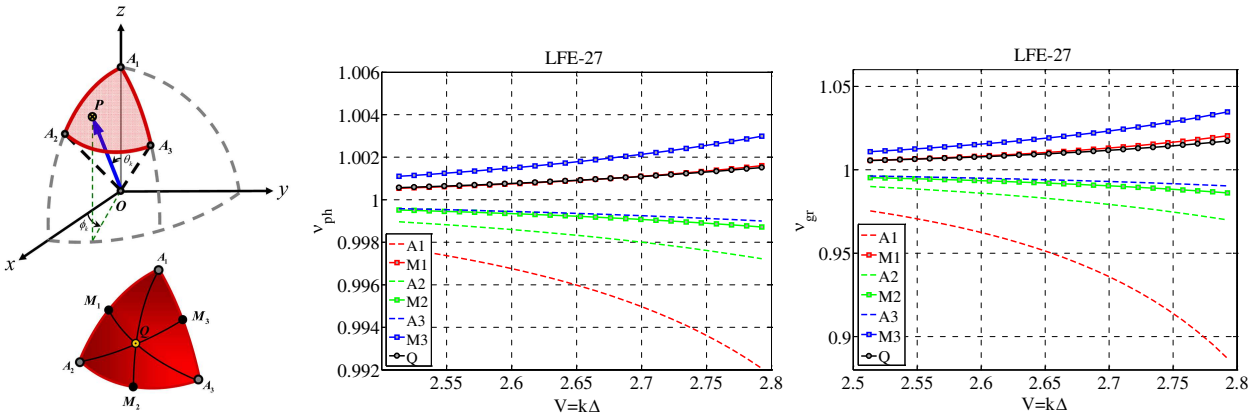

Figure 1: Numerical phase/group velocity for LFE-27 along various directions.

ACKNOWLEDGMENT

We are grateful to the support of the National Science Council of the Republic of China under the contracts NSC 100-100-2221-E-110-065.

REFERENCES

1. Chang, H.-W. and S.-Y. Mu, "Semi-analytical solutions of Helmholtz equation by the method of connected local fields," *Progress In Electromagnetics Research*, Vol. 109, 399–424, 2010.
2. Mu, S.-Y. and H.-W. Chang, "Theoretical foundation for the method of connected local fields," *Progress In Electromagnetics Research*, Vol. 114, 67–88, 2011.

FD-FD Analysis of SOI Based Micro-ring Cavities

Hung-Wen Chang
Department of Photonics, National Sun Yat-Sen University
70 Lien-Hai Rd., Kaohsiung 80424, Taiwan, R.O.C.

Abstract— Micro-ring cavities are important optoelectronic devices used in optical communication systems. The recently available silicon on insulator (SOI) technology allows us to reduce this micro-ring device to micron size. Traditionally the physics and working principles of micro-ring devices are well understood based on the assumption of uni-directional single and multi-mode traffic within the waveguides. Although waveguide material loss as well as bending loss can only be included in the theory, radiation and mode conversion loss are much harder to estimate. As the devices become smaller, we can no longer neglect the more complicated wave physics. The devices are too complex for analytical modal analysis.

Time-domain finite-difference (FD-TD) method is often used to study the transfer functions of micro-ring cavity devices. It is well-known that long time simulation is needed to resolve sharp resonances associated with the ring cavity. Also very small grid spacing must be chosen to capture the fine structure in the SOI circuit. Long simulation time plus small grid size will all contribute to the increased run time as well as the accumulated phase error due to FD grid dispersion. FD-TD simulation also posses errors due to the imperfect time-domain based absorbing boundary condition.

We combine highly accurate frequency-domain finite-difference (FD-FD) methods [1, 2], an index averaging scheme for FD coefficients and the wave extrapolation absorbing boundary condition to study SOI based micro-ring cavity devices.

ACKNOWLEDGMENT

We are grateful to the support of the National Science Council of the Republic of China under the contracts NSC 100-100-2221-E-110-065.

REFERENCES

1. Chang, H.-W. and S.-Y. Mu, "Semi-analytical solutions of Helmholtz equation by the method of connected local fields," *Progress In Electromagnetics Research*, Vol. 109, 399–424, 2010.
2. Mu, S.-Y. and H.-W. Chang, "Theoretical foundation for the method of connected local fields," *Progress In Electromagnetics Research*, Vol. 114, 67–88, 2011.

Guided Modes of Photonic Crystal Fiber Coupler Using Vector Boundary Element Method

Jung-Sheng Chiang, Rui-Sheng Wang, Yu-Liang Chen, and Nai-Hsiang Sun
Department of Electrical Engineering, I-Shou University, Kaohsiung, Taiwan

Abstract— We report a numerical approach, base on the surface integral equations formulations, to model the photonic crystal fiber for analysis of guided modes. Photonic crystal fibers, also called microstructured fibers or holey fibers, have aroused great attention, because of their unique advantages of control of light. PCFs are composed of a single material (generally silica) with multiple air-holes periodically arranged around the core that run along the length of the cladding. Coupler is one of essential components in optical fiber communication and optical fiber sensing systems. It can be applied as dividing/combining the optical power in optical fiber networks, wavelength division multiplexer, interferometric sensors, and so on. A single power can be divided into several branches and can be routed to different locations for additional purposes. With the fusion process, the coupler must be twisted and tapered during fabrication. It may be difficult to make 1×4 coupler using conventional optical fibers. The PCF has become possible to create multicores in a single fiber without fusion process. It is rather easy to split the light into surrounding cores in multicore PCFs. In this paper, we propose and investigate a new structure of the 1×4 PCF coupler that can divide a single optical power equally into four ports with 6 dB of power in each core. The structure consists of four identical cores surrounding an identical central core. We use the vector boundary element method (VBEM) and couple-mode theory to design and model the coupler.

Grating-assisted Coupling between Contra-propagated Modes

Nai-Hsiang Sun, Chia-Ming Hu, Shou-Feng Tsai, Tsum-Yen He, Shih-Cing Lei, and Jung-Sheng Chiang
Department of Electrical Engineering, I-Shou University, Kaohsiung, Taiwan

Abstract— The contra-directional propagating modes can be coupled by assisted gratings. The device is called the grating-assisted contra-directional coupler (GACC). Not like co-directional couplers, the grating period of contra-directional couplers is shorter than that of grating-assisted directional couplers (GADCs). In this paper, we analyze the contra-directional coupler with gratings by Floquet-Bloch theory (FBT). The field distributions of GACCs and the dispersion relationship of modes in the grating region are calculated by FBT. The discontinuity interfaces between the grating and the non-grating region are analyzed by Mahmoud-Beal's method. By overlapping integrals of the fields, we obtain the transmission efficiency and reflection efficiency of GACCs. The energy distribution in the grating region can be calculated as well. We successfully simulate the transmission and the reflection spectrum of the coupler.

Analysis of Fiber Bragg Gratings with Multi-grating Sections

Nai-Hsiang Sun, Chia-Ming Hu, Kun-Jhe Li, Fang-Jui Chang, and Jung-Sheng Chiang
Department of Electrical Engineering, I-Shou University, Kaohsiung, Taiwan

Abstract— Apodized fiber Bragg gratings (FBGs) have several properties such as superior filtering performance and high side lobe suppression. Apodized FBGs have been widely developed and applied in optical fiber technology. The coupled mode theory is the widely used numerical method to analyze the fiber Bragg gratings. For the structure of uniform FBGs, the coupled mode theory provides analytical solution of the transmission and reflection coefficients of the FBGs. On the other hand, apodized FBGs can be simulated by a FBG with multi-grating sections. In this paper, we use piecewise-uniform approach (PUA) with transfer matrix method (TMM) to simulate apodized grating structures. The apodization profile of gratings is discretized into numerous uniform grating sections. Moreover, Chebyshev-apodized Fiber Bragg Gratings are analyzed in this paper. The reflection spectrum and the group delay of the Chebyshev-apodized FBGs are evaluated in this paper.

Analysis of Surface Plasmon Phenomenon of Multi-pair Array of Silver Nanocylinders and Design

Po-Jui Chiang[1], **Fang-Chi Li**[1], **Nai-Hsiang Sun**[2], **and Chia-Ming Hu**[2]

[1]Department of Electronic Engineering
National Kaohsiung University of Applied Sciences, Kaohsiung, Taiwan
[2]Department of Electrical Engineering, I-Shou University, Kaohsiung, Taiwan

Abstract— The thesis mainly studies the local property of Surface Plasmon in the silver metallic nanocylinders structure and near-field optical phenomenon. Our numerical method based on the Finite-Element Methods has better convergence than Finite-difference the time-domain method in complex structures. The result is demonstrated through studying a single silver metallic nanocylinder. In addition, to efficiently enhance Surface Plasmon, we design several useful geometrical patterns and construct them from silver metallic nanocylinders.

Investigation of Frequency-domain Absorbing Boundary Conditions for the Helmholtz Equation

Hung-Wen Chang
Department of Photonics, National Sun Yat-Sen University
70 Lien-Hai Rd., Kaohsiung 80424, Taiwan, R.O.C.

Abstract— We present the analysis of various frequency-domain absorbing boundary condition (EM-ABC) for the Helmholtz equation. In addition to the well-known methods investigated by Engquist-Majda and Lindman we will also present our work based on layer-mode, LMABC [1] and the plane wave extrapolation method. For Engquist-Majda ABC the time-domain implementation of the one way equation is only first-order accurate in both temporal and spatial step size [2], in frequency-domain realization we are able to increase the accuracy of ABC.

There are two classes of FD-ABC, the global and the local ones. In global ABCs, such as the LMABC, all bordering points on the same edge/face are coupled. They are very accurate, capable of absorbing both propagating and evanescent waves, but are very difficult to implement for complex structures. On the other hand, for points on the edge of the computational domain implemented with local ABCs, they are coupled only to their immediate neighbors. Local ABCs are not as efficient in transmitting out-going waves but they are much easy to construct and can handle corner points much better than the global one can. Unlike the global ABCs, the resulting FD stencils for local ABCs are compact and do not increase the cost of solving the linear equation.

To compare effectiveness of various ABCs we shall compute the plane wave reflection coefficients of as function of the incident angle and grid size. Numerical results of computation of the 2D free space Green's function using various ABCs will also be discussed.

ACKNOWLEDGMENT

We are grateful to the support of the National Science Council of the Republic of China under the contracts NSC 100-100-2221-E-110-065.

REFERENCES

1. Chang, H.-W., W.-C. Cheng, and S.-M. Lu, "Layer-mode transparent boundary condition for the hybrid FD-FD method," *Progress In Electromagnetics Research*, Vol. 94, 175–195, 2009.
2. Chang, H.-W. and C.-Y. Lian, "Engquist-Majdat absorbing boundary condition for the Helmholtz equation," *International Photonics Conference 2011*, Tainan, Taiwan, 2011.

Comparison of Frequency-domain Absorbing Boundary Conditions for the Helmholtz Equation

Hung-Wen Chang
Department of Photonics, National Sun Yat-Sen University
70 Lien-Hai Rd., Kaohsiung 80424, Taiwan, R.O.C.

Abstract— We present the analysis of frequency-domain absorbing boundary condition (EM-ABC) for the Helmholtz equation. In addition to the well-known methods investigated by Engquist-Majda and Lindman we will also present of work based on LMABC [1] and plane wave extrapolation method. While the time-domain implementation of the one way equation is only first-order accurate in both temporal and spatial step size [2], in frequency-domain realization we are able to increase the accuracy of ABC. We derive the plane wave reflection coefficients of as function of the incident angle and grid size. Numerical results of computation of the 2D free space Green's function using various ABCs will also be discussed.

ACKNOWLEDGMENT

We are grateful to the support of the National Science Council of the Republic of China under the contracts NSC 100-100-2221-E-110-065.

REFERENCES

1. Chang, H.-W., W.-C. Cheng, and S.-M. Lu, "Layer-mode transparent boundary condition for the hybrid FD-FD method," *Progress In Electromagnetics Research*, Vol. 94, 175–195, 2009.
2. Chang, H.-W. and C.-Y. Lian, "Engquist-Majdat absorbing boundary condition for the helmholtz equation," *International Photonics Conference 2011*, Tainan, Taiwan, 2011.

Local Field Expansion Coefficients for Dielectric Media with Interfaces Based on the Method of Connected Local Fields

Hung-Wen Chang and Sin-Yuan Mu
Department of Photonics, National Sun Yat-Sen University, Taiwan

Abstract— We proposed the method of connected local fields, CLF [1, 2] as a semi-analytical technique for obtaining solutions of the Helmholtz equation. In CLF the EM fields are expressed as collection of overlapping local fields called patches. For wave in a 2D homogeneous medium we show that the local field in a given patch can be approximated by truncated Fourier-Bessel (F-B) series and the F-B coefficients are related to the control points on the surface of the given patch. This leads to a compact FD-FD stencil we called LFE-9 formulation.

In this paper, we report a modified stencil for field near a dielectric interface depicted in Figure 1 where two dielectric materials are met with a horizontal interface. We consider this case with two approaches. First, we use two F-B series one for the upper and the other for the lower region. We then require that both the tangential E and the H field be continuous across the interface to obtain the modified LFE-9 stencil. We may also consider the local field be approximated by multiple plane waves incident from all directions with transmitted and reflected plane waves that automatically satisfy the phase matching condition. The coefficients of these incident (plus reflected and transmitting) waves are determined from the surrounding eight fields on the square. Numerical results show that two coefficient sets agree well within one percent.

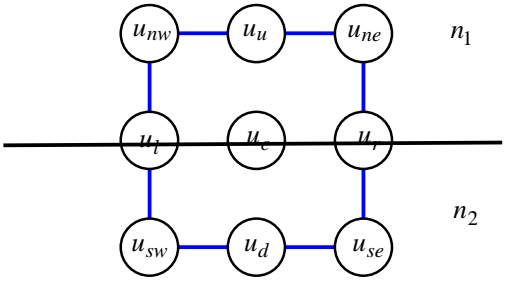

Figure 1: The unit square of a 2D local field showing nine control points and a horizontal dielectric interface.

ACKNOWLEDGMENT

We are grateful to the support of the National Science Council of the Republic of China under the contracts NSC 100-100-2221-E-110-065.

REFERENCES

1. Chang, H.-W. and S.-Y. Mu, "Semi-analytical solutions of Helmholtz equation by the method of connected local fields," *Progress In Electromagnetics Research*, Vol. 109, 399–424, 2010.
2. Mu, S.-Y. and H.-W. Chang, "Theoretical foundation for the method of connected local fields," *Progress In Electromagnetics Research*, Vol. 114, 67–88, 2011.

Session 2A7
Resonators, Filters, Interconnects, Packaging, MMIC

Effects of Residual Stress on Assembled SAW Strain Sensors
Jochen Hempel, Jürgen Wilde, Leonhard M. Reindl, ... 210

Design of Second-order Inductive-coupled Resonator-based Bandpass Filter with Controllable Multiple Transmission Zeros
Hui-Hsiang Huang, Tzyy-Sheng Horng, ... 211

Exact Synthesis of a Compact Dual-band Filter with an Asymmetric Response
Vincent Lunot, Chihming Tsai, ... 212

Design of Dual-band Coupling Matrix-based Matching Network
Chieh-Sen Lee, Chin-Lung Yang, ... 213

A Low-power K-band VCO Using Switchable Active Circuit Design
Szu-Ling Liu, Xin-Cheng Tian, Yue Hao, Yu-Chien Huang, Albert Chin, ... 214

Design and Characterization of Cryogenic Wideband LNA Using WIN 0.15 µm GaAs pHEMT Process
Ying Chen, Bin Li, Kun-Long Wu, Robert (Shu-I) Hu, ... 215

A 0.7 V Ka-band MMIC Amplifier in 65 nm CMOS Technology
Yu-Shao Jerry Shiao, Hsuan-Der Yen, Guo-Wei Huang, ... 216

A 3.5 GHz Single-Pole Double-Throw T/R Switch with High P1dB Implemented in a 0.35 µm GaN-on-Si HEMT Process
Hsuan-Ling Kao, Chih-Sheng Yeh, Hsien-Chin Chiu, ... 217

Effects of Residual Stress on Assembled SAW Strain Sensors

J. Hempel[1], **J. Wilde**[2], **and L. M. Reindl**[1]

[1]Laboratory for Electrical Instrumentation
Department of Microsystems Engineering, IMTEK
University of Freiburg, Germany
[2]Laboratory for Assembly and Packaging Technology
Department of Microsystem Engineering, IMTEK
University of Freiburg, Germany

Abstract— State of the art SAW strain sensors have a vast range of application as passive wireless sensing devices. The measurement principle has been already well investigated and frequently reported in literature. However the challenges in assembly and packaging of SAW sensors for structural integration in measurement applications still exist. Since residual stress affects the SAW sensor performance, it is mandatory to analyze these effects. This work focuses on investigations of stress factors in SAW strain sensors induced by the thermo mechanical load during sensor assembly.

In the presented work SAW strain sensors were assembled on heat-treatable steel carriers. Different adhesives have been used for sensor mounting, which were already pre-investigated and particularly suitable for SAW strain sensor application. The assembly process has been developed and adapted for SAW bare die devices. The sensor response was measured and analyzed with a network analyzer before and after assembly. The sensor deformation due to thermo mechanical stress was measured with white light interferometry. The sensor deformation was compared with the simulated sensor deformation, using a 3D FEM. The simulated and analytically computed sensor stress and the measurements from the SAW strain sensors were compared.

Additionally, the SAW strain sensor response was investigated with respect to the temperature dependency. A probe station with an integrated thermo-chuck has been used for the measurements up to 125°C. In conclusion, the whole assembly has been aged in a thermal step at 150°C and the sensor performance as well as the sensor deformation was analyzed.

The experimental and simulation results obtained in this work contribute to a better understanding of SAW strain sensor assembly and the effects of residual stress on the sensor performance. Furthermore, this work leads to consolidation of passive wireless SAW strain sensors as reliably measurement devices.

Design of Second-order Inductive-coupled Resonator-based Bandpass Filter with Controllable Multiple Transmission Zeros

H.-H. Huang and T.-S. Horng
Department of Electrical Engineering, National Sun Yat-Sen University, Kaohsiung 804, Taiwan

Abstract— This study proposes synthetic design for a compact LTCC bandpass filter with high rejection over a wide stopband for use in 2.4–2.5 GHz WLAN application. The presented design derives formulas for synthesizing a filter to meet the specification requirement in the passband insertion and return losses as well as the stopband attenuation. The presented bandpass filter has feedback paths for a coupled capacitor and a grounding inductor to provide controllable multiple transmission zeros at 5.0 GHz and 3.3 GHz stopband, resulting in high stopband rejection in 4.8 to 5.0 GHz range and 3.2 to 4.8 GHz range, which suppresses the second harmonic generation and Ultra-wideband (UWB) signal. Experiments results are very agreement with the full-wave simulation results.

Exact Synthesis of a Compact Dual-band Filter with an Asymmetric Response

Vincent Lunot and C.-M. Tsai
Department of Electrical Engineering, National Cheng Kung University
1 University Road, NCKU-EE, Tainan 70101, Taiwan

Abstract— Microstrip dual-band filters with commensurate transmission-line sections are usually designed based on the periodicity of the Richards' variable $j \tan \beta\ell$ [1]. The quarter-wavelength frequency is therefore between the two passbands. We propose here to directly synthesize a dual-band bandpass filter as a single-band filter whose band contains the two passbands. The quarter-wavelength frequency is therefore taken higher than the upper bound of the second passband and consequently all the transmission-line sections become shorter. Furthermore, when the periodicity of the Richards' variable is used in the traditional way, the second passband is a transformed version (mirror) of the first one, and therefore the number of zeros in each band is always the same. Synthesizing directly the two passbands as proposed allows to take a different number of zeros in each band. One problem of the method presented here is that when the two passbands are far from each other, realizing directly the filter is equivalent to designing a wideband filter, which is usually limited by the requirement of ideal coupling elements. We will consider such an example and therefore compute a filtering function that doesn't require any ideal coupling elements.

An example is studied with central frequencies for the two passbands at 2.45 GHz and 5.25 GHz and respective bandwidths of 10% and 3%. The quarter-wavelength frequency is taken at 10 GHz. We consider an all pole filtering function of order 7 to realize these specifications. We first compute a lowpass response thanks to a Remes-like algorithm [2] that guarantees an optimal rejection. Note that such an optimal function is not equiripple and that it has two complex conjugated zeros in the first band. We next transform the lowpass response to the real frequencies thanks to the classic lowpass to bandpass transformation. Since the lowpass response is asymmetric, the bandpass response is also asymmetric with respect to the real frequency zero, and consequently doesn't lead to a reflection function S_{11} with real coefficients. We therefore modify the bandpass response to obtain a reflection function with real coefficients by using only the right-hand plane zeros. The response of the modified function is close to the original one and both responses are plotted in Figure 1. Darlington's synthesis [3] is finally used to obtain a circuit with stub elements.

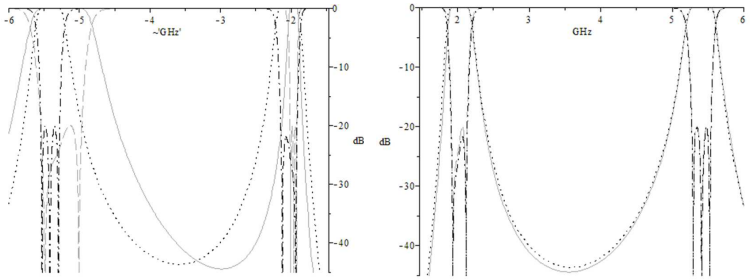

Figure 1: Comparison of the transformed low pass function (blue) and the obtained symmetric function (green) for (b) real frequencies and (a) "negative frequencies".

REFERENCES

1. Sun, Z., L. Zhang, Y. Yan, and H. Yang, "Compact dual-band bandpass filter using coupled three-line microstrip structure with open stubs," *IEEE 4th Int. Symp. on MAPE*, 2011.
2. Bila, S., R. J. Cameron, P. Lenoir, V. Lunot, and F. Seyfert, "Chebyshev synthesis for multi-band microwave filters," *IEEE Int. Microw. Symp.*, 2006.
3. Darlington, S., "Synthesis of reactance 4-poles which produce a prescribed insertion loss characteristics," *J. Math. Phys.*, Vol. 18, 257–355, 1939.

Design of Dual-band Coupling Matrix-based Matching Network

Chieh-Sen Lee and Chin-Lung Yang
National Cheng Kung University, Taiwan

Abstract— This study developed a novel dual-band matching technique based on a coupling matrix transformer that matches complex load impedances at two frequencies simultaneously. Matching performance can be significantly improved by the dual-band filter-based matching network at operation dual-bands. Especially, excellent selectivity at the operation frequencies and rejection capability in undesired bands can be achieved. A general design principle is analyzed, and the results of numerical examples demonstrated that complex impedances can be successfully matched at two arbitrary frequencies simultaneously with excellent performance rates.

A Low-power K-band VCO Using Switchable Active Circuit Design

Szu-Ling Liu[1], **Xin-Cheng Tian**[2], **Yue Hao**[2], **Y. C. Huang**[1], **and Albert Chin**[1]

[1]Department of Electronic Engineering, National Chiao Tung University, Hsinchu 300, Taiwan
[2]School of Microelectronics, Xidian University, Xi'an, China

Abstract— The CMOS-based VCO has been widely used for communication ICs. However, the VCO suffers from the relatively high $1/f$ noise of MOSFET, poor Q-factor of on-chip inductor, high RF loss Si substrate, and limited tuning range of varactor. These issues make the high performance and low-power goals more difficult in CMOS VCO.

To address the low-power challenge, transformer-based feedback VCO (TF-VCO) were proposed and demonstrated. Using TF-VCO architecture, larger dynamic V_{gs} voltage swing under a low supply voltage can be achieved to improve the signal-to-noise ratio (SNR) in VCO circuit. The higher Q-factor than on-chip inductor is other advantage of transformer in a similar size. However, it is difficult to design TF-VCO at high frequency due to the parasitic capacitance in transformer. Besides, the tuning range is still limited by the CMOS-based varactor and seldom exceeds 10%.

In this abstract, we demonstrated a novel low power K-band TF-VCO based a standard 90 nm CMOS technology. At $18 \sim 20$ GHz K band frequency, low power consumption of ≤ 3 mW, a wide 12.2% tuning range, low phase noise of $-115 \sim -114$ dBc/Hz (1 MHz offset), excellent figure-of-merit-with-tuning-range ($\mathrm{FOM_T}$) of $-182 \sim -192$ dBc/Hz and small core circuit area of 0.4-mm $\times$ 0.24-mm were achieved simultaneously. These performances were possible by the bias-varied method in circuit to control the DC power at different frequency ranges.

Design and Characterization of Cryogenic Wideband LNA Using WIN 0.15 μm GaAs pHEMT Process

Ying Chen[1], **Bin Li**[1], **Kun-Long Wu**[2], **and Robert Hu**[2]

[1]SHAO, Chinese Academy of Sciences, China
[2]College of Electrical and Computer Engineering, NCTU, Taiwan

Abstract— This manuscript describes our progress in the development of cryogenic wideband LNA for radio-astronomical applications. With technology maturity and fabrication cost taken into account, the WIN 0.15 μm GaAs pHEMT process is used for the 5–10 GHz and 8–20 GHz LNA design. Room-temperature S-parameters and noise temperature are measured first, with gain larger than 20 dB, input and output reflection coefficients below −10 dB within the intended bandwidth. As for the cryogenic noise measurement, the 6 dB cold-attenuator method is used to obtain the corresponding T_n at different ambient temperatures. A noise improvement factor of 3 is observed for cryogenic LNA designed with this 0.15 μm GaAs process.

A 0.7 V Ka-band MMIC Amplifier in 65 nm CMOS Technology

Yu-Shao Jerry Shiao[1], **Hsuan-Der Yen**[2], **and Guo-Wei Huang**[1, 3]

[1]National Nano Device Laboratories, Hsinchu 300, Taiwan, R.O.C.
[2]Institute of Electronics Engineering, National Tsing Hua University
Hsinchu 300, Taiwan, R.O.C.
[3]Department of Electronics Engineering, National Chiao Tung University
Hsinchu 300, Taiwan, R.O.C.

Abstract— Wideband satellite data communication at Ka-band frequency is gradually important due to globally mobile internet access demand. Low cost and low power CMOS MMICs are certainly the critical building blocks of Ka-band transceivers. Moreover, MMICs in CMOS technology are strongly suggested for consumer markets to further be combined with baseband digital circuits as a system-on-chip (SOC). However, portable battery-powered electronics may need low voltage devices to function properly most of the time. Unlike digital circuits may work at low voltage naturally, CMOS MMIC design may be difficult with such low supply voltage even in ultra-deep submicron technology. Thus, we have investigated and successfully designed a 26–30 GHz Ka-band low power CMOS MMIC amplifier in 65 nm CMOS technology. The amplifier only consumes 8 mW. The gain, S_{21}, is 19.6 dB while the supply voltage is 0.7 V. The bandwidth is about 4 GHz. The amplifier consists of three common source stages and two Pi-type matching networks. One of the matching networks is used to boost voltage gain at the first stage rather than power gain. Voltage gain is more important than power gain within MOS transistors. In this project, the technique successfully increases the overall power gain of the amplifier. The peaks of the return losses, S_{11} and S_{22} are lower than 10 dB. The chip size is 0.7 mm^2.

A 3.5 GHz Single-Pole Double-Throw T/R Switch with High P1dB Implemented in a 0.35 μm GaN-on-Si HEMT Process

Hsuan-Ling Kao, **Chih-Sheng Yeh**, **and Hsien-Chin Chiu**
Department of Electronic Engineering, Chang Gung University, Tao-Yuan, Taiwan

Abstract— This paper presents a high linear and power handling single-pole double-throw (SPDT) T/R switch for WLAN applications. The SPDT switch has been fabricated using 0.35 μm GaN HEMT on silicon substrate technology. The SPDT switch achieves 1.74 dB insertion loss and 35 dB isolation at 3.5 GHz. The switch exhibits 30 dBm (1 W) P1dB at 3.5 GHz with control voltage of 10/0 V. The low insertion loss and high P1dB are achieved by optimizing the transistor widths and minimizing the source/drain-to-body capacitances The fabricated SPDT switch chip size is $1.3 \times 1.85\,\mathrm{mm}^2$.

Session 2A8
Poster Session 1

Plasmonic Band Edge Effects in Periodic Metallic Gratings
Wei E. I. Sha, Ling Ling Meng, ... 221

Ridge-type Semiconductor Laser with a Partially Undoped Antiguiding Cladding Layer for Horizontal Transverse Modes
Guowei Chai, Takahiro Numai, ... 222

Enhanced Visible Photoluminescence of SnO_2/Gd_2O_3 Co-doped Glasses
Yu Tong, Yinyao Liu, Jing Ren, Guorong Chen, ... 223

Evaluation of Nonlinear Effect Impact on Optical Signal Transmission over Combined WDM System
Vjaceslavs Bobrovs, Aleksejs Udalcovs, Rolands Parts, Ilja Trifonovs, ... 224

Performance Improvement of Spectrum-sliced Passive Optical Network
Girts Ivanovs, Sandis Spolitis, Rolands Parts, Vjaceslavs Bobrovs, ... 225

Numerical Investigation of Mode Birefrigence and Confiment Loss of Different Air Hole Patterns in Photonic Crystal Fiber Cladding
Yuan-Fong Chau, Shinn-Fwu Wang, Yi Chu, Jeng-Hua Wei, Wayne Yang, ... 226

Design of an Optimal Benes WEX Architecture Based on Sufficient Permutations
Jieh-Chian Wu, Miao-Hsu Wei, ... 227

Analysis of Anisotropic Diffraction in Volume Gratings Using Liquid Crystal Composites
Akifumi Ogiwara, Hiromu Shichi, Hiroshi Kakiuchida, Akira Emoto, Hiroshi Ono, ... 228

Temperature Dependable Holographic Memory Using Holographic Polymer-dispersed Liquid Crystal
Akifumi Ogiwara, Minoru Watanabe, Retsu Moriwaki, ... 229

Investigation on Band Gap Characteristics in a Two-dimensional Photonic Crystal with Honeycomb Structure
Shang-Lin Hou, Rui Lv, Yan-Jun Liu, Jingli Lei, Suo-Ping Li, ... 230

Study on Characteristics of the Photonic Crystal Fibers with Three Zero-dispersion Points
Shang-Lin Hou, Yu Du, Rui Lv, Yan-Jun Liu, Jingli Lei, Suo-Ping Li, ... 231

Investigation on Slow Light of Uniform Fiber Bragg Gratings
Jingli Lei, Shang-Lin Hou, Rui Lv, Yan-Jun Liu, Suo-Ping Li, ... 232

Optical Fiber Nonlinear Coefficient Measurements Using FWM
Andis Supe, Jurgis Porins, Girts Ivanovs, ... 233

Multi-level Pores, Size-tunable Fe_3O_4 Nano/Submicrospheres for Electromagnetic Wave Adsorption
Xutang Qing, Xiaoxiao Yue, Yun Lu, ... 234

Design of Quantum Secure Communication System Based on FPGA
Jun Li, Jie Chen, Heping Zeng, Hui Li, ... 235

Numerical Study of Effective Plasma Frequency for a Plasma Photonic Crystal in the Presence of Magnetic Field
Heng-Tung Hsu, Jin-Jei Wu, Chi-Chung Liu, Chien-Jang Wu, ... 236

Mode Transformations of Surface Plasmons to Propagating and Back to Surface Plasmons in Metal Dielectric Interface with a Half Space Cloaking Region
D. Mahanta, P. Arora, Ananth Krishnan, ... 237

Characterization of Picosecond Laser Pulses Using a Single-shot Measurement Method
Hoon Jeong, Dongjoo Lee, Mi Joung Kim, ... 238

The Studies of Enhanced Optical Single Sideband Modulation Using by Laser's Cavity Mode and Nonlinear Optical Fiber Effect
Hsiang-Yun Shao, Wen-Shing Tsai, G. C. Lin, H. H. Lu, ... 239

A Study of Enhanced Optical Single Sideband Modulation Based on Scattering Effects and Semiconductor Laser Injection Locked Technology
Yi-Lin Chen, W. S. Tsai, G. Z. Lin, Hai-Han Lu, ... 240

Increasing the Luminous Efficiency of Flip-chip Light Emitting Diode with a Reflective Aluminum Layer
Ming-Jer Jeng, Wen-Yu Guo, Chia-Yi Yen, Liann-Be Chang, Boren Huang, ... 241

Asymmetric Permittivity and Permeability Sensitivities of Plasmonic Sensors
Yen-Kai Chang, Chih-Wei Chang, ... 242
Development of Optical Wave Microphone Measuring Sound Waves with No Diaphragm
Yoshito Sonoda, Takashi Samatsu, Toshiyuki Nakamiya, ... 243
Visualization of Electric Discharge Sound Fields in Atmospheric Pressure Plasma Using Fraunhofer Diffraction
Toshiyuki Nakamiya, Fumiaki Mitsugi, Yoichiro Iwasaki, Tomoaki Ikegami, Ryoichi Tsuda, Yoshito Sonoda, ... 244
An Overview of Metamaterials in Biomedical Applications
Singaravelu Raghavan, V. Rajeshkumar, ... 245
Interfacial Properties of Modified Natural Polysaccharide Carbohydrate Surfactants
Mou-Chuan Hwang, Li-Huei Lin, Wei-Min Hwang, ... 246
Indoor Broadband Spectrum Survey Measurements for the Improvement of Wireless Systems
Robert Urban, Tomas Kriz, Martin Cap, ... 247
Measurement of Inhomogeneity in the $\boldsymbol{B_0}$ and $\boldsymbol{B_1}$ Fields Performed via the Spin-Echo and Gradient-Echo MR Imaging Techniques
Radek Kubasek, Eva Gescheidtová, Karel Bartušek, ... 248
Processing of Magnetic Resonance Images of Adipose Tissues
Michaela Pokludová, Eva Gescheidtová, Jan Mikulka, ... 249
The Effect of Extremely Low Frequency (ELF) Pulsed Electromagnetic Field (PEMF) on Bacteria *Staphylococcus Aureus*
Istiaque Ahmed, Taghrid Istivan, Elena Pirogova, ... 250
The Effects of Visible Light Radiation (400–500 nm) on Enzymatic Activity of Collagenase
Jie Hu, Vuk Vojisavljevic, Elena Pirogova, ... 251
Scattering-induced Changes in the Degree of Polarization of a Stochastic Electromagnetic Plane-wave Pulse
Liuzhan Pan, Chaoliang Ding, ... 252
The Comparison of the Contrasts of Magnetic Resonance Images of Plants
Michaela Pokludová, Eva Gescheidtová, ... 253
Electromagnetic Structures and Inertias of Particles including the Higgs Boson
Michael James Underhill, ... 254
A Low Phase Noise CMOS VCO for the Millimeter Wave Application
Mingzhu Zhou, Jincai Wen, Jie Wang, Zhili Liu, ... 256
The Influence of an Electromagnetic Wave on the Acoustoelectric Current in a Rectangular Quantum Wire with an Infinite Potential
Nguyen Van Nghia, Nguyen Quang Bau, Nguyen Van Hieu, Nguyen Vu Nhan, ... 257
Influence of a Strong Electromagnetic Wave (Laser Radiation) on the Hall Coefficient in Doped Semiconductor Superlattices with an In-plane Magnetic Field
Nguyen Quang Bau, Nguyen Van Nghia, Nguyen Van Hieu, Bui Dinh Hoi, ... 258

Plasmonic Band Edge Effects in Periodic Metallic Gratings

Wei E. I. Sha and Ling Ling Meng
Department of Electrical and Electronic Engineering
The University of Hong Kong, Pokfulam Road, Hong Kong, China

Abstract— For photonic crystals, forward and backward traveling waves constructively interfere with each other, resulting in standing waves. Due to the Bragg scattering in periodic photonic structures with modulated refractive indices, the degenerate standing waves split into two band edge modes with field concentration in different regions. Between band edge frequencies, a band gap will be opened up due to the destructive interferences of traveling waves. Although it is non-intuitive that the phenomena could happen in metallic structures, no physical law forbids their existences. Critically different from traveling waves in photonic crystals, forward and backward surface plasmon waves constructively interfering with each other induce two plasmonic band edges with splitting resonance frequencies, which is due to the periodically modulated refractive indices of metallic grating structures. The plasmonic band edge resonance plays an important role in versatile engineering applications, such as surface enhanced Raman scattering, solar cells, nanoantennas, optical metamaterials, etc. To clarify the physical origin of plasmonic band edge resonance, both excitation and eigenvalue analyses for the metallic grating are carried out. Particularly, a universal eigenvalue solver is developed to compute the complex Bloch band diagram (dispersion relation) of dispersive periodic structures. The work provides a theoretical foundation and physical interpretation to the plasmonic band edge effect.

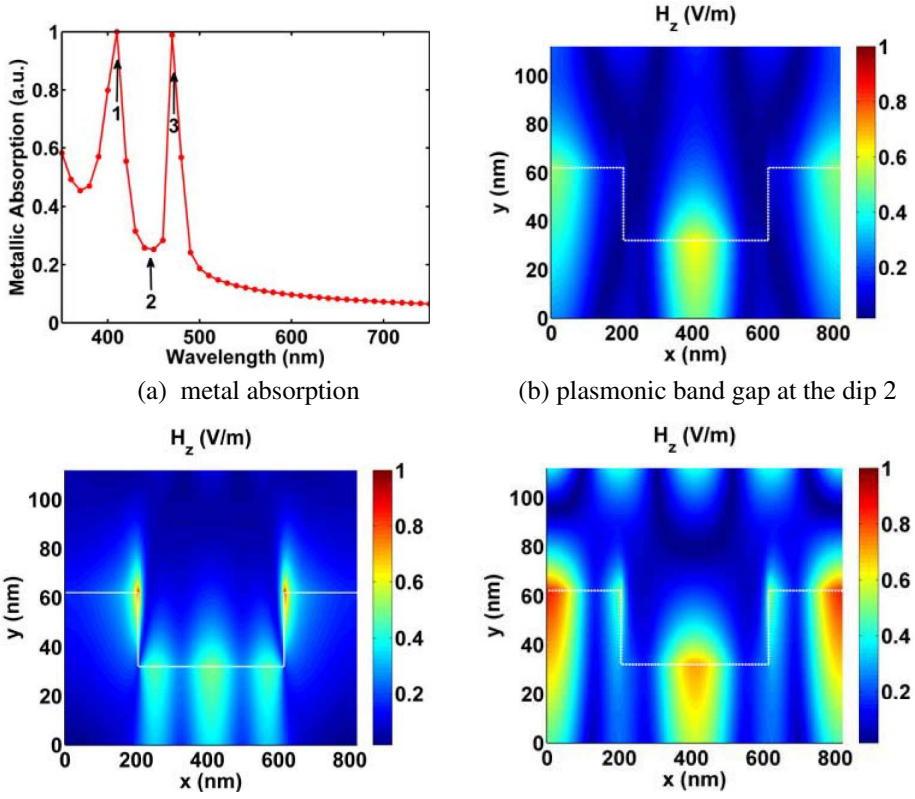

(a) metal absorption

(b) plasmonic band gap at the dip 2

(c) plasmonic band edge at the peak 1

(d) plasmonic band edge at the peak 3

Figure 1.

Ridge-type Semiconductor Laser with a Partially Undoped Antiguiding Cladding Layer for Horizontal Transverse Modes

Guowei Chai and Takahiro Numai
Ritsumeikan University, Japan

Abstract— High power 980-nm semiconductor lasers are indispensable for pumping sources of erbium doped optical fiber amplifiers. Generally, 980-nm semiconductor lasers have ridge structures so as not to expose their active regions to air during their fabrication, because the active regions are easily oxidized and degraded in air. In the ridge structures, higher-order transverse modes as well as the fundamental transverse mode are confined. As a result, with an increase in injected current, higher-order transverse modes lase; kinks appear in their current versus light-output ($I-L$) curves. These kinks are attributed to changes in the local gain profile and refractive index owing to spatial hole burning, the free-carrier plasma effect, and heating. To obtain high fiber-coupled optical power, semiconductor lasers with high kink levels operating in the fundamental transverse mode are required. To date, to increase kink levels, coupling of the optical field to the lossy metal layers outside the ridge, highly resistive regions in both sides of ridge stripe, and incorporation of a graded V-shape layer have been demonstrated. To increase kink level and decrease the threshold current further, a ridge structure with optical antiguiding layers have been proposed, but the fabrication process is fairly complicated. In order to make the fabrication process more simple and increase kink level, a ridge structure with an antiguiding cladding layer for horizontal transverse modes has been proposed. In this structure, the kink has not appeared, but the threshold current has increased.

In this paper, a novel ridge structure with a partially undoped antiguiding cladding layer for horizontal transverse modes is proposed, and lasing characteristics are simulated. In the proposed ridge structure, kink levels are improved by suppressing spatial hole burning and lowering optical gains for higher-order transverse modes with the step d of the antiguiding cladding layer. The spreading of the carriers is suppressed with the undoped cladding layer. For $90\,\mathrm{nm} \leq d \leq 210\,\mathrm{nm}$, kink-free laser operation is obtained up to the injected current of 2 A. The lowest threshold current with kink-free operation is 44.3 mA at $d = 125\,\mathrm{nm}$. This value is 77% of 57.5 mA in the previous work.

ACKNOWLEDGMENT

This research was partially supported by the Japan Society for Science, Grant-in-Aid for Scientific Research (C) 24560429, 2012.

Enhanced Visible Photoluminescence of SnO_2/Gd_2O_3 Co-doped Glasses

Yu Tong, Yinyao Liu, Jing Ren, and Guorong Chen
Key Laboratory for Ultrafine Materials of Ministry of Education
School of Materials Science and Engineering
East China University of Science and Technology, 130 Meilong Rd., Shanghai 200237, China

Abstract— Many investigations on optical glasses for different applications have been reported in recent years. This is because glasses can be used as the ultraviolet and visible transmitting matrices for hosting different functional ions, atoms or molecules. Although rare earth ions have been used as main functional centers, some special attention has also been given to semiconductive oxides, such as ZnO and SnO_2.

In the present work, SnO_2 doped strontium phosphate glasses ($75P_2O_5$-25SrO) are prepared and their enhanced visible photoluminescence properties are investigated by co-doping Gd_2O_3 of different concentrations (2.5, 5, 7.5, 10, 15 mol%). Absorption and photoluminescence (emission and excitation) spectra are presented and discussed. Results show that SnO_2 and Gd^{3+} can be co-stimulated by the 267 nm excitation source with both broad emission band of SnO_2 at 420 nm and sharp one of Gd^{3+} ions at 312 nm. Much enhanced visible emission from SnO_2 is observed with the increased Gd_2O_3 co-doping, while Gd^{3+} emission becomes weaker. Besides, excitation spectra show the doubled integrated excitation cross-section (ECS) upon SnO_2/Gd^{3+} co-doping, which benefits for energy harvesting of light sources, indicating an efficient sensitization effect of Gd^{3+} on SnO_2. The relevant mechanism is discussed with respect to the involved energy transfer and cross relaxation process between SnO_2 and Gd^{3+} ions.

Evaluation of Nonlinear Effect Impact on Optical Signal Transmission over Combined WDM System

V. Bobrovs, A. Udalcovs, R. Parts, and I. Trifonovs
Institute of Telecommunications, Riga Technical University, Latvia

Abstract— The transmission throughput over the existing wavelength division multiplexed (WDM) fiber-optic transmission systems (FOTS) can be increased in the following manner: using higher per channel bitrates, narrower channel spacing or wider amplifier bandwidth. The first approach used for achieving a higher system capacity throughput was the introduction into the systems new channels with higher per channel bitrate since such solution can be deployed on existing FOTS and is capable with current network architecture. Although it is a short term solution since it requires free and for transmission suitable band. Such band is limited not only with the "WDM-suitable" bandwidth of silica optical fiber but also with the bandwidth of FOTS elements such as inline optical amplifier (e.g., erbium doped fiber amplifier (EDFA)) and dispersion compensation module (e.g., based on the use of dispersion compensating fiber (DCF) or chirped fiber Bragg grating (FBG)). So, the increase of "for WDM-suitable" band utilization (or increase of spectral efficiency) allows to reduce the number of channel required for the transmission of the same data body as compared with relatively spectrally inefficient WDM systems (i.e., SE < 0.2 bit/s/Hz). As well as allows postpone the shortage of "for WDM-suitable" band and avoid the deployment of new optical fibers. That is why the method of increase of transmissions SE has some characteristics that are adequate for future needs and requirements of continuous traffic growth. Obviously, it is necessary to evaluate the impact of all fiber nonlinearities to optical signal transmission over the purposed model of combined WDM system designed for the future optical transport networks.

The authors have investigated the impact of nonlinear distortions to optical signal transmission over proposed configuration of combined wavelength division multiplexed (WDM) fiber-optic transmission system (FOTS). In chosen model of ultra-dense combined WDM system optical signals are transmitted with two different per channel bitrates (i.e., 10 and 40 Gbit/s) and three different optical signal modulation formats are used for the encoding of transmitted data body (i.e., non-return to zero encoded on-off keying or NRZ-OOK, orthogonal polarization shift keying or 2-POLSK and NRZ encoded differential phase shift keying or NRZ-DPSK) and in addition "non ITU-T" defined minimum and equal frequency intervals are used for the channels separation. Generally, investigated 9-channel combined WDM system complies with the following configuration scheme: [1st ($fc = 193.025$ THz), 4th and 7th channels: NRZ-OOK, $R = 10$ Gbit/s] — [2nd ($fc = 193.100$ THz), 5th and 8th channels: 2-POLSK, $R = 40$ Gbit/s] — [3rd ($fc = 193.175$ THz), 5th and 9th channels: $R = 40$ Gbit/s]. The developed concept of the combined WDM systems is offered as model for the future design of optical transport networks. This research revealed that 2-POLSK modulated signals are more susceptible to the impact of SPM in such ultra-dense combined transmission mode than, e.g., NRZ-DPSK signals.

Performance Improvement of Spectrum-sliced Passive Optical Network

G. Ivanovs, **S. Spolitis**, **R. Parts**, **and V. Bobrovs**
Institute of Telecommunications, Riga Technical University, Latvia

Abstract— Spectrum-sliced dense wavelength-division-multiplexed passive optical network (SS-DWDM PON) is an attractive and cost effective solution to satisfy the growing worldwide demand for transmission capacity in the next generation fiber optical access networks. Traditional WDM systems have multiple transmitter lasers operating at different wavelengths, which need to be wavelength selected for each individual channel operated at a specific wavelength. It increases complexity of network architecture, cost and wavelength (channel) management. The strength of spectrum-sliced WDM PON technology is use of one common broadband seed light source and its ability to place electronics and optical elements in one central office (CO), in that way simplifying the architecture of fiber optical network. Such optical systems benefit from the same advantages as WDM, while employing low cost incoherent light sources like amplified spontaneous emission (ASE) source or light-emitting diode (LED). One of the problems is that the ASE spectrum originally resulting on the output of EDFA is irregular and manipulation with EDFA parameters must be done to make it more flat. Flat optical spectrum of ASE source is an important premise to achieve minimal output power level fluctuations of obtained channels after spectrum-slicing operation and provide stable data transmission with BER $< 10^{-10}$ over the specified fiber optical link length. In this paper we successfully demonstrate the optical link reach improvement by implementation of chromatic dispersion compensation for cost effective spectrum-sliced DWDM PON system with data rate 2.5 Gbit/s per channel as well as realization of broadband ASE light source with output power +23 dBm, channel power variation less than 0.42 dBm and flat spectrum in wavelength range from 1545.32 nm to 1558.98 nm (C-band).

Investigated optical system is built on the ITU-T DWDM frequency grid, defined in recommendation G.694.1 and therefore it is potentially much more compatible with other already existing WDM PON optical systems. In this way it is possible to replace the classic WDM PON system with our proposed extended-reach spectrum-sliced WDM PON system and reduce complexity of network architecture as well as cost per one user. It is shown that CD compensation has an important role for guaranteed downstream optical link performance and maximum transmission line length of high speed SS-DWDM PON system.

Numerical Investigation of Mode Birefrigence and Confiment Loss of Different Air Hole Patterns in Photonic Crystal Fiber Cladding

Yuan-Fong Chau, Shinn-Fwu Wang, Yi Chu, and Wayne Yang
Department of Electronic Engineering, Chien Hsin University of Science and Technology
No. 229, Jianxing Rd., Zhongli City, Taoyuan County 32097, Taiwan, R.O.C.

Abstract— In this work, the optical mode birefringence and confinement loss of the photonic crystal fiber with different patterns of air holes are investigated by using a full-vector finite element method (FEM). Numerical results obtained from FEM show that a ultrahigh modal birefringence and low confinement loss of rectangular lattice PCF with rectangular air holes at excitation wavelength $\lambda = 1550\,\text{nm}$ can be achieved larger than a magnitude of 8.0×10^{-2} and less than $10^{-2}\,\text{dB/km}$, respectively. Noting that a ultrahigh birefringence up to 2.0×10^{-2} can be achieved from the case of circular air hole PCF, which is the highest value compared to conventional circular air holes PCF. The asymmetry formed by pressing air holes along x-axis in cladding of rectangular lattice PCFs is one of the vital factors in determining the localization extent of the transverse mode. We utilize the intrinsically large index contrast in PCFs in combination with asymmetric cladding designs. The merit of our designed PCFs is that the birefringence and confinement loss can be easily controlled by changing the air hole size along the direction of x-axis.

ACKNOWLEDGMENT

This work was supported by National Science Council of the Republic of China (Taiwan) under Grant Nos. NSC-100-2632-E-231-001-MY3 and NSC 99-2112-M-231-001-MY3.

Design of an Optimal Benes WEX Architecture Based on Sufficient Permutations

J.-C. Wu[1] and M. H. Wei[2, 3]

[1]Department of Computer and Communication Engineering
National Kaohsiung First University of Science and Technology, Kaohsiung, Taiwan
[2]Institute of Engineering Science and Technology
National Kaohsiung First University of Science and Technology, Kaohsiung, Taiwan
[3]Center of General Education, Kao Yuan University, Kaohsiung, Taiwan

Abstract— In order to achieve nonblocking connection, all the switching networks are designed to provide connections of full permutations. To reduce the hardware complexity, we propose designing wavelength-exchanging cross connect (WEX) to support sufficient permutations instead of full permutations. In this paper, we propose an algorithm to construct an optimal Benes WEX architecture with sufficient permutations. The idea is to select a minimal number of switching elements in a Benes WEX so that all connections of sufficient permutations can be provided. Our case study results show that the architectures of our proposed WEX based on sufficient permutations in the cases of 2 and 4 wavelengths in each fiber can to save up to half switching elements compared with that of the existing Benes WEXs based on full permutations.

Analysis of Anisotropic Diffraction in Volume Gratings Using Liquid Crystal Composites

A. Ogiwara[1], **H. Shichi**[1], **H. Kakiuchida**[2], **A. Emoto**[3], **and H. Ono**[4]

[1]Department of Electronic Engineering, Kobe City College of Technology, Japan
[2]Materials Research Institute for Sustainable Development
National Institute of Advanced Industrial Science and Technology (AIST), Japan
[3]Electronics and Photonics Research Institute
National Institute of Advanced Industrial Science and Technology (AIST), Japan
[4]Department of Electrical Engineering, Nagaoka University of Technology, Japan

Abstract— A micro-periodic structure composed of polymer and liquid crystal (LC) phases is called holographic polymer dispersed liquid crystal (HPDLC) grating.The HPDLC grating has been applied for grating formation to obtain both high optical efficiency and electric switching function. Moreover, HPDLC grating shows polarization dependence in diffraction efficiencies against the incident polarization state of laser light.The anisotropic diffraction is modulated by the distribution of submicrometer-scale liquid crystal (LC) droplet in a polymer matrix using interferometric laser exposure.The refractive-index modulations (n_x, n_y, n_z)in grating medium corresponding to the three dimensional directions are obtained by applying theoretical calculation based on the anisotropy for the experimental results of angular dependence of diffraction efficiencies in various grating structures.Also the microscopic origin of the anisotropic property is investigated by optical polarization microscopy and scanning electron microscopy (SEM). Our analysis shows that the diffraction efficiency and the characteristic ratio of diffraction efficiency in polarization parallel to the grating vector to that in polarization perpendicular to the grating vector are markedly affected by the refractive-index modulations. The variation of refractive-index modulations is considered to be produced by the orientation of the LC molecules in LC phase depending on the grating structure. The theoretical and experimental investigations clarify that the anisotropy in HPDLC grating is dependent on refractive-index modulation based on the orientation of LC molecules, and the order of LC orientation is obviously changed with grating configuration composed of small LC droplets such as grating thickness and slanted angle of grating.

Temperature Dependable Holographic Memory Using Holographic Polymer-dispersed Liquid Crystal

A. Ogiwara[1], **M. Watanabe**[2], **and R. Moriwaki**[2]

[1]Department of Electronic Engineering, Kobe City College of Technology, Japan
[2]Department of Electrical and Electronic Engineering
Faculty of Engineering, Shizuoka University, Japan

Abstract— Grating devices using photosensitive organic materials play an important role in the development of optical and optoelectronic systems. High diffraction efficiency and polarization dependence achieved in a holographic polymer-dispersed liquid crystal (HPDLC) grating are expected to provide novel polarization controllable optical devices, such as the holographic memory for optically reconfigurable gate arrays (ORGAs). However, the optical property is affected by the temperature change under environments where the HPDLC devices are applied. We propose the temperature dependable holographic memory using the combination of nematic LC and LC diacrylate monomer materials. Holographic polymer dispersed liquid crystal (HPDLC) memory is fabricated by a photo-induced phase separation technique using laser light interference exposures for the LC and polymer composites with different physical properties, such as refractive indices and the temperature at clearing point. The temperature dependence of the diffraction efficiency in holographic memory is investigated for various LC composites materials. The anisotropic diffraction induced by the alignment of LC in periodic structure in the HPDLC memory is confirmed to be maintained at high temperature over 100°C by adjusting the combination of refractive index of LC and polymer materials. The experimental results demonstrate that the holographic memory fabricated by the LC diacrylate monomer (Merck RM257) and the nematic LC (Merck MLC7023) of low refractive index between extra-ordinary and ordinary indices (n_e and n_o) can reconstruct the configuration contexts to implement optical reconfiguration under harsh environmental condition in the high temperature.

Investigation on Band Gap Characteristics in a Two-dimensional Photonic Crystal with Honeycomb Structure

Shanglin Hou, Rui Lv, Yanjun Liu, Jingli Lei, and Suoping Li
School of Science, Lanzhou University of Technology, Lanzhou 730050, China

Abstract— Photonic crystal is a periodic arrangement of dielectric materials in one, two or three dimensions, which exhibits a "forbidden" frequency region where electromagnetic waves cannot propagate along any direction. In a two-dimensional (2D) photonic crystal, the electromagnetic waves can be decoupled into two different polarized modes. These polarized modes are known as transversal magnetic (TM) polarized mode and transversal electric (TE) polarized mode. An absolute photonic band gap (complete TEM band gaps) exists for a 2D photonic crystal only when photonic band gaps in both polarization modes are present and they overlap each other. Photonic crystals have many potential applications and most of them rely on their band structures.

Photonic band gaps for TE and TM modes occur at different frequency regions and only in select structures both of them exist at the same frequency region giving rise to complete photonic band gap. In order to obtain a large absolute photonic band gap, a sufficient overlap between both TE and TM band gaps is important. Many attempts have already been made to design various kinds of photonic crystal structures, which are not easy for fabrication and the geometric shape is complex, although these structures can offer larger complete photonic band. Yuan et al. have studied the band gap characteristics of two- dimensional photonic crystal with triangular lattice structure and square lattice structure, however they haven't reported the TE band gaps and TM band gaps are responsible for the formation of complete TEM band gaps.

In this letter, we investigate the band gap characteristics of a two-dimensional photonic crystal consisting of honeycomb lattices for the TE mode, TM mode and complete TEM gaps by using the plane-wave expansion method. We concentrate on the effect of the relative dielectric constant and filling ratio. The results indicate that the TE band gaps and TM band gaps are responsible for the formation of complete TEM gaps; When $r/a = 0.32$, $\varepsilon_b = 26$, for the circular dielectric rods structure, the largest complete photonic band gap exists with the normalized gap width $\Delta G_{\max}/\omega_0 = 25\%$. The study provides useful basic theory in the design of various complete photonic band gap-based devices or integrated photonic circuits.

Study on Characteristics of the Photonic Crystal Fibers with Three Zero-dispersion Points

Shanglin Hou, Yu Du, Rui Lv, Yanjun Liu, Jingli Lei, and Suoping Li
School of Science, Lanzhou University of Technology, Lanzhou, Gansu 730050, China

Abstract— Photonic crystal fibers (PCFs) have attracted considerable attention as optical fiber transmission media and fiber-optic devices owing to the flexible tailor of their chromatic dispersion over a wide wavelength range, the controllability of their effective mode area and nonlinearities as well as their low confinement loss. So many novel optical properties are due to the position and size of the air-holes around the core of the PCFs. PCFs have been considered for fiber-optic devices but also as a candidate optical transmission medium for future large capacity photonic networks. And now wavelength division multiplexing (WDM) systems are widely used to improve the capacity of networks. Though the realization of higher bit-rate WDM transmission will be required in the future, the dispersion and the nonlinearity of the optical fiber degrade the transmission characteristics. So far people use dispersion compensation techniques to compensate for the dispersion and enlarge the effective area of optical fiber for reducing nonlinearity.

The photonic crystal fibers with three zero-dispersion points present a very rich phase-matching topology enabling enhanced control over the spectral locations of the four-wave-mixing and resonant-radiation bands emitted by solitons and short pulses, because of the presence of a third zero-dispersion point. The spectral evolution and the time-frequency characteristics of the soliton in PCFs owning three zero-dispersion wavelengths have been reported and the result shows that in high frequency normal dispersion region the blue-shifted dispersive wave was emitted by the dispersion wave solution.

In this paper, we investigate the properties of the PCFs, which have three zero-dispersion wavelengths, by adjusting the air-hole diameters of the structure parameters in the cladding and studied the influence of dispersion and nonlinearity on the structure parameters. The results show that in these PCFs broad anomalous dispersion region around the wavelength of 1550 nm, the lower dispersion in the normal dispersion region and larger effective mode area of the PCFs, where the effective mode area A_{eff} are sufficiently larger than that of the multicore fibers (effective area about 120 μm^2 at 1550 nm). These PCFs are expected to be used in optical networks with wavelength of 1260 nm–1625 nm (O-L bands), such as access networks and long haul networks.

Investigation on Slow Light of Uniform Fiber Bragg Gratings

Jingli Lei, Shanglin Hou, Rui Lv, Yan-Jun Liu, and Suo-Ping Li
School of Science, Lanzhou University of Technology, Lanzhou 730050, China

Abstract— The interest in slow light research has been attracted due to its potential applications in optical communication components and sensors devices. Such as slow light buffers, delay lines and laser radar, etc.. J. T. Mok reported the dispersionless slow light with 5-pulse-width delay in fiber Bragg gratingin 2007 and the excitation of gap solitons in a 30 cm fiber Bragg grating using 0.68 ns pulses, which emerge with a tunable delay of up to 3.2 ns corresponding to almost five pulse widths and without broadening. In 2008, Myungjun Lee, Ravi Pant and Mark A. Neifeld reported the improved slow-light delay performance of a broadband SBS system using fiber Bragg gratings, they presented a technique for improving the pulse-delay performance of a SBS based broadband slow-light system by combining with fiber Bragg grating and optimize the physical device parameters of three systems. Pump power consumption is reduced by 15% as compared to the broadband SBS system at the same bit rate. In 2009, Qian Kai, Zhan Li, etc. reported the tunable delay slow-light in an active fiber Bragg grating which achieved tunable optical delay by using the Er/Yb codoped fiber Bragg grating, a controllable delay of 0.9 ns can be obtained through changing the 980 nm pump power. It provides a very simple approach to control the light group delay.

In this paper, the slow light based on the uniform fiber Bragg gratings is investigated and the influence of the grating of length, "dc" index change spatially averaged over a grating period and fringe visibility of the index change on group delay is demonstrated by means of numeric simulation. The research results indicate that the impact of "dc" index change spatially averaged over a grating period on group delay is most obviously, the maximum value of the group delay of 140.087 ns can be obtained and slow light decays exponential at the edge of reflected spectrum of the fiber Bragg gratings.

Optical Fiber Nonlinear Coefficient Measurements Using FWM

A. Supe, J. Porins, and G. Ivanovs
Institute of Telecommunications, Riga Technical University, Azenes st. 12, Riga LV-1010, Latvia

Abstract— Telecommunication market needs for broadcasting channels determine the progress of development of high speed fiber optics telecommunication systems (FOTS). The total average demand for the data is increasing more and more rapidly [1].

Increasing data rates leads tomuch higher requirements to optical signal to noise ratio (OSNR) and bit error ratio (BER) which inevitably decreases as signal propagates along the optical fiber (OF) line due to linear effects (attenuation and dispersion) and non-linear effects. In addition nonlinear effects' influence is more dangerous because it is more complicated to compensateand it may eventually degrade an optical signal to be unrecognizable at the receiver.

Parameter that characterizes OF's nonlinearities is nonlinear coefficient γ. Traditional telecommunications OF's γ is not very high (around $2.5\,\mathrm{W^{-1}km^{-1}}$). But high optical radiation intensities in the OF core and long transmission distances lead to considerable nonlinear interaction. Therefore this parameter is very essential especially for the fibers that are used in high data rates FOTS.

In this research, γ parameter measurements using nonlinear phenomena four-wave mixing (FWM) are performed. Experimental measurement scheme is shown in the Fig. 1. Pump and signal laser wavelength are set to be in the OF's zero dispersion region to achieve better FWM interaction efficiency. It has been established that measured nonlinear coefficient value is decreasing according to increase in the pump and signal laser wavelength separation $\Delta\lambda$. This can be explained by phase matching condition deterioration as two optical components are located further away each from the other. Calculations are performed to find out exact $\Delta\lambda$ for which the γ parameter is constant.

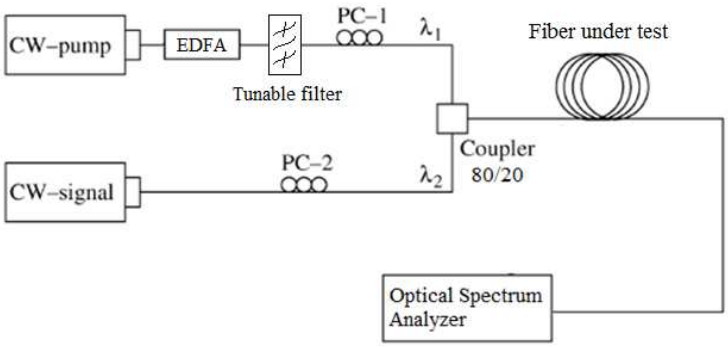

Figure 1: Measurement scheme for optical fiber γ parameter measurement using FWM.

REFERENCES

1. Hecht, J., "Recycled fiber optics, how old ideas drove new technology," *Optics and Photonics News*, Vol. 23, No. 2, 22–29, 2012.

Multi-level Pores, Size-tunable Fe_3O_4 Nano/Submicrospheres for Electromagnetic Wave Adsorption

Xutang Qing, Xiaoxiao Yue, and Yun Lu
State Key Laboratory of Coordination Chemistry, Department of Polymer Science and Engineering
School of Chemistry and Chemical Engineering, Nanjing University, Nanjing 210093, China

Abstract— Multi-level pores, size-tunable Fe_3O_4 nano/submicrospheres were prepared by one-pot solvothermal method using [BMIM][$FeCl_4$] as iron source, 25wt% $NH_3{\cdot}H_2O$ as alkali source and ethylene glycol as solvent. The electromagnetic data of the obtained Fe_3O_4 indicated that the incorporation of multi-level pores into bulk Fe_3O_4 enhanced the dielectric loss and made effective complementarities between the dielectric loss and the magnetic loss, which is a key to improve the reflection loss of electromagnetic wave absorbents. The reflection loss exceeded −40 dB at 1.4 GHz when the thickness of absorbents is 5.7 mm and shows high dual adsorption at both low frequencies and high frequencies.

Multi-level pores of 2 nm, 10 nm, 60 nm could be observed in SEM and TEM images, which is also proved by BJH model of isothermal N_2 adsorption and desorption. It is found that [BMIM][$FeCl_4$] and gas-producible alkali played a importance role in nucleation and formation of multi-level pores.

Varying the ratio of 25wt% $NH_3{\cdot}H_2O$ versus [BMIM][$FeCl_4$], particles sizes of Fe_3O_4 could be finely tuned from 411 nm to 23 nm and the saturated magnetization decreased from 89.2 emu/g to 74.9 emu/g simultaneously. With the increase of the import of alkali solution, the nucleation also increased and the reduction possibility of Fe^{3+} to Fe^{2+} was decreased.

The electromagnetic wave adsorption depended greatly on the thickness of absorbents. When the thickness of absorbent is below 3 mm or over 7 mm, the adsorption is relatively low; however, when the thickness is between 3 mm to 6 mm, the maximum adsorption is over −18 dB. Especially, when the thickness of absorbent is 5.7 mm, the adsorption reached a maximum of −40.0 dB at 1.4 GHz.

ACKNOWLEDGMENT

This work was supported by the National Natural Science Foundation of China (Nos. 20974043 & 21174059) and the Testing Foundation of Nanjing University.

Design of Quantum Secure Communication System Based on FPGA

Jun Li[1], **Jie Chen**[2], **Heping Zeng**[2], **and Hui Li**[1]

[1]Shenzhen Graduate School, Peking University, China
[2]State Key Laboratory of Precision Spectroscopy, ECNU, China

Abstract— Nowadays, quantum secure communication has been recognized as one of the most secure communication techniques, and plug-play scheme is one of the most practical case in QKD (quantum key distribution) experiment. This paper mainly introduces how to use FPGA (field programming gate array) to control the optical components in order to implement quantum key distribution system. The system works based on phase coding mode with optical pulse frequency being 10 MHz, communication distance being 50 km, code generating rate being 2 kbps and error rate being 10^{-6}. Also we have developed an application software which can take text chat and secure file transmit for the QKD hardware system using Qt IDE on Linux OS.

Numerical Study of Effective Plasma Frequency for a Plasma Photonic Crystal in the Presence of Magnetic Field

Heng-Tung Hsu[1], **Jin Jei Wu**[2], **Chi-Chung Liu**[3], **and Chien-Jang Wu**[4]

[1]Department of Communications Engineering, Yuan Ze University, Chungli 320, Taiwan, R.O.C.
[2]Department of Electrical Engineering, Chung Hua University, Hsinchu 300, Taiwan, R.O.C.
[3]Department of Electro-Optical Engineering
National Formosa University, Yunlin 632, Taiwan, R.O.C.
[4]Institute of Electro-Optical Science and Technology
National Taiwan Normal University, Taipei 116, Taiwan, R.O.C.

Abstract— In this paper, based on the transmittance spectrum calculated by making use of the transfer matrix method, we numerically study the effective plasma frequency for a ternary plasma photonic crystal (PPC) in the presence of static magnetic field. The results illustrate that the effective plasma frequency for the PPC will be red-shifted as a function of the static magnetic field. In the case of oblique incidence, we find that the effective plasma frequency is found to be insensitive to the angle of incidence in the TM wave.

Mode Transformations of Surface Plasmons to Propagating and Back to Surface Plasmons in Metal Dielectric Interface with a Half Space Cloaking Region

D. Mahanta, P. Arora, and A. Krishnan
Department of Electrical Engineering
Indian Institute of Technology Madras, Chennai 600 036, India

Abstract— John Pendry first proposed the considerations for an ideal optical cloak using anisotropic material media that mimic a curved co-ordinate system and this field became known as Transformation Optics (TrO) [1]. Since then, several research groups have used TrO to study guiding light around obstacles and to design practical metamaterial structures in different frequency regimes [2].

In this work, we present an interesting mode transformation that occurs when Surface Plasmon Polaritons (SPPs) encounter a semi-cylindrical metallic bump covered with a half-space cloaking medium. The anisotropic permittivity and permeability tensors of the cloaking medium were calculated using TrO and full wave electromagnetic simulations were performed. It was observed that when SPPs encountered the cloaking region, a mode transformation from tightly confined SPPs to loosely confined propagating wave occurred. This enabled SPPs to be guided around the bump as a propagating wave and another mode transformation back from propagating mode to tightly confined SPPs occurred on the second interface. It was observed that almost all the energy was transferred across the cloaking medium. Full wave simulations for Attenuated Total internal Reflection (ATR) configuration revealed that the angular SPP resonance characteristics for the glass-metal-air geometry was identical to the semicylindrical metallic bump coated with a half-space cloaking medium, resulting in a complete cloaking of the metallic bump from the SPPs.

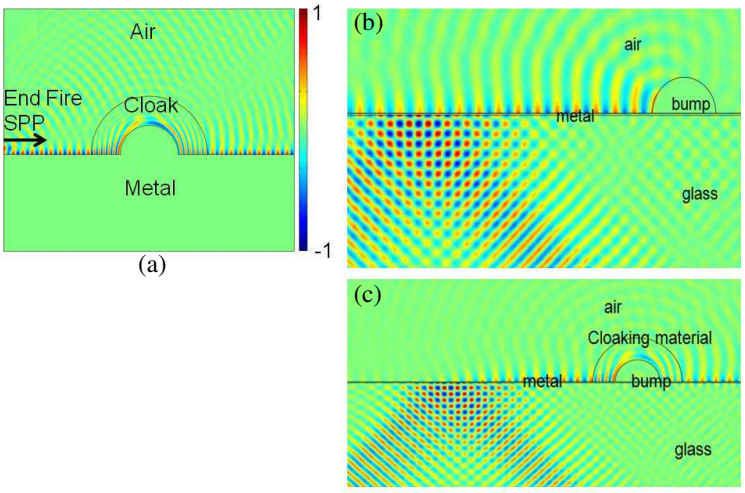

Figure 1: (a) Mode transformation in the semi-cylindrical cloaking region with end-fire SPP coupling. (b) Attenuated total internal reflection characteristics of glass-metal-air interface with a metallic bump. (c) Attenuated total internal reflection characteristics with the metallic bump covered with a cloak.

REFERENCES

1. Pendry, J. B., D. Schurig, and D. R. Smith, "Controlling electromagnetic fields," *Science*, Vol. 23, 1780–1782, 2006.
2. Schurig, D., J. J. Mock, B. J. Justice, S. A. Cummer, J. B. Pendry, A. F. Starr, and D. R. Smith, "Metamaterial electromagnetic cloak at microwave frequencies," *Science*, Vol. 314, 977–980, 2006.

Characterization of Picosecond Laser Pulses Using a Single-shot Measurement Method

Hoon Jeong[1], **Dongjoo Lee**[2], **and Mi Joung Kim**[1]

[1]Manufacturing System R&D Department, Korea Institute of Industrial Technology, South Korea
[2]Swamp Optics, Atlanta, Ga, USA

Abstract— High pulse energy picoseconds laser systems have emerged as universal tools for ablation almost any material without unwanted thermal effects in micromachining applications. Until now, however, the exact measurement method of the ps laser pulses has not developed even though the temporal pulse profile or pulse distortion could affect micromachining performance. This paper demonstrates the measurement method of several tens ps laser pulses based on the frequency-resolved optical gating (FROG). The huge pulse front tilt generated by a holographic grating increases the temporal range of the device which can make a single-shot measurement of several tens ps laser pulses. In order to prove the demonstrated measurement technique we generated double pulses using a Michelson interferometer. The duration of the single pulse is about 700 fs and the measured delay of two pulses is 50 ps, which implies that the maximum delay is 100 ps and the measurable maximum laser pulse duration is around 35 ps.

The Studies of Enhanced Optical Single Sideband Modulation Using by Laser's Cavity Mode and Nonlinear Optical Fiber Effect

H. Y. Shao[1], **W. S. Tsai**[1], **G. C. Lin**[1], **and H. H. Lu**[2]

[1]Department of Electrical Engineering, Ming Chi University of Technology, Taipei 24301, Taiwan
[2]Department of Electro-Optical Engineering, National Taipei University of Technology
Taipei 10608, Taiwan

Abstract— The conventional fiber optical communication system usually adopts light intensity modulation with optical double sideband (ODSB) modulation format. After transmission for a long distance, dispersion effect will make the microwave signal produced serious fading. Optical single sideband (OSSB) signal, which can remove a half of the optical spectrum, solving dispersion induce microwave signal degradation. Recently, radio-on-fiber systems have attracted considerable attention due to their superior capabilities for radar systems and commercial radio access applications.

The traditional optical double sideband (ODSB) modulation could cause severe optical dispersion in Radio-on-fiber (ROF) system. Optical single sideband (OSSB) modulation is usually used to solve it. OSSB modulation can suppress the power dissipation effectively and extend the signal transmission distance. The study proposes the improved and enhanced OSSB modulation method, which can suppress the dispersion caused between carrier and sideband, then can be transmitted over a longer distance.

Adjust the phase shifter for phase difference between the two paths of electrical signal; output signal is OSSB format in early method. Hence, we propose a transmission system based on injection-locked Fabry-Perot (FP) Laser and stimulated Brillouin scattering (SBS) to achieve modulation in fiber. These two kinds of technologies fall on frequency band approximately nearby 10.87 GHz $\sim$ 11 GHz to enhance optical single sideband (OSSB) signal. The first step based on injection-locked FP Lasers to achieve modulation. The right sideband is amplified and unlocked mode signal is attenuated by the cavity mode to produce OSSB modulation. The second step drive radio-frequency (RF) signal into the modulation and then used SBS effect to enhance performance of OSSB modulation. After 25-km of single-mode fiber (SMF) transmission, we can observe the sideband power ratio (SBPR) > 17 dB and phase noise < -80.07 dBc/Hz.

A Study of Enhanced Optical Single Sideband Modulation Based on Scattering Effects and Semiconductor Laser Injection Locked Technology

Y. L. Chen[1], **W. S. Tsai**[1], **G. Z. Lin**[1], **and H. H. Lu**[2]

[1]Department of Electrical Engineering, Ming Chi University of Technology, Taiwan
[2]Department of Electro-Optical Engineering, National Taipei University of Technology, Taiwan

Abstract— In Radio-on-fiber (ROF) transmission system, the microwave signal is converted into the optical signal and distributed to the remote base station by fiber link, which provide broad bandwidth and low attenuation characteristics. The conventional fiber optical communication system usually adopts light intensity modulation with optical double sideband (ODSB) modulation format. After transmission for a long distance, dispersion effect will make the microwave signal produced serious fading. Optical single sideband (OSSB) signal, which can remove a half of the optical spectrum, solving dispersion induce microwave signal degradation. By eliminating one of the sidebands, OSSB modulation not only immunizes to fiber dispersion, but it also increases the spectral efficiency twice. The study proposes the improved and enhanced OSSB modulation method, which can suppress the dispersion caused between carrier and sideband, then can be transmitted over a longer distance.

We propose a transmission system based on stimulated Brillouin scattering (SBS) and Distributed-Feedback (DFB) Lasers to achieve OSSB modulation in fiber. These two kinds of technologies fall on frequency band approximately nearby 10.87 GHz $\sim$ 11 GHz, to enhance OSSB signal. The first step drive radio-frequency (RF) signal into the modulation and then used SBS effect to produce of OSSB modulation. The second step based on injection-locked DFB Lasers to achieve modulation. The right sideband is amplified and unlocked mode signal is attenuated by the cavity mode to enhance performance OSSB modulation. After 25-km of single-mode fiber(SMF) transmission test, we can observe the sideband power ratio (SBPR) > 8.84 dB and phase noise < -86.09 dBc/Hz.

Increasing the Luminous Efficiency of Flip-chip Light Emitting Diode with a Reflective Aluminum Layer

Ming-Jer Jeng[1], **Wen-Yu Guo**[2], **Chia-Yi Yen**[1], **Liann-Be Chang**[1], **and Boren Huang**[2]

[1]Department of Electronic Engineering and Green Technology Research Center
Chang Gung University, Taiwan
[2]Department of Electronic Engineering
National Taiwan University of Science and Technology, Taiwan

Abstract— Many optoelectronic researchers focus their studies on the development of output power and efficiency performance in solid state light (SSL) illuminations. A standard flip-chip light emitting diode (FCLED) has many advantages. First, it can illuminate a light from the back side without electrode obstruction. Second, it can improve its efficiency by dissipating high heat through a thermal conductive submount. In this work, we investigate a reflective metal layer on the backside electrode of FCLEDs to reflect the emitting light for increasing output power. Aluminum is known to reflect well at the wavelength of visible light. In the process of device fabrication, an aluminum metal layer is deposited on the back side of FCLEDs and functioned as a light reflective layer to increase the output light. An electroluminescence measurement demonstrated that the light intensity of FCLED with a reflective layer is about 42% higher than that without a reflective layer under a current injection of 350 mA. In addition, its light output power in is also much higher than that without a reflective layer.

Asymmetric Permittivity and Permeability Sensitivities of Plasmonic Sensors

Yen-Kai Chang[1, 2] **and Chih-Wei Chang**[1]

[1]Center for Condensed Matter Sciences, National Taiwan University, Taipei 10617, Taiwan
[2]Department of Physics, National Taiwan University, Taipei 10617, Taiwan

Abstract— Subwavelength metal structures exhibiting plasmonic resonances determined by their geometries are like artificial plasmonic atoms whose optical responses can be tailored via engineering designs and advanced fabrication methods. In particular, the resonant frequencies of these plasmonic atoms are highly sensitive to the environmental media and can be utilized as optical refractive index sensors. In the past, it was predicted that the refractive index (RIU) sensitivities of various plasmonic atoms obey a simple universal scaling relation that the sensitivities linearly increase with the resonant wavelengths. However, because no magnetic responses exist at optical frequencies, these results are established exclusively in permittivity sensitivities only.

In this work, we employ electrodynamical simulations to study the fundamental electromagnetic duality of various plasmonic atoms by testing their sensitivities to environmental permeability changes. Interestingly, we find that electromagnetic duality is broken in various plasmonic atoms' sensitivities to the environmental permittivity and permeability. While the permittivity sensitivities vs. the resonant wavelengths relation follows a universal straight line at the visible to infrared ranges and is independent of the geometries of the plasmonic atoms, the permeability sensitivities deviate from the straight line with decreasing resonant wavelengths and is strongly geometrically dependent. Remarkably, for a given plasmonic atom, we can always find a particular resonant frequency beyond which the permeability sensitivity drops to zero. We numerically retrieve the effective dispersion relation from the simulation data and find that the conventional standing wave model can not explain the breakdown of the electromagnetic duality. Instead, the phenomena can be explained in terms of LC (L = inductance, C = capacitance) resonator model with added contributions from the inductance of kinetic electrons. We find that the effects are strongly correlated with the effective plasma frequency of the plasmonic atom and thus they can be further manipulated by introducing the concept of spoof plasmons. Unlike traditional electromagnetic systems such as microwave waveguides or antennas, our results provide a rare example that the fundamental electromagnetic duality can be broken in plasmonic systems.

Development of Optical Wave Microphone Measuring Sound Waves with No Diaphragm

Yoshito Sonoda, **Takashi Samatsu**, **and Toshiyuki Nakamiya**
Graduate School of Industrial Engineering, Tokai University, Toroku 9-1-1, Kumamoto 862-8652, Japan

Abstract— As a standard technique to measure sound waves, various types of microphone have been developed and used over one hundred years. However, they have many restrictions on practical applications because they use a diaphragm or any vibrating object to detect sound waves, which disturbs the sound field and cannot respond to the fast phenomena.

In this paper, the optical wave microphone with no diaphragm (or Optophone), which can detect sound waves wave-optically by using a laser beam without disturbing an air flow and a sound field, is presented as a nodal sound measurement technique.

The method is principally based on the interaction between light and sound and the Fourier optics. The sound signal is obtained by detecting ultra-small diffraction light generated from phase-modulation by sounds. In the optical receiving aparatus, the diffraction light generated from optical phase modulation by sound waves is passed through an optical information processing system or an optical Fourier-transform system and then is converted into an electric signal by a photodetector.

The principle and theory, which have been developed in the nuclear fusion research as a new plasma diagnostic technique to detect the electromagnetic radiation scattered by long-wavelength plasma waves, are briefly introduced. Based on it, property and merits as a wave-optical sound detection method are described. Furthermore, the fundamental experiments and results including the frequency property, the dynamic range and the directivity are described, in which it is shown that sounds from about 100 Hz to 100 kHz could be simultaneously detected by a visible laser beam of 5 to 20 mW. Finally, present main problems of the optical wave microphone for practical uses in the sound engineering field are shortly shown, adding the expected future technology.

Visualization of Electric Discharge Sound Fields in Atmospheric Pressure Plasma Using Fraunhofer Diffraction

Toshiyuki Nakamiya[1], **Fumiaki Mitsugi**[2], **Yoichiro Iwasaki**[1], **Tomoaki Ikegami**[2], **Ryoichi Tsuda**[1], **and Yoshito Sonoda**[1]

[1]Graduate School of Industrial Engineering, Tokai University
9-1-1,Toroku Higashi-ku, Kumamoto 862-8652, Japan
[2]Graduate School of Science and Technology, Kumamoto University
2-39-1, Kurokami Chuo-ku, Kumamoto 860-0082, Japan

Abstract— Most of electric discharges emit acoustic (20 $\sim$ 20,000 Hz) and ultrasonic (over 20 kHz) waves. Continuous and pulsed voltages initiate the electric breakdown which generates pressure deviation from equilibrium pressure. The sound waves are generated by the pressure change causing local compression and rarefaction. We have examined the sound signals which are emitted from the discharge area [1, 2]. Because the sound signals contain about the information of discharge and atmospheric condition around the discharge.

However, it's not easy to detect the sound signal in plasma reactor by the conventional condenser microphone technique. Therefore, we have developed a new diagnostic method, in which sound wave is measured by an optical sensor based on a Fraunhofer diffraction effect between the sound wave and laser beam. The light diffraction technique, which we call the "Optical Wave Microphone (OWM)" technique, is an effective sensing method to detect the sound. This technique is very useful to detect the sound wave without disturbing the sound field. Moreover, OWM can be applied for the visualization of sound field by computerized tomography (CT) because the ultrasmall modulation by the sound field is integrated along the laser beam path.

Applied voltage, current and the electrical discharge sound of coplanar dielectric barrier discharge are measured, and examined the relationship between the micro discharge and the acoustic properties. We expect that understanding of acoustic properties gives more details of electric discharges.

REFERENCES

1. Nakamiya, T., Y. Iwasaki, F. Mitsugi, R. Kozai, T. Ikegami, Y. Sonoda, and R. Tsuda, *Journal of Advanced Oxidation Technologies*, Vol. 14, No. 1, 63–70, 2011.
2. Nakamiya, T., F. Mitsugi, S. Suyama, T. Ikegami, K. Ebihara, Y. Sonoda, Y. Iwasaki, S.-I. Aoqui, H. Stryczewska, J. Pawlat, *Przeglad Elektrotechniczny (Electrical Review)*, 1/2011, 249–253, 2011.

An Overview of Metamaterials in Biomedical Applications

S. Raghavan and V. Rajeshkumar
Department of Electronics and Communication Engineering
National Institute of Technology, Tiruchirappalli 620015, India

Abstract— Communication technologies and biomedical sensors can provide services for the patient's vital signs to be monitored outside the clinical environment. The need for implantable telecommunication devices for medical applications has been growing rapidly over the past ten years. Microwave antennas and sensors are key components of telemetry systems related to medical applications. Metamaterials are artificial materials which have the electromagnetic properties that may not be found in nature. The unusual properties of a metamaterial have led to the development of metamaterial antennas, sensors and metamaterial lenses for miniature wireless systems which are more efficient than their conventional counterparts. Metamaterials exhibit a very sensitive response to the strain, dielectric media, chemical and biological sensing applications. A wide area of biomedical applications using metamaterials has been discussed in this review. The design concept of metamaterial antennas in ISM band is presented. Later, the fundamental theory and recent progress of metamaterial in sensors, lenses and absorbers are reviewed for various healthcare applications towards its practical implementation.

Interfacial Properties of Modified Natural Polysaccharide Carbohydrate Surfactants

Mou-Chuan Hwang[1], **Li-Huei Lin**[2], **and Wei-Min Hwang**[1]

[1]Department of Materials and Textiles, Oriental Institute of Technology
Pan-Chiao City, Taipei County 22061, Taiwan, R.O.C.
[2]Department of Cosmetic Science, Vanung University
Chung-Li City, Taoyuan County 32061, Taiwan, R.O.C.

Abstract— New natural polysaccharide carbohydrate derivatives of sodium alginate surfactants were prepared by condensation of sodium bisulfite onto the polysaccharide linkages at different hydrophobic chain of Fatty acids. We were synthesis and solution properties of hydrophobically modified alginate-ester derivatives in which dodecyl or octadecyl chains were grafted onto the polysaccharide backbone via ester functions. In semi-dilute aqueous solution, intermolecular hydrophobic associations result in the formation of physical networks, the physico-chemical properties of which can be controlled through polymer concentration, hydrophobic chain content and non-chaotropic salts such as sodium chloride. Alginate is a biomaterial widely used in the food industry as thickener and in biotechnological applications including cell encapsulation, protein delivery or tissue engineering. Alginate is a negatively charged polysaccharide obtained from marine algae and various bacteria, with solution properties ranging from viscous to gel-like structures in the presence of divalent cations. In this study, the structure of final products was confirmed by FT-IR and 1H-NMR. The interfacial properties were evaluated by surface tension, foaming properties and conductivity. The result showed that the novel material is capable of encapsulating both hydrophilic and hydrophobic molecules. Crucially, the all-important gelling and non-toxic properties of native alginate have been retained.

Indoor Broadband Spectrum Survey Measurements for the Improvement of Wireless Systems

R. Urban, T. Kriz, and M. Cap
Department of Theoretical and Experimental Electrical Engineering
Brno University of Technology, Kolejni 2906/4, Brno 612 00, Czech Republic

Abstract— This paper presents unique measurement campaign focused on indoor spectrum survey. This typeof the results which are achieved by the measurement should be used in many ways. Firstly, spectrum regulators have to know which frequencies are used at measured locations and also power limitations have to be accomplished. Secondly, spectrum survey data are used to simulate Cognitive Radio [1]. Cognitive radio is phenomena of the wireless communication during the last decade. It increases intelligence of transmitter and receiver to minimize Signal-to-Noise Ratio and interference with other users of shared frequency spectrum mainly by dynamic spectrum sharing. Generally, spectrum survey was presented is several papers e.g., [2], but presented measurements have significant differences. Instead of several directional antennas, in our case we use one wideband omnidirectional antenna, which enables us measure wideband results (up to 7 GHz). Portable wideband receiver (9 kHz–7.5 GHz) [3] is used, and it provides sufficient sensitivity (not worse than — 113 dBm) in the whole band. The receiver is controlled by specially designed program, which communicates via TCP/IP and provides fast connection to download huge amount of data to the controlling PC. The other advantages of presented system are portability and speed of measurement.Calibration was carefully made in anechoic chamber to measure baseline of the whole system. Results are processed to detect primary users (users of the frequency spectrum) and calculate utilization of the frequency spectrum. White spaces, part of the unused frequency spectrum at current location and time, that are possible to use for wireless communication, are detected and calculation of minimum, maximum and average white space duration is provided. Results are mainlyconcerned with the indoor spectrum survey, where the wireless traffic created by group of users is also taken into account. Based on the results one can see there is a potential of improvement ofwireless traffic by using principle of dynamic spectrum sharing [4]. The optimization of the radiated electromagnetic waves has beneficial effect for biological tissues.

ACKNOWLEDGMENT

This work was supported by the project CZ.1.07/2.3.00/30.0005 of Brno University of Technology.

REFERENCES

1. Mitola, J., *Cognitive Radio Architecture: The Engineering Foundations of Radio XML*, Wiley-Interscience, Hoboken, N.J., 2006.
2. Shared Spectrum Company (SSC), 2011, http://www.sharedspectrum.com/papers/spectrum-reports/.
3. R&S® PR100 Portable Receiver, 2011, http://www2.rohde-schwarz.com/en/products/radio-monitoring/receivers/PR100-|-Key_Facts-|-4-|-3473.html.
4. Cordeiro, C., K. Challapali, D. Birru, and N. Sai Shankar, "IEEE 802.22: The first worldwide wireless standard based on cognitive radios," *First IEEE International Symposium on New Frontiers in Dynamic Spectrum Access Networks (DYSPAN 2005)*, 328–337, 2005.

Measurement of Inhomogeneity in the B_0 and B_1 Fields Performed via the Spin-Echo and Gradient-Echo MR Imaging Techniques

R. Kubasek, E. Gescheidtova, and K. Bartusek
Department of Theoretical and Experimental Electrical Engineering
Brno University of Technology, Kolejni 4, Brno 612 00, Czech Republic

Abstract— The physical phenomenon in which the magnetic field of the nuclei of some atoms of the substance under examination reacts mutually with a rotating magnetic field is called NMR (Nuclear Magnetic Resonance). NMR spectroscopy and tomography require the basic magnetic field B_0 to be generated with a high homogeneity. The homogeneity of basic magnetic field can be distorted by measured object. It is not necessary to be magnetic, just different susceptibility can lead to distortion in images. Figure 1 shows the same specimen filed with water and with bubble at the top. The boundary between water ($\chi = -9.5 \times 10^{-6}$) and air ($\chi = 4{\times}10^{-7}$) leads to B_0 distortion. Figure 1(a) shows image obtained by SE (Spin Echo) pulse sequence. Figure 1(b) shows image obtained by GE (Gradient Echo) pulse sequence. Measuring techniques using SE compensate B_0 inhomogeneity and then the distortion in image is much less then in image obtained by GE. Properties of relaxation measurement techniques using SE and GE methods can be used to inhomogeneity estimation.

High homogeneity of RF field in the working space of MR tomograph depends on construction of a probe and on its adjustment. The mapping of RF magnetic field is commonly based on an MR image measurement of the homogenous testing specimen with optimally determined flip angle for obtaining the maximum contrast in the measured map of RF magnetic filed. The local B_1 field strength in each examination can be obtained using repeated acquisitions with different RF impulse amplitudes (transmit gain, flip angle). The inhomogeneity can be corrected by the use of a map of the spatial distribution of the B_1 field acquired either through computer simulation, or through the measurement of the field. The relaxation measurement using SE and GE sequences was firstly used for B_0 inhomogeneity estimation.

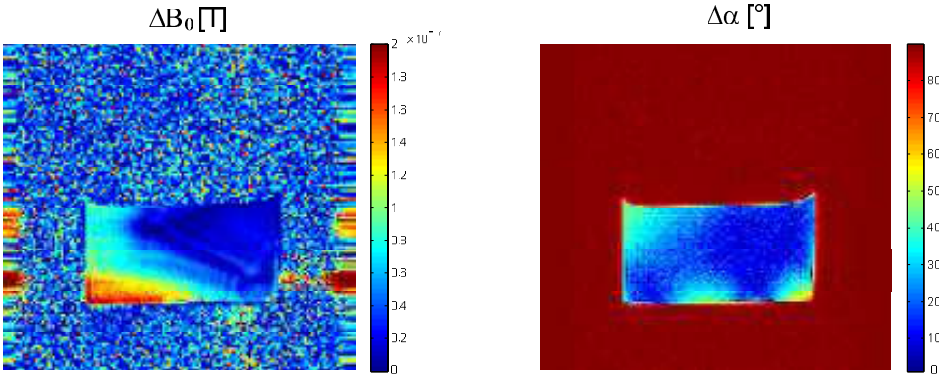

Figure 1: B_0 and B_1 inhomogeneity maps, specimen is a cube filled with water.

Processing of Magnetic Resonance Images of Adipose Tissues

Michaela Pokludová, **Eva Gescheidtová**, **and Jan Mikulka**
Department of Theoretical and Experimental Electrical Engineering
Brno University of Technology, Kolejni 4, Brno 612 00, Czech Republic

Abstract— Sufficiently meaningful picture of tissue structure can be obtained by the correct processing of the image data. This can be done by using image analysis, which takes place in several steps: acquisition of data, image adjustment, segmentation, and image description. At first, digital images are obtained, in our case these are the images of soft tissue obtained with using magnetic resonance tomograph (MR). This device is mainly used to display human tissue in medicine. MR is one of the non-destructive methods, does not cause harmful radiation, whose main advantage is the high contrast in the imaging of soft tissues. The contrast of the resulting images can be changed by setting of the pulse sequence (Spin Echo and Inversion Recovery) timing parameters used to measure the monitored tissue. The data acquired by tomograph is necessary reconstruct by using Fourier Transform reconstruction from K-space in to the MAT file as complex data. The next step of image analysis is image improvement, usually by suppression of noise, histogram equalization and segmentation. Noise should be suppressed to improve results of image processing. Linear transform of histogram was adjusted using a median filter. This is an expansion of the range of brightness in order to cover the entire width of the available brightness. The last step of image processing is multiparametric segmentation. It is a process that divides the image to objects of different characteristic. The main methods include the use of edge detector to highlight certain edges. The last step of the analysis is a description of the image; it is a statistical description of segmented objects in an image with subsequent classification. The aim of this paper is to demonstrate the internal morphology of chicken thigh by using MR. All MR images were evaluated using programs Marevisi and Matlab.

The Effect of Extremely Low Frequency (ELF) Pulsed Electromagnetic Field (PEMF) on Bacteria *Staphylococcus Aureus*

Istiaque Ahmed[1], **Taghrid Istivan**[2], **and Elena Pirogova**[1]

[1]School of Electrical and Computer Engineering
Royal Melbourne Institute of Technology (RMIT) University
Melbourne, Victoria 3001, Australia
[2]Department of Biotechnology and Environmental Biology, School of Applied Science
Royal Melbourne Institute of Technology (RMIT) University
Bundoora, Victoria 3083, Australia

Abstract— Current interest in the application of pulsed electromagnetic fields (PEMF) as alternative therapy for different medical conditions has proven to be successful. There are studies that demonstrate the effectiveness of low frequency PEMF in facilitating wound healing. There are many factors that can affect wound healing and cause improper or impaired tissue repair. Of particular interest are the infected wounds where bacteria or other microorganisms have colonized that cause either a delay in wound healing or deterioration of the wound. In most cases, wounds are typically contaminated by bacteria. In this study, we investigate the application of the applied PEMF on the selected bacterial cultures. In our previous study [1], we presented and discussed the design and development of an extremely low frequency (ELF) PEMF system that produces time varying magnetic field in the range of 0.5 mT to 2.5 mT for a frequency range of 2–500 Hz. Here, we report simulation results of the induced magnetic field distribution and the region of uniformity produced by the system of two pairs of air core Helmholtz coils. We also present the experimental evaluation of varying parametric changes in the applied ELF PEMF on the bacteria Staphylococcus aureus. The selection of this gram-positive bacterium for this study is attributed to the versatile role of these bacteria in infecting wounded tissues. These bacteria are also within easy reach and can be bred at a temperature of 37°C. Here, the Staphylococcus aureusbacteria in broth were exposed to the ELF PEMF of magnetic flux density, $B = 0.5$–2.5 mT, frequency (f) range of 2–500 Hz and time of exposure, $t = 30$ min. This is done in order to compare studied bacterial cultures viability (number of colony-forming units (CFU)). The number of colony-forming units aids in quantifying the experimental result. Fresh bacterial culture is used throughout the experiment. Findings from our investigation have direct implication in determining the optimal characteristics of the applied ELF PEMF for possible treatment of infected tissue and thus, wound healing promotion.

REFERENCES

1. Ahmed, I., V. Vojisavljevic, and E. Pirogova, "Design and development of extremely low frequency (ELF) pulsed electromagnetic field (PEMF) system for wound healing promotion," *IFMBE Proceedings World Congress on Medical Physics and Biomedical Engineering*, Vol. 39, 27–30, 2012.

The Effects of Visible Light Radiation (400–500 nm) on Enzymatic Activity of Collagenase

J. Hu, V. Vojisavljevic, and E. Pirogova
School of Electrical and Computer Engineering
RMIT University, Melbourne 3001, Australia

Abstract— Debridement is the process of removing necrotic burden or contaminated tissue from the wound bed until surrounding healthy tissue is exposed. It is an essential component of wound bed preparation (WBP) that aims to create an optimal wound healing environment. Enzymatic debridement helps to remove non-viable tissue which can otherwise delay wound healing and lead to infection [1]. Collagenase enzyme is known to be able to promote the cellular responses to injury and wound healing in vivo. Collagenase shows more selectively on denatured collagen in devitalized tissue. This selectivity is beneficial as it keeps the vital tissue and growth factors crucial to wound healing intact [2]. There are studies that showed the applied electromagnetic radiation (EMR) in the visible light range can modulate protein and cellular activity. Here we have studied experimentally the hypothesis of the Resonant Recognition Model (RRM) that selectivity of protein activities is based on specific resonant electromagnetic interactions [3]. The RRM theory proposes that an external electromagnetic field at a particular activation frequency would produce resonant effects on protein biological activity, and this activation frequency can be determined computationally [3]. The computational analysis of 28-collagenase sequences was carried out using the RRM. The activation frequency/wavelength range was determined to be between 450–460 nm. To evaluate this activation range experimentally the samples of the collagenase enzyme were irradiated by monochromatic visible light in a range of 400–500 nm. The kinetics of the irradiated collagenase was measured by continuous monitoring of the changes in digested collagen solution's absorption and optical density at 570 nm. The results reveal that collagenase activity can be modulated at the particular wavelength of 456 nm which is within the activation wavelength range defined computationally. This finding supports the hypothesis that protein function can be modified by an applied electromagnetic radiation of defined frequency, which may contribute to the development of a new clinical therapy for wound healing promotion.

REFERENCES

1. Panuncialman, J. and V. Falanga, "The science of wound bed preparation," *Surgical Clinics of North America*, Vol. 89, No. 3, 611–626, 2009.
2. Shi, L. and D. Carson, "Collagenase santyl ointment: A selective agent for wound debridement," *J. Wound Ostomy Continence Nurs.*, Vol. 36, No. 6S, S12–S16, 2009.
3. Vojisavljevic, V., E. Pirogova, and I. Cosic, "The effect of electromagnetic radiation (550–850 nm) on l-lactate dehydrogenase kinetics," *International Journal of Radiation Biology*, Vol. 83, No. 4, 221–230, 2007.

Scattering-induced Changes in the Degree of Polarization of a Stochastic Electromagnetic Plane-wave Pulse

Liuzhan Pan and Chaoliang Ding
Department of Physics, Luoyang Normal College, Luoyang 471022, China

Abstract— In recent years, the statistical properties of the light generated by scattering have been studied extensively due to their considerable interest in medical diagnostics and imaging, remote sensing of the atmosphere and ocean, and so on. However, in most cases, the treatment of scattering of the field was confined to the case that the incident field is statistically stationary. In this paper, the scattering of a stochastic electromagnetic plane-wave pulse on a deterministic spherical medium is investigated. Analytical formula for the degree of polarization (DOP) of the scattered field in the far zone is derived. Let pulse duration $T_0 \to \infty$, our formula can be applied to study the scattering of a stationary stochastic electromagnetic light wave. Numerical results show that the DOP of the far zone field is closely determined by the size of the spherical medium when the incident field is a stochastic electromagnetic plane-wave pulse, which is much different from the case when the incident field is a stationary stochastic electromagnetic light wave, where the degree of polarization of the far zone field is independent of the size of medium. One may obtain the information of the spherical medium by measuring the scattering-induced changes in the DOP of a stochastic electromagnetic plane-wave pulse.

The Comparison of the Contrasts of Magnetic Resonance Images of Plants

M. Pokludová and E. Gescheidtová
Department of Theoretical and Experimental Electrical Engineering
Brno University of Technology, Kolejni 4, Brno 612 00, Czech Republic

Abstract— To obtain an image with the largest information value is needed to achieve the best image contrast during the measurement of the object in the magnetic resonance tomograph. This contrast depends on the physical properties of the object, in particular a proton density and relaxation properties of the material. Furthermore, the contrast depends on parameters characteristic for each MR method: Spin Echo, Gradient Echo and Inversion Recovery. The echo time and repetition time are included between the two most important parameters of pulse sequence. We can create four different variants of contrast by combination of these two mentioned times: the contrast spin density, the T_1 weighted contrast, the T_2 weighted contrast, and the last one is inappropriate setting for the contrast. Each resulting contrast is suitable for displaying different plants stem tissue. Increasing in the contrast can also be achieved by adding contrast (paramagnetic) substances for differentiation of isomagnetic tissues. The aim of this paper is to display the internal morphology of plants by various methods with subsequent contrasts comparing and identification of appropriate method for the study of transport of substances in the stem of the plant. Euphorbia cactus was chosen for the study of the contrasts of images, which was inserted into working space of the tomograph. Images of the plant stem were acquired by magnetic resonance tomograph with the magnetic field induction 4.7 T (200 MHz). The evaluation of the results obtained by all used methods followed the last measurement. The data processing was performed by using programs Marevisi and Matlab. Monitored parameters of individual plant samples were inserted into a table and plotted on graphs. By evaluation and comparison between the relaxation times it can be determined that in the same selected points T_2 relaxation time has shorter values than the T_1 relaxation time, although it is a faster method but at the cost of the quality of the final image. On the contrary, respect to intensity of images where T_1 relaxation time has a lower value of intensities.

Electromagnetic Structures and Inertias of Particles including the Higgs Boson

Michael J. Underhill
Underhill Research Ltd, Lingfield, UK

Abstract— Electromagnetic string structures suitable for photons [1] and the main sub-atomic particles [2] have previously been presented. A photon is an 'electromagnetic string arrow' with a single line frequency spectrum. It is envisaged to be 'dark matter' with low inertia. A photon is a boson and has zero or unit spin. The unit spin can be taken to correspond to left-hand or right-hand circular polarisation. Protons, electrons and neutrons can be described by two or more interlaced toroidal string loops arguably having two or more dominant line frequency components in the particle's spectrum. The interlacing can be regarded as a representation of circular polarisation and characterises 'intrinsic spin'. These three particles have half unit spin and so are classified as 'fermions'. All these particle models have an electromagnetic frequency spectrum with discrete lines. The total energy of the spectral lines is the mass m of a particle according to $E = mc^2$. But the Higgs Boson is expected to have a wideband spectrum with no discrete lines.

An explanation for the existence of inertia in particles is shown in Figure 1. It is based on the concept of a delay in the formation or alteration of the potential 'atmosphere' surrounding the core of the particle with respect to any acceleration of the particle normal matter 'core'. The atmosphere is taken to be 'dark matter' which has gravitational mass in accordance with $E = mc^2$, and a much lower inertial mass.

The Higgs Boson has a mass of about $125\,\mathrm{GeV/c^2}$ (a proton is $0.938\,\mathrm{GeV/c^2}$) and a predicted mean lifetime of $1.56 \times 10^{-22}\,\mathrm{s}$. Its size, structure, (spherical) density profile and whether its inertial mass differs from its gravitational mass are unknown and under discussion. Size is difficult to measure or estimate with such a short lifetime. The internal structure of the Higgs Boson has not yet been discovered or unequivocally established by theory. Thus at this moment in time a simple electromagnetic structure for the Higgs Boson can be considered to have as much credence as any other offering from theoretical physics.

The proposed structure is a sphere with a core mass/energy density that is constant out to a radial distance at which it decays moderately rapidly towards zero density. The density law is assumed to be caused by (electromagnetic) self coupling. Surrounding the dense core is a region, an 'atmosphere' dominated by the (gravitational?) potential, giving an inverse square law of field/potential energy density. At some further distance the energy density decays more rapidly than the inverse square law to avoid the total field energy becoming greater than the core energy. With respect to Figure 1 the very short predicted Higgs particle lifetime may be comparable to the delay between core and atmosphere. Thus its inertia may be uncertain.

Energy and hence mass is assumed to be totally electromagnetic. Electromagnetic energy in general has a spectrum. In the case of the Higgs Boson the energy spectrum is postulated to be broadband covering a very wide band of frequencies, perhaps similar to that of a black body. Because of the short lifetime the spectrum of the electromagnetic energy, the highest spectrum frequency is expected to be at least a few tens of times the reciprocal of the lifetime, perhaps in excess of 10^{23} to $10^{24}\,\mathrm{Hz}$.

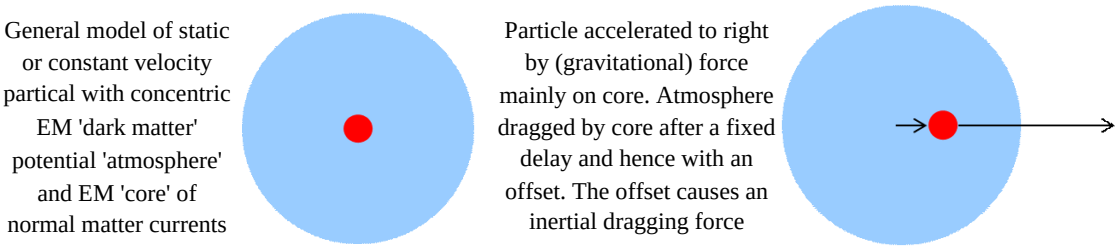

Figure 1: General model of a particle with an explanation for the inertia of normal matter.

REFERENCES

1. Underhill, M. J., "The phase noise spectrum and structure of photons?," *Proc. 16th EFTF-2010*, 8 pages, Noordwijk, Netherlands, April 13–16, 2010.
2. Underhill, M. J., "A physical model of electro-magnetism for a theory of everything," *PIERS Online*, Vol. 7, No. 2, 196–200, 2011.

A Low Phase Noise CMOS VCO for the Millimeter Wave Application

Mingzhu Zhou[1], **Jincai Wen**[1], **Jie Wang**[1], **and Zhili Liu**[2]

[1]The Institute of Electronic and Information Engineering
Hangzhou Dianzi University, China
[2]Hangzhou C-Sky Microsystems Co. Ltd., China

Abstract— In this paper, a low phase noise VCO for millimeter application is presented. The phase noise introduced by the NMOS channel current and the tank loss resistance are modeled to give approximate evaluation of the circuit character, and an optimization of the phase noise has been done according to this model. An inductor is inserted between the drain of one transistor and the gate of the other transistor, and then the transistor g_m generation efficiency is improved. To acquire an optimization inductor value, HFSS is used to model the device. The circuit has been simulated in a 90 nm CMOS technology. The result indicates that the frequency of the VCO is from 56 to 65.24 GHz, and the phase noise is −100.63 dBc/Hz @ 1 MHz in 65.24 GHz. The VCO core consumes 1.225 mA with 0.7 V power supply and the FOM is −197.62 dBc/Hz in 65.24 GHz. The chip layout occupies $500 \times 800\,\mu m^2$ areas.

Figure 1 is the architecture of the VCO circuit [1–3], and the inductor is modeled in HFSS which is shown in Fig. 2. Fig. 3 is the layout of the VCO.

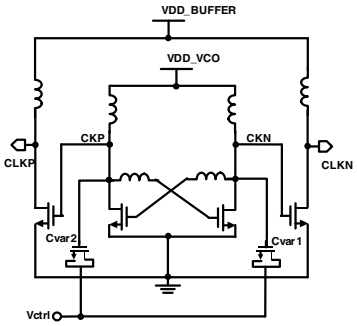

Figure 1: The VCO architecture.

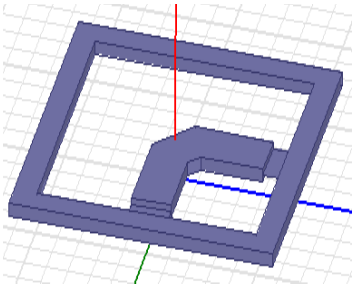

Figure 2: The inductor model in HFSS.

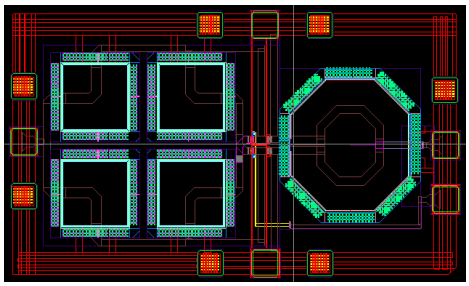

Figure 3: Layout of the VCO.

REFERENCES

1. Li, L. and P. Reynaert. "A 60-GHz CMOS VCO using capacitance-splitting and gate-drain impedance-balancing techniques," *IEEE Transactions on Microwave Theory and Techniques*, Vol. 59, No. 2, 406–413, 2011.
2. Li, L., P. Reynaert, and M. Steyaert. "A low power mm-wave oscillator using power matching techniques," *IEEE Radio Frequency Integrated Circuits Symposium*, 469–472, Boston, America, June 2009.
3. Chai, S. W., J. Yang, and B.-H. Ku, "Millimeter wave CMOS VCO with a high impedance LC tank," *IEEE Radio Frequency Integrated Circuits Symposium*, 545–548, Anaheim, America, May 2010.

The Influence of an Electromagnetic Wave on the Acoustoelectric Current in a Rectangular Quantum Wire with an Infinite Potential

Nguyen Van Nghia[1], **Nguyen Quang Bau**[2], **Nguyen Van Hieu**[2, 3], **and Nguyen Vu Nhan**[2]

[1]Department of Physics, Water Resources University, Hanoi, Vietnam
[2]Department of Physics, College of Natural Sciences, Hanoi National University, Hanoi, Vietnam
[3]Department of Physics, Danang University of Education, Danang University, Danang, Vietnam

Abstract— The analytic expression for the acoustoelectric (AE) current in the presence of an electromagnetic wave (EMW) induced by the electron-external acoustic wave (external phonons) interactions and electron-internal acoustic wave (internal phonons) scattering in a rectangular quantum wire (RQW) with an infinite potential is calculated by using the quantum kinetic equation for electrons. The dependence of the AE current on the temperature, the external acoustic wave frequency, the frequency of the EMW and the parameters of the RQW is analyzed. The theoretical results are numerically evaluated, plotted and discussed for the specific rectangular quantum wire with an infinite potential GaAs. These results are also compared with those for normal bulk semiconductors and RQW in the case of the absence of the EMW to show difference.

Influence of a Strong Electromagnetic Wave (Laser Radiation) on the Hall Coefficient in Doped Semiconductor Superlattices with an In-plane Magnetic Field

N. Q. Bau[1], **N. V. Nghia**[1], **N. V. Hieu**[1], **and B. D. Hoi**[1, 2]

[1]Department of Physics, College of Natural Science, Vietnam National University, Hanoi, Vietnam
[2]Department of Physics, National University of Civil Engineering, Hanoi, Vietnam

Abstract— The Hall effect is studied theoretically in a doped semiconductor superlattice (DSSL) with a periodical superlattice potential in z direction, subjected to a crossed dc electric field $\vec{E}_1 = (0, 0, E_1)$ and magnetic field $\vec{B} = (0, B, 0)$ ($\vec{B}$ is oriented in the plane of free motion of electrons) in the presence of a strong electromagnetic wave (EMW) characterized by electric field $\vec{E} = (E_0 \sin(\Omega t), 0, 0)$ (where E_0 and Ω are the amplitude and the frequency of EMW, respectively). By using the quantum kinetic equation method for electrons interacting with optical phonons at high temperatures, we obtain analytical expressions for the components σ_{zz} and σ_{xz} of the Hall conductivity as well as the Hall coefficient with a dependence on B, E_1, E_0, Ω, temperature T of the system and the characteristic parameters of DSSL. These expressions are fairly different in comparison to those obtained for bulk semiconductors. The influence of the EMW is interpreted by using the dependencies of the Hall conductivity and the Hall coefficient on the amplitude E_0 and the frequency Ω of EMW. The numerical results for the n-GaAs/p-GaAs DSSL show that the Hall coefficient reaches saturation when the magnetic field or the EMW frequency increases. The Hall coefficient varies strongly at small values and reaches saturation at large values of doped concentration.

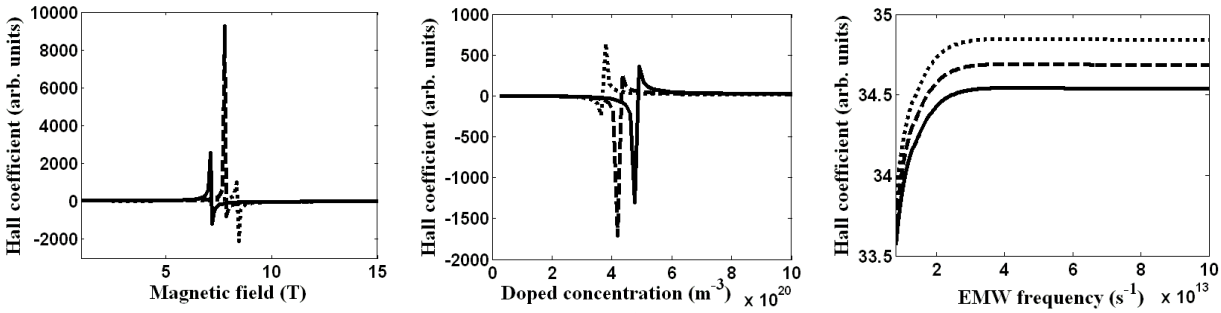

Figure 1.

Session 2P1a
Manipulating Wave with Metamaterials and Photonic Crystal 2

Fabrication and Applications of Polymer Photonic Crystals
Yanlin Song, ... 260
Effective Medium of Periodic Electromagnetic Composites
Ying Wu, ... 262
Dirac Points in Two-Dimensional Photonic Crystals
Jun Mei, Yan Li, Ying Wu, ... 263
Optical Force in Parallel-plate Metamaterial
Zhi Hong Hang, Z. Marcet, D. Guan, S. B. Wang, Hui Liu, H. B. Chan, Penger Tong, Che Ting Chan, ... 264
Effects of Broken Time-reversal Symmetry on Periodic Resonator Arrays
Kin Hung Fung, Jin Wang, Ross Chin Hang Tang, Che Ting Chan, Nicholas X. Fang, ... 265
Dispersion in Drude DNG Stacks: Infinite Density and Line Gaps
Gilad Rosenblatt, Meir Orenstein, ... 266
Bending and Cloaking for a Surface Plasmonic Wave
Hongyi Xu, Su Xu, Hongsheng Chen, Handong Sun, Baile Zhang, ... 267
The Manipulation of Heat Flow by Affine Transformation Thermodynamics
Hongyi Xu, Handong Sun, Baile Zhang, ... 268

Fabrication and Applications of Polymer Photonic Crystals

Yanlin Song
Institute of Chemistry, Chinese Academy of Sciences, Beijing 100190, China

Abstract— Photonic crystals (PCs) not only have beautiful colours, but also could effectively modify the emission and propagation of light with minimal losses, thus the fabrication and applications of PCs have attracted extensive research interest. In our group, PCs with high strength were prepared from latex spheres with a hard PS core and an elastometric PMMA-PAA shell [1–3]. The mono-dispersed latex spheres were synthesized via one-step emulsion polymerization without purification [4]. PC films with brilliant colours covering the wavelength period from the UV to the IR can be fabricated over large areas by vertical deposition method and even spray coating [5, 6]. The wettability of the PCs could be well controlled from superhydrophilicity to superhydrophobicity by adjusting the assembly temperature or pH [7–9]. Furthermore, functional polymer inverse opals were achieved by using the PCs as template, such as high stable polyimide inverse opal PCs [10] and an electrically tunable polypyrrole inverse opal [11]. Additionally, as the PC stop band is sensitive to its lattice constant and the relative index of its components, the colorful humidity-sensitive PC hydrogel [12] and oil-sensitive inverse opals [13, 14] were achieved. Moreover, the PCs could be used as wavelength-selective concentrator and effectively improve the output power of dye-sensitive solar cells [15]. The PCs could also be used to enhance the fluorescence emission [16] of dyes and energy transfer of plasmonic device [17].

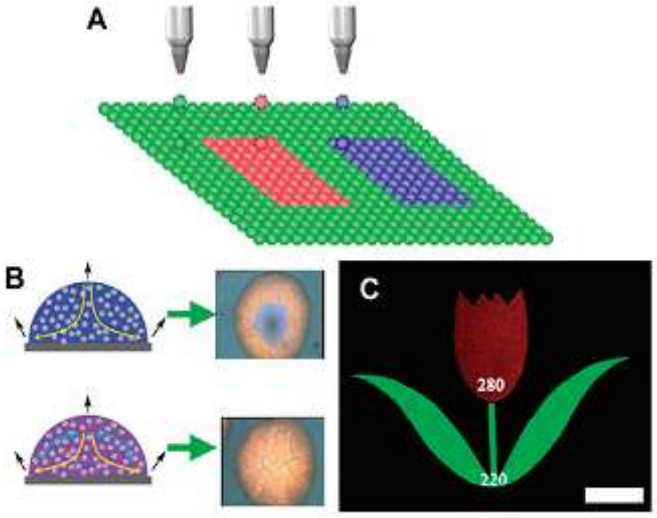

Figure 1: Photonic crystals pattern prepared by inkjet printing.

REFERENCES

1. Wang, J. X., Y. L. Song, et al., *Acc. Chem. Res.*, Vol. 44, 405–415, 2011.
2. Huang, Y., Y. L. Song, et al., *Adv. Funct. Mater.*, Vol. 21, 4436–4441, 2011 (Cover).
3. Huang, Y., Y. L. Song, et al., *J. Am. Chem. Soc.*, 2012 (in press).
4. Wang, J. X., Y. L. Song, et al., *Macromol. Chem. Phys.*, Vol. 207, 596–604, 2006 (Cover).
5. Tian, E. T., Y. L. Song, et al., *Macromol. Rapid Commun.*, Vol. 30, 509–514, 2009 (Cover).
6. Cui, L. Y., Y. L. Song, et al., *Macromol. Rapid Commun.*, Vol. 27, 598–603, 2009 (Cover).
7. Wang, J. X., Y. L. Song, et al., *Macromol. Rapid Commun.*, Vol. 27, 188–192, 2006.
8. Wang, J. X., Y. L. Song, et al., *Adv. Funct. Mater.*, Vol. 17, 219–225, 2007 (Inside cover).
9. Wang, J. X., Y. L. Song, et al., *Chem. Mater.*, Vol. 18, 4984–4986, 2006.
10. Chen, X., Y. L. Song, et al., *J. Mater. Chem.*, Vol. 18, 2262–2267, 2008.
11. Xu, L., Y. L. Song, et al., *Chem. Mater.*, Vol. 20, 3554–3556, 2008.

12. Tian, E. T., Y. L. Song, et al., *J. Mater. Chem.*, Vol. 18, 1116–1122, 2008.
13. Li, H. L., Y. L. Song, et al., *Adv. Funct. Mater.*, Vol. 18, 3258–3264, 2008.
14. Li, H. L., Y. L. Song, et al., *J. Mater. Chem.*, Vol. 18, 5098–5103, 2008.
15. Zhang, Y. Z., Y. L. Song, et al., *J. Mater. Chem.*, Vol. 18, 2650–2652, 2008 (Inside cover),
16. Zhang, Y. Q., Y. L. Song, et al., *J. Mater. Chem.*, Vol. 17, 90–94, 2007.
17. Li, M. Z., Y. L. Song, et al., *Appl. Phys. Lett.*, Vol. 91, 203516, 2007.

Effective Medium of Periodic Electromagnetic Composites

Ying Wu
Computer, Electrical and Mathematical Sciences and Engineering
King Abdullah University of Science and Technology, Thuwal 23955-6900, Saudi Arabia

Abstract— In the framework of multiple-scattering theory, we studied the effective medium properties of two-dimensional periodic electromagnetic composites, such as photonic crystals and metamaterials, in the long-wavelength limit. The composites considered are cylindrical inclusions of magnetodielectic materials embedded in air host. We derived the effective medium theory for two particular cases: complex cell and high filling ratio of the scatter. For the complex cell case, in which there are two distinct scatterers in a unit cell, we investigated the effective medium in the zero-frequency limit as well as at finite frequencies. For such cases, we show that the effective medium is anisotropic in general but it exhibits isotropic behavior when the relative position of the two scatterers satisfies certain conditions. The isotropic effective medium parameters are functions of the summation of the scattering coefficients. For the case of large scatterers, in which there is only one scatterer in a unit cell and the filling ratio of the scatterer is high even close to the tight-packing, we studied the zero-frequency effective medium properties. We found that, if the lattice has four- or six-fold symmetry, the effective medium is isotropic regardless of the concentration of the scatterer. While one effective parameter (dielectric constant for TM waves and permeability for TE waves) always remains the same form as the Maxwell-Garnett formula, the other effective parameter deviates from its leading order dipole solution and becomes lattice structure dependent in a certain range of filling ratios. The analytic expressions of the effective parameters are given and verified by the finite-element simulations.

Dirac Points in Two-Dimensional Photonic Crystals

Jun Mei[1], **Yan Li**[1], **and Ying Wu**[2]

[1]Department of Physics, South China University of Technology, Guangzhou 510640, China
[2]Computer, Electrical and Mathematical Sciences and Engineering
King Abdullah University of Science and Technology, Thuwal 23955-6900, Saudi Arabia

Abstract— A perturbation theory, in the spirit of $\vec{k}\cdot\vec{p}$ method in electron systems, is developed to study the origin of Dirac points in two-dimensional photonic crystals composed of common dielectric materials. Our methods take the degenerate eigen-functions on a high symmetry point in the Brillouin zone as the basis set to expand the unknown Bloch states around that point. It is shown that the existence of linear dispersions around the Brillouin zone center requires that the mode-coupling integrals between the degenerate Bloch statesat the Γ point, in the form of perturbation matrix elements, should be nonzero. The linear slopes of band structures in the vicinity of the Brillouin center can be very accurately reproduced by our perturbationformulae, which agree excellently with the rigorous band structure calculations given by COMSOL Multiphysics, a commercial package based on finite element method. In addition, a selection rule is established which provides an easy and quick check for the existence of Dirac pointsby identifying the spatial symmetry of the Bloch states and evaluating the direct product of the irreducible representations for a vector differential operator and the Bloch states at the Γ point. Such a selection rule gives a conclusive prediction on the existence of linear dispersion, and it makes no assumption on if the accidental degeneracy of Bloch states is already achieved, and if there is an effective medium theory. With all the multiple-scatterings of electromagnetic waves in the photonic crystals fully taken into account, our general theory is applicable to different photonic crystal systems independent of wave polarizations, lattice types, and components' properties.

Optical Force in Parallel-plate Metamaterial

Z. H. Hang[1, 2], Z. Marcet[2, 3], D. Guan[2], S. B. Wang[2], H. Liu[2, 4], H. B. Chan[1], P. Tong[2], and C. T. Chan[2]

[1]Department of Physics, Soochow University, Suzhou, Jiangsu 215006, China
[2]Department of Physics, The Hong Kong University of Science and Technology
Clear Water Bay, Kowloon, Hong Kong, China
[3]Department of Physics, University of Florida, Gainesville, FL 32611, USA
[4]National Laboratory of Solid State Microstructures, Department of Physics
Nanjing University, Nanjing 210093, China

Abstract— Artificial electromagnetic resonating material, also known as metamaterials have successfully been used to demonstrate various interesting wave guiding properties, including negative refraction, super-imaging, cloaking et al. at a broad frequency range from optics to microwave. In addition, the use of laser paved the path to non-contact particle manipulation by light induced forces, which leads to various applications in physics, chemistry and biology. Here we show by both theory and experiments that by combining the concept of metamaterial and optical manipulation, we can induce enhanced optical force orders of magnitude larger than the normal incident photon pressure to achieve mechanical movement of macroscopic objects.

The prototypical system we studied is a parallel-plate metallic cavity. Under the light illumination with wave vector normal to the plate surface and the magnetic field polarized parallel to the surface, anti-parallel current can be induced on the top and bottom plates [Fig. 1]. In the plasmonic regime, the strong attractive force is induced by field penetration into the metal [1]. In the microwave regime, leakage of electric field at the edge of the cavity leads to a net repulsive force [2]. Using a differential capacitance technique, we successfully measured the repulsive force induced between the cavity walls in the microwave regime, which is about two orders larger than the microwave radiation pressure provided at resonance. Using dynamic mode atomic force microscope, we can measure the enhanced optical force of a plasmonic resonant cavity at infrared frequency.

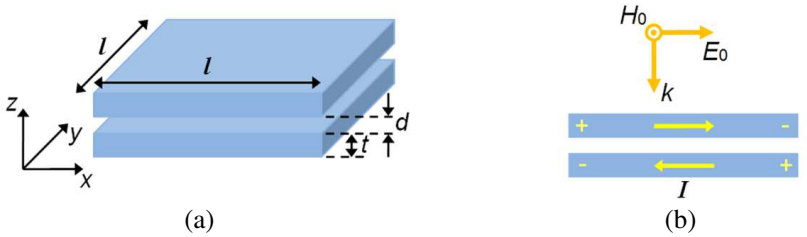

Figure 1: (a) Schematic representation of a parallel-plate resonant cavity showing the geometric parameters and coordinate system. (b) The direction of the incident plane wave and polarization are shown. The anti-parallel induced current I is indicated by the yellow arrows at a certain instance of time.

REFERENCES

1. Liu, H., J. Ng, S. B. Wang, Z. F. Lin, Z. H. Hang, C. T. Chan, and S. N. Zhu, *Phys. Rev. Lett.*, Vol. 106, 087401, 2011.
2. Wang, S. B., J. Ng, H. Liu, H. H. Zheng, Z. H. Hang, and C. T. Chan, *Phys. Rev. B*, Vol. 84, 075114, 2011.

Effects of Broken Time-reversal Symmetry on Periodic Resonator Arrays

Kin Hung Fung[1, 3, 4], **Jin Wang**[2, 4], **Ross C. H. Tang**[3], **C. T. Chan**[3], **and Nicholas X. Fang**[4]

[1]The Hong Kong Polytechnic University, Hong Kong, China
[2]Southeast University, Nanjing, China
[3]The Hong Kong University of Science and Technology, Hong Kong, China
[4]Massachusetts Institute of Technology, Cambridge, MA 02139, USA

Abstract— We discuss the effects associated with the broken time-reversal symmetry on periodic resonator arrays. In particular, we discuss the effect of decoupling between resonators by static magnetic field and the splitting of leaky modes by absorption.

To show the first effect, we consider the wave propagation in periodic arrays of gyromagnetic resonators. When the external staic magnetic field is off, electromagnetic waves can propagate in the array with a finite group velocity. When the external static magnetic field is on, even nearly touching resonators can be decoupled so that almost no wave propagation is allowed. The wave is thus localized within one single resonator. This interesting effect is explained by the splitting of photon angular momentum states by external static magnetic field [1].

For the second effect, we consider a linear array of plasmonic resonators [2, 3]. When there is no absorption, the degeneracy of two leaky modes is protected by time reversal symmetry. When absorption exists, two modes split and thus lead to two different exponential decays together with an additional long-range power-law decay [2].

These two effects are of different origins although both are associated with broken time-reversal symmetry. The first one has a broken reciprocity while the second one does not. We will also have some discussions on distinguishing different types of broken symmetries in Green's functions that are associated broken time-reversal symmetry.

REFERENCES

1. Wang, J., K. H. Fung, H. Y. Dong, and N. X. Fang, "Zeeman splitting of photonic angular momentum states in gyromagnetic cylinder," *Phys. Rev. B*, Vol. 84, 235122, 2011.
2. Fung, K. H., R. C. H. Tang, and C. T. Chan, "Analytical properties of the plasmon decay profile in a periodic metal-nanoparticle chain," *Opt. Lett.*, Vol. 36, 2206, 2011.
3. Fung, K. H. and C. T. Chan, "Plasmonic modes in periodic metal nanoparticle chains: A direct dynamic eigenmode analysis," *Opt. Lett.*, Vol. 32, 973, 2007.

Dispersion in Drude DNG Stacks: Infinite Density and Line Gaps

G. Rosenblatt and M. Orenstein
Department of Electrical Engineering, Technion, Israel

Abstract— Double negative media (DNG), having negative permittivity and permeability, suggested by Veselago and realized by Smith et al., were proposed by Pendry to act as perfect lenses. Significant research effort followed towards DNG-based devices and applications. A periodic stack of alternating DNG and DPS (double positive) layers, was shown to exhibit some unique features including: complex modes [1], discrete Fabry-Perot modes [2], and giant resonance absorption [3].

Nevertheless, a study of its actual band dispersion, without assuming constant media responses over the frequency range of interest, is still missing and it is crucial since the assembly of meta-materials is based on highly dispersive dipoles. Herein we present such a detailed study, applying Drude dispersion for both the DNG permittivity and permeability ($\varepsilon, \mu_{\mathrm{DNG}} = 1 - \omega^2/\omega_{p,\varepsilon,\mu}^2$).

The frequency vs. propagation constant plain — Figs. 1(a) and 1(b) is divided by the dispersive light-lines, and supports three types of possible bands: (i) Infinite number, converging to the DPS light-line at high frequencies (purple); (ii) two surface-wave converging at a resonant frequency, similar to plasmonic bands, but in both polarizations (yellow); (iii) unique complimentary of (i): Infinite number, condensed in a finite frequency domain converging to the DNG light-line with a negative slope, lacking an equivalent in non-DNG stacks (light blue).

Cases of special interest are further scrutinized. Especially, for $\varepsilon_{\mathrm{DNG}} = \mu_{\mathrm{DNG}}$ we show no complete band gap can form, unless both layer thicknesses are equal — resulting in overlapping surface-wave bands along a flat boundary at the frequency for which $\varepsilon_{\mathrm{DNG}} = \mu_{\mathrm{DNG}} = -1$ (Fig. 1(c)), with no power allowed via the stack (a single-frequency 'band gap') — as expected for zero average index media.

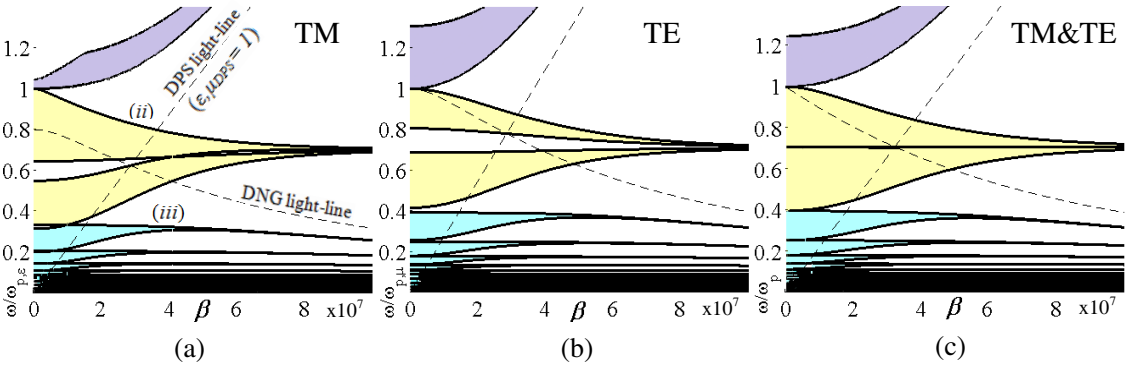

Figure 1: Band structure dispersion for a DNG-DPS (40 nm–50 nm) periodic stack in (a) TM, and (b) TE polarizations, and (c) the special case $\varepsilon_{\mathrm{DNG}} = \mu_{\mathrm{DNG}}$ with equal layer thicknesses (40 nm).

REFERENCES

1. Wu, L., S. He, and L. F. Shen, *Phys. Rev. B*, Vol. 67, 2003.
2. Li, J., L. Zhou, C. T. Chan, and P. Sheng, *Phys. Rev. Lett.*, Vol. 90, 2003.
3. Yanai, A., M. Orenstein, and U. Levy, *Opt. Express*, Vol. 20, 2012.

Bending and Cloaking for a Surface Plasmonic Wave

Hongyi Xu[1, 2], **Su Xu**[3, 4], **Hongsheng Chen**[3, 4], **Handong Sun**[1, 2], **and Baile Zhang**[1, 2]

[1]Division of Physics and Applied Physics, School of Physical and Mathematical Sciences
Nanyang Technological University, Singapore 637371, Singapore
[2]Centre for Disruptive Photonic Technologies
Nanyang Technological University, Singapore 637371, Singapore
[3]Department of Information Science and Electronic Engineering
Zhejiang University, Hangzhou 310027, China
[4]The Electromagnetics Academy at Zhejiang University
Zhejiang University, Hangzhou 310027, China

Abstract— Surface plasmonics, a subject bearing expectations in building next-generation ultra-compact on-chip photonic technologies, is subject to a long-standing issue: the propagation of surface plasmonic polaritons suffers from strong scattering when encountering a sharp corner linking two unparallel surfaces, or an obstacle on a flat surface. This disadvantage shadows the efficient routing and interconnection of surface signals in plasmonic circuits.

In our recent research, we address this issue by adapting the method of nonmagnetic transformation optics. Theoretically and experimentally, the transmission of surface plasmonic polaritons across a sharp bending corner and through an abrupt bump can approach unity in broadband.

The Manipulation of Heat Flow by Affine Transformation Thermodynamics

Hongyi Xu, Handong Sun, and Baile Zhang
Division of Physics and Applied Physics, School of Physical and Mathematical Sciences
Nanyang Technological University, Singapore 637371, Singapore

Abstract— While transformation optics has incubated exciting applications such as invisibility cloaks and light harvesting devices, the method residents yet not limited in fields of electromagnetics. Its extension brings forth an effective way of heat manipulation, when the idea of coordinate transformation marries thermodynamics. Although there have been interesting results regarding this subject, the complex transformation method leads to a harsh requirement of material selection and implementation, whereas low cost material with simple fabrication technique is highly demanding in thermal management. We address this issue by proposing a simple, clear affine transformation method, and the design of metallic thermal cloak is demonstrated as an example. The method offers a direct, effective solution of heat flow manipulation, and finds its application in the thermal management of electronic devices and heat engine.

Session 2P1b
Electromagnetic Theory, Analysis and Simulation in Photonics

Controlling the Dynamics of Quantum Mechanical Processes Using Meta-atoms
Carsten Rockstuhl, R. Filter, S. Muhlig, T. Eichelkraut, S. Fischer, J. C. Goldschmidt, Falk Lederer, 270
Engineering the Response of Fano-resonant Plasmonic Systems for Sensing at the Ultimate Scale
Benjamin Gallinet, Thomas Siegfried, Hans Sigg, Olivier J. F. Martin, ... 271
Real-space vs Fourier-space Homogenization of Metamaterials
Vadim A. Markel, Igor Tsukerman, Xiaoyan Xiong, Lijun Jiang, ... 272
Scattering Problem in s-SNOM: Novel Model for Interaction between Near-field Probe and Inhomogeneous 3D Sample
Alexander A. Govyadinov, F. Huth, Martin Schnell, P. Scott Carney, Rainer Hillenbrand, ... 273
Surface Waves in Electromagnetic Metamaterials and Their Effect on Effective Parameters
Xiaoyan Y. Z. Xiong, Lijun Jiang, Vadim A. Markel, Igor Tsukerman, ... 274
Signal Formation in Scanning Nearfield Optical Microscopy
Ralf Vogelgesang, M. Esslinger, ... 275

Controlling the Dynamics of Quantum Mechanical Processes Using Meta-atoms

C. Rockstuhl[1], **R. Filter**[1], **S. Mühlig**[1], **T. Eichelkraut**[1], **S. Fischer**[2], **J. C. Goldschmidt**[2], **and F. Lederer**[1]

[1]Institute of Condensed Matter Theory and Optics, Abbe Center of Photonics
Friedrich-Schiller-Universität Jena, Germany
[2]Fraunhofer Institute for Solar Energy Systems, Germany

Abstract— Optical meta-atoms are metallic nanostructures with complex geometries that provide a desired resonant scattering response. They are the basic building blocks of metamaterials upon closely packing them. However, already individual structures attracted considerable research interest in the past and their theoretical treatment, analysis and their simulation by solving Maxwell's equations is a prime challenge for nanoscience. Optical nanoantennas, as they are usually dubbed then, promise to provide electromagnetic fields on the nanoscale with predefined spatial and spectral characteristics. A prominent class of applications of optical nanoantennas consists in mediating the interaction of light with other nanoscopic systems. Here, we provide an overview of our latest activities on using optical meta-atoms to mediate the interaction of light with molecular systems described by rate equations. The first subject concerns the control of the dynamics of quantum mechanical systems featuring dipole-forbidden transitions. There, the meta-atoms provide local fields that exhibit a large electric quadrupole moment. The second issue is related to the enhancement of the upconversion process in erbium-doped crystals. There, the optical meta-atom has to show resonances at multiple frequencies which match the transition frequencies of the erbium ion. Unique to our work is a rigorous analysis of the optical properties of the meta-atoms and the treatment of the entire dynamics in the molecular and/or the atomic system on the basis of rate equations. The required nanoantennas resemble meta-atoms which sustain resonances at multiple frequencies and/or resonances which are characterized by higher order multipole moments. Such meta-atoms are currently accessible by both bottom-up or top-down approaches and will find use in future. In conclusion, optical meta-atoms represent a promising approach to access weak processes in a quantum mechanical system. We strongly believe, that as a consequence, in the future this will allow ground breaking applications.

REFERENCES

1. Filter, R., S. Mühlig, T. Eichelkraut, C. Rockstuhl, and F. Lederer, "Controlling the dynamics of quantum mechanical systems sustaining dipole-forbidden transitions via optical nanoantennas," *Phys. Rev. B*, Vol. 86, 035404, 2012.
2. Filter, R., J. Qi, C. Rockstuhl, and F. Lederer, "Circular optical nanoantennas," *Phys. Rev. B*, Vol. 85, 125429, 2012.
3. Mühlig, S., C. Menzel, C. Rockstuhl, and F. Lederer, "Multipole analysis of meta-atoms," *Metamaterials*, Vol. 5, 64, 2011.
4. Fischer, S., F. Hallermann, T. Eichelkraut, G. Von Plessen, K. W. Krämer, D. Biner, H. Steinkemper, M. Hermle, and J. C. Goldschmidt, "Plasmon enhanced upconversion luminescence near gold nanoparticlessimulation and analysis of the interactions," *Opt. Express*, Vol. 20, 271, 2012.
5. Fischer, S., H. Steinkemper, P. Loper, M. Hermle, and J. C. Goldschmidt, "Modeling upconversion of erbium doped microcrystals based on experimentally determined Einstein coefficients," *J. Appl. Phys.*, Vol. 111, 013109, 2012.
6. Dorfmüller, J., R. Vogelgesang, W. Khunsin, C. Rockstuhl, C. Etrich, and K. Kern, "Plasmonic nanowire antennas: Experiment, simulation and theory," *Nano Letters*, Vol. 10, 3596, 2010.

Engineering the Response of Fano-resonant Plasmonic Systems for Sensing at the Ultimate Scale

B. Gallinet[1, 2], **T. Siegfried**[3], **H. Sigg**[3], **and O. J. F. Martin**[2]

[1]CSEM Centre Suisse d'Electronique et de Microtechnique SA
Tramstrasse 99, Muttenz CH-4132, Switzerland
[2]Nanophotonics and Metrology Laboratory
Swiss Federal Institute of Technology Lausanne, Switzerland
[3]Laboratory for Micro- and Nanotechnology, Paul Scherrer Institut
Villigen-PSI CH-5232, Switzerland

Abstract— Over the last five years, there has been a surge of interest for Fano resonances in plasmonic systems. This interest is motivated by the possibility of engineering the spectral response of a plasmonic system using Fano resonances, in particular by creating spectrally narrow features, which should exhibit enhanced sensitivity to their environment for sensing applications. Such engineering requires full mastering of the underlying modal structure that produces the Fano resonance. To address this, we have recently established an *ab initio* theory for Fano resonances in plasmonic nanostructures and metamaterials using the Feschbach formalism [1]. The resulting generalized Fano formula can be used to describe the spectra observed for any Fano-resonant plasmonic system. Furthermore, this formalism provides access to the modal structure associated with the Fano resonance and can be used to tune some of its specific spectral features by adjusting the geometry of the system [2]. With this approach, we are able to identify different electromagnetic coupling regimes in Fano-resonant plasmonic systems, with rather different properties. Some configurations are associated with large energy storage (i.e., strong evanescent near-field), while other configurations exhibit an extremely high sensitivity to geometrical changes and can be used for sensing with unprecedented sensitivity [3]. Using arrays of periodic plasmonic nanostructures fabricated with extreme-UV lithography [4], we verify experimentally these different electromagnetic coupling regimes in Fano-resonant systems and demonstrate optical sensing with visible light with a sensitivity down to a few Angstroms!

REFERENCES

1. Gallinet, B. and O. J. F. Martin, "*Ab initio* theory of Fano resonances in plasmonic nanostructures and metamaterials," *Phys. Rev. B*, Vol. 83, 235427, 2011.
2. Gallinet, B. and O. J. F. Martin, "Influence of electromagnetic interactions on the lineshape of plasmonic Fano resonances," *ACS Nano*, Vol. 5, 8999–9008, 2011.
3. Gallinet, B., T. Siegfried, H. Sigg, P. Nordlander, and O. J. F. Martin, "Plasmonic radiance: Probing structure at the Angstrom scale with visible light," *Nano Lett.*, 2013, in Press.
4. Siegfried, T., Y. Ekinci, H. H. Solak, O. J. F. Martin, and H. Sigg, "Fabrication of sub-10 nm gap arrays over large areas for plasmonic sensors," *Appl. Phys. Lett.*, Vol. 99, 263302, 2011.

Real-space vs Fourier-space Homogenization of Metamaterials

Vadim A. Markel[1], **Igor Tsukerman**[2], **Xiaoyan Xiong**[3], **and Lijun Jiang**[3]

[1]Departments of Radiology and Bioengineering and
the Graduate Group in Applied Math and Computational Science
University of Pennsylvania, Philadelphia, PA 19104, USA
[2]Department of Electrical and Computer Engineering
The University of Akron, OH 44325-3904, USA
[3]The University of Hong Kong, China

Abstract— A large variety of effective medium theories for periodic electromagnetic structures (metamaterials) have emerged over the last decade. Many of these theories strive to extend the classical Fourier-space description of electromagnetic waves from natural materials to metamaterials; other theories operate in real space.

This paper argues, first, that Fourier-space theories have, in the case of metamaterials, very serious limitations. The key drawback of Fourier methods is that they are not suitable in the presence of boundaries (all spatial harmonics become coupled). But without interface boundaries, i.e. for an infinite medium, the permittivity and permeability cannot be separately defined as a matter of principle. Indeed, the **H** and **D** fields can be re-gauged in such a way that Maxwell's equations remain unaffected but the material parameters change. (This re-gauging is sometimes referred to as the "Serdyukov-Fedorov" transformation).

Some Fourier-based methods assume a "forced" excitation of waves by hypothetical plane-wave sources. Such sources are not directly realizable, but two physical setups leading to them are conceivable. First, a small (point-like) physical source inside an infinite material may be mathematically expanded into plane waves. Second, there may be an incident wave coming from the outside, and the field inside the material could again be expanded into plane waves. In both cases, boundaries cannot be effectively handled because all spatial harmonics are coupled. Also in both cases, the waves everywhere in the material outside the source itself are still a superposition of normal eigenmodes, not "forced" modes.

With regard to real-space methods, the fundamental principle is that coarse-grained fields must be defined in such a way that Maxwell's equations and boundary conditions hold. The paper describes methods that satisfy this requirement and discusses methods that do not. A complete analytical study is available in one dimension and is presented in the paper. Illustrative numerical examples for 3D metamaterials are also given.

Scattering Problem in s-SNOM: Novel Model for Interaction between Near-field Probe and Inhomogeneous 3D Sample

A. A. Govyadinov[1], **F. Huth**[1, 2], **M. Schnell**[1], **P. S. Carney**[4], **and R. Hillenbrand**[1, 3]

[1]CIC Nanogune Consolider, Donostia-San Sebastian, Spain
[2]Neaspec GmbH, Martinsried, Germany
[3]IKERBASQUE, Basque Foundation for Science, Bilbao, Spain
[4]ECE Department and Beckman Institute
University of Illinois, Urbana-Champaign, Urbana, USA

Abstract— We present a novel rigorous three-dimensional model that can describe the near-field interaction between the metallic s-SNOM probe and an arbitrary three-dimensional (3D) inhomogeneous sample.

Scattering-type scanning near-field optical microscopy (s-SNOM) is a versatile scanning probe technique for nondestructive optical imaging with wavelength-independent nano-scale spatial resolution [1]. The imaging is typically performed by scanning an AFM tip above the sample surface, subject to an external illumination. The field scattered by the tip depends on the near-field interaction between the probe and the sample, and can thus provide important information about the local sample properties, e.g., its composition.

In particular, s-SNOM has recently demonstrated the ability to perform infrared (IR) spectroscopic identification of minerals in biological materials [2] and polymer particles with 20 nm spatial resolution [3] via direct comparison against standard FTIR databases. While such nano-FTIR technique works well for *on-surface* (2D) studies of a wide range of organic and biological samples, the determination of sample structure *below* its surface and in three dimensions presents both theoretical and experimental challenges.

From the theoretical standpoint the determination of the 3D sample structure from s-SNOM images requires the solution of the near-field inverse scattering problem. This, in turn, necessitates a tractable model which accounts for the near-field interaction between the relatively large metallic tip employed in IR s-SNOM and an inhomogeneous sample. Previous approaches, which treat such tips as point-dipoles, can only provide qualitative description of the depth dependence [4]. Here we present a novel model that is able to describe scattering by the tip-sample system beyond treating the former as a point polarizability. Our model is based on the multiple multipolar expansions of the scattered field and is a generalization of the finite-dipole model [5]. Finally, we describe our progress towards optical near-field tomography.

REFERENCES

1. Taubner, T., R. Hillenbrand, and F. Keilmann, *Appl. Phys. Lett.*, Vol. 85, 5064, 2004.
2. Amarie, S., P. Zaslansky, Y. Kajihira, et al., *Beilstein J. Nanotechnol.*, Vol. 3, 312, 2012.
3. Huth, F., A. A. Govyadinov, S. Amarie, et al., *Nano Letters*, Vol. 12, No. 8, 3973, 2012.
4. Krutokhvostov, R., A. A. Govyadinov, J. M. Stiegler, et al., *Opt. Express*, Vol. 20, No. 1, 593, 2011.
5. Cvitkovic, A., N. Ocelic, and R. Hillenbrand, *Opt. Express*, Vol. 15, No. 14, 8550, 2007.

Surface Waves in Electromagnetic Metamaterials and Their Effect on Effective Parameters

Xiaoyan Y. Z. Xiong[1], **Lijun Jiang**[1], **Vadim A. Markel**[2], **and Igor Tsukerman**[3]

[1]The University of Hong Kong, China
[2]Departments of Radiology and Bioengineering and
the Graduate Group in Applied Math and Computational Science
University of Pennsylvania, Philadelphia, PA 19104, USA
[3]Department of Electrical and Computer Engineering
The University of Akron, OH 44325-3904, USA

Abstract— Many applications of periodic electromagnetic composites (metamaterials) involve a metamaterial slab with cubic elementary cells. It is important to understand how the characteristics of such a slab depend on the number of lattice layers in it. Physical and numerical experiments published in the literature indicate that the material can be accurately characterized by an effective bulk parameter tensor even if the number of layers is surprisingly small (five or even less). These findings, however, are largely heuristic, and the purpose of this paper is to provide a solid analytical and numerical foundation for them.

We argue that the dependence of effective medium parameters on the number of layers is due to the surface wave (surface plasmon polariton, or SPP). In homogeneous materials, SPPs can be excited only by an evanescent incident wave, i.e., from the near-field, or from a medium with a higher refractive index (Kretschmann geometry). However, in periodically modulated media, SPPs can be exited by both propagating and evanescent incident waves and are, therefore, unavoidable. The paper demonstrates that the role of surface waves diminishes rapidly as the vacuum wavelength increases beyond a certain threshold.

The effective parameters of the periodic structure are determined from the recently developed non-asymptotic homogenization theory applicable to all cell sizes, not necessarily vanishingly small relative to the vacuum wavelength. The main underlying principle of the new theory is that the coarse-grained fields must satisfy Maxwell's equations and interface boundary conditions. Consequently, $\mathbf{E}$ and $\mathbf{H}$ are sought as *curl-conforming* interpolants of the respective rapidly varying fields $\mathbf{e}$ and $\mathbf{b}$ — i.e., as interpolants preserving the tangential continuity of fields across all interfaces. At the same time, $\mathbf{B}$ and $\mathbf{D}$ are sought as *div-conforming* interpolants preserving the normal continuity across all interfaces.

The actual microscopic fields in the structure are approximated by suitable basis functions (b.f.) For lattice cells in the bulk, such basis functions could be chosen as Bloch waves traveling in different directions. In the present paper, however, the basis is defined differently — by illuminating a metamaterial sample with incident waves at varying angles. This allows us to construct a basis set not only in the bulk but also at the surface, where traditional Bloch modes are not applicable. This approach also has a computational advantage: transmission and reflection of a given incident wave is less difficult to calculate than eigenmodes.

Illustrative numerical examples for three-dimensional periodic structures are presented.

Signal Formation in Scanning Nearfield Optical Microscopy

R. Vogelgesang[1] **and M. Esslinger**[2]

[1]University of Oldenburg, Germany
[2]Max Planck Institute for Solid State Science, Germany

Abstract— Nearfield optical microscopy renders optical images with deep-subwavelength resolution. However, the analysis of recorded signals still suffers from considerable uncertainty about the exact nature of the image forming mechanisms. Inevitably, a probing tip has to penetrate the nearfield zone of the sample. In the general case it is far from obvious, to what degree its interaction with the sample distorts the resulting images.

We develop a fully general framework based on the reciprocity theoretical formulation of Maxwell theory. This approach has been used in the past by Carminati, Greffet, et al. who have formulated a description of the measurable signals in the form of integrals over an infinite plane separating the probe and sample. Using the volume equivalent representation and a convenient angular spectrum description of the vectorial Green function for the Helmholtz operator, we re-cast the main relation into an integral over the volume of the perturbing probe tip volume. This allows for an intuitive interpretation of measured signals.

Our formalism is applicable to aperture-type probes as well as apertureless probes. As we show with several examples, it is able to predict recorded signals for various experimentally relevant situations. In particular, for point-like dipolar probe tips, the analysis simplifies dramatically. If a Born-series description of the sample-probe interaction may be used, our results show that the main recordable signal is directly proportional to the local field of the excited sample — at the location of the dipole probe. This has been an empirically established rule for a number of years, already, which is now set on a more formal basis.

Session 2P2a
Biological Effects and Medical Applications of Electromagnetic Energy 2

Effects of Tuning Condition, Head Size and Position on the SAR of a MRI Dual-row Transmit Array at 400 MHz
Mikhail Kozlov, Robert Turner, ... 278
Active Implantable Medical Devices and Electromagnetic Compatibility
Veronica Ivans, Chung-Kwang Chou, ... 280
Interesting Issues of Mobile Phones and Base Stations in Taiwan
Ji-Shing Lin, ... 281
Impact of Planning Based Restrictions on Operation of Mobile Networks
Jack Rowley, ... 282
Occupational Over-exposure to RF Radiation in TV Tower
Maila Hietanen, ... 283
Update of IEEE C95.1 Exposure Standard Revision
Chung-Kwang Chou, J. Patrick Reilly, R. Kavet, Bertram J. Klauenberg, Marvin C. Ziskin, Art Thansandote, Thanh Dovan, R. A. Tell, Ken Gettman, Ralf Bodemann, R. C. Petersen, ... 284

Effects of Tuning Condition, Head Size and Position on the SAR of a MRI Dual-row Transmit Array at 400 MHz

M. Kozlov and R. Turner
Max Planck Institute for Human Cognitive and Brain Sciences, Leipzig, Germany

Abstract—

Purpose: It is becoming well understood that the performance of RF transmit coils used in MRI benefit from dual-row array design. Safety assessment is significantly complicated for a dual-row array because matching dual-row array conditions in numerical and actual domains is very complicated. In typical RF coil simulations SAR can be calculated for several excitation modes and even complex pTX pulse but on base of assumption of ideally decoupled array elements [1] or in best case for a single array tuning condition with comparison of magnitude of complex array circuit level measures: element matching and adjacent element coupling. Influence these measure phases on SAR has generally been neglected. In our previous works we developed simulation work-flow closely corresponds to fabrication steps of an array, but results reported were obtained for circuit level optimization reached their global minima [2].

Our numerical simulation goals were: a) to investigate effect of different tuning condition on dual-row array SAR; b) to explore the sensitivity of SAR both to the head size, and to position of the head inside an array, which would be used without adjustment of array variable components for each subject.

Method: We numerically investigate already fabricated 9.4 T dual row array [3] using RF circuit and 3-D EM co-simulation. The realistic 3-D EM model of the arrays included all coil construction details for the resonance elements, simulated with precise dimensions and material electrical properties. The loads utilized were the multi-tissue Ansoft human body models, cut in the middle of the torso, with different scaling factor: head #1 with scaling $X = 0.9$, $Y = 0.9$, $Z = 0.9$ simulating an average head, head #2 with scaling $X = 0.85$, $Y = 0.85$, $Z = 0.9$ simulating a small head, and head #3 with scaling $X = 0.95$, $Y = 0.975$, $Z = 0.9$ simulating a large head. We analyzed: geometry case #1 — head placed symmetrically in transverse plane and geometry case #2 — head shifted from case #1 position for 22 mm downwards to provide space for mirror of visual stimulus system. In each case four axial positions of the human models were defined with 5 mm step, and in case #1 the head #1 was also shifted to both sideward by 5 and 10 mm. In circuit domain the inductors of the decoupling networks were placed in series with distributed capacitors; Q factor of all capacitors was equal to 200; all inductor were simulate with actual inductor size and copper wire diameter; array decoupling pin diode resistance was 0.2 Ohm.

To obtain values of array variable components — decoupling inductors, tune and match capacitors — we used two circuit-level array optimization strategies: 1) optimization based on S parameters, mimicked the commonly used optimization during fabrication, where the reflection coefficient ($\mathbf{S}_{xx}$) for each individual array element and the coupling coefficient ($\mathbf{S}_{xy}$) for the each decoupled pair of array elements were minimized at the array operating frequency ($\mathbf{F_{MRI}}$); 2) mode optimization, minimized an error or cost function (**EF**), which consisted of individually weighted sums derived from **S** parameter matrix and power reflected by array rows for given set of excitation modes [2].

All optimizations were independently performed in two steps: 30 000 random tries, followed by "Quasi-Newton" method until no further improvement was possible. This resulted in a set of eight values for variable components and a correspondent set of E and H fields (on an equidistant 1 mm mesh) for each independently excited radiative element. The fields were exported from 3-D EM domain to files in Matlab format. The peak SAR averaged over 10 gram ($\mathbf{SAR}_{10\,\mathrm{g}}$) was calculated for CP and some other excitation modes by an in-house Matlab procedure, which was developed in consistence with IEEE 1528.1 standard and which reliability was proved during IEEE TC 34 interlab comparison study [4]. For each 3D EM domain simulation total amount of calculated $\mathbf{SAR}_{10\,\mathrm{g}}$ values was equal 96 (to number of head positions (4) multiply by number of circuit level strategies (2) multiply by number of excitation modes (12)).

Results and Discussion: For circuit level optimization strategy #1 and geometry case #1 magnitude of the $\mathbf{S}_{xx}$ (< -40 dB) and $\mathbf{S}_{xy}$ (< -18 dB) were similar for each axial position of head #1 but mutual inductor coupling coefficient $\mathbf{K}_{di}$ for decoupling inductors and $\mathbf{S}_{xy}$ phases were significantly different between position #3 and other positions. When variable component

values were used from another head #1 position the $\mathbf{S}_{xx}$ magnitude slightly increased (remaining below $-20\,\mathrm{dB}$) and the $\mathbf{S}_{xy}$ slightly decreased. Therefore in all configurations array looked as properly tuned. Variation of the $\mathbf{S}_{xx}$ and $\mathbf{S}_{xy}$ for head #2 and head #3 simulations was more pronounced but still in all configurations array looked near to be reasonable (only a couple of $\mathbf{S}_{xx}$ were about $-16\,\mathrm{dB}$, others $\mathbf{S}_{xx} < -20\,\mathrm{dB}$ and all $\mathbf{S}_{xy} < -18\,\mathrm{dB}$) tuned.

For circuit level optimization strategy #1 and geometry case #2 all four circuit level optimization resulted in similar magnitude values of the $\mathbf{S}_{xx}$ and $\mathbf{S}_{xy}$. The $\mathbf{S}_{xx}$ and $\mathbf{S}_{xy}$ behaviour for different head positions and head sizes was similar to case #1. For geometry case #2 and given excitation mode $\mathbf{SAR}_{10\,\mathrm{g}}$ variations were less than $\pm 5\%$ for each optimization strategy and less than $\pm 10\%$ when results for both optimization strategies were taken into account.

If results for head position #3 tuning of geometry case #1 would be excluded from database $\mathbf{SAR}_{10\,\mathrm{g}}$ variations for both geometry cases would be very similar. But if these results were taking into account $\mathbf{SAR}_{10\,\mathrm{g}}$ variations increased up to 30% for some excitation modes. When head position #3 tuning was applied i) significant variation of current through radiative elements was observed; ii) the constructive E-field interference had a different pattern; iii) finally, value and spatial location of peak $\mathbf{SAR}_{10\,\mathrm{g}}$ significantly changed.

To perform sensitivity analysis circuit level optimization strategy #1 was applied 100 times for geometry case #1. We obtained solutions where values of $\mathbf{K}_{di}$ were grouped to two values with small dispersion: the first value was closed to value of the original optimization for head in head positions #1, #2 and #4 and the second value were closed to value of the original optimization of head positions #3. Probability to obtain the first value was 83%.

Conclusion: A precise match of dual row array conditions in numerical and actual domains is vital for reliable SAR assessment. Tuning condition may provide a significant impact on $\mathbf{SAR}_{10\,\mathrm{g}}$ of a dual row array. When array diameter is relative large and variation of head position resulted in non-significant variations of array circuit level measures, $\mathbf{SAR}_{10\,\mathrm{g}}$ differences are expected to be relative small (less than 20%) and can be easily covered by array safety margin. However it is impossible to provide a general conclusion that a variation of an array property provides negligible influence on $\mathbf{SAR}_{10\,\mathrm{g}}$ for any dual row array. Given dual row array should be comprehensively and reliable investigated (including sensitivity analysis) for defining scanner SAR assessment parameters. If the precise match of conditions or sensitivity analysis cannot be obtained safety margin should be increased considerably.

REFERENCES

1. Guerin, B., M. Gebhardt, E. Adalsteinsson, and L. Wald, *Proceedings of the 20th ISMRM*, 2215, 2012.
2. Kozlov, M. and R. Turner, *Proceedings of 34th IEEE EMBS*, 1089–1092, 2012,
3. Shajan, G., J. Hoffmann, K. Scheffler, and R. Pohmann, *Proceedings of the 20th ISMRM*, 308, 2012.
4. Monebhurrun, V., Y. Braux, H. Devos, M. Kozlov, W. Simon, and T. Wittig, *Proceedings of the BEMS2012*, 315–317, 2012.

Active Implantable Medical Devices and Electromagnetic Compatibility

Veronica Ivans[1] **and Chung-Kwang Chou**[2]

[1]IMDS, LLC, USA
[2]Motorola Solutions, Inc., USA

Abstract— This presentation gives an overview of active implantable medical devices (AIMD), which include implantable pacemakers and ICDs (implantable cardioverter defibrillators), requirements in a newly published international standard ISO 14117 (2012) [1] addressing safety in the presence of ElectroMagnetic Fields (EMF).

During recent years there has been a rapid proliferation of emitters across the entire electromagnetic frequency spectrum. Majorities of these emitters are intended to broadcast radiofrequency energy for communication or other applications. On the other hand, there has been a demand for smaller size AIMDs, and more advanced systems (distant telemetry communication, more leads, etc.) with more sophisticated features that would allow physicians to provide, and their patients to receive, better health care and quality of life. The above factors combined have raised the visibility to potential interference from EMF and their effects on patient safety.

As a result, the International Standard Organization (ISO)/International Electrotechnical Commission (IEC) Joint Working Group 1 has developed an international standard ISO 14117 comprising immunity requirements for AIMDs in these environments to minimize interference from EMF emitters. In general, AIMDs shall not cause any harm because of susceptibility to electrical influences due to external EMF, whether through malfunction of the device, damage to the device, heating of the device, or by causing local increase of induced electrical current density within the patient. The standard defines implantable cardiovascular systems, and describes basic operation of pacemakers and ICDs. EMF sources in non controlled and controlled and medical environments are identified. Test procedures for various frequency ranges and environments of the AIMDs are specified in the ISO 14117 standard. Main elements of the standard will be presented in the meeting. For increased safety of the patients, it is highly recommended the AIMDs comply with the standard to minimize electromagnetic interference from various EMF sources.

REFERENCES

1. ISO 14117, "Active implantable medical devices — Electromagnetic compatibility — EMC test protocols for implantable cardiac pacemakers, implantable cardioverter defibrillators and cardiac resynchronization devices," July 2012, http://www.iso.org/iso/catalogue_detail.htm?csnumber=54472.

Interesting Issues of Mobile Phones and Base Stations in Taiwan

Ji-Shing Lin
Office of Board of S&T, The Executive Yuan (Cabinet), Taiwan

Abstract— There are 5 telecom operators in Taiwan, a small island of 36,188 km^2, crammed with thousands of base stations spreading around the country. Fueled by local activists and the media that enjoy cherry-picking foreign news or researches fitting their EMF scare, Taiwan has been much under the siege of mis-information that both mobile-phone sets and base stations are endangering people's health, especially, causing cancers which is a serious driving force for mobilizing peoples' protests.

There have been several studies of their health effects, provided by local regulatory authorities and operators. For example, the impact on infants due to mothers' using mobile phones. Most of these show that exposure to telecom EMF is not causing health problems.

Another related issue is electromagnetic hypersensitivity (EHS), which, according to a local study, seems to be quite prevalent in Taiwan, with 13.5% of Taiwanese claiming suffering from it. At least one provocative study has been done on this issue, and the result indicates that the symptoms are not associated with telecom EMF.

Here, an overview of the prevalence of mobile phone uses, base station set-up, media coverage of health effects, activist "propaganda," and responses of regulatory authorities is presented. Then, related research work on health concerns, including EHS, follows.

Impact of Planning Based Restrictions on Operation of Mobile Networks

Jack Rowley
GSM Association, 7th Floor, 5 New Street Square, London EC4A 3BF, UK

Abstract— Around the world mobile networks continue to be expanded in response to growth in subscribers and increasing demands for data services. In some countries there is concern about possible health risks from the radio signals used for mobile communications and national or local policy makers have responded with a range of measures including restrictions related to siting of antennas near schools. In Australia the radio frequency (RF) exposure limits are consistent with international recommendations and there are no mandatory planning exclusion zone policies. Therefore, we studied the hypothetical impact upon existing networks of radio base stations in the Melbourne metropolitan area and the potential for such a policy (if applied) to negatively impact the future enhancement of these networks.We used publicly available geographical information system data on the location of community facilities and the location of base stations to construct a series of overlays to allow the testing of the impact of different size exclusion zones on the siting of existing base stations. In this paper we present the results of the analysis of the impact of a hypothetical 500 m exclusion zone. The main findings of the analysis include that across the Melbourne metropolitan area, 54.1% of all existing radio base stations would be impacted if such an exclusion zone was applied around community facilities (schools,pre-school and medical facilities). The impact increases in dense urban areas and for larger radius zones. A reason given for adopting such policies is to reduce the RF exposure in schools and hence the potential for a health risk to the students. However, measurements at schools in the US with and without monopoles for mobile communication antennas show that geometric mean RF exposures in either group of schools are generally more than 100,000 times below the US federal RF exposure limits. This study shows that planning based exclusions would significantly impact the ability to operate mobile networks and consequently the ability of subscribers to obtain services. Importantly, such a policy would not significantly reduce the RF exposure on school properties.

Occupational Over-exposure to RF Radiation in TV Tower

Maila Hietanen
Finnish Institute of Occupational Health, Finland

Abstract— There are only few reports of the effects of acute exposure to radiofrequency exposures from high power transmitting antennas, as it is a commonly adopted rule that it is safe for staff staff to climb through radio and television towers only when the antennas are transmitting with reduced power. This Case Report describes an event in which a worker was accidentally exposed to high levels of radiofrequency radiation (85–100 MHz) while working on transmission mast. The mast worker experienced various adverse health effects, such as headache, pain in chest and stomach, diarrhea, sweating, changes in blood pressure and heart rate, and other similar somatic symptoms. A measurement survey was carried out after the accident, indicating that the average power density in front of the antenna, at the approximate site of the worker, was 36 W/m^2, and the corresponding peak reading was 87 W/m^2. Hence, the exposure level was significantly higher than the occupational reference guideline (10 W/m^2) given by the International Commission on Non-Ionizing Radiation Protection [1].

RF over-exposure at 100 MHz is not immediately detectable by the human body which makes difficult for workers to avoid high fields without an alarming meter. In order to give advice to proper health risk management at typical work situations, a project on safe working on transmission towers with transmitting antennas in liaison with the telecommunications industry will be undertaken in Finland.

REFERENCES

1. International Commission on Non-Ionizing Radiation Protection (ICNIRP), "Guidelines for limiting exposure to time-varying electric, magnetic, and electromagnetic fields (up to 300 GHz)," *Health Phys.*, 74, 494–522, 1998.

Update of IEEE C95.1 Exposure Standard Revision

C-K. Chou, J. P. Reilly, R. Kavet, B. J. Klauenberg, M. Ziskin, A. Thansandote, T. Dovan, R. A. Tell, K. Gettman, R. Bodemann, and R. C. Petersen
IEEE International Committee on Electromagnetic Safety, TC95, Piscataway, NJ, USA

Abstract— The IEEE International Committee on Electromagnetic Safety (ICES) develops standards for the safe use of electromagnetic energy in the range of 0 Hz to 300 GHz. Presently, two IEEE exposure standards, C95.6-2002 [1] (0–3 kHz) and C95.1-2005 [2] (3 kHz to 300 GHz) specify levels to protect against established adverse health effects in humans caused by exposure to electric, magnetic and electromagnetic fields, and the associated induced currents, and contact currents and voltages. The standards draw upon comprehensive reviews and evaluations of the scientific literature including studies conducted under many different exposure conditions, some using levels of radio frequency energy too low to produce significant (or measureable) heating in animal or *in vitro* test systems (sometimes called "non-thermal" exposures).

This presentation is a report of the Editorial Working Group (EWG) on the progress of combining the two IEEE exposure standards into a single standard C95.1-201X "Standard for Safety Levels with Respect to Human Exposure to Electric, Magnetic and Electromagnetic Fields, 0 Hz to 300 GHz." Also, under a Technical Cooperation Agreement between NATO and IEEE, ICES TC95 is developing a "Standard for the Evaluation and Control of Personnel Exposure to Electric, Magnetic and Electromagnetic Fields, 0 Hz to 300 GHz" for consideration by the NATO member countries as a replacement for NATO STANAG 2345 [3].

Defining terminology associated with different interaction mechanisms above and below 100 kHz represents one of the challenges in combining the standards. This is important since appropriate safety factors must be defined that result in adequate safety margins for protection against hazards and adverse health effects. Several terms have been changed to address these differences and to make the meaning of each term more obvious. Thus far, 15 EWG meetings and 6 TC-95 Subcommittee 3 and 4 combined meetings have been held to discuss details and approve these changes. Presently, only the exposure limits for contact current at radio frequencies have been changed. A special exposure zone with relaxed limits restricted to selected experts has been established for the NATO standard to enable multinational interoperability.

Conclusion: Both C95.6 and C95.1 standards protect against established adverse health effects and include safety margins for human exposure. Work to combine C95.6-2002 and C95.1-2005 into a single standard for frequencies between 0 Hz and 300 GHz is ongoing. ICES continues to critically review the relevant scientific information while updating its standards. ICES considers harmonization with ICNIRP [4] and the proposed European Union Directive important, with an ultimate goal of internationally-harmonized EMF exposure criteria.

REFERENCES

1. C95.6-2002, "IEEE standard for safety levels with respect to human exposure to electromagnetic fields, 0–3 kHz," The Institute of Electrical and Electronics Engineers, Inc. 3 Park Avenue, New York, NY 10016-5997, USA, 2002.
2. C95.1-2005, "IEEE standard for safety levels with respect to human exposure to radio frequency electromagnetic fields, 3 kHz to 300 GHz," The Institute of Electrical and Electronics Engineers, Inc. 3 Park Avenue, New York, NY 10016-5997, USA, 2005.
3. STANAG 2345 MED, "Evaluation and control of personnel exposure to radio frequency fields −3 kHz to 300 GHz," *NATO Standardization Agency Standardization Agreement (STANAG)*, Edition 3, Feb. 13, 2003, http://www.everyspec.com/NATO/NATO-STANAG/STANAG_2345_3RD_ED_14299/.
4. ICNIRP, "Guidelines for limiting exposure to time-varying electric, magnetic, and electromagnetic fields (up to 300 GHz)," *Health Physics*, Vol. 74, No. 40, 494–522, 1998.

Session 2P2b
Medical Electromagnetics, Medical Imaging, MRI

A Review on Electrical Property Retrieval in a Noninvasive Way
Shao Ying Huang, Shaohui Foong, ... 286
Quantification Error in Local Maxwell Tomography (LMT) Introduced by $\boldsymbol{B_1}$ Map Inaccuracy
Longfei Hou, Shao Ying Huang, Shaohui Foong, Jiu Hui Wu, ... 287
A Economical Surface Coil Design without Lumped Elements for MRI Application
Siya Mi, Yee Hui Lee, ... 288
Resonant RF Biosensors for Immature Cells Identification
Ling Yan Zhang, Aurelie Lacroix, Claire Dalmay, Alaeddine Landoulsi, Annie Bessaudou, Christophe Bounaix Morand Du Puch, Christophe Lautrette, Serge Battu, Fabrice Lalloué, Marie-Odile Jauberteau, Pierre Blondy, Arnaud Pothier, ... 289
Feasibility of Microwave Dental Imaging
Chun-Sen Wu, Hsien-Nan Kuo, George G. Cheng, Yong Zhu, Jan Alexander Grzesik, ... 291
Microwave Medical Imaging Techniques
George G. Cheng, Yong Zhu, Jan Alexander Grzesik, ... 292
Three Dimensional Radar Imaging by Using Spherical Near Field Range
Dau-Chyrh Chang, Chih-Hung Lee, Tsung-Yuan Yang, ... 293

A Review on Electrical Property Retrieval in a Noninvasive Way

Shao Ying Huang[1, 2] **and Shaohui Foong**[2]

[1]Massachusetts Institute of Technology, USA
[2]Singapore University of Technology and Design, Singapore

Abstract— Knowledge of the spatial distribution of electrical properties, namely dielectric constant and conductivity, is valuable to various diagnostic and therapeutic technologies, for example, transcranial magnetic stimulation (TMS) or *in vivo* specific absorption rate (SAR) mapping in high-field magnetic resonance imaging (MRI). It could probably provide information on microstructure and function of tissues and materials which would be complementary to that provided by traditional imaging modalities. Recently, MRI has become a new tool for noninvasive electrical property retrieval without the assistance of additional sensing equipment. Mainly there are two categories, namely electric properties tomography (EPT) [1, 2] based on the integration version of the Maxwell's equations, and local Maxwell tomography (LMT) [3] based on the Maxwell's equations. EPT requires the absolute phase of and it works based on the assumption that $\varphi^+ = (\varphi^+ + \varphi^-)/2$ at 3 T or below. The assumption is referred as half phase assumption in this content. LMT has no assumptions on the phase and it works at arbitrary field strength. In the coming International Society for Magnetic Resonance in Medicine (ISMRM) annual meeting and exhibition in April 2013, we propose a new method called Local Electrical Property Retrieval (LEPR) to retrieve the electrical properties of tissues at 3 T or below.

In this paper, we present a review on the technical details for the aforementioned different methods that retrieve electrical properties in a noninvasive ways, from an electromagnetic point of view. The methods are implemented, commented, and compared. SEMCAD X based on FDTD is used for full-wave simulations [4]. This study may provide insights to the future study on this topic.

REFERENCES

1. Katscher, U., et al., *IEEE Trans. Med. Imaging*, Vol. 28, 1365, 2009.
2. Voigt, T., *Magn. Reson. in Med.*, Vol. 66, 456, 2011.
3. Sodickson, D. K., *ISMRM*, 387, 2012.
4. SEMCAD X by Speag, www.speag.com.

Quantification Error in Local Maxwell Tomography (LMT) Introduced by B_1 Map Inaccuracy

Longfei Hou[1,3], **Shao Ying Huang**[2,3], **Shaohui Foong**[3], **and Jiuhui Wu**[1]

[1]Xi'an Jiaotong University, Xi'an, China
[2]Massachusetts Institute of Technology, USA
[3]Singapore University of Technology and Design, Singapore

Abstract— Maps of the spatial distribution of conductivity, σ, or dielectric constant, ε_r are valuable to various diagnostic and therapeutic technologies such as *in vivo* specific absorption rate (SAR) mapping in high-field magnetic resonance imaging (MRI). There are mainly two existing approaches that have been proposed for the estimation of ε_r and σ based on MRI; electric properties tomography (EPT) [1, 2] based on the integral version of the Maxwell's equations, and local Maxwell tomography (LMT) [3]. EPT requires the absolute phase of B_1^+ and it works based the assumption that $\varphi^+/2 = \varphi^-/2$ which holds at 3 T or below. LMT has no assumptions on the phase and it works at arbitrary field strength.

In this work, we evaluate the accuracy of the retrieved ε_r and σ obtained from LMT when B_1^+ and B_1^- are noisy. Three kinds of effects are reported. They are the effects introduced by the effect of the tissue types, that of Larmor frequencies, f's, and the effect of the number of excitations and B_1 maps. A spherical phantom in Fig. 1 with a radius of 0.1 m is used for the study. The excitation sources are planes waves ($\widehat{k}_i$ in Fig. 1). SEMCAD X based on FDTD is used for full-wave simulations [5].

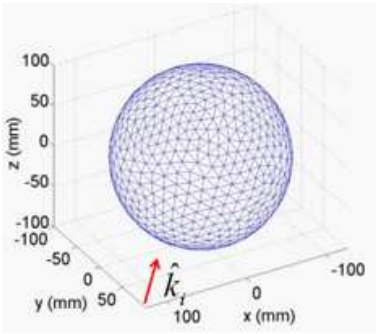

Figure 1: The spherical phantom.

REFERENCES

1. Katscher, U., et al., *IEEE Trans. Med. Imaging*, Vol. 28, No. 1365, 1.3, 2009.
2. Voigt, T., *Magn. Reson. in Med.*, Vol. 66, No. 456, 2011.
3. Sodickson, D. K., *ISMRM*, 387, 2012.
4. http://niremf.ifac.cnr.it/tissprop.
5. SEMCAD X by Speag, www.speag.com.

A Economical Surface Coil Design without Lumped Elements for MRI Application

Siya Mi and Yee Hui Lee
School of Electrical and Electronic Engineering, Nanyang Technological University, Singapore

Abstract— Radio frequency (RF) coils are used to receive signals in magnetic resonance imaging (MRI) scanners, among which surface coils have been widely used because of their narrow bandwidth and high signal to noise ratio (SNR). In a surface coil, one of the most important components is the capacitor. Usually,at least one capacitor is organized in parallel at the input port, which are used to tune the desired resonant frequency. However, the capacitor is made of lumped elements, so its hard to fabricate to adjust the capacity in surface coil. This factor leads the surface coils to be at a high price. If the cost of the coils is reduced, then the MRI scanners will be affordable by more clinics and hospitals.

In this paper, we design a economical surface coil without the tuning capacitor. Specifically, we use a couple of interdigital microstrip lines instead of the lumped capacitor in the RF coil. In the interdigital microstrip lines, the stretched strips and slots are used to tune the gap between neighboring lines, which control the capacitance of the equivalent RLC circuit. By adjusting the microstrip length and insert depth of the stretched strip, the capacitance can be adjusted and the resonant frequency can be tuned over a wide range. This design allows us to tune the resonant frequency without changing the coil size, which reduces the fabrication expense of surface coisl. Our simulation shows this design of RF coil achieves the comparable performance as the traditional RF coil with lumped elements, which shows its potential utility in (MRI) scanners.

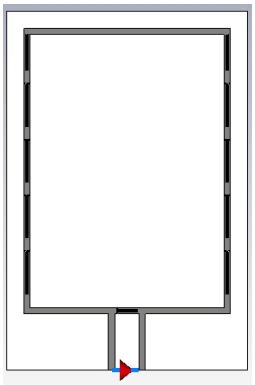

Figure 1: The surface coil without lumped capacitor.

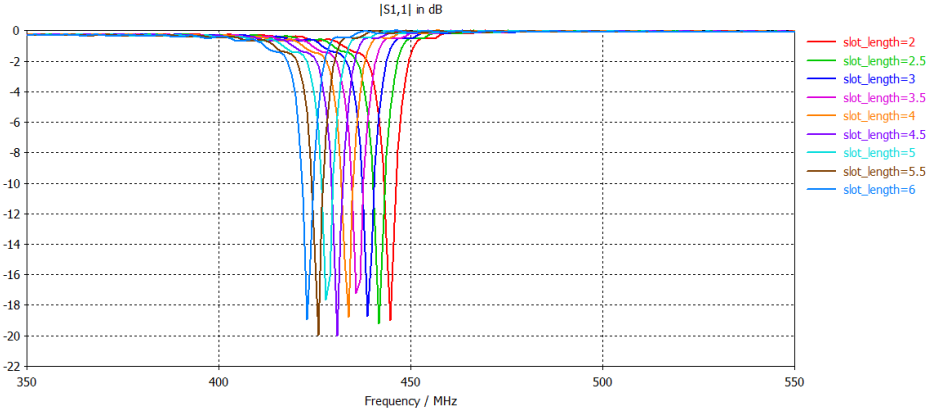

Figure 2: The scattering parameter S_{11} for various slot length (mm).

Resonant RF Biosensors for Immature Cells Identification

Ling Yan Zhang[1], **Aurelie Lacroix**[2], **Claire Dalmay**[1], **Alaeddine Landoulsi**[1], **Annie Bessaudou**[1], **Christophe Bounaix Morand du Puch**[3], **Christophe Lautrette**[3], **Serge Battu**[2], **Fabrice Lalloué**[2], **Marie-Odile Jauberteau**[2], **Pierre Blondy**[1], **and Arnaud Pothier**[1]

[1]XLIM institute UMR 7252 CNRS, University of Limoges, Limoges 87060, France
[2]Homéostasie Cellulaire et Pathologies — EA 3842, University of Limoges, Limoges 87025, France
[3]Oncomedics, 1 Avenue d'Ester, Limoges 87069, France

Abstract— Since biological cell membranes are transparent at RF or microwave frequencies, such high frequency signals can penetrate inside cells and interact with their intracellular content. There is so a high interest to use microwave to perform biological cell analysis. Hence, in this paper, we will show that such frequencies can be especially used to identify the cell maturity state (from differentiated cell up to stem cell). Indeed, we have used surface micro-machined biosensors derived from RF resonators (Fig. 1) to probe individually the content of cells and measure their intrinsic dielectric properties. The high sensitivity detection achieved thanks to these detectors allows performing analysis without requiring any cell labeling; only measuring intrinsic physical parameters of cells under analysis. Especially, this work is focused on cells coming from a glioblastoma cell line known for their cancerous aggressiveness and high proliferation capabilities. Interestingly, by changing culture conditions of such cells, in terms of medium and oxygen rate, we have selected different cells pools with an increasing immaturity level looking for reaching a high stem cell concentration. These different pools have been specifically analyzed with several of our biosensors in order to measure their dielectric permittivity characteristics depending on several frequencies. Thanks to these collected data, we have established a representative electromagnetic signature for each of the different cells pools we obtained. Hence, as illustrated in Fig. 2, we have extracted from these pools significant electromagnetic signature differences that can be relied to the increasing cell immature/undifferentiated level. Indeed, as shown on Fig. 2, we can observe that cells coming from well differentiated cell pool "NN" seem to present an intrinsic permittivity following a dispersive behavior versus frequency (linked to their water content) with much lower values that ones coming from "DH" pool. This "DH" pool is in fact made up cells with the higher immaturity level we have successfully grown and selected including a large amount of cancerous stem cells.

In the final paper, more details about the cell culture selection and the used measurement methodology will be discussed. In addition, we will further comment biological analysis performed to characterize these cell pools and evaluate their immaturity level with biological criteria.

To conclude this abstract, we wish to underline that looking-introduced results; this sensing method appears very promising especially to develop new powerful tools for label free cancerous

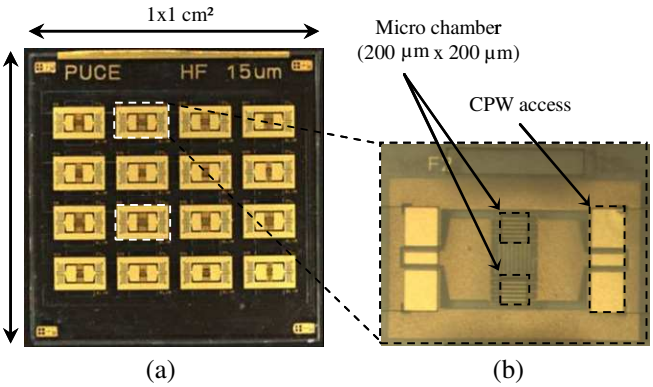

Figure 1: (a) Top-view of biosensor chip micro-machined on fused silica substrate and (b) individual biosensor photograph.

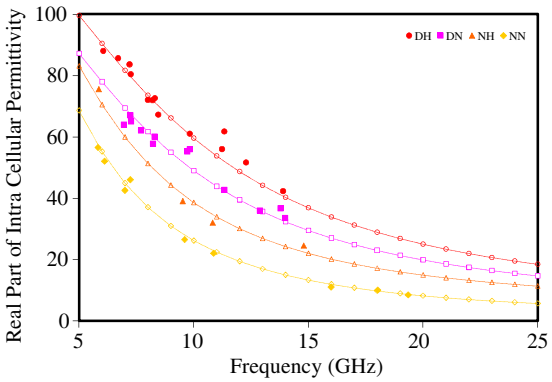

Figure 2: Example of dielectric relative permittivity signatures extracted from measurements achieved on glioblastoma cells with an increased immaturity level and their associated Cole-Cole modeling.

stem cell discrimination and sorting. Indeed cancerous stem cells, which are nowadays still difficult to fully discriminate with conventional biological technics, are currently focusing an increasing attention in the clinical research community since they might be the cause of a majority of cancer recurrences that too often follow chemotherapy or radiotherapy treatments.

REFERENCES

1. Dalmay, C., et al., "Ultra sensitive biosensor based on impedance spectroscopy at microwave frequencies for single cell analysis," *Sensors and Actuators, A: Physical*, Vol. 162, No. 2, 189–197, 2010.
2. Dalmay, C., et al., "Microwave sensors for stem cell identification and discrimination," *IEEE MTT-S International Microwave Symposium Digest*, 620–623, 2010.
3. Zhang, L., et al., "Microwave biosensors for identifying cancer cell aggresiveness grade," *IEEE MTT-S International Microwave Symposium Digest*, Artical No. 6259539, 2012.

Feasibility of Microwave Dental Imaging

Chun-Sen Wu[1], **Hsien-Nan Kuo**[1], **George Cheng**[2], **Yong Zhu**[2], **and Jan Grzesik**[2]

[1]Metal Industries Research & Development Centre, Taiwan
[2]Allwave Corporation, USA

Abstract— In this presentation we seek to advocate the use of microwave (**RF**) reflection imaging as an adjunct and, ultimately, a robust dental diagnosis competitor to the prevailing technique of computerized tomography (**CT**) with x-rays as probe. Since x-rays inevitably ionize intervening tissue along their path, their use, in no matter how small an amount, must always be viewed as a potential carcinogenic trigger. Penetrating microwaves, by contrast, are totally exempt from posing any such threat, and are thus *a priori* superior from the standpoint of safety.

We have evolved both measurement procedures and computer codes centered around our unique Field Mapping Algorithm (**FMA**), which provides full three-dimensional structural imaging based upon either transmitted or reflected (**T/R**) microwave fields. In particular, our **FMA**, utilizing a **T/R** tangential microwave data capture along some suitable surface (preferentially planar, cylindrical, or spherical), permits a full structural reconstruction of the material traversed. Such reconstruction is achieved essentially in real time, fully apace with the imaging procedure under way, and is altogether unburdened by the delays, spatial imprecision, and massive **CPU** demands accompanying optimization schemes, schemes, indeed, which are altogether foreign to the makeup of our **FMA**, but otherwise central to most other microwave imaging initiatives.

In the proposed context of dental diagnosis, an **FMA** embodiment would minimize instrument intrusion into patient tissue. Both transmit source and receive array would be placed in proximity to, but entirely exterior to the patient's cheek. There would be no need for an internal (and most uncomfortable) image capture, be it on film or direct digital sensor, or else the massive x-ray dosage inflicted from a multitude of directions during a standard **CT** session. In particular, there would be no adverse carcinogenic legacy bequeathed by x-ray ionization.

There does not appear to be any **RF** hardware impediment in implementing the diagnosis setup thus suggested, since ingredients such as source and receive array are commercially available. Equally as important, the structural **FMA** reconstruction objectives, which, in a specifically dental setting would take the form of searching for cavities and, say, root pathologies and/or congenital abnormalities, have been tested with promising results in software simulations based upon analytic and numerical examples, a few of which will be on view herein.

Microwave Medical Imaging Techniques

George G. Cheng, **Yong Zhu**, **and Jan Grzesik**
Allwave Corporation, 3860 Del Amo Blvd., #404, Torrance, CA 90503, USA

Abstract— A wide swath of medical imaging techniques will be summarized and individually assessed as to their comparative efficacy. Ultimately, however, we intend to focus our emphasis upon microwave imaging We shall begin with traditional, pulse-based measurements, typified by heartbeat rate, blood pressure, and EEG/EKG readings and then continue on to X-ray imaging and the still more sophisticated procedures embodied in computerized tomography (**CT**), Ultrasonics, Magnetic Resonance Imaging (**MRI**), Positron Emission Tomography (**PET**), and so on. Both underlying principle and hardware implementation will be outlined and discussed along the way.

Medical imaging utilizing electromagnetic waves as probes has been studied for at least the past half century, and, despite its long gestation period, in recent years it has finally claimed its proper role as an emerging alternative to X-rays. These evolving electromagnetic techniques now embrace several varieties of bioinstrumentation, microwave thermography and microwave microscopy, radar imaging, microwave holography, diffraction tomography, and on to inverse scattering methods, the latter largely reliant upon an optimization-based, computer-intensive underpinning. Our survey will conclude with a comprehensive comparison roster

In 2004 we developed the Field Mapping Algorithm (**FMA**) in the arena of electromagnetic fields. In addition to its natural antenna and radar cross section (**RCS**) applications, we have recently found it to be ideally suited for use in medical imaging. Our **FMA** provides direct solutions to **3D** inverse scattering problems, allowing images of internal biological organs to be obtained simply on the basis of the scattered fields detected by sensors that are proximate, yet fully external to living tissue. In particular, with the low-power microwave probing which is organized beneath the control of our **FMA**, one is able to bypass altogether the carcinogenic threat of *in situ* ionization which inevitably accompanies X-ray transit. Test measurements conducted with *bona fide* biological samples have consistently shown convincing results.

Three Dimensional Radar Imaging by Using Spherical Near Field Range

Dau-Chyrh Chang[1], **Chih-Hung Lee**[2, 3], **and Tsung-Yuan Yang**[3]

[1]Oriental Institute of Technology, Taiwan
[2]Yuan Ze University, Taiwan
[3]Electronics Testing Center, Taiwan

Abstract— Usually, the high quality inverse synthetic aperture radar (ISAR) radar image is generated inside anechoic microwave chamber with far field test range or compact far field test range. In this paper, a high performance three dimensional radar image with size 1.5 meter by 1.5 meter and far field RCS versus aspect angle is performed by using the spherical near field range. By using the near field to far field transformation, the high fidelity radar image and radar cross section (RCS) can be generated. The radar system is impulse time domain system. The pulse width and pulse repetition frequency of radar are 30 ps and 1 MHz respectively. Figure 1 shows the simulation image result of 12 scatter points target model, distributed on 1.5 meter by 1.5 meter plane, by using the near field spherical range. Figure 2 shows the structure of near field scanner. The target is mounted on the horizontal positioner. By the rotation of the target, the near field ISAR image can be generated at special aspect angle. The impulse time domain radar system is moved along the arch. By using the radar movement along the arch and the target rotation on the postioner the three dimensional near field ISAR radar image can be generated. By using the field transformation from near field to far field, the high performancee radar image and RCS can be generated. The details, such three dimensional image and RCS, will be included at the full paper and oral presentation.

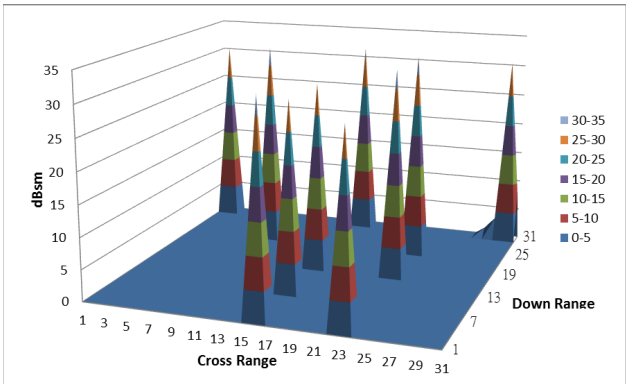

Figure 1: Simulation results of points scatter target.

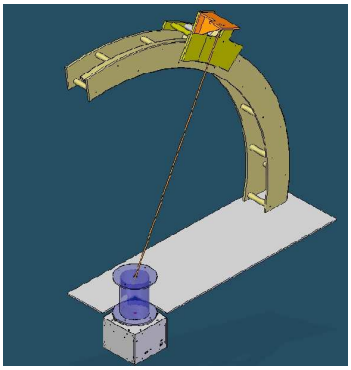

Figure 2: Spherical near field scanner.

Session 2P3a
Earth Electromagnetic Environment and Radiowaves Propagation & Scattering: Modeling, Observation and Measurements

Measuring ELF-EMF Levels in the State of Kuwait
Fuad M. Alkoot, Essa M. Alkoot, Ahmad A. Dashti, Mahdi B. Abdulaziz, ... 296

An Investigation on Ionospheric Total Absorption of Radio Waves in High Latitude Region
Wei Tao, Jiankui Shi, Guojun Wang, X. Wang, G. A. Zherebtsov, Alexander P. Potekhin, E. B. Romanova, K. G. Ratovsky, A. Stepanov, ... 298

Oblique Sounding of the Ionosphere Layer F2 by Powerful Wave Beams
Barbara Atamaniuk, I. A. Molotkov, Alexei Popov, ... 299

Evaluation of Correlation Detector for Ship Detection with HF Radar
A. Gupta, Thomas Heinrich Fickenscher, ... 300

Compensation of Mutual Coupling for Antenna Array with Application of Ground Penetrating Radar
Qiang Hou, He Ping Pan, Feng Zhou, Guo Hong Wang, Si Pei Liao, ... 302

Integration of Multi Instrument Ionospheric Plasma Diagnostics Used for Description of the Near Earth's Plasma Environment
Hanna Rothkaehl, A. Krankowski, D. Przepiórka, E. Słomińska, ... 304

Analysis of Radio Signals Spatial Structure in Relation with Ionospheric Perturbations
Rachid Talhi, G. Rogerie, ... 305

Passive Ionospheric Sounding and OTH Radar Using DRM Signals
Michael James Underhill, ... 306

Measuring ELF-EMF Levels in the State of Kuwait

Fuad M. Alkoot[1,*], **Essa M. Alkoot**[2,**], **Ahmad A. Dashti**[3,***], **and Mahdi B. Abdulaziz**[3,****]

[1]HITN, PAAET, P. O. Box 4575, Alsalmia, Kuwait
[2]PAI, Kuwait
[3]KOC, Kuwait

Abstract— Extremely low frequency magnetic field, ELF-MF around power lines has increasingly gained the attention and concerns of the public and officials. Scientists have conducted many studies to find the relation between ELF-MF and many health disorders including cancer. Research on the health effects of electromagnetic field began in the late 1960's and was originally focused on electric fields. In 1979 Wertheimer et al. [1] reported a statistical association between magnetic field exposure and distance between a power line and someone's home, and two- to three-fold increases in leukemia risk among U.S. children. This early research brought the issue of magnetic field-related health risks to the attention of scientists and the public. Two studies by Green et al. [2] and Schuz et al. [3] have reported an association between ELF-EMF and Leukemia. Ahlbom [4] found the strongest link between exposure and childhood leukemia, where a statistically significant association between childhood leukemia and average exposure for 24–48 hours of 0.4 μT or greater was found, (0.4 μT = 4 mG). Many studies link between exposure to power frequency fields and breast cancer, lymphoma, liver cancer, skin cancer and brain cancer in animals. while Loomis [5] showed a clear association of female breast cancer with occupational exposure to power low frequency fields. Strongest evidence for a connection between power frequency fields and many diseases in addition to cancer was found by Neutra et al. (2002) [6]. In addition to different types of cancer, ELF-EMF was found to be a possible cause of miscarriage among women living close to power lines. This finding was also reported in Geraldine et al. (2002) [7]. International Association for Research on Cancer, (IARC) [8], and The U.S. National Institute of Environmental Health Sciences (NIEHS), [9] have assigned EMF radiation to group 2B, which means it is a possible carcinogenic.

Based on the surveyed literature we believe there is a health hazard associated with extremely low frequency magnetic fields. However, studies were not able to find and confirm the exact dangerous levels due to the complex nature of the problem. This study aims at measuring magnetic field levels close to power transmission lines and transformer substations, in order to provide an unbiased data to the scientific community and the public. We aim to present information regarding this project in addition to results on field levels at some of the surveyed locations in Kuwait. For each location spot measurements were conducted at various distances from the power lines and substations, at a height of one meter. The visit to a location is repeated at three times of the day at four seasons of the year.

REFERENCES

1. Wertheimer, N. and E. Leeper, "Electrical wiring configurations and childhood cancer," *Am. J. Epidemiol.*, Vol. 109, 273–284, 1979.
2. Green, L. M., A. B. Miller, D. A. Agnew, M. L. Greenberg, J. Li, P. J. Villeneuve, and R. Tibshirani, "Childhood leukemia and personal monitoring of residential exposures to electric and magnetic fields in Ontario, Canada," *Cancer Causes and Control*, Vol. 10, 233–243, 1999.
3. Schuz, J., J. Grigat, K. Brinkmann, and J. Michaelis, "Residential magnetic fields as a risk factor for childhood acute leukaemia: Results from a german population-based case-control study," *International Journal of Cancer*, Vol. 91, 728–735, 2001.
4. Ahlbom, A., N. Day, M. Feychting, E. Roman, J. Skinner, J. Dockerty, M. Linet, M. McBride, J. Michaella, J. H. Olsen, T. Tynes, and P. K. Verkasalo, "A pooled analysis of magnetic fields and childhood leukaemia," *British Journal of Cancer*, Vol. 83, No. 5, 692–708, 2000.
5. Loomis, D. P., et al., "Breast cancer mortality among femal electrical workers in the United States," *Journal of National Cancer Institute*, Vol. 86, 921–925, 1994.

*: Fuad M. Alkoot (f_alkoot@yahoo.com).
**: Essa M. Alkoot (e.alkoot@hotmail.com).
***: Ahmad A. Dashti (aamdashti@kockw.com).
****: Mahdi B. Abdulaziz (Mahdi-shirazi@hotmail.com).

6. Neutra, R. R., V. DelPizzo, and G. M. Lee, "An evaluation of the possible risks from electric and magnetic fields (EMFs) from power lines, internal wiring, electrical occupation and appliances," California EMF Program Final Report, June 2002.
7. Lee, G. M., et al., "A nested case-control study of residential and personal magnetic field measures and miscarriages," *Epidemiology*, Vol. 13, No. 1, 21–31, January 2002.
8. International Agency for Research on Cancer, http://www.iarc.fr.
9. US National Institute of Environmental Health Sciences, "Health effects from exposure to power-line frequency electric and magnetic fields," Research Triangle Park, NC, 1999.

An Investigation on Ionospheric Total Absorption of Radio Waves in High Latitude Region

W. Tao[1], **J. K. Shi**[1], **G. J. Wang**[1], **X. Wang**[1], **G. A. Zherebtsov**[2], **A. Potekhin**[2], **E. B. Romanova**[2], **K. G. Ratovsky**[2], **and A. Stepanov**[3]

[1]State Key Laboratory of Space Weather
Center for Space Science and Applied Research, CAS, Beijing, China
[2]Institute of Solar-Terrestrial Physics, RAS, Irkutsk, Russia
[3]Institute of Cosmophysical Research and Aeronomy, RAS, Yakutsk, Russia

Abstract— The ionogram data obtained by DPS-4 digisonde at the high-latitude Station Norilsk (Dip lat. 60°N) in 2006 were used to study properties of Ionospheric Total Absorption of Radio waves (ITAR), such as its diurnal variation, seasonal variation, and response to geomagnetic activity. In winter and some months of equinox, the ITAR occurrence rate was much higher in nighttime than in daytime, and its maximum was about 90%. In summer, the occurrence rate dropped in nighttime and went up in daytime, thus the difference between the occurrence in nighttime and that in daytime was reduced. The total duration of ITAR declined from April to July and ascended from August to December. The ITAR occurrence ascended with the increase of Kp. The physical mechanism of the ITAR is also discussed.

Oblique Sounding of the Ionosphere Layer F2 by Powerful Wave Beams

B. Atamaniuk[1], **I. A. Molotkov**[2], **and A. Popov**[2]

[1]Space Research Centre of the Polish Academy of Sciences, Warsaw, Poland
[2]Institute of Terrestrial Magnetism, Ionosphere and Radio Wave Propagation, RAS
Troitsk, Moscow 142190, Russia

Abstract— The presentation is devoted to modeling and analysis of the interaction of a powerful obliquely incident wave beam of decameter radio waves with the ionospheric layer F2. Much like the linear case, propagation through the natural anti-waveguide layer F2 splits the initial beam. Part of its energy propagates trough the ionospheric layer, the other part goes back along a downward trajectory. However, nonlinearity leads to further stratification of the ionospheric layer. A new feature, in comparison with the linear case, is appearing a narrow waveguide beneath the F2 layer maximum which traps a small part of the beam energy. We study the relationship between these parts of the wave field in a simplified model of parabolic F2 layer, with nonlinearity caused by thermal plasma expulsion from the high field intensity region. Analytical results are supplemented with numerical estimates of the effects.

- We model and analyze of the interaction of a powerful obliquely incident wave beam of decameter radio waves with the ionospheric layer F2.
- Oblique propagation of a powerful HF wave beam in the ionospheric F2 layer leads to additional plasma stratification, in particular — to the formation of an artificial waveguide controlled by the beam intensity.
- The formation of the artificial waveguide is a nonlinear effect.
- The problem of efficient feeding the artificial waveguide depends on the ability to create in the F2 layer high values of the HF electric field compared with the characteristic "plasma fields".

ACKNOWLEDGMENT

This research is supported by grant O N517 418440.

Evaluation of Correlation Detector for Ship Detection with HF Radar

A. Gupta and T. Fickenscher
Helmut Schmidt University/University of the Federal Armed Forces Hamburg, Hamburg, Germany

Abstract—

Summary: HF radar finds applications in various fields such as oceanography, maritime surveillance, search and rescue operations, and Tsunami warning. Probability of ship detection P_{detect} for HF Surface Wave Radar (SWR) can hardly be justified purely by either theoretical or experimental investigations. We propose to evaluate the performance of recently invented Correlation Detector using synthetic targets in the background of measured sea clutter data. Various datasets for a wind speed of 1.5 m/s prove that reliable estimation of P_{detect} is achieved with proposed approach. Results are provided for values of Radar Cross Section RCS from 10–40 dBsm.

Motivation: For the detection of ships by using HF Surface Wave Radar (HF SWR) the primary obstacle is first-order ocean clutter identified as so-called Bragg lines in the Range-Doppler (RD) map. Recently a new detector has been proposed which uses the property that azimuth variation of received power for a Range Doppler (RD) cell including a target will be more correlated across the adjacent RD cells as compared to a RD cell without a target [1, 2]. Detection of targets within the first and second order Bragg sea scatter on measured data has been shown. In this paper the performance of the Correlation Detector is investigated by evaluating the probability of ship detection using synthetic targets in the background of measured clutter data. In particular the impact of the window length (number of azimuth bins) considered for calculating the correlation of azimuth vectors is investigated. Application is advantageous for both ship detection and oceanography as detection list can be used to improve the quality of oceanographic data.

Concept: The evaluation of P_{detect} in case of HF SWR is not straightforward. Since the statistics of sea clutter is not fully understood it is not possible to calculate the value of P_{detect} theoretically. On the other hand experimental investigations using measured targets and Automatic Identification System (AIS) data for verification are also prone to error as AIS data are often incomplete (leading to a high number of false alarms) and sometimes even incorrect. Therefore, in this paper we propose to implant a synthetic target of variable RCS and range in 100 measured data sets and make a statistical estimate. To evaluate the value of P_{detect} for a given data set the synthetic target of a given RCS is inserted in middle of the range Doppler bin. The target signal is weighted by Sommerfeld surface wave attenuation function and corresponding complex voltage is added to the voltage of measured signal after range transform. The correlation detector is used to detect the presence of the target. The process was sequentially repeated for ranges from 10–200 km and Doppler frequencies from ±2.5 Hz. By evaluating the number of successful detections the value of P_{detect} has been calculated for various RCS values and window lengths as seen in Fig. 1 and Fig. 2 respectively.

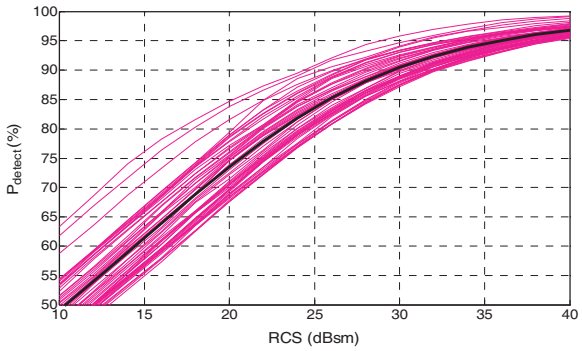

Figure 1: Probability of detection, P_{detect} versus target Radar Cross Section, RCS for window length of 25. Black line represents the mean P_{detect}.

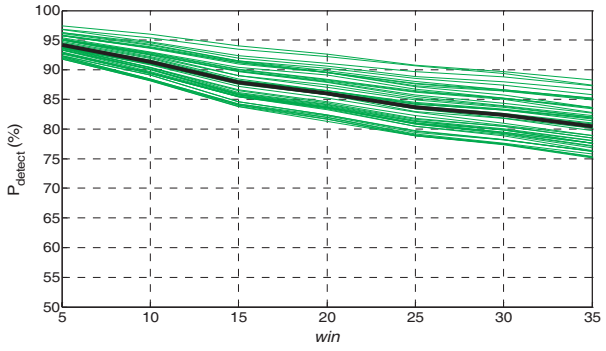

Figure 2: Probability of detection, P_{detect} versus window length, *win* for a target RCS of 25 dBsm. Black line represents the mean P_{detect}.

REFERENCES

1. Gupta, A. and T. Fickenscher, "Correlation detector for HF surface wave radar," *IET Radar 2012*, Glasgow, October 2012.
2. Gupta, A. and T. Fickenscher, "Hard threshold correlation detector for mobile HF surface wave radar," *International Radar Symposium (IRS) 2012*, Warsaw, May 2012.

Compensation of Mutual Coupling for Antenna Array with Application of Ground Penetrating Radar

Qiang Hou[1], **He Ping Pan**[2], **Feng Zhou**[1], **Guo Hong Wang**[1], **and Si Pei Liao**[1]

[1]Faculty of Mechanical & Electronic Information, China University of Geosciences
Hubei 430074, China
[2]Institute of Geophysics & Geometrics, China University of Geosciences
Hubei 430074, China

Abstract— Ground-penetrating radar (GPR) technology finds applications in many areas such as geophysical prospecting, archaeology, civil engineering, environmental engineering, and defense applications as a non-invasive sensing tool. One key component in any GPR system is the receiver/transmitter antenna. Desirable features for GPR antennas include efficient radiation of ultra-wideband pulses into the ground, good impedance matching over the operational frequency band, and small size. As the attenuation of radio waves in geophysical media increases with frequency, ground-penetrating radars typically operate at frequencies below 1 GHz. For either impulse or stepped frequency continuous-wave applications, the wider the frequency range, the better the range resolution of the radar. Continuous wave multi-frequency radars are advantageous over impulse radars in coping with dispersion of the medium, the noise level at the receiver end, and the controllability of working frequency. It requires, however, mutual coupling between the transmit (Tx) and receive (Rx) antennas, which determines the dynamic range of the system, to be kept as small as possible.

In this paper, the full-wave analysis of electromagnetic coupling mechanisms between resistively loaded wideband dipole antennas operating in realistic GPR scenarios is carried out. To this end, a locally conformal finite-difference time-domain (FDTD) technique, useful to accurately model electromagnetic structures having complex geometry, is adopted. Such a scheme, necessary to improve the numerical accuracy of the conventional FDTD algorithm, by avoiding staircase approximation, is based on the definition of effective material parameters, suitable to describe the geometrical and electrical characteristics of the structure under analysis. By doing so, the losses in the soil, as well as the presence of ground-embedded inhomogeneities with arbitrary shape and material parameters, are properly taken into account. Emphasis is devoted to the investigation of the antenna pair performance for different Tx-Rx separations and elevations over the ground, as well as on scattering from dielectric and metallic pipes buried at different depths and having different geometrical and electrical characteristics. Novelty of the analysis lies in the fact that at the lowest operational frequency both the receive antenna and a pipe are situated in the near-field, whilst at the highest operational frequency only the far field is playing the role. The obtained numerical results provide a physical insight into the underlying mechanisms of subsurface diffraction and antenna mutual coupling processes. This information in turn can be usefully employed to optimize the performance of detection algorithms in terms of clutter rejection.

Finally, a frequency-independent equivalent circuit model of antenna pairs is provided in order to facilitate the design of the RF front-end of ground-penetrating radars by means of suitable software CAD tools. The procedure employed to extract the equivalent circuit is based on a heuristic modification of the Causer's network synthesis technique useful to model ohmic and radiation losses. In this way, one can obtain a meaningful description of the natural resonant modes describing the electromagnetic behavior of antenna pairs for GPR systems.

REFERENCES

1. Caratelli, D. and R. Cicchetti, "A full-wave analysis of interdigital capacitors for planar integrated circuits," *IEEE Trans. Magnetics*, Vol. 39, No. 3, 1598–1601, 2003.
2. Caratelli, D., R. Cicchetti, G. Bit-Babik, and A. Faraone, "A perturbed E-shaped patch antenna for wideband WLAN applications," *IEEE Trans. Antennas Propagat.*, Vol. 54, No. 6, 1871–1874, 2006.
3. Caratelli, D., A. Yarovoy, and L. P. Ligthart, "Antennas for ground-penetrating radar applications," Tech. Rep. IRCTR-S-032-07, Delft University of Technology, 2007.
4. Caratelli, D., A. Yarovoy, and L. P. Ligthart, "Full-wave analysis of cavity-backed resistively-loaded bow-tie antennas for GPR applications," *Proc. European Microwave Conference*, 204-207, Amsterdam, the Netherlands, 2008.

5. Chuma, J., C. W. Sim, and D. Mirshekar-Syahkal, "Computation of resonant frequencies of dielectric loaded rectangular cavity using TLM method," *IET Electron. Lett.*, Vol. 35, No. 20, 1712–1713, 1999.
6. Dey, S. and R. Mittra, "A conformal finite-difference time-domain technique for modeling cylindrical dielectric resonators," *IEEE Trans. Microwave Theory Tech.*, Vol. 47, No. 9, 1737–1739, 1999.
7. Freundorfer, A., K. Iizuka, and R. Ramseier, "A method of determining electrical properties of geophysical media," *J. Appl. Phys.*, Vol. 55, 218–222, 1984.
8. Gürel, L. and U. Oguz, "Simulations of ground-penetrating radars over lossy and heterogeneous grounds," *IEEE Trans. Geosci. Remote Sensing*, Vol. 39, No. 6, 1190–1197, 2001.
9. Gürel, L. and U. Oguz, "Optimization of the transmitter–receiver separation in the ground-penetrating radar," *IEEE Trans. Antennas Propagat.*, Vol. 51, No. 3, 362–370, 2003.
10. lizuka, K., A. P. Freundorfer, K. H. Wu, H. Mori, H. Ogura, and V. Nguyen, "Stepfrequency radar," *J. Appl. Phys.*, Vol. 56, 2572–2583, 1984.
11. Kaneda, N., B. Houshmand, and T. Itoh, "FDTD analysis of dielectric resonators with curved surfaces," *IEEE Trans. Microwave Theory Tech.*, Vol. 45, No. 9, 1645–1649, 1997.
12. Maloney, J. G. and G. S. Smith, "A study of transient radiation from the Wu-King resistive monopole — FDTD analysis and experimental measurements," *IEEE Trans. Antennas Propagat.*, Vol. 41, No. 5, 668–676, 1993.
13. Montoya, T. P. and G. S. Smith, "A study of pulse radiation from several broad-band loaded monopoles," *IEEE Trans. Antennas Propagat.*, Vol. 44, No. 8, 1172–1182, 1996.
14. Moray, R. M., "Continuous subsurface profiling by impulse radar," *Proc. Eng. Found. Conf. Amer. Soc. Civil Eng.*, 213–232, 1974.
15. Peter, Jr., L., J. D. Young, and J. Daniels, "Ground penetration radar as a subsurface environmental sensing tool," *Proc. IEEE*, Vol. 82, 1802–1822, 1994.
16. Timmins, I. and K. Wu, "An efficient systematic approach to model extraction for passive microwave circuits," *IEEE Trans. Microwave Theory Tech.*, Vol. 48, No. 9, 1565–1573, 2000.
17. Yee, K. S., "Numerical solution of initial boundary value problems involving Maxwell's equations," *IEEE Trans. Antennas Propagat.*, Vol. 14, No. 3, 302–307, 1966.
18. Daniels, D., *Ground Penetrating Radar*, 2nd Edition, IEE Press, 2004.
19. Fletcher, R., *Practical Methods of Optimization*, John Wiley, 1980.
20. Guillemin, E. A., *Synthesis of Passive Network: Theory and Methods Appropriate to the Realization and Approximation Problems*, John Wiley, 1965.
21. Taflove, A. and S. C. Hagness, *Computational Electrodynamics: The Finite Difference Time Domain Method*, 3rd Edition, Artech House, 2005.

Integration of Multi Instrument Ionospheric Plasma Diagnostics Used for Description of the Near Earth's Plasma Environment

H. Rothkaehl[1], **A. Krankowski**[2], **D. Przepiórka**[1], **and E. Słomińska**[1]

[1]Space Research Center Polish Academy of Sciences (SRC PAS), 00-716 Bartcka 18-A, Wasaw, Poland
[2]Geodynamics Research Laboratory (GRL/UWM), University of Warmia and Mazury in Olsztyn
1 Oczapowski, Olsztyn 10-957, Poland

Abstract— In order to enhance our understanding of the rich plasma physical processes that drives the solar-terrestrial space environment we need to dramatically increase our ability to perform multi point measurements with sensors of different types. The magnetosphere-ionosphere thermosphere system is strongly affected by electric and magnetic fields, particle precipitation, heat flows and small scale interactions. The changes of the near Earth plasma conditions are produced mainly by natural perturbations, but some of them also have anthropogenic origin. The diagnostics of the ionospheric plasma property as electron and ion density, temperature and velocity can provide essential inputs for modeling the Space Weather conditions.

The aim of this presentation is to show global distribution of main plasma parameters during different geomagnetic conditions and seasons diagnosed by various measuring techniques as: in situ wave and plasma diagnostics registered on board of DEMETER satellite, GPS observations collected at IGS/EPN network, GPS observation carried out at the Antarctic and Arctic IGS (International GNSS Service) stations used and the data retrieved from FORMOSAT-3/COSMIC radio occultation measurements. We are willing to present and validate the properties of the ionospheric electron density profiling retrieved from FORMOSAT-3/COSMIC radio occultation measurements. The comparison of radio occultation data with ground-based measurements indicates that usually COSMIC profiles are in a good agreement with ionosonde profiles both in the F2 layer peak electron density (NmF2) and the bottom side of the profiles. For this comparison ionograms recorded by European ionospheric stations (DIAS network) during 2008 year were used.

We would like also to discuss the limitation of presented diagnose techniques with respect to different geomagnetic condition and localization in space.

ACKNOWLEDGMENT

This research is supported by grant No. 517 418440.

Analysis of Radio Signals Spatial Structure in Relation with Ionospheric Perturbations

R. Talhi and G. Rogerie
C.N.R.S-LPC2E, University of Tours, Orleans 45071, France

Abstract— This paper presents an analysis of statistical properties of radio signals reflected from the ionosphere, focusing on the scattered wave intensity and the wave polarization rate, among other important parameters related to fluctuations of the radio propagation channel. As we know, the high spatio-temporal ionization variability of the ionosphere requires a statistically accurate predictions at all times and under all kind of geophysical conditions in order to lead to a reliable performance in many applications like HF communications. Although empirical methods are used, there is no efficient theory (or method) able to predict and to explain the physical process which is at the origin of the ionospheric behaviour.

In this study, we performed an optimization of a series of numerical simulations based on Monte Carlo method, using typical condition and ionospheric parameters, total electron content values, turbulence spectrum. The evolution of the predicted scattered wave intensity and wave polarization rate with frequency, incidence angle, electron density, and turbulence strength, is analysed and the relevant phenomena to take into account during simulations are specified. Finally, results and comments are presented and discussed to illustrate the use of the method.

Passive Ionospheric Sounding and OTH Radar Using DRM Signals

Michael J. Underhill
Underhill Research Ltd., Lingfield, UK

Abstract— A novel technique for passive ionospheric sounding was published in May 2012 in a paper entitled "Estimation Of Ionospheric Layer Heights and Velocities Using Available DRM Signals" [1]. DRM (Digital Radio Mondiale) signals are used for high fidelity and long distance HF broadcast transmissions. DRM has a high immunity to multipath interference from delayed versions of the original transmitted signal. It is an OFDM (Orthogonal Frequency Division Multiplex) signal with a 10 kHz wide flat-topped spectrum of 200 to 500 equally spaced 16 or 64-QAM (Quaternary Amplitude Modulation) carriers of equal amplitude.

Figure 1 shows the signal and immediate past history time waterfall of the 10 kHz wide 15 kW signal of RUVR (Voice of Russia) transmitted on 9850 kHz from Bolshakovo, Kaliningrad Oblast, and received 30 km south of London, UK, on an RFspace SDR-IQTM software receiver. The direct path length is 1500 km.

Figure 1 shows a time waterfall of reflections delayed relative to the shortest 'direct' path interfering and combining to give the patterns shown. The distance of a reflection has been shown [1] to be inversely proportional to the horizontal period of the pattern component. The velocity of a reflection is given by the slope of the pattern troughs or peaks. A slope corresponding to a decreasing frequency with time is a receding reflection, and an increasing frequency with time is an approaching reflection. Speed can also be estimated from Doppler shifts measured vertically on the waterfall. By inspection we can identify three distinguishable delayed reflections. These are: (a) a layer reflection at a spacing of about 210 km receding at a velocity of 185 kph, (b) a layer reflection at about 120 km with an apparent velocity 1830 kph and (c) seen faintly at right of centre at the bottom of the waterfall, a discrete object reflection at 530 km travelling at 870 kph. The first two reflections (a) and (b) are from ionospheric layers, and (c) would appear to be an OTH (Over The Horizon) aircraft reflection at a distance of at least 530 km. The velocity of 1830 kph is too high to correspond directly to ionospheric layer movements. This mystery is under investigation.

The problem is to find what signal processing algorithms could best separate and measure these kind of targets automatically. A 'successive unwrapping' de-convolution approach is being examined. The concept is to identify the strongest reflection first by taking a Fourier transform of the 10 kHz wide spectrum and observing which is the strongest component. This component is then both subtracted and used to correct the periodic phase reversals that this signal causes on all other components. The next strongest component is then extracted, subtracted and used to correct the phase reversals on the remaining less strong components. And so on until all

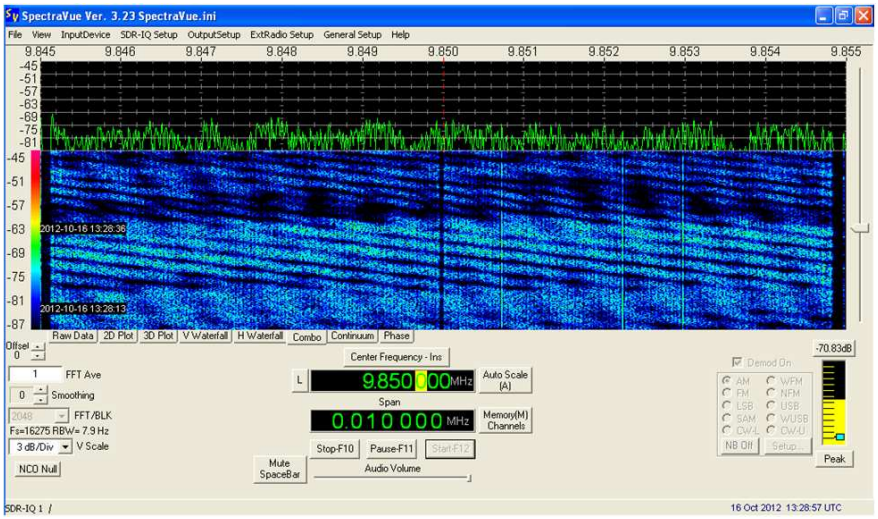

Figure 1: SpectraVue display of 9850 kHz DRM signal over a 1500 km path with at least 3 different delayed reflections of the original signal.

identifiable components have been extracted. The final step is to find the reflection component velocities from the time waterfalls of the separated components.

REFERENCES

1. Underhill, M. J., "Estimation of ionospheric layer heights and velocities using available DRM signals," *IET Conf. on Ionospheric Radio Systems and Techniques 2012*, Royal York Hotel, York, UK, May 15–17, 2012.

Session 2P3b
Present and Future of Terahertz Science & Technology, Including Applications in Radio-sciences

Study of DNA Fingerprint of Pine Wood Nematode Based on Terahertz Spectroscopic Technology at 0–10 THz
Ling Jiang, Chun Li, Lin Huang, Zhenwei Zhang, Cunlin Zhang, Yunfei Liu, ... 310
Terahertz Functional Tissue Imaging
Seongsin Margaret Kim, Patrick Kung, ... 311
Characterization of High Intense Pulse Amplified by Yb-doped Fiber Chirped Pulse Amplification System for THz Wave Generation
Junichi Hamazaki, Norihiko Sekine, Shingo Saito, Iwao Hosako, ... 312
The Transmission Spectra of Semiconductor Based Samples Using the Terahertz Spectroscopy System
Weixin Lu, Bo Hou, ... 313

Study of DNA Fingerprint of Pine Wood Nematode Based on Terahertz Spectroscopic Technology at 0–10 THz

Ling Jiang[1], **Chun Li**[1], **Lin Huang**[2], **Zhenwei Zhang**[3], **Cunlin Zhang**[3], **and Yunfei Liu**[1]

[1]College of Information Science and Technology, Nanjing Forestry University, Nanjing 210037, China
[2]Forest Resources and Environment Institute, Nanjing Forestry University, Nanjing 210037, China
[3]Terahertz Laboratory, Department of Physics, Capital Normal University, Beijing, China

Abstract— In this paper, we investigate the fingerprint characteristics of harmful Bursaphelenchus xylophilus (*Bx*) nematode and harmless Bursaphelenchus mucronatus (*Bm*) nematode by applying terahertz spectroscopic techniques. We measure and analyze the transmission features of the deoxyribose nucleic acid (DNA) of the *Bx* and the *Bm* samples, and their corresponding polymerase chain reaction (PCR) amplification segments of the DNA molecules by using terahertz domain spectroscopy (THz-TDS) and Fourier transform infrared spectroscopy (FTIR). The low-frequency absorption features measured by THz-TDS exhibits different absorption peaks (i.e., 0.07 and 0.11 THz) for the *Bx* and the *Bm* samples respectively. The calculated relative refractive index of the *Bm*-PCR segment is found to be much smaller compared with other three samples. The higher frequency characteristics of the four samples measured by the FTIR spectroscopy shows similar absorption peaks, except that the *Bm*-DNA provides a smooth differential feature of absorption at 5.46 THz. These measurement results indicate the *Bm* samples including DNA and PCR segment indeed have unique signature behaviors different from the *Bx* samples. It demonstrates that the terahertz spectroscopic technique is a useful method to distinguish the *Bx* and the *Bm*'s DNA and PCR segments by locating the absorption frequency.

Terahertz Functional Tissue Imaging

S. M. Kim and P. Kung
Department of Electrical and Computer Engineering
The University of Alabama, Tuscaloosa, USA

Abstract— In recent years, biomedical imaging techniques using electromagnetic radiation in the terahertz (THz) spectral band, between 0.2 THz and 10 THz, has drawn considerable interest and made progress due to the ability of THz radiation to interact with biological tissue at the molecular structure level, in addition to being non-ionizing. For example, THz waves have been used to identify tissue changes in tooth enamel, cartilage, and malignant cancer cells. Terahertz Time-Domain Spectroscopy (THz-TDS) is one of the most versatile methods for spectroscopic image acquisition because of its ability to simultaneously determine the amplitude and phase of the traveling wave over a broad spectral range.

In this study, we develop and investigate the use of THz-TDS imaging techniques to uniquely identify changes in tissue samples for both forensic and treatment applications. Using THz-TDS imaging in both transmission and reflection modes, we examine tissue samples that have been damaged using a variety of acids, thermal burns, and other chemical compounds. Each method causes structural deterioration to the tissue through a different mechanism, thus a distinct fingerprint on it that can lead to contrast visible in the THz. In this study, we correlate the observed spectroscopic change in the THz time domain spectra, the frequency spectra, as well as phase shift for each damage type to the mechanisms and severity of the deterioration caused. Once these correlations are established, we further investigate the forensic viability of such THz techniques by allowing natural rotting to damage the cellular structures so that the time window of effectiveness for this identification method can be determined.

Characterization of High Intense Pulse Amplified by Yb-doped Fiber Chirped Pulse Amplification System for THz Wave Generation

J. Hamazaki, **N. Sekine**, **S. Saito**, **and I. Hosako**
National Institute of Information and Communications Technology, Japan

Abstract— Terahertz (THz) spectroscopy is suitable for identifying molecules of interest with fingerprints in the THz region, including gas molecules, illicit drugs, and so on. In the THz spectroscopy, high power THz wave generation is required for precise measurements. To generate high-power THz wave by nonlinear optical effects, high-intense pump pulse with shorter pulse width is desired. This is because generated THz wave increases superlinearly with increase in peak electric field intensity of the pump pulse.

Since Yb-doped fiber has large gain and broad gain spectrum (1.0–1.1 μm), a combination of Yb-doped fiber laser oscillator and Yb-doped fiber amplifier has attracted much attention as a promising candidate of ultra-short high-intense pulse source, an alternative to a commonlyused Er-doped fiber laser system. To date, by using Yb-doped fiber laser oscillators and Yb-doped fiber amplifiers, ultra-short (< 150 fs) and high-intensity pulses (100 μJ) have been reported.

There are reports of THz wave generation by using ultra-short high-intensity pulse amplified by Yb-doped fiber amplifier. However, they simply input the pulse to nonlinear crystal. Detailed investigation of THz generation depended on input pump pulse condition (e.g., pulse width, dispersion of pulse and so on) is not well examined.

In this paper, we demonstrate our Yb-doped fiber chirped pulse amplification system. As a seed oscillator, we used mode-locked Yb-doped fiber laser oscillator with a pulse width of $100 \sim 150$ fs. We obtained high intense pulse with an average power over 1 W. We characterized this high-power amplified pulse. Moreover, we used this pulse to generate THz wave by nonlinear optical effects. Optimal condition of pump pulse for THz wave generation will be discussed.

The Transmission Spectra of Semiconductor Based Samples Using the Terahertz Spectroscopy System

Weixin Lu and Bo Hou
School of Physical Science and Technology, Soochow University
1 Shizi Street, Suzhou 215006, China

Abstract— We used the ultrafast laser pulses to generate and detect the terahertz (THz) radiation by ZnTe. This coherent THz spectroscopy system, using optical rectification and electro-optic sampling, was used to measure the transmission spectra of semiconductor based samples within the wide bandwidth, beyond 3 THz.

Session 2P4
Advanced Mathematical and Computational Methods in Electromagnetic Theory and Their Applications

Numerical Steepest Descent Method for Computing Highly Oscillatory Physical Optics Integral on Saddle Surfaces
Yumao Wu, Weng Cho Chew, Lijun Jiang, ... 316

Scattering of a Plane Wave by a Half Plane with a Sinusoidally Deformed Edge
Akira Komiyama, ... 317

Reflection and Transmission of Electromagnetic Waves from the Boundaries of Anisotropic Magneto Dielectric Plate in the Waveguide
Eduard A. Gevorkyan, V. I. Steshkin, ... 318

Optical Gausson Perturbation
Anjan Biswas, ... 319

Wiener-Hopf Method for Problems of Diffraction of Asymmetric Waves by a Circular Cylinder
Seil S. Sautbekov, Gulnar K. Alkina, Merey S. Sautbekova, ... 320

Exact Axisymmetric Solutions for the Magnetic Force between Disk Coils
John Thomas Conway, ... 321

Advances in the Theory of the Circular Waveguide with an Azimuthally Magnetized Ferrite Cylinder and a Dielectric Toroid
Mariana Nikolova Georgieva-Grosse, Georgi Nikolov Georgiev, ... 323

DOA Estimation via Phase Measurement
Andrew Im, Matthew Gialich, Zekeriya Aliyazicioglu, H. K. Hwang, ... 325

Universal Properties of Electromagnetic Pulses
John Lekner, ... 326

Approximate Solution Method of Nonlinear Helmholtz Equation
Merey S. Sautbekova, Seil S. Sautbekov, ... 327

Reconstruction Parameters of Local Scattering Sources of a Cylindrical Object from the Backscattering Pattern
Stanislav Nikolaevich Kutishchev, ... 328

Universal Properties of Electromagnetic Beams
John Lekner, ... 329

Numerical Steepest Descent Method for Computing Highly Oscillatory Physical Optics Integral on Saddle Surfaces

Yu Mao Wu[1], **Weng Cho Chew**[1, 2], **and Li Jun Jiang**[1]

[1]Department of Electrical and Electronic Engineering
The University of Hong Kong, Pokfulam Road, Hong Kong, China
[2]Department of Electrical and Computer Engineering
University of Illinois, Urbana, Champaign, USA

Abstract— When the electrical sizes of considered objects are on the order of tens to thousands of the working wavelength, the analysis of the electromagnetic scattering problem belongs to the high frequency regime. In this regime, the physical optics (PO) current approximation has been utilized to analyze the electromagnetic scattering problem. Then, the scattered electromagnetic field in terms of the PO current can be represented by a PO surface integral. Moreover, the kernel of the PO integral becomes more oscillatory with increasing wave frequency. Direct solvers, such as the method of moment, make the computational efforts that increase dramatically with the frequency. Traditional asymptotic expansion approximation is a frequency independent approach for analyzing the highly oscillatory PO integral. However, it leads to limited accuracy since the asymptotic approximation procedure is used.

In this work, we develop the numerical steepest descent path (NSDP) method to calculate the highly oscillatory PO integral on saddle surfaces. Physically, the critical points contributions, including the stationary phase point, the resonance points, and the vertex points are comprehensively studied in terms of the NSDP method. Importantly, the PO integrands defined on the NSDPs decay exponentially after the contour deformation on the complex plane. Hence, the NSDP method provides a frequency independent approach to evaluate the PO integral. Compared with the asymptotic expansion approach, our NSDP method has significantly improved the accuracy for evaluating the PO integral on the saddle surface. The proposed NSDP method for the PO integral is frequency independent in computational cost and error controllable in accuracy.

Scattering of a Plane Wave by a Half Plane with a Sinusoidally Deformed Edge

Akira Komiyama
Osaka Electro-Communication University, Hatsu-cho Neyagawa-shi 572-8530, Japan

Abstract— A periodic grating scatters an incident plane wave in only discrete directions and the scattered wave is expressed as a sum of diffracted plane waves. To calculate the powers of the diffracted plane waves many methods have already been proposed [1]. In case of a periodic surface with finite extent the scattering in all directions takes place and the scattered wave is expressed in the form of a Fourier integral [2]. It is expected that in case of a half plane with a periodically deformed edge from a straight edge an incident plane wave is scattered in only discrete directions in the same manner as a periodic grating. Authors are interested in scattering phenomena by the edge and its mathematical description from a theoretical point of view.

The boundary perturbation method [3] is an efficient tool to treat the scattering by a slightly deformed object from a simple shape for which an exact solution of a scattering problem has been known. Only the effect of the deformation can be extracted by the method. Although the exact solution of the scattering by the straight edge has been well-known [4] it is very hard to apply the perturbation method to a deformed edge.

Levien and Schwinger have dealt with the scattering of a plane wave by an aperture in an infinite screen by the variational method and there have given the integral equation for the unknown function on the screen [5, 6]. By applying the procedure to an edge diffraction problem we can easily obtain an integral equation. However, it is very hard to solve analytically and numerically the integral equation.

In this paper we deal with the scattering of a scalar plane wave by a half plane with a sinusoidally deformed edge by the physical optics approximation. The oblique incidence of a plane wave to the edge is assumed. A contribution of an edge to the field integral is asymptotically evaluated and basic properties of the edge scattering are clarified. It is shown that the results are in good agreement with the results obtained by the GTD method.

REFERENCES

1. Petit, R., editor, *Electromagnetic Theory of Grating*, Springer, 1980.
2. Kashihara, A. and J. Nakayama, "Scattering of TM plane wave from a finite periodic surface," *IEICE Trans. Electron.*, Vol. J88-C, No. 7, 493–501, 2005.
3. Yeh, C., "Perturbation method in the diffraction of electromagnetic waves by arbitrarily shaped penetrable obstacles," *J. Math. Phys.*, Vol. 6, 2008–2013, 1965.
4. Morse, P. M. and H. Feshbach, *Methods of Theoretical Physics*, 1038–1064, McGraw-Hill, 1953.
5. Levien, H. and J. Schwinger, "On the theory of diffraction by an aperture in an infinite plane screen. I," *Phys. Rev.*, Vol.74, 958–974, 1948.
6. Levien, H. and J. Schwinger, "On the theory of diffraction by an aperture in an infinite plane screen. II," *Phys. Rev.*, Vol. 75, 1423–1432, 1949.

Reflection and Transmission of Electromagnetic Waves from the Boundaries of Anisotropic Magneto Dielectric Plate in the Waveguide

E. A. Gevorkyan and V. I. Steshkin
Moscow State University of Economics, Statistics and Informatics
7, Nezhinskaya Str., Moscow 119501, Russia

Abstract— The propagation of transverse-electric (TE) and transverse-magnetic (TM) electromagnetic waves in the waveguide of arbitrary cross section with anisotropic magneto dielectric plate is considered. With help of received generalized Fresnel's formulas the power reflection and transmission coefficient for the plate are obtained. The dependence of these coefficients on thickness of the plate at various values of the parameters describing the parametric interaction of TE and TM waves with anisotropic and magneto dielectric plate in the waveguide is found.

Optical Gausson Perturbation

Anjan Biswas
Department of Mathematical Sciencers, Delaware State University
Dover, DE 19901-2277, USA

Abstract— This talk will be on the dynamics of Gaussons in optical fibers that is governed by the nonlinear Schrodinger's equation (NLSE) with log law nonlinearity. There are a few advantages of considering NLSE with log law nonlinearity as opposed to the NLSE with Kerr law nonlinearity which is the norm in optical sciences. Gaussons do not support radiations and consequently no shedding of energy occurs during the soliton transmission through nonlinear optical fibers. This is a great advantage that gives Gaussons an edge over solitons. The soliton perturbation theory will be first addressed for Gaussons in presence of several perturbation terms that will be considered with full nonlinearity. The adiabatic dynamics of the Gausson amplitude and frequency will be obtained by the aid of this theory. Additionally, the slow change of the soliton velocity will also be given. The fixed point of the corresponding dynamical system will be computed that will lead to optical soliton cooling for log law nonlinearity. The multiple-scale perturbation analysis will then be carried out for the governing equation. The secular terms or resonances will be removed by the aid of Fredholm's Alternative. This will lead to four constraint relations, between the Gausson parameters. One of these constraint conditions is recoverable by the soliton perturbation theory, while the remaining three are not. This gives multiple-scales an edge over soliton perturbation theory. Finally, the quasi-stationary solution will be given.

Wiener-Hopf Method for Problems of Diffraction of Asymmetric Waves by a Circular Cylinder

Seil Sautbekov, Gulnar Alkina, and Merey Sautbekova
Eurasian National University, 5, Munaitpassov Str., Astana, Kazakhstan

Abstract— Diffraction of an unsymmetrical electromagnetic wave by a long pipe coaxially oriented inside an infinite waveguide is considered. The corresponding boundary value problem is reduced to a system of singular integral equations concerning the Fourier component of the surface current density. The exact solution of the above system of equations is constructed by the Wiener-Hopf-Fok method in a class of analytical functions and it is defined in the form of sum of partial waves.

REFERENCES

1. Weinstein, L. A., *The Theory of Diffraction and the Factorization Method*, The Golem Press, Boulder, Colorado, 1969.
2. Daniele, V. G. and G. Lombardi, "Wiener-Hopf solution for impenetrable wedges at skew incidence," *IEEE Trans. Antennas and Propagation*, Vol. 54, No. 9, 2472–2485, 2006.
3. Noble, B., *Methods Based on the Wiener-Hopf Technique*, 2nd Edition, Chelsea, New York, 1988.

Exact Axisymmetric Solutions for the Magnetic Force between Disk Coils

John T. Conway
University of Agder, Norway

Abstract— For the axisymmetric case, a closed form solution in terms of elliptic integrals has been found for the axial force F_z between a disk coil and a circular loop. The relative sizes and axial locations of the disk and ring coils are arbitrary. The disk coil is assumed to have N turns uniformly spaced between an inner radius R_1 and an outer radius R_2, and to lie in the plane $z = z_1$ in cylindrical coordinates (r, ϕ, z). The circular loop is assumed to lie in the plane $z = z_2$ and to have a radius R. The two coils carry currents I_1 and I_2 respectively. This solution is based on the Bessel function expression for the force between two coaxial current loops of radii r and R, lying in the planes $z = z_1$ and $z = z_2$, which is given by [1]:

$$F_z = -\mu_0 \pi I_1 I_2 rR\text{sgn}(z_2 - z_1) \int_0^\infty s J_1(sr) J_1(sR) \exp(-s|z_2 - z_1|) ds. \quad (1)$$

Integrating this equation from $r = R_1$ to $r = R_2$ gives the force between a disk and a ring coil in the form:

$$F_z = -\mu_0 \pi I_1 I_2 \sigma_R R\text{sgn}(z_2 - z_1) \int_{R_1}^{R_2} \int_0^\infty s J_1(sr) J_1(sR) \exp(-s|z_2 - z_1|) dsdr \quad (2)$$

where the disk coil radial current density is given by:

$$\sigma_R = \frac{N}{R_2 - R_1}. \quad (3)$$

The double integration in (2) can be evaluated in closed form by linear superposition of two terms of the form:

$$I_A(R, a, |z_2 - z_1|) = \int_0^a \int_0^\infty sr J_1(sR) J_1(sr) \exp(-s|z_2 - z_1|) dsdr. \quad (4)$$

Recently, in the context of nuclear radiation calculations [2], the related integral below was evaluated in terms of complete elliptic integrals:

$$I_B(R, a, h) = \int_0^a \int_0^\infty J_1(sR) J_0(sr) \exp(-sh) dsdr \quad (5)$$

as:

$$I_B(R, a, h) = \frac{\left(R^2 + h^2\right)^{1/2} + a}{2R} \Lambda_0(\beta_1, k) + \frac{a - \left(R^2 + h^2\right)^{1/2}}{2R} \Lambda_0(\beta_2, k) - \frac{hk}{\pi} \left(\frac{a}{R^3}\right)^{1/2} K(k) \quad (6)$$

where:

$$k = \left(\frac{4aR}{(R+a)^2 + h^2}\right)^{1/2}, \ \beta_1 = \arcsin\left(\frac{\sqrt{(R+a)^2 + h^2}}{\sqrt{R^2 + h^2} + a}\right) \text{ and } \beta_2 = \arcsin\left(\frac{\sqrt{R^2 + h^2} - a}{\sqrt{(R-a)^2 + h^2}}\right).$$

Integrating the radial integral in Eq. (4) by parts with $h = |z_2 - z_1|$ gives:

$$I_A(R, a, h) = I_B(R, a, h) - a I_{(0,1,0)}(R, a, h) \quad (7)$$

where the Bessel-Laplace integral in Eq. (7) is given [3] in terms of elliptic integrals as:

$$I_{(0,1,0)}(R,a,h) = \frac{a}{2R}\left(1 - \frac{hkK(k)}{\pi\sqrt{aR}} + \operatorname{sgn}(R-a)\left(1 - \Lambda_0(\beta_3,k)\right)\right) \tag{8}$$

where: $\beta_3 = \arcsin(\frac{h}{\sqrt{(R-a)^2+h^2}})$.

The equations above give an analytical solution for the force between a disk coil and a ring coil. This solution can then be integrated radially using a package such as Mathematica [4] to give the exact solution for the force between two ring coils as a a single integration of analytical expressions. This can be evaluated to any desired accuracy.

The full paper will present numerical results for a selection of disk/ring and disk/coil combinations.

REFERENCES

1. Conway, J. T., "Forces between thin coils with parallel axes using Bessel functions," *IEEE Trans. Magn.*, Vol. 48, No. 1, Jan. 2012.
2. Conway, J. T., "Geometric efficiency for a circular detector and a linear source of arbitrary orientation and position," *Nucl. Instr. and Meth. Phys. Res. A*, Vol. 622, 555–566, 2010.
3. Conway, J. T., "Exact solutions for the magnetic fields of solenoids and current distributions," *IEEE Trans. Magn.*, Vol. 37, No. 4, 2977–2988, 2001.
4. Wolfram, S., *The Mathematica Book*, 5th Edition, Wolfram Media, Champaign, IL, 2003.

Advances in the Theory of the Circular Waveguide with an Azimuthally Magnetized Ferrite Cylinder and a Dielectric Toroid

Mariana Nikolova Georgieva-Grosse[1] and Georgi Nikolov Georgiev[2]

[1]Consulting and Researcher in Physics and Computer Sciences
Meterstrasse 4, Gerlingen D-70839, Germany
[2]Faculty of Mathematics and Informatics
University of Veliko Tirnovo "St. St. Cyril and Methodius", Veliko Tirnovo BG-5000, Bulgaria

Abstract— The analysis of the circular waveguides, comprising a co-axially positioned ferrite cylinder or toroid of azimuthal magnetization, under normal TE_{0n} modes excitation, faces serious mathematical difficulties [1–16]. One of the most promising ways to overcome them is that, using the complex Kummer (or the complex Kummer and Tricomi) confluent hypergeometric function(s) [8–15]. Its main advantage is the well-developed theory of the latter and the relative simplicity (the single-valuedness) of the first of them [14, 17].

This work extends the recent results [13] on the phase behaviour for the aforesaid sets of fields of a waveguide of the family pointed out, containing a ferrite cylinder, magnetized in azimuthal direction, stuffed in a dielectric toroid in contact with its wall. Following the approach, suggested in the Reference cited, the complex Kummer [14, 17] and the real Bessel and Neumann functions are accepted as wave functions for propagation in the ferrite and dielectric medium, resp. Further, the procedure, employing the purely imaginary roots of the structure's characteristic equation [13], determined numerically, is applied to figure out in normalized form the phase curves of the configuration examined for both signs of the ferrite magnetization. To ease the investigation, the relative permittivities of both strata are assumed identical which diminishes the number of parameters, participating in the equation in question. It is accepted also to normalize the guide radius r_0 and the phase constant of the supported wave β towards frequency and relative permittivity of the ferrite and to denote these generalized quantities by bars, written above the relevant symbols ($\bar{r}_0$ and $\bar{\beta}$, resp.) [8–16].

A set of phase pictures of the transmission line considered is plotted, presenting the dependence of $\bar{\beta}$ on $\bar{r}_0$ with the off-diagonal ferrite permeability tensor element α as parameter, which correspond to various ferrite cylinder to waveguide radius ratios ρ. Their inspection discloses that the phase behaviour of the geometry is much more complicated in relation to that of the circular and coaxial ferrite waveguides [8, 12, 15, 16]. Simultaneously, it possesses similar features to the ones of the structure in which the places of the layers are interchanged [9–12]. Particularly, for specific $|\alpha|$ there are two phase curves $\bar{\beta}_+(\bar{r}_0)$ and $\bar{\beta}_-(\bar{r}_0)$, pertinent to positive and negative ferrite magnetization $\alpha > 0$ and $\alpha < 0$, resp. The characteristics for $\alpha > 0$ are situated completely to the right of the point at the horizontal axis in the phase diagram, depicting the cut-off frequency (the critical guide radius). They are single-valued with respect to $\bar{r}_0$ and describe forward-wave propagation. Unlike them those for $\alpha < 0$ might lie entirely or partially to the left of the point mentioned. In the first case they might be single- or double-valued, conforming to backward or backward- and forward-wave transmission. In the second one their part below cut-off is double-valued, resp. backward- and forward-wave propagation is observed. When the $\bar{\beta}_-(\bar{r}_0)$ — curve is double-valued, there is one (inversion) point at which its direction is reversed. The cut-off itself is magnetically controlled. Above it the character of the $\bar{\beta}_-(\bar{r}_0)$ — phase line and of the concurring wave is like of those, provided $\alpha > 0$. If a part of the $\bar{\beta}_-(\bar{r}_0)$ — characteristic lies to the right of cut-off, it is situated above the $\bar{\beta}_+(\bar{r}_0)$ — one. Accordingly, for $\bar{r}_0$ larger than the critical radius, always it is fulfilled $\bar{\beta}_- > \bar{\beta}_+$ and the structure in this case may afford differential phase shift $\Delta\bar{\beta} = \bar{\beta}_- - \bar{\beta}_+$ ($\Delta\bar{\beta} > 0$).

Similar to the structure with ferrite toroid both phase curves are finite. Likewise, there are special envelope curves for both signs of off-diagonal ferrite tensor element α at which the same end. This is a consequence of the springing up of the $L_{3\pm}$ numbers, connected with the roots of characteristic equation [13]. Physically this result means that the TE_{0n} modes may get excited in the configuration studied in bounded frequency ranges both for $\alpha < 0$ and $\alpha > 0$, as in the one whose outer area is taken by ferrite [9–12]. For comparison the waveguides, entirely filled with the anisotropic medium regarded sustain the fields referred to in a restricted band in case $\alpha < 0$ and beyond the frequency range above for $\alpha > 0$ [8, 12, 15, 16].

The change of ratio ρ influences substantially the phase pattern. Diminishing it from 1 to 0 leads to a shortening of the phase characteristics for both signs of α (of the bands in which propagation may take place). The envelopes are strongly deformed and the cut-off frequencies become smaller. This entails a shrinking of the area in which the structure produces phase shift (operates as digital phase shifter), as well.

REFERENCES

1. Bolle, D. M. and G. S. Heller, "Theoretical considerations on the use of circularly symmetric *TE* modes for digital ferrite phase shifters," *IEEE Trans. Microwave Theory Tech.*, Vol. 13, No. 4, 421–426, July 1965; Correction, *IEEE Trans. Microwave Theory Tech.*, Vol. 34, No. 4, 427, Apr. 1986.
2. Clarricoats, P. J. B. and A. D. Olver, "Propagation in anisotropic radially stratified circular waveguides," *Electron. Lett.*, Vol. 2, 37–38, Jan. 1966.
3. Eaves, R. E. and D. M. Bolle, "Perturbation theoretic calculations of differential phase shifts in ferrite-loaded circularly cylindrical waveguides in the TE_{01} mode," *Electron. Lett.,* Vol. 2, No. 7, 275–277, July 1966.
4. Ince, W. J. and G. N. Tsandoulas, "Modal inversion in circular waveguides, Part II. Application to latching nonreciprocal phasers," *IEEE Trans. Microwave Theory Tech.*, Vol. 19, No. 4, 393–400, Apr. 1971.
5. Samaddar, S. N., "Special functions associated with azimuthally magnetized ferrite rod phase shifters," *J. Appl. Phys.*, Vol. 50, No. 1, 518–520, Jan. 1979.
6. Lindell, I. V., "Variational methods for nonstandard eigenvalue problems in waveguide and resonator analysis," *IEEE Trans. Microwave Theory Tech.*, Vol. 30, No. 8, 1194–1204, Aug. 1982.
7. Baden-Fuller, A. J., *Ferrites at Microwave Frequencies*, IEE Electromagnetic Waves Series 23, Peter Peregrinus, London, UK, 1987.
8. Georgiev, G. N. and M. N. Georgieva-Grosse, "A new property of the complex Kummer function and its application to waveguide propagation," *IEEE Antennas Wireless Propagation Lett.*, Vol. 2, 306–309, Dec. 2003.
9. Georgiev, G. N. and M. N. Georgieva-Grosse, "Phase behaviour of a two-layered circular ferrite-dielectric waveguide with azimuthal magnetization," *Progress In Electromagnetics Research Symposium Abstracts*, 742, Moscow, Russia, Aug. 18–21, 2009; *PIERS Proceedings*, 1473–1477, Moscow, Russia, Aug. 18–21, 2009.
10. Georgiev, G. N. and M. N. Georgieva-Grosse, "Effect of the dielectric filling on the phase behaviour of the circular waveguide with azimuthally magnetized ferrite toroid and dielectric cylinder," *Proc. Asia-Pacific Microwave Conf. APMC-2009*, 870–873, in CDROM, Singapore, Dec. 7–10, 2009.
11. Georgieva-Grosse, M. N. and G. N. Georgiev, "Transmission properties of the circular waveguide, containing an azimuthally magnetized ferrite toroid and a dielectric cylinder," *Proc. 5th Europ. Conf. Antennas Propagat. EuCAP 2011*, 1870–1874, Rome, Italy, Apr. 11–15, 2011.
12. Georgieva-Grosse, M. N. and G. N. Georgiev, "Transmission properties of the circular waveguide completely or partially filled with azimuthally magnetized ferrite: Review of recent results," *Proc. 1st IEEE-APS Topical Conf. Antennas Propagat. Wireless Commun. IEEE APWC'11*, 865–868, in CDROM, Turin, Italy, Sep. 12–16, 2011, Invited Paper in the Special Session "Advances in wireless communications and their applications," organized by M. N. Georgieva-Grosse and G. N. Georgiev.
13. Georgiev, G. N. and M. N. Georgieva-Grosse, "Propagation in the circular waveguide, containing an azimuthally magnetized ferrite cylinder and a dielectric toroid," *Proc. 6th Europ. Conf. Antennas Propagat. EuCAP 2012*, 1141–1145, Prague, Czech Republic, Mar. 26–30, 2012.
14. Georgiev, G. N. and M. N. Georgieva-Grosse, "On the confluent hypergeometric functions and their application: Basic elements of the Tricomi theory. Case of waveguide propagation," *Telecomm. Radioeng.*, Vol. 71, No. 3, 209–216, 2012.
15. Georgiev, G. N. and M. N. Georgieva-Grosse, "Advanced computational methods for analysis of the circular waveguide completely filled with azimuthally magnetized ferrite: Review of recent results," *Proc. Fourteenth Int. Conf. Electromagn. Adv. Applicat. ICEAA'12*, 62–65, in CDROM, Cape Town, South Africa, Sept. 2–7, 2012, Invited Paper in the Special Session "Modern problems of mathematical and computational electromagnetics and their advanced applications," organized by M. N. Georgieva-Grosse and G. N. Georgiev.
16. Georgiev, G. N. and M. N. Georgieva-Grosse, "Circular waveguide, completely filled with azimuthally magnetized ferrite," *Wave Propagation*, Academy Publish, Cheyenne, Wyoming, USA, 2013, in print.
17. Tricomi, F. G., *Funzioni Ipergeometriche Confluenti*, Edizioni Cremonese, Rome, Italy, 1954.

DOA Estimation via Phase Measurement

Andrew Im, Matthew Gialich, Zekeriya Aliyazicioglu, and H. K. Hwang
Electrical and Computer Engineering, California State Polytechnic University-Pomona
3801 W. Temple Ave, Pomona, CA 91768, USA

Abstract— This paper investigates direction of arrival (DOA) estimation using array antenna with large inter-element spacing. The estimation technique is based on measuring the phases of the array elements. Since the inter-element spacing is larger than signal wavelength, the measured phase of each element has ambiguity. The possible phase combination of array elements is a large number. The proper phase combination is derived from the least square method. Once the proper phase combination is defined, the signal's DOA can be computed. Simulation results are presented in this paper.

Universal Properties of Electromagnetic Pulses

John Lekner
MacDiarmid Institute and School of Chemistry and Physics
Victoria University, Wellington, New Zealand

Abstract— We survey the existing known universal properties of electromagnetic pulses, and discuss their consequences. The established universal properties are (i) the time invariance of the total electromagnetic energy U, momentum cP_z and angular momentum J_z of the pulse, and (ii) the inequality $cP_z < U$. (Pulse propagation is along the z-direction.) In both (i) and (ii) the theorems follow directly from Maxwell's equations [1–3].

The conservation of energy, momentum and angular momentum is no surprise, but the inequality $cP_z < U$ implies that all localized electromagnetic pulses have a zero-momentum frame (not a 'rest' frame, waves are never at rest). The above is of course in contradistinction to Einstein's light quantum, for which the momentum P is purely in one direction, and $cP = U$. The implication seems to be that we cannot form a model of the photon by any pulse wave-function satisfying Maxwell's equations.

The momentum P and energy U form a four-vector $(cP,\ U)$, and $U^2 - c^2P^2$ is a Lorentz invariant. We show that $\langle U^2 - c^2P^2 \rangle$ is positive, reinforcing the above inequality.

We also discuss the helicity of electromagnetic pulses, and the counter-intuitive relation between the helicity and angular momentum of certain exactly calculable examples, one of which is illustrated below [4].

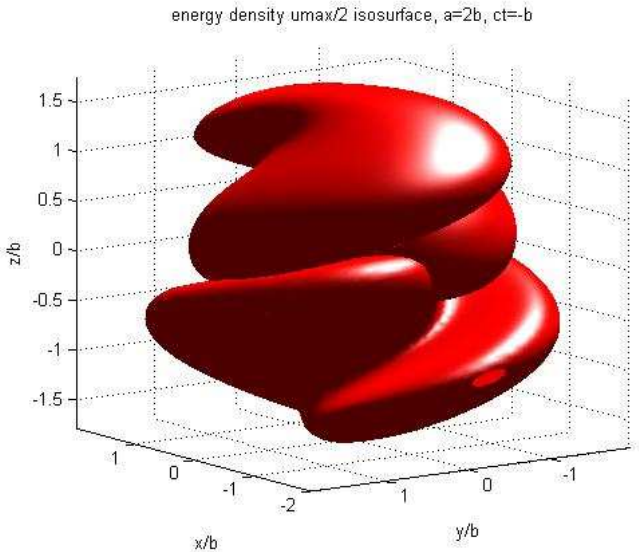

REFERENCES

1. *J. Opt. A: Pure Appl. Opt.*, Vol. 5, L15, 2003.
2. *J. Opt. A: Pure Appl. Opt.*, Vol. 6, 146, 2004.
3. *J. Opt. A: Pure Appl. Opt.*, Vol. 6, S128, 2004.
4. *J. Opt. A: Pure Appl. Opt.*, Vol. 5, L29, 2003.

Approximate Solution Method of Nonlinear Helmholtz Equation

M. S. Sautbekova and S. S. Sautbekov
Eurasian National University, Kazakhstan

Abstract— In recent work a new method of approximate solution of nonlinear equations is proposed. Analytical solution is obtained by the method of successive approximations in the form of an infinite series, where successive term is convolution of the last. The main contribution to the asymptotic solution is given. The condition of solution convergence is considered. The proposed method for one-dimensional nonlinear problem is tested. Results that are obtained by using the convolutions and the numerical method are compared.

We consider nonlinear Helmholtz equation of the form

$$(k_0^2 + \Delta)U = -\alpha|U|^2U + f, \tag{1}$$

where k_0 and α are constants ($|\alpha| \ll 1$). For parameter k:

$$\left(k_0^2 + \frac{k^2}{r^2} + \Delta\right)U = \left(\frac{k^2}{r^2} - \alpha|U|^2\right)U + f, \tag{2}$$

where k is constant. Let ε be a fundamental solution of operator $\left(k_0^2 + \frac{k^2}{r^2} + \Delta\right) := T$,

$$T\varepsilon = \delta. \tag{3}$$

Then by taking convolution of (2) from the right and the left hand side we get the next:

$$U = \left(\frac{k^2}{r^2} - \alpha|U|^2\right)U * \varepsilon + f * \varepsilon. \tag{4}$$

We choose k such, that it satisfy the following condition:

$$\left|\frac{k^2}{r^2} - \alpha|U|^2\right| \ll 1. \tag{5}$$

If the initial approximation is

$$U_0 = f * \varepsilon. \tag{6}$$

And its important to note that

$$\left|\frac{k^2}{r^2} - \alpha|f * \varepsilon|^2\right| \ll 1 \tag{7}$$

Afterwards we come to the following:

$$k^2 = \alpha r^2|f * \varepsilon|^2, \quad r \gg 1, \tag{8}$$

or

$$k = \sqrt{\alpha}r|f * \varepsilon|. \tag{9}$$

Note that on the infinity $f * \varepsilon$ behaviour itself proportionally to $\frac{1}{r}$. It means that the value of k is a constant.

Then from (4) we obtain the iterated solution

$$U_{n+1} = \left(\frac{k^2}{r^2} - \alpha|U_n|^2\right)U_n * \varepsilon + f * \varepsilon. \tag{10}$$

The one-dimensional case is considered in $\mathbb{R}^1$. Easily finds ε [1].

REFERENCES

1. Vladimirov, V. S., *Equations of Mathematical Physics*, Nauka, Moscow, 1981 (in Russian).
2. Polyanin, A. D., V. F. Zaitsev, and A. I. Zhurov, *Methods for Solving Nonlinear Equations of Mathematical Physics and Mechanics*, Fizmatlit, Moscow, 2005 (in Russian).

Reconstruction Parameters of Local Scattering Sources of a Cylindrical Object from the Backscattering Pattern

S. N. Kutishchev
Department of Physics and Chemistry
Voronezh State University of Architecture and Civil Engineering
Voronezh, Russia

Abstract— In this work I prove the ability of quantity reconstruction, amplitudes and coordinates of cylindrical object local scattering sources from the backscattering pattern. They are performed as the results of numerical solution for the infinite perfect conducting cylinder of the triangular cross section in case of E-polarization of the incident plane electromagnetic wave. The analysis of the obtained numerical results allows to make the conclusion, that in the considered example the absolute error of reconstruction of the transverse coordinates of the local scattering sources is $\Delta y \approx 0.25\lambda$ (λ — length of the incident plane electromagnetic wave) and the absolute error of reconstruction of their longitudinal coordinates is $\Delta x \approx 0.3\lambda$. So this method lets us reconstruct from the backscattering pattern the parameters (quantity, amplitudes and coordinates) of isotropic stiff-tied and electrodynamically independent local scattering sources of the cylindrical object. In this case it is necessary to fulfill the following conditions. The local scattering sources amplitudes should be the same order, in transverse and longitudinal directions the local scattering sources should be separated into distances more than apparatus resolution $\delta = \lambda/(2\Delta\varphi)$ ($\Delta\varphi$ — value of sector of aspect angles), and the object maximum size does not have to be more than approximately 50λ. It was shown the limit and ability of the further development of the offered method.

Universal Properties of Electromagnetic Beams

John Lekner
MacDiarmid Institute and School of Chemistry and Physics
Victoria University, Wellington, New Zealand

Abstract— We survey the existing known universal properties of electromagnetic beams, and discuss the possibility of a new one. The established universal properties are (i) the existence of beam invariants, which follow from conservation laws, and (ii) various non-existence theorems arising out of beam localization transversely to the direction of propagation. In both (i) and (ii) the theorems follow directly from Maxwell's equations.

The conservation of energy, momentum and angular momentum lead to seven beam invariants, the simplest of which is the integral across a transverse section of an electromagnetic beam of the time-averaged longitudinal component of the momentum density. This integral is the same for any transverse section: it is an *invariant*. This particular invariant comes from the conservation of energy; the conservation of momentum leads to three invariant integrals over components of the electromagnetic stress tensor, and likewise three more invariants come from the conservation of angular momentum [1, 2].

The non-existence theorems show that the properties of the textbook electromagnetic plane wave cannot be realized for real (transversely finite) beams. They assert the non-existence of: 1: Pure TEM beam modes, 2: Beams of fixed linear polarization, 3: Beams which are everywhere circularly polarized in a fixed plane, and 4: Beams within which the energy velocity is everywhere in the same direction and magnitude c [3].

In addition to these established facts, we argue in favour of the universality of rings of zeros of the beam wave function in the focal plane, leading to wave vortices, as illustrated below.

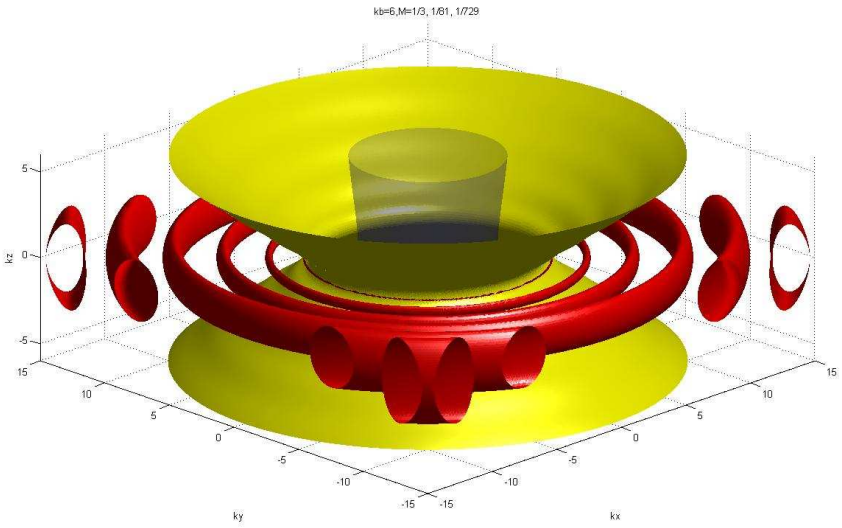

REFERENCES

1. Lekner, J., "Invariants of electromagnetic beams," *J. Opt. A: Pure Appl. Opt.*, Vol. 6, 204–209, 2004.
2. Lekner, J., "Invariants of three types of generalized bessel beams," *J. Opt. A: Pure Appl. Opt.*, Vol. 6, 837–843, 2004.
3. Lekner, J., "Polarization of tightly focused laser beams," *J. Opt. A: Pure Appl. Opt.*, Vol. 5, 6–14, 2003.

Session 2P5
Wideband and Multi-band Antennas

Wide Band Open Ended Air Gap RLSA Antenna at 26 GHz Frequency Band
Imran Mohd Ibrahim, Tharek Bin Abdul Rahman, Mursyidul Idzam bin Sabran, Ulaganathen Kesavan, T. Purnamirza, ... 332
Design of Wideband Monopole Antennas Using a Simple Tapered Feed Line and Slot
Li Liu, X. J. Yang, Sing Wai Cheung, ... 333
A Grounded CPW Transparent UWB Antenna for UHF and Microwave Frequency Application
Thomas Peter, Sing Wai Cheung, Sharul Kamal Bin Abdul Rahim, Tharek Bin Abdul Rahman, ... 335
A Printed Dipole Antenna with U-line Matched for Dual-band WiFi Applications
Churng-Jou Tsai, Bo-Yuan Tsai, ... 336
Compact Dual-band Monopole Antenna for 2.4/3.5 GHz WiMAX Applications
Xiao Lei Sun, Sing Wai Cheung, Tung Ip Yuk, ... 337
Dual-band Transparent Antenna for ISM Band Applications
Mohd Subri Bin Abdul Rani, Sharul Kamal Bin Abdul Rahim, Tharek Bin Abdul Rahman, Thomas Peter, Sing Wai Cheung, ... 338
Developing Alternatives of Small Monopole Antenna Design for Achieving 4G-LTE Requirements in a Limited Antenna Size
Nassrin Ibrahim Mohamed Elamin, Tharek Bin Abdul Rahman, Amuda Yusuf Abdulrahman, ... 339
Investigation on CPW Koch Antenna Durability for Microwave Imaging
Roshayati Yahya, Muhammad Ramlee Bin Kamarudin, Norhudah Seman, Mursyidul Idzam bin Sabran, Mohd Faizal Jamlos, ... 340
P-shape Monopole Antenna Design for WBAN Application
Ebrahim Sailan Alabidi, Muhammad Ramlee Bin Kamarudin, Tharek Bin Abdul Rahman, Hashimu Uledi Iddi, ... 342
Planar UWB Antenna with Dual Band Notch Characteristics
Rezaul Azim, Mohammad Tariqul Islam, Ahmed Toaha Mobashsher, ... 343

Wide Band Open Ended Air Gap RLSA Antenna at 26 GHz Frequency Band

I. M. Ibrahim[1], **T. A. Rahman**[2], **M. I. Sabran**[2], **U. Kesavan**[2], **and T. Purnamirza**[2]

[1]Faculty of Electronics and Computer Engineering, Universiti Teknikal Malaysia Melaka, Malaysia
[2]Wireless Communication Centre, Universiti Teknologi Malaysia, Malaysia

Abstract— RLSA antenna is a popular candidate for many applications such as Direct Broadcast Satellite Reception, Point to Point Microwave Link, RFID and Wimax Application. This is due to its capability of carrying high speed signal with high directivity characteristic and capability of beam steering and beam shaping. This paper will introduce the RLSA antenna designed at the frequency of 26 GHz for wireless backbone application. The antenna design was utilize open ended air gap as a separator between radiation surface and ground plane. The open air gap cavity structure normally implemented in broadband planar antennas. This structure normally provide a wide bandwidth and good return loss on the desired frequency. Therefore, an investigation of this technique and hybrid with FR4 board as a cavity material will be very interesting due to condition of easy to manufacture, lighter the antenna weight and durable. The model of RLSA antenna at 26 GHz has been simulated. The results obtained a −25 dB of reflection coefficient, 23.68 dBi of directivity gain with wide antenna bandwidth capability. This research found an opportunity of utilizing RLSA antenna concept for extreme high frequency band application.

Design of Wideband Monopole Antennas Using a Simple Tapered Feed Line and Slot

L. Liu, X. J. Yang, and S. W. Cheung
Department of Electrical and Electronic Engineering
The University of Hong Kong, Hong Kong, China

Abstract— This paper presents the results from a study of a simple wideband monopole antenna. The antenna has a half-elliptical shaped radiator with microstrip-fed and a total size of $24 \times 30 \times 0.762\,\text{mm}^3$. The extremely wideband characteristic from 3.1–40 GHz of the antenna is achieved by simply using a tapered feed line and a small square slot on the ground plane.

Introduction: Planar ultrawideband (UWB) monopole antennas, due to low cost, low power and low complexity, have been developed quickly for uses in wireless communications [1]. To achieve wideband operation and stable performance for planar UWB antennas, different methods have been proposed. These methods included using resonant structures [2], parasite elements [3], filters [4], slots [5], different shaped radiators [6], modifying the shape of the radiator [7], adding slots on the ground plane [8], and modifying the shapes of the ground planes [9, 10]. Some researchers also combined several methods together to optimize the designs [11–13].

In this study, a simple planar monopole antenna with a half-elliptical shaped radiator and microstrip-fed is used. The feed line connected to the radiator is tapering toward it. A simple rectangular slot is etched at the top edge of the ground plan on the other side of the substrate right underneath the feed line. Results show that, with a compact size $24 \times 30 \times 0.762\,\text{mm}^3$, an extremely bandwidth of 3.1–40 GHz can be easily obtained by optimizing the dimensions of the tapering and the slot.

REFERENCES

1. Chen, Z. N., M. J. Ammann, X. Qing, X. H. Wu, T. S. P. See, and A. Cai, "Planar antennas," *IEEE Microwave Magazine*, Vol. 7, 63–73, 2006.
2. Sadeghzadeh-Sheikhan, R. A., M. Naser-Moghadasi, E. Ebadifallah, H. Rousta, M. Katouli, and B. S. Virdee, "Planar monopole antenna employing back-plane ladder-shaped resonant structure for ultra-wideband performance," *IET Microwaves, Antennas & Propagation,* Vol. 4, No. 9, 1327–1335, September 2010.
3. Martins, T. C., R. M. S. de Oliveira, and C. L. S. Sobrinho, "Use of square parasite elements to increase the bandwidth of planar monopole antenna for UWB systems," *2007 SBMO/IEEE MTT-S International Microwave and Optoelectronics Conference*, 427–431, October–November 2007.
4. Barakat, A. and M. El-Khamy, "Bandwidth extension of UWB planar antenna with band-notched characteristics," *2010 IEEE Middle East Conference on Antennas and Propagation (MECAP)*, 1–5, October 2010.
5. Wang, H. and Y. Li, "Bandwidth enhancement of a wide slot UWB antenna with a notch band characteristic," *2011 IEEE 3rd International Conference on Communication Software and Networks (ICCSN)*, 365–368, May 2011.
6. Naktong, W. and A. Ruengwaree, "Increasing bandwidth of flambeau-shape monopole antenna for UWB application," *2011 8th International Conference on Electrical Engineering/Electronics, Computer, Telecommunications and Information Technology (ECTI-CON)*, 172–175, May 2011.
7. Zaker, R. and A. Abdipour, "A very compact ultrawideband printed omnidirectional monopole antenna," *IEEE Antennas and Wireless Propagation Letters*, Vol. 9, 471–473, 2010.
8. Sun, Y. Y., M. T. Islam, S. W. Cheung, T. I. Yuk, R. Azim, and N. Misran, "Offset-fed UWB antenna with multi-slotted ground plane," *2011 International Workshop on Antenna Technology (iWAT)*, 432–436, March 2011.
9. Chang, D., J. Liu, B. Zeng, and M. Liu, "Impedance bandwidth enhancement for UWB slot antenna," *2007 International Workshop on Antenna Technology: Small and Smart Antennas Metamaterials and Applications*, 184–187, March 2007.
10. Leib, M., M. Frei, and W. Menzel, "A microstrip-fed Ultra-wideband slot antenna," *2009 IEEE Antennas and Propagation Society International Symposium,* 1–4, June 2009.

11. Nashaat, D., H. A. Elsadek, E. Abdallah, H. Ellhenawy, and M. F. Iskander, "Enhancement of ultra-wide bandwidth of microstrip monopole antenna by using metamaterial structures," *2009 IEEE Antennas and Propagation Society International Symposium*, 1–4, June 2009.
12. Wu, Q., R. Jin, J. Geng, and M. Ding, "Printed omni-directional UWB monopole antenna with very compact size," *IEEE Transactions on Antennas and Propagation,* Vol. 56, No. 3, 896–899, March 2008.
13. Koohestani, M., M. N. Moghadasi, and B. S. Virdee, "Miniature microstrip-fed ultra-wideband printed monopole antenna with a partial ground plane structure," *IET Microwaves, Antennas and Propagation,* Vol. 5, No. 14, 1683–1689, November 2011.

A Grounded CPW Transparent UWB Antenna for UHF and Microwave Frequency Application

T. Peter[1], **S. W. Cheung**[2], **S. K. A. Rahim**[3], **and A. R. Tharek**[3]

[1]Department of Electronics and Computer Engineering
Brunel University, Uxbridge, Middlesex, UK
[2]Department of Electronics and Electrical Engineering
University of Hong Kong, Pokfulam Road, Hong Kong, China
[3]Wireless Communication Centre, Faculty of Electrical Engineering
University Technology Malaysia, Malaysia

Abstract— A grounded CPW transparent ultra-wideband (UWB) antenna for Ultra High Frequency (UHF) and microwave frequency application is proposed in this paper. The proposed antenna covers a bandwidth starting from as low as 500 MHz to the upper limit of the FCC UWB bandwidth of 10.6 GHz. This enables the antenna to be used for a very wide range of applications ranging from narrow band UHF devices to high data rate UWB transceivers. The antenna is fabricated using AgHT-8 for the CPW and radiator patch on a 1 mm thick glass substrate with an Indium Tin Oxide (ITO) ground. The AgHT-8 has a sheet resistance of $8\,\Omega\cdot$m while the ITO, a sheet resistance of $4\,\Omega\cdot$m. The overall size of the antenna is $64 \times 67\,\text{mm}^2$. The antenna has a consistent flat 10 dB return loss across the entire bandwidth. The antenna is suitable for integrating onto window glass of homes and buildings as it does not affect the aesthetics of the building. The AgHT-8 layer of the antenna additionally provides sun-shielding from harmful sun-rays and keeps the building cool thus conserving energy required for air-conditioning in hot climates. As such the antenna provides an integrated wireless communication and energy conservation solution for modern day homes and buildings.

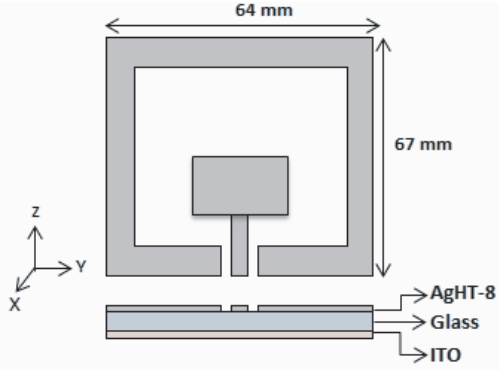

Figure 1: Geometry of the proposed transparent UWB antenna.

A Printed Dipole Antenna with U-line Matched for Dual-band WiFi Applications

Churng-Jou Tsai and Bo-Yuan Tsai
Graduate School of Computer and Communication, Kun Shan University, Tainan, Taiwan, R.O.C.

Abstract— A dual-band WiFi printed dipole antenna is presented in this paper, its PCB size is 7.35 mm × 53 mm × 1 mm. This long and narrow PCB antenna will be applied to the wireless AP and has the omni-directional radiation patterns. This double-sided designed antenna uses a U-line to match and control the bandwidth. The antenna only has 2.36–2.57 GHz and 4.85–6 GHz WiFi bands, the return loss of the remaining frequency maintains in the region of reflection loss larger than −6 dB to reduce interference from outside of the WiFi bands. The simulation results of the architecture, bandwidth and pattern will be presented in this paper by using the simulation of Ansoft HFSS.

Compact Dual-band Monopole Antenna for 2.4/3.5 GHz WiMAX Applications

X. L. Sun, S. W. Cheung, and T. I. Yuk
Department of Electrical and Electronic Engineering
The University of Hong Kong, Hong Kong, China

Abstract— The design of a microstrip-fed dual-band monopole antenna with compact size for use in wireless devices of the 2.4 and 3.5 GHz worldwide interoperability for microwave access (WiMAX) system is presented. The antenna has two radiating branches resonating at around 2.4 GHz and 3.5 GHz. One is folded and the other one is meandered to achieve a size of $40 \times 20\,\text{mm}^2$. The two working bands can be independently set using the lengths of the two radiating branches. The antenna is designed and optimized using the EM simulation tool CST on a $40 \times 35\,\text{mm}^2$ dielectric substrate with a relative permittivity (ε_r) of 3.5, thickness of 0.8 mm, and loss tangent ($\tan\delta$) of 0.004. For verification of simulation results, the antenna is fabricated and measured using the antenna measurement system, Satimo Starlab. In measurement, a feeding cable is used to connect the antenna to the measurement system, which affects the measured results and produces disagreements between the simulated and measured results. To evaluate the cable effects, the cable is modeled using CST and included in simulation. Simulation results with and without the cable model and the measurement results are presented in this paper. With the cable model, the simulated results show better agreements with the measurements. The simulated and measured radiation patterns, efficiencies and gains of the proposed antenna are also presented in this paper. The results show that the proposed antenna has good monopole-like radiation characteristics in the 2.4 GHz and 3.5 GHz operating bands.

Dual-band Transparent Antenna for ISM Band Applications

M. S. A. Rani[1], **S. K. A. Rahim**[1], **A. R. Tharek**[1], **T. Peter**[2], **and S. W. Cheung**[3]

[1]Wireless Communication Centre, Faculty of Electrical Engineering
University Technology Malaysia, Malaysia
[2]Department of Electronics and Computer Engineering
Brunel University, Uxbridge, Middlesex, UK
[3]Department of Electronics and Electrical Engineering
University of Hong Kong, Pokfulam Road, Hong Kong, China

Abstract— A compact dual-band transparent antenna with co-planar waveguide (CPW)-fed for wireless applications in the unlicensed industrial, scientific and medical (ISM) band is proposed in this paper. The proposed antenna generates two bands at 2.4 and 5.8 GHz for Wireless Local Area Network (WLAN) access points and point-to-point applications, respectively. The CPW technique is used to feed the circular radiating element. Two slots lines are introduced in the antenna to obtain the desired resonating frequencies. Results and analysis from introduction of the slot lines are highlighted in this paper. The antenna utilizes a conductive silver coated film (AgHT) as the core material as the substrate, making the antenna almost 82% transparent. The proposed antenna is very small, having an overal size of $60 \times 60 \times 0.175 mm^3$, when compared to other conventional non-transparent antenna operating at the same frequencies of 2.45 and 5.8 GHz. The combination of transparency and small size enables the antenna to be integrated into any flat surface with low chances of being noticed. The antenna can be integrated into the window glass of a building and performs as an access point to provide wireless signal around it. In addition, the antenna can also serve as a tinted film to provide an extra layer of protection from the sun radiation when integrated into the buildings' windows. The integration of the antenna into building windows will reduces the space consumption and remove the space limitation problems faced when using the conventional non-transparent antenna. The proposed prototype antenna has acceptable performances in terms of return loss, gain, efficiency and omni-directional radiation pattern. Simulated and experimental results are discussed.

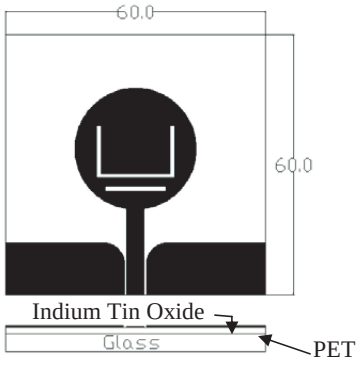

Figure 1: Geometry of proposed design (mm).

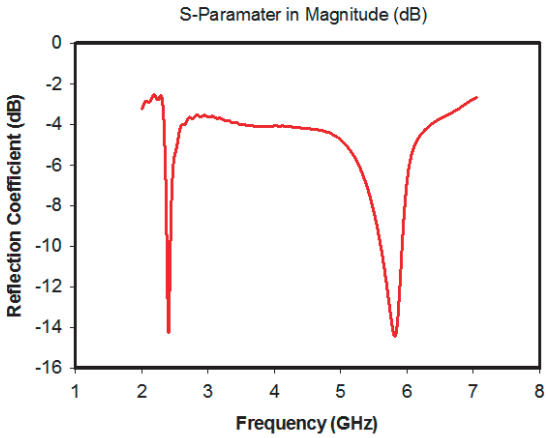

Figure 2: Simulated reflection coefficient (dB).

Developing Alternatives of Small Monopole Antenna Design for Achieving 4G-LTE Requirements in a Limited Antenna Size

N. I. Mohamed, T. A. Rahman, and A. Y. Abdulrahman
Wireless Communication Center (WCC), Faculty of Electrical Engineering
Universiti Teknologi Malaysia (UTM), Malaysia

Abstract— Achieving Long Term Evolution (LTE) frequency bands (the second generation (2G), third generation (3G), and the proposed fourth generation (4G) frequency bands) using a small-size antenna in a compact device remains a major technical challenge. This paper surveys the recent literature on two types of Universal Serial Bus USB LTE antennas, the Meander Line Antenna (MLA) which is one of the alternatives of the small monopole antenna and the Slot Patch multiband antenna (SPA), which is vital for multiband through slotting patch radiators. Consequently a new geometrical design of multiband antenna is proposed in this paper. The proposed antenna design operates at four separate bands: 1.5, 1.8, 1.9, and 2.6 GHz for supporting LTE wireless device of USB Dongle.

Investigation on CPW Koch Antenna Durability for Microwave Imaging

R. Yahya[1, 2], **M. R. Kamarudin**[2], **N. Seman**[2], **M. I. Sabran**[2], **and M. F. Jamlos**[3]

[1]Department of Communication Engineering, Faculty of Electrical and Electronic Engineering
Universiti Tun Hussein Onn Malaysia (UTHM), Parit Raja, Batu Pahat, Johor 86400, Malaysia
[2]Wireless Communication Center (WCC)
Universiti Teknologi Malaysia (UTM), Skudai, Johor Bahru, Johor 81310, Malaysia
[3]Advanced Communication Engineering Center (ACE)
School of Computer and Communication Engineering
Universiti Malaysia Perlis (UniMAP), Kampus Pauh Putra
Arau, Perlis 02600, Malaysia

Abstract— Recently, there is much interest in flexible and wearable communication system specifically for fabric based antenna. In the near future, fabric based antenna will become good candidate to be used in Microwave Imaging of medical application due to ease integration with clothes, light, and compact. In this paper, the investigation on the durability of fabric antenna (shown in Figure 1) is presented. This antenna is inspired by the author in [1]. However, the antenna in [1] is fabricated on FR4 strip board and it is not either flexible or wearable antenna. Here, an antenna which made from pure copper fabric and patched onto a denim jean with $\varepsilon_r \approx 2.3$ is fabricated. This fabric antenna has wider operating frequency from 1.2–8.2 GHz (bandwidth = 6 GHz) which is 2.6 GHz bandwidth greater than antenna in [1]. Figure 2 shows the simulation and measurement result of S_{11}. It can be seen clearly that good agreement between simulation and measurement result is obtained. The antenna is then investigated on its durability (crumpled, ironed, wetted, washed, and dried). The results of investigated items are shown in Figure 3 and Figure 4. From these figures, it can be noticed that the antenna provides almost the same bandwidth from 1.2–8 GHz for crumpled, ironed, wetted, and dried, except washed.

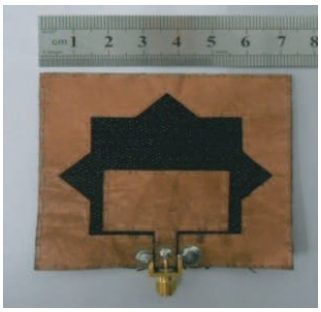

Figure 1: Fully textile Koch antenna.

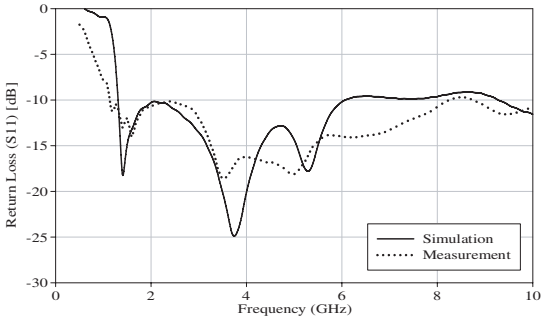

Figure 2: Return loss of the Koch antenna.

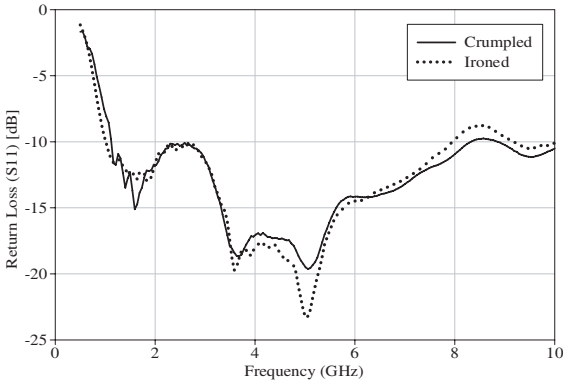

Figure 3: Return loss of crumpled and ironed antenna.

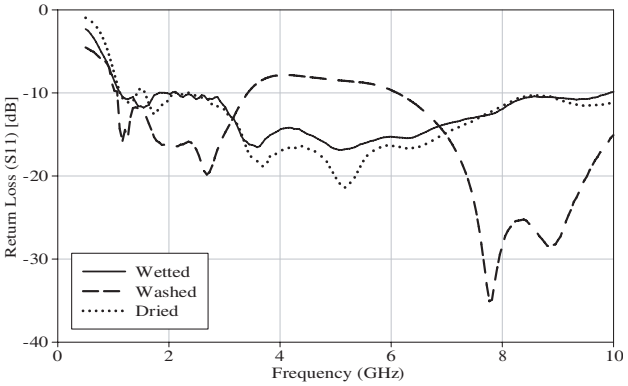

Figure 4: Return loss of wetted, washed, and dried antenna.

This is caused by high water content in the fabric which decreases the performance of the washed antenna. However, after it is dried, the performance become back to the normal. In conclusion, this fabric antenna is stable for most conditions and can be used for flexible and wearable antenna in microwave imaging of medical application.

REFERENCES

1. Zhang, H., H. Xu, B. Tian, and X. Zeng, "CPW-fed fractal slot antenna for UWB application," Vol. 2012, 3–6, 2012.

P-shape Monopole Antenna Design for WBAN Application

Ebrahim Sailan Aabidi, M. R. Kamarudin, T. A. Rahman, and Hashimu Uledi Iddi
Wireless Communication Centre (WCC)
Universiti Teknologi Malaysia, UTM Skudai, Johor 81310, Malaysia

Abstract— This paper presents P-shape monopole antenna for wireless body area network (WBAN) application at 3.1 to 5.1 GHz. The proposed antenna is designed on FR4 substrate with dielectric constant (ε_r) of 4.4 and thickness of 1.6 mm. The final optimized design is $32 \times 28\,\text{mm}^2$. Figure 1 shows the prototype of P-shape antenna. The small size of P-shape antenna is suitable for WBAN application as it provide wide bandwidth (about 2 GHz of bandwidth). Figure 2 shows the measurement and simulation result of the P-shape antenna for the return loss. For body simulations, the three layers of the body tissue model have been used. As the antenna provides wide bandwidth, thus not much different can be seen in the return loss results. However, for other parameters such as gain and specific absorption rate (SAR) are influenced by the factor of distance between the antenna and the body. Here, the specific absorption rate (SAR) is increased when the antenna is placed near the body especially when the frequency is increased. The SAR values of the proposed antenna are 17.3, 18 and 19.92 w/kg at 3.1 GHz, 4.1 GHz and 5.1 GHz, respectively. On the other hand, the gains of P-shape antenna in the free space are 2.7 dBi, 1.4 dBi and 2.2 dBi at 3.1 GHz, 4.1 GHz and 5.1 GHz, respectively. In contrast, the gains obtained when it brought closer to numerical human phantom are 0.7 dBi at 3.1 GHz, 0.9 dBi at 4.1 GHz and 1.1 dBi at 5.1 GHz. In conclusion, the gains are reduced as the distance between the antenna and the body is very close.

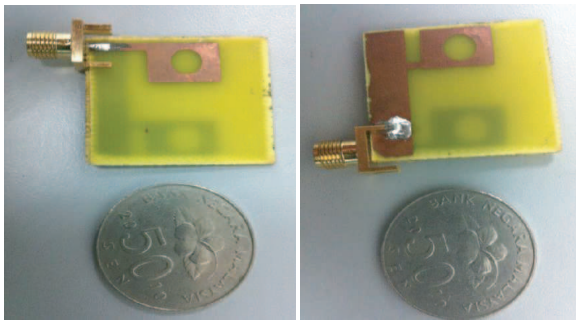

(a) (b)

Figure 1: Prototype of P-shape antenna, (a) front view, (b) back view.

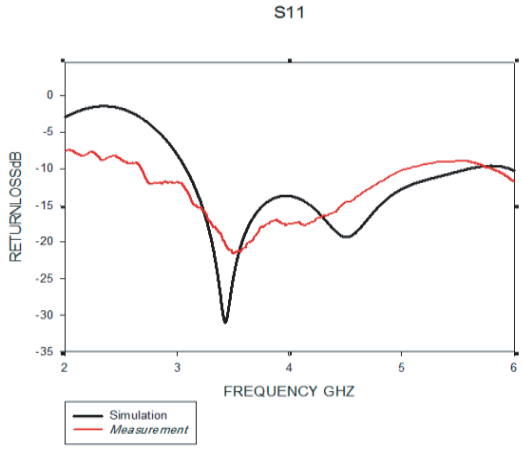

Figure 2: Return loss results in free space.

Planar UWB Antenna with Dual Band Notch Characteristics

Rezaul Azim[1], **Mohammad Tariqul Islam**[1], **and Ahmed Toaha Mobashsher**[2]

[1]Institute of Space Science (ANGKASA), Universiti Kebangsaan Malaysia
UKM Bangi 43600, Malaysia
[2]School of Information Technology and Electrical Engineering
The University of Queensland, Brisbane St Lucia, QLD 4072, Australia

Abstract— In February 2002, the US the Federal Communications Commission (FCC) released the frequency spectrum of 3.1 to 10.6 GHz as an unlicensed band for ultra-wideband (UWB) radio communication. However, over the assigned ultra-wideband frequency band there are some other narrow band services such as WiMAX (3.3–3.7 GHz) and WLAN (5.15–5.825 GHz). These existing narrowband may cause potential electromagnetic interference with the UWB systems. Therefore, it is necessary to design antennas that are capable of notching the frequency band from 3.3–3.7 GHz and 5.15–5.825 GHz in UWB systems to minimize the possible interference between UWB and existing WiMAX and WLAN systems, i.e., antennas with dual band-notched characteristics.

In this paper, a dual band notch planar monopole antenna is proposed for UWB applications. The antenna consists of rectangular radiating patch and a partial ground plane. The microstrip line-fed radiating patch is printed on one side of an inexpensive FR4 dielectric substrate of thickness 1.6 and dielectric constant 4.6 while the partial ground plane of side length 5.5 mm is printed on the other side of the substrate. The length and width of the microstrip feed line are fixed at 2.75 mm and 6 mm respectively to achieve a 50 Ω characteristics impedance. An SMA is connected to the port of the feeding microstrip line. To realize dual band-notch characteristics, a three arm parasitic element has been inserted on the back side of the substrate and couple to the radiating patch. The lengths of the vertical arms of the parasitic element are 5 and 6.5 mm respectively while the length of horizontal arm is 22.5 mm. At the notch frequencies, the current flows are more dominant around the parasitic element and they are oppositely directed between the parasitic element and the radiating patch. Therefore, the resultant radiation fields cancel out and high attenuation near the notch frequency is proposed. It is observed that by properly designing the three arm parasitic element above the partial ground plane, good frequency rejection of 3.3–3.65 GHz and 5.12–5.52 GHz with a wide operating band from 3.08 to more than 11 GHz can be obtained. Compared to the recently reported dual band notch UWB antennas, the proposed antenna has a simple structure to achieve the dual notch-band characteristics to reduce the potential interference between UWB and existing WIMAX and WLAN systems. Furthermore, a stable radiation pattern and gain except in the notch frequency bands makes the proposed antenna a suitable candidate for future UWB applications.

Session 2P6
Optics and Photonics, Fiber, Lasers, Gyrotrons

Can There Be WDM Solitons in Fibers?
Cavour Yeh, F. I. Shimabukuro, ... 346

Investigation of Two Bidirectional C + L Band Fiber Amplifiers with Pumping Sharing and Wavelength Reused Mechanisms
Shien-Kuei Liaw, Yi-Lin Yu, Y. C. Wang, W. F. Wu, R. Y. Liu, ... 347

Optical-circulator-based Single-frequency Fiber Laser Using Absorber and Subring Cavity in the Linear Cavity
Shien-Kuei Liaw, H. Wang, Haiyin Hsu, C. S. Shin, R. Y. Liu, ... 348

Generation of Terahertz, Microwave, Radio Waves from a Laser-excited Wire Antenna
Kuan-Yan Huang, Chia-Hsiang Chen, Ming-Hsiung Wu, Yen-Chieh Huang, ... 350

An Improved Method for SNR Estimation on Optical Remote Sensing Images
Xinhong Wang, Chuanrong Li, Bo Zhu, Lingli Tang, Hong Yuan, ... 351

Arc-induced Long Period Fiber Gratings Based on Flat-clad Fibers
Zhi-Zong Zheng, Chai-Ming Li, Cheng-Ling Lee, Jing-Shyang Horng, ... 353

Optical Properties of Raman-enhancing Substrates
Hui-Hsin Hsiao, Juen-Kai Wang, Hung-Chun Chang, ... 354

Analysis of Frequency Coded Quantum Key Distribution for Secure Communication
Hum Nath Parajuli, Reinhold Herschel, Stefan Schwarz, C. G. Schäffer, ... 355

Transmitted Characterization of 625 Mbps/15 GHz ROF Signal Using a Direct Modulated Baseband Signal and Twice Optical Carrier Suppression Modulation
Yu-Peng Chang, Wen-Jeng Ho, Jhe-Min Lin, Peng-Chun Peng, Hai-Han Lu, ... 356

Experimental Study of All-optical Frequency Conversion Using Period-one Dynamics of Semiconductor Lasers
Yu-Han Hung, Sheng-Kwang Hwang, ... 357

A Fault-tolerant Mechanism on Star-ring Based Ethernet Passive Optical Networks
Zen-Der Shyu, I-Shyan Hwang, I. C. Lin, ... 358

A New Mechanism to Improve Bandwidth Utilization and QoS of IPTV in Ethernet Passive Optical Network
I-Shyan Hwang, Andrew Tanny Liem, Ali Akbar Nikoukar, Ku Chieh Chen, ... 359

The Influence of the Electromagnetic Wave on the Nonlinear Quantum Acoustoelectric Current in a Quantum Well
Nguyen Van Hieu, Nguyen Quang Bau, Nguyen Van Nghia, ... 360

Can There Be WDM Solitons in Fibers?

Cavour Yeh and F. I. Shimabukuro
California Advanced Studies, 2432 Nalin Dr., Los Angeles, CA 90077, USA

Abstract— The existence of solitons on single wavelength beam in fiber is a marvel of nature. For a pulse propagating on a single wavelength beam in a fiber, it is amazing that the linear dispersive effect of pulse broadening can be cancelled exactly by the non-linear self-phase modulating effect of pulse compression such that the pulse will not degrade as it propagates along the fiber. This pulse is called a soliton. This delicately balanced condition can easily be perturbed or destroyed, when there are co-propagating pulses on different wavelength beams, called wavelength division multiplexed (WDM) beams, in this fiber. This degradation is due to the presence of the non-linear cross-phase modulation effect which can act on co-propagating pulses on WDM beams. Can nature provide another condition under which pulses on WDM beams can be formed into WDM solitons? This paper will address this problem.

Investigation of Two Bidirectional C + L Band Fiber Amplifiers with Pumping Sharing and Wavelength Reused Mechanisms

S. K. Liaw[1], Y. L. Yu[1], Y. C. Wang[1], W. F. Wu[2], and R. Y. Liu[3]

[1]Department of Electronic Engineering
National Taiwan University of Science and Technology, Taipei 106, Taiwan
[2]Department of Mechanical Engineering, National Taiwan University, Taipei 106, Taiwan
[3]National Space Organization, Hsin Chu 300, Taiwan

Abstract— The rapid growth of data traffic in optical communications and optical networks demands extensive research into wideband optical amplifiers as the roles they play have become increasingly important. Both L and Erbium-doped fiber amplifier (EDFA) and Raman fiber amplifier operating in C + L band wavelength-division-multiplexing (WDM) systems are now a mature technology. So far, there are many methods to amplify the C + L band signals such as EDFA, Raman fiber amplifier (RFA) and semiconductor optical amplifier (SOA). For the C band, EDFA is a mature and widely used technology, owning to its higher gain and lower noise figure (NF) than other methods. RFA is a convenient method to amplify various wavebands, and it has even lower NF than that of EDFA We have studied theoretically both serial-type scheme and parallel-type hybrid amplifier scheme. Both dispersion compensation and power equalization are realized by adjusting the fiber Bragg grating (FBG) reflectivity and the pumping ratio. In addition, compared to the unidirectional EDFA, bidirectional EDFAs can not only reduce the complexity of the optical system, but also reduce the cost of transmission optical fiber. In this paper, we proposed and experimentally demonstrated two kinds of bidirectional fiber amplifiers. The amplification range covers both the C band and L band signals. We use a singlewavelength pump laser diode for both the C band and L band. Moreover, we employ concept of residual pumping power reuse to optimize both the gain efficiency of C + L band signals. Figure 1(a) shows the proposed bidirectional C + L band hybrid amplifiers, including an EDFA and a RFA. A pump reflector is used to optimize the performance of two fiber amplifiers. Figure 1(b) shows the proposed bidirectional C + L band EDFAs. For improving the fiber amplifiers' performance, a ratio coupler and a pump reflector are used.

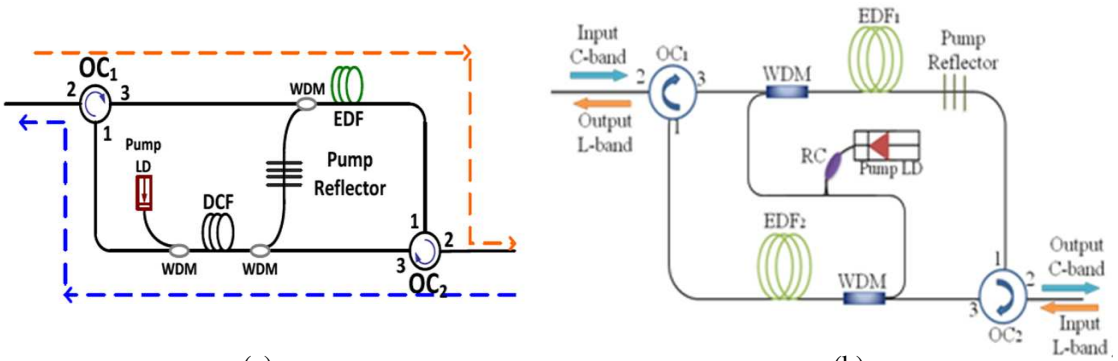

Figure 1: (a) The proposed C + L band hybrid amplifiers using a single-wavelength pump laser source, and (b) the proposed C + L band Erbium doped fiber amplifiers using a single-wavelength pump laser source.

Optical-circulator-based Single-frequency Fiber Laser Using Absorber and Subring Cavity in the Linear Cavity

S. K. Liaw[1], **H. Wang**[1], **H. I. Hsu**[1], **C. S. Shin**[2], **and R. Y. Liu**[3]

[1]Department of Electronic Engineering
National Taiwan University of Science and Technology, Taipei 106, Taiwan
[2]Department of Mechanical Engineering, National Taiwan University, Taipei 106, Taiwan
[3]National Space Organization, Hsin Chu 300, Taiwan

Abstract— Single frequency lasers have attracted much research interest because of their potential applications in long-haul and/or high-speed optical communications. Up to now, various techniques have been investigate to obtaina stable singlefrequency operation, such as using fiber Bragg gratings (FBGs), the Fabry–Pérot etalon, saturable-absorber filter inside the cavity, passive multiple-ring cavities, integrating two cascaded FFP filters, using an un-pumped erbiumdoped fiber (EDF) as a narrow bandwidth auto tracking filter for fiber ring lasers and so on. Linear cavity fiber laser requires fewer intracavity components and connecting fiber than that of a unidirectional ring-cavity fiber laser. This makes it more attractive. However, single frequency operation in a linear-cavity fiber laser is seldom addressed when compares to ring-cavity fiber lasers. In this paper, we report a single-frequency fiber laser using a saturable absorber Incorporated subring cavity as mode filters. The linear-cavity based fiber laser is constructed using an optical circulator and a partial reflectance fiber Bragg grating as the cavity ends. At 1550.82 nm, the laser output is 6.25 dBm and the signal-to-noise-ratio is 53.2 dB with linewidth less than 1 MHz in stable operation. The pumping efficiency is 10% improved by recycling the residual pump power to gain medium.

Figure 1 shows the proposed single frequency operation by adding one subring cavity and a piece of un-pumped EDF as saturable absorber. The Er^{3+} ion density, fiber core radius, numerical aperture and meta-stable lifetime are $5.0 \times 10^{24}(1/m^3)$, 1.4 μm, 0.28 and 10 ms, respectively, 6.24 dB/m at 1530 nm.

To analyze the laser characteristics, Fig. 2(a) shows lasing power stability of < 0.09 dB and wavelength variation of < 0.03 nm are observed in 30 minutes interval.

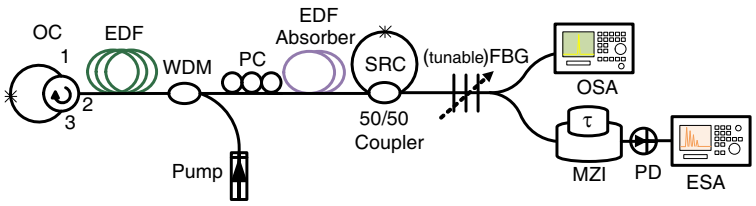

Figure 1: (a) The OC-based linear-cavity fiber laserand, (b) the proposed linear-cavity fiber laser including a subring cavity incorporated a piece of absorber.

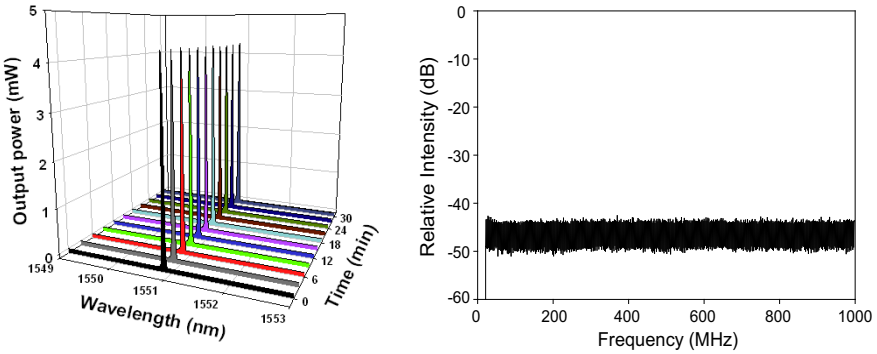

Figure 2: (a) Lasing power stability and wavelength variation in 30 minutes observation, and (b) measured frequency spectrm for the proposed fiber laser with both subring cavity and absorber, respectively.

As shown in Fig. 2(b), the laser can successfully suppress multimode operation and obtain a narrow line width of 967 kHz with both subring cavity and absorber. The proposed linear-cavity fiber laser has a number of potential applications in long-haul and high-speed optical communications.

Generation of Terahertz, Microwave, Radio Waves from a Laser-excited Wire Antenna

Kuan-Yan Huang, **Chia-Hsiang Chen**, **Ming-Hsiung Wu**, **and Yen-Chieh Huang**
HOPE Laboratory, Institute of Photonics Technologies
National Tsinghua University, Hsinchu 30013, Taiwan

Abstract— We report a laser-excited wire antenna (LEWA) generating radiation covering a spectrum from radio to THz frequencies. When the wire was irradiated by a mode-locked Ti:sapphire laser with a 160-fs pulse width, focused to 280 GW/cm^2 intensity on the wire, we detected the THz radiation with a 3-THz bandwidth, reaching the detection limit of our electro-optic sampling system. The amplitude of the detected THz signal was comparable to that generated from a ZnTe emitter under the same experimental condition. The microwave LEWA was driven by a Nd:YAG laser amplifier producing 40-mJ pulse energy in a 460-ps pulse width. We installed the LEWA in front of an S-band metal waveguide, which functions as a spectral filter to pass and reject the radiation above and below the cutoff frequency of the dominant TE10 waveguide mode. By using a ring antenna, we measured 1.7 and 2.6 GHz microwave signal before and after the waveguide, respectively. The radio wave was produced from a LEWA with its laser-excited tip biased at an anode voltage +500 V. When irradiated with a laser pulse with 42 mJ energy in a 7 ns pulse width, the LEWA generated radiation power 3–4 orders of magnitude higher than that from a direct laser-excited antenna without the biased voltage. The radiation power scales with the square of the laser induced photocurrent between the antenna tip and the anode (800 A in our case). With a higher biased anode field and shorter-wavelength excitation laser, this antenna has a potential to reach MW-GW radiation power in the microwave or even in the millimeter-wave spectrum.

An Improved Method for SNR Estimation on Optical Remote Sensing Images

Xinhong Wang, Chuanrong Li, Bo Zhu, Lingli Tang, and Hong Yuan
Academy of Opto-Electronics, Chinese Academy of Sciences, China

Abstract— Signal-to-Noise Ratio (SNR) is one of the basic and commonly used statistical parameters to evaluate the imaging quality of optical sensors. A number of typical SNR estimation algorithms have been developed in various research fields. Within them, the local standard deviation method proposed by Bo-Cai Gao has been a widely used one for a variety of remote sensing images, including panchromatic images, multi-spectral images, and even imaging spectrometer data. However, a relatively large region (usually hundreds of pixels by hundreds of pixels at least) with rather good uniformity in the image is needed when using the local standard deviation method. This precondition is not easy to be met, for in a common remote sensing image, uniform regions usually would not extend so large due to multiplicate limitations. Nevertheless, it is not hard to find some relatively small regions with sufficient uniformity. But unfortunately the local standard deviation method behaves unstable and may lead to severe errors when it is used on small size image regions.

In this paper, an improved method which is suitable for estimating SNR on a small image region is presented and algorithm tests with simulated noisy image and actual remote sensing image are performed. In addition, estimated values are compared with those derived from the conventional local standard deviation method, and the advantages of the improved method can be easily observed.

In brief, the improved method for SNR estimation proposed in this paper consists of the following steps:

1. A relatively uniform region is chosen from the remote sensing image which is to be investigated the SNR quality. Note that absolute uniformity is not required, and relative uniformity is enough (as uniform as possible is better, of course).
2. Select a small block size for oncoming image dividing. For example, the block size of 3×3 is assumed now.
3. Use certain pixel of the image region chosen in step 1 as the starting pixel for image division. For the first turn, the most upper-left pixel (i.e., the pixel $(1, 1)$ in the region) acts as the starting pixel.
4. The image region chosen in step 1 is divided into small blocks sized 3×3 pixels. For each small block, the local mean (LM) and the local standard deviation (LSD) of pixels within this block is calculated and recorded.
5. Set the pixel $(2, 1)$ as the new starting pixel, and carry out step 3 and step 4 for the second turn. Similarly, set the pixel $(3, 1)$ as starting pixel for the third turn. Afterwards, set the pixel $(1, 2)$ as starting pixel for the fourth turn .... Finally, set the pixel $(3, 3)$ as starting pixel for the ninth turn.
6. The mean value of LSDs of all the small blocks generated by the former steps is calculated, and the minimum and maximum of LSDs of all blocks are also found.
7. A number of bins with equal width are set up, within the range from the minimum of the LSDs to the 1.2 times of the mean of the LSDs. The LSDs of all blocks are then grouped into these bins. The number of blocks having LSDs within each bin is counted and recorded. Now a statistical histogram about the number of blocks with respect to the bin can be generated.
8. Perform a low-pass filtering processing on the statistical histogram, and a filtered histogram will be produced.
9. The bin having the peak value on the filtered histogram will be considered standing for the mean noise level of the image region.
10. The mean value of all pixels within the image region is computed and considered as the mean signal level.
11. In the end, the SNR of the image region is obtained by ratioing the mean signal produced in step 10 against the mean noise determined in step 9.

The first outstanding attribute of this SNR estimation method is that it performs multiple turns of image dividing (step 3 $\sim$ step 5) so that plenty of small blocks can be generated even on a relatively small image region, which can lead to more stable evaluation results. The second

merit of this method comes from the filtering processing in step 8, and it can effectively alleviate interferences due to some possibly unexpected big counts in step 7. Algorithm tests based on simulated noisy images show the method is more stable and accurate in comparison with the conventional local standard deviation method, especially when the evaluation region is not large (50×50 pixels for example). Tests on actual remote sensing image acquire by SPOT satellite produce some similar results.

Arc-induced Long Period Fiber Gratings Based on Flat-clad Fibers

Zhi-Zong Zheng, Chai-Ming Li, Cheng-Ling Lee, and Jing-Shyang Horng
Department of Electro-Optical Engineering, National United University, Miaoli 360, Taiwan, R.O.C.

Abstract— Arc-induced long-period fiber gratings (AI-LPFG) written by electric-arc discharge techniques are so popular because they do not need to be hydrogen loaded or highly germanium-doped for the expensive UV-laser exposure fabrication. Many kinds of AI-LPFGs, based on single mode fibers (SMF), dual concentric core fibers, special-doped (nonstandard) fibers, photonic crystal fibers, and photonic band gap holy fibers have been presented. By use of the heating and thermal effect, a flexible and low-cost arc-induced technique which can fabricate a periodical LPFG structure in any kinds of material and structure waveguides will be possible and easy. Therefore, in this study, a successful fabrication of an arc-induced LPFG based on a flat-clad fiber (FCF) is presented to investigate the birefringence of the structure and the sensing capabilities of the devices. Comparing with a standard SMF LPFG, asymmetrical structure of the FCF LPFG could be expected to induce more obvious birefringence effect. Figure 1 indicates the experimental setup of proposed flat-clad AI-LPFG. Inset shows the cross-sectional micrograph of the flat clad fiber. For fabrication process, a bare flat-clad fiber without its protective coating was placed between the electrodes of a fusion splicer machine, while its electrode-arc direction was fixed along the minor axis of the FCF. For measurement process, a broadband light source is launched into the fiber and the transmission spectra is measured by using an Optical Spectrum Analyzer. The transmission spectra of the proposed FCF AI-LPFG with a grating-period of 500 μm and 600 μm are shown in Figure 2. The experimental results with very deep attenuation band and narrow bandwidth are well compared with those results of the general UV-written LPFGs. We would further analyze the transmission spectral characteristics of many specifications for the designed FCF AI-LPFGs when a polarized light launched. Furthermore, the sensitivity of the devices for the strain, curvature, and temperature variations will be measured.

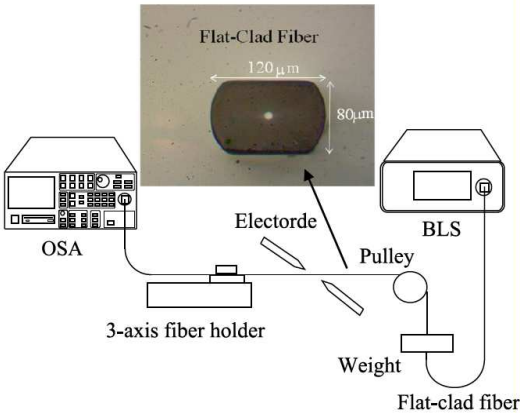

Figure 1: Experimental setup for the fabrication of flat-clad AI-LPFGs.

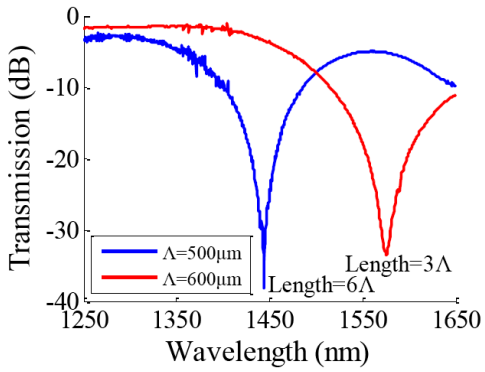

Figure 2: Experimental spectra of the fabricated flat-clad AI-LPFGs with different grating period.

Optical Properties of Raman-enhancing Substrates

Hui-Hsin Hsiao[1], **Juen-Kai Wang**[2, 3], **and Hung-Chun Chang**[1, 4, 5]

[1]Graduate Institute of Photonics and Optoelectronics, National Taiwan University
Taipei 10617, Taiwan, R.O.C.
[2]Institute of Atomic and Molecular Sciences, Academia Sinica, Taipei 10617, Taiwan, R.O.C
[3]Center for Condensed Matter Sciences, National Taiwan University, Taipei 10617, Taiwan, R.O.C.
[4]Graduate Institute of Communication Engineering, National Taiwan University
Taipei 10617, Taiwan, R.O.C.
[5]Department of Electrical Engineering, National Taiwan University, Taipei 10617, Taiwan, R.O.C.

Abstract— Localized surface plasmon resonance (LSPR) within metallic nanoparticles gives arise to large enhancement of the local electromagnetic field at the nanostructure surface, which leads to surface-enhanced Raman scattering (SERS) and other surface-enhanced spectroscopic processes [1]. For practical applications of the SERS phenomenon, many efforts have been done in developing uniform and reproducible SERS substrates. One of such structures is arrays of silver nanoparticles (Ag-NPs) partially buried into anodic aluminum oxide (AAO) layers [2, 3]. However, the opaqueness of Ag-NP/AAO substrates obstructs visualization of microscopic details for observing objects such as bacteria. Therefore, Wang et al. [3] further used an ion-drift process to enhance transparency of Ag-NP/AAO substrate. As shown in Fig. 4(b) in [3], *S. aureus* bacteria can now be clearly distinguished from the transparent SERS substrate. The image of each bacterium exhibits a darker center with bright surroundings. This is a breakthrough improvement because we usually need to dye the sample before observing if we use the traditional glass substrate. However, the reason that causes the higher-contrast image for transparent Ag-NP/AAO substrate is not clear.

In this research, we use our in-house developed three-dimensional (3D) finite-difference time-domain (FDTD) method program to simulate transmittance, total scattering cross section (TSCS), and radar cross section (RCS) for AAO substrate, Ag-NP/AAO substrate, and those with a bacterium above these two substrates. The transmittance shows a good correspondence to the experimental result with a LSPR dip near 400 nm–600 nm. By analyzing the RCS, we found that within the range of LSPR, the existence of a bacterium among the Ag-NP/AAO substrate causes more light to be scattered around the edge of the bacterium and less light to be reflected, which may be due to the sensitivity of LSPRs to the change of the refractive index and the geometry of the bacterium. Besides, the Ag-NP array acts as an antenna array amplifying those non-evanescent signals to transmit to the far field. Therefore, we can obtain a high-contrast image for the bacteria within the Ag-NP/AAO substrate.

ACKNOWLEDGMENT

This work was supported in part by the National Science Council of the Republic of China under grants NSC100-2628-M-002-008 and NSC100-2221-E-002-182-MY2, in part by the Excellent Research Projects of National Taiwan University under grant 10R80919-1, and in part by the Ministry of Education of the Republic of China under "The Aim of Top University Plan" grant.

REFERENCES

1. Willets, K. A. and R. P. Van Duyne, "Localized surface plasmon resonance spectroscopy and sensing," *Annu. Rev. Phys. Chem.*, Vol. 58, 267–297, 2007.
2. Wang, H.-H., C.-Y. Liu, S.-B. Wu, N.-W. Liu, C.-Y. Peng, T.-H. Chan, C.-F. Hsu, J.-K. Wang, and Y.-L. Wang, "Highly Raman-enhancing substrates based on silver nanoparticle arrays with tunable sub-10 nm gaps," *Adv. Mater.*, Vol. 18, 491–495, 2006.
3. Wang, H.-H., T.-Y. Cheng, P. Sharma, F.-Y. Chiang, S. W.-Y. Chiu, J.-K. Wang, and Y.-L. Wang, "Transparent Raman-enhancing substrates for microbiological monitoring and in situ pollutant detection," *Nanotech.*, Vol. 22, 385702, 2011.

Analysis of Frequency Coded Quantum Key Distribution for Secure Communication

Hum Nath Parajuli, Reinhold Herschel, Stefan Schwarz, and C. G. Schäffer
Helmut-Schmidt-Universität/Universität der Bundeswehr, Hamburg, Germany

Abstract— Quantum cryptography addresses ultimate secure communication by exploiting fundamental properties of quantum mechanics. We present with numerical simulations a photonic interference phenomena in sidebands of phase modulated light also known as frequency coded quantum key distribution (FC-QKD) which can be effectively employed for quantum cryptography. In this paper, a comparative analysis of two commonly used protocols (BB84 and B92) for quantum cryptography employing frequency coding in terms of different modulation schemes is presented along with security aspects.

Transmitted Characterization of 625 Mbps/15 GHz ROF Signal Using a Direct Modulated Baseband Signal and Twice Optical Carrier Suppression Modulation

Yu-Peng Chang[1], **Wen-Jeng Ho**[1], **Jhe-Min Lin**[1], **Peng-Chun Peng**[1], **and Hai-Han Lu**[1, 2]

[1]Institute of Electro-Optical Engineering, National Taipei University of Technology, Taipei 106, Taiwan
[2]Department of Information Technology and Communication, Tungnan University
New Taipei City, 222, Taiwan

Abstract— In this paper, we experimentally demonstrated the optical frequency quadrupling generation and characterized a directly modulated 625 Mbps baseband data carried upon a 15 GHz radio over fiber (ROF) signal by using twice optical carrier suppression (OCS) modulation. The distribution of radio frequency (RF) signals over optical fiber link has advantages of low attenuation, high capacity, broadband bandwidth, and low cost. Under these advantages, ROF is interesting for the applications such as mobile communications, wireless large area networks, and fixed wireless access services. The optical millimeter-wave (mm-wave) used in ROF is a promising frequency resource for optical-wireless access networks, but the optical mm-wave is difficult to generate in electrical domain which it must be spend more costs to purchase electrical configure devices to achieve. Hence, it is a attracting way that mm-waves/microwave is generated and processed in optical domain.

In this work, the generation of optical mm-wave using two cascaded low-speed optical intensity modulators (IMs) and a tunable electrical phase shifter without any optical filter was experimentally demonstrated. A distributed-feedback laser diodes (DFB-LDs) directly modulated with a 625 Mbps baseband signal is used as an optical carrier. Instead of using external modulation with a high frequency electrical mixer, the proposed direct modulation in this work is a low cost approach. The 1550 nm modulated optical carrier was then coupled into the first optical modulator (IM1). On the other hand, 3.75 GHz RF driving signal was split two branches, one branch is directly applied to IM1. Another branch of RF signal was firstly coupled to a tunable electrical phase shifter which can adjust the phase of RF signal and then applied to the second modulator (IM2). DC bias voltage applied on two modulators is adjusted to a value of the minimum transmission point of optical modulator to obtain two second-order optical sideband with optical carrier suppression. The obtained 625 Mbps/15 GHz ROF signal was amplified by an Erbium doped fiber amplifier (EDFA) for optical power compensation before transmitted through a single mode fiber (SMF) link. After 10 km transmission, the ROF signal is detected and down-conversion to baseband signal. The measured results show that the 625 Mbps/15 GHz signal was successfully transmitted and the low power penalty of only 0.5 dB was obtained. The effectiveness of the proposed technique was experimentally verified without high frequency mixer and narrow band optical notch filter to generate frequency quadrupling ROF signal.

ACKNOWLEDGMENT

The authors would like to thank the National Science Council of the Republic of China for financial support under grant NSC-100-2622-E-027-029-CC3.

Experimental Study of All-optical Frequency Conversion Using Period-one Dynamics of Semiconductor Lasers

Yu-Han Hung[1] **and Sheng-Kwang Hwang**[1, 2]

[1]Department of Photonics, National Cheng Kung University, Tainan, Taiwan
[2]Advanced Optoelectronic Technology Center
National Cheng Kung University, Tainan, Taiwan

Abstract— When an external optical field injects into one semiconductor laser, the necessary gain in the injected laser cavity decreases. The gain reduction increases the refractive index of the injected laser cavity through the antiguidance effect, thus shifting the cavity resonance toward a lower frequency. This red-shifted cavity resonance attempts to pull the laser oscillation toward the shifted cavity frequency. Such a pulling effect competes with the external optical field which on the other hand attempts to pull the laser oscillation toward the optical injection frequency. A number of different nonlinear dynamics therefore emerge. With proper injection level and frequency, the injected laser can enter period-one dynamics through Hopf bifurcation. Such a dynamical state possesses a characteristic of multiple spectral components equally separated around the injection frequency, which can therefore be used for all-optical conversion between frequency channels. Compared with other conversion schemes such as Electrical-Optical-Electrical conversion or cross gain modulation using semiconductor optical amplifier, this conversion scheme requires only one laser as the main conversion unit, where the converted frequency can be varied by simply adjusting injection level and frequency. A power penalty of less than 3 dB can be obtained at a bit-error-ratio of 10^{-9} for 2.5 Gb/s non-return-to-zero ASK data. PSK and FSK data format are also studied and proposed numerically. Furthermore, a conversion range of more than 100 GHz for a power penalty of less than 3 dB at BER of 10^{-9} is achieved. A wider conversion range is possible by using different operating conditions of the laser under study.

A Fault-tolerant Mechanism on Star-ring Based Ethernet Passive Optical Networks

Z. D. Shyu[1], **I. S. Hwang**[2], **and I. C. Lin**[3]

[1]Department of General Education, Army Academy, Taoyuan City, Taiwan
[2]Department of Information Communication, Yuan-Ze University, Taoyuan City, Taiwan
[3]Department of Computer Science and Engineering, Yuan-Ze University, Taoyuan City, Taiwan

Abstract— Ethernet Passive Optical Networks (EPONs) are proposed to overcome the bandwidth bottleneck at access networks due to its simplicity, cost effectiveness and wide spread deployment. The traditional PON architecture is bounded by the nature of tree topology, where data must be transmitted from node to central node before it could be redirected to another node which causes performance waste. To resolve this issue, a Sub-OLT component is assigned on the proposed star-ring based EPON architecture to control the partial traffic in the ring. All ONU's AF and BE traffics will be sent to Sub-OLT then transport to the OLT. On the other hand, all ONU's EF traffic (including Sub-OLT traffic) is transmitted directly at the assigned DBA time. In addition, to achieve high reliability and low-cost for deployment, a significant fault-tolerant mechanism on star-ring based EPON architecture is proposed in this article to provide protection against link fiber failure and ring fiber failure. This paper also proposes a Star-Ring Dynamic Bandwidth Allocation (SR-DBA) scheme on star-ring based EPON to handle dynamic bandwidth allocation process by OLT and Sub-OLT respectively. The simulation results show that the fault-tolerant SR-DBA can provide high system performance for different failure situations in terms of average delay and expedited forwarding (EF) jitter, especially in high traffic loads.

A New Mechanism to Improve Bandwidth Utilization and QoS of IPTV in Ethernet Passive Optical Network

I-Shyan Hwang[1, 2], **Andrew Tanny Liem**[2], **Ali Akbar Nikoukar**[2], **and Ku Chieh Chen**[2]

[1]Department of Information Communication, Yuan-Ze University, Chung-Li 32003, Taiwan
[2]Department of Computer Science and Engineering, Yuan-Ze University, Chung-Li 32003, Taiwan

Abstract— Newly evolving multimedia applications such as high-definition television (HDTV), Internet Protocol Television (IPTV), and Video-on-Demand (VoD) in recent times become one of the most key services for network operators. These applications have brought the network operators to offer higher bandwidth to their residential and business subscribers. Among these applications, IPTV is one of the killer multimedia applications for the next-generation network, yet provides exciting new revenue and opportunities for service providers. IPTV offers digital television services over Internet Protocol (IP) for the subscribers at a lower cost. These IPTV services can include live television (i.e., with or without interactivity), time-shifted television (i.e., catch-up TV or start-over TV) and video on demand (VoD) (i.e., browse a catalog of videos, not related to TV programming). IPTV has a different infrastructure from conventional TV services, which use a push metaphor in which all the content is pushed to the users. However, IP infrastructure is based on subscribers' personal choices. It can be the combination of push and pull schemes, depending on user needs and interests. Despite all the attractive IPTV services, it also requires high-speed access networks with the functions of multicasting, Quality-of-Services (QoS) guarantee and so on. In the access networks, EPON is regarded as one of the best technologies to meet the higher bandwidth demands. Moreover, EPON will fit the characteristics of IPTV services, since the broadcasting nature of the EPON systems. We have identified the use of single copy broadcast (SCB) over EPON systems for efficiently distribute the video traffic, particularly for delivering live IPTV traffics. Therefore, in this paper we propose broadcasting mechanisms for IPTV in EPON by using the SCB. Our architecture emulates the multicasting mechanism by employing SCB without using IGMP multicasting protocol. In our mechanism the Reconciliation Sublayer (RS) of ONUs and OLT contain a table to handle the IPTV request. When the OLT broadcasts the channel data via SCB, the ONU's table helps the ONU to accept or reject the data. The ONU table contains the channel name and user address. The OLT uses the table records to decide start/stop broadcasting the channel data. The OLT table contains the channel name and ONUs LLID which request for the channel. Simulation results have shown that our propose mechanism can improve the QoS metrics in terms of start-up delay, and packet dropping. Moreover, it also improves the bandwidth utilization at the feeder fiber.

The Influence of the Electromagnetic Wave on the Nonlinear Quantum Acoustoelectric Current in a Quantum Well

N. V. Hieu[1, 2], **N. Q. Bau**[1], **and N. V. Nghia**[1]

[1]Faculty of Physics, Hanoi University of Science, Vietnam National University, Hanoi, Vietnam
[2]Faculty of Physics, Danang University of Education, Danang, Vietnam

Abstract— The influence of the electromagnetic wave on the nonlinear quantum acoustoelectric (QAE) current in a quantum well (QW) is investigated by using the quantum kinetic equation method for an acoustic wave whose wavelength $\lambda = 2\pi/q$ is smaller than the mean free path ℓ of the electrons and in the region $q\ell \gg 1$ (where q is the acoustic wave number). The dependence of the QAE current j^{QAE} on the frequency of external acoustic wave ω_q, the temperature T, the amplitude E_0 and the photon energy $\hbar\Omega$ of the electromagnetic wave are obtained by using the quantum kinetic equation in the case of relaxation time of momentum τ constant approximation. Numerical calculation is done, and the result is discussed for a typical AlGaAs/GaAs/AlGaAs QW. The computational results show that the dependence of the QAE current j^{QAE} on the external acoustic wave frequency ω_q, the temperature T and the photon energy $\hbar\Omega$ is non-monotonic, the cause of appearance peaks attributes the transition between mini-bands $n \to n'$. The quantum theory of the QAE current in a QW is newly developed.

Session 2P7
Electromagnetics of Gradient Nanostructures and Heterogeneous Media

Dyson Equations for Dense Random Media Composed of Dielectric or Metallic Nanoscale Scatterers
Gerard Berginc, ... 362

Dyson Equations for Dense Random Media Composed of Dielectric or Metallic Nanoscale Scatterers

Gerard Berginc
Thales, France

Abstract— In this paper, we consider the coherent component [1] of the electromagnetic wave field inside random media composed of dielectric or metallic nanoscale particles. The subject of our interest concerns a random medium consisting of a statistical ensemble of different scattering species and artificial material structures developed on base of dielectric or metallic resonant particles. Under some assumptions, it can be shown that the average electric field propagates as if the medium is homogeneous with a renormalized permittivity, which is called the effective permittivity. The intent of this paper is to establish new formulas for the effective dielectric constant which characterizes the coherent part of an electromagnetic wave propagating inside a random medium . The starting point of our theory is the multiple scattering theory, the averaged electric field satisfies a Dyson equation with a mass operator related to the effective dielectric permittivity of the homogenized structure [2]. Quantum multiple scattering theory has been transposed in this electromagnetic case. We give a formal solution for the mass operator by introducing the T-matrix formalism. We show that the T-matrix satisfies a Lippman-Schwinger equation. Then, we introduce the Quasi-Crystalline Coherent Potential Approximation (QC-CPA), which takes into account the correlation between the particles with a pair-distribution function. This function describes the correlation between two distinct particles and the hard sphere model (impenetrable particles). We add some new approximations to the QC-CPA approach, which give us a tractable equation for the effective permittivity. In the low frequency limit, the expression is identical with the usual result obtained under the QC-CPA scheme, and in the high frequency limit the expression includes the vectorial case generalization of the result obtained by Keller [3], which has been derived, using a scalar theory, but seems to be in good agreement with experimental data for particles whose diameter is larger than one wavelength.

This new expression of the permittivity has been extended to random media with different types of particles. This extended formulation of the effective permittivity is then used to calculate the coherent and incoherent intensities scattered from a three-dimensional disordered medium bounded by randomly rough interfaces [4]. Some examples will be given in the paper.

REFERENCES

1. Soubret, A. and G. Berginc, "Electromagnetic wave scattering from a random layer with rough interfaces I: Coherent field," *Physics*, 0312133, 2003.
2. Soubret, A. and G. Berginc, "Effective dielectric constant for a random medium," *Physics*, 0312117, 2003.
3. Keller, J. B., "Stochastic processes in mathematical physics and engineering," *Proceedings of Symposia in Applied Mathematics*, Chapter Stochastic Equations and Wave Propagation in Random Media, Vol. 16, 145–170, AMS, Providence, Rhode Island, 1964.
4. Berginc, G. and C. Bourrely, "Light scattering from 3-D nanoscale disordered media," *PIERS Online*, Vol. 6, No. 8, 730–734, 2010.

Session 2P8
Poster Session 2

Compact LTCC-based Identification Reader Modules with Thermal Consideration for Ku-band Application
Yu Ye, Liang Wu, Lingyun Li, Wei Wang, Shu-Na Wang, Xiao-Wei Sun, ... 365
A Model the Production of Nanoparticles in an Inductively Coupled Plasma Reactor: Application to the Design of an Industrial Unit
Silvania Lopes, Patrick Rambaud, Pierre Proulx, ... 367
Investigations of Plane Wave Scattering on Ferrite Posts Configurations Using Hybrid Technique
Adam Kusiek, Rafal Lech, Jerzy Mazur, ... 368
Analysis of Parameter Sensitivity of Electromagnetic Railgun System
Na Pan, Zejun Shen, Peng Zuo, Jiansheng Yuan, ... 369
Analysis of Approaches for Modeling the Contact Resistance on Conductor Interface by the Finite Element Method
Zejun Shen, Li Hao, Peng Zuo, Jiansheng Yuan, ... 370
Analysis of the Electric Field Environment around Railway Platform
Yuyi Lin, Li Hao, Zejun Shen, Jun Zou, Jiansheng Yuan, ... 371
The Multi-component Signal Model and Learning Algorithm of Blind Source Separation
Tiao Jun Zeng, Quanyuan Feng, Xiao-Hui Yuan, Hongbo Ma, ... 372
Near-weightlessness Movements in Electromagnetic Fields
Zi-Hua Weng, ... 373
Electromagnetic Radiation
Ilias J. Tyrovolas, ... 374
Tunable Quantum Interference in a Four-level Atomic System for Photonic Device Design
Shengtao Mei, Hang Zhao, Jian Qi Shen, ... 376
Focusing on the Moiré Effect
Sara Liyuba Vesely, Alessandro Alberto Vesely, ... 377
Response of Multilayer Materials to Electromagnetic Waves
Radim Kadlec, Petr Marcon, Eva Kroutilová, Pavel Fiala, ... 379
Analysis of Distortion Factor of Three Phase Linear Synchronous Motor
Koichi Nakaiwa, Hiroyuki Wakiwaka, ... 380
Simulation of 3-D SAR Imaging Based Outdoor RCS Measurement Technique
Ke-Fei Liao, Sanyuan Xu, Xiao-Ling Zhang, Jun Shi, ... 381
GRECO Based Spotlight SAR Imaging Simulation Method
Min Su, Jia Liu, Ning Fang, Bao Fa Wang, ... 382
A Multi-baseline InSAR DEM Reconstruction Approach Based on Proportional Subband Filtering
Shuang Li, Huaping Xu, ... 383
Bridgeless SEPIC-derived LED Driver without Electrolytic Capacitor for Multistring Application
Hongbo Ma, Quanyuan Feng, Tiao Jun Zeng, Xiao-Hui Yuan, ... 384
Investigation of Irregularities Induced from Medium-scale Traveling Ionospheric Disturbances Using Global Positioning System and Digisonde
Wei-Sheng Chen, Chien-Chih Lee, Fang-Dar Chu, ... 385
A Study of Equatorial Ionospheric Irregularities over the Indian-Ocean Sector during Solar Maximum by Using the Global Positioning System
Fang-Dar Chu, Wei-Sheng Chen, Chien-Chih Lee, W. H. Tseng, Huang-Tien Lin, Chia-Shu Liao, 386
Multi-instrument Observations of F-region Irregularities near the Crest of Equatorial Ionization Anomaly
Chien-Chih Lee, Wei-Sheng Chen, Fang-Dar Chu, ... 387
Satellite Monitoring for Elasto-plastic Behavior of Plate around Epicenter in a Process Tsunami Earthquakes
Shigehisa Nakamura, ... 388

A Geomagnetic Polar Drifting Path Evolution on the Geographic Earth Surface
Shigehisa Nakamura, ... 389
Electromagnetic Process at a Crustal Fault Formation for Tsunami Earthquake on the Planet Earth
Shigehisa Nakamura, ... 390
Advancing Climate Studies in the Australasian Region Using Ground and Space-based GPS Techniques — An Overview of Recent Progress
Yuriy Kuleshov, Erjiang Fu, Sue-Lynn Choy, Fabrice Chane-Ming, Yuei-An Liou, Alexander G. Pavelyev, ... 391
Scattering of Light from Rough Surfaces, the Limits of Validity of Geometric Optics Approximation Method
Imed Sassi, Mehdi Khemiri, ... 392
Modulation in the Spectral Degrees of Polarization of Stochastic Electromagnetic Higher-order Bessel-Gauss Pulsed Beams
Weimin Peng, Haixia Wang, Chaoliang Ding, ... 393
Weighted Multi-frequency Imaging of Thin, Crack-like Electromagnetic Inhomogeneities
Young Deuk Joh, Young Mi Kwon, Joo Young Huh, Won-Kwang Park, ... 394
Broad-band Spectrum Control with Polarization
Pin Han, ... 395
Estimating Properties of Subsurface Layers from GPR Spectral Attributes
Zhonglai Huang, Jianzhong Zhang, ... 396
Identification of Subsurface Thin Layers Using Cepstrum of GPR Data
Zhonglai Huang, Jianzhong Zhang, ... 397
Monitoring System for Space Weather
Edwin Andres Quintero Salazar, Ivan Dario Arellano Ramirez, Jimmy Alexander Cortes Osorio, ... 398
Principle of Locality and Remote Sensing from Space
Alexander G. Pavelyev, Yuei-An Liou, Alexey A. Pavelyev, Keifei Zhang, Yuriy Kuleshov, ... 399
Design and Implementation of Bandgap References Voltage Circuit for SOC Module Applications
Min-Chin Lee, Chi-Jing Hu, Wen-Shiang Jung, ... 400
Spatial Interpolation for Mapping Geoclimatic Factor $\boldsymbol{K}$ in South Africa
Mike Omondi Asiyo, Thomas Joachim Odhiambo Afullo, ... 401
Non-parametric and Parametric Modelling and Characterization of the Effective Earth Radius Factor for South Africa
Abraham M. Nyete, Thomas Joachim Odhiambo Afullo, ... 402
A Novel Imaging Formation Algorithm Based on Lagrange Interpolation for SweepSAR Data Processing
Wei Yang, Hongcheng Zeng, Jie Chen, Pengbo Wang, ... 403
Proposal of Technical Measures for a Partial Discharge Detection System Based on Real Measurement
Radek Myška, Petr Drexler, Tomas Kriz, ... 404
A 60 GHz Marchand Balun with Floating Ground Centre-tap in CMOS Technology
Leijun Xu, Henrik Sjoland, Markus Tormanen, Tianhong Pan, Xue Bai, ... 405
Compact UWB Monopole Antenna with Tapered Ground Plane
Akkala Subbarao, Singaravelu Raghavan, ... 406
The Effects of Low Power Microwaves at 500 MHz and 900 MHz on Yeast Cells Growth
Hamad Suliman Alsuhaim, Vuk Vojisavljevic, Elena Pirogova, ... 407
Design of 4 GHz Multiplier Based on Sigma-Delta Modulation in a 0.18-µm CMOS Technology
Xiao Dan Guo, Qiao Meng, Yiong Liang, ... 408
Effect of Low-power Microwave Radiation on Seed Growth Rate
Manu Fuangfoong, K. Eaipresertsak, T. Chim-Oye, K. Dungkanya, ... 409
An Optical Imaging Lift Using a Birefringent Homogeneous Crystal
Chia-Wei Chu, Zhi Chen, Yubo Duan, Yuan Luo, ... 410

Compact LTCC-based Identification Reader Modules with Thermal Consideration for Ku-band Application

Yu Ye[1,2], Liang Wu[1], Ling-Yun Li[1], Wei Wang[1], Shu-Na Wang[1], and Xiao-Wei Sun[1]

[1]Key Laboratory of Terahertz Solid-State Technology
Shanghai Institute of Micro-system and Information Technology, Shanghai 200050, China
[2]Graduate University of Chinese Academy of Sciences, Beijing 100049, China

Abstract— A millimeter-wave identification readers for Ku-band short-range high data-rate backscattering communications is presented. The reader is composed of an oscillator, an amplifier, and a down converter based on GaAs pHEMT technology and integrated on a low temperature co-fired ceramic substrate. Power transmitted of the module is 7-dBm while the receiver 1 dB compression points are −5.5-dBm for Ku-band reader. The reader module achieves 2 GHz-wide IF bandwidth with miniaturized sizes of 15-mm × 11-mm for application.

MMID Reader Architecture: The application of near field communication (NFC) can be enlarged with high data rate and high operation frequency, which can be seen as a tendency to implement millimeter-wave identification (MMID) in NFC. The presented MMID reader is operating at Ku-band, which consists of GaAs monolithic micro-wave integrated circuits (MMICs) on a LTCC board. Oscillator, amplifier, and down converter have been realized in 0.15-µm GaAs pHEMT technology. Ferro A6-M system low tem-perature co-fired ceramic (LTCC) is utilized for integration and assembling. The architecture of the reader is shown in Fig. 1(a). Fig. 1(b) depicts the photograph of the LTCC mo-dule in which the designed MMIC chips are wire-bonded on the surface. The module size is only 15-mm × 11-mm.

MMID Reader Assembling and Testing: In LTCC assembling, the thermal and electro-magnetic properties of the thermal through via with a long distance need to be considered. As in Fig. 2, the thermal through via arrangement adopted in this work is optimized as via-array with 100-µm diameter and 250-µm pitch, which shows good performance in mm-wave application. In simulation, a steady uniformed 0.5-W heat source is placed on a 1 mm × 1 mm top layer with

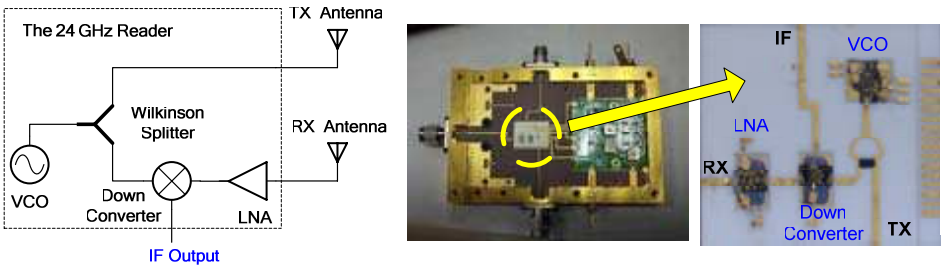

(a) (b)

Figure 1: Architecture of the 24 GHz MMID reader. The VCO, LNA, and Down Converter are implemented in GaAs pHEMT then integrated on LTCC. (a) Block diagram of the reader. (b) Photograph of the reader.

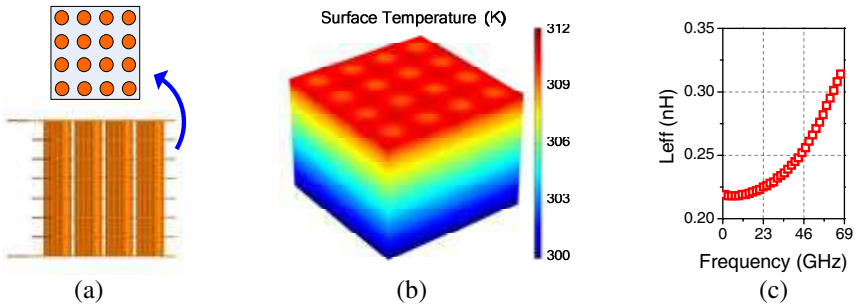

(a) (b) (c)

Figure 2: Configurations of thermal via arrangement. (a) Schematic con-figuration. (b) Surface temperature distribution. (c) Effective Inductance.

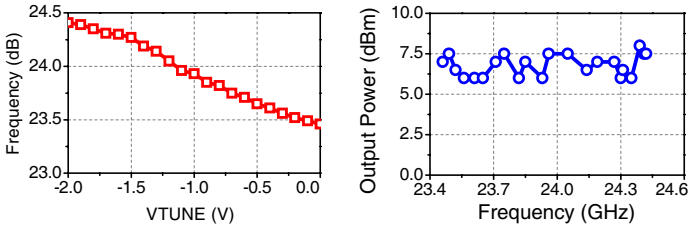

(a) (b)

Figure 3: Measured transmitted frequency and power tuning curve of the reader. (a) Transmitted frequency vs. VTUNE. (b) Transmitted power vs. tuning frequency.

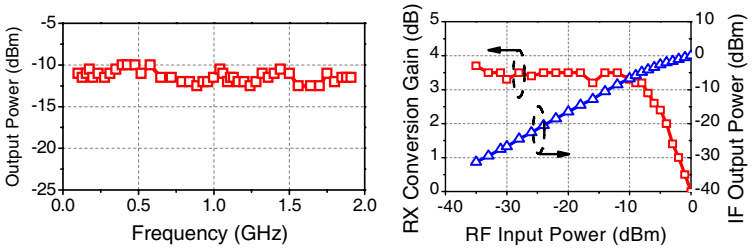

(a) (b)

Figure 4: Measured RX chain results. (a) Measured IF output power with a −15 dBm frequency-tuned RF signal and a fixed 24 GHz LO signal. (b) Measured RX conversion gain and IF output power with a power-tuned 24.4 GHz RF signal and a fixed 24 GHz LO signal.

the temperature of bottom fixed to 27°C. The top surface temperature distribution has only 2°C deviation and the maximum temperature is 12°C higher than the room temperature. The simulated effective inductance of via arrangement is 0.22-nH up to 60-GHz.

The output signal has a linear tuning frequency range of 1 GHz (from 23.4 GHz to 24.4 GHz). The average transmitted power is 7-dBm, as in Fig. 3. The output IF signal has a low power variation, ±1-dB around −11-dBm, which can provide a broad-band IF operation region with steady performance. The RX has a gain of 3.5-dB with input 1-dB compression point at −5.5-dBm, as featured in Fig. 4.

A Model the Production of Nanoparticles in an Inductively Coupled Plasma Reactor: Application to the Design of an Industrial Unit

Silvania Lopes, Patrick Rambaud, and Pierre Proulx
von Karman Institute for Fluid Dynamics
Chaussée de Waterloo, 72, Rhode Saint Genèse 1640, Belgium

Abstract— In this study, we present the development and design an inductively coupled plasma (ICP) reactor for the production of nanoparticles at an industrial scale. The design of the process first involves mathematical modelling of the r.f. inductively coupled plasma torch, as well as the injection and evaporation of microparticules as precursors. In order to apply the model to the design of the process unit, it is necessary to further model the nucleation and growth of the nanoparticles, including the morphology of the particles. The full coupling, in the resulting model, of the electromagnetic r.f. power, the Navier-Stokes equations, the microparticles temperature and trajectory histories, the radiative losses of the plasma and the population balance equations describing the nanoparticle's size and morphological characteristics, is done using the open-source package OpenFOAM. The multiple physical phenomena involved in the process are all described on a unique numerical grid, in a fully integrated model.

The mathematical model of the process is used to optimize the production of the nanoparticles, taking into account the important aspect of aggregation, i.e., the formation of non-spherical agglomerates typically assuming shapes similar to fractals. The model used to solve the population balance equations describing the nanoparticles dynamics is based ont the method of moments with interpolative closure (MOMIC) and includes an additional moment used to describe the fractal nature of the agglomerated powders. The model enables to design the reactor and quenching system in order to maximize the quality of the powers, measured in terms of size, uniformity and agglomeration characteristics. A parametric modelling study is presented, and the choice of the optimal design is discussed. Comparison of the model's results is made in terms of the inductively coupled plasma characteristics as well as the nanoparticles sizes and morphology.

Investigations of Plane Wave Scattering on Ferrite Posts Configurations Using Hybrid Technique

A. Kusiek, R. Lech, and J. Mazur
Gdansk University of Technology, Poland

Abstract— The analysis of scattering from an arbitrary or periodic set of objects is crucial in many recent civil and military applications (e.g., antenna systems for wireless communication [1, 2] or objects identification in radar systems). The single configuration of posts placed in near field of antenna are utilized as a beam-forming structures. The periodic in two directions arrangement of scatterers creates the frequency-selective surface (FSS). The multilayered FSSs are utilized as an electromagnetic band structure (EBG) in microwave wavelength range or photonic band structure (PBG) in optical range [1]. Recently, EBGs and PBGs are of great interest due to their extraordinary properties and potential applications, e.g., filters, polarizers, substrates for radiating elements, or optical switches [1, 2]. FSSs find also application in polarizers and polarization rotators to change the polarization state of an electromagnetic wave.

The wide interest in the analysis of scattering problems creates the demand for highly efficient and accurate analysis techniques of this phenomenon. In the analysis of structures composed of objects with complex geometry the most numerically powerful techniques are hybrid methods [3, 4] which combine the partially-differential equation (PDE) based methods (e.g., finite-difference time-domain (FDTD) method, finite element method (FEM)) with analytical ones (e.g., Mode Matching (MM) technique, method-of-moments (MoM)). In these techniques the discrete approach (FDTD, FEM) is only used in the limited area surrounding the post, where the analytical solution of the problem is difficult to determine. In the outer homogenous region the continuous analytical form of the fields is assumed. The advantage of this approach is that the complexity of the problem can be reduced, and time and memory efficiency algorithms can be achieved.

In this paper the investigations of structures composed of arbitrary or periodic set of ferrite posts are presented. The main advantage of considered structures is the possibility of tuning their electromagnetic properties by the change of biasing magnetic field. In the analysis of such configurations the hybrid technique based on transmission matrix approach is applied [4, 5]. The transmission matrix of single post is determined with the use FDFD/MM technique. In order to determine scattering field from arbitrary set of objects we utilize the analytical iterative scattering procedure (ISP) [4]. Finally, when the scattering parameters of multilayered periodic structure are of interest, the lattice sum technique is applied [5]. The developed technique is applied to the analysis of beam-forming structures and frequency-selective surfaces composed of ferrite posts with irregular shape. The validity and accuracy of approach is verified by comparing the presented results with those obtained from alternative numerical methods.

ACKNOWLEDGMENT

This work was supported by the Polish Ministry of Science and Higher Education from sources for science in the years 2012-2013 under Contract IP2011 028271 (decision No. 0282/IP3/2011/71).

REFERENCES

1. Jandieri, V., K. Yasumoto, and Y.-K. Cho, "Rigorous analysis of electromagnetic scattering by cylindrical EBG structures," *Progress In Electromagnetics Research*, Vol. 121, 317–342, 2011.
2. Kim, S.-H., T. T. Nguyen, and J.-H. Jang, "Reflection characteristics of 1-D EBG ground plane and its application to a planar dipole antenna," *Progress In Electromagnetics Research*, Vol. 120, 51–66, 2011.
3. Dunn, E. A., J.-K. Byun, E. D. Branch, and J.-M. Jin, "Numerical simulation of BOR scattering and radiation using a higher order FEM," *IEEE Trans. on AP*, Vol. 54, No. 3, 945–952, March 2006.
4. Kusiek, A. and J. Mazur, "Analysis of scattering from arbitrary configuration of cylindrical objects using hybrid finite-difference mode-matching method," *Progress In Electromagnetics Research*, Vol. 97, 105–127, 2009.
5. Kusiek, A., R. Lech, and J. Mazur, "Analysis of electromagnetic plane wave scattering from 2-D periodic arrangements of posts," *Progress In Electromagnetics Research*, Vol. 129, 69–90, 2012.

Analysis of Parameter Sensitivity of Electromagnetic Railgun System

Na Pan[1], **Zejun Shen**[2], **Peng Zuo**[2], **and Jiansheng Yuan**[2]

[1]Department of Electrical Engineering, Northeast Dianli University, Jilin 132012, China
[2]Department of Electrical Engineering, Tsinghua University, Beijing 100084, China

Abstract— By using the simulation of the electromagnetic railgun system, the influence effect of several parameters to the performance of the system characteristics is analyzed, including the number of capacitance groups in the pulse power source, the value of capacitances and their sequence trigger time, the value of adjustable wave inductance and resistance, current-carrying diode resistance and thyristor resistance, rail resistance gradient and inductance gradient parameters. The acceleration time and the exit velocity of armature are taken as the system performance. On the basic of parameter sensitivity analysis, an electromagnetic rail gun system is designed.

The basic structure of electromagnetic railgun is composed of high pulse power supply, two root conductor rails, and an armature sandwiched between the rails, but which can slide. The working principle of the system is that: a huge value of current produced by the high pulse power source flows through the rails and the armature, the current produces a big magnetic field interacted with the current inside the armature, and the electromagnetic force is formed which speeds the armature forward.

In the sensitivity analysis of capacitance, the influence degree to the system by different number of capacitor groups, the value of their voltage and triggering time, is given in the paper. Based on the analysis results, more reasonable values of the parameters can be determined and designed. In the sensitivity analysis of adjustable wave inductance, by observing the current waveform regulation characteristics within the scope of certain value, the suggestion to choose the value of inductance is provided. In the analysis of the resistance of adjustable wave inductance, the maximum allowed value is given, as the resistance only plays a role in negative effect to the system. It is similar to the analysis of other resistance. The inductance gradient of rails is proportional to the force to armature. In principle, the bigger is the inductance gradient, the better to the system. The relationship between the acceleration of armature as well as the performance of system and the inductance gradient is given. The sensitivity analysis of the parameters to the system can provide a basis for optimizing the system design.

Analysis of Approaches for Modeling the Contact Resistance on Conductor Interface by the Finite Element Method

Zejun Shen, Li Hao, Peng Zuo, and Jiansheng Yuan
Department of Electrical Engineering, Tsinghua University, Beijing 100084, China

Abstract— There may be an additional contact resistance on the interface of conductor regions caused by the change of material property, i.e., the resistivity. The simulation of the contact resistance is very important to get the Joule-heat losses of the conductors. However, it is difficult or impossible to model and calculate the contact resistance by using the traditional finite element method (FEM). More capable or efficient approaches should be found for the simulation.

With the traditional FEM, a "thin-layer" has to be placed on the interface to express the contact resistance, which has been proposed in some articles. This approach is simple, but the simulation accuracy depends heavily on the thickness of the layer and the value of the conductivity. Moreover, the number of employed mesh elements can be huge, as the thin layer occupies much less space than the surrounding domains. Therefore, it takes large computer resource to solve practice problems.

A new method to model the contact resistance has been proposed in this article, with the help of the contact element in FEM software ANSYS. The contact element is a kind of surface element which can mesh the interface of conductors and model different contact resistances using its special parameter named "surface conductivity". The contact element meshes the interface between conductors directly, while not the whole contact region. The number of employed surface elements is few. With the parameter of "surface conductivity", equations can be set up to couple the elements of the conductors, and different value of contact resistance can be easily modeled just by regulating the value of "surface conductivity".

Furthermore, by setting different values of "surface conductivity" in the contact elements at different positions of the meshed interface, we have implemented the simulation of another kind of contact resistance caused by the current shrinking. By this approach the distribution of current on the interface influenced by the shrinking contact resistance can be simulated. Some examples of contact resistance calculation under different contact conditions will be given and analyzed in the full version of the paper.

Analysis of the Electric Field Environment around Railway Platform

Yuyi Lin, Li Hao, Zejun Shen, Jun Zou, and Jiansheng Yuan
Department of Electrical Engineering, Tsinghua University, Beijing 100084, China

Abstract— The calculation of the power frequency electric and magnetic fields around high-speed railway accurately is of importance to evaluate the living situation of residents along railway. In this paper, the power frequency electric field around high-speed railway is calculated by using the finite element method (FEM). In the calculation, the mesh generation with the freedom coupling method on interfaces is adopted to model the thin transmission lines and the large surrounding air region. This method is able to reduce the demand of element number and increase the calculation accuracy heavily.

The traditional FEM requires the continuity of the mesh on the interface of domains, i.e., all the nodes on the interface must be used by the neighborhood domains. The characteristic of the simulation is that the size of transmission lines are very small, but the air region form the lines the ground is very large relatively. Therefore, if the transmission lines with small region are generated small size of elements, the size of elements in the air and near the transmission lines must be also small, which will generate huge number of elements in the air with large region. Consequently, large computer resource is needed for the simulation by the traditional FEM.

An efficient method is adopted for the simulation, which is the freedom coupling method. By this method, the continuity of mesh is not required, and the mesh can be generated as shown in Fig. 1, in which the circle can be the transmission line. It is clear that the number of mesh in the air can be made mush less than the traditional FEM. The freedom coupling method is included in software ANSYS. By the software the freedom coupling method, we calculate the electric field environment on the ground, and acceptable results have been obtained.

Actually, the transmission lines are very close. Therefore, a region can be created to enclose all the lines as shown in Fig. 2 where there are four lines enclosed by a circle, and small size of elements are generated in the circle. In this way the calculation accuracy can be increased, the number of required mesh can be reduced. A calculation result that is the distribution of equipotential lines is given in Fig. 3, which contains the roof of the platform shell and the train carriage. More results and the analysis of the electric field environment in the plat-form will be given in the full version of the paper.

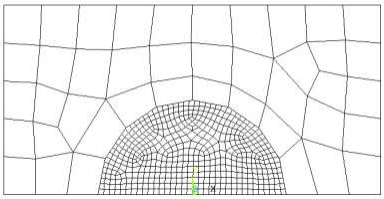

Figure 1: Mesh for the freedom coupling method.

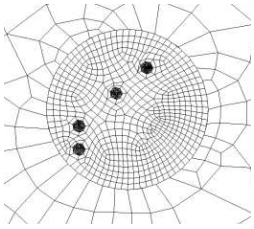

Figure 2: Mesh for the simulation of four lines.

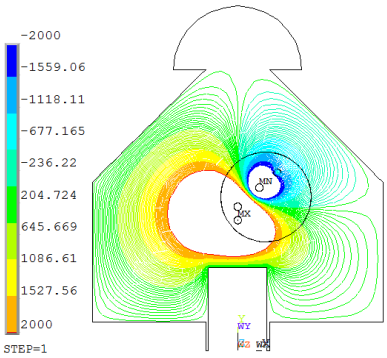

Figure 3: Distribution of equipotential lines around the platform.

The Multi-component Signal Model and Learning Algorithm of Blind Source Separation

T.-J. Zeng[1], **Q.-Y. Feng**[1], **X.-H. Yuan**[1], **and H.-B. Ma**[2]

[1]School of Information Science and Technology, Southwest Jiaotong University, Sichuan 610031, China
[2]School of Electric Engineering, Southwest Jiaotong University, Sichuan 610031, China

Abstract— The blind signal separation (BSS) problem consists of re-covering a set of statistically independent sources from a group of sensor observations. The challenge of this problem lies in the fact that the separation is blinded; without the knowledge of the sources nor the mixing environment. In the last few year, blind signal separation has become an important research area, since it has wide potential applications. For example, the problems of image enhancement and recognition such as face and fingerprint recognition, signal equalization and reconstruction in digital communication, medical diagnosis such as EEG and ECG, geophysical analysis, etc.. In this paper, the proposed polynomial mixture model, difference from general ones, has better precision to describe real situations. The signal separation is achieved through an information maximization criterion no requiring the PDF (Probability Density Function) of observed signals. In the separating stage, a novel variable-step-size and two-separating-systems algorithm is employed, moreover, a new Performance Index (PI) is presented, its theoretic properties which we have proved in this paper, and simulations indicate that is more practical than the wide-using PI recently. At last part of the paper, two numerical simulations are provided to illustrate the efficiency of the proposed method.

Near-weightlessness Movements in Electromagnetic Fields

Zi-Hua Weng
School of Physics and Mechanical & Electrical Engineering, Xiamen University
Xiamen 361005, China

Abstract— The near-weightlessness movements in the electromagnetic field can be described by the algebra of octonions. The octonion decomposes into the quaternion and S-quaternion. The quaternion is suited to describe the property of the gravitational field, while the S-quaternion is adaptive to depict the feature of the electromagnetic field.

The similarity between the quaternion and S-quaternion allows the concepts of weightlessness and near-weightlessness in the gravitational field to spread across the electromagnetic field. From the condition of near-weightlessness movements of electromagnetic fields, it is found that the electromagnetic potential impacts the 'orbit' movement of the test charge in the S-quaternion space, and then to interfere the measurement precision.

The above inferences agree with the A-B experimental results and the Uncertainty Principle in the quantum mechanics to a certain extent. This means that the applications of present measurement methods cannot avoid disturbing the 'orbit' movement of the test charge from the electromagnetic potential in the S-quaternion space.

ACKNOWLEDGMENT

The authors are grateful for the financial support from the National Natural Science Foundation of China under grant number 60677039.

Electromagnetic Radiation

Ilias J. Tyrovolas
Agricultural University of Athens, Athens, Greece

Abstract— In the Compton effect the frequency of photon reduces.

Lower energy (E) means lower frequency (ν): $E = h\nu$. But what is frequency meaning for one or a few photons? The question has been answered by Luis de Broglie since 1923: $\nu = mc^2/h$. So, it becomes obvious that frequency expresses the photon mass or size and thereby there are various photon sizes. That's why its mass is not defined yet. Its assumed rest mass has experimentally been found less than 10^{-27} eV.

In 2010 photons observed in the condensation Bose-Einstein where required a nonzero effective mass [1]. Moreover, virtual photons have mass.

But then, can go to c? Answer: how much energy is consumed by neutrinos in the recent experiment OPERA?

Varying size is the reason for many observable effects, as the followings:

- Different refractive index of different colors
- Short radio waves reflection from the ionosphere
- Long radio waves large permeability (submarines radio)
- UHF and microwaves reflected from objects more than the above
- Light waves reflected from objects more than radio waves
- Light waves are more absorbable than radio waves

As we know there are free electrons within a metal pipe. When they are accelerated (by an electric field for example) they are forced to jump from a lower to a higher energy level (stimulation). The gap among levels depends on the force (acceleration). Then (when the electric current is stabilized) each electron goes to lower energy level releasing a quantum of energy (photon). This effect is observed when we switch on/off (current starts or stop running, this is acceleration) electrical devices: radio waves produced.

Oscillation is also acceleration. In alternating current (A.C.) because metal's free electrons oscillate fast there is huge acceleration so that released photons. In this way radio waves are produced. With increasing oscillation frequency increases the acceleration. In A.C. free electrons oscillate in high frequency, which means big acceleration, between two energy levels emitting photons. As we said above, the gap among levels depends on acceleration. So, the higher frequency, the larger energy level gap. The larger energy gap, the more energy (bigger size or higher frequency of photon) is emitting. When this photon collides and is absorbed by a free electron antenna captures this energy.

There is also oscillation due to heat. Increasing the temperature increases the frequency of oscillation. As already explained, this represents a greater stimulation and higher frequency (bigger photon) emission. In this way infrared rays are produced. In nonmetals, due to thermal motion of atoms orbital electrons collide with and stimulate each other similarly to the fluorescence effect.

It appears as if photons are electrons fragments. Energy is quantized because each photon is composed of a natural number of pieces (elemental photons). When the photon produced by laser the pieces have a normal distribution, so the shape of photon is spherical. When emitted spontaneously by an atom the pieces follow the Poisson distribution, so the photon has the drop shape. If you collide two beams of different sizes photons then produced photons with the average size of the two original [2]. In the Compton effect, some elemental photons are absorbed by the electron, so the photon mass decreases. If the collision is temporary plastic, then fluorescence and phosphorescence effects appear.

In incandescent lamp electrons forced to pass through a thin pipe and collide with each other thus detached photons of various sizes.

When X-rays produced electrons collide with nuclei so generated photons from both pieces. As a result X-photon consists of quark and electron fragments, such as γ-photon (rest mass) consists of an electron and a positron fragments.

The mass decreases with speed: $m = m_o\alpha^u$, $0 \ll \alpha < 1$, m_o: rest mass, u: velocity.

It is not true that electromagnetic waves are unaffected by electric fields. Scientists choose to ignore what all the technicians know, how the antenna-TV amplifier does works: electricity fed to the antenna. It seems like the electric current to pull the waves.

But this is not the electric force. This is the force which holds the photons inside electron, the fifth force in universe. Perhaps black holes are strong fields of this force. Doppler Effect appears in waves produced by oscillators which have "peaks" and "hollows". These peaks can be "condensed" or "diluted" by the Doppler effect.

Radio oscillators pulsating emit photons "in waves". But photons are not only produced by oscillators (i.e., by nuclear reactions). Incandescent lamp and most stars (except pulsars) emit photons continuously, irregularly and randomly (by random nuclear explosions), not in pulsed waves. These light waves are not polarized and not pulsed. On these waves the wavelength as a distance does not make sense. To them frequency ($\nu = c/\lambda$) has meaning only as a measure of their energy or mass.

Stars emit particles of all sizes such as UV-rays, X-rays, radio waves, γ-rays and ions. The radiation is continuous, not in pulsed waves. If an ion departs from a star and travels towards earth, except of a possible collision, it will arrive on earth integer, regardless to star's motion. That is also true for a photon: we do not expect change its size on the way because the star is moving. A γ-photon emitted from a far star will not arrive on earth as an X-photon. An X-photon will not arrive as a UV-photon. Blue photons will arrive as they are and make man's eye to feel the blue color. Therefore, any calculation based on redshift or blueshift is false. In 1987, Jan Pierre Vigier and Jan Claude Pecker blamed the cosmic dust for redshift. Now, their speculation becomes reasonable: Blue photons because of bigger size absorbed more by cosmic dust than the red ones. The bigger size, the much more collisions occur leading to higher absorbance. The longer distance among star and earth, there is more dust between them. The more dust between them, the less blue photons arrive on earth than the reds. For the same reason the old lighthouses had red lamps. Another possible explanation involving dust is due to Compton effect.

Consequently, we can't be sure about the speeds of stars or galaxies and so the existence of the dark matter. Also, the supposed acceleration of the universe and the attendant concept of "dark energy" is a mistake.

REFERENCES

1. Schmitt, W. and K. Vewinger, "Bose-Einstein condensation of photons in an optical micro cavity," *Nature*, Vol. 468, 545–548, 2010.
2. *Physical Review Letters*, DOI: 10.1103/physrevlett.107.083602.

Tunable Quantum Interference in a Four-level Atomic System for Photonic Device Design

Shengtao Mei[1], **Hang Zhao**[1], **and Jian Qi Shen**[2]

[1]Centre for Optical and Electromagnetic Research
Zhejiang University, Zijingang Campus
No. 5 East Building, Hangzhou 310058, China
[2]State Key Laboratory of Modern Optical Instrumentations
Department of Optical Engineering
Zhejiang University, Yuquan Campus, Hangzhou 310027, China

Abstract— Four-level atomic systems that can exhibit nontrivial double-control quantum coherence have attracted intensive attention of researchers. Since a four-level system is driven by two control laser beams and one probe laser beam, one can coherently manipulate the probe transition (and hence the optical properties of the four-level atomic vapor) with double-control destructive and constructive quantum interference between the two transition paths driven by the two control fields. Take a tripod-configuration system for example. The three lower levels can form a three-level dark state that can be viewed as a generalization of the concept of two-level dark state appearing in a conventional three-level EIT system. The optical properties of the atomic vapor can be dramatically modified by the double-control quantum interference (such a double-control quantum interference can be realized by tuning the ratio of the intensities of the two control fields). Thus, the wave propagation of one light can be controlled by the tunable quantum interference caused by the other two light waves. We shall consider the destructive and constructive quantum interference occurring in such a multilevel system by solving the equation of motion of density matrix of the atomic system, and suggest a new application in photonic device design (e.g., photonic logic gates and optical switches) based on the present double-control quantum interference effects.

Focusing on the Moiré Effect

S. L. Vesely[1] and A. A. Vesely[2]

[1]I.T.B. — C.N.R., Italy
[2]Via L. Anelli 13, Milano, Italy

Abstract— Wireless reception of images avails itself of two kinds of receivers, based on quite different principles. In optics, catadioptric systems detect images of objects that diffuse natural light. In telecommunications, both transmission and reception are encoded, often digitally. In the latter case, image transmission implies a priorly established encoding. Algorithms can be tuned by comparing the directly viewed scene with the rendering of the transmitted one, so as to remove encoding artifacts. In remote sensing, on the other hand, the encoding of the reflectivity is assumed to be statistically distributed. Since the visual nature of bodies depend on the frequency range of the radiation as well as on other illumination conditions, the comparison of reconstructions with ordinary photographs bears a somewhat limited significance. As we interpret visual scenes by accommodation, the tuning phase may sometimes require us to compare the reconstructions of echo returns with data obtained under the same illumination conditions, and heterodyned to a frequency range fit for sharp images, without appreciably altering the information transmitted. In the synthetic aperture radar (SAR) of the 60's, data were processed optically, and compared with holographic images. In our opinion, the analysis of the detector's response can never be fully substituted by attributing properties to the scattered radiation, such as an elementary nature, a spectral dispersion, or the capability to exhibit space/time patterns.

Elementary Nature: The double nature of radiation, photon/wave-packet, is the accepted result of the analysis of light propagation through a single and a double slit. When just one slit is open, the light path towards the target screen passes through it. The blur on that surface is interpreted as the probability density of a photon hitting it. When both slits are open, the wavy pattern on the screen is interpreted as the joint probability that a photon passes through either slit, calculated without assigning the probability that it passes through a given one of them. However, the problem of the nature of radiation is different from that of signal reception. The ability to compute the fast Fourier transform (FFT) of encoded signals does not, by itself, imply a statistical distribution of sinusoidal vibrations in general. Likewise, we may say that the stigmatic image of a point, its point spread function (PSF), does not entail that light consists of photons.

Spectral Dispersion: The harmonic analysis of the response applies the Fourier transform, by which space-time and spectral domains are dual of one another. Classically, the solutions of differential equations obtained by the Laplace transform method have to be transformed back to be interpreted. In quantum theory, the linear momentum p and the free coordinate q become non-commuting operators P and Q. The uncertainty principle applies at atomic scale, and causes a probabilistic interpretation of the Fourier transform independently of the scale. If the wave function, which carries position information, is expressed as a Fourier series, the coefficients of the packet's "frequency" terms belong to the impulse space, which is reciprocal to the configuration space. That hardly applies to images, for example those of some birds' feathers and their interference colors, which can be seen sharp on focus simultaneously.

Space/time Patterns: In optics, moiré refers to beat patterns produced by superposed gratings. Originally, the name "moiré" designates the watered look of a kind of silky fabric. In digital images, the Nyquist sampling rate of the passband can produce a moiré-like aliasing effect, which is an artifact observed on the screen. The moiré on which we focus is the irregularly streaked appearance of fine-textured, folded drapery against an uniformly lit background. Usually a diffractive optical system displays both the image and the diffraction pattern of a subject, but if the corresponding planes cannot be detected separately it is not possible to discern which is which. The planes mingle if the depth of a nearby subject is considerable with respect to the effective focal length of the lens, or if the subject is far away, so that both planes move towards the back focal plane. The latter case applies to folded curtains. Eyes are mainly well described by diopters, and seldom behave as diffractive systems. On the other hand, it is not always clear what to expect from algorithmically reconstructed images of unencoded received radiations.

In conclusion, the moiré effect belongs to the common visual experience. If it affects images taken under other illumination conditions without being recognized as such, it contributes artifacts and noise. It cannot be easily attributed to the local details of the objects' structure, nor to the

nature of the radiation. It could be hinted at by comparing reconstruction algorithms with the performance of focusing detectors.

Response of Multilayer Materials to Electromagnetic Waves

R. Kadlec, P. Marcoň, E. Kroutilová, and P. Fiala
Department of Theoretical and Experimental Electrical Engineering
Brno University of Technology, Kolejní 2906/4, Brno 612 00, Czech Republic

Abstract— The authors report on an analytical solution of the propagation, reflection and refraction of broadband electromagnetic signals within multilayer optical materials. The presented solution is processed in the Matlab program, which is suitable for a specifically oriented detailed analysis of a general problem.

The paper includes a theoretical analysis and references to the generated algorithms. Comparison of the parameter changes is supported by graphical outputs of the algorithms. Algorithms created in the Matlab environment are verified by means of programs based on the finite element method, namely the ANSYS program.

Inhomogeneities and regions with different parameters generally appear even in the cleanest materials. During the electromagnetic wave passage through a material there occurs an amplitude decrease and a wave phase shift; these phenomena are due to the material characteristics such as conductivity, permittivity, or permeability. Any incidence of a wave on an inhomogeneity results in a change in its propagation. The change manifests itself in two forms, namely in the reflection and refraction. In addition to this process, polarization and interference may appear in these waves.

The methods described in this paper are well-suited for the analysis of beam refraction to the other side from the perpendicular line during the passage through the boundary. This phenomenon occurs in metamaterials.

ACKNOWLEDGMENT

The research described in the paper was financially supported by the research program of Ministry of Industry and Trade of the CR (Diagnostics of Superfast Objects for Safety Testing, FR-TI1/368), Czech Science Foundation (102/09/0314), project of the BUT Grant Agency FEKT-S-11-5/1012 and project from Education for Competitiveness Operative Programme CZ.1.07.2.3.00.20.0175, (Electro-researcher).

REFERENCES

1. Dedek, L. and J. Dedková, *Elektromagnetismus*, Vol. 2, 232, Vitium, Brno, 2000, ISBN 80-214-1548-7.
2. Nešpor, D., "Electromagnetic wave propagation study in heterogeneous structures," Ph.D. Thesis, 20, Supervisor Doc. Ing. Pavel Fiala, 2009.
3. Fiala, P., R. Kadlec, P. Drexler, and P. Dohnal, "Tuned periodical structures — Model, experiments in THz band applied in safety application," *PIERS Proceedings*, Cambridge, USA, July 5–8, 2010.
4. Steinbauer, M., R. Kubásek, and K. Bartušek, "Numerical method of simulation of material influences in MR tomography," *Progress In Electromagnetics Research Letters*, Vol. 1, 205–210, 2008.

Analysis of Distortion Factor of Three Phase Linear Synchronous Motor

Koichi Nakaiwa[1] **and Hiroyuki Wakiwaka**[2]

[1]Tamagawa Seiki Corporation, Japan
[2]Shinshu University, Japan

Abstract— It is important to take into account of the influence of distortion factor in the design of a linear motor. A distortion factor expresses the grade of distortion of a waveform, and it is a ratio of the effective value of the overall higher harmonic wave contained in the distorted wave to the effective value of a fundamental wave. Since a current effective value will also increase if a distortion factor becomes high, electric power increases by I^2R, and it becomes important whether a high thrust can lower the distorted rate of the E.M.F wave pattern from a point of vibration and the overheat. This report describes a distortion factor and verifies the distortion factor change analysis by the changes of the aspect ratio of the magnets in three linear synchronous motors of the density uniformity. The summary specification of three models is shown in Table 1. Software is inner product, and analysis is estimating an E.M.F waveform and distortion factor.

As an example, from the calculated result of E.M.F waveform, Halbach array is considered that a thrust becomes highest, and it is presumed that magnet arrangement acts on distortion factor. And, distortion factor was analyzed also in the change aspect ratio of Halbach array (refer Fig. 1).

The relation between the E.M.F and distortion factor by magnet arrangement was compared and verified. The use of linear motor suitable for each magnet arrangement was drawn from a viewpoint of magnetic energy efficiency (for example: generator use, industrial use high speed drive use etc.)

Table 1: Summary specification.

Type / Item	Radial array	Halbach array	Interior array
External dimensions	12 mm		
stroke	30 mm		
Number of pole & slot	8 p–18 s		
Structure of magnet	Radial magnet	Radial & Thrust magnet	Radial & Thrust magnet + magnetic ring

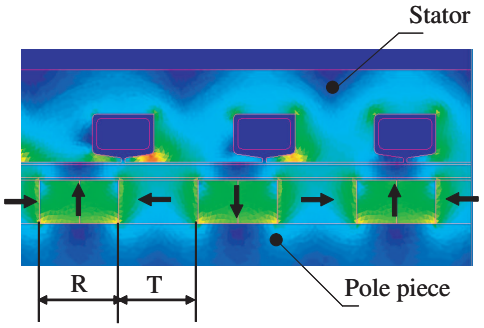

Figure 1: Change of aspect ratio of Halbach array.

REFERENCES

1. Nakaiwa, K., H. Wakiwaka, and K. Tashiro, "Thrust characteristic comparison of interior magnet type pencil size cylinder linear motor," *Journal of the Japan Society of Applied Electro Magnetics and Mechanics*, 509–512, 2011.

Simulation of 3-D SAR Imaging Based Outdoor RCS Measurement Technique

Kefei Liao[1], **Sanyuan Xu**[2], **Xiaoling Zhang**[1], **and Jun Shi**[1]

[1]Lab. B504, School of Electronic Engineering
University of Electronic Science and Technology of China, Chengdu, China
[2]Unit 95784 of PLA, China

Abstract— Most traditional RCS Measurement systems need to be placed in anechoic chamber to reduce noise, but the sizes of targets are limited by the anechoic chamber. To overcome these defects, RCS Measurement technique based on 3-D SAR imaging is developed, which can be used outdoor and to measure large targets, such as flights and tanks.

3-D SAR imaging technique can spatially distinguish the scattering characteristic and RCS of the different parts of complex objects, or distinguish the targets' RCS from noise. By selecting the region of interested manually (pick out the electric/magnetic currents in the region of interested using the prior information on the target's shape), or by cancelation technique (for example, subtract the image of the empty box from the "box + target" image), we can obtain the scattering characteristic in the ROI, and calculate its RCS easily.

The mechanism of RCS Measurement via 3-D SAR imaging can accurately be explained using the Stratton-Chu equation. For perfect conductor, the 3-D image is related to the electric current density, and the received Electric-field is related to the electric current density, as a result, the RCS can be calculated as the ratio of the received Electric-field to the transmit Electric-field.

As validation, the scattering fields are computed using widely accepted software FEKO based on physical optics. The IFFT algorithm is adopted for step-frequency data to form a high-resolution range image, and the 3-D BP algorithm is adopted to form a focused 3-D image. The technique of imaging and the measurement of RCS for a 3-D complex-shaped perfect electric conductor electric-large target, such as a flight-like object, are presented.

GRECO Based Spotlight SAR Imaging Simulation Method

Min Su, Jia Liu, Ning Fang, and Baofa Wang
School of Electronic Information Engineering, Beihang University, Beijing, China

Abstract— SAR (Synthetic Aperture Radar) simulation plays a significant role in radar target recognition for its convenience in data supporting. Radar signal and EM scattering characteristic are usually two independent sources of SAR simulation, which are based on different method. The former is currently the main contribution to SAR research. Since GRECO (Graphical Electromagnetic computing) could compute the EM scattering characteristic of complex electrically large target with fast speed and acceptable error, generating SAR image based on it has great practical values. This paper introduces a GRECO based spotlight SAR imaging simulation method, which simulates and calculates the target scattered field and generates the SAR data, and then further processes the SAR image. The result of the real complex target proves the method's effectiveness.

A Multi-baseline InSAR DEM Reconstruction Approach Based on Proportional Subband Filtering

Shuang Li and Huaping Xu
Bei Hang University, No. 37 Xue Yuan Road, Hai Dian District, BeiJing 100191, China

Abstract— Comparing to the single-baseline interferometric synthetic aperature radar (InSAR) system, multi-baseline InSAR system can offer additional observation information and enhance estimate accuracy of height reconstruction. In multi-baseline InSAR system, the short baseline makes phase unwrapping much more easily but has higher height ambiguity, while the long baseline usually causes phase unwrapping more complicated but has lower height ambiguity. It is significance to combine the SAR images from different baselines. However, the equal baselines is better than the different baselines in terms of CRLB of height estimation, and proportional subband filtering is equivalent to equal baseline. Therefore, this paper presents a multi-baseline InSAR digital elevation model (DEM) reconstruction approach based on proportional subband filtering. This method mainly includes two steps: the first step is about how to obtain interferometric phase images from different baselines, and the second one is the proportional subband filtering mechanism. Then, through simulation, the achieved results not only demonstrate the higher DEM reconstruction accuracy and practicability of the approach proposed in this paper, but also prove that the performance of the proposed approach is much better than multi-baseline InSAR.

Bridgeless SEPIC-derived LED Driver without Electrolytic Capacitor for Multistring Application

H.-B. Ma[1], **Q.-Y. Feng**[2], **T.-J. Zeng**[2], **and X.-H. Yuan**[2]

[1]School of Electrical Engineering, Southwest Jiaotong University, Chengdu, Sichuan 610031, China
[2]Institute of Microelectronics Technology, Southwest Jiaotong University, Chengdu, Sichuan 610031, China

Abstract— High brightness light-emitting-diode (HB-LED) has attracted a lot of attention for its high efficacy, simple to drive, environmentally friendly, long lifespan and compact size. The power supply for LED also requires long life while maintaining high efficiency, high power factor and low cost. However, a typical power supply design employs electrolytic capacitors as storage capacitors, which is not only bulky, but also with short lifespan, thus hampering the development of the entire LED lighting system. In this paper, a novel bridgeless SEPIC-derived AC/DC converter is proposed. The proposed converter has the following features: 1) The totem-pole configuration is employed to decrease the number of semiconductors in the line-current path. 2) Special DCM operation make the intermediate capacitor wok as the power decoupling capacitor, thus it make the elimination of electrolytic capacitor be possible in the presented converter. This bridgeless topology is then developed for driving multiple LED strings. By allowing a relatively large voltage ripple allowable in the AC/DC converter, the electrolytic capacitor with large capacitance can be replaced by the film or ceramic capacitor with small capacitance while maintaining high power factor and high efficiency. A 50-W prototype has been built to verify the proposal. The experimental results have shown that the proposal has the features of high power factor over 0.95 and high efficiency over 85% under universal input voltage operation.

Investigation of Irregularities Induced from Medium-scale Traveling Ionospheric Disturbances Using Global Positioning System and Digisonde

Wei-Sheng Chen[1], **Chien-Chih Lee**[1], **and Fang-Dar Chu**[2]

[1]General Education Center, Chien Hsin University of Science and Technology, Taiwan
[2]National Standard Time and Frequency Lab, Chunghwa Telecom Co. Ltd., Taiwan

Abstract— This study is intended to investigate the irregularities induced from medium-scale traveling ionospheric disturbances (MSTIDs) over Wuhan (30.51°N, 114.41°E) in China. We employed the data came from the GPS receiver and the digisonde at Wuhan. The data were limited in 2000 when sun was in high solar activity period. The events of MSTIDs were derived from the perturbations of total electron content (TEC) of GPS data. The GPS phase fluctuation index and the spread F occurrences were calculated and examined from the GPS and digisonde observations, respectively. We explored the seasonal and nighttime occurrence rates as well as the one-to-one correspondences for these phenomena. We discovered that, for the seasonal variations, three phenomena all are highly active in summer, which confirms that irregularities over Wuhan mainly relate to MSTIDs. Moreover, all spread F types have a minor occurrence peak in winter but none for the MSTIDs and the GPS phase fluctuations. Besides, none of large GPS phase fluctuations event had occurred during observation periods, which indicates that the strength of irregularities related to MSTIDs are weaker than that of equatorial plasma bubbles. For the nighttime variations, the frequency spread F occurs earlier than other spread F types which implies that disturbances start at the altitude near the F-region peak. For the one-to-one correspondences, the occurrence rates of each spread F type and GPS phase fluctuations are low during MSTIDs occurred. This implies that smaller scale irregularities which are observed as spread F or GPS phase fluctuations may only appear in some phase of MSTIDs.

A Study of Equatorial Ionospheric Irregularities over the Indian-Ocean Sector during Solar Maximum by Using the Global Positioning System

F. D. Chu[1], **W. S. Chen**[2], **C. C. Lee**[2], **W. H. Tseng**[1], **H. T. Lin**[1] **and C. S. Liao**[1]

[1]National Time and Frequency Standard Lab, Chunghwa Telecom Co., Ltd., Taiwan
[2]General Education Center, Chien Hsin University of Science and Technology, Taiwan

Abstract— Ionospheric irregularities will exert scintillations on electromagnetic waves if the waves pass through them. So they are interesting for ionospheric propagation at the magnetic equator and low latitudes. The irregularities during solar maximum period were examined by tracking stations of the global position system, which were located in the India-Ocean sector in both southern and northern hemispheres. The results show that the significant nocturnal ionospheric irregularities appear equinoctial dominance at low latitudes. Besides, there is an equinoctial asymmetry of occurrence rate of irregularities, i.e., the rate seems larger during spring (March–April) than autumn (September–October) over the eastern sector, while appears larger during autumn than spring over the western sector. Moreover, the equinoctial asymmetry can reverse over the eastern sector when solar activity is going to reach maximum during the rising phase of a solar cycle.

Multi-instrument Observations of F-region Irregularities near the Crest of Equatorial Ionization Anomaly

Chien-Chih Lee[1], **Wei-Sheng Chen**[1], **and Fang-Dar Chu**[2]

[1]General Education Center, Chien Hsin University of Science and Technology
No. 229, Jianxing Rd., Zhongli City, Taoyuan County 32097, Taiwan
[2]National Standard Time and Frequency Lab of Telecommunication Laboratories
Chunghwa Telecom Co. Ltd., No. 99, Dianyan Rd., Yangmei City, Taoyuan County 32601, Taiwan

Abstract— This work concurrently studies the occurrence probability of F-region irregularities near the crest of equatorial ionization anomaly (EIA). The data were recorded by an ionosonde, a GPS receiver, and ROCSAT-1 during 2000. Results show that the occurrences of the range spread F (RSF) differ from those of the frequency spread F (FSF). For the seasonal variation, the RSF occurrence has the maximum values in March and September; while the FSF occurrence peaks at June. For the nighttime variation, RSF and FSF peak at 2300 and 0300 LT, respectively. Regarding the GPS phase fluctuations, an index, Fp, is applied to characterize the irregularity strength. The similarity between the $50 < \mathrm{Fp} \leq 200$ and RSF occurrences demonstrates that the characteristics of F-region irregularities forming $50 < \mathrm{Fp} \leq 200$ are mainly related to RSF. The occurrence of $200 < \mathrm{Fp}$ is almost absent. The rare event is also found in the observation of plasma bubbles by ROCSAT-1. Furthermore, the seasonal variations in GPS phase fluctuations at the EIA crest and the dip equator have similar trends. This indicates that the F-region irregularities of RSF and $50 < \mathrm{Fp} \leq 200$ at the EIA crest are originated from the equatorial ionosphere. On the other hand, the seasonal variation in occurrence probability of FSF at the EIA crest is close to that of spread F at mid-latitudes. This suggests that the generation mechanisms of FSF and mid-latitude spread F might be same, but the further study is required.

Satellite Monitoring for Elasto-plastic Behavior of Plate around Epicenter in a Process Tsunami Earthquakes

Shigehisa Nakamura
Kyoto University, Japan

Abstract— This is a note to crustal plate creeping process for a trigger of great destructive earthquake accompanied tsuman. A simple model is introduced in order to have this dynamical understanding at an informed attention of the sliding shift of the eastern boundary of the Eurasian plate in a form of a fluidized elasto-plastic material. This process was observed at the seismic event on 11 March 2011 though it is necessary to consider on the possible energetic process of this earthquake tsunamis. This process could be seen when it is a process found in the plates in a global scale. A possibility might be expected for satellite monitoring of disturbance in positioning of the settled stations on the plate in order to track this process effectively.

A Geomagnetic Polar Drifting Path Evolution on the Geographic Earth Surface

Shigehisa Nakamura
Kyoto University, Japan

Abstract— This work concerns to a geomagnetic polar drifting projected on the geographic earth surface. Under serveral assumptions, a specific sun spot positioning is considered for a convenient reference at modeling of the geomagnetic poloidal and toroidal modes is taken to be possible instead of the case of the solar spot model of eleven year cycle. This may lead to a consistent geomagnetic polar drifting path evolution on the geographic earth surface.

Electromagnetic Process at a Crustal Fault Formation for Tsunami Earthquake on the Planet Earth

Shigehisa Nakamura
Kyoto University, Japan

Abstract— This work concerns to an electromagnetic process at a crustal fault as a seismic tsunami generation. Special references are the data of satellite monitoring, and of geophysical process at a specific tsunami earthquake. The data shows that the pattern of the earth surface displacement is quite similar to a water flow pattern out of a reservoir through a conduit in a hydraulic field. This fact tells us that the earth surface displacement pattern indicates the crust is in motion pointing to an epicenter of the earthquake for forcing the crust driven by the magma under the crust. This process might be consistent to induce an impulsive impact in the ionospheric layers just above the seismic epicenter.

Advancing Climate Studies in the Australasian Region Using Ground and Space-based GPS Techniques — An Overview of Recent Progress

Yuriy Kuleshov[1, 2], Erjiang Fu[3], Sue-Lynn Choy[2], Fabrice Chane-Ming[4], Yuei-An Liou[5], and Alexander G. Pavelyev[6]

[1]National Climate Centre, Bureau of Meteorology, Melbourne, Australia
[2]School of Mathematical and Geospatial Sciences, RMIT University, Melbourne, Australia
[3]Climate and Water Division, Bureau of Meteorology, Melbourne, Australia
[4]Laboratoire de l'Atmosphère et des Cyclones, Université de la Réunion St Denis
Ile de la Réunion, France
[5]Center for Space and Remote Sensing Research (CSRSR)
National Central University, Jhongli, Taiwan
[6]Kotelnikov Institute of Radio Engineering and Electronics, Russian Academy of Sciences
Fryazino, Moscow Region, Russian Federation

Abstract— We describe recent results on advancing climate studies in the Australasian region using the global positioning system (GPS) radio occultation (RO) and GPS ground-based observations. Temperature trends in the troposphere and the lower stratosphere over the Australian region and the Antarctic were examined using atmospheric temperature records obtained by the GPS RO and *in-situ* radiosonde observations. The GPS RO data provide detailed vertical structure of temperature trends and demonstrate overall cooling in the lower stratosphere and warming in the troposphere, in agreement with radiosonde measurements. The potential of using ground-based GPS observations for studying severe weather events has been demonstrated using the March 2010 Melbourne thunderstorm as a case study. Strong spatial and temporal correlation between variations of the ground-based GPS-PWV (precipitable water vapour) estimates and the thunderstorm passage has been found. This finding demonstrates that the ground-based GPS technique can supplement conventional meteorological observations in studying, monitoring, and potentially predicting thunderstorms. Daily radiosonde and GPS RO data over the South Indian Ocean have been examined, signatures of tropical waves have been identified and their spatial and temporal distribution have been analysed. Relationships of the tropical waves with convective activity such as tropical cyclones have been also investigated. An innovative analytical technique based on the relationships among the derivatives of the phase, eikonal and Doppler frequency over time and the intensity of GPS transmitted radio waves through the Earth' atmosphere has also been further developed. Application of this innovative technique could advance our understanding of tropical cyclone genesis and development.

Scattering of Light from Rough Surfaces, the Limits of Validity of Geometric Optics Approximation Method

Imed Sassi and Mehdi Khemiri
Laboratory of Physico-chemical of Materials, Faculty of Science of Monastir
University of Monastir, Monastir, Tunisie

Abstract— The geometric optics approximation (GOA) for predicting wave scattering from rough surfaces is developed. The GOA consists of ray tracing the energy incident on a rough surface until it leaves the surface after having incurred multiple rebounds. The effects of the direction of incident light and optical properties of rough surfaces on the scattering and the backscattering of light are presented. For one-dimensional rough surfaces, the GOA is quantified by comparisons with the exact electromagnetic theory calculations. The regions of validity of the approximation method for TE and TM polarization are quantified. For dielectric rough surfaces, the integral method (IM) is used to determine the domains of validity of the GOA. Using that method represents a significant reduction in computational time and memory.

Modulation in the Spectral Degrees of Polarization of Stochastic Electromagnetic Higher-order Bessel-Gauss Pulsed Beams

Weimin Peng, **Haixia Wang**, **and Chaoliang Ding***
College of Physics and Electronic Information, Luoyang Normal University, Luoyang 471022, China

Abstract— Using the coherence theory of non stationary field, the analytical expression for the spectral degree of polarization of stochastic electromagnetic HBGP beams propagating in free space is derived. The effect of beam order, radial spatial frequency, pulse duration and temporal coherence length on the spectral degree of polarization of electromagnetic HBGP beams is illustrated through numerical calculations. It is shown that the position z of the spectral degree of polarization $P = 0$ increases with increasing beam order and pulse duration, whereas it decreases with increasing radial spatial frequency and temporal coherence length, respectively.

*Corresponding author: Chaoliang Ding (dingchaoliang2006@126.com).

Weighted Multi-frequency Imaging of Thin, Crack-like Electromagnetic Inhomogeneities

Y.-D. Joh, Y. M. Kwon, J. Y. Huh, and W.-K. Park
Department of Mathematics, Kookmin University, Seoul 136-702, Korea

Abstract— In recent work [2], a MUltiple SIgnal Classification (MUSIC)-type algorithm has been designed and demonstrated to be a useful technique for imaging of thin, crack-like electromagnetic inhomogeneities. Unfortunately, this algorithm offers a result of poor resolution whenever one tried to obtain such inclusion both dielectric and magnetic contrasts with respect to the embedding homogeneous space, an improved multi-frequency based subspace migration has been considered [1]. However, although this technique has been proven to be effective for imaging of such inhomogeneities, owing to its heuristic application, a mathematical study is still required in order to investigate its properties. In this paper, we discuss the structure and properties of existing subspace migration, introduce an improved weighted multi-frequency imaging algorithm, and explore some properties of the proposed algorithm. This is based on the fact that the measured scattered field can be written as an asymptotic expansion formula. Some numerical results are computed in order to demonstrate the feasibility of the proposed algorithm.

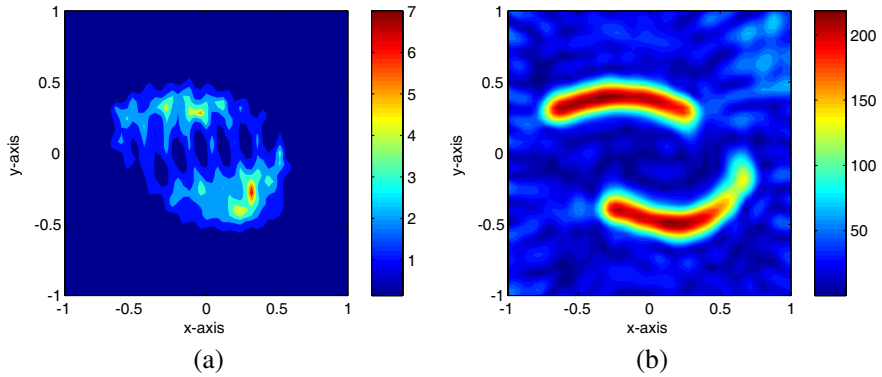

Figure 1: (a) Imaging results via MUSIC and (b) weighted multi-frequency algorithms.

REFERENCES

1. Park, W.-K., "Non-iterative imaging of thin electromagnetic inclusions from multi-frequency response matrix," *Progress In Electromagnetics Research*, Vol. 106, 225–241, 2010.
2. Park, W.-K. and D. Lesselier, "MUSIC-type imaging of a thin penetrable inclusion from its far-field multi-static response matrix," *Inverse Problems*, Vol. 25, 075002, 2009.

Broad-band Spectrum Control with Polarization

Pin Han
Graduate Institute of Precision Engineering, National Chung Hsing University
250, Kuo Kuang Road, Taichung 402, Taiwan, R.O.C.

Abstract— In this paper, we study the reflection wave from an interface for a broad band light field. We show that the reflected spectra can be controlled to show the blue-shift or red-shift with the change of polarization. The behavior of the reflectance of an interface with different incident angles and polarizations are investigated. Using the Fresnel equations the reflected spectrum can be calculated and studied numerically. Also the spectral switch can be turned on/off with the variation of p-light or s-light.

Estimating Properties of Subsurface Layers from GPR Spectral Attributes

Z. L. Huang[1,2] **and J. Z. Zhang**[1]

[1]College of Marine Geosciences, Ocean University of China, China
[2]School of Information Science and Technology, Xiamen University, China

Abstract— Inferring properties of subsurface layers is the main task of ground penetrating radar (GPR) detection. It is difficult to infer the properties of thin layers in time domain because of the interference of waves reflected from the top and base of each thin layer. Based on the different influence of the geometric and the electric parameters of subsurface layers on the GPR frequency spectra, we use the different GPR spectral attributes to estimate the different parameters of subsurface layers. For example, consider a three-layer model. The frequency of the first spike in the amplitude spectrum of GPR response to the model is equal to the inverse of double temporal thickness of the middle layer, and the period of the notches in the amplitude spectrum is equal to the inverse of the thickness. So the temporal thickness of the middle layer can be estimated from the frequency of the first spike in the amplitude spectrum, or from the period of the notches. The frequencies of the extremes in the phase spectrum depend only on the depth and the thickness of the middle layer. When the thickness has already been obtained, the temporal depth can be estimated using only the extreme value positions of the phase spectrum. When the thickness and the depth of the middle layer are fixed, the permittivities of the three layers and the conductivity of the middle layer can be estimated from only the phase spectrum. In consequence, we propose a step-by-step GPR spectral inversion method for the estimation of thicknesses, depths, permittivities and conductivities of subsurface layers.

Identification of Subsurface Thin Layers Using Cepstrum of GPR Data

Z. L. Huang[1, 2] **and J. Z. Zhang**[1]

[1]College of Marine Geosciences, Ocean University of China, China
[2]School of Information Science and Technology, Xiamen University, China

Abstract— A new method is presented for identification subsurface thin layers using cepstrum of GPR data. First, spectrum of the reflection coefficients series is estimated, then instead of using the traditional cepstrum of it, we calculated the real and image part of the pseudo-cepstrum of the series. This kind of cepstrum does not apply logarithmic operation on the spectrum. It's found that the real part of the pseudo-cepstrum can be represented by cosine functions of different quefrencies, while the image part of the cepstrum can be represented by sine functions. The quefrencies of these functions are the positions of the reflection coefficients. Due to the existence of noise, the analysis band is limited, which makes it impossible to directly obtain the time positions by simply applying the Inverse Fourier Transform (IFT) on the cepstrum, since the result of IFT on the cepstrum of GPR data from a thin layer would look the same as that from a single reflection interface. In order to make a difference of these two situations, we add the real part with a phase-shifted image part of the cepstrum. The shift parameter depends on the peak of the magnitude cepstrum. If the peak turns out to be the result of a single reflection interface, the adding would make the quefrency component disappear. The residual would still be strong if the cepstrum is a result of a thin layer reflection. So from the different results we can decide the existence of subsurface thin layers.

Monitoring System for Space Weather

Edwin A. Quintero, Iván D. Arellano, and Jimmy A. Cortés
Department of Physics, Technological University of Pereira
Vereda La Julita, Pereira, Colombia

Abstract— Solar fulguration or flares, protuberances, sunspots, and coronal mass ejection (CME), release large amounts of radiation composed of ions, which upon reaching the outer layers of the earth interact with the particles present there modifying their electrical characteristics. The set of events resulting from this series of phenomena gives rise to the term "space weather". Among the possible complications caused by space weather, interferences are presented in geolocation, telecommunications, satellite operations, space monitoring, radio navigation, electrical networks and fuel transportation networks. In order to begin monitoring space weather, the Alfa Orion astronomy research group planned and executed a project for the design and construction of a signal detection system to operate in the very low frequency band of the electromagnetic spectrum (17–25 kHz VLF band). This system is formed by a detection stage composed of an array of loop antennas, a filtering and signal conditioning stage, and a processing and visualization stage based on a computer graphic interface. The system enables quantitative measurement of variable frequency, signal strength, signal to noise ratio, and power spectral density (PSD) of the received signals.

Principle of Locality and Remote Sensing from Space

A. G. Pavelyev[1], **Y. A. Liou**[2], **A. A. Pavelyev**[1], **K. Zhang**[3], **and Yu. Kuleshov**[4]

[1]Kotelnikov Institute of Radio Engineering and Electronics, Russian Academy of Sciences
Fryazino, Moscow, Russia
[2]Center for Space and Remote Sensing Research, National Central University
Chung-Li 320, Taiwan
[3]School of Mathemathical & Geospatial Sciences, RMIT University
GPO Box 2476V, Melbourne 3001, Australia
[4]National Climate Centre, Bureau of Meteorology, Melbourne, Australia

Abstract— A fundamental principle of local interaction of radio waves with a refractive spherical medium is formulated and illustrated using the radio occultation (RO) method of remote sensing of the atmosphere and ionosphere of the Earth and planets. In accordance with this principle, the main contribution to variations of the amplitude and phase of radio waves propagating through a medium makes a neighborhood of a tangential point where gradient of the refractive index is perpendicular to the radio wave trajectory. A necessary and sufficient condition (a criterion) is established to detect the displacement of the tangential point from the radio ray perigee using analysis of the RO experimental data. This criterion is applied to the identification and location of layers in the atmosphere and ionosphere by use of GPS RO data. RO data from the CHAllenge Minisatellite Payload (CHAMP) are used to validate the criterion introduced when significant variations of the amplitude and phase of the RO signals are observed at the RO ray perigee altitudes below 80 km. The detected criterion opens a new avenue in terms of measuring the altitude and slope of the atmospheric and ionospheric layers. Depending on the sign of the refractive attenuations the displacement of a plasma layer from the RO ray perigee should be positive (in the direction to a GPS satellite and vice versa). The magnitude of the displacement can be found from a ratio of the refractive attenuation's difference to the magnitude of the refractive attenuation from the RO phase data. The altitude and slope of a plasma layer can be found from the known value of its displacement. Therefore the standard estimation of a layer's altitude as a height of RO ray perigee should be revised due to underestimation of the altitude of inclined plasma structures in the lower ionosphere. The accuracy of the current radio-holographic back-propagation method depends on the form of the Green function used for the back-propagation. If the Green function corresponding to the propagation in the free space is used, then the inaccuracy of back-propagation method is proportional to the bending angle. The analytic technique based on the locality principle is simpler and more precise than the back-propagation method. By use of the introduced criterion the RO method is capable of locating and determining the direction and magnitude of the gradient of electron density in the lower ionosphere. This is important for the location determination of the wind shear and the direction of internal wave propagation in the lower ionosphere, and possibly in the atmosphere.

ACKNOWLEDGMENT

The work is partly supported by RFBR grant No. 10-02-01015-a.

Design and Implementation of Bandgap References Voltage Circuit for SOC Module Applications

Min-Chin Lee, Chi-Jing Hu, and Wen-Shiang Jung
Orient Institute of Technology, New Taipei City, Taiwan

Abstract— All kinds of portable electronic products in the current market have an orientation toward light, slim and small. They have both a variety of applications and long operation time. Thus a high-efficiency power management module is necessary such as low-power power converter or low dropout regulator to integrate with mixed-mode signal circuit into a single chip (SOC) to achieve the different kinds of low-power applications. Therefore it requires a low-power bandgap reference voltage circuit to offer different reference bias voltage source for power management circuits of portable SOC module. In this paper, we design a low-power bandgap reference voltage circuit that can operated from a nominal 1.3 to 1.8 V power supply. The circuit provides an output reference voltage of 1.124 V close to the bandgap voltage having a low output resistance and allows resistive loading. It does not use an operational amplifier and dissipates low power of 0.1 mW. And no resistors are used in its design and hence it can be fabricated in any digital CMOS technology. The circuit uses a NIC current conveyor and current mirrors to convert the proportional to absolute temperature voltage into a current using a MOSFET. The current is converted back to a voltage by using the functional inverse of the diode-connected MOSFET characteristics. This makes the voltage gain linear and temperature independent. This proposed circuit is design and implemented using the TSMC 0.18 µm CMOS process. Based on simulated and measured results, the chip size is $0.502 \times 0.583\,\mathrm{mm}^2$ with power dissipation about 0.1 mW, and the operation temperature range form $-40^\circ\mathrm{C} \sim 85^\circ\mathrm{C}$ with temperature coefficient about 25.53 ppm/°C. The chip suply voltage can from 1.3 to 1.8 V with PSRR about 70 dB, and its output reference voltage can stable at 1.12 V. Therefore it is suitable for power management circuits of SOC module or low power wireless receiver applications.

Spatial Interpolation for Mapping Geoclimatic Factor K in South Africa

M. O. Asiyo and T. J. O. Afullo
Department of Electrical, Electronic and Computer Engineering
University of KwaZulu-Natal, King George V Ave., Durban 4041, South Africa

Abstract— A deep fading prediction technique is the most important element of practically all methods for estimating multipath outage on terrestrial microwave line-of-sight links (LOS). Most of these techniques are based on empirical fits of Rayleigh-type distributions to the fading data for individual countries and are characterized in terms of climatic conditions. ITU-R provides a global method for predicting the percentage of time that a certain fade depth is exceeded in the average worst month. Apart from link variables, the ITU-R method, has additional variable — the geoclimatic factor K. This variable takes into account the variability of climate and terrain. It is recommended that the geoclimatic factor K be obtained from fading data in the vicinity links of the planned link if such data exist. However, since in most cases such data is not available, prediction methods based on refractivity gradient statistics are recommended. In this paper, geoclimatic factor K derived from radiosonde data for five locations in South Africa are used to estimate and map the values for all the regions in South Africa. Three spatial interpolation techniques: Kriging, Inverse Distance Weighting and Thin-Plate Spline are used in estimating the geoclimatic factor in places where data is not observable. Statistical assessment of these methods is done by calculating the mean absolute error (MAE) and the mean squared error (MSE) between a set of control points and the interpolated results. The best performing method estimated values is used to map the seasonal geoclimatic factor K for the entire study region. The estimated values of geoclimatic factor will improve accuracy in predicting multipath outage in LOS links in the region.

Non-parametric and Parametric Modelling and Characterization of the Effective Earth Radius Factor for South Africa

A. M. Nyete and T. J. O. Afullo
Department of Electrical, Electronic and Computer Engineering
University of Kwa-Zulu Natal, South Africa

Abstract— The effective earth radius factor (k-factor) is an important parameter in the planning and design of both terrestrial microwave and UHF/VHF line-of-sight links. It is for this reason that the structure and variations in the effective earth radius factor in the first 200 m of the atmosphere is critical to radio link planners and optimization engineers alike. The atmospheric composition changes from time to time, place to place and even with height and hence the need for accurate determination and prediction of the k-factor. The four thirds (4/3) value given for the median k-factor in average temperate climate should only be used for gross planning but where data is available, the actual values of the same should be determined. This will ensure well designed links with minimum outage experienced due to k-factor related problems i.e., diffraction (k-type) fading and thus avoiding expensive reverse engineering and optimization procedures. In this presentation, three years radiosonde measurements data sourced from the South African Weather Service (SAWS) has been processed and only k-factor statistics for the first 200 m above ground level considered for further analysis. Both non-parametric and parametric methods have been used to model solutions for the distribution characteristics of the k-factor across seven locations in South Africa. For the non-parametric approach, the kernel density estimate has been used. The so-called 'curve-fitting' method (Gaussian distribution modelling) has been used for the parametric technique. The Integral of Squared Error (ISE) has been applied to optimize the solutions in both cases. Using the foregoing procedures, both median ($k_{50\%}$) and k-factor values exceeded 99.9% of the time (k_e) have been determined. From the results obtained, the kernel density estimate is found to out-perform the curve-fitting method in terms of the ISE. Also, we observe that both techniques give very close k-factor values and so the error performance may be the only key performance indicator between both. The Rectangular kernel is observed to produce superior ISE performance in five out of the seven locations considered. It thus comes out as the more favourable kernel compared to the other three kernels used i.e., Gaussian, Triangular and Epanechnikov kernels. It is also observed that with the optimum choice of the window width or bandwidth, h, there is little to choose from in terms of the kernel function, $K(k)$. Finally, we draw comparisons between the measured, curve-fitting and kernel values of the k-factor obtained.

A Novel Imaging Formation Algorithm Based on Lagrange Interpolation for SweepSAR Data Processing

Wei Yang, Hongcheng Zeng, Jie Chen, and Pengbo Wang
School of Electronic and Information Engineering, Beihang University, Beijing, China

Abstract— Synthetic Aperture Radar (SAR) is playing an significant role in remote sensing science. In past years, an innovative SweepSAR mode was proposed to satisfy the requirements that space-borne SAR systems possess the capability to image with high-resolution wide-swath (HRWS). In this SweepSAR mode, pulse repetition frequency (PRF) is changing along azimuth time, which will avoid the occlusion of transmitted pulse. However, the periodic variation of PRF leads to non-uniform sampling in azimuth and the reformation of range cell migration (RCM). So the traditional imaging algorithm is not suitable for SweepSAR data processing. In order to solve these problems abovethis paper conducted thorough research to the theory of the space-borne SweepSAR data image formation. Firstly, the characteristic of SweepSAR mode is analyzed in detail. Then, the impaction of the sweeping of PRF on the focused quality of imaging is further discussed. By mathematic derivation and theoretical analysis, a valuable conclusion is given: the shorter period of the sweeping of PRF, the farther the paired echo deviates from the main-lobe, and vice versa. Based on this deep analysis result, a novel efficient and accurate imaging formation algorithm based on Lagrange interpolation for SweepSAR data processing is presented, which handles the azimuth non-uniform sampling caused by sweeping of PRF well. At last, numerical simulations are implemented to justify the validity and precision of our proposed algorithm. And the fine focused quality of high resolution images achieved in the point target simulation experiment demonstrate that the perfect performance of the presented imaging algorithm.

Proposal of Technical Measures for a Partial Discharge Detection System Based on Real Measurement

R. Myska, P. Drexler, and T. Kriz
Department of Theoretical and Experimental Electrical Engineering
Brno University of Technology, Kolejni 2906/4, Brno 612 00, Czech Republic

Abstract— The article presents results of the measurement of partial discharge (PD) activity in power oil transformers. The method is based on measurements of electromagnetic waves in UHF spectrum produced by PD. Typical spectrum of the PD radiofrequency (RF) signal ranges from hundreds of MHz to units of GHz. This measurement method has been described in paper [1]. The RF signal is detected by sensing heads that enter the transformer through its casing. Each sensing head contains an antenna and a set of high-frequency components which adapt the signal from the antenna. The signals from the sensing heads are processed by a digitizer and evaluated by custom-made software in real time. This software also comprises a graphic user interface. The interface displays signal waveforms from each sensing head and a vector diagram, which indicates the time position of a partial discharge within a single period of voltage. The measurement of PD activity has been made on eight power transformers in the Dukovany nuclear power plant in the Czech Republic. The initial experimental measurement, which was under full working arrangements, has been accompanied by some issues. The recorded signals contained strong interference. It has been estimated that the source of the interference is probably situated in the high voltage bushings, which feed the transformer from a turbo-generator. The interfering signal in form of electromagnetic waves has propagated through the air vicinity and it has coupled to the sensing heads. It has been found that the proper shielding is a crucial factor, while the PD signal level is far below the level of the interference. Moreover, the current sensor shielding was not sufficient and it allowed to penetrate the interference in to the sensor casing. Further experiments have been conducted with an additional shielding and the interference level significantly decreased. The report on the results of the experimental measurement is given in the paper. There are shown waveform examples of the interfering signal and waveform examples of PD signal. Further, the design of construction measure of the sensor casing, which allows to improve the shielding, is presented also.

ACKNOWLEDGMENT

The research described in the paper was performed within the grant of Czech ministry of industry and trade No. FR-TI1/001 and it was also financially supported by project of the BUT Grant Agency FEKT-S-11-5.

REFERENCES

1. Myska, R. and P. Drexler, "The development of methods for estimation of time differences of arrival of pulse signals," *PIERS Proceedings*, 709–713, Kuala Lumpur, Malaysia, March 27–30, 2012.
2. Markalous, S. M., "Detection and localization of partial discharge in power transformers using acoustic and electromagnetic signals," *Institut fur Energieubertragung und Hochspannungtechnik der Universitat Stuttgard*, 2006, ISBN 978-3-933893-97-0.

A 60 GHz Marchand Balun with Floating Ground Centre-tap in CMOS Technology

Leijun Xu[1], **Henrik Sjöland**[2], **Markus Törmänen**[2], **Tianhong Pan**[1], **and Xue Bai**[1]

[1]Jiangsu University, Zhenjiang 212013, China
[2]Lund University, Lund 22100, Sweden

Abstract— With the increase of the circuit frequency, more balanced structures are used in millimeter-wave designs for reducing noise and high order harmonics, such as Mixers and Amplifiers. As a passive component, Balun plays an important role in the design of balance circuit. To reduce size and provide a simple DC bias for active devices in designs, transformer baluns are commonly used for their easy connected centre-tap to bias. However, one of the problems for millimeter-wave transformer is that its primary side connected to ground will lead unbalance in layout, which will degrade the performance of balun at such high frequency. In this paper, a Marchand Balun with floating ground centre-tap is proposed for silicon-based millimeter-wave applications.

Based on 65 nm CMOS technology, the Marchand Balun is designed with broadside coupling lines by using two top metals. To reduce the size, the balun was folded and both ends of the two secondary side lines are connected together to floating ground, two by-bass capacitances are connected between the real ground and floating ground, as shown in Fig. 1. The balun is simulated by ADS Momentum and different width of the lines are compared to find the optimal value. The insertion loss of the balun is 1.2 dB at 60 GHz, the Amplitude imbalance is less than 1 dB and the Phase imbalance is less than 2.5° in the frequency range from 50 GHz to 70 GHz. The diameter of the designed balun is 100 μm under the output load of 50 Ω resistor.

The proposed balun has small size and floating ground centre-tap for feeding DC bias conveniently. Compared with transformer balun, the layout of this Marchand balun is more symmetric due to the open-end of its primary side, which also improves the bandwidth and imbalances of the balun.

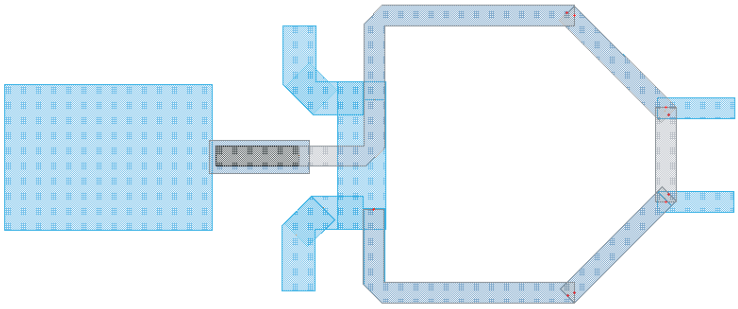

Figure 1: The layout of the proposed Marchand balun.

Compact UWB Monopole Antenna with Tapered Ground Plane

A. Subbarao and S. Raghavan
National Institute of Technology, Tiruchirappalli 620015, India

Abstract— Ultra-wideband is one of emerging technologies in wireless filed due to various merits such as faster data transfer and lower power consumption. A compact ultra-wideband monopole antenna with band-notched characteristic is presented in this paper. It has compact size of $30 \times 32\,\mathrm{mm}^2$. The antenna is fed by coplanar waveguide feed which supports higher bandwidth and lower dispersion. A slot is etched to achieve notched band from 4.9 GHz to 6 GHz to reject interference from WLAN. The proposed antenna operates from 3 GHz to 11.5 GHz for return loss below −10 dB. Parametric study is performed to study effect of different geometrical parameters of antenna on return loss and bandwidth. IE3D electromagnetic simulator is used to analyze this antenna. Various characteristics such as such as return loss, radiation patterns are presented. The radiation patterns are omni directional in H-plane and bi-directional in E-plane. The antenna has consistent gain in operating band. The antenna can be easily integrated with monolithic microwave integrated circuits and is useful for potable UWB systems.

The Effects of Low Power Microwaves at 500 MHz and 900 MHz on Yeast Cells Growth

Hamad S. Alsuhaim[1], **Vuk Vojisavljevic**[1], **and Elena Pirogova**[1, 2]

[1]School of Electrical and Computer Engineering
Royal Melbourne Institute of Technology (RMIT) University
Melbourne, Victoria 3001, Australia
[2]Health Innovation Research Institute, RMIT University, Victoria, Australia

Abstract— In the last few decades, the use of microwave radiation has greatly increased in radar and communication systems, food-processing technology, and other industrial applications. The development of consumer and medical microwave devices for clinical diagnosis and therapy has also prompted widespread interest and stimulated much research into the mechanisms of interaction between microwave radiation and living matter. Two types of effects can be ascribed to microwaves, i.e., thermal and non-thermal. Non-thermal biological effects are measurable changes in biological systems that may or may not be associated with adverse health effects. It was demonstrated that extremely low power microwaves can affect enzymes activities. Little is known about the molecular mechanisms involved in putative non-thermal effects. One hypothesis is that low power microwave radiation can induce dipole oscillations in a protein's active site and thus, can alter its function. Our study evaluates the effect of weak radiofrequency microwave (RF/MW) radiation on the proliferation response of the yeast Saccharomyces cerevisiae. S. cerevisiae strains type II (Sigma) were exposed to the microwaves at the frequencies 900 MHz and 500 MHz and the selected powers of 0 dBm, 10 dBm, −10 dBm, 13 dBm, −13 dBm, 17 dBm and −17 dBm using the Transverse Electro-Magnetic (TEM) cell. The average specific absorption rate (SAR) for a single cell was 0.12 W/kg. SAR was calculated by averaging the individual parameters of the cell components in accordance with their volume fraction in live cells. A comparative analysis of changes in the proliferation rate of the irradiated yeast cells vs. non-radiated cells was performed for the selected frequencies and powers. Changes in yeast culture growth were monitored using the spectrophotometer (Ocean Optics). The findings of this experimental study will be presented and discussed.

Design of 4 GHz Multiplier Based on Sigma-Delta Modulation in a 0.18-μm CMOS Technology

Xiao-Dan Guo[1, 2], **Qiao Meng**[1, 2], **and Yiong Liang**[1, 2]

[1]Institute of RF- & OE-ICs, Southeast University, China
[2]Engineering Research Center of RF-ICs & RF-Systems, Ministry of Education, China

Abstract— This paper presents an implementation of high speed multiplier for direct Sigma-Delta Modulated (SDM) signals. Compared with several other conventional ones, the structure of this multiplier can reduce the circuit-loop delay and work efficiently at a high speed. The integrated circuit (IC) has also been improved with a pipe-line structure and source coupled logic (SCL) technology. It is fabricated in a TSMC's 0.18-μm CMOS process. Simulation results show that the chip meets the function and performance demand of the design and have zero bit error ratio at a frequency higher than 4 GHz. Analysis of the multiplier's noise performance is also presented.

Figure 1 shows the layout of the multiplier. Fig. 2 is the key module of the multiplier with small circuit-loop-delay.

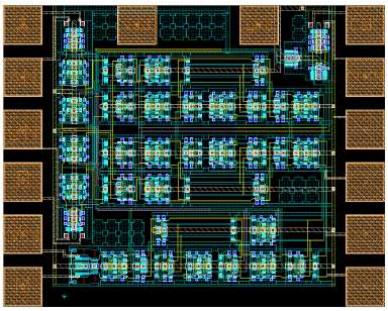

Figure 1.

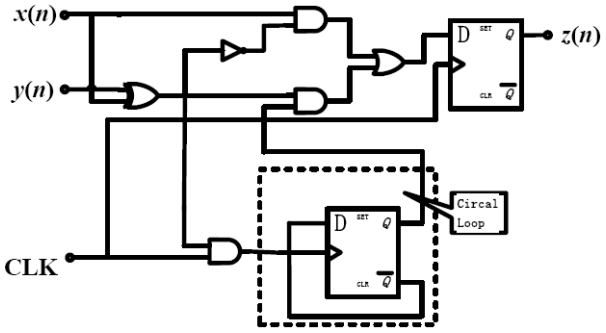

Figure 2.

REFERENCES

1. Matic, T., T. Svedek, and M. Herceg, "An analog multiplier based on asynchronous sigma-delta pulse amplitude modulation," *10th International Conference on Telecommunication in Modern Satellite Cable and Broadcasting Services (TELSIKS)*, 707–710, 2011.
2. Liang, Y., Z. G. Wang, Q. Meng, and X. D. Guo, "Design of high speed high SNR bit-stream adder based on Sigma-Delta modulation," *Electronics Letters*, Vol. 46, 752–753, 2010.
3. Fujisaka, H., M. Sakamoto, C. J. Ahn, T. Kamio, and K. Haeiwa, "Sorter-based arithmetic circuits for sigma-delta domain signal processing — Part II: Multiplication and algebraic functions," *IEEE Transactions on Circuits and Systems I: Regular Papers*, Vol. PP, 1–14, 2012.

Effect of Low-power Microwave Radiation on Seed Growth Rate

M. Fuangfoong, K. Eaipresertsak, T. Chim-Oye, and K. Dungkanya
Department of Physics, Faculty of Science and Technology
Thammasat University, Rangsit Center, Klongluang, Pathum Thani 12120, Thailand

Abstract— In this paper, the influence of power density and exposure time of low power microwave radiation on seeds growth rate had been studied. A 9.44 GHz X-band from Gunn diode based microwave test bench has been used as a source of microwave for the experiment. Seed samples were mung bean. The experiments divided into two methods, first method, the effect of microwave radiation power on seeds germination and root length were studied under irradiation for 7 days. The second method, the effect of seeds watered from water treatment on % germination as well as length of stems at 7th days after sowing. The treatment water was irradiated by varying exposure time from 10 minute, 20 minute, 30 minute, 40 minute, 50 minute and 60 minute.

An Optical Imaging Lift Using a Birefringent Homogeneous Crystal

Chia-Wei Chu[1, 2], **Zhi Chen**[3, 4], **Yubo Duan**[3, 4], **and Yuan Luo**[1, 2]

[1]Center of Optoelectronic Biomedicine, College of Medicine
National Taiwan University, Taipei, Taiwan
[2]Molecular Imaging Center, National Taiwan University, Taipei, Taiwan
[3]Singapore-MIT Alliance for Research and Technology (SMART) Centre, Singapore
[4]National University of Singapore, Singapore

Abstract— Recently, using the invariance of Maxwell's equation, transformation optics has provided a new method to manipulate light propagation. Based on transformation optics, we report and experimentally demonstrate the realization of such an optical elevator, lifting a two-dimensional (2D) sheet underneath upwards optically with broad viewing angles, while the sheet is still at the original height. The proof-of-concept experimental device is made using a single piece of calcite crystal with $n_e = 1.65$, and $n_o = 1.48$, which is a natural homogeneous birefringent material with low-loss in visible regime. The device lifts a sheet with 2.2 mm, and the dimension of the device is 1 cm in width, 3 cm in length, and 20 mm in height. The results show good agreement with simulations through finite element analysis. In addition, a Michelson low-coherent interferometer is used for optical phase measurements. It is important to note that the optical elevation does not alter the optical path or phase, so that the optical elevation is phase-preserved, fundamentally different from the other commonly observed optical illusion such as the mirage effect. Our design adopts affine expansive transformation to expand the electromagnetic space vertically such that the entire sheet can be elevated at different viewing angles. This concept also provides further possibility of concealing exterior hardware in the surrounding environment, presenting great advantages in camouflage for industrial and military purposes.

Session 3A1
Plasmonic Nanophotonics 1 - Experiment and Fabrication

Using Human Cells to Synthesize Plasmonic Nanoparticles
Shourya Dutta-Gupta, Guillaume Suárez, Christian Santschi, Lucienne Juillerat-Jeanneret, Olivier J. F. Martin, ... 412

Narrow-band Thermal Radiation by Metal Metasurface
Junichi Takahara, ... 413

Biansiotropic Property of Analuminum Nanorod Arrayfabricated by Glancing Angle Deposition
Yi-Jun Jen, Meng-Jie Lin, Huang-Ming Wu, ... 414

Bioanalytics Using Single Plasmonic Nanostructures
Thomas Schneider, Norbert Jahr, J. Wirth, Frank Garwe, O. Stranik, Andrea Csaki, Wolfgang Fritzsche, ... 415

Efficient Mode Converters for Plasmonic Optical Nanocircuits
Jer-Shing Huang, ... 416

Additional Efficiency Enhanced for DL-ARC Triple-junction GaAs/Ge Solar Cells Based on Indium Nanoparticles Surface Plasmon Light Scattering
Chi-He Lin, Wen-Jeng Ho, Yi-Yu Lee, Jheng-Jie Liou, Po-Hung Tsai, Yu-Peng Chang, ... 417

Metallodielectric Hybrid Optical Antennas for Ultrastrongly Enhancing and Directing Single-photon Emission
Xuewen Chen, Vahid Sandoghdar, ... 418

Localized Surface Plasmon Resonance in Single Gold Nanowires and Edges of Gold Film Patterns
Sheng-Yung Lo, Wei-Yu Chen, Ly-Yun Wang, Heh-Nan Lin, ... 419

Direct Visualization of Nano-plasmonic Waveguide Devices Using a Modified Near-field Spectroscopy
Ming-Yang Pan, En-Hong Lin, Pei-Kuen Wei, ... 420

Large-scale Plasmonic Nanostructures Fabricated with Nanospherical-lens Lithography
Yun-Chorng Chang, Yung-Chiang Lan, ... 421

Fabrication of Three-dimensional Plasmonic Devices Using Highly Ordered Anodic Porous Alumina
Hideki Masuda, Takashi Yanagishita, Kazuyuki Nishio, Toshiaki Kondo, ... 422

Using Human Cells to Synthesize Plasmonic Nanoparticles

S. Dutta-Gupta[1], **G. Suárez**[1], **Ch. Santschi**[1], **L. Juillerat-Jeanneret**[2], **and O. J. F. Martin**[1]

[1]Nanophotonics and Metrology Laboratory, Swiss Federal Institute of Technology Lausanne, Switzerland
[2]University Institute of Pathology, Centre Hospitalier Universitaire Vaudois & University of Lausanne
Lausanne 1011, Switzerland

Abstract— Plasmonic nanoparticles, with their ability to enhance light and heat locally, have tremendous application potentials in biology and medicine. In this presentation, we will discuss our effort toward the direct biosynthesis of metal nanoparticles by human cells. One of the main advantages of using biosynthesized nanoparticles in a biological context is their enhanced biocompatibility towards cells, compared to chemically synthesized nanoparticles. Hence, cellular incorporation of such biosynthesized nanoparticles does not require any additional functionalization steps. Although it is well known that biosynthesis takes place when the cells are incubated with metallic salts, it is not yet clear what exactly facilitates the synthesis of these nanoparticles in human cells. In this work, we study the biosynthesis of gold nanoparticles by human cerebral endothelial cells (HCEC) and investigate the chemical species involved in the biosynthesis process. Our results clearly show that addition of auric salt to the cell culture medium turns the colorless solution to the typical pink color of non-aggregated gold nanoparticles. Moreover, a correlation between the average size of the biosynthesized nanoparticles with the intracellular concentration of glutathione (GSH) is established. In our experiments, the level of intracellular GSH is increased, respectively decreased, by addition of N-acetyl cysteine (NAC) and buthionine sulfox (BSO), respectively. Noticeably, the average size of the biosynthesized gold nanoparticles increases with the level of intracellular GSH and decreases when the GSH concentration becomes lower. Finally, the average size of the synthesized nanoparticles increases when the cells are stressed, e.g., by addition of cadmium. Overall, these results indicate that cell metabolism controls the size of the biosynthesized nanoparticles.

REFERENCES

1. Dutta-Gupta, S., G. Suárez, C. Santschi, A. Lovera, C. Schütz, L. Juillerat-Jeanneret, and O. J. F. Martin, "The cellular oxidative metabolism controls the intracellular biosynthesis of gold nanoparticles by human cells," *ACS Nano*, 2013, in Press.

Narrow-band Thermal Radiation by Metal Metasurface

Junichi Takahara[1, 2]

[1]Photonics Advanced Research Center (PARC), Osaka University
2-1 Yamadaoka, Suita, Osaka 565-0871, Japan
[2]Graduate School of Engineering, Osaka University
2-1 Yamadaoka, Suita, Osaka 565-0871, Japan

Abstract— Though an incandescent lamp is widely used for a long time, it is known as an inefficient light source compared to a fluorescent lamp or a light emitting diode (LED). This is because the fraction of invisible infrared (IR) radiation is dominant (more than 90%) in thermal radiation spectra at 2800 K. Since early 2007 almost all OECD governments have announced policies aimed at phasing-out incandescent lighting; more efficient replacement lighting sources such as compact fluorescent lamps or LEDs have been recommended to use. In contrary to recent main stream on lighting technology, here we would like to stress that "an incandescent lamp is efficient" from the viewpoint of energy conversion from electric power to radiated power; a thermal emitter has a high potential as an energy converter [1].

In this presentation, we review recent progress of our study about thermal radiation control by periodic microstructures on metal surface, so called metasurface. We show experimental results of modification of thermal radiation spectra by resonant electromagnetic modes inside single micro-cavity fabricated on tungsten and discuss its applications to efficient light sources [2]. In addition, we propose new types of narrowband thermal emitter using spoof-surface plasmon mode on a periodic array of microcavity [3] or surface plasmon mode on metasurface [4]. These emitters are tunable on resonant frequency by structural parameters and can be applied to wide-range of emitting device from THz to IR range.

REFERENCES

1. Takahara, J., Y. Ueba, and T. Nagatsuma, *KOGAKU (Japanese Journal of Optics)*, Vol. 39, No. 10, 482, 2010 (in Japanese).
2. Kusunoki, F., J. Takahara, and T. Kobayashi, *Japanese Journal of Appl. Phys.*, Vol. 43, No. 8A, 5253, 2004.
3. Ueba, Y., J. Takahara, and T. Nagatsuma, *Opt. Lett.*, Vol. 36, No. 6, 909, 2011.
4. Ueba, Y. and J. Takahara, 2012 (submitted).

Biansiotropic Property of Analuminum Nanorod Arrayfabricated by Glancing Angle Deposition

Yi-Jun Jen, Meng-Jie Lin, and Huang-Ming Wu
Department of Electro-Optical Engineering, National Taipei University of Technology
No. 1, Sec. 3, Chung-Hsiao E. Rd., Taipei 106, Taiwan

Abstract— A recent research has shown that the optical property of a typical metamaterial film should take the bianisotropy into account, and a bianisotropic parameter should be added to permittivity and permeability to represent the associated electromagnetic parameters of a metamaterial thin film. In measurement of theses parameters, the reflection and transmission coefficients have to be measured from both sides of the thin film. In this work, the walk-off interferometer is adopted here to measure the reflection and transmission coefficients.

In fabrication, the sample was a film composed of aluminum nanorods prepared by glancing angle deposition. The deposition angle between the substrate normal and the direction of deposited vapor flux was kept at 87 degree. The deposition rate was maintained at 1 nm/sec. These measurements were carried out at five wavelengths of 476, 514, 568, 647, and 676 nm.

The derived permittivity, permeability and bianisotropic parameters are equivalent to the optical parameters: refractive index, forward impedance and backward impedance. The optical parameters are used to show the wave propagation through the metamaterial thin film. The reflected waves from both sides of the film can interfere with each other. It is also demonstrated that the reflectance spectrum of the film can be interpreted as a result of interference effect and the reflectance is mainly dominated by the first-order and second-order reflected wave. The transmittance is mainly dominated by the first-order transmitted wave.

Bioanalytics Using Single Plasmonic Nanostructures

T. Schneider, N. Jahr, J. Wirth, F. Garwe, O. Stranik, A. Csaki, and W. Fritzsche
Institute of Photonic Technology (IPHT), A.-Einstein-Str. 9, Jena, Germany

Abstract— Plasmonic nanostructures promise to provide sensing capabilities with the potential for sensitive and robust assays in a high parallelization. We present here the use of individual nanostructures for the detection and manipulation of biomolecules such as DNA based on optical approaches [1].

The change in localized surface plasmon resonance of individual metal nanoparticles is utilized to monitor the binding of DNA directly or via DNA-DNA interaction. The influence of different size (length) as well as position (distance to the particle surface) is thereby studied [2].

Holes in a Cr layer present another interesting approach for bioanalytics. They are used to detect plasmonic nanoparticles as labels or to sense the binding of DNA on these particles. This hybrid system of hole and particle allows for simple (just using RGB-signals of a CCD [3]) but a highly sensitive (one nanoparticle sensitivity) detection. On the other hand, the binding of molecular layers around the particles can be detected using spectroscopic features of just an individual one of these systems.

Besides sensing, individual plasmonic nanostructures can be also used to manipulate single biomolecular structures such as DNA. Attached particles can be used for local destruction [4] or cutting as well as coupling of energy into (and guiding along) the molecular structure [5].

REFERENCES

1. Csaki, A., T. Schneider, J. Wirth, N. Jahr, A. Steinbrück, O. Stranik, F. Garwe, R. Müller, and W. Fritzsche, *Philosophical Transactions A*, Vol. 369, 3483–3496, 2011.
2. Schneider, T., N. Jahr, A. Csaki, O. Stranik, and W. Fritzsche, 2012, submitted.
3. Jahr, N., N. Hädrich, M. Anwar, A. Csaki, O. Stranik, and W. Fritzsche, *Int. J. Environ. Anal. Chem.*, Vol. 92, 2012.
4. Csaki, A., F. Garwe, A. Steinbrück, G. Maubach, G. Festag, A. Weise, I. Riemann, K. König, and W. Fritzsche, *Nano Letters*, Vol. 7, No. 2, 247–253, 2007.
5. Wirth, J., F. Garwe, G. Haehnel, A. Csaki, N. Jahr, O. Stranik, W. Paa, and W. Fritzsche, *Nano Letters*, Vol. 11, No. 4, 1505–1511, 2011.

Efficient Mode Converters for Plasmonic Optical Nanocircuits

Jer-Shing Huang[1, 2]

[1]Department of Chemistry, National Tsing Hua University, Hsinchu 30013, Taiwan
[2]Frontier Research Center on Fundamental and Applied Sciences of Matters
National Tsing Hua University, Hsinchu, 30013, Taiwan

Abstract— Using surface plasmons as information and power carriers is promising for future sub-wavelength nanocircuits working in the optical frequencies. Among various waveguides, plasmonic two-wire transmission line (TWTL) has been studied theoretically and experimentally. Due to the phase difference between the displacement current on each wire of TWTL, guided modes exhibit distinctly different properties that are suitable for various circuit functions. Therefore, it is important to switch the modes at will in order to maximize the performance of a multi-functional nanocircuit. Here, we show efficient the mode conversion in a gold nano-sized plasmonic circuit. Instead of pure optical interference, strong near-field coupling of surface plasmons results in great momentum splitting and modal profile variation. We propose using the bonding and antibonding resonance of an optical nanoantenna to excite the TE and TM guided modes. Finally, we demonstrate control over nanoantenna radiation and discuss the possibility to enhance nanoscale light-matter interaction. The converters may find important applications in future optical nanocircuits.

Additional Efficiency Enhanced for DL-ARC Triple-junction GaAs/Ge Solar Cells Based on Indium Nanoparticles Surface Plasmon Light Scattering

Chi-He Lin, Wen-Jeng Ho, Yi-Yu Lee, Jheng-Jie Liu, Po-Hung Tsai, and Yu-Peng Chang
Department of Electro-Optical Engineering
National Taipei University of Technology, Taipei 106, Taiwan

Abstract— In this paper, we experimentally demonstrated the photovoltaic performance enhancement of a double layer (DL) anti-reflective coating (ARC) triple-junction GaAs/Ge solar cells by using indium nanoparticles due to the surface plasmonics light scattering. The epitaxial structure of triple-junction GaAs/Ge solar cell was grown by metal-organic chemical vapor deposition (MOCVD) and DL anti-reflective coating is consisted of a TiO_2 and Al_2O_3 layers with quarter wavelength thickness, respectively. The 3-nm thick indium film was then deposited on ARC-layer surface by e-beam evaporation system and subsequently annealed at 200°C for 20 min in H_2 ambient to obtain nano-size indium nanoparticles. The measured performance of the fabricated cell after anti-reflective coating the short circuit current (I_{SC}) of 12.46 mA, open circuit voltage (V_{OC}) of 2.53 V, fill factor (FF) of 0.87, and conversion efficiency (η) of 32.59% are obtained under 1 sun AM1.5G solar simulation. As the cell with the indium nanoparticles on the top surface, however, I_{SC} increase to 12.59 mA and η increase to 33.18% are presented. Additionally, the average reflectance of cell decreasing by 0.84% at wavelengths 350–700 nm and −0.28% at wavelengths 700–900 nm are also shown in reflective spectrum as the cell having indium nanoparticles. The increase in I_{SC} and η and decrease in reflectance of the top cell are attributed this enhancement to the indium nanoparticles surface plasmonics light scattering. Furthermore, the external quantum efficiency (EQE) measurement is undergoing study, in this work, to examine the enhanced mechanism of the nanoparticles surface plasmonics light scattering.

ACKNOWLEDGMENT

The authors would like to thank the National Science Council of the Republic of China for financial support under grant NSC-100-2221-E-027-053-MY3.

Metallodielectric Hybrid Optical Antennas for Ultrastrongly Enhancing and Directing Single-photon Emission

Xuewen Chen and Vahid Sandoghdar
Max Planck Institute for the Science of Light and Department of Physics
Friedrich-Alexander University Erlangen-Nürnberg, Erlangen 91058, Germany

Abstract— Controlling the emission of single quantum emitters has been a topic of theoretical and experimental investigations over the past decades both for fundamental studies and emerging applications. Two features of central interest in this line of research are the enhancement of spontaneous emission rate and the engineering of the emission pattern that funnels the photons into well-defined modes. In this presentation, we report on a class of metallo dielectric hybrid optical antenna to simultaneously achieve ultra strong enhancement of spontaneous emission rate of a single emitter and near-unity efficiency in collecting its emission.

Recent reports have shown that metallic nanoparticles can enhance emission in analogy with antenna concepts from radio engineering. However, due to the dissipation in the metal, it is difficult to achieve ultra strong enhancement of the emission without invoking quenching. Here we combine metallic antennas with planar dielectric structures and exploit design strategies from antennas and concepts from Cavity QED to maximize the emission and minimize the losses. We show that the new metallo dielectric antenna can reduce the excited-state lifetimes from the typical values of nanoseconds to the range of 100 fs while maintaining quantum efficiencies of about 80% [1]. The radiation pattern of such metallo dielectric hybrid antenna is similar to that of a vertical dipole antenna above a high-index substrate and most of the emission funnels to the substrate. In a recent publication [2], we have reported on a broad-band scheme with a layered full-dielectric antenna structure to collect more than 96% of the emitted photons from a vertically-oriented molecule. To improve on the performance of our first experiment, we put a metallic mirror on top of the dielectric antenna and achieved beyond 99% collection efficiency of single emitters with arbitrary orientation of the dipole moment [3]. Here the metallo dielectric antenna concept is fully compatible with the high collection-efficiency schemes. By introducing a thin high refractive index layer in the hybrid antenna structure, we could collect 99% of the emission with ultra strongly enhanced emission rate.

This brings about the prospect of triggered single-photon sources at the μW power level. The resulting hybrid antennas open the door to an unprecedented paradigm where the radiative processes become comparable with or faster than many vibrational (phenolic) interactions, leading to unexplored regimes of photo physical dynamics.

REFERENCES

1. Lee, K. G., X. W. Chen, H. Eghlidi, P. Kukura, R. Lettow, A. Renn, V. Sandoghdar, and S. Götzinger, *Nat. Photonics*, Vol. 5, 166, 2011.
2. Chen, X. W., S. Götzinger, and V. Sandoghdar, *Opt. Lett.*, Vol. 36, 3545, 2011.
3. Chen, X. W., M. Agio, and V. Sandoghdar, *Phys. Rev. Lett.*, Vol. 108, 233001, 2012.
4. Chen, X. W., M. Agio, and V. Sandoghdar, to be submitted.

Localized Surface Plasmon Resonance in Single Gold Nanowires and Edges of Gold Film Patterns

Sheng-Yung Lo, Wei-Yu Chen, Ly-Yun Wang, and Heh-Nan Lin
Department of Materials Science and Engineering, National Tsing Hua University
Hsinchu 30013, Taiwan

Abstract— We report on a study of localized surface plasmon resonance (LSPR) in single Au nanowires (NWs) and edges of microscale Au film patterns. The NWs are fabricated by atomic force microscopy nanolithography and have a length of a few micrometers widths ranging between 50 and 110 nm and thicknesses between 7 and 30 nm. Two LSPR peaks at around 630 (red) and 490 (blue) nm in wavelength are observed. The red peak wavelength is linearly proportional to the NW width. In addition, the intensity is strongest when the incident electric field is parallel to the length direction. The chemical sensing capability of the NWs is investigated by spin-coating a thin layer of PMMA on the NWs. A sensitivity of 104 nm per refractive index unit is obtained for the red peak of an 85 nm thick NW.

For Au film patterns, the edge effect allows the occurrence of LSPR similar to that in Au NWs. At edges of patterns with thicknesses ranging between 10 and 60 nm, three LSPR peaks are observed. The peak wavelengths are 517, 588, and 646 nm for a 40 nm thick pattern. Furthermore, the intensity of the middle peak is much weaker than the other two. From transmission electron microscopy analysis, these modes are likely to originate from electron oscillations along three directions at the edges. It has been found that the peak wavelength of the first mode (shortest wavelength) increases as the film thickness is increased, whereas the third mode (longest wavelength) decreases slightly. For chemical sensing, a highest sensitivity of 104 nm per refractive index unit is obtained for the 60 nm thick pattern. This sensitivity is close to that of the NWs and indicates the usefulness of structurally simple Au patterns for chemical sensing.

Additionally, plasmonic heating in the NWs under optical irradiation has also been investigated by measuring heating-induced NW resistance change. By creating contact electrodes between the NWs, the resistance change is found to be a few tens percents when the NWs are irradiated by a white light source. The temperature rise is estimated to be a few tens degrees Celsius based on comparison with the resistance change due to non-optical heating.

REFERENCES

1. Chen, H.-A., H.-Y. Lin, and H.-N. Lin, "Localized surface plasmon resonance in lithographically fabricated single gold nanowires," *J. Phys. Chem. C*, Vol. 114, 10359, 2010.
2. Lin, H.-Y., H.-A. Chen, and H.-N. Lin, "Fabrication of a single metal nanowire connected with dissimilar metal electrodes and its application to chemical sensing," *Anal. Chem.*, Vol. 80, 1937, 2008.

Direct Visualization of Nano-plasmonic Waveguide Devices Using a Modified Near-field Spectroscopy

Ming-Yang Pan[1], **En-Hong Lin**[1], **and Pei-Kuen Wei**[2, 3, 4]

[1]Department of Optoelectronics, National Tsing Hua University, Hsinchu 300, Taiwan
[2]Research Center for Applied Sciences, Academia Sinica, Taipei, Taiwan
[3]Institute of Biophotonics, National Yang-Ming University, Taipei, Taiwan
[4]Department of Optoelectronics, National Taiwan Ocean University, Keelung, Taiwan

Abstract— We present a method to directly visualize the surface plasmon polariton (SPP) propagation on various nanophotonic waveguide devices. The method combined the transmission-mode near-field spectroscopy with a leakage radiation optical microscope. The near-field fiber probe converts incident photons into SPP through evanescent wave coupling. Real-time color SPP radiation images were taken through of a high NA oil lens. This setup takes advantages of nanoscale excitation, lower background and controlled excitation positions. The recording of SPP image is real-time with tunable wavelength. In this presentation, wavelength-dependent propagation lengths of dielectric loaded SPP waveguides (DLSPPW) with silver and gold films were measured and compared. It confirmed that silver-based SPP has a propagation length longer than gold-based one about 1.5 times. To further increase the propagation length, a slot-loaded waveguide consisted of two dielectric layers (high-index/low-index) on a silver film was proposed. Compared with the DLSPPW, this new SPP waveguide increases the propagation length of SPP mode by about 1.6 times due to a concentrated optical field in the low-index region. The 90° waveguide with 3 μm radius showed the bending loss was smaller than 2 dB. In addition, the resonance coupling as a function of wavelength in dual DLSPPWs was measured. The coupling lengths analyzed from leakage radiation images were in good agreement with vector finite difference simulation.

Large-scale Plasmonic Nanostructures Fabricated with Nanospherical-lens Lithography

Yun-Chorng Chang and Yung-Chiang Lan
Department of Photonics, National Cheng Kung University, Tainan, Taiwan

Abstract— Nanophotonics is a research field that studies how to manipulate the incident photons with either a dielectric photonic crystal or surface plasmon of metal nanostructure. Localized surface plasmons are collective oscillation of conductive electrons propagating at the surface of noble metal nanoparticles. The electric field is highly localized and very strong at the surface, which is ideal for electric field-related applications such as surface-enhanced Raman scattering (SERS) The light scattering induced by localized surface plasmon resonance (LSPR) of metal nanoparticles is also very sensitive to the dielectric environment and is widely used for ultrasensitive chemical and biological sensing applications. Therefore, plasmonic-related studies have been booming research topics in recent years. However, the high fabrication cost and low throughput for the common precise nanofabrication techniques, such as focused ion beam milling or electron-beam lithography, have severely the applications of these plasmonic-related applications.

In this research, we have presented an economic nanofabrication that uses polystyrene nanospheres as nanoscale focusing lenses. The incident ultraviolet light is collimated and focused by nanospheres to exposure the underlying photoresist film. This method is referred as Nanospherical-Lens Lithography (NLL) by us. Cylindrical photoresist hole arrays reveals after developing the photoresist. Metal nanodisk arrays can be fabricated after metal evaporation and lift-off processes. The fabricated metal-insulator-metal nanodisk arrays have been applied to study plasmon hybridization. Dark plasmon mode in this vertically aligned configuration is the bonding mode, which is dominated by absorption mechanism. This dark plasmon mode is also widely tunable by changing the diameters of the nanodisk and the spacing between the metal nanodisks. In addition, the fabricated Ag and Au nanodisk arrays have been investigated as a sensitive localized surface plasmon resonance (LSPR) sensors that demonstrate high sensitivity figure of merit (FOM). Nanodisk arrays with diameter as small as 75 nm and cover an area as large as $1\,\mathrm{cm} \times 1\,\mathrm{cm}$ are successfully fabricated. The minimum LSPR linewidth is about 27 nm, which corresponding a index sensing FOM of 9.

In conclusion, we have demonstrated that NLL can economically fabricate nanodisk arrays that cover large area. We have used these nanodisk arrays to investigated plasmon hybridization and ultrasensitive LSPR sensors. We believe NLL will attract more attentions in the future nanophotonic studies.

Fabrication of Three-dimensional Plasmonic Devices Using Highly Ordered Anodic Porous Alumina

Hideki Masuda[1, 2], **Takashi Yanagishita**[1], **Kazuyuki Nishio**[1], **and Toshiaki Kondo**[2]

[1]Department of Applied Chemistry, Tokyo Metropolitan University
1-1 Minamiosawa, Hachioji, Tokyo 192-0397, Japan
[2]Kanagawa Academy of Science and Technology
5-4-30 Nishihashimoto Midoriku, Sagamihara, Kanagawa 252-0131, Japan

Abstract— The use of naturally occurring self-ordered structures is effective for the preparation of functional optical devices based on a localized surface plasmon (LSP) because of its ability of the formation of precisely controlled fine structures. To optimize the performance of the obtained LSP devices, formation of precisely controlled geometrical structures of metal is essential [1, 2]. In this presentation, we describe the fabrication of several types of three-dimensional (3D) plasmonic devices using highly ordered anoodic porous alumina in addition to two-dimensional (2D) devices. The anodic porous alumina, which is formed by anodization of Al in acidic electrolyte, is one of typical self-ordered material [3]. Based on the highly ordered nanostructures of anodic porous alumina, 2D and 3D LSP devices can be prepared easily without the use of any expensive apparatus. As a typical process for the preparation of 2D structures of metal particles, vacuum deposition of metals using porous alumina as a mask can be applied [3]. The structures of the obtained metal particles can be controlled based on the geometrical structures of the porous alumina used for the mask. The ordered structures with high aspect features of anodic porous alumina can be also applied to the fabrication of 3D structures of metals. The preparation of 3D structures of metals contributes to the enlargement of the active surface area in the samples, and also allows the formation of small gaps, which are effective for the enhancement of the electric field of the incident light. One of typical examples of the 3D structures of metal particles is a multi-layered ordered array of metal nanoparticles in alumina matrix [4]. In this structure metal nanoparticles are arranged in a multilayered structure with uniform intervals in an anodic alumina matrix. In addition, metal hole arrays and coaxial cable array structures were also prepared as 3D structures using anodic porous alumina. The 2D and 3D structures of metals obtained by the ordered structures of anodic porous alumina showed unique optical properties originated form the LSP, and could be applied to the measurement of surface-enhanced Raman scattering (SERS).

REFERENCES

1. Jin, R., Y. C. Cao, E. Hao, G. S. Métraux, G. C. Schatz, and C. A. Mirkin, *Nature*, Vol. 425, 487, 2003.
2. Lee, K.-S. and M. A. El-Sayed, *J. Phys. Chem. B*, Vol. 110, 19220, 2006.
3. Masuda, H. and M. Satoh, *Jpn. J. Appl. Phys.*, Vol. 35, L126 1996.
4. Kondo, T., K. Nishio, and H. Masuda, *Appl. Phys. Express*, Vol. 2, 032001, 2009.

Session 3A2
Power Electronics

Analysis and Construction of Output Capacitance Filter for High Power LLC Resonant Converter
Jiri Lettl, Ondrej Plhak, ... 424
Stable Adaptive Signal Generation in Current Based MRAS Induction Motor Sensorless Speed Control
Miroslav Bednar, Jiri Lettl, Martin Vlcek, ... 425
Comparison of DTC and Sliding Mode Control of IM Drive
Jiri Lettl, Stanislav Fligl, Jan Bauer, ... 426
Design and Implementation of a Variable-frequency Multiphase VRM with Optimized Phase-reduction Control
Shengyuan Ou, Yi-Peng Lin, Jui-Chien Wang, ... 427
An Adaptive Current-sharing Control Technology for Multi Power Module with Hot Swapping
Shengyuan Ou, Fu-Sung Chen, ... 428
Implementation and Study of Super-capacitor Cell Power Management System
Shao-Wei Chieh, Wen-Hsien Ho, Chung-Bo Tsai, Po-Chou Chen, Shengyuan Ou, ... 429
Design and Implementation of an LED Switching Regulator Using Inverse Buck Topology
Shengyuan Ou, Hong-Hsiang Chang, ... 430

Analysis and Construction of Output Capacitance Filter for High Power LLC Resonant Converter

J. Lettl and O. Plhak
Department of Electric Drives and Traction, Faculty of Electrical Engineering
Czech Technical University in Prague, Technicka 2, 166 27 Prague 6, Czech Republic

Abstract— Resonant inverter type of DC/DC found their application in construction of medium power inverters such as in the design of adapters, power automotive technology etc. The most famous is the type of LLC. The use of the resonant principle in other areas such as the area of static converters in traction is Analysis and Construction of Output Capacitance Filter for High Power LLC Resonant Converter considered today.

Most of the problems related to the design of resonant converters LLC is known and described in many technical articles. But there is very small discussion about problems that arise in the design of high power converters, especially in traction. The requirements for static converters used in traction are very strict and places greater demands on the design in: form of: a wide range input voltage (high tolerance), high quality outputs, electrically isolated inputs and outputs with high insulation capacity (several kV), modularity for quick repairs. These problems make more complex design of resonant converters for this use.

One problem of the design is a construction of the input and output filter of resonant converter. This article therefore intends to focus on technical issues related to the design and subsequent construction output filter for resonant converter LLC type for high performance.

Output filter of static converter is usually connected to the traction batteries that are recharged with relatively large currents. The output filter must be dimensioned for that. The usage of resonant converters leads through resonance circuit used in large ripple currents (RMS) that flow through the output filter, which makes the very difficult design and construction of the filter.

Conventional capacitors cannot be used due to small current-carrying capacity, because it leads to increase in the total volume of the converter. Snubber capacitors meet the current-carrying capacity, but have a low capacity. The use of electrolytic capacitors increases the power output capacity of the converter, which increases the control constants to unbearable values. The overall converter system is uncontrollable — the regulator is then very unstable. In the contrary undersizing and overloading the filter is not possible due to the required high life. The point is to use capacitors with very low ESR (parasitic resistance), to achieve a small temperature rise and therefore perhaps greater ripple current. It appears that the optimal solution is to use parallel connection of electrolytic capacitors in the design of the printed circuit board.

The use of printed circuit brings many benefits and design versatility. The disadvantage is the complexity of the proposal in the form of compliance with the relevant distances and thicknesses of each layer so as not to exceed the permissible temperature rise of utilized components. Final hilarious and labour input filter design leads to the consideration of the economics of this variant. Another possibility is modified topology to LC output filter type or an application of complex solutions such as filter type CLC. We have to consider context if we want to help decrease size of output filter and we achieve high switching frequency. This article summarizes the experimental results of different designs.

Stable Adaptive Signal Generation in Current Based MRAS Induction Motor Sensorless Speed Control

M. Bednar, J. Lettl, and M. Vlcek
Department of Electric Drives and Traction, Faculty of Electrical Engineering
Czech Technical University in Prague, Technicka 2, 166 27 Prague 6, Czech Republic

Abstract— Realization of the induction machine sensorless drive control is quite difficult technical problem. Many solutions with different quality degree have been found, but many of them have stability problems in some operating mode. The current based MRAS (Model Reference Adaptive Signal) method was chosen as one of the best from the point of view of accuracy and dynamic of the speed estimation. The only values needed for the estimation algorithm are parameters of the controlled machine substitute scheme, actual values of phase currents and voltages. In the designed scheme of the current based MRAS the most important value for the speed estimation is an adaptive signal that has to enable the stable speed estimation in the whole speed range (except the situation when rotor flux vector $\vec{\psi}_r = 0$) and in both operating modes (motor and generator). The proper adaptive signal finding is the aim of this contribution.

If correct adaptive machine model parameters are available and the model input voltage is the same like the reference machine terminal voltage, it can be found that the difference between measured and estimated stator current depends on the difference between the real and estimated speeds. We can write

$$\Delta\vec{i}_s \frac{\vec{\psi}_r^*}{|\vec{\psi}_r|^2} = \Delta\omega \cdot \vec{z},$$

where Δi_s is per unit current difference, $\Delta\omega$ is angular speed difference, $\vec{\psi}_r$ is per unit rotor flux vector, $\frac{\vec{\psi}_r^*}{|\vec{\psi}_r|^2}$ is a term of transformation into the system rotating synchronously with $\vec{\psi}_r$, $z = f(\omega_r, \omega_s)$ could be called the machine steady state impedance for purpose of the current based MRAS (where ω_r is slip angular speed and ω_s is stator flux angular speed). It can be deduced by comparison of the equations of the both models (reference and adaptive) and the curve of this function can be depicted in the complex plane. Its imaginary part (see Fig. 1) has a potential to be an adaptive signal in the MRAS structure, but it does not fulfil the stability criterion in the whole operating range. Especially, it changes its sign in the low speed braking area. The main merit of the contribution is finding of the formula that transforms the z function into the form available for using as an adaptive signal (see Fig. 2).

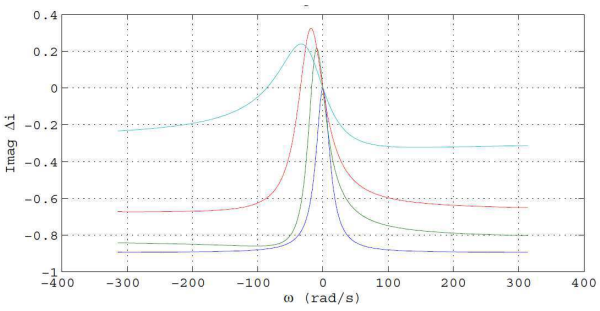

Figure 1: Non-transformed adaptive signal.

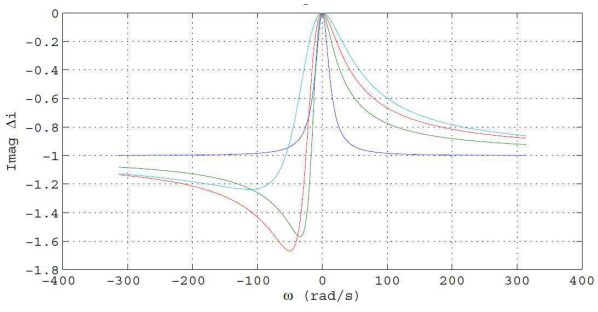

Figure 2: Transformed adaptive signal.

Comparison of DTC and Sliding Mode Control of IM Drive

J. Lettl, **S. Fligl**, **and J. Bauer**
Department of Electric Drives and Traction, Faculty of Electrical Engineering
Czech Technical University in Prague, Czech Republic

Abstract— Recently used induction machines (IM) are often applied as a part of controlled electric drives. They are robust, durable and they do not need much maintenance. However, their control is more difficult compared to DC machines or permanent magnet synchronous machines due to the absence of the electromagnetic flux separate source. Therefore the output of the control algorithm for the IM must be the desired current or voltage vector, the application of which on the IM terminals will produce the desired flux and torque of the IM. This requirement can be reached by splitting IM control into two separate arms. One component is responsible for the flux production and the second one is responsible for the torque production. The demanded vector is then vector combination of both components.

Several control algorithms are known that offer possibility of separate control of torque and flux current components. The Field Oriented Control (FOC) or Direct Torque Control (DTC) belongs to them. The DTC offers high dynamics and utilization of the drive; but it requires greater computational power of the controller. The control of switching frequency and thus necessary reduction of current harmonics is a problem, too. The DTC controller does not include modulator; the IM voltage switching is more or less based on the switching table. Therefore also modified DTC strategies were developed. However, for their operation most of them need information about hardly measurable IM inner values like electromagnetic flux and torque. To estimate these values, models of the machines are used. Models based on the machine's equations are commonly used. Nevertheless, it seems to be useful to employ a model of the IM based on the state space variables, because apart from the information about the electromagnetic flux and torque values it also enables to analyze analytically the IM behaviour.

This contribution strives to compare behaviours of the IM drive controlled by classical DTC and modified direct torque control strategy based on the state space variable description of the induction machine.

Design and Implementation of a Variable-frequency Multiphase VRM with Optimized Phase-reduction Control

Sheng-Yuan Ou, Yi-Peng Lin, and Jui-Chien Wang
Department of Electrical Engineering, National Taipei University of Technology, Taiwan

Abstract— This paper proposes a control method to improve voltage regulator module (VRM) efficiency under light-load situations. The VRM is an important application on the motherboard in a personal computer (PC) that supplies power to the central processing unit (CPU) and other ICs requiring a low-voltage high-current power supply. The proposed control strategy utilizes a hybrid control method comprised of variable-frequency control and phase-reduction control. The proposed variable-frequency control method is used to modulate the switching frequency higher as the load becomes lower or lighter to achieve zero voltage switching (ZVS) on both high-side and low-side switches to significantly improve the light-load efficiency. The phase-reduction control is associated with the proposed variable-frequency control to enhance the efficiency improvement further as the load gradually becomes lighter. Compared to conventional control methods, one advantage of the proposed variable-frequency control method is that it keeps the ripple low enough to meet the desired design specification even under light-load situations.

This paper provides the illustration for the control techniques and theory, including variable-frequency control rule, conduction loss analysis and the output voltage ripple derivation for multiphase VRM. The proposed control scheme is also explained in this paper. An eight-phase VRM is implemented for verification with the design specification including 81 A output current, 1.3 V output voltage, 100 W maximum power and ripple below 1% for full-range loads. The switching frequency is modulated from 240 kHz to 550 kHz as the load varies. The experimental results verify the theoretic analysis and feasibility of the proposed control method, and show comparisons between the proposed control method and other conventional constant-frequency techniques and the proposed method increases efficiency up to 30%.

An Adaptive Current-sharing Control Technology for Multi Power Module with Hot Swapping

Sheng-Yuan Ou and Fu-Sung Chen
Department of Electrical Engineering, National Taipei University of Technology, Taiwan

Abstract— This paper proposes an adaptive current sharing control strategy for multi power module to solve the output current imbalance problem caused by hot swapping while some power modules are paralleled or removed to provide higher or lower power the load requires. The conventional hot swapping techniques used in multi power module are easy to perform flexibility and precision, but generally easy to result in both the output voltage and current imbalances of operating modules so that some paralleled modules will be overloaded to mistake the operation even damage. Therefore, one of the solutions to balance the each module voltage and current while hot swapping uses the current control IC in each modules, but it increases complexity, cost and volume of each power circuit as well as degrades the efficiency under tiny-load and no-load situations. This paper provides a simple and low-cost adaptive current-sharing control method using off-the-shelf PWM control IC which only needs to be simply and easily modified.

This paper discussed and illustrates the issues caused by hot swapping, the current-sharing control theory, and the proposed control scheme to easily implement the required control function. A multi power supply comprised of two power modules is implemented for verification of the proposed control in which one module has the design specification including 19 V output voltage, 7.1 A maximum output current, and 135 W maximum output power, the other has 19 V output voltage, 3.4 A maximum output current, and 65W maximum power. The total multi power module has 10.5 A maximum output current and 200 W maximum output power.

The experimental results verify the theoretic analysis and feasibility of the proposed control method, and show the required current sharing function with actually-measured waveforms.

Implementation and Study of Super-capacitor Cell Power Management System

Shao-Wei Chieh[1], **Wen-Hsien Ho**[2], **Chung-Bo Tsai**[2], **Po-Chou Chen**[2], **and Sheng-Yuan Ou**[1]

[1]Department of Electrical Engineering, National Taipei University of Technology, Taiwan
[2]Taiwan Textile Research Institute, Taiwan

Abstract— This paper proposes a novel super-capacitor cell power management system to monitor current and balance state of charge for each cell while charging and discharging a multi-cell super-capacitor stack. Generally, the super-capacitor cells are in series connection to form a multi-cell stack for practical applications due to the much lower operating voltage of super-capacitor. The cells should suffer from the imbalance charging issue caused by intrinsic property differentials among separate cells even labeled the same specification. The imbalance charging phenomenon can cause some super-capacitor cells in stack overcharging to be destroyed and decrease their lifetime. The imbalance charging also results in other super-capacitor cells in the same stack undercharging and makes the cells as well as the cell stack utilization and performance very low. One popular conventional balance charging control method uses some passive networks comprised of resistors so that there are some fatal disadvantages, including the poor efficiency resulting from the resistor dissipation and the difficulty for resistor selection and setting as well as the accuracy degrading. Therefore, this paper provides an active balancing circuit which can maintain equal voltages across each super-capacitor cell and clamp the peak voltage across each cell to a selectable maximum value by monitoring cell state of charge in the stack. The proposed adaptive and active charging balance control method utilizes off-the-shelf control IC which only needs to be simply and easily modified in which charging strategy is the constant-current/constant-voltage method which is implemented easily and simply in view of super-capacitor lifetime and fast charging.

The experimental results verify the theoretic analysis and feasibility of the proposed control method and show the performance superior to the prior arts.

Design and Implementation of an LED Switching Regulator Using Inverse Buck Topology

Sheng-Yuan Ou and Hong-Hsiang Chang
Department of Electrical Engineering, National Taipei University of Technology, Taiwan

Abstract— This paper proposes an LED switching regulator using inverse buck topology to achieve dimming improvement, eliminating spike from diode reverse recovery time and LED string short and dimming short operation and protection. The used pulse width modulation technique is fixed off time adjustment by easily setting the additional elements comprised of a resistor and a capacitor to achieve variable-frequency control under continuous current mode (CCM) or discontinuous current conduction mode (DCM). Recently, LED is largely used in lighting system to save energy and space in human life instead of cold-cathode fluorescent lamps so that current-sharing issue is very important to make the brightness uniform while using LED strings as the lighting system. This paper therefore provides an LED switching regulator to achieve the required active current-equalization function even dimming is up to near 100%. In addition, this paper also implements both dimming short protection and dimming open protection that are quite major considerations in LED lighting system in addition to elimination of spike caused by diode reverse recovery time. In this paper, analysis of the used inverse buck topology and the active current-equalization effect with dimming are illustrated. Finally, an LED switching regulator using inverse buck topology is implemented and measured with specifications including 206.4 V/260 mA for a 3 LED string panel to verify the theoretic analysis and feasibility of the proposed control method and show the performance superior to the prior arts. The experimental results show good confirm and the active current-equalization is within 5% that meets the required specification.

Session 3A3
EM Scattering Models and Applications

Efficient Solutions of Volume Integral Equations with Inhomogeneous Materials
K. Yang, Y. Q. Zhang, M. H. Wei, Mei Song Tong, ... 432
A General Overview on the Microwave Remote Sensing of Tropical Vegetation
Yu Jen Lee, Hong Tat Ewe, Hean-Teik Chuah, ... 433
Electromagnetic Scattering from Aggregates Embedded in Absorbing Media
Romain Ceolato, Nicolas Riviere, Matthew J. Berg, Beatrice Biscans, ... 434
A New Parallel Version of the DDSCAT Code for Electromagnetic Scattering from Big Targets
Robert W. Numrich, Thomas L. Clune, Kwo-Sen Kuo, ... 435
Analysis of Electromagnetic Scattering from Absorptive Dielectric Rough Surfaces with Underneath Target
Yinhui Wang, Yang Du, ... 436
Investigating the Radar Returns of a Wind Turbine
Muhammad Bilal Raza, Thomas Heinrich Fickenscher, ... 437
EM Plane Wave Diffraction by a Moving Half-plane
Adam Ciarkowski, ... 438
Backscattering Coefficient Laboratory Measurements in Ka Band and at Small Incidence Angles
Pierre Borderies, Christophe Fatras, Guillemette Caulliez, Sébastien Pioch, Jean-Claude Lalaurie, Roger Fjørtoft, ... 439

Efficient Solutions of Volume Integral Equations with Inhomogeneous Materials

K. Yang, Y. Q. Zhang, M. H. Wei, and M. S. Tong
Department of Electronic Science and Technology, Tongji University
4800 Cao'an Road, Shanghai 201804, China

Abstract— Volume integral equations (VIEs) are indispensable for solving electromagnetic (EM) problems with inhomogeneous or anisotropic materials by integral equation approach. Traditionally, the VIEs are solved by the method of moments (MoM) in which the unknown volumetric electric and magnetic currents are represented with the Schaubert-Wilton-Glisson (SWG) basis function. The SWG basis function is defined over a pair of tetrahedrons with a common face and requires conformal tetrahedral meshes in geometric discretization. The conformal meshes will result in a high cost in discretization, especially for multiscale structures in which the meshes with different sizes need to perfectly merge near material interfaces.

The conformal meshes imply that the tetrahedral elements cannot stride across material interfaces or each tetrahedron cannot include inhomogeneous materials in the geometric discretization. This is because the SWG basis function cannot be defined over a discontinuous material boundary. Therefore, we have to locate the material boundaries for a given arbitrarily inhomogeneous structure and discretize each material individually without striding across its boundary. However, if we need to discretize the geometries along their material boundaries, why do we need to bother the VIEs? The surface integral equations (SIEs) can also be used and are more convenient to implement if we must locate the boundaries because they only require discretizing the material interfaces. Hence, it seems that solving the VIEs is unnecessary in the case when the material boundaries are impenetrable in geometric discretization.

In this work, we propose a Nyström-like point-matching scheme to solve the VIEs. The scheme does not use any basis function and only works with individual tetrahedrons instead of tetrahedron pairs. Therefore, the scheme allows an inhomogeneity of materials in each tetrahedron or permits to stride across material boundaries without enforcing a conformity in geometric discretization. Due to this distinctive feature, the scheme can handle arbitrarily inhomogeneous or anisotropic structures with much convenience. Numerical examples for electromagnetic scattering will be presented to demonstrate the scheme and its robustness can be observed.

A General Overview on the Microwave Remote Sensing of Tropical Vegetation

Y. J. Lee, H. T. Ewe, and H. T. Chuah
Universiti Tunku Abdul Rahman, Malaysia

Abstract— This paper presents a general overview of the application of microwave remote sensing towards vegetation in the tropics. In the tropics, where agriculture plays an important role towards the economic growth of the region and also acts as its food source, proper management and monitoring of crop growth and yield is important. In addition, tropical rainforests play an important role towards the regulation of oxygen and water retention as well as the survival of a variety of endangered species of flora and fauna. It is important to highlight that due to the vast expanse of crop fields and forests, it is almost impossible to collect data and monitor all areas on foot. The use of microwave remote sensing via airborne SAR systems or satellites serves as a means to solve such problems. However, proper scattering models to understand how microwaves interact with various types of vegetation need to be developed first prior to the utilization of such technology. In addition, proper measurements need to be carried out to collect data for the validation of such models. Image classification techniques to properly classify different areas of crops from other landscape, as well as to differentiate different stages of growth are equally important. A summary of the various developments and results from these areas are discussed in this paper.

Electromagnetic Scattering from Aggregates Embedded in Absorbing Media

R. Ceolato[1], **N. Riviere**[1], **M. J. Berg**[2], **and B. Biscans**[3]

[1]Onera, The French Aerospace Lab, FR 31000, France
[2]Department of Physics and Astronomy, Mississippi State University
Mississippi State, MS 39762, USA
[3]LGC, UMR CNRS 5503, Universite de Toulouse, FR 31432, France

Abstract— The scattering of electromagnetic waves by objects is of crucial interest for research and engineering problems in remote-sensing, telecommunication, microwave and optics. Scattering may occur by the presence of particles. It results in a change of the wave propagation depending on the ratio of particle size to wavelength. Particles often form three-dimensional systems by aggregation in various situations as combustion, turbulent jets or dense particulate media. The scattering properties of an aggregate depend upon primary particle parameters as their size, shape or complex refractive index in addition to aggregate structure as its fractal dimension or gyration radius. Such properties are retrieved by solving the scattering problem. Analytical solutions are known only for particles with regularly shaped particles. Dedicated numerical methods are required for complex systems of particles.

We present an electromagnetic computational method derived from the discrete-dipole approximation (DDA). It solves the Maxwell equations using the volume-integral equation. Our method computes accurately the full scattering signature of arbitrary three-dimensional objects. We report numerical results using our method for aggregates of particles with averaged orientation in absorbing host media. The spectral and angular scattered intensities is calculated over for a broadband continuous incident radiation. Radiative parameters of interest are retrieved as the full spectral Mueller matrix or spectral scattering, absorption and extinction cross-sections.

We study theoretically and numerically the electromagnetic scattering properties of fractal-like aggregates of silicon dioxide particles embedded in water at 193.4 THz or 1550 nm. Such properties are of interest in a range of scientific and industrial applications in the fields of remote-sensing as RADAR or LiDAR but also materials characterization.

A New Parallel Version of the DDSCAT Code for Electromagnetic Scattering from Big Targets

R. W. Numrich[1], **T. L. Clune**[2], **and K.-S. Kuo**[2, 3]

[1]The Graduate Center, City University of New York, New York, New York, USA
[2]NASA Goddard Space Flight Center, Greenbelt, Maryland, USA
[3]Earth System Science Interdisciplinary Center, University of Maryland
College Park, Maryland, USA

Abstract— We have modified the publicly available electromagnetic scattering code called DDSCAT to handle bigger targets with shorter execution times than the original code. A big target is one where the effective radius of the target is large compared with the incident wavelength. The code uses the discrete-dipole approximation, and an accurate result requires that the spacing between cells be small relative to the wavelength. This requirement, along with the big target size, implies that the number of discrete points defining the computational box surrounding the target must be large. The memory requirement is large and the execution time is long. The original version of the code cannot handle the problems we want to consider because the memory requirement exceeds the memory on a single node of our machine and the execution time extends to days of computer time.

We have removed two limitations of the original version of the code. First, to lower the execution time, the original code assigned one MPI process to each independent target orientation. We have removed this limitation by assigning teams of processes to each orientation. Second, the original code allocated all the memory for the full problem for each MPI process. We have removed this limitation by decomposing the data structures across the members of a team. With these changes, for big targets, the new version of the code exhibits strong scaling for fixed problem size. The execution time decreases very nearly $1/p$ as the processor count p increases. Execution time measured in days with the original code can now be reduces to fractions of an hour with the new code.

Analysis of Electromagnetic Scattering from Absorptive Dielectric Rough Surfaces with Underneath Target

Yinhui Wang and Yang Du
Department of Information Science and Electronics Engineering
Zhejiang University, Hangzhou 310027, China

Abstract— Electromagnetic scattering from absorptive dielectric rough surfaces with underneath target carries rich information of the target and medium, which can be used for many important ends. The main concerns of conducting the analysis lie in the capability of the proposed numerical approach to be computationally efficient, robust, and able to handle large scale problems. Also since the popular spectral acceleration (SA) technique can deal with both time and storage complexity, it is desirable to extend its applicability to absorptive media as well.

In our previous work, we have proposed a highly efficient and robust numerical approach for the analysis of scattering from dielectric rough surfaces. It is based on the design of an appropriate right preconditioner (RP) in combination with the GMRES approach. Since knowledge of the distribution of the impedance matrix spectrum is not required, the GMRES-RP method is expected to be of wide applicability. In the current work we extend this method to the case of coupling between a rough surface and a target beneath it. Moreover, the medium under the rough surface is allowed to be absorptive, which represents more realistic conditions. The extension from nonabsorptive or highly absorptive medium to the case of slightly or moderate absorptive medium when the spectral acceleration technique is used without compromising accuracy has been proposed in our previous work. In this paper we take advantage of this capability to make a more realistic study.

The proposed method has shown to be very accurate through comparison of its predictions against that of direct matrix inversion (DMI). The conservation of energy holds very well. Sensitivity to a number of parameters, such as target size, roughness, has been systematically investigated.

In conclusion, we have proposed a highly efficient and robust numerical approach for the analysis of scattering from a rough surface with a target beneath it. The medium under the rough surface is allowed to be absorptive. The proposed method is useful in a number of important applications such as target detection.

Investigating the Radar Returns of a Wind Turbine

M. B. Raza and T. H. Fickenscher
Helmut Schmidt University, Hamburg, Germany

Abstract— As a consequence of the global push for green energy, the growing number of wind farms being deployed leads to an increase in the possibility of electromagnetic interference with nearby radio communication systems. Wind turbines located in the vicinity of radar installations can cause deterioration in the performance of the radars. The signals reflected from the physical structure of the turbine may be reflected back to the radar, resulting in an increase in the strength of the undesired echoes that come from objects other than the intended target. Moreover, the rotation of the blades of a turbine causes a frequency shift owing to the Doppler Effect. The Doppler frequency shift generated by this rotation is a time varying frequency function and a periodic time-varying modulation is imposed onto the carrier frequency. Consequently, the ability of the radar to detect desired targets can be severely affected. Different studies about the radar returns from a wind turbine have been carried out in the past, however, the impact of the rotating blades of a turbine on RCS and Doppler shift have not been comprehensively characterized.

In this paper, an analysis of the radar returns of a wind turbine is presented. EM Simulation Software FEKO is used to obtain the Radar Cross Section (RCS) of entire wind turbine geometry, including the mast, the nacelle, and the blades. Different orientations of the rotor blades are incorporated to account for the rotation of the blades which results in a path length change versus time. Short time Fourier transform (STFT) is used to obtain time-dependent frequency information for the extraction of Doppler features. The impact of varying blade positions and material on RCS and Doppler shift is discussed. Doppler features due to multiple scattering and unique blade shapes are also reported.

EM Plane Wave Diffraction by a Moving Half-plane

A. Ciarkowski
Warsaw University of Life Sciences, Poland

Abstract— This contribution is concerned with 2D diffraction of an electromagnetic, harmonic plane wave by a perfectly conducting half-plane moving in a free space. The scatterer velocity can attain values from zero to relativistic ones. This, and related problems involving moving scatterers with edges, have recently met with much interest (e.g., [1–4]). In this contribution known results are confirmed and new ones are presented.

In [2] and in [3] it was shown that in the diffraction by a *moving* half-plane the shadow boundaries of both the incident and reflected wave are not parallel to the rays pertinent to those waves, and thus the illuminated and shadow regions are modified as compared to the stationary diffraction. It was shown that the diffracted wave is also modified. The final results in [2] are a little bit complex in form. The analysis in [3] is carried out with the help of integrals defined in a complex frequency plane.

Here we consider the case wherein the velocity of the half-plane is perpendicular to both the normal to the screen surface and its edge. We arrive at the field peculiarities occuring at relativistic velocities of the scatterer in a simple way.

The starting point of the analysis is the exact solution for both E and H polarizations and the stationary case, given in terms of Fresnel integrals. With the help of Lorentz transformation and by the use of Frame Hopping Method we transform the solution from the stationary frame (where the scatterer remains motionless) to the laboratory frame, where it is moving with a constant velocity. The modification of the incident and shadow boundaries is readily inferred from the change of incident (reflected) and diffracted eiconals in this transformation. It is shown that the surfaces of the diffracted wave are dynamically growing cylinders with their centres moving together with the edge of the half-plane. We show the relation between the phase of the incident wave and the phase of the diffracted wave. The quantitative estimation of the Doppler effect is readily seen from the results obtained. In the analysis we depend on the exact solution given in the closed form. Hence the radiation pattern of the diffracted wave and its change with scatterer velocity can be obtained without resorting to asymptotic considerations (which introduce singularities at particular directions).

REFERENCES

1. De Cupis, P., P. Burghignoli, G. Gerosa, and M. Marziale, "Electromagnetic wave scattering by a perfectly conducting wedge in uniform translational motion," *Journal of Electromagnetic Waves and Applications*, Vol. 16, No. 8, 345–364, 2002.
2. Ciarkowski, A. and B. Atamaniuk, "Electromagnetic diffraction by a moving half-plane," *Journal of Technical Physics*, Vol. 46, No. 4, 203–212, 2005.
3. Idemen, M. and A. Alkumru, "Relativistic scattering of a plane-wave by a uniformly moving half-plane," *IEEE Transactions on Antennas and Propagation*, Vol. 54, 3429–3440, 2006.
4. Ciarkowski, A., "Scattering of an electromagnetic pulse by a moving wedge," *IEEE Transactions on Antennas and Propagation*, Vol. 57, No. 3, 688–693, 2009.

Backscattering Coefficient Laboratory Measurements in Ka Band and at Small Incidence Angles

Pierre Borderies[1], **Christophe Fatras**[1], **Guillemette Caulliez**[2], **Sébastien Pioch**[2], **Jean-Claude Lalaurie**[3], **and Roger Fjørtoft**[3]

[1]ONERA-DEMR, 2, Avenue Edouard Belin, Toulouse 31400, France
[2]Mediterranean Institute of Oceanography (MIO)
163, Avenue de Luminy, case 901, Marseille 13009, France
[3]CNES, 18, Avenue Édouard Belin, Toulouse 31400, France

Abstract— The present paper describes laboratory experiments designed for investigating the Ka-band radar response at incidences close to nadir over continental water surfaces. This study was made in the controlled environment of the large Marseille-Luminy wind wave facility and aimed at collecting data about radar backscattering coefficient σ_0 and the associated water surface roughness and wind parameters. To illuminate the water surface of interest with a narrow angular distribution, we chose to work in the near field of the reflector antenna (tubular zone). The measurements were made using two configurations, the first one consisting in a system built for outside measurements over rivers enabling to investigate a limited range of incidences, and the second one built more specifically for such experiments, then enabling to investigate a broader range of incidences with a wider backscattering water surface footprint. The two laboratory campaigns lead to similar values of the measured incoherent backscattering coefficient, which are also consistent with airborne measurements. When wind increases, it is shown σ_0 first increases rapidly up to a maximum observed for a wind speed of 3 m/s about, and then exhibits a continuous but slowly decrease with wind. At very small wind speeds, typically below 2 m/s, the σ_0 variation with incidence angle exhibits a peculiar non monotonous trend with round peaks located around $\pm 3°$ while at higher winds, a more classical behavior is observed. There, the curves which characterize the σ_0 dependence on incidence reach lower levels and become flatter when the water surface roughness increases with wind. Furthermore, the calibration method for retrieving the backscattering coefficient and the impact of the experimental configurations on the observations will be discussed as well as the perspectives opened by this study for modelling the Ka radar response over real continental water surfaces.

(a) (b)

Figure 1: (a) Views of the wind tunnel and (b) the water surface ruffled by wind waves.

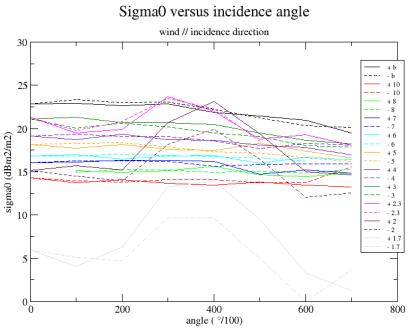

Figure 2: σ_0 versus incidence angle as observed for increasing wind speeds.

Session 3A4
Design and Simulation of Electromagnetic and Optical Devices 1

Modal Analysis of Post-wall Waveguides Based on a Model of Two-dimensional Photonic Crystal Waveguides
Kiyotoshi Yasumoto, Hiroshi Maeda, Vakhtang Jandieri, ... 442

Design and Simulation of Three-dimensional Woodpile Photonic Crystal Defect Cavities
Ying-Lung Daniel Ho, Mike P. C. Taverne, Xu Zheng, Lifeng Chen, Martin Lopez Garcia, John G. Rarity, ... 443

Electromagnetic Scattering from Imperfectly Periodic Array of Circular Cylinders
Koki Watanabe, Yoshimasa Nakatake, ... 445

Tapered Fiber Mach-Zehnder Interferometer for Liquid Level Sensing
Hun-Pin Chang, Chai-Ming Li, Cheng-Ling Lee, Jui-Ming Hsu, ... 446

Analysis of Plasmonic Devices Using the Frequency-dependent Fundamental 3D-LOD-FDTD Method
Jun Shibayama, Tomoyuki Hirano, Y. Wakabayashi, Junji Yamauchi, Hisamatsu Nakano, ... 447

Computational Accuracy of a Hybrid Scheme for Maxwell-Schrödinger Equations
Shinichiro Ohnuki, Takashi Takeuchi, T. Sako, Yoshito Ashizawa, Katsuji Nakagawa, Masahiro Tanaka, Weng Cho Chew, ... 448

Reflection and Transmission Characteristics of Lattice Grid with Lossy Clad for Optical CT
Yasumitsu Miyazaki, Koichi Takahashi, Nobuo Goto, ... 449

Reconstruction of Dielectric Objects by Solving Volume Integral Equations with Tetrahedral Discretization
Guochun Wan, Q. F. Li, K. Yang, Mei Song Tong, ... 451

Numerical Technique Based on Superposition Solution Combined with Method of Moments
Masahiro Tanaka, K. Tanaka, ... 452

Distance Property of Electric Field Patterns for an Antenna Mounted on a Car in UHF Band
R. Aoyama, Kenji Taguchi, Suguru Imai, Tatsuya Kashiwa, H. Kuribayashi, S. Komatsu, ... 453

Low SAR, Compact and Multiband Antenna
Kamel Salah Sultan, Haythem Hussein Abdullah, Esmat Abdel-Fattah Abdallah, Essam Abdel Haleem Hashish, ... 454

Modal Analysis of Post-wall Waveguides Based on a Model of Two-dimensional Photonic Crystal Waveguides

Kiyotoshi Yasumoto[1], **Hiroshi Maeda**[1], **and Vakhtang Jandieri**[2]

[1]Faculty of Information Engineering, Fukuoka Institute of Technology, Fukuoka 811-0295, Japan
[2]School of Electrical Engineering and Computer Science, Kyungpook National University
Daegu 702-701, Republic of Korea

Abstract— The post-wall waveguide, also called laminated waveguide or substrate integrated waveguide, has received a growing attention because of their promising applications to planar circuit components operating in the microwave and millimeter wave frequency range. Their modal properties have been extensively investigated using various numerical techniques [1]. In this paper, we shall present a novel semi-analytical approach for analyzing the post-wall waveguide using a model [2] of two-dimensional photonic crystal waveguides.

The post-wall waveguide, as illustrated in Fig. 1, is composed of periodic arrays of conducting circular posts embedded in a dielectric substrate that connect two parallel conducting plates. Although the post arrays in both sides may be N-layered, Fig. 1 shows the structure formed by a single array. Since the substrate is very thin ($b << \lambda$), the fields are uniform ($\partial/\partial y = 0$) in the y direction. This periodic waveguide is quite similar to a two-dimensional photonic crystal waveguide formed by parallel circular rods which are infinitely long in the y direction. The modal properties of the post-wall waveguide can be analyzed using the generalized reflection matrix of N-layered post arrays viewed from the guiding region [2], which is expressed in term of the T-matrix of the isolated circular rod and the lattice sums for the periodic arrangement of the rods. Applying the long wavelength approximation, which is valid when only the fundamental Froquet mode is propagating and all other diffraction orders are evanescent, the generalized reflection matrix is reduced to a scalar reflection coefficient. The long wavelength application is applicable to most of practical post-wall waveguide structures. Using the reduced reflection coefficient, the propagation constant of the fundamental mode of the post-wall waveguide and the effective width of the equivalent rectangular waveguide are calculated and their accuracy is validated by various numerical tests.

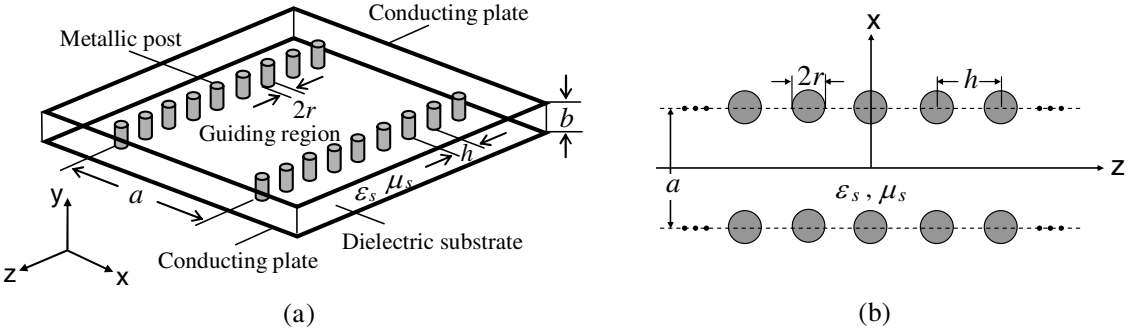

Figure 1: Schematic of a post-wall waveguide: (a) 3-D view and (b) transversal view in the x-z plane.

ACKNOWLEDGMENT

This work was supported in part by Grant-in-Aid for Scientific Research (C) 24560430.

REFERENCES

1. Deslandes, D. and K. Wu, "Accurate modeling, wave mechanisms, and design considerations of a substrate integrated waveguide," *IEEE Trans. Microwave Theory Tech.*, Vol. 54, No. 6, 2516–2526, 2006.
2. Yasumoto, K., H. Jia, and K. Sun, "Rigorous modal analysis of two-dimensional photonic crystal waveguides," *Radio Sci.*, Vol. 40, No. 6, RS6S02, 2005.

Design and Simulation of Three-dimensional Woodpile Photonic Crystal Defect Cavities

Y. -L. D. Ho[1,2], **M. P. C. Taverne**[1,2], **X. Zheng**[1,2], **L. Chen**[1,2], **M. L. Garcia**[1,2], **and J. G. Rarity**[1,2]

[1]Centre for Communications Research, Department of Electrical and Electronics Engineering University of Bristol, United Kingdom
[2]Centre for Quantum Photonics, H. H. Wills Physics Laboratory, University of Bristol, United Kingdom

Abstract— In the last few years, there has been significant interest in developing photonic crystal (PhC) based optical cavities with long photon life times (high Q-factors) and small modal volume (V_{eff}). These parameters are the key figures of merit measuring the strength of interaction between the cavity and a two-level system. Potential applications of these systems include ultra-small optical filters, nonlinear optical devices, ultralow-power and ultrafast optical switches, quantum information processing and low threshold lasers. Light localization, coupling, and emission of photons by defect cavities in two-dimensional (2D) PhC waveguides with a triangular lattice structure and suspended 1D PhC cavities have been experimentally demonstrated. The confinement of light in 1D and 2D systems is always partly reliant on total internal reflection at a low refractive index boundary (often air), hence a key loss component is out-of-waveguide scattering. Fabricated structures often show much lower Q-factors than predicted in theory because of surface scattering and the difficulties of trapping of light in low refractive index defects. Hence, we are investigating a system where these losses are fully suppressed because the cavity is fabricated in a structure with a full 3D bandgap at the resonant frequency.

Here, we report on our latest numerical study of defect cavities in inverse 3D photonic crystals building on work first reported in [1]. We will report results obtained from models of nanocavities in woodpile structures showing full photonic bandgaps. These microcavity resonators are the world's smallest dielectric resonators [cavity volume $< 0.2(\lambda/2n)^3$] and show potential Q-factors $> 10^6$. As these structures are inside full bandgap materials we expect also to be able to trap light in low refractive index defects and will report modeling results at the conference. We are also studying woodpile structures made from high refractive index materials, two different materials and dispersive materials. We have recently installed a two-photon polymerization based 3D lithography system capable of directly writing 3D woodpile structures. Hence the modelling will be guided by the experimentally achievable log sizes and refractive index contrasts. Once we have determined good bandgap candidates in extended single crystals we will model finite structures containing defect cavities using our in house FDTD software. We've already seen promising initial results from cube defect in woodpile structures [2].

This proposed 3D system is a promising platform for quantum information processing and quantum communication schemes. The ultimate goal is the simulation and eventual fabrication of a high-Q nanocavity containing a two-level 'atom' showing strong coupling with the electromagnetic field. This can be used to implement efficient single photon sources, ultra-low power optical switches and quantum memory based on spin [3].

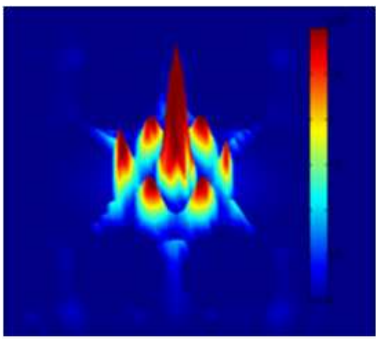

Figure 1: Resonant frequency snapshot of a single-cell defect cavity mode intensity distribution ($\varepsilon|E_x|^2 + |E_y|^2 + |E_z|^2$) in x plane in a 3D inverse FCC photonic crystal. The cavity volume is $0.152(\lambda/2n)^3$ [1], much smaller than any other dielectric confined cavities.

REFERENCES

1. Ho, Y.-L. D., et al., "FDTD simulation of inverse three-dimensional face-centered cubic photonic crystal cavities," *IEEE J. Quantum Electron.*, Vol. 47, 1480–1492, 2011.
2. Ho, Y.-L. D., et al., "Modelling, fabrication and measurement of 3-D photonic crystal defect layer in woodpile structures," *Photon*, Vol. 12, Durham, UK, September 3–6, 2012.
3. Hu, C. Y., et al., "Loss-resistant state teleportation and entanglement swapping using a quantum-dot spin in an optical microcavity," *Phys. Rev. B*, Vol. 47, 115303, 2011.

Electromagnetic Scattering from Imperfectly Periodic Array of Circular Cylinders

Koki Watanabe and Yoshimasa Nakatake
Fukuoka Institute of Technology, Japan

Abstract— The electromagnetic scattering problem of periodic structures has been extensively studied for a long time as wavelength and polarization selective components in microwave, millimeter-wave, and optical wave regions. The Floquet theorem asserts that the fields in periodic structures are expressed in a superposition of the Floquet-modes, which are the eigenmodes with pseudo-periodic property. The plane-wave excites only one Floquet-mode in a perfectly periodic structure, and the excited fields have a pseudo-periodic property. This implies that the analysis region can be reduced to only one periodicity cell and the fields have equidistant discrete spectra in the wavenumber space. Therefore, the field components can be expressed in the generalized Fourier series expansions, and many numerical approaches to periodic structures are based on the Floquet theorem.

Recently, structures in which the periodicity is locally broken have also received much interest because they induce distinct properties; for example, the field localization induced by defects in the electromagnetic bandgap structures. In such structures, the numerical approaches based on the Floquet theorem is no longer applicable, and the numerical analyses are usually performed with the finite differences time-domain method, the finite element method, the time-domain beam propagation method, the method of fictitious sources, etc. In this work, we consider the scattering problems of imperfectly periodic structures, and present an efficient and accurate spectral-domain technique to characterize the electromagnetic scattering from periodic circular cylinder arrays, in which structural periodicity is locally broken. The present formulation is based on the recursive transition-matrix algorithm (RTMA) with the help of the concept of the pseudo-periodic Fourier transform (PPFT). The RTMA is one of the most commonly used approaches to the electromagnetic scattering problem of a finite number of parallel cylinders and also extended to the plane-wave scattering problem of periodic cylinder array consisting of in finite number of cylinders with the use of the concept of the Floquet theorem. When the structural periodicity is not perfect, an artificial discretization is generally necessary for practical computation. The present formulation introduces the discretization in the wavenumber space by using the concept of the PPFT.

Tapered Fiber Mach-Zehnder Interferometer for Liquid Level Sensing

Hun-Pin Chang, Chai-Ming Li, Cheng-Ling Lee, and Jui-Ming Hsu
Department of Electro-Optical Engineering, National United University
Miaoli 360, Taiwan, R.O.C.

Abstract— Fiber-optic liquid level sensors (FOLLSs) with many smart and hybrid structures have been proposed in recent years. These FOLLSs especially based on the in-line fiber interferometer have attracted much attention due to their compact and highly sensitive properties.

In this study, we present a low cost, simple, and in-line liquid level sensor by using a tapered fiber Mach-Zehnder interferometer (TFMZI) which can be effectively fabricated by tapering a single-mode fiber (SMF) twice with an interval of certain length. The TFMZI subsequently pasted onto a slice of uniform elastic-plastic to form a sensing element of bending cantilever, a stick of polyamide adheres to the cantilever and droops into the liquid. Figure 1 indicates the configuration of the proposed FOLLS.

The cantilever is the most curved initially, it is driven by the buoyancy of the liquid and reduces its bending curvature during the liquid level rises. The coupling cladding modes, which dominate the interference in the TFMZI, are determined upon the evanescent mechanism resulted from the bending taper regions. Therefore, the interference spectra will shift during the liquid level rises or drops. The quantitative data of the liquid level is then obtained from the wavelength shifts based on the the above-mentioned bending interference.

Experimental results show that the proposed TFMZI sensor is extremely sensitive; a sensitivity of about 5 nm/cm has been achieved (displayed in Figure 2). The proposed simple liquid level sensor has considerable potential applications, and can be further improved to enhance the sensing capabilities of multi-sensing parameters, such as refractive index and specific gravity of liquids.

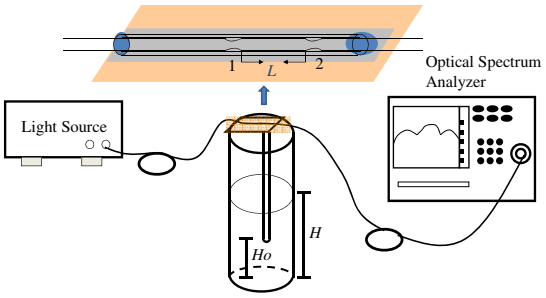

Figure 1: Configuration of the proposed liquid level sensor.

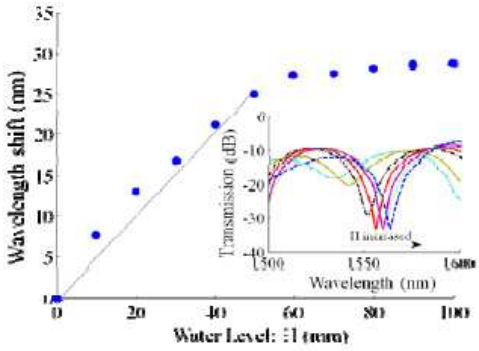

Figure 2: Sensitivity of the proposed liquid level sensor. Inset shows the experimental interference spectra shifts during the liquid level increases.

Analysis of Plasmonic Devices Using the Frequency-dependent Fundamental 3D-LOD-FDTD Method

J. Shibayama, **T. Hirano**, **Y. Wakabayashi**, **J. Yamauchi**, **and H. Nakano**
Faculty of Science and Engineering, Hosei University, Tokyo 184-8584, Japan

Abstract— The finite-difference time-domain (FDTD) method has widely been used for the numerical analysis of plasmonic waveguides. One major drawback is the limitation of a time step caused by the Courant-Friedrichs-Lewy (CFL) condition. In particular, the time step becomes extremely small, when plasmonic devices are analyzed in which spatial meshes should be reduced to $\cong \lambda/300$ (λ represents a wavelength). This gives rise to long computation time.

To tackle this problem, we have utilized the locally one-dimensional (LOD) FDTD [1–4] because of the ability to use a large time step beyond the CFL limit. We have shown that the frequencydependent LOD-FDTD using the trapezoidal recursive convolution (TRC) technique [5] can provide efficient calculations for the analysis of plasmonic devices, when compared with the traditional explicit FDTD. In addition, the LOD-FDTD has an advantage over the alternating-direction implicit FDTD in that the algorithm is quite simple.

In this article, a novel 3D formulation of the LOD-FDTD using the fundamental scheme [6] is presented. The metal dispersion of Ag is expressed by the Drude model, which is taken into account with the TRC technique. The calculation procedure based on the fundamental scheme is improved, in which implicit and explicit equations are alternatingly calculated. This leads to the requirement of only 10 field arrays, while the traditional explicit FDTD needs 12 arrays. Using the present method, we analyze several plasmonic devices composed of metal-insulator-metal structures. It is shown that this method is equivalent to the conventional LOD-FDTD without the fundamental scheme, even in matrix-operator-free forms in the right-hand sides of the resultant equations [7]. Numerical results of plasmonic devices will be shown in the presentation.

REFERENCES

1. Shibayama, J., M. Muraki, J. Yamauchi, and H. Nakano, "Efficient implicit FDTD algorithm based on the locally one-dimensional scheme," *Electron. Lett.*, Vol. 41, No. 19, 1046–1047, 2005.
2. Do Nascimento, V. E., B.-H. V. Borges, and F. L. Teixeira, "Split-field PML implementations for the unconditionally stable LOD-FDTD method," *IEEE Microw. Wireless Compon. Lett.*, Vol. 16, No. 7, 398–400, 2006.
3. Tan, E. L., "Unconditionally stable LOD-FDTD method for 3-D Maxwell's equations," *IEEE Microw. Wireless Compon. Lett.*, Vol. 17, No. 2, 85–87, 2007.
4. Ahmed, I., E. K. Chua, E. P. Li, and Z. Chen, "Development of the three-dimensional unconditionally stable LOD-FDTD method," *IEEE Trans. Antennas Propagat.*, Vol. 56, No. 11, 3596–3600, 2008.
5. Shibayama, J., A. Nomura, R. Ando, J. Yamauchi, and H. Nakano, "A frequency-dependent LOD-FDTD method and its application to the analysis of plasmonic waveguide devices," *IEEE J. Quantum Electron.*, Vol. 46, No. 1, 40–49, 2010.
6. Tan, E. L., "Fundamental scheme for efficient unconditionally stable implicit finite-difference time-domain methods," *IEEE Trans. Antennas Propagat.*, Vol. 56, No. 1, 170–177, 2008.
7. Shibayama, J., T. Hirano, J. Yamauchi, and H. Nakano, "Efficient implementation of frequency-dependent 3D LOD-FDTD method using fundamental scheme," *Electron. Lett.*, Vol. 48, No. 13, 774–775, 2012.

Computational Accuracy of a Hybrid Scheme for Maxwell-Schrödinger Equations

S. Ohnuki[1], **T. Takeuchi**[1], **T. Sako**[1], **Y. Ashizawa**[1], **K. Nakagawa**[1], **M. Tanaka**[2], **and W. C. Chew**[3]

[1]College of Science and Technology, Nihon University, Japan
[2]Faculty of Engineering, Gifu University, Japan
[3]University of Illinois, USA

Abstract— Novel photonic devices operating under the principle of quantum effects play an important role for development of next generation technology [1]. However, phenomena in such devices are considered as mesoscopic physics which cannot be expressed by only using classical or quantum theories. Hybrid simulation is an essential tool to analyze such mesoscopic problems and coupled methods of Maxwell-Schrödinger equations have been proposed recently [2, 3].

In this talk, we will investigate the interaction between electrons and light by using the hybrid scheme of Maxwell-Schrödinger equations. Computational results are compared with those obtained by another scheme of Maxwell-Newton equations. The computational accuracy of those hybrid schemes will be discussed.

REFERENCES

1. Aoki, K., D. Guimard, M. Nishioka, M. Nomura, S. Iwamoto, and Y. Arakawa, "Coupling of quantum-dot light emission with a three-dimensional photoniccrystal nanocavity," *Nature Photonics*, Vol. 2, 688–692, 2008.
2. Pierantoni, L., D. Mencarelli, and T. Rozzi, "A new 3-D transmission line matrix scheme for the combined Schrödinger — Maxwell problem in the electronic/electromagnetic characterization of nanodevices," *IEEE Trans. MTT*, Vol. 56, No. 3, 654–662, 2008.
3. Takeuchi, T., S. Ohnuki, T. Sako, Y. Ashizawa, K. Nakagawa, M. Tanaka, and W. C. Chew, "Hybrid simulation of an electron constrained by a harmonic oscillator potential using the FDTD method for the Maxwell-Schrödinger equations," *Proceedings 2012 IEEE International Symposium on Antennas and Propagation and USNC/URSI Radio Science Meeting*, Chicago, USA, IF22.8, July 2012.

Reflection and Transmission Characteristics of Lattice Grid with Lossy Clad for Optical CT

Yasumitsu Miyazaki[1], **Koichi Takahashi**[1], **and Nobuo Goto**[2]

[1]Department of Media Informatics, Aichi University of Technology
50-2 Manori, Nishihasama-cho, Gamagori 443-0047, Japan
[2]Institute of Technology and Science, The University of Tokushima
2-1 Minamijosanjima-cho, Tokushima 770-8506, Japan

Abstract— Medical image diagnosis and computer aided diagnosis are modern important medical techniques developed with computer technology. Particularly, medical image diagnosis using optical waves of lasers is very important technical tools for physiological examination of human body. Image responses of optical transmitted projection include optical scattering characteristics that disturb transmission properties through biological structures depending on optical absorption effects due to biological characteristics consisting of atomic and molecular structure. We have studied spatial filtering for optical scattering superposed on transmitted and attenuated waves to improve image diagnosis. Spatial filtering characteristics of grid structure are shown for exact image optical projection excluding scattering effects through physiological media by FDTD method. In waveguide-type grid filters with lossy clads, scattered fields from biological structures with large scattering angles have large attenuations. Transmitted and scattered fields of small scattering angles have small attenuations and can pass through the waveguide grids. We studied statistical scattering characteristics of biological objects surrounded by inhomogeneous biological media using FDTD method and showed that spatial filtering by waveguide-type grid filter with lossy clads is very effective to suppress scattered waves with large scattering angles and to obtain accurate target object image.

In this paper, reflection and transmission characteristics of waveguide-type spatial filter consisting of clad and core with relatively long length and complex refractive index of lossy clad for incident angles of the incident beam are studied by FDTD method comparing with approximate analytical method, such as physical and geometrical optics for optimum design of structure of spatial filter to accomplish accurate image diagnosis by optical CT. For periodic structures of lattice grid spatial filter, width of lossy clad $d = 1$–$3\,\mu$m, width of transparent core $D = 10$–$50\,\mu$m with complex refractive index n_g^*, length of grid $\ell_g = 30$–$100\,\mu$m are considered for filtering evaluation. Fig. 1 shows the FDTD analysis model for lattice grid with $d = 1\,\mu$m, $D = 2\,\mu$m, $\ell_g = 4\,\mu$m and $n_g^* = 2.0 - j0.5$ and the amplitudes of transmitted and attenuated waves in core and clad regions are evaluated. For large incident angles of the incident beam, attenuation of the amplitudes of transmitted waves become large due to the absorption by lossy clads and realization of effective spatial filter is expected. In this study, electric field distributions in waveguide-type grids are shown precisely using FDTD method. Also, field distributions are studied by approximate analytical method which gives physical interpretation for numerical results obtained by FDTD. The numerical and analytical methods can provide optimum design of lattice grid spatial filter with desired performance for accurate image diagnosis by optical CT.

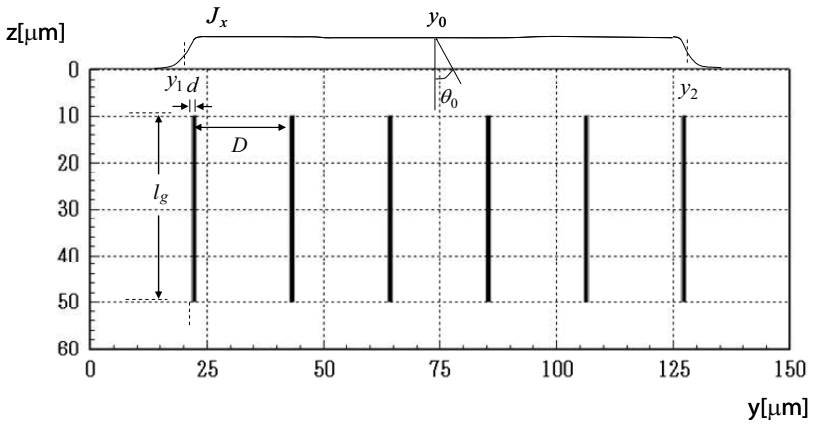

Figure 1: Analysis model of lattice grid for optical CT.

REFERENCES

1. Miyazaki, Y., *Jpn. Appl. Phys.*, Vol. 13, 1238–1248, 1974.
2. Miyazaki, Y., *Proc. of APMC 2007*, 527–530, Bangkok, 2007.
3. Miyazaki, Y. and K. Kouno, *IEEJ Trans. FM*, Vol. 129, No. 10, 693–698, 2009.

Reconstruction of Dielectric Objects by Solving Volume Integral Equations with Tetrahedral Discretization

G. C. Wan[1, 2], **Q. F. Li**[1, 2], **K. Yang**[1, 2], **and M. S. Tong**[1, 2]

[1]Department of Electronic Science and Technology, Tongji University
4800 Cao'an Road, Shanghai 201804, China
[2]State Key Laboratory of Millimeter Waves, Nanjing 210096, China

Abstract— In the integral equation method for reconstructing dielectric objects through the Born iterative method (BIM) or distorted Born iterative method (DBIM), the volume integral equations (VIEs) are solved because the imaging domain including both real unknown objects and part of background is inhomogeneous. There are forward scattering integral equation (FSIE) and inverse scattering integral equation (ISIE) in the reconstruction and we need to alternatively solve them in the context of BIM or DBIM. The FSIE is used to calculate the total electric field in the imaging domain by assuming that the material property of the imaging domain is known, while the ISIE is used to solve the material property of the imaging domain by assuming that the total electric field is known.

The FSIE is mainly solved by the conventional method of moments (MoM) though other schemes can also be used. However, the MoM may not be convenient for solving inverse scattering problems because the imaging domain is inhomogeneous and the Schaubert-Wilton-Glisson (SWG) basis function requires conforming meshes. In this work, we employ the Nyström method to replace the MoM for solving the FSIE. The advantages of this method include the fast preprocessing, lower requirement on mesh quality, and removal of basis and testing functions. On the other hand, the ISIE is insolvable by direct inversion because the matrix equation is inherently ill-posed due to the limited data diversity of measurement in general. One usually transforms the inversion of model parameters from measured data into an optimization problem and it can be solved by the Gauss-Newton minimization approach (GNMA) with a regularization scheme. The determination of regularization parameter is a key in the regularization and we use the multiplicative regularization method (MRM) in this work. The MRM was proposed for gradient-type algorithms and was adapted by Habashy and Abubakar for Newton-type algorithms in the inversion by the finite difference time domain (FDTD) approach, but we use it for integral equation approach by modification here. The method can adaptively vary the regularization parameter as the iteration proceeds and a large number of numerical experiments are unnecessary in the inversion. Numerical examples for reconstructing typical dielectric objects are presented to illustrate the approach and good results can be observed.

Numerical Technique Based on Superposition Solution Combined with Method of Moments

M. Tanaka and K. Tanaka
Gifu University, Gifu 501-1193, Japan

Abstract— Electromagnetic scattering from multiple objects is an important problem, and it has been investigated for a long time. The examples of scattering from multiple objects are frequency selective surface, photonic crystal structure, metamaterial structure, and so no. They contain periodic structure of small objects. Another example is electromagnetic propagation through rain medium. It consists randomly distributed raindrops.

When objects are spherical in shape, the superposition solution combined with Mie's theory gives an exact solution for electromagnetic scattering from multiple spheres. The solution can be analytically calculated by using the additional theorem to transform a spherical harmonic from one coordinate origin to another. In the method, each sphere has arbitrary in radius, position, and index of refraction, however, the shape of each object is restricted to spherical only.

In order to solve electromagnetic scattering from multiple objects arbitrary in shape, we replace the method of moments with Mie's theory. Namely, we employ the superposition solution combined with the method of moments.

When one treat electromagnetic scattering from multiple objects, the method of moments is applied into the entire structure of multiple objects. Therefore, one need to solve a linear equation in large number of variables. It is a time-consuming part in the method of moment to solve the linear equation.

On the other hand, since the method of moments is applied into each object in our method, we need to solve a linear equation in small number of variables. It is not a time-consuming part in our method to solve the linear equation. A time-consuming part is calculation of scattering field.

We will discuss strong and weak points of our method, and we will also show some numerical results.

Distance Property of Electric Field Patterns for an Antenna Mounted on a Car in UHF Band

R. Aoyama[1], **K. Taguchi**[1], **S. Imai**[1], **T. Kashiwa**[1], **H. Kuribayashi**[2], **and S. Komatsu**[2]

[1]Kitami Institute of Technology, Kitami, Japan
[2]Honda R&D Co., Ltd., Tochigi, Japan

Abstract— With the development of mobile communication technology, it is becoming important to design car antennas for communication service using the UHF band, such as digital terrestrial broadcasting, a mobile communication, an inter-vehicle communication and so on, in Japan. In the measurement, radiation patterns for an antenna mounted on a car are always measured at finite distance by using a large-scale anechoic chamber or an open site. Therefore, it is indispensable to know distance property of electric field patterns at finite distance, and distance from a car to boundary between near and far fields. However, it is difficult to clarify the above-mentioned characteristics by measurement. In this paper, the distance property of electric field patterns for an antenna mounted on a standard compact sedan in UHF band was investigated for the first time by the electromagnetic simulation. As a result, it was shown that field patterns at finite distance depended on frequencies, antenna positions, polarizations, ground conditions, origin positions to observe field patterns.

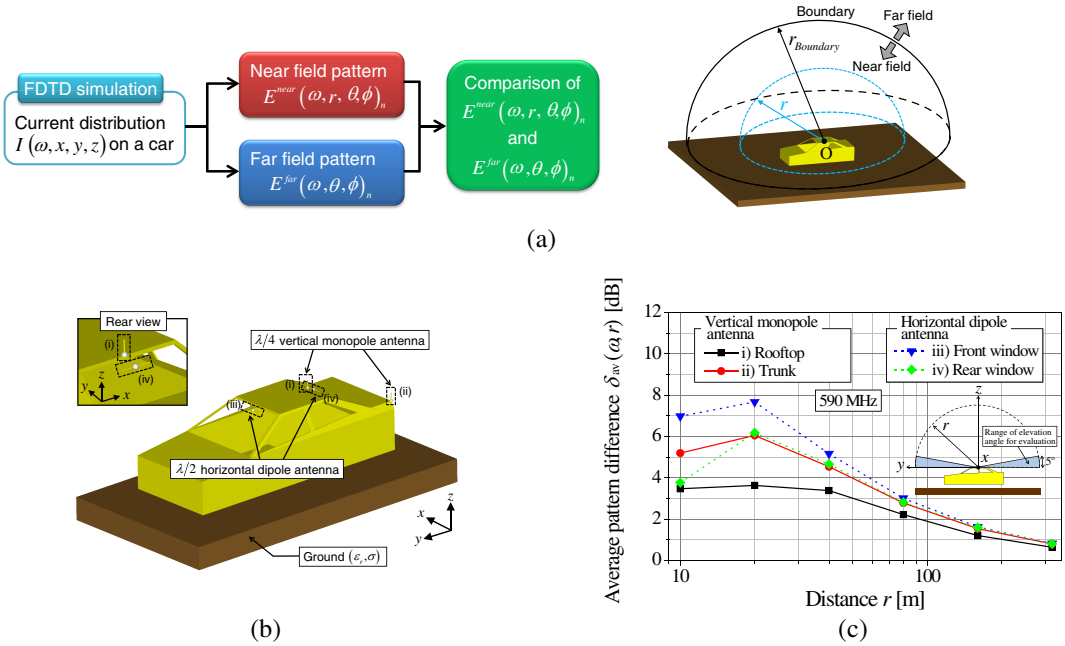

Figure 1: (a) Flowchart of analysis method for distance property of electric field patterns. (b) Car model and antennas. (c) Average pattern difference between near and far fields for 590 MHz, where the ground is assumed to be asphalt.

ACKNOWLEDGMENT

A part of this work was supported by MEXT, KAKENHI (23560433 and 22760260).

Low SAR, Compact and Multiband Antenna

Kamel S. Sultan[1], **Haythem H. Abdullah**[1],
Esmat A. Abdallah[1], **and Essam A. Hashish**[2]

[1]Electronics Research Institute, Dokki, Giza, Egypt
[2]Faculty of Engineering, Cairo University, Giza, Egypt

Abstract— With the advent of mobile communications, researchers quick to go through the introduction of competitive mobile handsets. The features of interest in the competitions are the compact size, multiband operation, low cost and the low SAR. Thus, a compact multiband antenna is proposed to cover most of the mobile operating bands and other wireless applications. The covered bands are the GSM 900, DCS 1800, PCS 1900, UMTS 2100, and most of the LTE bands. Furthermore, it covers the ISM, WiMAX and the WLAN bands. The antenna is constructed from two parts a monopole and a meander line antenna. The operating bands ranges from (830–1030 MHz) and (1.71–7.8 GHz). Moreover, the first resonant band of the antenna can be tuned by using various meander line lengths or by adjusting the spacing between the monopole and the meander line, while the second band can be tuned by adjusting the monopole length or the meander line area. The interaction between the human head and handset antennas needs to be reduced, so an EBG structure is applied to the antenna to reduce the surface waves and to prevent the undesired radiation from the ground plane. This technique reduces the radiation pattern toward the direction of human head and reduces the specific absorption rate (SAR) value. The advantages of the EBG technique are its low cost and its ease of implementation. These periodic structures have high electromagnetic surface impedance, which is capable of suppressing the propagation of surface currents and acting as a perfect magnetic conductor in a certain frequency range. Before applying the EBG structure, the antenna dimensions were $(24 \times 20 \times 1.5)\,\text{mm}^3$ and its dimensions were reduced to $(20 \times 20 \times 1.5)\,\text{mm}^3$. After applying the EBG structure the gain and front to back ratio are increased with the use of the EBG structure. The planar EBG structure is positioned between the user and the handset antenna. It consists of a periodic square patches with dimensions of $(9 \times 9)\,\text{mm}^2$ and gaps of 1 mm. The SAR calculations were done by using the CST 2011 commercial package. The SAR values are calculated at different operating bands, distances, and orientations. The effect of the human body on the performance of the antenna is tested by calculating the radiation pattern in the presence of the body head. The antenna was fabricated and its performance was measured. The simulation results are compared to the experimental measurements and a good agreement is observed.

Session 3A5
Microstrip and Printed Antenna, Antenna Theory

Creeping Wave Antenna Design and Application for On-body Surface Communication
Shih-Chung Tuan, Hsi-Tseng Chou, Ching-Hui Chen, ... 456
Compact Folded Meander PIFA Antennas in MedRadio Bands
Chiu-Yueh Huang, Chi-Lin Tsai, Chin-Lung Yang, ... 457
Band Notch Characteristics of a UWB Planar Antenna with an Elliptical Element Comprising Single Slots
Siti Fatimah Jainal, Toshio Wakabayashi, Mohamad Kamal Abd Rahim, ... 458
Dual-polarized and Dual-band Omni Directional Antenna
Ming Hui Chen, ... 459
Metamaterial Loaded Wideband Patch Antenna
Singaravelu Raghavan, Anoop Jayaram, ... 461
Wideband Small Loop-monopole HF Transmitting Antenna with Implications for Maxwell's Equations and the Chu Criterion
Michael James Underhill, ... 462
Performance Characteristics of Loop Antennas above a Ground Plane of Finite Extent
Ayotunde Abimbola Ayorinde, Sulaiman Adeniyi Adekola, Alex Ike Mowete, ... 464
Design and Analysis of a Stripline Archimedean Snail Antenna
Teng-Kai Chen, Gregory H. Huff, ... 465

Creeping Wave Antenna Design and Application for On-body Surface Communication

Shih-Chung Tuan[1], **Hsi-Tseng Chou**[2], **and Ching-Hui Chen**[2]

[1]Department of Communication Engineering, Oriental Institute of Technology, Pan-Chiao, Taiwan
[2]Department of Communication Engineering, Yuan Ze University, Chung-Li, Taiwan

Abstract— This paper presents Creeping Wave Antenna (CWA) design and application for on body surface communication, the basic characteristic of CWA has largest radiation energy coupling for on body surface communication. An array antennas have high gain and directivity, slotted microstrip patch antenna have light, low profile and thin characteristic for on body surface communication put into the dress material are better choice. The 1×6 Slotted Patch Antennas Array are designed which operation frequency at 5.8 GHz and make use of microstrip line path length produce phase difference for each antenna's elements to approach largest radiation direction is our desired. So this designed antenna can through wireless on body surface communication system for human body vital and physical signal detection. The Purpose for control immediately and look after at home can be realized.

Compact Folded Meander PIFA Antennas in MedRadio Bands

Chiu-Yueh Huang, Chi-Lin Tsai, and Chin-Lung Yang
National Cheng Kung University, Tainan 701, Taiwan

Abstract— As biomedical microwave systems grow and develop fast and widely, many implantable antenna designs are proposed such as implantable loop antenna, implantable monopole antenna, implantable helical antenna, and implantable planar inverted-F antenna (PIFA) for implantation systems [1].

This study proposes a novel miniaturized antenna design for MedRadio Band (401–406 MHz) The basic structure is based on the PIFA antenna. As the geometry shown in Fig. 1, the ground plane is bent to the other side of the substrate to reduce the size The point of C is connected to the C′ The proposed miniaturized antenna is printed on the PCB board (FR4 substrate with thickness of 0.8 mm, dielectric constant of 4.4), with a total size of 320 mm^3 ($0.0266\lambda_0 \times 0.0266\lambda_0 \times 0.00106\lambda_0$ mm^3). The proposed antenna is the single layer design, which total size is compact. Fig. 2 shows the simulated return loss of the proposed antenna. Its return loss is more than 15 dB at 404 MHz. In Fig. 3, the antenna simulated gain and efficiency are −25 dBi and 0.25% Moreover, its bandwidth covers the whole MedRadio band (401–406 MHz) This compact antenna is suitable for implantable applications.

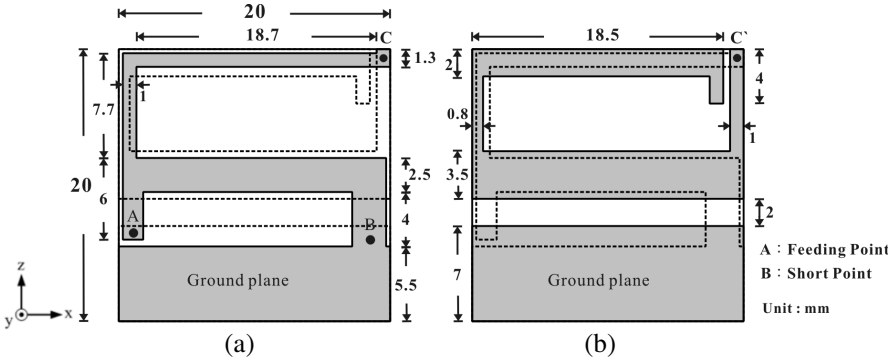

Figure 1: (a) Top view of the proposed antenna; (b) Bottom view of the proposed antenna.

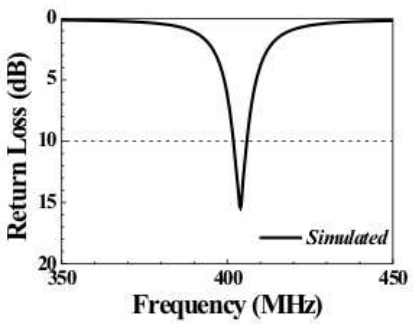

Figure 2: The simulated return loss of the proposed.

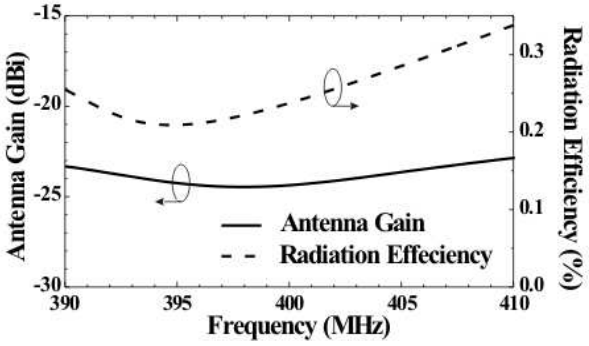

Figure 3: Gain and efficiency plot for 400 MHz.

REFERENCES

1. Soontornpipit, P., C. M. Furse, and C. C. You, "Design of implantable microstrip antenna for communication with medical implants," *IEEE Transactions on Microwave Theory and Techniques*, Vol. 52, No. 8, 1944–1951, Aug. 2004.

Band Notch Characteristics of a UWB Planar Antenna with an Elliptical Element Comprising Single Slots

Siti Fatimah Jainal[1], **Toshio Wakabayashi**[1], **and Mohamad Kamal A. Rahim**[2]

[1]Electronic System Engineering, Malaysian-Japan Institute of Technology (MJIIT)
Universiti Teknologi Malaysia (UTM), UTM International Campus
Jalan Semarak, Kuala Lumpur 54100, Malaysia
[2]Radio and Communication Engineering Department (RACED)
Faculty of Electrical Engineering (FKE)
Universiti Teknologi Malaysia (UTM), UTM Skudai, Johor 81310, Malaysia

Abstract— A single slot elliptical element planar antenna in the means of creating band notch characteristics suitable for ultra-wideband (UWB) application which operates between 3.1–10.6 [GHz] is presented. There are other existing frequency band such as wireless local area network (WLAN) with an operating bandwidth of 5.15–5.35 and 5.725–5.85 [GHz] in the UWB communication system. Thus, causing electromagnetic interruptions between these wireless networks. The proposed antenna is designed in order to filter these operating bandwidth frequencies. Single etching at the left part of the elliptical antenna significantly gives some band notch characteristics to the antenna performances. Band notch characteristics are concentrated at the desired frequency on the WLAN communication system. The proposed antenna is fabricated on an FR4 substrate. An elliptical element and ground plane are both composed on top of the substrate. The single slot parameters and the distance between the feed point and ground plane have been taken into account in the means of creating the notch band. The length and width of the single slot are adjusted purposely to increase the notch band in the common method. In this study, the distance between the feed point and the ground plane is similarly been given an attention as the impedance matching also plays an important role to increase the notch. Parametric study of the proposed antenna characteristics is studied. The comparable simulation and experimental results are obtained.

Dual-polarized and Dual-band Omni Directional Antenna

Ming Hui Chen
Victory Microwave Corporation, Xizhi District, New Taipei City, Taiwan

Abstract— Dual polarizations have recently been used in recent wireless MIMO (multiple in and multiple out) systems. However, when two antennas, one vertically polarized and one horizontally polarized, are placed side by side (as shown in Figure 1), interference results between the two polarizations. In particular, the vertically polarized signal is affected significantly.

We have been able to eliminate such interference by developing an omni directional slot array antenna with both vertical and horizontal polarizations on a single quadruple ridge waveguide

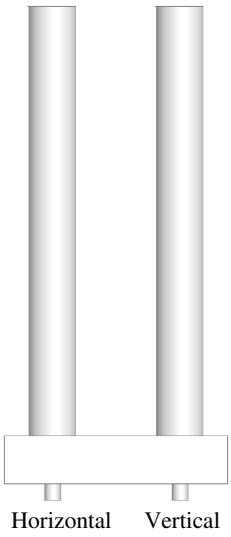

Figure 1: Dual polarized antenna with separate elements.

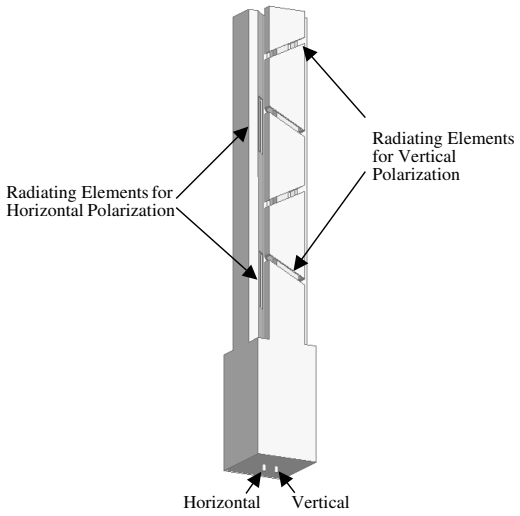

Figure 2: Dual polarized ridge waveguide slot array with horizontal and vertical polarizations.

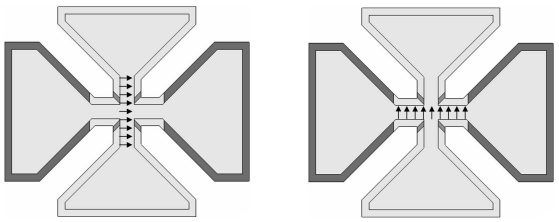

Figure 3: Waveguide modes for horizontal and vertical radiation.

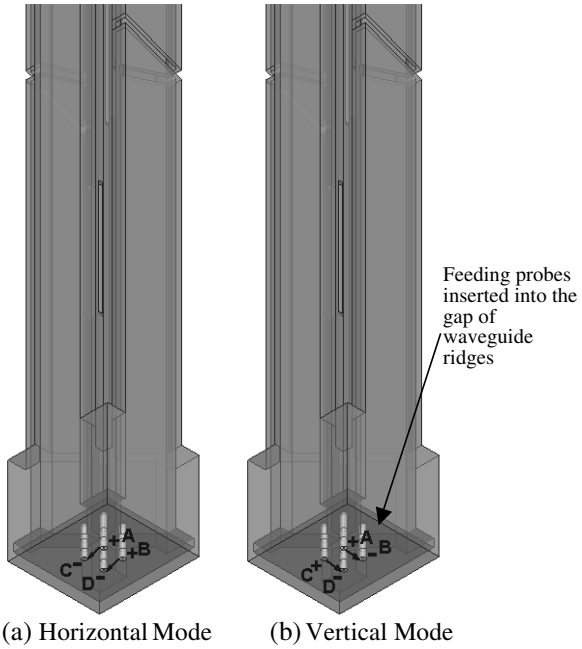

Figure 4: Feeding method for dual polarized antenna.

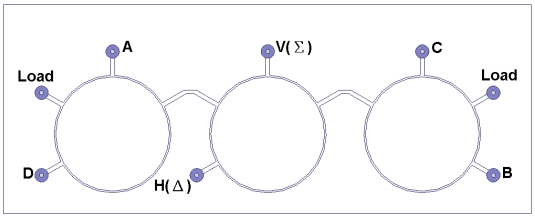

Figure 5: Network of 180° hybrid coupler for achieving horizontal and vertical excitation.

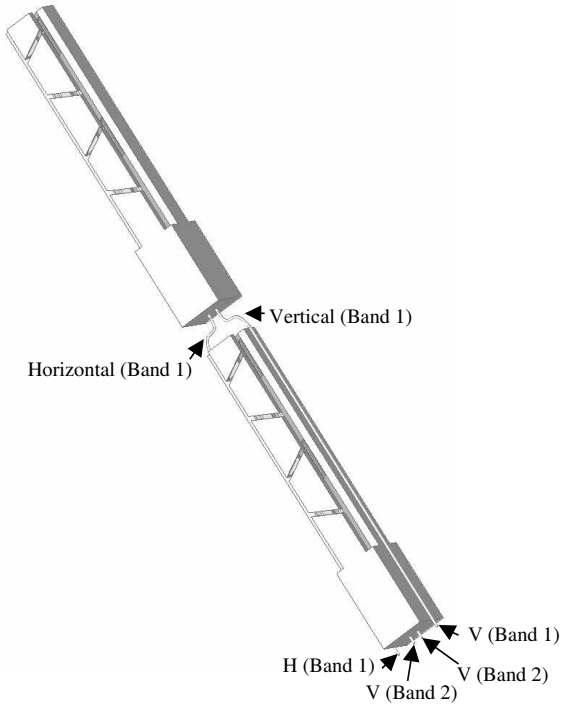

Figure 6: Method of integration for dual band antenna.

(shown on Figure 2). The radiating slots and mode of operation for each polarizations are further explained in Figure 3. The modes for both polarizations can be excited through the gaps of the ridges by four probes as shown in Figure 4. A network as shown in Figure 5 can drive the inputs of the vertical and horizontal polarization ports.

By stacking two antennas vertically, it is possible to construct a dual-band omni-directional antenna on a single post. However, there may be challenges in feeding the upper antenna without interfering with the lower one. One possible solution is shown in Figure 6 where the waveguide slot array has two metallic surfaces which can be used to support transmission lines for feeding the upper antenna. The measured data of this prototype will be presented at the conference.

Metamaterial Loaded Wideband Patch Antenna

S. Raghavan[1] and Anoop Jayaram[2]

[1]Electronics and Communication Department, National Institute of Technology, Trichy, India
[2]National Institute of Technology, Trichy, India

Abstract— A new design technique for producing wideband patch antenna is introduced in this paper. The methodology involves complementary square split ring resonators and an inset fed rectangular patch antenna both designed to resonate at the same frequency. The dimensions of the complementary square split ring resonator are same as that of the split ring resonator's physical dimensions, which are optimized using Artificial Neural Network. A Cascade Forward Backpropogation neural network using Levenberg Marquardt learning algorithm is utilized for optimization. The proposed neural network for optimization contains four hidden layers with variable number of neurons in each layer, which is created and trained using neural network toolbox 5.1 of MATLAB. The proposed antenna is constructed by cutting out the split ring resonator from the two corners of the patch where the feed is given to antenna. HFSS simulation of the proposed antenna shows improved bandwidth and return loss at the centre frequency of 2.4 GHz. The simulation result shows remarked improvement in antenna parameters when compared to a normal inset fed rectangular patch antenna, the only loss being a negligible decrement in the antenna gain.

Wideband Small Loop-monopole HF Transmitting Antenna with Implications for Maxwell's Equations and the Chu Criterion

Michael J. Underhill
Underhill Research Ltd, Lingfield, UK

Abstract— A versatile small antenna has been developed originally to meet the need for a highly portable broadband transmitting antenna for wave-tilt measurements in the HF band [1]. Figure 1 is a picture and Figure 2 is a schematic of a 0.9 m loop version of the antenna. This novel loop-monopole consists of a 1 cm diameter copper loop vertical loop that is top fed directly by a sufficiently long 50 Ohm coaxial cable. Two (or three) turns of the coaxial cable are loosely twisted around the copper loop. The lowest usable frequency is obtained with the copper loop connected to the coaxial cable as shown. In the case shown the lower coil of coaxial cable is about 25 m in length. The total vertical extent of the antenna is 1.45 m. It can be completely contained in a sphere of 1.5 m diameter, or 0.75 m radius. This loop-monopole design can thus be considered to be a 'small' antenna up to a frequency of about 64 MHz. The vertical E-field monopole part is formed by the unbalanced feed of the loop causing the loop self-capacity to act together with the vertical part of the feeder as the monopole. To avoid the suggestion that this antenna operates by radiation from a feeder outside the 1.5 m diameter sphere, a MiniVNApro Bluetooth connected, but otherwise isolated, Vector Network Analyser is used for impedance measurements. It can be seen at the bottom of the picture, Figure 1.

The 0.9 m loop-monopole, as shown, has Standing Wave Ratio (SWR) $< 11:1$ above 1.7 MHz corresponding to an antenna system $Q < 6.6$. Above 2.9 MHz, the SWR is $< 6:1$, corresponding to a system $Q < 4$ This antenna can radiate 700 watts continuous power at 3.5 MHz without appreciable heat being generated. The antenna efficiency is thus estimated to be in excess of 90%. These Q and antenna efficiency results firmly contradict the Chu Small Antenna Criterion. The claim is that the Chu criterion is derived directly from Maxwell's Equations, and if this is the case Maxwell's Equations should also be modified and improved to account for these measured results [2].

The unexpectedly low value of effective antenna Q is shown to be the result of strongly (electromagnetically) coupled and approximately equally excited electric and magnetic modes occupying the same near-field volume. The existence and importance of 'electromagnetic coupling' is once again demonstrated [3]. The equal excitation also explains the polar diagram of the loop-monopole antenna, which has been found to be usefully uni-directional (3 to 12 dB) over significant parts of the operating frequency range. Further improved variants of the loop-monopole appear to be feasible.

Figure 1: Picture of 90 cm loop-monopole with MiniVNApro (Bluetooth connected) vector network analyser at bottom.

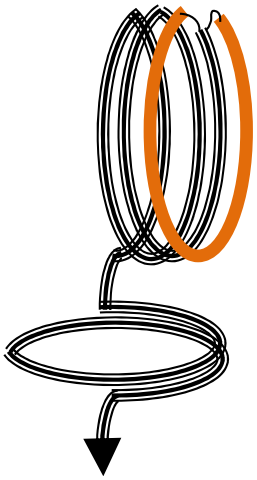

Figure 2: Schematic of loopmonopole seen in Figure 1.

REFERENCES

1. Underhill, M. J., "Anomalous ground wave tilt measured over wet ground," *IET Conf. on Ionospheric Radio Systems and Techniques 2012*, Royal York Hotel, York, UK, May 15–17, 2012.
2. Underhill, M. J., "Maxwell's transfer functions," *PIERS Proceedings*, 1766–1770, Kuala Lumpur, Malaysia, March 27–30, 2012
3. Underhill, M. J., "A physical model of electro-magnetism for a theory of everything," *PIERS Online*, Vol. 7, No. 2, 196–200, 2011.

Performance Characteristics of Loop Antennas above a Ground Plane of Finite Extent

A. A. Ayorinde[1], **S. A. Adekola**[1, 2], **and A. Ike Mowete**[1]

[1]Department of Electrical and Electronics Engineering, Faculty of Engineering
University of Lagos, Lagos, Nigeria
[2]Department of Electrical and Electronics Engineering, Niger Delta University
Wilberforce Island, Yenegoa, Nigeria

Abstract— This paper examines the characteristic behaviors of the feed-point input impedance and radiation fields of two thin-wire loop antenna types (one a circular-loop and the other, a square-loop antenna) both, one wavelength long at operating frequency, and located over a ground plane which is of the wire-grid variety [1], and whose extent is finite.

Using the moment-method approach, computational results are obtained in the presentation, for the antennas' performance parameters alluded to in the foregoing, to suggest that the square loop antenna resonates when located at a distance of 0.054λ above the ground plane; whereas the corresponding distance for the circular-loop emerges as 0.132λ. The results also indicate that the antennas' directive gains and input impedance profiles are such as to suggest that they may be suitable for practical applications over a wide range of frequencies.

A comparison carried out in the paper, between computed values of input impedance and corresponding measurement results reported elsewhere [2], very clearly indicate that the approach described in this presentation is valid.

REFERENCES

1. Wait, J. R. and K. P. Spies, "On the radiation from a vertical dipole with an inductive wire-grid system," *IEEE Transactions on Antennas and Propagation*, Vol. 18, No. 4, 414–415, April 1984.
2. Rojavayanout, B. and C. Sekiguchi, "One-element loop antenna with finite reflector," *Electronics and Communications in Japan*, Vol. 59-B, No. 5, 68–75, 1976.

Design and Analysis of a Stripline Archimedean Snail Antenna

T.-K. Chen and G. H. Huff
Department of Electrical and Computer Engineering
Texas A&M University, College Station, TX 77843, USA

Abstract— This paper presents an analysis of a stripline Archimedean snail antenna on its impedance properties and radiation mechanism. The Archimedean snail antenna has similar structure to the spiral one but with asymmetric spiral turns on arm structures. The stripline implementation of spiral center (Dyson balun) acts as a mode converter and a power splitter. Power can be transmitted from stripline mode to spiral radiating mode because of impedance matching between the two transmission line structures, i.e., stripline and parallel elevated slot-lines in periodicity. The radiation occurs when the two elevated slot-line modes are in-phase. Specifically, the spiral-radiating mode can be explained as a common mode radiation of two elevated slot-lines. A design method is then developed and proposed for the stripline Archimedean snail antenna, which uses a simple design concept by impedance matching. This design process can determine the spiral parameters step by step without performing a numerical simulation on entire spiral antenna structure to optimize the design. Designing the transmission line structures with analytical formulas can save a lot of computational time. A compact (45 mm × 40 mm × 1.016 mm) stripline-fed snail antenna is fabricated for demonstration. The measurement shows a good agreement with the simulated result from 2 GHz to 20 GHz. The snail type antenna has better performance than the spiral antenna due to its radiation mechanism. Compared to the traditional spiral antenna, this antenna design is a completely planar antenna, which provides a platform for integration of impedance matching circuits or other circuit elements easily inside the antenna structure without additional need of wideband balun and matching circuit designs.

Session 3A6
Electromagnetic Theory and Design on the Optical Dispersive Materials, Invisible Cloak and Photonic Crystals

Terahertz Super Thin Planar Lens Based on Generalized Huygens' Principle
Yan Zhang, Jia-Sheng Ye, Dan Hu, Xinke Wang, Shengfei Feng, Wenfeng Sun, ... 468

Light Speed Is an Irrational Number
Ganquan Xie, Jianhua Li, Feng Xie, Lee Xie, ... 469

Transmission Characteristics of a Plasmonic Open Waveguide Based on Low Frequency Spoof Surface Plasmon Polaritions
Yao-Huang Kao, Jin-Jei Wu, Her-Lih Chiueh, Tzong-Jer Yang, Da Jun Hou, Chien-Jang Wu, Linfang Shen, ... 470

Unidirectional and Wavelength-selective Photonic Sphere-array Nanoantennas
Yang G. Liu, Wallace C. H. Choy, Wei E. I. Sha, Weng Cho Chew, ... 471

Sensitivity Enhancement of Surface Plasmon Resonance (SPR) Sensor in a Phase-shift Interferometry (PSI) System
Wen-Kai Kuo, Chi-Xian Chen, Chien-Jang Wu, ... 472

Experimental Verification of the Suppression of Crosstalk between Bended Parallel Microstrips via Designer Surface Plasmon Polaritons
Hung Erh Lin, Tzong-Jer Yang, Yao-Huang Kao, Jin-Jei Wu, Clark Li, Chien-Jang Wu, Xianmin Zhang, ... 473

A New Proof on Boundary Conditions in Electromagnetic Theory
Cavour Yeh, F. I. Shimabukuro, ... 474

Frequency Spectra of Absolute Optical Instruments
Tomas Tyc, Aaron J. Danner, ... 475

Terahertz Super Thin Planar Lens Based on Generalized Huygens' Principle

Yan Zhang[1, 2], **Jiasheng Ye**[1, 2], **Dan Hu**[1, 2],
Xinke Wang[1, 2], **Shengfei Feng**[1, 2], **and Wenfeng Sun**[1, 2]

[1]Beijing Key Lab for Terahertz Spectroscopy and Imaging
Key Laboratory of Terahertz Optoelectronics, Ministry of Education, China
[2]Department of Physics, Capital Normal University, Beijing 100048, China

Abstract— Terahertz radiation has attracted extensive attentions in the past decades. Many developments have been made in the fields of sources, detector, and applications. However, due to the long wavelength property of the THz radiation, the size of the optical elements for dominating THz beam is quite large. They are not suitable for THz system integration. Based on the diffractive optics theory, the thickness of an element, for example, a lens can be reduced from several millimeters for bulk elements to several hundred micrometers for diffractive optical elements. However, this size is still too large for some applications. Is it possible to reduce the thickness of the THz lens?

A recently published paper presents a possible approach to reduce the thickness of the THz lens further. For a V shaped metal antenna, the illuminating radiation will resonate with the chargers generated on the surface of metal. By accurately selecting the lengths of two arms and the angle between two arms of the antenna, the amplitude and phase of the resonance wave can be effectively controlled. According to the Huygnes' principle, if the wavefront is modulated on a subwavelength scale, every point can be considered as the second light source and then the desired field can be generated at the predesigned plane. In this work, eight antennas are selected with same resonance amplitude but different phase sampled from 0 to 2π with equal step, one can use these antennas to from arbitrary elements based on the theory of diffractive optics.

The amplitudes and phases of transmitted waveforms of the antennas with different arm lengths and angles have been theoretically calculated using the finite difference time domain method. Eight antennas with same transmitted light amplitude are selected. The phase difference between two adjacent antennas is $\pi/4$. Using the diffractive optics theory, a lens with 4 mm focus length for 0.75 THz is design and the phase distribution is quantized. The corresponding antennas are selected to generate difference phase difference. The samples are fabricated on a 100 nm thick gold film on a silicon wafer substrate with the traditional optical lithography method.

The sample is characterized with a THz focusing plane imaging system. The range of the THz radiation is 0.2–2.6 THz. The sample is located 4 mm away from the detection crystal and under the plane wave illuminating. The waveform at each point on the detection crystal can be achieved via scanning the time delay. After the Fourier transform, the complex amplitude distribution on the focusing plane for 0.75 THz can be obtained. The THz wave has been well focused to a point. The FWHM of the focus point is about 400 μm. The thickness of the lens is only 1/4000 of the illuminating wavelength.

Light Speed Is an Irrational Number

Ganquan Xie[1, 2], **Jianhua Li**[1, 2], **Feng Xie**[1], **and Lee Xie**[1]

[1]Hunan Super Computational Sciences Center, China
[2]GL Geophysical Laboratory, USA

Abstract— A Poem say that "Familiarly reading mathematics and physics, and more talk about the rational and the irrational, the important things wrong popularity, the speed of light is an irrational." The ratio between the rectangle and Circle is a irrational number. The ratio between Time and Light motion is an irrational number. Therefore, the light speed is a irrational number. Recent, light speed in the publication is the 299,792,458 metres per second, that should be corrected. By searching in the www.google.com, we get the URL *Speed of light* — Wikipedia, the free encyclopedia. To open it, we found that the **speed of light** in vacuum, commonly denoted c, is a universal physical constant important in many areas of physics. Its value is 299,792,458 metres per second, a figure that is exact because the length of the metre is defined from this constant and the international standard for time. Why is the light speed 299,792,458 metres per second? It is not from measured, because the length of the metre is defined from this constant and the international standard for time. In this article, we say that the light speed is an irrational number. The traditional "light speed = 299,792,458 m/s" that has to be corrected. The light speed is an irrational number. The "light speed = 299,792,458 m/s" is just the approximation number to close to the light speed irrational number. The copyright and patent and all right are reserved by authors in GL GEOPHYSICAL Laboratory. The GL Geopysical Laboratory agree The abstract to publish in PIERS 2013 in Taipei, Taiwan, China.

Transmission Characteristics of a Plasmonic Open Waveguide Based on Low Frequency Spoof Surface Plasmon Polaritions

Yao-Huang Kao[1], **Jin Jei Wu**[2], **Her-Lih Chiueh**[4], **Tzong-Jer Yang**[3], **Da Jun Hou**[2], **Chien-Jang Wu**[5], **and Linfang Shen**[6]

[1]Department of Communication Engineering, Chung Hua University, Hsinchu 300, Taiwan
[2]Department of Electrical Engineering, Chung Hua University, Hsinchu 300, Taiwan
[3]College of Engineering, Chung Hua University, Hsinchu 300, Taiwan
[4]Department of Electronic Engineering, Lunghwa University of Science and Technology Tayouan 333, Taiwan
[5]Institute of Electro-Optical Science and Technology, National Taiwan Normal University Taipei 116, Taiwan
[6]Institute of Space Science and Technology, Nanchang University, Nanchang, China

Abstract— A kind of plasmonic open waveguide, which is made of periodic subwavelength metallic brick array, is investigated both theoretically and experimentally in this paper. Based on the guiding mechanism of spoof surface plasmon polaritions (spoof SPPs), the transmission properties of this waveguide are controlled by altering the geometric parameters of the brick cell. Numerical results show that periodic metallic brick can greatly improve the confinement property of electromagnetic field while the asymptotic frequency is nearly fixed. Compared with the metallic brick structure, our hollow periodic metallic brick with the same lattice period has wider transmission frequency bandwidth. Experimental results of this open metallic waveguide at microwave frequency verify the high efficiency of wave guiding predicted by the theoretical analysis.

Unidirectional and Wavelength-selective Photonic Sphere-array Nanoantennas

Yang G. Liu[1,2], **Wallace C. H. Choy**[2], **Wei E. I. Sha**[2], **and Weng Cho Chew**[2,3]

[1]Institute of Applied Physics and Computational Mathematics, Fenghao East Road, Beijing, China
[2]Department of Electrical and Electronic Engineering, The University of Hong Kong
Pokfulam Road, Hong Kong, China
[3]Department of Electrical and Computer Engineering, University of Illinois
Urbana-Champaign, Illinois, USA

Abstract— We design a photonic sphere-array nanoantenna (NA) exhibiting both strong directionality and wavelength selectivity. The photonic NA with the silicon material comprises a reflector with a single sphere and a director with a sphere chain. Although the geometric configuration of the photonic NA resembles a plasmonic Yagi-Uda NA, it has different working principles and, most importantly, reduces the inherent metallic loss from plasmonic elements. For any selected optical wavelength, a sharp Fano resonance by the reflector is tunable to overlap spectrally with a wider dipole resonance by the sphere-chain director, leading to a high directionality. In particular, the wavelength selectivity by the narrow and sharp Fano resonance is required to resolve and match the vibrational mode of the target molecule. As an accurate and fast solution to Maxwell's equations, the T-matrix method with a Hertzian dipole source is adopted to analyze and optimize the far-field response of the photonic sphere-array NA. This work provides design principles for directional and selective photonic NAs, which are particularly useful for photon detection and spontaneous emission manipulation.

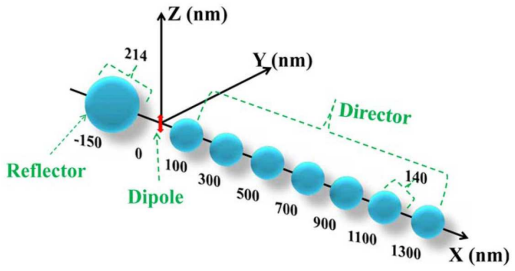

Figure 1: Schematic design for an optimized photonic sphere-array NA at the selected wavelength of 603 nm.

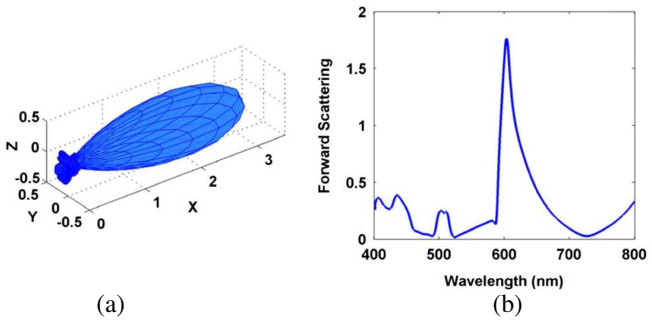

Figure 2: (a) Radiation pattern of the optimized photonic NA at a selected wavelength of 603 nm. (b) Forward scattering intensity (along the x direction) of the photonic NA as a function of the wavelength.

Sensitivity Enhancement of Surface Plasmon Resonance (SPR) Sensor in a Phase-shift Interferometry (PSI) System

Wen-Kai Kuo[1], **Chi-Xian Chen**[1], **and Chien-Jang Wu**[2]

[1]Institute of Electro-Optical and Material Science
National Formosa University, Huwei, Yunlin 63208, Taiwan, R.O.C.
[2]Institute of Electro-Optical Science and Technology
National Taiwan Normal University, Taipei 11677, Taiwan, R.O.C.

Abstract— In this paper, we utilize phase-shift interferometer to measure the phase retardation of a grating-coupled surface plamson resonance (SPR) sensor. The grating structure of the sensor device was fabricated by nano-imprinting technique and a thin meal film was thermally evaporated onto the grating surface. In our experimental system, two liquid-crystal modulators (LCM) were stacked to produce over one wavelength phase shift. A low-cost web-camera with 130 Mega pixels was used to capture the phase shift image. The phase detection sensitivity was enhancement by rotating a polarizer in front of the web-camera. The detection sensitivity of 1.23×10^6 RIU was obtained.

Experimental Verification of the Suppression of Crosstalk between Bended Parallel Microstrips via Designer Surface Plasmon Polaritons

Hung Erh Lin[1], **Tzong-Jer Yang**[1], **Yao-Huang Kao**[2], **Jin-Jei Wu**[3], **Clark Li**[3], **Chien-Jang Wu**[4], **and Xianmin Zhang**[5]

[1]College of Engineering, Chung Hua University, Hsinchu 30012, Taiwan, R.O.C.
[2]Department of Communication Engineering, Chung Hua University, Hsinchu 30012, Taiwan, R.O.C.
[3]Department of Electrical Engineering, Chung Hua University, Hsinchu 30012, Taiwan, R.O.C.
[4]Institute of Electro-Optical Science and Technology, National Taiwan Normal University
Taipei 11677, Taiwan, R.O.C.
[5]Department of Information Science and Electronic Engineering, Zhejiang University
Zhejiang 310027, China

Abstract— In this report, we propose a novel microstrip using the concept of designer surface plasmon polaritons (designer SPPs) to construct the bended parallel microstrips to suppress the crosstalk in between, which is realized by introducing subwavelength periodic corrugations onto the edges of one conventional microstrip. The transmission properties of this microstrip are numerically analyzed. The suppression effect of the coupling between the bended corrugated microstrip and conventional microstrip is also investigated experimentally, especially in time domain signal measurement. The agreement between the numerical and experimental results in this microstrip structure is found well. Such structure can be effectively achieved to suppress the cross talk in the high speed digital signal transmission.

A New Proof on Boundary Conditions in Electromagnetic Theory

Cavour Yeh and Fred Shimabukuro
California Advanced Studies, 2432 Nalin Dr., Los Angeles, CA 90077, USA

Abstract— Although electromagnetic waves have been the subject of intense study by many researchers for many years, there still exist elementary yet fundamental aspects of the theory that have not been carried out. It is well known that, for time varying fields, satisfying the continuity of the tangential electric and magnetic fields across the boundary surface of two different material media automatically implies the continuity of the normal magnetic induction vector and electric displacement vector across that boundary surface. However, the converse is not true. A proof on this statement has not been found in the literature. Here, we shall provide this proof. In addition, it will be shown that unlike the case for the time-varying fields, for the static field case, satisfying the boundary conditions on the tangential electric and/or magnetic fields does not imply the satisfaction of the boundary conditions on the normal electric displacement and/or magnetic induction fields.

Frequency Spectra of Absolute Optical Instruments

Tomáš Tyc[1] and Aaron Danner[2]

[1]Department of Theoretical Physics and Astrophysics, Masaryk University
Kotlářská 2, Brno 61137, Czech Republic
[2]Department of Electrical and Computer Engineering, National University of Singapore
Singapore 117576, Singapore

Abstract— Absolute optical instrument (AI) is a device that provides a stigmatic (sharp) image of all points from some 3D region of space. In other words, an infinite number of light rays emerging from a point A from that region reach a point B — the image of A [1]. The simplest example of an AI is a plane mirror that gives a virtual image of whole half-space. A less trivial but more interesting AI is Maxwell's fish eye [2], discovered by J. C. Maxwell in 1854, where all rays form circles and the whole space is stigmatically imaged. In the recent years, there has been an increased interest in AIs which has led to proposing previously unknown devices of various types, e.g., AIs that perform imaging of the whole space or of optically homogeneous regions [3], or provide magnified images [4]. A general method has also been proposed for designing spherically symmetric AIs [5]. All this research was based on geometrical optics.

Recently AIs attracted attention also from the point of view of wave optics. In particular, it has been demonstrated both theoretically [6] and experimentally [7] that Maxwell's fish eye has the ability to focus light beyond the diffraction limit, the property that had been attributed to negative index materials only [8]. Further experiments have shown that such super-resolution exists also in other absolute instruments [7]; the necessary condition seems to be that all rays emerging from the source A reach the image B.

Another interesting question, apart from focusing, is related to the eigenfrequency spectra of absolute instruments [9]. In particular, many important AIs are devices of a finite volume and therefore their spectrum is discrete. Is there any distinct characteristic in which the spectra of AIs differ from those of non-AIs?

There are at least two ways how to investigate this question. One is based on an analysis of a light pulse propagating in the AI and on the natural assumption that a pulse emitted at a point A during a short time can also be absorbed at its image B during a short time. The second method is based on the WKB approximation and on the general property of AIs that the optical path from the source A to its image is equal for all the rays.

Both of these methods give the same result for the spectra of AIs and show that the answer to the above question is positive. In particular, the spectra of AIs consist of tight groups of levels with almost equidistant spacing between them. This strong degeneracy is necessary for obtaining the correct geometrical-optics limit when the wavelength goes to zero, and it in fact enables the unique focusing properties of AIs. In addition, the WKB method enables us to calculate not just the spacing of the level groups but their offset as well which is related to the Gouy phase. We will also show that the numerically calculated spectra of various AIs confirm our theoretical result very well.

REFERENCES

1. Born, M. and E. Wolf, *Principles of Optics*, Cambridge University Press, Cambridge, 2006.
2. Maxwell, J. C., *Camb. Dublin Math. J.*, Vol. 8, 188, 1854.
3. Mi nano, J. C., *Opt. Express*, Vol. 14, 9627, 2006.
4. Tyc, T., *Phys. Rev. A*, Vol. 84 031801(R), 2011.
5. Tyc, T., L. Herzánová, M. Šarbort, and K. Bering, *New J. Phys.*, Vol. 13, 115004, 2011.
6. Leonhardt, U., *New J. Phys.*, Vol. 11, 093040, 2009.
7. Ma, Y. G., S. Sahebdivan, C. K. Ong, T. Tyc, and U. Leonhardt, *New J. Phys.*, Vol. 14, 025001, 2012.
8. Pendry, J. B., *Phys. Rev. Lett.*, Vol. 85, 3966, 2000.
9. Tyc, T. and A. Danner, *New J. Phys.*, Vol. 14, 085023, 2012.

Session 3A7
Microwave and Millimeter Wave Circuits and Devices, CAD

Variable Gain Low Noise Amplifier Using Mutual Inductor for Input Matching Network
George Chang-Lin Guu, Chien-Chang Huang, ... 478

Design of Ultra Low-power Voltage Controlled Oscillator in 0.18-μm CMOS Technology
Shao-Ping Yu, Chin-Lung Yang, ... 480

Road-vehicle Cooperation for Lateral Guidance
Nabil Houdali, Thierry Ditchi, Emmanuel Geron, Jerome Lucas, Stephane Holé, ... 482

A Compact Wilkinson Power Divider Utilizing Coupled Lines for Unequal Power Division and Equal Port Impedance
Yi Fan Chen, Yi-Hsin Pang, ... 483

A New Lowpass-to-broadband Synthesis Method which Preserves DC Connection
Tao-Yi Lee, Li-Han Chang, Yu-Jiu Wang, ... 484

Design of a Ku-band High Gain Low Noise Amplifier
Muhammad Adil Bashir, M. Mansoor Ahmed, Umair Rafique, Qamar-ud-Din Memon, ... 486

A Novel Ultra-wideband Range Bandstop Filter Using Electromagnetic Bandgap Structure with Triangular Unit Cells
Shao Ying Huang, Yee Hui Lee, ... 487

Wide Band Band-stop Filters with a Rectangle and a Unsymmetrical T-shape DGS
Jin-Ling Zhang, Cui Juan He, Yu-Lei Du, Nan Zhang, Lei Shu, Ying-Hua Lu, ... 489

Contactless Power Transmission Track with Core Array Structure Unit for Mobile Apparatuses
Jiayou Lee, Hung-Yu Shen, Yi-Ying Lee, ... 490

Broadband Characterization of Connector's Degradation Level by Frequency Domain Reflectometry
Florent Loete, Cedric Gilbert, ... 491

Using Contactless RF Power Transfer Technique to Improve the Power Supply Issue of Implanted Neurostimulator
Jiayou Lee, Hung-Yu Shen, Yan-Tian Liu, ... 492

Variable Gain Low Noise Amplifier Using Mutual Inductor for Input Matching Network

George Chang-Lin Guu and Chien-Chang Huang
Department of Communication Engineering, Yuan Ze University
No. 135, Yuan-Tung Rd., Chung-Li, Taoyuan 320, Taiwan

Abstract— This paper presents a 5.8 GHz 0.18 µm CMOS gain-control low noise amplifier (LNA) using mutual coupled stack inductors as input impedance matching for dedicated short-range communication (DSRC) applications. To improve the receiver dynamic range, the designed LNA requires gain control function which is accomplished by the bias current sharing from the amplifier component with the mutual inductors at gate and source terminals to stabilize the amplifier and tune the input impedance but maintain the chip area in $0.57 \times 0.63\,\mathrm{mm}^2$. In addition, the cascode configuration is adapted for its high gain, low noise, low power consumption, and good input/output isolation. The measured results show 10.5 dB in high gain-mode operation and 1.8 dB in low-gain mode operation for the designed LNA to fulfill the requirements of DSRC applications.

Circuit Design and Measurement Results: The circuit schematic is shown in Fig. 1. By adding a transistor M_3 shunting to the common-gate stage M_2 of the cascode structure, a fraction of bias current directly bypasses M_2 to this gain-control transistor which is adjusted by the M_3 gate voltage V_C to determine the gain value. This control mechanism can provide about 9 dB gain-control range for the LNA with an advantage of insignificant affecting the input/output impedance conditions and less circuit complexity. Moreover, there is a gain enhancement feature for the gain control circuit before reaching the gain compression point as performing input power sweep test. Consequently, this bias current sharing method can extend the P1 dB and IIP3 of the LNA, thereby improving the linearity. Another feature of the proposed method is its DC consumed current kept in almost constant for the high-/low-gain mode operations.

Source inductive degeneration technique is adopted for the LNA design to adjust the input impedance of the common-source stage M_1 to 50 Ω. However, two inductors are needed for this kind of operation. To save the chip area, one can replace the two individual inductors by a mutual coupled stack inductor as part of input matching network as designated in L_1 and L_2 for the circuit schematic shown in Fig. 1. The polarity of mutual inductance between two inductors is determined by how the magnetic coupling is constructed. The scattering parameters (S-parameters) of the mutual coupled inductors are simulated by using the commercial electromagnetic software and the coupling coefficient k can be extracted. The final designed k value is chosen as -0.06 to provide the negative feedback effect for better stability.

The designed LNA is fabricated by using TSMC 0.18 µm one-poly-six-metal (1P6M) CMOS technology in chip area of $0.57 \times 0.63\,\mathrm{mm}^2$. The measurement results including S-parameter

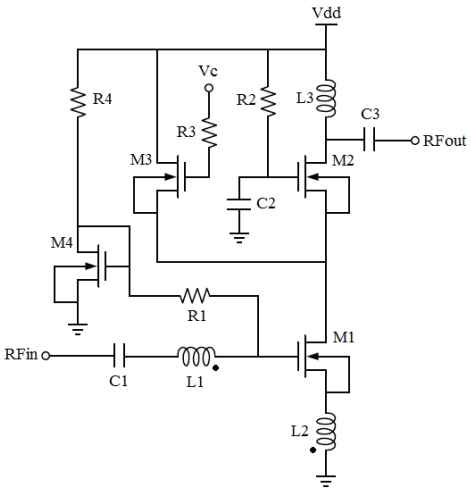

Figure 1: Complete schematic of designed gain-control LNA.

and noise figure (NF) for high-gain mode operation is shown in Fig. 2, with 10.5 dB and 3.6 dB in gain and NF, respectively. For low-gain mode operation, 1.8 dB and 6.7 dB in gain and NF, respectively, are observed as the control voltage is changed from 0.9 V to 1.3 V, and the current is about 3.4 ± 0.1 mA with 1.2 V supplied voltage. The measured P1 dB and IIP3 for high-gain mode operation are -15 dBm and -4 dBm, respectively, and the linearity can be improved for 11 dB in low-gain mode operation. For both of the high-/low-gain mode operations, the input and output return losses are better than 10 dB. The measured results show the applicability of the designed LNA for DSRC applications.

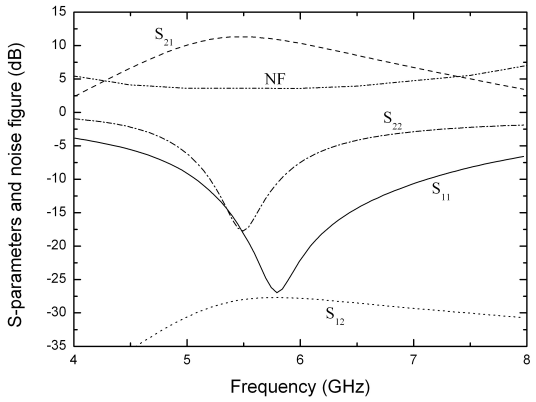

Figure 2: Measured S-parameter and noise figure of gain-control LNA for high-gain mode operation.

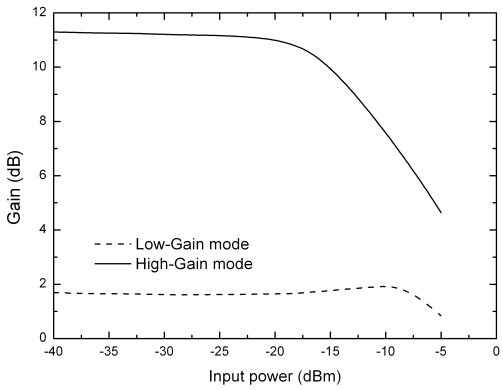

Figure 3: Gain compression point of high- and low-gain mode operations.

Design of Ultra Low-power Voltage Controlled Oscillator in 0.18-μm CMOS Technology

Shao-Ping Yu and Chin-Lung Yang
National Cheng Kung University, Tainan 701, Taiwan

Abstract— A design of low-power voltage controlled oscillator (VCO) is presented and fabricated in TSMC 1P6M CMOS 0.18-μm technology. In 0.18-μm CMOS technology, the performance of 24 GHz VCO is as good as 90 nm CMOS technology, which is much more costly though In [1, 2], VCOs are oscillating in lower frequency and followed by the frequency multiplier to up-convert to the desired frequency. The advantage is its wider tuning range at a cost of the increase of power consumption. This paper presents a 24 GHz VCO in relatively low-cost 0.18-μm CMOS process and realizes excellent performance in its low power consumption. The proposed VCO circuit combines Colpitts with a current-reused topology (Figure 1). The power consumption is reduced by current-reused topology combined with PMOS and NMOS cross pair. Moreover, using differential Colpitts topology achieves an easy start-up oscillation, low power consumption and also improves phase noise. The feature of g_m-boosted Colpitts VCO is enhanced by the differential characteristics. The negative conductance of g_m-boosted Colpitts VCO is amplified by $(2 + C_2/C_1)$ compared with that of a traditional Colpitts VCO. It means that the power consumption can be saved by $(2 + C_2/C_1)$. C_2 and C_1 can be designed to small-sized, and the ratio C_2 to C_1 can be appropriately designed to obtain lower phase noise [3]. Therefore, the initial oscillating condition is improved by g_m-boosted Colpitts VCO; low phase noise and low power consumption can be achieved at the same time. Besides, the gate of M_2 is connected to the supply voltage and M_4 is connected to the ground. This can further increase the negative conductance of VCO to relax the startup oscillation conditions. The principle of a current-reused VCO is applied to succeed in oscillating by PMOS and NMOS pair which produces a negative impedance based on the same biased current, implying to lower the power consumption as well as the operating cycles. Because PMOS and NMOS are opened and closed at same time, the current is only half of a traditional VCO; Our proposed architecture reaches to similar amount of negative conductance by using 50% biasing current. A design of low-power voltage controlled

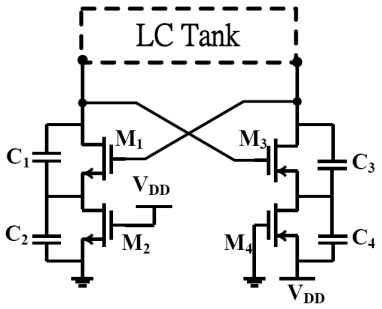

Figure 1: Schematic of 24 GHz VCO.

Table 1: Performance summary of 24 GHz VCO (TT & Temp=27°C).

Specification	Post-Simulation
Tuning range (GHz)	22.74 ∼ 24.63
FTR (%)	7.98
Phase noise (dBc/Hz) @ 1 MHz offset	−102.39
Phase noise (dBc/Hz) @ 10 MHz offset	−123.31
Power consumption (mW)	2.448
FOM (dBc/Hz)	−186.07
FOM_T (dBc/Hz)	−184.11
Chip size (mm^2)	0.34

oscillator in 0.18-μm CMOS technology utilizing Colpitts and current-reused topology achieves extremely low power consumption. The simulation results show that when the supply voltage is 1.8 V, the frequency tuning range is from 22.74 to 24.63 GHz, phase noise is −102.4 dBc/Hz @ 1 MHz, power consumption is merely 2.4 mW. Compared to state-of-art, the power consumption is reduced by 14% ∼ 78%. FOM is −186.1 dBc/Hz (Table 1). The proposed VCO can achieve lowest power consumption so far while remaining other performances outstanding. This work reveals potential low power local oscillators in low cost CMOS process for future applications.

REFERENCES

1. Ozis, D., N. M. Neihart, and D. J. Allstot, "Differential VCO and passive frequency doubler in 0.18 μm CMOS for 24 GHz applications," *2006 IEEE Radio Frequency Integrated Circuits (RFIC) Symposium*, 4 pp, June 11–13, 2006.
2. Tsai, P. K. and T. H. Huang, "Integration of current-reused VCO and frequency tripler for 24-GHz low-power phase-locked loop applications," *IEEE Transactions on Circuits and Systems II: Express Briefs*, Vol. 59, No. 4, 199–203, April 2012.
3. Aparicio, R. and A. Hajimiri, "A noise-shifting differential Colpitts VCO," *IEEE Journal of Solid-State Circuits*, Vol. 37, No. 12, 1728–1736, December 2002.

Road-vehicle Cooperation for Lateral Guidance

N. Houdali, T. Ditchi, E. Géron, J. Lucas, and S. Holé
Laboratoire de Physique et d'Étude des Matériaux, LPEM
ESPCI-ParisTech, CNRS, UPMC Univ Paris 06,
UMR8213, 10 rue Vauquelin, Paris 75005, France

Abstract— Numerous traffic accidents result from a loss of control. Consequently, Advanced Driver Assistance Systems are being studied in order to laterally locate the vehicle on the road in real time for warning as early as possible a forthcoming run-off-road collision. An Advanced Driver Assistance System should work in any environmental conditions (fog, heavy rain, snow, tunnels, . . .), therefore optical sensors, radars or global positioning system (GPS) are not suitable. A cooperation between the vehicle and the road using magnetism is however a promising solution. One existing example consists in magnetic markers buried in the roadway and acting as a lateral position reference, and inboard magnetic sensors used to detect the static magnetic field generated by these markers. However, those systems imply a high building cost for the installation or the withdrawal of the markers. A work around has been successfully tested by using a magnetic strip deposited on the middle of the road, but it may not be allowed because of the potential disturbance the strip could induce to the driver. Unfortunately, putting the magnetic strip under the lateral white strips would generate a magnetic field too weak for being correctly detected.

The approach described in this paper consists in an electromagnetic system in the UHF band including flat passive transponders integrated under the lateral white strips and inboard transmitter/receiver devices interacting with these transponders. Because transponders are passive and integrated under the lateral white strips, the installation cost is drastically reduced and the system can easily be withdrawn or adapted to any situations, for instance in the case of temporary roadwork. Figure 1(a) illustrates the system principle.

Each transponder includes a $\lambda/2$ dipole antenna to receive and re-transmit electromagnetic waves and a resonator to generate a phase transition. The resonator allows inboard system to extract the signal received from the transponder among the background noise resulting from parasitic reflections. An optimized algorithm is applied to the received signal in order to extract precisely a parameter corresponding to the time of flight of electromagnetic waves between the transceiver and the transponder. This parameter is finally processed to find out the distance between the transponders and the inboard devices.

The system described in this paper was characterized in an anechoic chamber, which represents an ideal environment. Reflectors, such as metallic plates, have been added to study the robustness of the detection system. In any cases the efficiency of the lateral position estimation is very good since errors less than ± 2 cm can be observed in a range of 2 m as shown in Figure 1(b). Such a precision should allow very early abnormal driving behaviors to be detected and thus help Advanced Driver Assistance Systems to limit dangerous situations.

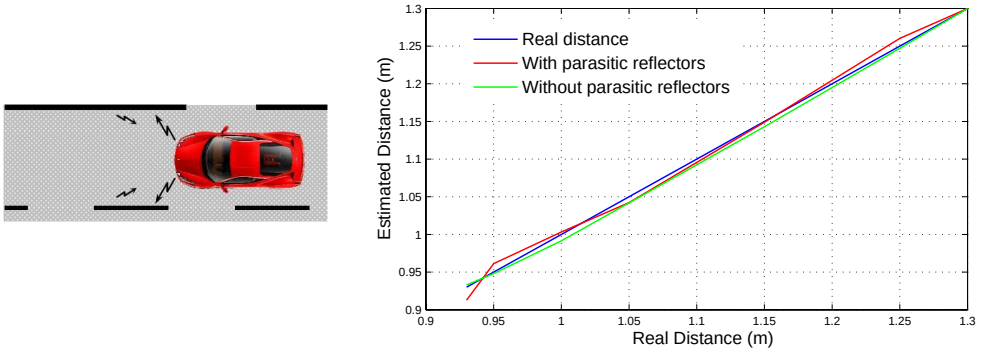

Figure 1: (a) Principle of the cooperative road- vehicle system. Inboard transmit- ter/receiver devices detect flat passive transponders included in the lateral white strips. (b) Lateral position estimation with and without parasitic reflectors.

A Compact Wilkinson Power Divider Utilizing Coupled Lines for Unequal Power Division and Equal Port Impedance

Yi-Fan Chen and Yi-Hsin Pang
Department of Electrical Engineering, National University of Kaohsiung, Taiwan, R.O.C.

Abstract— A Wilkinson power divider of compact size is presented for unequal power distribution. The quarter-wavelength ($\lambda/4$) impedance transformers in a conventional Wilkinson power divider are replaced by coupled lines. In a conventional unequal-split Wilkinson power divider, the port impedances are different so that an additional quarter-wavelength transformer is required for port impedance transformation of each output terminal. Extra area would be occupied. The proposed circuit, as shown in Fig. 1, is designed with only a pair of $\lambda/4$ coupled lines and exhibits the characteristic of equal port impedance. No additional quarter-wavelength transformer is necessary. Size of the proposed power divider is therefore reduced compared with a conventional one. The two coupled lines have different even- and odd-mode characteristic impedances for unequal power splits. In Fig. 1, the even- and odd-mode characteristic impedances of the coupled line between ports 1 and 2 are, respectively, Z_{eA} and Z_{oA}. For the coupled line between ports 1 and 3, they are, respectively, Z_{eB} and Z_{oB}. The electrical length of each coupled line is $\theta = 90°$ at the center frequency. A resistor of normalized resistance r is presented for good isolation between port 2 and port 3. Analytic formulae are also derived. An unequal-split Wilkinson power divider operating at 2 GHz is designed with the power ratio $k^2 = P_3/P_2 = 1.44$. The design parameters are $Z_0 = 50.0\,\Omega$, $Z_{eA} = 229.4\,\Omega$, $Z_{oA} = 73.2\,\Omega$, $Z_{eB} = 170.2\,\Omega$, and $Z_{oB} = 40.0\,\Omega$. Fig. 2 shows the simulation results where Agilent ADS circuit simulator with ideal transmission line model is used. Good impedance matching and isolation are achieved. The simulated data $|S_{31}| = -2.29$ dB and $|S_{21}| = -3.87$ dB at 2 GHz reveal the required unequal power division. The design theory is hence validated.

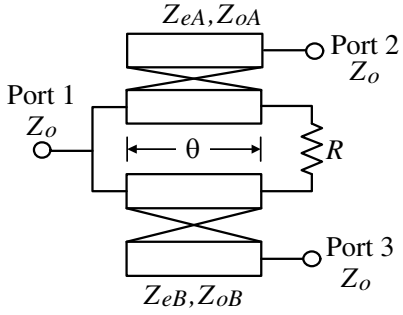

Figure 1: Proposed Wilkinson power divider.

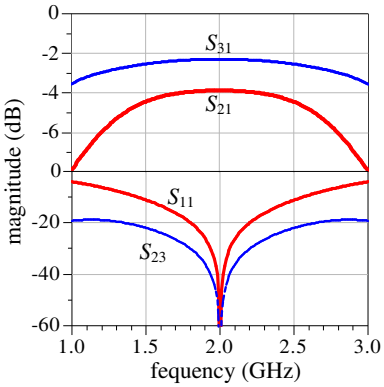

Figure 2: Simulated results with ideal transmission line mode.

A New Lowpass-to-broadband Synthesis Method which Preserves DC Connection

Tao-Yi Lee, **Li-Han Chang**, **and Yu-Jiu Wang**
Institute of Electronics, National Chiao-Tung University, 1001 Ta-Hsueh Road Hsinchu, 30010, Taiwan

Abstract— Standard filter approximation technique with the aid of frequency transformation is a proven way to synthesize passive frequency-selective matching networks. For example, to transform a prototype low-pass filter to its band-pass counterpart, an $s \rightarrow s + s^{-1}$ mapping is almost universally adopted. Nonetheless, there are several disadvantages of using this technique: 1.) The order of the network and the number of passive components are both doubled. 2.) An inductor in the prototype is transformed to a serial LC resonator which blocks DC path. 3.) Realizing the serial LC on a planar process requires critical etching formality along metal edges. 4.) Strong electric fields around the resonant gaps can excite undesired substrate mode.

A new method for synthesizing broadband (ω_L to ω_H), frequency selective, impedance transformation networks from a low-pass prototype transfer function is proposed. Starting from a generalized normalized non-elliptic low-pass transfer function $|S_{21}|^2 \equiv 1/1 + X(\omega^2)$, if this transfer function is even-ordered, an $\omega^2 \rightarrow \frac{(\omega^2-\omega_L^2)}{2\omega_H^2-\omega_L^2}$ substitution of variables converts it into a broadband transfer function, while normalized frequencies (DC, 1) in the prototype is mapped to frequencies (ω_L, ω_H) in the realized domain. Furthermore, if this low-pass prototype is optimum, i.e., equi-ripple, this ω^2-shifted technique preserves its optimality. Closed-form solutions are derived in this case.

In the case of odd-ordered transfer function, there is no simple transformation as ω^2-shifted technique due to a violation of the positive real property of any realizable passive networks. To deal with this problem, $X(\omega^2)$ can be furtherer formulated as $X(\omega^2) = C \times (\omega^2 + z_0^2) \times \Pi_1^M(\omega^2 - z_m^2)^2$. A mini-max optimization is adopted to find the real zeros $(z_1^2, z_2^2, \ldots)$ with prescribed z_0, ω_L and ω_H. Once the optimization is converged, a symbolic ladder permutator/synthesizer implemented in MATLAB will be carried out transfer function synthesis to find all possible ladders and associated component values. The same program is used for synthesizing even-ordered network. Compared with an even-ordered network, an odd-ordered network requires more order to achieve the same ripple, impedance transformation ratio and bandwidth in theory. However, an odd-ordered network offers a favorable advantage by absorbing parasitic shunt capacitances at both ports, which makes it very useful in real applications. In addition, impedance transformation ratio can be traded-off for shunt capacitances by choosing different values of z_0^2.

The proposed method is verified through the designs of an eleventh-order 0.9–4.5 GHz 50-to-250 Ω impedance transformation network and a three-port 0.45–4 GHz Wilkinson power divider, both on 1.6-mm FR-4 PCB.

Comparing with the broadly-adopted lowpass-to-bandpass ($s \rightarrow s + s^{-1}$) frequency transformation technique, this new approach realizes passive networks with reduced orders, while preserving

Table 1: Comparison of the proposed method and other broadband matching techniques from an n-th order prototype. (Note 1): A Norton transformation is usually necessary if a different impedance conversion ratio and port parasitic capacitance are required.

Synthesis Method	This Work	$s \rightarrow s + s^{-1}$ Transformation
Lumped elements	n	$2n$
Feasibility in planer process	Good	Fair
Design Trade-offs	Frequency selectivity, in-band ripples, broadband impedance conversion ratio, port parasitic capacitance	Frequency selectivity, in-band ripples, (Note 1)
Input-to-output DC Impedance	Short	Open

DC characteristics between input and output. This unique property is useful for designing broadband MMICs on a technology without high-quality bypass components.

The full paper will be organized as follows: with an introduction in Part 1, Part 2 will formulate the framework problem theoretically, and identify key network properties. Part 3 describes the details about ω^2-shifting and the numerical approach for odd-ordered counterparts. Parts 4 and 5 will be on the experimental results with a conclusion.

Design of a Ku-band High Gain Low Noise Amplifier

M. A. Bashir[1], **M. M. Ahmed**[2], **U. Rafique**[2], **and Q. D. Memon**[3]

[1]Department of Electrical Engineering, Bahauddin Zakariya University, Multan, Pakistan
[2]Department of Electronic Engineering, Mohammad Ali Jinnah University, Islamabad, Pakistan
[3]Department of Electrical Engineering, University of Faisalabad, Faisalabad, Pakistan

Abstract— A single stage low noise amplifier is developed for Ku-band applications. The design is aimed to provide low noise figure and high associated gain. Submicron gate length GaAs MESFET is used as an active device because of its superior high frequency properties. Device equivalent circuit parameters are first evaluated with and without pad capacitors using measured S-parameters. Low noise amplifier is then designed by employing common source configuration. Additional circuit components are employed to achieve unconditional stability whereas; matching networks of different types are evaluated to achieve $VSWR$ closer to unity. Simulated data showed a bandwidth of 2.3 GHz with minimum noise figure 1.02 dB and 14.1 dB associated gain.

A Novel Ultra-wideband Range Bandstop Filter Using Electromagnetic Bandgap Structure with Triangular Unit Cells

Shao Ying Huang[1, 2] **and Yee Hui Lee**[3]

[1]Massachusetts Institute of Technology, USA
[2]Singapore University of Technology and Design, Singapore
[3]Nanyang Technological University, Singapore

Abstract— Ultra-wideband (UWB) from 3.1 GHz to 10.6 GHz is released by the Federal Communications Commission (FCC) in 2002 for the use of indoor and hand-held systems [1]. Wireless communication utilizing UWB signals has obtained great attention among industry groups, academia, and standardization and regulation bodies. UWB technology has obtained great development with intensive research and development work on UWB components and systems. It has become one of the popular short range wireless systems in indoor wireless communications.

The UWB range bandpass filter becomes indispensable in order to enable the transmission of signals using UWB frequency range. It has been a fast growing research field in the pass ten years or so [2–4]. On the other hand, a UWB range bandstop filter is becoming more and more important nowadays for devices working in non UWB bands.

In this paper, we proposed a UWB range bandstop filter using electromagnetic bandgap (EBG) structure with triangular unit cells. The design is implemented and both simulated and measured data are shown. The design shows a 15 dB bandwidth from 3 GHz to 7.8 GHz and small ripple level of 1.5 dB in the passbands. Tapering technique is applied to the etched patches in the ground plane to improve matching. It is a good alternative to attenuate a wide range of signals in the UWB range.

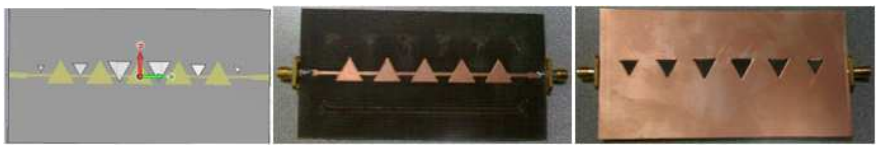

(a) (b) (c)

Figure 1: The proposed bandstop filter (a) schematic, (b) top view of the fabricated structure, (c) bottom view.

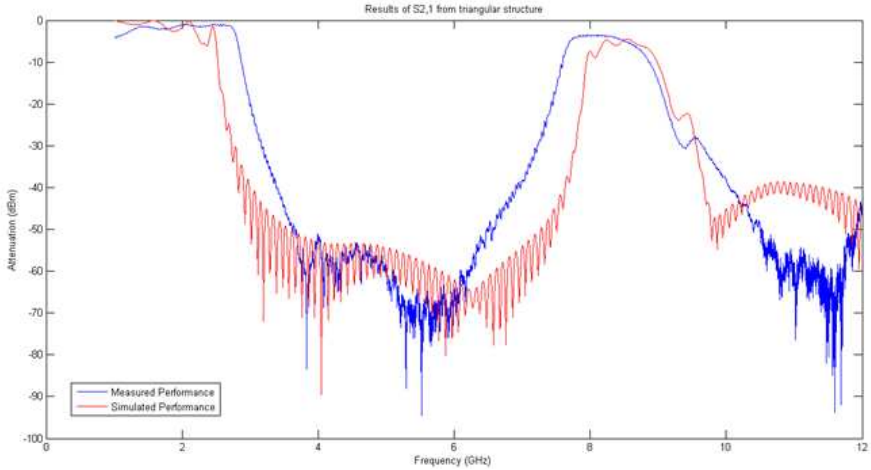

Figure 2: Simulated and measured results.

REFERENCES

1. Commission, F. C., Technical Report, Vol. ET-Docket 98-153, FCC02–48, Apr. 2002.
2. Kuo, J.-T. and E. Shih, *IEE Proc. — Microw. Antennas Propag.*, Vol. 149, No. 5/6, 243–247, Oct./Dec. 2002.
3. Ishida, H. and K. Araki, *IMS*, Jun. 2004.
4. Shaman, H. and J. Hong, *IEEE Microwave and Wireless Components Letters*, Vol. 17, No. 7, 516–518, Jul. 2007.

Wide Band Band-stop Filters with a Rectangle and a Unsymmetrical T-shape DGS

Jin Ling Zhang, Cui Juan He, Yu Lei Du, Nan Zhang, Lei Shu, and Ying Hua Lu
School of Electronic Engineering, Beijing University of Posts and Telecommunications
Beijing 100876, China

Abstract— A kind of miniaturization wide band-stop filter with a rectangle and an unsymmetrical T-shape defected ground structure (DGS) is presented and simulated using the finite-integral time domain modeling method. The filter not only creates two transmission zeroes near the pass band, but also exhibits a wide stop band. The filter centers at 5.54 GHz and 6.10 GHz with insertion loss of −28.99 dB and −42.34 dB is designed and implemented, −10 dB bandwidth is 1.62 GHz. By tuning a different DGS aperture width and space between, the proposed filters exhibit the stepped impedance effect, resulting in ultra-wide stop band. These wide band resonant devices can be used for various applications such as wide band-stop filter to suppress the harmonics in wireless communication system.

A novel wide band band-stop filter with a rectangle and an unsymmetrical T-shape DGS been fabricated. The DGS band stop filters have shown a sharp cutoff frequency response and a wide stop band bandwidth. The above filter experimental data are in good agreement with the simulation results. The DGS configuration can be applied for some compact and wide band microwave communication system.

Contactless Power Transmission Track with Core Array Structure Unit for Mobile Apparatuses

Jia-You Lee, Hung-Yu Shen, and Yi-Ying Lee
Department of Electrical Engineering, National Cheng Kung University, Tainan, Taiwan, R.O.C.

Abstract— The contactless power transmission track with core array structure unit for mobile apparatuses is proposed in this research. Traditionally, this can be hazardous and unreliable to deliver energy to mobile apparatuses by using conventional power cord under certain extreme condition, i.e., environment with dampness, overfilling of explosive gases and so on. The objective of this paper is to investigate the contactless power transmission techniques to enhance the above inconvenience.

Therefore, the core array structure unit is proposed in this paper so as to supply power stably to mobile apparatuses. A uniform magnetic field is established by arranging several cores in a square array with area of $13 \times 15\,\mathrm{cm}^2$. Electromagnetic simulation software, Maxwell is adopted to analyze and design the arrangement of core array structure unit and pick up coil. In addition, the connection of each coil of proposed core array structure unit would be discussed to clarify the distribution and density of its magnetic field. For industrial applications, the operating route of mobile apparatuses can be pre-arranged by burying the core array structure unit in the ground of working area. Finally, driving circuit and control circuit of the proposed contactless power transmission track with core array structure unit are implemented. Experimental results show that the contactless power transmission track system in this research can deliver power 1.4 W stably to mobile apparatus under the condition of air gap 5 mm.

The feasibility and reliability of the concept which is presented in this research is verified by analyzing the magnetic field distribution of core array structure unit and executing the experiment for test system. Fig. 1(a) displays the photo of contactless power transmission track with core array structure unit for mobile apparatuses proposed by this paper, including driving circuit, control circuit, coupled structure and remote circuit. Besides, Fig. 1(b) represents the magnetic field simulation result of core array structure unit, consists of 41 coils arranged like square array with area of $13 \times 15\,\mathrm{cm}^2$.

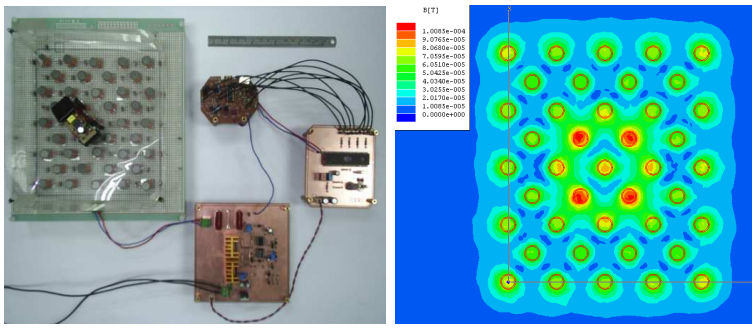

(a) (b)

Figure 1: (a) The photo of contactless power transmission track with core array structure unit for mobile apparatuses and (b) the magnetic field simulation result of core array structure unit.

Broadband Characterization of Connector's Degradation Level by Frequency Domain Reflectometry

F. Loete and C. Gilbert
Laboratoire de Genie Électrique de Paris SUPELEC
11 rue Joliot Curie 91190, Gif sur Yvette, France

Abstract— Because of the increasing size of electrical networks in automotives, the degradation of wires and connectors has become a major concern. As a matter of fact, severe system failures are often merely due to broken wires, bad crimping or degraded connectors. Furthermore, the difficulty to localize those kinds of defects using nowadays techniques generally leads to costly repair.

Reflectometry is a well known method used to monitor the health of lines and wired networks.

Wiring networks can be affected with two types of faults: "soft ones" are created by the change of the impedance along the line due to different kinds of defects (insulation, radial crack, and degradation of connector . . .) in the wire. "Hard faults" correspond to open and short circuits. For the first type of faults, the frequency-domain response of the faulty wiring presents a modification of the impedance, in the defect location.

For that reason, this paper focuses on the application of the reflectometry technique to the broadband characterization of a degraded Cu-Sn connector by fretting. Once the Sn plating is removed, the electrical properties of the contact interface are entirely modified. The results presented in this paper show that observing such kind of transition can be used as criteria for estimating the degradation level of the connector.

Using Contactless RF Power Transfer Technique to Improve the Power Supply Issue of Implanted Neurostimulator

Jia-You Lee, Hung-Yu Shen, and Yan-Tian Liu
Department of Electrical Engineering, National Cheng Kung University, Tainan, Taiwan, R.O.C.

Abstract— In this paper, the contactless RF power transfer technique is investigated to overcome the drawbacks of supplying energy to implanted neurostimulator. The major problem of implanting the medical electronic device in the human body is the way to provide enough energy for this device. Embedding disposable battery is commonly adopted but it still possesses some potential jeopardy, i.e., leakage of battery electrolyte and replacement of battery. The purpose of this research is to solve the above-mentioned issues by applying contactless RF power transfer technique to the implanted neurostimulator.

Owing to decreasing dimension of implanted neurostimulator, the PCB coil is employed as coupled structure and the exciting source operated in radio frequency is chosen. Different shape, trackwidth, and turns of PCB coil are analyzed and discussed in this paper to select the appropriate coil for the implanted neurostimulator. To prevent the tissue from self-heating, the current-regulated mode with delayed pseudomonophasic pulse (DPS) is adopted as the electrical stimulation waveform of the proposed implanted neurostimulator.

Experiments of proposed contactless RF power transfer system for implanted neurostimulator are carried out, including the horizontal displacement test, perpendicular displacement test, and transfer efficiency measurement. According to the experimental results, an efficiency of about 34.5% has been achieved for the proposed implanted neurostimulator under the air gap 10 mm. Even though the air gap between primary and secondary of system is enlarged to 30 mm, the implanted neurostimulator gets enough energy to operate normally.

The concept of using the contactless RF power transfer technique to improve the power supply issue of implanted neurostimulator is achieved by this research. Furthermore, introducing the integrated circuit technology can totally diminish the size of implanted neurostimulator. Fig. 1 shows the photo of proposed contactless RF power transfer system for implanted neurostimulator. Fig. 1(a) represents the primary of proposed system, including oscillator, class E exciting source, gate driver, and PCB coil. Fig. 1(b) demonstrates the secondary of proposed system with area of $35 \times 50\,\text{mm}^2$, including PCB coil, rectifier, voltage regulator, D/A converter, MCU, and neurostimulator.

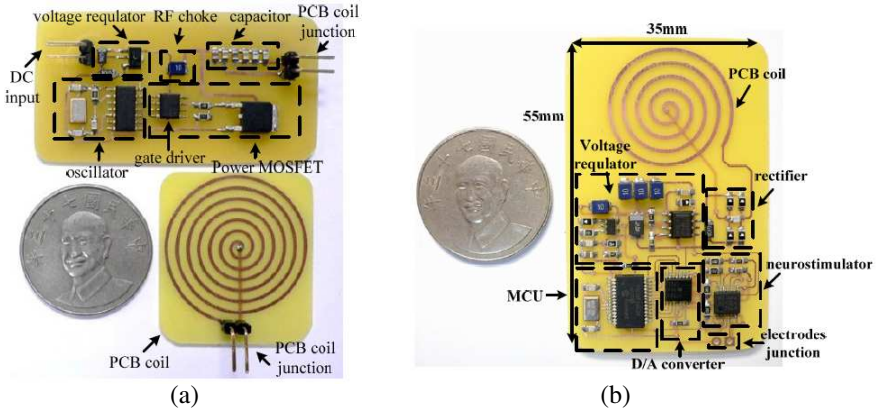

Figure 1: The photo of proposed contactless RF power transfer system for implanted neurostimulator, (a) primary and (b) secondary of proposed system.

Session 3A8
Poster Session 3

Improved Circularly Polarized Bandwidth in Dielectric Resonator Antenna for L-band Satellite Application
Abrahim Heshmati, F. Geran, Ramezan Ali Sadeghzadeh, ... 495

UWB Microstrip Antennas on a Cylindrical Surfaces
Rafal Lech, Wojciech Marynowski, Adam Kusiek, ... 496

The Improvement of Open-ended Waveguides Used As Probes in Near Field Antenna Measurements
Mateusz Mazur, Wlodzimierz Zieniutycz, Lukasz Sorokosz, ... 497

The Probes Dedicated for Multiband or Wideband Antennas Patterns Measurements in Near Field
Mateusz Mazur, Wlodzimierz Zieniutycz, Adam Kusiek, Wojciech Marynowski, ... 498

Real Time Parallel PSO and CFO for Adaptive Beam-forming Applications
Eman Ahmed Fahmy, Korany Ragab Mahmoud, Safwat Helmy Hamad, Zaki Taha Fayed, ... 499

Design of a Novel Dual-band Microstrip Patch Antenna for WLAN/WiMAX Applications Using Complementary Split Ring Resonators and Partially Defected Ground Structure
Debdeep Sarkar, Kushmanda Saurav, Kumar Vaibhav Srivastava, ... 500

A Moment-method Analysis of the Thin-wire Circular-loop Zigzag Antenna
Sulaiman Adeniyi Adekola, Hisham Abubakar Muhammed, Alex Ike Mowete, ... 501

Influence of Probe Positioning Precision in Near Field Antenna Measurement System on Far Field Calculation
Wojciech Marynowski, Adam Kusiek, Mateusz Mazur, ... 502

Design of MIMO Antenna with Enhanced Isolation Elements for USB Dongle Applications
Wen-Shan Chen, Ke-Ming Lin, ... 503

Mutual Coupling Effects on the Linear Microstrip Array Self-impedance
Cheng-Nan Hu, Kai-Hong Jheng, Esther Lee, ... 504

Design of the MIMO Antenna Using Cavity-backed Structure
Se-Hwan Choi, Yemin Hein, Jae-Young Lee, ... 505

A Compact UHF Antenna for Handheld RFID Reader
Wei Che Hung, Hsin-Lung Su, Sung-Lin Chen, Chang-Tsun Lin, ... 506

Dual-band Slot Antenna Using CPW Feed Line and Metasurface
Hailiang Zhu, Sing Wai Cheung, Tung Ip Yuk, ... 507

Loaded Circular Patch Rectangular Slit Ultra-wideband (UWB) Microstrip Antenna
Chao Wang, En Li, Gaofeng Guo, ... 508

Printed Modified Bow-tie Dipole Antenna with Band-notch Structure
Huai-Yu Lin, I-Fong Chen, Ching-Chih Hung, Chia-Mei Peng, ... 509

Printed Dual-polarization Broadband Directional Antenna
Lu-I Yams, Chia-Mei Peng, I-Fong Chen, Kang-Ling Li, ... 510

A Y-shaped Microstrip-line-fed Wide-slot Antenna with Band-controlled for Multiband Applications
Sheng-Jun Wei, Quanyuan Feng, Ding-Hong Jia, ... 511

Wide Band Frequency Control of Circularly Polarized Patch Antenna with Movable Dielectric
Kazuhiro Kitatani, Masahiro Wada, Yasuyuki Okamura, ... 512

Crosstalk Modeling and Analysis of Through-Silicon-Via Connection in 3D Integration
Xiang He, Wensong Wang, Qunsheng Cao, ... 513

FDTD Study on Transmission Characteristics Affected by Air-gap between Noise Suppression Sheet and Strip Conductor
Kyota Otsuka, Tatsuya Suzuki, Sho Suzuki, Kota Kiyomi, Takanobu Ohno, Kouichi Ishii, ... 514

Portable Wireless Power Transmission Demonstration System with Low Power Consuming and Compact Size
Chun-Hao Hsu, Ko-Wen Hsu, Wen-Hua Tu, ... 515

Effect of Electromagnetic Interference (EMI) on the DC Shift of NMOSFET Current-mirror
Muhammad Taher Abuelma'atti, Ali M. T. Abuelmaatti, ... 516

Effect of Electromagnetic Interference (EMI) on the DC Shift of NMOSFET Current Mirror with Capacitor Between Mirror Node and Ground
Muhammad Taher Abuelma'atti, Ali M. T. Abuelmaatti, ... 517
Behavioral Modeling of a 12-bit 500-MS/s Multi-stage ADC
Wen Wei He, Qiao Meng, ... 518
The Impact of USB 3.0 Module on Wireless Communication with Improved Solution for EMI Problem of High Speed Connectors
Han-Nien Lin, Wei-Hua Huang, Wei-Jr Lai, ... 519
Verification Analysis of Electromagnetic Coupling between Display Module and Antenna of Mobile Devices for Wireless Communications
Han-Nien Lin, Allen Laio, Yen-Lin Tseng, Ming-Shan Lin, ... 520
Resonant Capability of Multilayer Spheroidal Nanoparticles as Plasmonic Nanoantennas
Mahdie Khosravi, Ramezan Ali Sadeghzadeh, Mohammad Sadegh Abrishamian, ... 521
Electromagnetic Equations in Curved Octonion Compounding Spaces
Zi-Hua Weng, ... 523
Theoretic Analysis on a Periodic Array of Broadband Plasmonic Nanoantenna
Yuan-Fong Chau, Wayne Yang, Shinn-Fwu Wang, Yi Chu, ... 524
Analysis of the Bonding and Anti-bonding Modes on Periodic Array of Nanometals
Yuan-Fong Chau, Wayne Yang, Ci-Yao Jheng, San-Cai Jheng, Shinn-Fwu Wang, Yi Chu, ... 525
Design of Three-coupled Finline Bandpass Filter Using Full Wave Analysis
V. Madhusudana Rao, B. Prabhakara Rao, ... 526
Reconstruction of Electromagnetic Scatterers with Different Boundary Conditions
Rencheng Song, Xiuzhu Ye, Xudong Chen, ... 527
Compressive-sensing-based Phaseless Imaging
Li Pan, Rencheng Song, Swee Ping Yeo, Xudong Chen, ... 528
Perturbation Influence Analysis on the RCS of Dynamic Targets
Jia Liu, Min Su, Ning Fang, Bao Fa Wang, ... 529
Electromagnetic Interference on Metal Sandwiched Quartz Crystal
Kuei-Jie Tseng, Wen-Teng Chang, ... 530
Efficient Characterization of Fabry-Perot Resonator Antennas
Yuehe Ge, Wang Can, ... 531
Transparent Antenna Design for Wireless Access Point Application
A. S. Azini, Muhammad Ramlee Bin Kamarudin, Tharek Bin Abdul Rahman, Sharul Kamal Bin Abdul Rahim, Mohd Subri Bin Abdul Rani, ... 532
Design of a Programmable Low-pass Filter for UHF RFID ZIF Receivers
Changchun Zhang, Chao Wang, Yufeng Guo, Yuming Fang, Leilei Liu, Deyuan Chen, Wei Li, ... 533
Experimental Evaluation of Cytotoxicity Effects in Cancer and Normal Cells Exposed to Far Infrared Radiation
Pantea Peidaee, Taghrid Istivan, Ravi Shukla, Elena Pirogova, ... 534
The Effect of Pulse Parameters and Medium Information on the Temporal Coherence Length of a Partially Coherent Pulse on Scattering
Chaoliang Ding, Liuzhan Pan, ... 535
Investigating Embedded Planar Electromagnetic Band Gap (EPEBG) Structure for Noise Suppression in PCBs
Yao-Te Shu, Jiun-Hwa Lin, ... 536
High Isolation Pencil Beams Antenna Array for IEEE802.11a MIMO Application
Dau-Chyrh Chang, Chia-Ping Huang, Fong-Yi Lin, Chih-Hung Lee, Ming-Ching Yen, Yau-Jyun Tsai, 538

Improved Circularly Polarized Bandwidth in Dielectric Resonator Antenna for L-band Satellite Application

A. Heshmati[1], **F. Geran**[1], **and R. A. Sadeghzadeh**[2]

[1]Faculty of Engineering Research and Science, Islamic Azad University, Iran
[2]Faculty of Electrical and Computer Engineering, Khajeh Nasir Toosi University of Technology, Iran

Abstract— In this paper, a new configuration for circularly polarized dielectric resonator antenna (DRA) is presented. The idea is to use two different dielectric materials and parasitic patches to obtain bandwidth improvement of the axial ratio and return loss properties. In the operating frequency range of this antenna, return loss is less than −10 dB in which the axial ratio is less than −3 dB around the main direction of the antenna. In this paper, a dielectric resonator antenna is used for the GPS and to satellite communications (Inmarsat) with strip line feed [1]. For increasing return loss frequency bandwidth used two different dielectric materials [2]. However, the interest of circular polarized DRA has increased recently. In this paper, to improve circular polarization parasitic patches were used [3]. The proposed DRA can take the advantages of circular polarized, broadband return loss and axial ratio.

Simulation and Figures: The proposed antenna is simulated with CST MWS. The results confirm the capability of our idea to use the proposed configuration in achieving broadband, circular polarization and almost fix gain of antenna. Fig. 1 shows return loss of proposed antenna. As seen in Fig. 2, a significant axial ratio bandwidth enhancement achieved. Fig. 3 shows the gain of proposed antenna.

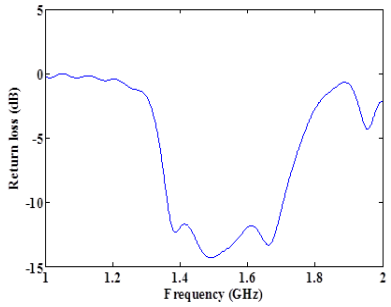

Figure 1: Return loss.

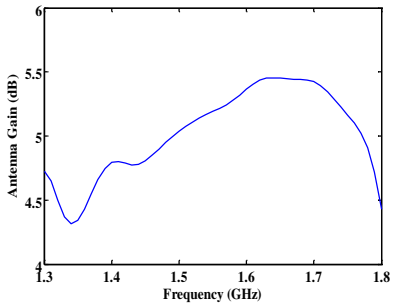

Figure 2: Axial ratio.

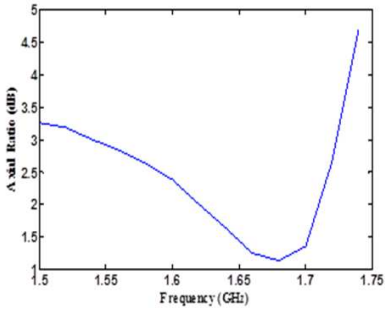

Figure 3: Gain (theta and phi is zero).

REFERENCES

1. Jeon, S., H. Choi, H. Kim, J. Yeom, and H. Kim, "Design of GPS antenna using dielectric resonator," *The 23rd International Technical Conference Circuit/Systems, Computer and Communication*, 2008.
2. Li, B. and K. W. Leung, "Strip-fed rectangular dielectric resonator antenna with/without a parasitic patch," *IEEE Transaction on Antenna and Propagation*, Vol. 53, No. 7, July 2005.
3. Ge, Y. and K. P. Esselle, "A UWB probe-fed dielectric resonator antenna," Department of Physics and Engineering, Macquarie University, Sydney, NSW 2109, Australia.

UWB Microstrip Antennas on a Cylindrical Surfaces

R. Lech, W. Marynowski, and A. Kusiek
Gdansk University of Technology, Poland

Abstract— Conformal antennas are becoming popular due to their many advantages and possibilities of applications they offer. The advantages of using antennas with a curved surface arise not only from the possibility of integrating them with the object on which they are mounted on but also from the increase, relatively to planar antennas, of their visible angular range. The circular antenna arrays, or arrays of radiators located on the surface of a cylinder may be the examples of such antenna that provide omni-directional radiation patterns in azimuth plane or provide, in this plane, the possibility of beam control. Such antennas can be used, e.g., in base stations for mobile communications systems. In the analysis of conformal antennas one encounters the electromagnetic problem which consists in finding the electromagnetic field resulting from radiation sources placed on curved surfaces. It is a boundary problem, where the fields in the area outside antenna surface and the fields or current distribution on the radiating elements have to be matched. Determination of radiation characteristics is reduced to finding the electromagnetic field in the antenna far zone. For this case, the simplified relations are often used. Determination of the mutual-couplings between the radiators requires finding the fields in the antenna near zone and is therefore more difficult issue, because no simplifications can be utilized. The inclusion of mutual-coupling effect is of great importance in pattern synthesis problems [1, 2], where if the mutual-coupling is neglected, poor results are obtained especially in the shaped beam region.

The microstrip Ultra Wideband (UWB) antennas are very attractive to short pulse technology and have been proposed for wireless communication systems to transmit coded signals. Their compact and simple structures with small dimensions and light weight are suitable for easy integration with system components of phased and active antenna arrays [3, 4].

The analysis of UWB microstrip antennas mounted on a circular cylinder is being conducted in the paper. The influence of curvature of the antennas on their reflection coefficients and radiation patterns is investigated and the comparison between planar and conformal radiators is made. A commercial softwares are used to design the UWB radiators and investigate the influence of the curvature.

ACKNOWLEDGMENT

This work was supported from sources of National Science Center under grant decision No. DEC-2011/01/D/ST7/06639.

REFERENCES

1. Josefsson, L. and P. Persson, "Conformal array synthesis including mutual-coupling," *Electroinic Letters*, Vol. 35, No. 8, 625–627, April 1999.
2. Xu, Z., H. Li, Q.-Z. Liu, and J.-Y. Li, "Pattern synthesis of conformal antenna array by the hybrid genetic algorithm," *Progress In Electromagnetics Research*, Vol. 79, 75–90, 2008.
3. Chen, M. and J. Wang, "Compact CPW-fed circular slot antenna for ultra-wideband applications," *8th International Symposium Antennas, Propagation and EM Theory*, 7881, November 25, 2008.
4. Marynowski, W. and J. Mazur, "Design of UWB coplanar antenna with reduced ground plane," *Journal of Electromagnetic Waves and Applications*, Vol. 23, No. 13, 1707–1713, 2009.

The Improvement of Open-ended Waveguides Used As Probes in Near Field Antenna Measurements

Mateusz Mazur, Włodzimierz Zieniutycz, and Łukasz Sorokosz
Gdansk University of Technology, Poland

Abstract— The purpose of work was to develop the family of relatively cheap electric field probes that may be successfully utilized in near field antenna measurements. The open ended waveguides were chosen and investigated. Such probes are achievable in the market, but their dimensions are usually related to waveguide standards. These investigations allow to design probes directly dedicated to certain antenna measurements with reduced aperture comparing to standard probes or ability to make dual polarization measurements simultaneously.

The accuracy of antenna pattern obtained from near field measurements depends on many factors. Among them are environmental parameters (jamming, reflections), precision in positioning probe vs. AUT, sensitivity of measurement equipment. The impact of probe on antenna measurements in near field may be significant. The known radiation pattern of probe allows to take it into account in far field pattern building and correction. The probe should enable to minimize losses in measured signal and be characterized by relatively low VSWR and losses. On the other hand the probe should have minimal impact on AUT pattern.

A probe working in C band based on square profile is described below as an representative example. It consists of square flange aluminum profile, shorted on one side and open on other. With optimized feeding element fabricated from SMA flange connector with long inner pin cut at chosen experimentally appropriate length and placed at distance about $\lambda/4$ at $f = 5.6\,\mathrm{GHz}$ from shorted end of profile. Obtained VSWR was below 1.3 in band from 5 GHz up to 6 GHz. The measurements of probe in anechoic chamber show that a high level of radiation was observed in back directions. According to a low gain of open-end waveguide, the level of Front to Back radiation (F/B) is not expected to be significant, nevertheless F/B ratio about 7–10 dB was not satisfied. The reason of high emission in back direction is caused by diffraction effect on edges of open waveguide. The second considered reason is backward leakage of em wave from shorted end of waveguide. To investigate and reduce these effects the 10 mm loss foam LS22 (Eccosorb) was utilized in two ways. In first method all the probe was covered outside with foam. It allowed to improve F/B ratio to more than 15 dB. In the second case only the aperture was coated outside with foam. Obtained F/B ratio was more than 13 dB in C band. The absorbing foam shouldn't cause mechanical or environmental problems and may cover all the probe for better performance.

Application of the square profile gave us ability to construct dually polarized probe with two orthogonal linear polarizations. The advantage of such construction is ability to measure diagonal patterns of antenna simultaneously, or if equipment is not sufficient for such measurements the cable should be rearranged only. The change of polarization doesn't cause the necessity to change the mechanical orientation of probe causing additional random errors in near field measurements. The LS22 material was also used to coat two polarization probes having standard isolation about 30 dB in C band. The 2–3 dB improvement of isolation between two orthogonal polarizations in C band was observed so it is farther advantage of absorbing material application

Conclusions: The basic calculations and experimental trials allowed to achieve low level of VSWR in probes. Futher improvement of probes was achieved by utilizing an absorbing material to coat waveguide probe. It allowed to:

- improve F/B ratio in probe radiation characteristics;
- improve cross polarization in dually polarized probe.
- reduce interaction between AUT and measurement system.

All these aspects have positive impact on near field antenna pattern measurements. Described here effects refer to other designed open ended waveguide probes, but absorbing material must be chosen adequately to frequency band.

ACKNOWLEDGMENT

This work was supported by the Polish Ministry of Science and Higher Education and carried out within the framework of The National Center for Research and Development under agreement LIDER/21/94/L-2/10/NCBiR/2011.

The Probes Dedicated for Multiband or Wideband Antennas Patterns Measurements in Near Field

Mateusz Mazur, Włodzimierz Zieniutycz, Adam Kusiek, and Wojciech Marynowski
Gdansk University of Technology, Poland

Abstract— The novel antenna systems may integrate in one aperture different antennas working in different frequency band. Such expanded multifrequency or wideband systems require multifrequency probes for single measurement or repeated scans with narrow band probes. The aim of the investigations described in that paper was to develop wideband or multiband probes dedicated to such antennas near field measurements. As single near field measurement may be time consuming procedure, the utilization of wideband probes gives noticeable benefits.

The test probe should allow good transfer of signal from/to Antenna Under Test (AUT) and minimize impact on AUT radiation pattern. Standard, high efficiency, for example waveguid probe size is strongly correlated to the wavelength. To illustrate it, assume that antenna works at two frequencies f_0 and $4\times f_0$ (L and C bands). The probe should work also at these frequencies. Standard probes for L band have $4\times$ longer linear dimension comparing to the second frequency. So high impact of such probe on measurements in C band may be expected. According to dimensions and limited frequency band for single mode the waveguide probes are not acceptable for single scan.

The investigations for proper element that may work as wideband probe led us to modify and improve Vivaldi and dipole antennas to obtain multiband or wideband performance with limited back scattering. All the antennas are fed with TEM or quasi-TEM mode so no cutoff frequency is defined. The antennas should be small, have regular radiation pattern, high front to back ratio (F/B) and good transmission parameters (low losses and VSWR) also polarization clarity and mechanical durability are important. The proposed Vivaldi antennas fed from microstrip line via slot gave quite good electrical characteristics with the exception of F/B ratio. Modified dipoles fed with parallel line allow for multi-frequency work as well, but F/B ratio was low again. There are two ways to reduce that problem. The first method is to put the metal screen functioning as reflector behind antennas or second: implementing loss material. In first case F/B ratio is raised significantly over 15 dB, but shift of frequencies in presence of reflector is observed especially for dipoles. The application of lossy material causes additional losses for tested probe (about 1–2 dB), small changes of of VSWR and improvement of F/B ratio to 10–15 dB. Comparing TEM probes based on microwave laminate to waveguide ones the degradation of electrical parameters is observed, antenna patterns are waved and losses are higher also mechanically it is more difficult to integrate them in measurement equipment ensuring high stability. It is also difficult to introduce correction procedures related to probe impact on near field measurements. However TEM probes give ability to make multiple scan of antenna by once and reduce measurement time.

Conclusions: Proposed wideband and multiband probes based on microwave laminate have limited electrical performance, nevertheless they may be used in near field measurement of wideband and multiband antenna systems. Higher measurement errors may be achieved comparing to waveguide probes, but as proposed probes are wideband the measurements of multiband antenna will not require multiple scans with different probes.

ACKNOWLEDGMENT

This work was supported by the Polish Ministry of Science and Higher Education and carried out within the framework of The National Center for Research and Development under agreement LIDER/21/94/L-2/10/NCBiR/2011.

Real Time Parallel PSO and CFO for Adaptive Beam-forming Applications

Eman Ahmed[1], **K. R. Mahmoud**[2], **Safwat Hamad**[1], **and Z. T. Fayed**[1]

[1]Faculty of Computer and Information Sciences
Ain Shams University, Abbassia, Cairo 11566, Egypt
[2]Faculty of Engineering, Helwan University, Cairo, Egypt

Abstract— The scientific community is still interested in heuristic techniques and optimization algorithms that could be applied in complex problems such as the antenna adaptive beam forming problem. In this paper, we present an empirical study of placing nulls in the antenna patterns to suppress interference and maximizing their gain in the direction of desired signal using Central Force Optimization (CFO) algorithm and compared the results with those obtained using Particle Swarm Optimization (PSO) algorithm. In this work, the complex excitations, amplitudes and phases of the adaptive antenna array elements are calculated for a given 24-antenna elements in a uniform circular array (UCA). The algorithms were implemented using Compute Unified Device Architecture (CUDA) then applied on a graphics processing unit (GPU). Extensive experimentations were applied to compare their performance through a number of case studies. PSO showed to have a good performance, low computational complexity, and gives good results. On the other hand, CFO has a higher computational complexity but it gives better results. The experimentations showed that the resulting beam-pattern optimized by the PSO and CFO required a large processing time which is not acceptable for an on line applications. Hence, the demand for a parallel solution that accelerates these computations is considered. Therefore, a parallel version of PSO and CFO is proposed and implemented using (CUDA) then applied on a (GPU). The comparison is presented to show how the parallel version of the PSO and CFO outperforms the sequential one, thus an online procedure is available for time-critical applications of the antenna adaptive beam-forming.

Design of a Novel Dual-band Microstrip Patch Antenna for WLAN/WiMAX Applications Using Complementary Split Ring Resonators and Partially Defected Ground Structure

Debdeep Sarkar, Kushmanda Saurav, and Kumar Vaibhav Srivastava
Department of Electrical Engineering, Indian Institute of Technology, Kanpur, India

Abstract— Designing compact multi-band antennas for state-of-art wireless communication systems like portable Wi-Fi enabled laptops and smart-phones is one of the challenging problems for microwave engineers. Microstrip patch antennas are attractive candidates for this purpose due to their low-profile and compatibility with planar monolithic microwave integrated circuit (MMIC) components, but they suffer from disadvantages like narrow bandwidth, poor scan performance etc. [1]. Since the practical realization of artificially engineered metamaterials in the beginning of 21st century [2], researchers have focused on using metamaterial paradigm in performance-enhancement as well as miniaturization of antennas. Use of various shaped slots and meta-resonators (like normal and complementary split ring resonators, SRR and CSRR) as well as meta-surfaces like AMC (Artifical Magnetic Surfaces), EBG (Electromagnetic Band-gap) structures have recently caught the attention of metamaterial-inspired antenna designers [3]. This paper proposes a novel low-profile (single-layer) CSRR-loaded microstrip patch antenna placed on a partially defected ground structure (PDGS). The proposed compact dual-band antenna simultaneously satisfies WLAN (Wireless Local Area Network) and WiMAX (Worldwide Interoperability for Microwave Access) application requirements, providing a significantly wide (20.6%) impedance bandwidth ($S_{11} < -10\,\text{dB}$) in the WLAN and upper WiMAX frequency regions. The gain and efficiency of the antenna are also satisfactory in the frequency bands of operation.

One coax-fed microstrip patch antenna operating at its fundamental resonance frequency of 5.24 GHz is chosen as the reference design. The reference rectangular patch antenna is placed on FR4-epoxy substrate ($\varepsilon_r = 4.4$, $\tan\delta = 0.02$) having thickness 1.6 mm. In the proposed antenna, crossed-stripline gaps are etched on one side of the ground-plane creating a partially defected ground structure (PDGS). Furthermore, two CSRRs are etched near the radiating edge of the patch which is over the normal ground-pane. The proposed antenna is of the same physical size as compared to the reference antenna. The characteristics of this modified antenna system along with that of the original patch antenna are obtained from simulations in FEM based electromagnetic solver HFSS. It is observed that the CSRRs etched on the patch generates resonances at 3.45 GHz ($S_{11} = -20.85\,\text{dB}$) and 3.70 GHz ($S_{11} = -18.17\,\text{dB}$) which are well within the middle WiMAX band (3.2–3.8 GHz). Also due to the PDGS, the proposed antenna achieves wide impedance bandwidth (4.81–5.90 GHz) around resonant frequency of 5.29 GHz ($S_{11} = -45.75\,\text{dB}$) which covers the entire WLAN band (5.15–5.85 GHz) as well as the upper WiMAX band (5.2–5.8 GHz). The simulated peak-gains of the antenna are 2.051 dBi, 1.286 dBi and 4.475 dBi at frequencies 3.45 GHz, 3.70 GHz and 5.29 GHz respectively. This proposed compact dual-band metamaterial-inspired microstrip patch antenna can be used in wireless communication systems where embedded antennas covering both WiMAX and WLAN bands are required.

REFERENCES

1. Balanis, C. A., *Antenna Theory: Analysis and Design*, 2nd Edition, John Wiley and Sons Inc., Wiley Reprint, New Delhi, India, 2007.
2. Smith, D. R., W. J. Padilla, D. C. Vier, S. C. Nemat-Nasser, and S. Schultz, "A composite medium with simultaneously negative permeability and permittivity," *Physical Review Letters*, Vol. 84, No. 18, 4184–4187, 2000.
3. Dong, Y., H. Toyao, and T. Itoh, "Design and characterization of miniaturized patch antennas loaded with complementary split-ring resonators," *IEEE Transactions on Antennas Propagation*, Vol. 60, No. 2, 772–785, 2012.

A Moment-method Analysis of the Thin-wire Circular-loop Zigzag Antenna

S. A. Adekola[1, 2], **H. A. Muhammed**[1], **and A. Ike Mowete**[1]

[1]Department of Electrical and Electronics Engineering, Faculty of Engineering
University of Lagos, Lagos, Nigeria
[2]Department of Electrical and Electronics Engineering, Niger Delta University
Wilberforce Island, Yenegoa, Nigeria

Abstract— Using closed-form expressions developed in an earlier presentation [1], this paper describes a moment-method analysis of the thin-wire circular-loop zigzag antenna. Analytical expressions obtained in [1], (where a uniform current distribution was assumed) for the vector magnetic potential, are evaluated using the better approximation of a distribution of current provided by the moment-method treatment.

Computational results subsequently obtained for current distribution, far-zone (radiation) field, and input impedance characteristics for this antenna are compared with those for a regular circular loop antenna as well as the zigzag antenna, in which current is uniformly distributed.

And from the comparisons, we find that whereas the antenna types share quite a few characteristics, they differ sharply in others; for example, in input reactance, for which our results suggest, the zigzag geometry introduces a significant level of capacitive reactance.

REFERENCES

1. Adekola, S. A., A. I. Mowete, and H. A. Muhammed, "Analysis of a circular-loop Zigzag thin-wire antenna," *PIERS Proceedings*, 1648–1654, Kuala Lumpur, Malaysia, March 27–30, 2012.

Influence of Probe Positioning Precision in Near Field Antenna Measurement System on Far Field Calculation

W. Marynowski, A. Kusiek, and M. Mazur
Gdansk University of Technology, Poland

Abstract— The determination of antenna far field characteristics based on near field measurements has become popular in recent years [1, 2]. This approach allows to avoid the main limitation of an anechoic chamber measurement which is the electric size of the antenna determining the Fraunhofer distance. Moreover, the knowledge of the fields in the near zone allows to determine the radiation of the antenna in all directions while in the anechoic chamber measurements the radiation patterns only in two orthogonal cross section are known.

In the radiation pattern determination using near field measurement very complex systems are required. Such systems are composed of two main parts: The mechanical one which allows to make the field measurement in two planes in front of the antenna and the software one used for the calculation of the far field characteristic based on measured data. The errors related with the mechanical positioning precision of the probe during measurement process have the crucial influence on the correctness of the final far zone characteristics. These are the one of the most important sources of the errors in such systems and their influence depend on the type of measurement and used algorithm for far zone characteristic calculation.

In our system, we use the amplitudes of radiated field measured in two rectangular planes in front of antenna. Next, the own hybrid phase retrieval algorithm is applied to derive the whole information about the field in near zone [3]. The algorithm is based on a combination of the iterative method [4] and the global minimum optimization techniques, e.g., Simulated Annealing or Particle Swarm Optimization [5]. Finally the amplitud and phase of the field in near zone are used to determine the whole far field characteristic of the antenna under test. The presented algorithm offers a significantly higher accuracy than the iterative process and requires less time than optimization technique with random initial point.

In this paper the influence of probe positioning precision in near field antenna measurement system on far field calculation is investigated. Using the near fields obtained from commercial software the random errors of the probe positions with specified maximum value are introduced. The random positioning errors were considered for each point of the measured field separately and as a displacement of the whole plane of the measurement. In the tests the errors of the positioning in three planes are considered, i.e., in plane of measurement (x, y) and in the propagation direction (z). The performed analysis allows to determine the maximum value of the probe positioning errors in all directions which ensures the acceptable correctness of the far field characteristics. Such information derives the minimal precision of the probe positioning in complex mechanical system required for proper characteristics determination.

ACKNOWLEDGMENT

This work was supported by the Polish Ministry of Science and Higher Education and carried out within the framework of The National Center for Research and Development under agreement LIDER/21/94/L-2/10/NCBiR/2011.

REFERENCES

1. Isernia, T., G. Leone, and R. Pierri, "Radiation pattern evaluation from near-field intensities on planes," *IEEE Trans. on AP*, Vol. 44, No. 5, 701, May 1996.
2. Yaccarino, R. G. and Y. Rahmat-Samii, "Phaseless bi-polar planar near-field measurements and diagnostics of array antennas," *IEEE Trans. on AP*, Vol. 47, No. 3, 574–583, March 1999.
3. Kusiek, A., W. Marynowski, and M. Mazur, "Phase retrieval algorithm combining iterative and optimization technique for near field antenna measurements," *Progress In Electromagnetics Research Symposium Abstracts*, 318, Moscow, Russia, August 19–23, 2012.
4. Anderson, A. P. and S. Sali, "New possibilities for phaseless microwave diagnostics. Part1: Error reduction techniques," *IEE Proc. of Microwaves, Antennas and Propag.*, Vol. 132, No. 5, 291–298, 1985.
5. Robinson, J. and Y. Rahmat-Samii, "Particle swarm optimization in electromagnetics," *IEEE Trans. on AP*, Vol. 52, No. 2, 397–407, February 2004.

Design of MIMO Antenna with Enhanced Isolation Elements for USB Dongle Applications

Wen-Shan Chen and Ke-Ming Lin
Southern Taiwan University of Science and Technology, Taiwan, R.O.C.

Abstract— To obtain higher data throughput and longer propagation range, Multiple-input and multiple-output (MIMO) technology is proposed and used in wireless communication systems. Other important features in wireless devices are small and compact, which are important for the devices to be portable to attract consumers. In the article, two PIFA antennas fabricated on both ends of an FR4 substrate are introduced for MIMO application. The isolation mechanism is accomplished through T-shaped stubs, which is extended from the ground plane and located between the PIFAs. The two identical PIFAs excite resonant bands (S_{11} and S_{22}) both at 2.45 GHz for WLAN application; however, the operating band cannot cover the entire range of the WLAN 2.4 GHz. To increase the operating bandwidth of the proposed antenna the T-shaped stubs are designed to excite another resonant mode at 2.45 GHz. The resonances of the PIFAs and T-shaped stubs gather to meet the WLAN 2.4 GHz application band The T-shaped stubs also block the mutual coupling between the two PIFAs, which decrease the radiating emission between the PIFAs and the conducting emission through the ground plane. The overall dimensions (20 mm × 45 mm) of the proposed MIMO antenna including an antenna portion (10 mm × 20 mm) and a system ground (20 mm × 35 mm) are suitable for applying in a dongle device. The experimental results of radiation patterns, diversity gain, ECC (envelope correlation coefficient) and radiation efficiency of the proposed design will be presented in the conference.

ACKNOWLEDGMENT

This work was supported by the National Science Council of Taiwan under grant numbers of NSC 101-2632-E-218-001-MY3 and NSC 101-2221-E-218-032.

Mutual Coupling Effects on the Linear Microstrip Array Self-impedance

Cheng-Nan Hu, Kai-Hong Jheng, and Esther Lee
Oriental Institute of Technology, Taiwan, R.O.C.

Abstract— The multi-input multi-output (MIMO) system, employing multi-antenna signal processing at both ends of a wireless link, has shown promising performance in delivering high spectral efficiency with reasonable constellation. In most of previous MIMO antenna performance analyses, mutual coupling between the antenna elements was ignored by assuming the antenna elements to be isolated from each other and the self-impedance of antenna was identical by viewing the antenna elements to be the same as that of a single antenna. In practical elements of an antenna array have mutual coupling, which in turn affect the gain, self-impedance, and beamwidth, etc., of the array. Mutual coupling becomes particularly significant as the inter-element spacing is decrease. This study numerically and experimentally investigates the mutual coupling effects on the self-impedance of a five-element microstrip antenna array. Experimental validation shows the effectiveness of the numerical method using *GEMS EM Simulator* for the further analysis on the communication system performance.

Design of the MIMO Antenna Using Cavity-backed Structure

Sehwan Choi, Yemin Hein, and Jaeyoung Lee
Korea Electronics Technology Institute, Republic of Korea

Abstract— Nowadays, multiple input multiple output (MIMO) antenna is widely used to increase the data rate after LTE service starts. The rayleigh fading effect in mobile communication environment can be reduced by that MIMO antenna providing the space diversity. Space diversity technique can get rid of fading dips that can be occurred while mobile handsets are moving. In order to develop effective MIMO antenna, single antenna must have higher mean effective gain (MEG) and multiple antenna must meet the requirements such as isolation, correlation and diversity gain. But it is difficult that antennas satisfy these specifications because recent wireless communication systems requires small-size and multi-mode.

In this paper, MIMO antenna fed by rectangular patch antenna is designed. This antenna operates at E-UTRA frequency band 5 (824 MHz $\sim$ 894 MHz). We can get the characteristics of the high isolation between 2 ports by using power divider feeding structure and orthogonal linear polarization. MIMO antenna consists of two patches and a metal structure. This metal structure plays a role of a cavity-backed antenna and can improve a front-back ratio. Lower patch is fed by microstrip power divider and generates the coupling between lower and higher patch.

The proposed antenna size is $145 * 145 * 20\,\mathrm{mm}^3$, and it is fabricated on the FR-4 substrate. Antenna is simulated by Ansys HFSS and measured by Agilent E5071c network analyzer. The antenna has the bandwidth of about 70 MHz, the realized gain of 5.3 dBi and front-back ratio of 15 dB. MIMO antenna has the isolation of -30 dB. This antenna can be used for commercial small base station by reason of that this antenna satisfied the requirements of mobile communication system.

A Compact UHF Antenna for Handheld RFID Reader

W. C. Hung[1], **H. L. Su**[1], **S. L. Chen**[2], **and C. T. Lin**[2]

[1]Department of Computer Science and Information Engineering
National Pingtung Institute of Commerce, Taiwan
[2]China Steel Corporation, Taiwan

Abstract— This work presents a compact antenna for a handheld ultra-high-frequency (UHF) RF identification (RFID) reader. This antenna has the bandwidth of VSWR smaller than 2 from 917 MHz to 934 MHz and the center frequency is 925 MHz. The gain is bigger than 2 dBi at concern band and the maximum gain is 2.55 dBi. The antenna structure is an invert-F patch antenna and is composed of an aluminum stand with 60 mm × 20 mm × 17.5 mm and a radiation metal with 14.5 mm × 56 mm. Because the antenna is for handheld device, the effect of the body of the RFID reader and human hand are also study. Two cases of the material, metal and plastic, of the body of the RFID reader are discussed. When the antenna mounted on the plastic body of the RFID reader, the bandwidth of the antenna become broader slightly. When the human hand, which relative permittivity is 41.5 and conductivity is 0.98, hold on the antenna reader, the antenna has better matching and broader bandwidth. The peak gain has 0.4 dB reduction but the gain in the concern band is still bigger than 2 dBi. The effect of the distance between of the antenna and hand is also discussed. When the distance is smaller than 5 mm, the antenna becomes mismatching. When the body of the RFID reader is metal, the center frequency will shift to low frequency. The reason is that the metal-body provides a long current path. Finally, the antenna is fabricated and verified.

Dual-band Slot Antenna Using CPW Feed Line and Metasurface

Hailiang Zhu, S. W. Cheung, and T. I. Yuk
Department of Electrical and Electronic Engineering
The University of Hong Kong, Hong Kong, China

Abstract— Metasurface is the two-dimensional equivalent of metamaterial. Due to its planar structure, metasurface can be easily combined with planar antenna (which is called source antenna) to achieve performance enhancement in terms of bandwidth, gain and radiation pattern. Among reported metasurface antennas using metasurface, the metasurface and source antenna were fabricated on different dielectric substrates and placed a certain distance away from each other, although the distance between source antenna and metasurface was very close, the thickness of metasurfaced antenna has been increased considerably compared to source antenna, in addition, the complexity of antenna was also increased due to assembly problem. Even so, this is necessary when the source antenna is fed by microstrip line because both planes of the source antenna has conductors and there is no space for metasurface. However, things will be different if the coplanar waveguide (CPW) feed line is used, because all the conductors are fabricated on the same plane of the dielectric substrates, therefore, if we place the metasurface on the other side, the metasurface and source antenna will be combined perfectly as one single antenna, the thickness of the metasurfaced antenna does not even change at all compared to that of the source antenna.

A simple CPW-fed slot antenna, of which the radiation pattern is bi-direction and only one resonant point exists, is used as the source antenna in this paper and we propose to add a metasurface directly onto the plane which has no conductors of a CPW-fed slot antenna to design a dual-band antenna working at 3.4 and 5 GHz for illustration purpose. According to simulated and measured results, it was novel that the metasurface played complete opposite role at different frequency bands. On one hand, at the lower band around 3.4 GHz, the metasurface acts like a load, receiving the signal from the source antenna and re-radiated the signal in the direction away from source antenna, here the function of the metasurface is similar with that of most reported metasurfaces, on the other hand, at the upper band around 5 GHz, the metasurface acts like a reflector, reflecting the signal from the source antenna to the direction of source antenna. Therefore, under the manipulation of metasurface, the proposed antenna can radiate signal around 3.4 GHz mainly to one direction while the signal around 5 GHz is mainly radiated to the opposite direction.

Loaded Circular Patch Rectangular Slit Ultra-wideband (UWB) Microstrip Antenna

Chao Wang, **En Li**, **and Gaofeng Guo**
University of Electronic Science and Technology of China, China

Abstract— This paper brings forward a small printed rectangular slit ultra-wideband microstrip antenna loaded with a plane of circular patch. Different from the common circular slit microstrip antennae, the circular patch is loaded in the middle of the rectangular slit in order to obtain ultra-wideband characteristics and maintain small physical size at the same time. Experimental results show that the impedance of the antenna bandwidth is 2.7 GHz $\sim$ 6.2 GHz, the width of the lobe level of $\pm$30 degrees, and the pitch beamwidth is $\pm$20 degrees. And the physical size of the antenna is only 75 mm (length) $\times$ 70 mm (width) $\times$ 7 mm (thickness), which is suitable for ultra-wideband wireless communication system.

Printed Modified Bow-tie Dipole Antenna with Band-notch Structure

Huai-Yu Lin, I-Fong Chen, Ching-Chih Hung, and Chia-Mei Peng
Institute of Computer and Communication Engineering
Jinwen University of Science and Technology, Taiwan, R.O.C.

Abstract— The ability of a modified bow-tie dipole antenna with band-notch slot, which has an asymmetric-feed structure to operate at UHF-band (470–82 MHz) and dual ISM-band (2.4 GHz and 5.8 GHz) is demonstrated. An asymmetric-feed structure to yield broad bandwidth, and the terminal resistance is approximately 50 Ω. The arms of modified bow-tie dipole are shifted position to yield an asymmetrical structure. The impedance matching of the modified bow-tie dipole structure is obtained by tuning the shifted distance. The band notch of the dipole structure is obtained by inserting some slots on the dipole-arms. Experimental results indicate that the VSWR 2.5 : 1 bandwidths achieved were 60.6%, 20.48% and 20% at 660 MHz, 2.45 GHz and 5.5 GHz. The measured radiation patterns for free space at 0.66 GHz, 2.45 GHz and 5.5 GHz in the xy-plane (H-plane) and xz-plane (E-plane), respectively. The maximum gains in the E-plane are 0.24 dBi, 1.12 dBi and 0.97 dBi. The maximum gains in the H-plane are 0.1 dBi, 0.078 dBi and 0.24 dBi. The operating bandwidth of the proposed antenna with usable broadside radiation patterns is consistent with the specification of DVB and WLAN system. Stable radiation patterns are observed. Acceptable radiation characteristic for the practical applications is obtained for the proposed antenna. The proposed modified bow-tie dipole exhibits a nearly omni-directional radiation pattern with very easy to fabricate structure, and so is suitable for various commercial wideband applications.

Printed Dual-polarization Broadband Directional Antenna

Lu-I Yams, Chia-Mei Peng, I-Fong Chen, and Kang-Ling Li
Institute of Computer and Communication Engineering
Jinwen University of Science and Technology, Taiwan, R.O.C.

Abstract— A four layer odd function symmetric dual-polarization coplanar waveguide (CPW)-fed slot antenna for broadband communications is proposed in this literature. The proposed antenna has a very simple antenna structure and wide impedance bandwidth ($\sim 400\%$ for $|S_{11}|$ and $|S_{22}|$ VSWR $\leqq 3$) which can cover the $1.5 \sim 6$ GHz frequency band for Global Positioning System (GPS, 1575 MHz) and dual ISM band (2.4 GHz and 5.8 GHz) applications. Good isolation between the two input ports ($|S_{21}| \leqq -15$ dB) is also achieved at the operating band. The radiation pattern and efficiency of the proposed antenna are also measured, and radiation pattern data are compared with simulation results.

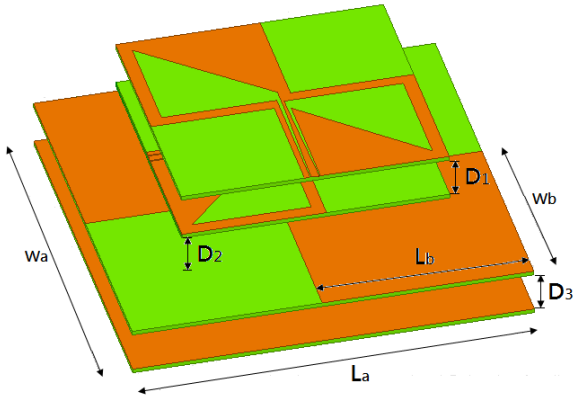

A Y-shaped Microstrip-line-fed Wide-slot Antenna with Band-controlled for Multiband Applications

S.-J. Wei, Q.-Y. Feng, and D.-H. Jia
School of Information Science and Technology
Southwest Jiaotong University, Chengdu, Sichuan 610031, China

Abstract— In this paper, a printed wide-slot antenna with a Y-shaped microstrip-fed line for multiband applications is proposed and studied. A simple Y-shaped microstrip line is used for exciting the wide slot carved on the ground plane. With the use of equilateral triangle wide-slot reversed along the equilateral triangle ground plane, multi-frequency is obtained. The prototype designed on FR4 substrate occupies the dimensions of $125 \times 108\,\mathrm{mm}^2$ with the thickness of 1.6 mm, relative permittivity 4.4 and dielectric loss tangent of 0.02. The simulated results demonstrate that a single frequency is achieved while the angle of the Y-shaped microstrip line is 120 degree. The resonant frequency with great matching impedance occurs at 7.95 GHz. The −10 dB band is 7.54–8.34 GHz. Meanwhile, dual-band is obtained while the angle is 90 degree. The frequency band appears at 2.43 GHz and 7.68 GHz. The −10 dB bands are located at the range of 2.28–2.63 GHz and 6.19–8.07 GHz. However, tri-band could be acquired while the angle is set as 60 degree. The center operating frequencies, which are 2.35 GHz, 4.15 GHz and 7.65 GHz, are obtained. The −10 dB bands are located at the range of 2.21–2.54 GHz, 3.82–4.84 GHz and 6.16–7.95 GHz. It could be observed that the resonant frequency of the proposed antenna is greatly affected by the angle of the Y-shaped microstrip line. Thus, the band is proved to be controllable. One-band, dual-band and tri-band antenna could be obtained by adjust the angle of the Y-shaped microstrip line. In addition, the current distribution on the radiating patch for the proposed antenna, which corresponds to the frequency band, is presented and discussed. Meanwhile, the radiation patterns of the proposed antenna are simulated with XY plane and YZ plane for both co-polarization and cross-polarization. It could be suitable for multiband wireless applications.

Wide Band Frequency Control of Circularly Polarized Patch Antenna with Movable Dielectric

K. Kitatani, M. Wada, and Y. Okamura
Graduate School of Engineering Science, Osaka University
1-3 Machikaneyama-cho, Toyonaka, Osaka 560-8531, Japan

Abstract— A service of radio communication systems is being diversified. A variety of these usages require a reconfigurable antenna operating at different frequencies. A patch antenna of interest here is one of the typical microstrip antennas. The frequency control of the patch antenna was reported in 1982 using a semiconductor device. In recent years, the frequency control of the circularly polarized patch antenna has been achieved by using the ferrite, the semiconductor, and the mechatoronics technology. In them, the bandwidth of the frequency control has been reported to be able to 13% by using variable reactance elements in the experiment. We proposed a circularly polarized patch antenna using partial dielectric filling whose resonant frequency is controllable using mechatoronics technology. This frequency change can be achieved by changing the effective dielectric constant by the dielectric plate moving in the air layer between the ground and the patch. The control range of operating frequency was able to obtain 10% in the experiment. Furthermore, we reported the frequency control of 44% in calculation. Thus, we have been studying continuously changing the resonance frequency of the patch antenna using mechatronics technology.

This paper presents circularly polarized microstrip patch antenna for frequency control. Wide band operating frequency of circular polarization of the proposed antenna can be control by using a movable dielectric. The frequency control bandwidth was able to obtain 67.7% from 6.4 GHz to 12.95 GHz with axial ratio less than 3 dB.

Crosstalk Modeling and Analysis of Through-Silicon-Via Connection in 3D Integration

Xiang He, Wensong Wang, and Qunsheng Cao
Nanjing University of Aeronautics and Astronautics, China

Abstract— For the wider bandwidth and the smaller form factor, high-speed I/O channel design in three-dimensional integrated circuit (3D IC) becomes more important. Through-Silicon-Via (TSV) is regarded as a critical component in 3D integration that extends Moore's Law. In TSV based 3D-IC systems, a significant design consideration is the coupling noise between TSVs. This paper focuses on the TSV crosstalk analysis under high speed operations using a 3D electromagnetic field solver and a SPICE simulator. Effects of the TSV radius, insulator thickness, and TSV pitch are investigated in details. In addition, the crosstalk performance of different TSV bus configurations is also evaluated and compared, which is one important consideration in high speed interconnection systems.

FDTD Study on Transmission Characteristics Affected by Air-gap between Noise Suppression Sheet and Strip Conductor

K. Otsuka, T. Suzuki, S. Suzuki, K. Kiyomi, T. Ohno, and K. Ishii
Kisarazu National College of Technology, Japan

Abstract— In this paper, transmission characeristics affected by air-gap between a noise suppression sheet (NSS) and a transmission line are examined. A microstrip line (MSL) based on IEC standard (IEC62333-2) is fabricated, and a transmission characteristic of the MSL attached with an NSS is simulated and measured.

Figure 1 shows the simulation model of the MSL attached with an NSS. The substrate shown in Fig. 1 assumes DiClad522 ($\varepsilon_r = 2.55$, $\tan\delta = 0.0022$) manufactured by ARLON. Fig. 2 shows the schematic model of the air-gap between an NSS and a strip conductor. The distance of the air-gap is defined as d. Fig. 3 shows the simulated and measured transmission characteristics in the case of $d = 0.0$ [mm] or $d = 0.1$ [mm]. The maximum difference of transmitted electric power between simulated and measured results is 1.38% in $d = 0.0$ [mm], and is 2.45% in $d = 0.1$ [mm], respectively. Therefore, the simulation model shown in Fig. 1 is available from above results. The simulated transmission characteristics varying the distance of the air-gap are shown in Fig. 4. In Fig. 4, whereas increasing the air-gap distance from 0.0 to 0.4 mm deteriorates the transmission characteristic in high frequency side, the transmission characteristic at 1 GHz is improved from −2.10 dB to −0.30 dB. Moreover, the cutoff-frequency is shifted to higher frequency. As a result, it is important to consider the distance of the air-gap between an NSS and a transmission line.

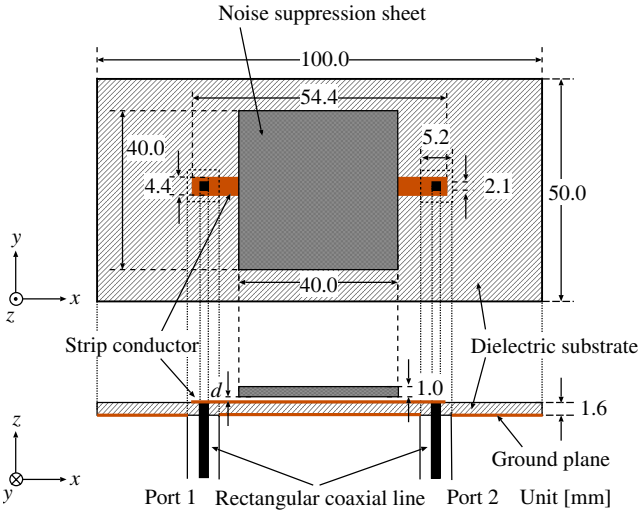

Figure 1: Simulation model of the MSL with NSS.

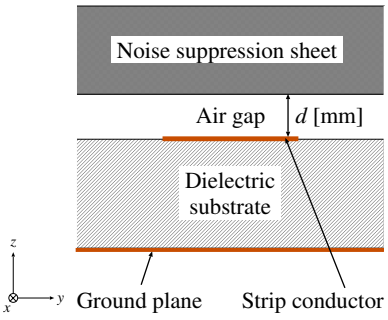

Figure 2: Air-gap between NSS and strip conductor.

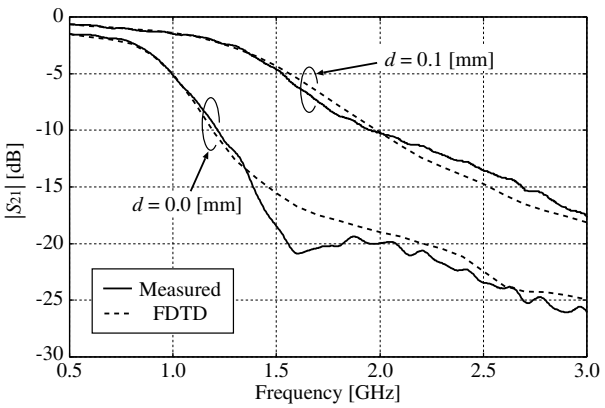

Figure 3: Simulated and measured results of Fig. 1.

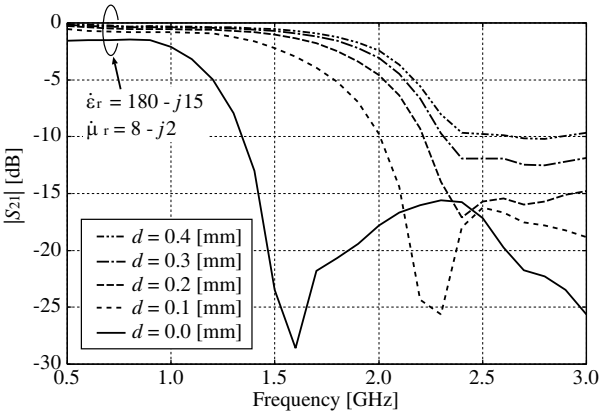

Figure 4: Simulated results of NSS with different air-gap.

Portable Wireless Power Transmission Demonstration System with Low Power Consuming and Compact Size

Chun-Hao Hsu, **Ko-Wen Hsu**, **and Wen-Hua Tu**
Department of Electrical Engineering, National Central University, Taoyuan 32001, Taiwan

Abstract— In this study, a portable wireless communication system with low power-consuming and compact size is presented. The module is composed of the transmitter and receiver. The transmitter consists of oscillator and antenna. The receiver consists of antenna, bandpass filter, low noise amplifier, AC/DC modulation, and power density display. The proposed system features easily assembling and disassembling components since they connect one another by SMA connectors. Users can replace the existing components to meet the demands for various teaching goals. Furthermore, there is no power amplifier in the entire system. Power is transmitted directly from oscillator to antenna. To implement the lowest power-consuming structure, the output DC connects to LM3914C for detecting minor voltage, which needs no amplifier.

The operating frequency of the module is designed at 1.575 GHz for Global Position System. For the oscillator, the input voltage is 3 V and the current is 6 mA. The power supply is used by cascading two 1.5 V batteries and the output power is 9.3 dBm. For the antenna, patch antenna and dipole antenna are provided to exchange. For the bandpass filter, the dual-mode bandpass filter is employed. It consists of one wavelength ring and two capacitors for feeding. For the low noise amplifier, the input voltage is of 3 V and the current is of 6 mA. The power supply is used by cascading two 1.5 V batteries and the output power is of 19 dBm. For the AC/DC modulation, one order voltage doubler is used to modulate the single from AC to DC. To display the wireless signal density, the thirty LEDs are arranged to shine. As the signal density is more powerful, the more LEDs are turned on. The operating current is 394 mA as all LEDs shine. The driven voltage is of 5 V. The whole system can be charged up by using laptops or rechargeable battery kits with USB connector.

Effect of Electromagnetic Interference (EMI) on the DC Shift of NMOSFET Current-mirror

Muhammad Taher Abuelma'atti[1] and Ali M. T. Abuelmaatti[2]

[1]King Fahd University of Petroleum and Minerals, Box 203, Dhahran 31261, Saudi Arabia
[2]18 Lynas Place, Evenwood, Bishop Auckland, County Durham, DL14 9RF, UK

Abstract— In this paper a new approximation is presented for the nonlinear relationship between the input-current and the output-current of an NMOSFET current-mirror. Using this approximation closed-form expressions are obtained for the DC component of the output current resulting from exciting the NMOSFET current-mirror by a DC biasing current plus a superimposed sinusoidal electromagnetic interference. Comparison between calculated and simulated results is included.

Effect of Electromagnetic Interference (EMI) on the DC Shift of NMOSFET Current Mirror with Capacitor Between Mirror Node and Ground

Muhammad Taher Abuelma'atti[1] and Ali M. T. Abuelmaatti[2]

[1]King Fahd University of Petroleum and Minerals, Box 203, Dhahran 31261, Saudi Arabia
[2]18 Lynas Place, Evenwood, Bishop Auckland, County Durham, DL14 9RF, UK

Abstract— In this paper, a new procedure is presented for predicting the effect of electromagnetic interference (EMI) on the DC shift of an NMOSFET current mirror with a capacitor connected between the mirror node and the ground. Closed-form expressions are obtained for the DC output current component resulting from exciting the mirror by a DC biasing current plus a superimposed multisinusoidal EMI. Simulation results are included.

Behavioral Modeling of a 12-bit 500-MS/s Multi-stage ADC

Wen Wei He and Qiao Meng
Institution of RF- & OE-ICs, Southeast University, Sipailou 2, Nanjing 210096, China

Abstract— This paper describes a behavioral model of 12-bit@500 MS/s Multi-Stage analog to digital converter (ADC) and its non-ideal parameters are presented. A new multiplying digital-to-analog converter (MDAC) architecture (4.5 bit/stage) is used to reduce the capacitor matching requirements. By simulation, the optimum performance is Signal to Noise and Distortion Ratio (SNDR) = 73.3 dB, Spurious Free Dynamic range (SFDR) = 95.6 dB, Effective Number of Bits (ENOB) = 11.89 bit when the input signal is 17.7 MHz and the sampling clock rate is 500 MHz. The proposed model can provide a reference for the error and dynamic analysis for multi-stage ADC system.

The Impact of USB 3.0 Module on Wireless Communication with Improved Solution for EMI Problem of High Speed Connectors

Han-Nien Lin[1], **Wei-Hua Huang**[2], **and Wei-Jr Lai**[1]

[1]Department of Communications Engineering, Feng-Chia University, Taiwan, R.O.C.
[2]Training Research Co., LTD
6F.-1, No. 3-1, Park St., Nangang Dist., Taipei City 115, Taiwan, R.O.C.

Abstract— With the development of Ultrabook in recent years, the main and auxiliary antennas for WLAN are moved down to PC base because the LCD panel is too thin to install antennas inside. On top of that, there are also more and more laptops equipped with super high-speed USB 3.0 ports. Unfortunately, the USB 3.0 modules will usually radiate the EMI noise to affect the receiving performance of WLAN antennas in the Ultrabook if USB dongle is inserted or the USB cable is plugged in. To analyze and quantify the effect of the USB 3.0 EMI noise on the WLAN antennas of Ultrabook, several experiments have been conducted for root cause analysis (RCA) including measurement for throughput rate and EMI noise power received by the antennas.The root cause of USB 3.0 EMI problem is closely related to its structure design and termination scheme. For the structure issue of USB 3.0 module, there exist many discontinuities from IC to receptacle, and also from the receptacle to plug. As to the termination issue, there exists design problem about impedance mismatch between plug and cable. The improper design of structure and termination for USB 3.0 module will result in common mode current and thus lead to EMI problem. Besides, the differential signal of USB 3.0 TX and RX pair may also cause EMI problem in the Ultrabook due to compact design restriction. Therefore, some equipment will be presented, such as Microwave Power Clamp, SNA (System Noise Analyzer), NFS (Noise Floor Measurement System), and PNS (Platform Noise Scanner), which have been developed to help trouble-shooting and identifying the root cause of EMI problem relevant to the radiated EMI noise from various IC chips, modules, devices, and so on. In addition to the USB 3.0 module, the EMI diagnosis procedure also applies to other high speed modules such as HDMI, LVDS, SATA, PCI Express, Display Port, and EDP. Finally, the possible solution to USB 3.0 EMI problem will also be discussed in this paper. The design technique for improved design of the USB 3.0 structure will be illustrated in detail, and the new USB 3.0 design will also show better performance than the old USB 3.0 module.

Verification Analysis of Electromagnetic Coupling between Display Module and Antenna of Mobile Devices for Wireless Communications

Han-Nien Lin[1], **Allen Laio**[2], **Yen-Lin Tseng**[1], **and Ming-Shan Lin**[3]

[1]Department of Communications Engineering, Feng-Chia University
No. 100, Wenhua Rd., Xitun Dist., Taichung City 407, Taiwan, R.O.C.
[2]Training Research Co., LTD, 6F.-1, No. 3-1, Park St.
Nangang Dist., Taipei City 115, Taiwan, R.O.C.
[3]Bureau of Standards, Metrology and Inspection, MOEA
No. 4, Sec. 1, Jinan Rd., Zhongzheng Dist., Taipei City 100, Taiwan, R.O.C.

Abstract— Since the display modules occupy the largest area of various smart phones nowadays, they may either act as an EMI noise radiators or a noise receivers. The EMI noise on mobile platform may couple with display module via traces of PCB, FPC, or the panel ICs. Because the antenna of a smart phone is usually located around the display module, the EMI noise generated from display module would strongly couple with nearby antenna and cause sensitivity degradation of communications. On the other hand, the antenna will radiate a higher level power to keep the link effectively when the phone initiates a call connection, and it may thus affect the function of display module due to electromagnetic coupling. We will analyze here the RF tests needed to be performed by vendors for those display modules before they are to be integrated into smart phones with accepted performance. The 1st test is near field emission test of display module measured with an EMC surface scanner. The test is to scan the operating display module with horizontal near field probe, and to limit the radiated power from the whole display module (including control Panel ICs and FPC connectors) in the designated communication bands. The test also has to ensure that the EMI noise is from the display module itself by filtering power supplier or other PCB traces. The 2nd test is the S-parameter test for radiated emission by performing with microstrip. The test is to measure electromagnetic coupling between the selected dominant noisy lines and microstrip. There are two purposes for this test: (1) Evaluate the EMC performance of display module under test in terms of emissions from the dominant lines, and (2) Validate the relationship between simulation model and the corresponding S-parameter results. The 3rd test is RF immunity test by performing with display module against the high level power transmitted from mobile phone without any specific image degraded. The base station simulator will make a connection to mobile phone to control the radiated power during the test, and the quality of image (including display module state, image color, and tone) should not be degraded under RF interference. To achieve better performance of wireless communications, we will summarize the principle and applications of various RF test for display modules to be integrated in mobile devices.

Resonant Capability of Multilayer Spheroidal Nanoparticles as Plasmonic Nanoantennas

M. Khosravi, **R. A. Sadeghzadeh**, **and M. S. Abrishamian**
Department of Electrical and Computer Engineering, K. N. Toosi University of Technology
Shariati Street, P. O. Box 16314, Tehran, Iran

Abstract— Guiding light in nanostructures are important challenges for current research and development. A proper solution to these kinds of nanoscale problems is applying metallic nanoantennas [1]. In recent years, a variety of schemes taking advantage of localized optical near-fields generated by metallic nanoparticles have been proposed to use them as optical nanoantennas [2]. Optical antennas consisting of nanometer size metallic particles can be used to improve the size mismatch between the diffraction limited spot of the excitation light and fluorescent molecules that are much smaller than the excitation wavelength. Such antennas which act in optical regime-support a localized surface plasmon resonance. In certain condition, light exited plasmons lead to strong light scattering and absorption, and also an enhancement of the local field.Plasmon modes exist in a number of geometries and in various metals especially in noble metals such as gold and silver [3, 4]. It is noticeable that metalsare no longer a perfect electric conductor at optical frequencies. At radio frequencies, metals behave very similarly to a perfect conductor that can instantaneously cancel out time-varying fields by generating a surface current. Although metals are still highly reflective at visible frequencies, light can penetrate into metals due to the skin effect leading to dissipation. In optical frequency range many materials, especially metals, have strong dispersions, i.e., their permittivitychange significantly with light frequency.

Here, we study the effect of changing different parameters on the resonant behavior of a single element nanoantenna in the form of multilayer nanosphere (Fig. 1). Thickness and number of layers are parameters that their variations have been focused. As final step, the gradual transformation from sphere to both oblate and prolateellipsoids has been considered (Fig. 2). This alteration in symmetry has interesting results on outputs.In this paper, we discuss different cross sections as special outputs which their considerations are essential in studying parameters variation. The

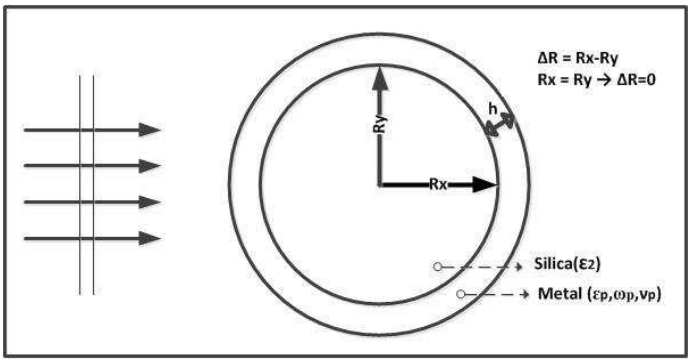

Figure 1: Silica nanosphere coated by a noble metal (basic model).

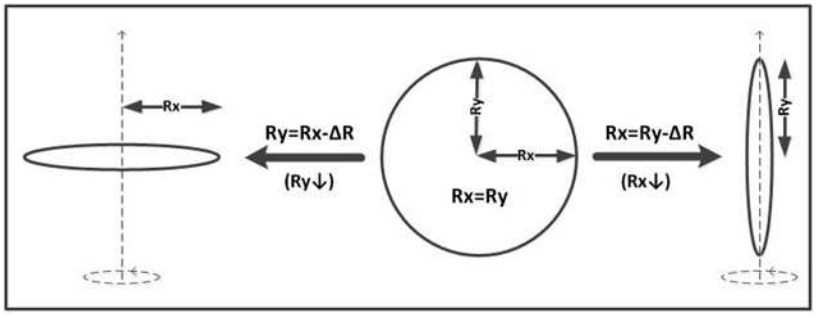

Figure 2: Transform from sphere to ellipsoid by a gradual increase in difference (ΔR).

CST Microwave Studio (full-wave 3D software) is applied as main tool for simulationsMoreover, it is good to know that the dielectric response of noble metals (gold or silver) modeled by Drude function.

The paper is organized as follow. Some theoretical concepts such as scattering from nanoparticles and dispersive behavior of metals at optical frequencies are main subjects which concerned in the opening part. In next parts, simulation results for different parameters variation (thickness and number of layer) have been presented by order.As an important step, a gradual transformation from sphere to ellipsoid has been taken into account. Final section includes conclusions after a logical review of all achieved results.

REFERENCES

1. Novotny, L., "Optical antennas for enhanced light-matter interactions," Report, The Institute of Optics, University of Rochester, 2010.
2. Thomas, R., J. Kumar, R. S. Swathi, and K. G. Thomas, "Optical effects near metal nanostructures: Towards surface-enhanced spectroscopy," *Current Science*, Vol. 102, No. 1, Jan. 2012.
3. Brongersma, M., "Plasmonics engineering optical nanoantennas," *Nature Photonics*, Vol. 2, 2008.
4. Maier, S. A., *Plasmonics: Fundamentals and Applications*, Springer, 2007.

Electromagnetic Equations in Curved Octonion Compounding Spaces

Zi-Hua Weng
School of Physics and Mechanical & Electrical Engineering
Xiamen University, Xiamen 361005, China

Abstract— J. C. Maxwell first described the electromagnetic theory with the algebra of quaternions, while A. Einstein first adopted the curved Four-spacetime to depict the gravitational field. Those methods enlighten the subsequent scholars to introduce the curved octonion space to characterize simultaneously the features of the electromagnetic and gravitational fields.

In the octonion space, the radius vector can be combined with the integral of field potential to become the compounding radius vector, which can be considered as the radius vector of the octonion compounding space (that is one kind of function space). In the octonion compounding space, it can be discussed the influence of velocity and rotation on the object's movements.

In the curved octonion compounding space, the paper studies the impacts of the coefficients and the curvatures on the field potential, velocity, field strength, rotation, and field source etc. This means that the extent of the space bending will impact directly the electromagnetic equations and the movement of charged particle.

ACKNOWLEDGMENT

The authors are grateful for the financial support from the National Natural Science Foundation of China under grant number 60677039.

Theoretic Analysis on a Periodic Array of Broadband Plasmonic Nanoantenna

Yuan-Fong Chau, Wayne Yang, Shinn-Fwu Wang, and Yi Chu
Department of Electronic Engineering, Chien Hsin University of Science and Technology
No. 229, Jianxing Rd., Zhongli City, Taoyuan County 32097, Taiwan, R.O.C.

Abstract— We numerically simulate a periodic array of plasmonic nanoantennas by varying the structural parameters on the antenna resonance conditions, such as peak resonance wavelengths, electric field intensity, propagation properties, three component field distributions, total field distribution, charge density and electrical filed stream lines at spectral points of interest. Besides, the characteristics of transmittance spectral of a periodic antenna array corresponding to bonding modes and anti-bonding modes are also investigated. Through these simulations, we found that it can be tuned a periodic nanoantenna array with a fixing size over a wide spectral. These results will inspire further developments in the periodic plasmonic nanoantennas array with complex geometries and will have future applications in more range spectra of spectroscopy and sensing.

ACKNOWLEDGMENT

This work was supported by National Science Council of the Republic of China (Taiwan) under Grant Nos. NSC-100-2632-E-231-001-MY3 and NSC 99-2112-M-231-001-MY3.

Analysis of the Bonding and Anti-bonding Modes on Periodic Array of Nanometals

Yuan-Fong Chau, Wayne Yang, Ci-Yao Jheng, San-Cai Jheng, Shinn-Fwu Wang, and Yi Chu

Department of Electronic Engineering, Chien Hsin University of Science and Technology
No. 229, Jianxing Rd., Zhongli City, Taoyuan County 32097, Taiwan, R.O.C.

Abstract— We numerically investigate the SPR mode and coupling effect of the periodic silver-shell nanopearl and its periodic dimer arrays. The proposed structure of silver-shell nanopearl arrays is an important novel geometry for plasmonic metal nanoparticles, combining the highly attractive nanoscale optical properties of both dielectric nanorods and metallic nanoshells. Numerical investigations by using the 3-D finite element method (FEM) indicate that the periodic silver-shell nanopearl arrays exhibit two SPR modes corresponding to bonding and anti-bonding modes, respectively. The boundary symmetry at inner and outer surface of the periodic silver-shell nanopearl arrays can be broken by increasing the filling permittivities inside the dielectric holes (DHs). On the basis of our simulations, it is possible to excite the anti-bonding modes by breaking the material symmetry of structures directly, i.e., by varying the filling permittivities inside the DHs. It is worth noting that the depth of transmittance dips is sensitive to the period (Λ), and the depth of transmittance dips is increased as the value of period reduced due to the coupling effect of shorter period among the periodic silver-shell nanopearl arrays is stronger than those of longer period cases. This unique property of periodic silver-shell nanopearl arrays and periodic silver-shell nanopearl dimer arrays are highly attractive for serving as resonant nanocavity to hold and probe smaller nanostructures, such as biomolecules or quantum dots. Periodic silver-shell nanopearl arrays also show significant applications for nano-switch devices, sensing, and surface-enhanced spectroscopy, due to their strong and tunable SPRs.

ACKNOWLEDGMENT

This work was supported by National Science Council of the Republic of China (Taiwan) under Grant Nos. NSC NSC-100-2632-E-231-001-MY3 and 99-2112-M-231-001-MY3.

Design of Three-coupled Finline Bandpass Filter Using Full Wave Analysis

V. Madhusudana Rao[1] and B. Prabhakara Rao[2]

[1]Jawaharlal Nehru Technological University, Kakinada 533003, India
[2]Electronics and Communication Engineering Department
Jawaharlal Nehru Technological University, Kakinada 533003, India

Abstract— This paper presents a systematic procedure for designing a bandpass filter with wide bandwidth based on parallel coupled three finline structures. Normal mode parameters like propagation constants, characteristic impedance and equivalent voltage eigenvector of multiple coupled unilateral finlines are evaluated by using full wave modal analysis. A design graph for symmetric three unilateral finline structure is presented for the design of bandpass filter. A bandpass Chebyshev filter of order 3 having center frequency of 10 GHz with fractional bandwidth of 20% is designed on RT-duroid 5880^{TM} substrate using unilateral three finlines and simulated in HFSS (High Frequency Structure Simulator).

The finline is a wave guiding structure which is increasingly used as millimeter wave component due to various advantages such as reducing size, weight and cost. At millimeter wave frequency the finline filter has been implemented, which are mostly based on ladder/cascaded shape. Limited analysis is available on finline filter, which is based on coupled finline. This paper presents the design of bandpass filter using three coupled unilateral finlines. The advantage of present filter is low loss and wider bandwidth over the ladder/cascaded type filter. The full wave modal analysis for unilateral finline coupling section and an admittance inverter circuit are derived.

Reconstruction of Electromagnetic Scatterers with Different Boundary Conditions

Rencheng Song, Xiuzhu Ye, and Xudong Chen
Department of Electrical and Computer Engineering
National University of Singapore, Singapore

Abstract— In practical electromagnetic inverse scattering problems, the targets to be reconstructed usually own different boundary conditions like Dirichlet (perfect electric conductor), transmission (dielectric) or Robin (impedance) et al.. However, most known inverse scattering methods are only designed for dealing with one particular boundary above. Although some qualitative inverse scattering methods like linear sampling method can retrieve the shape of scatterers with mixed boundary conditions, it can not further classify their physical characteristics. Therefore, there is a demand to develop a quantitative method to solve such problems. It is well known that it is challenging to solve such an inverse scattering problem where scatterers with different boundaries coexist.

In this paper, we introduce a T-matrix method to reconstruct simultaneously the scatterers with different boundary conditions like Dirichlet, Neumann, Robin, and transmission boundaries without any prior information. The scattering problem is modeled by the T-matrix method and the cost functional is built and reformulated according to the subspace based optimization method. The characteristics of scatterers are further classified by the zeroth order coefficients of T-matrix and other related parameters. Various numerical examples show that the new method can recover both the shapes and the physical parameters of scatterers.

Compressive-sensing-based Phaseless Imaging

Li Pan[1], **Rencheng Song**[2], **Swee Ping Yeo**[2], **and Xudong Chen**[2]

[1]Agency for Science, Technology and Research (A*STAR), Singapore
[2]National University of Singapore, Singapore

Abstract— A novel method is proposed to address the phaseless imaging problem, i.e., to image point-like dielectric objects with intensity-only measurement. Since the method was motivated by the recent development of compressive sensing (CS) in the area of signal processing and applied mathematics, we conveniently refer to it as the compressive-sensing-based phaseless imaging (CPI) method. The CPI method enables us to obviate the difficulty of measuring phase information, which was reported to be inaccurate and expensive at high frequency.

In the absence of phase information, the phaseless imaging problem becomes far more nonlinear than the full data imaging problem, due to the terms of products of contrasts. Thus it seems that the CS algorithm (which is for linear system) cannot be directly applied to the nonlinear problem of phaseless imaging. In CPI method, however, we transform the intrinsically nonlinear phaseless imaging to a linear system by introducing additional independent variables representing the product terms. Besides, we also perform the random sampling by employing random sensor arrays, which is a good way of realizing incoherence measurement. The nonlinear-to-linear conversion, random sampling, and the sparsity of objects validate the applicability of compressive sensing in imaging point-like scatterers with phaseless measurement. Once the linear formulation is established, the contrast information can be reconstructed efficiently by convex optimization.

To test the CPI method, our numerical experiments cover both noiseless and noisy cases, and both homogeneous and heterogeneous background media cases. The results show that the exact internal constitution of the domain of interest can be efficiently reconstructed with good resolution. Furthermore, since Green's function is employed in the formulation, this method is not restricted in far field measurement.

Perturbation Influence Analysis on the RCS of Dynamic Targets

Jia Liu, **Min Su**, **Ning Fang**, **and Bao Fa Wang**
Department of Electronic and Information Engineering
Beijing University of Aeronautics and Astronautics, Beijing 100191, China

Abstract— The computation of the electromagnetic scattering for flying target usually has more practical meanings in stealth performance evaluation and weapon design. As a fast RCS prediction method with acceptable error, GRECO (Graphical Electromagnetic Computing) provides the possibility of broad-scale RCS computation for electrically large dynamic targets. In the actual environment, flying target (like aircraft) is influenced by the unpredictable factors, like atmospheric interference, fuselage shake and flying operation, etc. These factors usually bring perturbation in both flight and radar view point, which are commonly not considered in the simulation. The high sensitivity of the target's RCS in high frequency region indicates the potential influence on radar target characteristic simulated from the simulation results without perturbation consideration. In this paper, the perturbation of the aircraft is modeled as the uniformly distributed random variables on pitch, yaw and roll planes individually. The application of the Monte-Carlo simulation in GRECO is used for analyzing the perturbation effects on the aircraft's RCS. Gaussian model is proposed as the description of the RCS difference, whose sensitivity on frequency, polarization and turbulence extents are also studied. The conclusion could be used as the consultation on the comparison of RCS between measurement and simulation.

Electromagnetic Interference on Metal Sandwiched Quartz Crystal

Kuei-Jie Tseng and Wen-Teng Chang
Department of Electrical Engineering, National University of Kaohsiung, Kaohsiung, Taiwan

Abstract— Elimination of electromagnetic interference (EMI) is an important issue to normally operate electronic devices. A frequency generator, such as oscillator, is one of the major sources in an electronic system to emit EMI. Many literatures have discussed different approaches and the cause to reduced EMI, however, not many of them have ever discussed the impact of EMI to an oscillator. Since quartz crystal (QC) is the one of the most commonly device used as oscillator due to its high stability of operating frequency. This work first addresses the radiation effect of EMI on QC by applying an external AC source as interference source. The experiment operated frequencies of the AC generator from 0 to 80 MHz and connected to a customized copper slate to emit electromagnetic radiation on the QCs. The nominal frequencies of the QCs composed of 4 MHz, 6 MHz, 8 MHz and 10 MHz. The At-cut QCs were sandwiched by coating aluminium and plugged into an oscillator circuit separately, to demonstrate the radiation impacts of EMI. Within the measurement distance of less than 10 mm from the slate to a QC, the frequency shift was found to highly depend on operating frequency. Additionally, the results showed that the normalized frequency shift would reach to maximum when the AC generator was operated around 45 to 50 MHz. The shorter radiation distance showed a stronger interference on frequency shift. The results should indicate that the induced surface current on the metal is strongly related to radiation distance because of the nature of EMI. Besides, the induced surface current is frequency dependent and the frequency mixing effect should be considered.

Efficient Characterization of Fabry-Perot Resonator Antennas

Yuehe Ge[1, 2] and Wang Can[1]

[1]College of Information Science and Engineering, Huaqiao University
Xiamen, Fujian 361021, China
[2]State Key Laboratory of Millimeter Waves, Nanjing 210096, China

Abstract— Inspired by the development of electromagnetic band-gap (EBG) structures and metamaterials, Fabry-Perot leaky-wave antennas have been well studied in the recent decade. Such antennas are mainly composed of a Fabry-Perot resonant cavity and excited by a normal antenna or an antenna array. A ground plane and a partially reflective surface (PRS) form the Fabry-Perot cavity. The advantages of this kind of antennas include simple structure, high directivity and low cost of production.

The methods to characterize Fabry-Perot resonator antennas include the ray tracking method, the transmission line method, and numerical methods including the finite element, the method of moments and the finite-difference time-domain method. Among them, the ray tracking method and transmission line method are analytical methods and hence efficient. The numerical method can characterize the entire antenna structure including the feeding antenna and give accurate result, but consume a large amount of the computer resource and computational time. In some cases of two-dimensional (2D) or three-dimensional (3D) EBG based Fabry-Perot resonator antennas, the numerical methods, based on the use of commercial softwares such as HFSS and CST Microwave Studio, cannot converge to the designated accuracy and hence give the reliable result, due to the limitation of the computer resource.

In this paper, the transmission line method, which was applied to the analysis of dielectric Fabry-Perot resonator antennas before, is extended to that of 2D and 3D EBG based Fabry-Perot resonator antennas. ABCD network is used to represent 2D or 3D EBG structures or partially reflective surfaces (PRSs), leading to an equivalent transmission network (ETN) method that can be applied to the characterization of one-dimensional (1D), two-dimensional (2D) and three-dimensional (3D) Fabry-Perot resonator antennas. Reciprocity is used together with the ETN model to characterize the radiation properties of Fabry-Perot resonator antennas. The method occupies less memory and resources of computers.

Wideband and dual-band Fabry-Perot resonator antennas are applied to demonstrate the effectiveness of the extended transmission line method. The wideband and dual-band design principles, which are based on a single EBG superstrate and have been developed to design high-gain, low-profile Fabry-Perot resonator antennas before, have been verified using the extended transmission line method. This in turn demonstrates the effectiveness of the ETN method. Both theoretical and experimental results of low-profile 2D wideband and dual-band Fabry-Perot resonator antennas will be presented at the Symposium.

Transparent Antenna Design for Wireless Access Point Application

A. S. Azini, M. R. Kamarudin, T. A. Rahman, S. K. A. Rahim, and M. S. A. Rani
Wireless Communication Centre (WCC), Faculty of Electrical Engineering
Universiti Teknologi Malaysia, UTM Skudai, Johor 81310, Malaysia

Abstract— In this paper a wideband transparent planar monopole antenna has been presented. There are three types of transparent conductive films that are mainly used by many researchers for antenna development such as indium tin oxide (ITO), fluorine-doped tin oxide (FTO) and silver coated polyester film (AgHT) [1]. Figures 1 and 2 below clearly indicate the dimensions of the proposed transparent monopole antenna. As shown in Figures 1 and 2, a transparent planar monopole antenna consists of a rectangular patch (front view) and an arc shape slot (back view) is proposed for 2.4 GHz wireless local area network (WLAN) application. The radiating element and ground plane are both designed using AgHT while the substrate is made of glass. The normal monopole antenna was tuned at 4 GHz without the arc shape slot on the ground plane. By having a suitable arc shape slot on the ground plane, a wide impedance bandwidth of 48.89% (1.9611 to 3.23 GHz) that cover WLAN system in the 2.4 GHz has been obtained. This is due the fact that the arc shape slot helps the current flowing much longer and consequently makes the antenna tuned at lower frequency of 2.4 GHz. Besides that, the 50 × 40 mm ground frame makes the antenna have broadside radiation pattern. The return loss result clearly indicates good agreement between the measurement and simulation as shown in Figure 3. The prototype of the proposed antenna is shown in Figure 4. The dimensions of the proposed transparent monopole antenna are designed and optimized using the CST simulation tool.

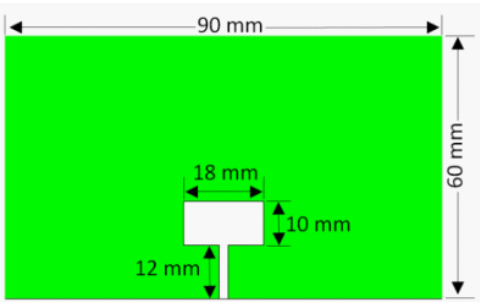

Figure 1: Front view.

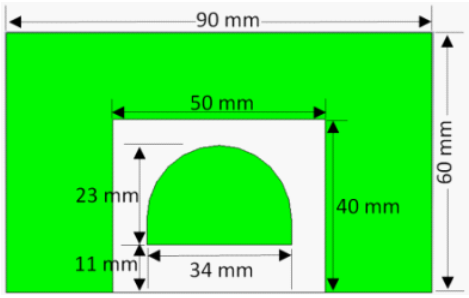

Figure 2: Back view.

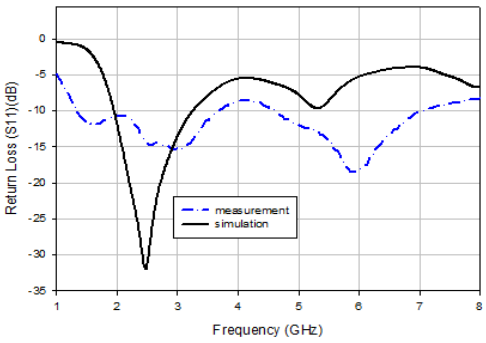

Figure 3: Simulated and measured return loss of the proposed antenna.

Figure 4: Prototype of antenna.

REFERENCES

1. Song, H. J., et al., "A method for improving the efficiency of transparent film antennas," *IEEE Antennas and Wireless Propagation Letters*, Vol. 7, 753–756, 2008.

Design of a Programmable Low-pass Filter for UHF RFID ZIF Receivers

C. C. Zhang[1, 2], **C. Wang**[1], **Y. F. Guo**[1], **Y. M. Fang**[1], **L. L. Liu**[1], **D. Y. Chen**[1], **and W. Li**[1]

[1]Power and RF Microelectronic Research Centre
Nanjing University of Posts and Telecommunications, Nanjing 210046, China
[2]Nanjing Research Institute of Electronics Technology, Nanjing 210013, China

Abstract— A programmable low-pass filter for 860 $\sim$ 960 MHz UHF RFID ZIF (zero IF) receivers was designed in 0.18 µm CMOS process. Taking into account the high linearity requirements, the Active-RC filter was selected. Moreover, a fully differential operational amplifier with common-mode feedback (CMFB) was employed as a critical building block. With a 4th-order butterworth low-pass-type topology, based on the tow-thomas biquad, the filter was synthesized. Its bandwidth can be programmed to 480/600/700/900/1100/1680 kHz with an attenuation greater than 50dB at frequencies of $10 \times f_c$ (cutoff frequency). The filter exhibits many advantages, such as low order, low power consumption, small size, wide cutoff frequency selection range and high linearity. From a single 1.8 V power supply, simulations show that the filter has an input referred noise of 74.3 nV/$\sqrt{}$Hz, a third-order intercept point (IIP3) of 24.25 dBm, and a power consumption of 12.42 mW.

Experimental Evaluation of Cytotoxicity Effects in Cancer and Normal Cells Exposed to Far Infrared Radiation

P. Peidaee[1], **T. Istivan**[2], **R. Shukla**[3, 4], **and E. Pirogova**[1, 4]

[1]School of Electrical and Computer Engineering, RMIT University, Melbourne, Australia
[2]Department of Biotechnology and Environmental Biology, School of Applied Sciences
RMIT University, Bundoora, Victoria, Australia
[3]Department of Applied Chemistry, School of Applied Sciences
RMIT University, Bundoora, Victoria, Australia
[4]Health Innovation Research Institute, RMIT University, Australia

Abstract— It has been proven that many of biological processes are frequency selective processes that relate to quantum energy state of photosensitive molecules. Here we have studied experimentally the hypothesis of the Resonant Recognition Model (RRM) that proposes that an external electromagnetic field at a particular activation frequency would produce resonant effects on protein biological activity, and this activation frequency can be determined computationally.

In this study, we designed an exposure system based on IR-LED to irradiate the selected cancer and normal cells in the wavelength range predicted computationally by the RRM. The experimental evaluation of the attained far infrared (IR) wavelengths of 3400 nm, 3600 nm, 3800 nm, 3900 nm, 4100 nm and 4300 nm was conducted on a murine melanoma (B16F0) and Chinese Hamster Ovary (CHO) cells. CHO cells are normal cells and used here as a control and B16F0 is cancer cell line.

A comprehensive quantitative analysis of the exposed and sham-exposed B16F0 and CHO cells has been carried out. The results obtained from LDH cytotoxicity test of B16F0 and CHO cells exposed to the computationally predicted wavelengths of far IR light presented and discussed here. In addition qualitative analysis of the effects of applied radiation on cancer and normal cells was performed using the light microscopy. The results obtained demonstrate the changes in cell viabilities of ofB16F0 cells exposed to far infrared light radiation.

The Effect of Pulse Parameters and Medium Information on the Temporal Coherence Length of a Partially Coherent Pulse on Scattering

Chaoliang Ding* **and Liuzhan Pan**
College of Physics and Electronic Information, Luoyang Normal University, Luoyang 471022, China

Abstract— The changes of the temporal coherence length of partially coherent plane-wave pulse produced by scattering from quasi-homogeneous random medium are studied with the accuracy of the first Born approximation. It is shown that the temporal coherence length of scattered partially coherent plane-wave pulse, depending on the medium properties and incident pulse parameters, varies non-monotonously with increasing scattering angle. The numerical calculation results are given.

*Corresponding author: Chaoliang Ding (dingchaoliang2006@126.com).

Investigating Embedded Planar Electromagnetic Band Gap (EPEBG) Structure for Noise Suppression in PCBs

Yao-Te Shu and Jiun-Hwa Lin
Department of Electrical Engineering, National Taiwan Ocean University, Keelung, Taiwan

Abstract— The embedded planar electromagnetic band gap (EPEBG) structure has been studied and discussed in recent years [1]. It provides an additional reference plane for current return path, so EPEBG has better signal integrity (SI) than the traditional planar EBG structures.

The EPEBG structure is mainly divided into the metal patches, metal branches and shorting vias. We found that the metal branch placements would have effect on the results of noise suppression performance. We investigate three types of metal branches placements: the branches at the middle of the patches, the branches at the corner of the patches, and the branches either at the middle or at the corner of the patches, as shown in Fig. 1(a). We observe that the EPEBG with hybrid placements of the metal branches can achieve the widest noise suppression bandwidth (red line), as shown in Fig. 1(b).

Many scholars studied the EPEBG structures of the noise suppression by a 3D full-wave electromagnetic simulation software, such as CST or HFSS, but it takes a lot of time in simulation, usually more than an hour. In this thesis, we propose the equivalent circuit models for the EPEBG structures, as shown in Fig. 2(a), Fig. 2(b). Cases of different EBG dimensions, dielectric constant, bridges between patches, and locations of excitation and observations are studied. Both equivalent circuit and full wave results are very similar. Most simulations of the equivalent circuits can be completed in less than a minute.

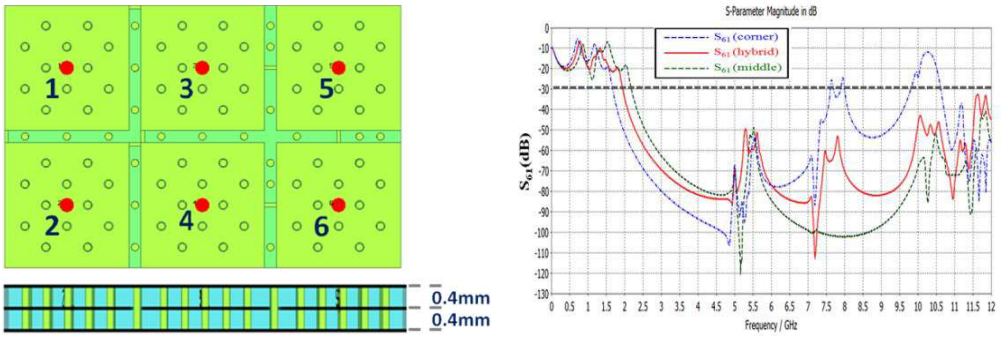

(a) (b)

Figure 1: (a) Hybrid placements of the metal branches. (b) S_{61} comparison of three type branch placements.

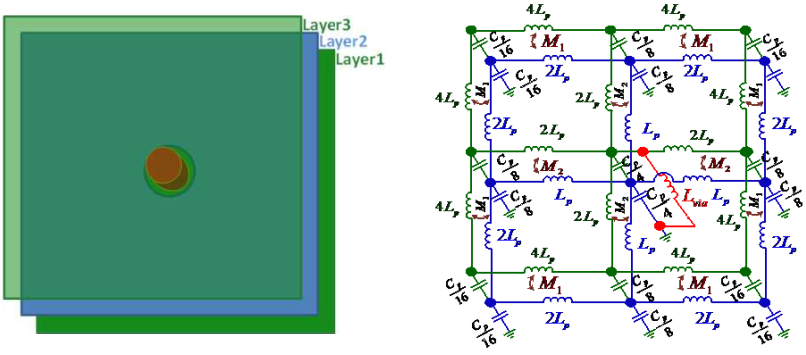

(a) (b)

Figure 2: (a) EPEBG structure. (b) Equivalent circuit model.

REFERENCES

1. Huh, S. L. and M. Swaminathan, "A design technique for embedded electromagnetic band gap structure in load board applications," *IEEE Transactions on Electromagnetic Compatibility*, 443–456, Vol. 54, No. 2, April 2012.

High Isolation Pencil Beams Antenna Array for IEEE802.11a MIMO Application

Dau-Chyrh Chang[1], **Chia-Ping Huang**[1], **Fong-Yi Lin**[1], **Chih-Hung Lee**[2, 3], **Ming-Ching Yen**[1], **and Yau-Jyun Tsai**[1]

[1]Oriental Institute of Technology, Taiwan
[2]Yuan Ze University, Taiwan
[3]Electronics Testing Center, Taiwan

Abstract— The effect of multipath fading will decrease the communication data throughput or increase the bit error rate. In order to reduce the multipath fading, the MIMO (multiple input multiple output) communication system is widely used in nowadays. The performance of MIMO communication system will be dominated by the port isolation. Usually, the ECC (envelope correlation coefficient) will be used to describe the performance of MIMO communication system. The lower the port isolation the higher the ECC (envelope correlation coefficient) value will be. In order to increase the communication range with high data throughput, dual pencil beams with high isolation is developed.

In this paper, two independent antenna array with dual linear polarization (vertical polarization and horizontal polarization) is developed for IEEE802.11a MIMO application. Figure 1 shows the simulation model and hardware implementation. Figure 2 shows the peak gain comparisons for simulation and measurement at vertical polarization port and horizontal polarization port. The 3 dB beamwidth for E-plane and H-plane is about 35 degrees. The measured peak gain of two pencil beams is around $12 \sim 13$ dBi for the desired frequency band.

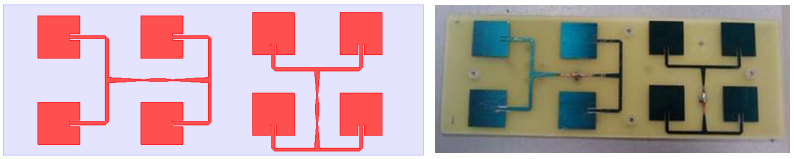

(a) (b)

Figure 1: Simulation model and hardware implementation. (a) Simulation model. (b) Hardware implementation.

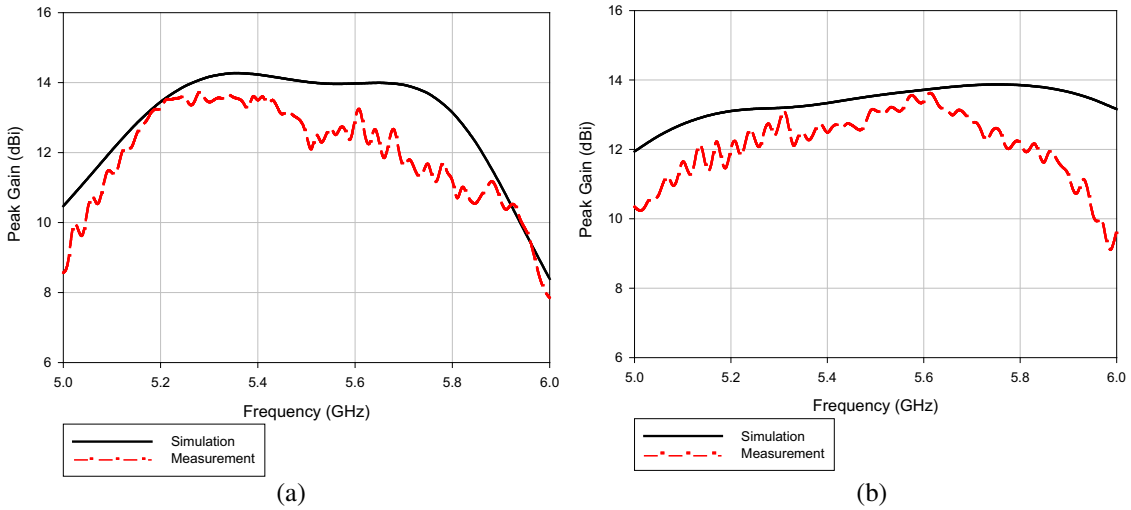

Figure 2: Simulated and measured peak gain comparisons for different polarizations. (a) Peak gain for vertical polarization. (b) Peak gain for horizontal polarization.

Session 3P1
Plasmonic Nanophotonics 2 - Analysis, Theory, Calculation and Simulation

Universal Scaling Relation of Plasmonic Refractive Index Sensors
Yen-Kai Chang, Zong-Xing Lou, Kao-Der Chang, Chih-Wei Chang, ... 540

Dispersion Relation, Zero Refraction, and Nano-focusing in 1D Chiral Metamaterials
Wei-Chih Liu, ... 541

Magnetic Plasmon Induced Transparency in Three Dimensional Metamolecule
Chun Yen Liao, Pin Chieh Wu, Wei Ting Chen, Kuang Yu Yang, Greg Sun, Ai Qun Liu, Nikolay I. Zheludev, Din Ping Tsai, ... 542

Addressable Nanoscale Light Localizations in Hybrid Plasmonic Nanostructures
Minghui Hong, Tsung Sheng Kao, Mohsen Rahmani, ... 543

Optical Refractive Index Sensor Based on Upright U-shape Metamaterials
Hsiang-Lin Huang, Pin Chieh Wu, Kuang Yu Yang, Ta-Jen (David) Yen, Din Ping Tsai, Hai-Pang Chiang, ... 544

Electromagnetic Scattering Field Computation on Plasmonic Structures
Yong-Gu Lee, ... 545

Plasmonic Gap Modes in a Nano-antenna with Particle-film Configuration
Chua-Zu Huang, Ting-Hao Wang, Lingling Tang, Shiuan-Yeh Chen, ... 546

Radiative and Non-radiative Channels of Molecule Fluorescence Near Hyperbolic Half Space
Vasily V. Klimov, Dmitry V. Guzatov, Vitaly Savinov, ... 547

Enhancing Efficiency of Electromagnetic Simulation in Time-domain with Transformation Optics
Jian-Shiung Hong, Wei-Ming Cheng, Ruei-Cheng Shiu, Yung-Chiang Lan, Kuan-Ren Chen, ... 548

Chiral Surface Plasmon Modes on Metallic Nanorods
Chih-Min Chen, Chih-Kai Yang, Yung-Chiang Lan, ... 549

Analysis of Transmission Characteristics and Multiple Resonances in Plasmonic Gratings Coated with Homogeneous Dielectrics
P. Arora, Ananth Krishnan, ... 550

Universal Scaling Relation of Plasmonic Refractive Index Sensors

Yen-Kai Chang[1], **Zong-Xing Lou**[1, 2], **Kao-Der Chang**[3], **and Chih-Wei Chang**[1]

[1]Center for Condensed Matter Sciences, National Taiwan University, Taipei 10617, Taiwan
[2]Department of Physics, National Taiwan University, Taipei 10608, Taiwan
[3]Nanotechnology Research Center, Industrial Technology Research Institute, Hsinchu 31040, Taiwan

Abstract— Subwavelength metal structures exhibiting plasmonic resonances have enabled widespread interests in their potential applications in chemical sensing and super-resolution imaging. Since the optical responses of these metal structures are largely determined by their geometries, each metal structure can be considered as an artificial atom (plasmonic atom) for light. The great design flexibilities of these plasmonic atoms have led to many extraordinary optical phenomena that can be manipulated by advanced chemical synthetic or nano-lithographic methods. Because the resonant frequencies of these plasmonic atoms are highly sensitive to the environmental media, they have been utilized as subwavelength refractive index sensors. Previous intensive experimental studies on plasmonic atoms of varieties of geometries have stimulated a lot of interests. However, these works mainly focus on highlighting the specialties of each plasmonic atoms, only few works have devoted to understanding the universal behaviors. " Here we establish experimental and numerical evidence that the refractive index sensitivities of subwavelength plasmonic atoms and molecules obey a simple universal scaling relation that the sensitivities linearly increase with the resonant wavelengths and exhibit a slope 1/RIU instead of 2/RIU predicted theoretically. The universal scaling relation is independent of the geometrical structures or contributions of multipolar resonances of plasmonic atoms. It is also independent of spatial distributions or field enhancements of electromagnetic hot spots in plasmonic molecules. The universal scaling relation reveals the fundamental standing wave resonances for all plasmonic atoms and the predominant near-field electric couplings for most plasmonic molecules. It also helps to exclude some magnetically coupled plasmonic molecules for practical refractive index sensors due to their reduced sensitivities.

Dispersion Relation, Zero Refraction, and Nano-focusing in 1D Chiral Metamaterials

Wei-Chih Liu
Department of Physics, National Taiwan Normal University, Taiwan, R.O.C.

Abstract— Chiral metamaterials provide an approach to achieve negative refraction without negative ϵ or negative μ. Due to the chiral nature of biological molecules, chiral metamaterial is also expected to play an important role on future bio-medicine research. Since research works in metamaterials grow quickly in recent years, it is possible to study the chiral metamaterial with large anisotropy in permittivity and in permeability. This work is to understand the optical properties of the chiral metamaterials which has rotational permittivity and permeability on the different principal optical axes. The dispersion relation for light propagating in 1D periodic chiral metamaterials is solved analytically and numerically. Besides having different circularly polarization states, the two optical modes have folded band structures. These folded bands do not extend to entire first Brillouin zone, and they imply the peculiar feature where the large refractive index transfers from positive to negative through different frequency regions. Both negative and positive refractive index can happen for the different modes in the same frequency. Moreover, there is zero refractive index, which is due to optical anisotropy instead of frequency-dependent large anomalous dispersive materials. Numerical simulations demonstrate light propagation properties in the chiral metamaterials near the zero refractive index and large refractive index. Nano-focusing of the selected circularly light is observed, while the orthogonal circularly light is diffused or absorbed.

Magnetic Plasmon Induced Transparency in Three Dimensional Metamolecule

C. Y. Liao[1], P. C. Wu[2], W. T. Chen[2], K.-Y. Yang[2], G. Sun[3], A. Q. Liu[4], N. I. Zheludev[5], and D. P. Tsai[1, 2, 6]

[1]Department of Physics, National Taiwan University, Taipei 10617, Taiwan
[2]Graduate Institute of Applied Physics, National Taiwan University, Taipei 10617, Taiwan
[3]Department of Physics, University of Massachusetts Boston, MA 02125, USA
[4]School of Electrical and Electronic Engineering
Nanyang Technological University, Singapore 639798, Singapore
[5]Optoelectronics Research Centre and Centre for Photonic Metamaterials
University of Southampton, Southampton SO17 1BJ, UK
[6]Research Center for Applied Sciences, Academia Sinica, Taipei 11529, Taiwan

Abstract— In a laser-driven atomic quantum system, a continuous state couples to a discrete state resulting in quantum interference that provides a transmission peak within a broad absorption profile the so called electromagnetically induced transparency (EIT). In the field of plasmonic metamaterials, the sub-wavelength metallic structures play a role similar to atoms in nature. The interference of their near-field coupling at plasmonic resonance leads to a plasmon induced transparency (PIT) that is analogous to the EIT of atomic systems. A sensitive control of the PIT is crucial to a range of potential applications such as slowing light and biosensor. So far, the PIT phenomena often arise from the electric resonance, such as an electric dipole state coupled to an electric quadrupole state. Here we report the first three dimensional photonic metamaterial consisted of an array of erected U-shape plasmonic gold nanostructures that exhibits PIT phenomenon with magnetic dipolar interaction between magnetic metamolecules a promising approach to achieve magnetic plasmon devices. We further demonstrate using a numerical simulation that the coupling between the different excited pathways at an intermediate resonant wavelength allows for a π phase shift resulting in a destructive interference. A classical RLC circuit was also proposed to explain the coupling effects between the bright and dark modes of EIT-like electromagnetic spectra.

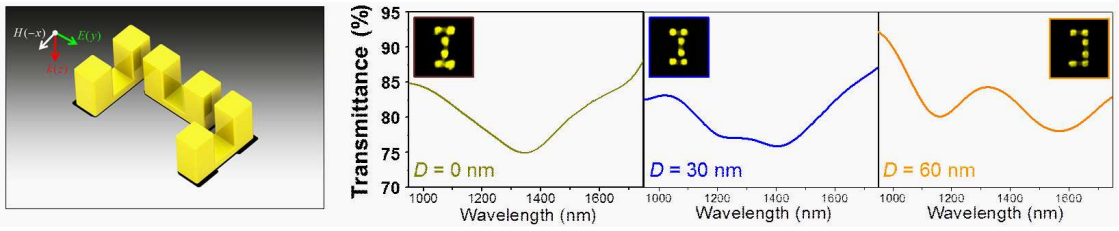

(a) (b)

Figure 1: (a) Schematic diagram of a single SRR metamolecule unit cell. Each unit cell consisted of three erected gold SRRs with 600 nm period in both x and y directions. The optical properties of such metamolecule are studied in the case of y-polarized illumination. (b) The experimental transmittance spectra upon varying distance parameter D. All the insets show the top-view SEM images of the corresponding samples.

Addressable Nanoscale Light Localizations in Hybrid Plasmonic Nanostructures

Minghui Hong[1], **Tsung Sheng Kao**[1], **and Mohsen Rahman**[1, 2]

[1]Department of Electrical & Computer Engineering
National University of Singapore, Singapore
[2]Data Storage Institute, ASTAR, Singapore

Abstract— With the rapid development of nanophotonics and the strong demand on improvement of microscope techniques, there has been increasing attention on localizing and concentrating the optical energy of a light beam to form a subwavelength focused spot. Thus, within the last few decades, a number of promising concepts of subwavelength optical field generation and detection have been widely proposed and experimentally demonstrated, some of which have made significant breakthroughs in biological specimen imaging and nanostructure fabrication. Meanwhile, a great deal of effort has been made in controlling and manipulating focused subwavelength spots flexibly. However, it is found that most of these techniques are restricted to certain wavelengths, limited nanosystems or fail to achieve nanoscale accuracy in optical manipulation.

To overcome the limitations above, this paper will focus on manipulating characteristics of light and using various kinds of nanostructures, with the aim of easily and precisely creating and controlling nanoscale light localizations. Fundamental theories and experimental methods relevant to this theme will be discussed. Through this work, a new scheme of light localization can be developed and hence applied in practical areas such as super-resolution imaging, ultra-high density data storage, optical nanolithography and nanoluminescent bio-assay labeling.

Optical Refractive Index Sensor Based on Upright U-shape Metamaterials

Hsiang Lin Huang[1], **Pin Chieh Wu**[2], **Kuang Yu Yang**[2], **Ta Jen Yen**[3], **Din Ping Tsai**[2, 4], **and Hai-Pang Chiang**[1, 5]

[1]Institute of Optoelectronic Sciences, National Taiwan Ocean University, Keelung, Taiwan, R.O.C.
[2]Department of Physics, National Taiwan University, Taipei, Taiwan, R.O.C.
[3]Department of Materials Science and Engineering, National Tsing Hua University, Hsinchu, Taiwan
[4]Research Center for Applied Sciences, Academia Sinica, Taipei Taiwan, R.O.C.
[5]Institute of Physics, Academia Sinica, Taipei, Taiwan, R.O.C.

Abstract— Surface plasmon resonance (SPR) [1, 2], and metamaterials have attracted more and more attentions in the research field of nano-optics. Metamaterials are artificial substances in nature and its optical properties are determined by the geometry of the subwavelength structures rather than the optical properties of material which the structures made of. At the beginning of the research field of metamaterials, the main goal is to explore the material with optical properties of negative refractive index. In recent years, sensor applications of metamaterials have been reported in many literatures. In 2009, metamaterial made of nanorods has been employed as surface plasmon resonance sensor substrate, and sensitivity as low as 10^{-4} RIU can be achieved [3].

In this paper, using COMSOL Multiphysics software with algorithm of three-dimensional finite element method (FEM) and Fourier Transform Infrared Spectroscopy (FTIR), computer simulation and experimental verification of the refractive index sensing characteristics of plasmonic arrays based on upright U-shape split ring resonators (SRR) [4] were investigated by observing the displacement of far-field transmittance spectra in the visible region. The upward nano gold split ring resonator coupling with plasmon resonance will cause a phenomenon similar to electromagnetically induced transparency and its transmittance spectra will change according to the change of ambient refractive index. Discrepancies between computer simulation and experimental results will be discussed.

REFERENCES

1. Chiang, H. P., J. L. Lin, and Z. W. Chen, "High sensitivity surface plasmon resonance sensor based on phase interrogation at optimal incident wavelengths," *Appl. Phys. Lett.*, Vol. 88, 141105, 2006.
2. Peng, T.-C., W.-C. Lin, C.-W. Chen, D. P. Tsai, and H.-P. Chiang, "Enhanced sensitivity of surface plasmon resonance phase-interrogation biosensor by using silver nanoparticles," *Plasmonics*, Vol. 6, 29, 2011.
3. Kabashin, A. V., P. Evans, S. Pastkovsky, W. Hendren, G. A. Wurtz, R. Atkinson, R. Pollard, V. A. Podolskiy, and A. V. Zayats, "Plasmonic nanorod metamaterials for biosensing," *Nat. Mater.*, Vol. 8, No. 11, 867–871, 2009.
4. Chen, W. T., C. J. Chen, P. C. Wu, S. Sun, L. Zhou, G. Y. Guo, C. T. Hsiao, K. Y. Yang, N. I. Zheludev, and D. P. Tsai, "Optical magnetic response in three-dimensional metamaterial of upright plasmonic meta-molecules," *Optics Express*, Vol. 19, 12837–12842, 2011.

Electromagnetic Scattering Field Computation on Plasmonic Structures

Yong-Gu Lee
Gwangju Institute of Science and Technology, Gwangju, Korea

Abstract— When electromagnetic beams are illuminated on plasmonic structures, the resulting scattering field exhibit extraordinary strong field enhancement. This strong field can be effectively used for various applications ranging from monitoring of nanoscale particles to nanometric optical trapping of such. The wavelength of incident light, proper material selection and the shape of the structure plays significant role in the result. In this study, we investigate the computer simulation of this intense field enhancement made possible in the proximity of plasmonic structures where plasmonic structures are modeled as holes on gold films and the resulting electromagnetic field is computed using the Finite-Difference Time-Domain method.

Plasmonic Gap Modes in a Nano-antenna with Particle-film Configuration

Chua-Zu Huang, Ting-Hao Wang, Lingling Tang, and Shiuan-Yeh Chen
Department of Applied Materials and Optoelectronic Engineering
National Chi Nan University, Puli 54561, Taiwan

Abstract— In this study, the plasmonic modes of a nano-antenna formed by a particle/film structure are characterized. The plasmonic nano-antennas draw a lot of attention due to their capabilities to convert external excitation into localized field and couple emission originating around them into the far-field region. We have shown that this nano-antenna can "broadcast" the enhanced Raman scattering through the gap dipole mode. In addition to dipole mode, this nano-antenna supports several plasmonic gap modes which have distinct mode profiles. However, these plasmonic modes are usually damped by internal material loss and then overlapped with adjacent modes. These modes can be resolved by experimentally analyzing the scattering pattern and simulating their near-field distribution. These modes also have different responses to p- and s-polarized excitation. Investigation of these high order modes may further help us understand the interaction within the nano-scale regime when the nano-antenna is coupled to a molecule or other active materials nearby. This may be extended as design rules for active plasmonic devices.

Radiative and Non-radiative Channels of Molecule Fluorescence Near Hyperbolic Half Space

Vasily Klimov, Dmitry Guzatov, and Vitaly Savinov
Lebedev Physical Institute, Russian Academy of Sciences, Russia

Abstract— Now hyperbolic metamaterials (HMM) are considered as promising media to enhance decay rate of simple quantum systems [1]. Due to huge local density of photon states the decay rate of molecule near surface of HMM tends to infinity as

$$\Gamma^{rad} \propto \frac{2\sqrt{|\varepsilon_x|\varepsilon_z}}{d^3(1+|\varepsilon_x|\varepsilon_z)} \tag{1}$$

where $d \to 0$ is distance between molecule and HMM surface and $\varepsilon_x = \varepsilon_y, \varepsilon_z$ are lossless components of permittivity tensor.

However if we take into account losses in HMM it is easy to show that non-radiative (Joule) losses also tend to infinity when molecule gets closer to surface of HMM

$$\Gamma^{rad} \sim \frac{\operatorname{Im}\varepsilon}{d^3} \tag{2}$$

In this work we will present results of investigation of relations between (1) and (2) for different materials, molecule positions and orientations of its dipole momentum, and find conditions where nonradiative losses are minimal.

ACKNOWLEDGMENT

The authors thank the Russian Foundation for Basic Research (grants ## No. 11-02-91065, No. 11-02-92002, No. 11-02-01272 and No. 12-02-90014) for financial support of this work.

REFERENCES

1. Jacob, Z., J. Y. Kim, G. V. Naik, A. Boltasseva, E. Narimanov, and V. M. Shalaev, "Engineering photonic density of states using metamaterials," Paper 696, Birck and NCN Publications, 2010, http://docs.lib.purdue.edu/nanopub/696.

Enhancing Efficiency of Electromagnetic Simulation in Time-domain with Transformation Optics

Jian-Shiung Hong[1], **Wei-Ming Cheng**[2], **Ruei-Cheng Shiu**[1], **Yung-Chiang Lan**[1], **and Kuan-Ren Chen**[1, 3, 4, 5]

[1]Institute of Electro-Optical Science and Engineering, National Cheng Kung University
1 University Road, Tainan 70101, Taiwan, R.O.C.
[2]Institute of Space, Astrophysical and Plasma Sciences, National Cheng Kung University
1 University Road, Tainan 70101, Taiwan, R.O.C.
[3]Department of Physics, National Cheng Kung University
1 University Road, Tainan 70101, Taiwan, R.O.C.
[4]Advanced Optoelectronic Technology Center, National Cheng Kung University
1 University Road, Tainan 70101, Taiwan, R.O.C.
[5]Research Center for Energy Technology and Strategy, National Cheng Kung University
1 University Road, Tainan 70101, Taiwan, R.O.C.

Abstract— Applying transformation optics (TO) for converting non-uniform physical grids, we propose a novel method to enhance the electromagnetic finite-difference time-domain simulation efficiency. In contrast to designing applications of TO devices, the non-uniform physical grids and the homogeneous mediums are mapped into uniform numerical grids with the corresponding inhomogeneous mediums so that one can use a common simulation package that attaches the implement of anisotropic medium without any further modification of the source code. This makes the proposed method superior to conventional non-uniform grid methods. The Courant condition is verified in both physical and numerical coordinates. We demonstrate, as an example, the simulation of an electromagnetic wave propagating through a rectangle subwavelength slit in an infinite film of nearly perfectly electric conductor. The physical grids are designed to be non-uniform in one dimension with the cell sizes to be smaller around the slit area as required by resolution and to be larger at other areas for reducing the overall cell number. We show that the efficiency of the simulation is enhanced by the proposed method, which saves 11 times of the memory and 5 times of loop time. It is expected, if the coordinate transform is extended to three-dimension, the efficiency could be enhanced to the power of three.

Chiral Surface Plasmon Modes on Metallic Nanorods

Chih-Min Chen, Chih-Kai Yang, and Yung-Chiang Lan
Department of Photonics, National Cheng Kung University, Taiwan, R.O.C.

Abstract— Chiral surface plasmon (CSP) mode on metallic nanorods has been found recently. This special mode is formed by combination of TM_0 and HE_1 SP modes. However, the CSP modes that are composed of higher-order SP modes have never been observed on metallic nanorods. Neither has propagation of the CSP modes on metallic nanocones been investigated.

In this study, the CSP modes on silver (Ag) nanorods and nanocones are explored by performing both FDTD simulations and theoretical analyses. The radius of Ag nanorod is 60 nm. For the truncated cone, the radii of lower and upper bases and the height are 120 nm, 60 nm and 9000 nm, respectively. The Drude model of Ag is used in the simulation with the plasma frequency and collision frequency set to 1.32×10^{16} and 0.68×10^{14}, repsectively. The surrounding material is the matching oil with the relative permittivity of 2.25. The incident wave length is 632.8 nm. The propagation constants and field patterns of SP modes on Ag nanorods are acquired by solving their dispersion relations.

The CSP modes that are composed of higher-order HE_1 and HE_2 SP modes are observed in FDTD simulation. The HE_1 and HE_2 modes have dipole- and quadrupole-like, respectively, field pattern on the metallic nanorods. Dependent on the rotation direction of the HE_1 and HE_2 modes parallel or opposite to each other, the time-averaged electric field energy of the CSP modes exhibit single-strand or three-strand, respectively, spiral patterns. The simulated spiral pitches agree well with those obtained from theoretical calculation. When the CSP mode that is composed of the TM_0 and HE_1 modes propagates along the truncated cone from the larger base side, the spiral pitch of the mode decreases gradually. Furthermore, the field energy intensity increases to a maximum value and then falls.

Analysis of Transmission Characteristics and Multiple Resonances in Plasmonic Gratings Coated with Homogeneous Dielectrics

P. Arora and A. Krishnan
Department of Electrical Engineering, Indian Institute of Technology Madras, Chennai, India

Abstract— Grating Coupled and Waveguide Coupled Surface Plasmon Resonances (GCSPR and WCSPR) are alternatives to Kretschmann's configuration to excite the Localized Surface Plasmons (LSPs), forward and backward propagating Surface Plasmons (SPs) and waveguide coupled plasmonic modes [1]. GCSPR and WCSPR offer the possibility of using near normal incidences to excite the Plasmon modes, and provide a method to integrate surface Plasmon devices on a planar chip along with other optical devices [1].

In this paper, we present the transmission characteristics of two different structures involving a single grating layer for easiness of fabrication. Firstly, a Binary Metal Grating (BMG) of finite thickness and period, on a BK-7 glass substrate was analyzed for its sensitivity to a homogeneous dielectric film (acting as a superstrate) with different refractive indices and thicknesses. Secondly, a Metal binary Grating on top of a homogeneous Metal film (MGM) coated on a bulk glass substrate was investigated. These structures have potential to be used in transmission based experiments involving normal incidences as in the case of using a high numerical aperture objective in a transmission optical microscope. Simulations of these structures were performed using home made Rigorous Coupled Wave Analysis (RCWA) [2] and the field distributions were obtained using a commercial finite elements full wave solver.

A systematic analysis of the effect of geometrical parameters of the gratings, refractive index of the superstate, polarization etc. were performed on BMG and MGM structures to extract the origin of the multiple plasmonic resonances in these structures. Under normal incidence, in BMG three distinct modes could be excited corresponding to WCSPR, SP mode, leaky mode (at metal/glass substrate interface) as shown in Fig. 1(a). The field distributions for these resonances are shown in Figs. 1(b), 1(c) and 1(d) respectively. Both the WCSPR and SP modes of BMG offer a sensitivity of 500nm/RIU, however the Full Width at Half Maximum (FWHM) of the waveguide modes is 35nm which is much lower compared to 95nm of the SP mode. Secondly, the thickness of the superstrate can be ascertained using the spectral position of the SP mode and the WCSPR mode. However, it should be noted that the WCSPR mode occurs only after a critical thickness of superstrate. A third mode excited in these structures corresponds to the leaky modes coupled to the metal substrate interface and offer no effect to the sensitivity.

The MGM structure showed a FWHM of 15 nm and less than 50% of the FWHM compared to BMG structure, which was attributed to the excitation of LSPs. In this structure, since the grating has no variation in sizes between difference grooves, the LSP resonance is spectrally narrow. These structures under normal incidences provided a sensitivity of similar to BMG structure, however, the narrower spectral dips in transmission provide a clearly observable change in refractive indices of the superstrate. An analysis of polarization dependence was performed on BMG structures with TE waves revealed SP and WCSPR resonances with no leaky mode coupling.

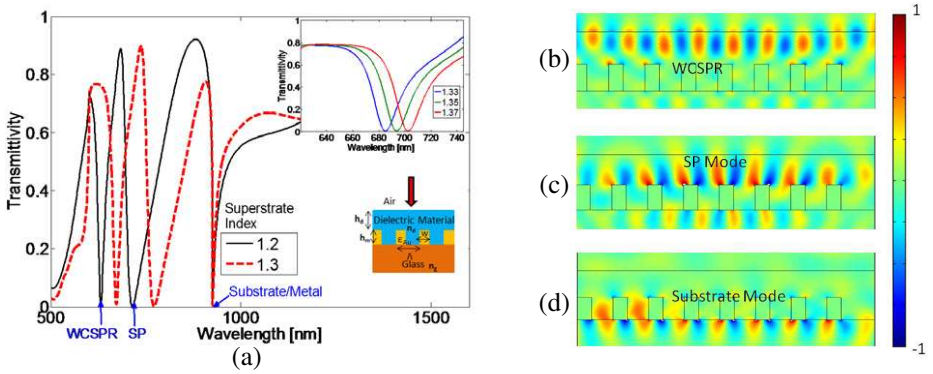

Figure 1: (a) Transmittivity for BMG configuration (b), (c) and (d) E-field distributions at different resonances.

We conclude that a single grating layer based GC/WCSPR offer easiness of fabrication and provide reasonable sensitivities of the order of 500 nm/RIU with broadband visible wavelength excitation under different polarizations, compatible with technologies that involve integrated sensors based on normal incidences. These structures also involve transmission based experimental setups that are widely available as microscopes with high numerical aperture objectives.

REFERENCES

1. Homola, J., et al., "Surface plasmon resonance sensors: Review," *Sensors and Actuators B*, Vol. 54, 3–15, 1999.
2. Moharam, M. G., et al., "Formulation for stable and efficient implementation of the rigorous coupled wave analysis of binary grating," *J. Opt. Soc. Am. A*, Vol. 12, 1068–1076, 1995.

Session 3P2a
Intelligent Electronics

The Design and Implementation of a MISO Fuzzy Logic Controller Based on CPLD
Chien-Nan Lee, Kai-Teng Jheng, ... 554
Mobile Mouse Pad
Li-Lin Chen, ... 555
An ECG Signal Enhancement Based on Improved EMD
Mei-Lin Su, Keh-Shih Chuang, ... 556
A Rehabilitation Device for the Patients of Carpal Tunnel Syndrome
Li-Lin Chen, ... 557

The Design and Implementation of a MISO Fuzzy Logic Controller Based on CPLD

Chien-Nan Lee and Kai-Teng Jheng
Department of Electronic Engineering, Oriental Institute of Technology
New Taipei City, Taiwan

Abstract— The main purpose of this approach is designing and realizing a MISO (Multi-Input Single-Output) fuzzy logic controller based on CPLD. The power control system for a mobile radio channel that was regarded as the example, two input variables are signal error and error-change, output variable is the signal power increment. The main component of a fuzzy logic controller include the fuzzification interface, knowledge base, decision- making logic and defuzzification interface. This approach design the fuzzification interface with the truth table, design the database and decision logic with decoder, ROM and comparator, etc., design the defuzzification interface with multiplier, adder, divider and truth table, etc. According to the design method may realize a fuzzy logic controller very much easily.

Mobile Mouse Pad

Li-Lin Chen
Electronic Engineering Department, Oriental Institute of Technology
New Taipei City, Taiwan, R.O.C.

Abstract— Carpal tunnel syndrome is a common modern occupational disease, which is often diagnosed among people whose work requires their wrists repeating the same action or exerting excess strength over a long period. For example, personnel who use the computer for long periods employ the mouse for hours every day, inducing repeated and excess movements of the wrist joints. This may compress or damage the median nerve that travels through the wrist and block nerve conduction, thereby numbing the hand and obstructing hand movements [1, 2].

To prevent suffering resulting from carpal tunnel syndrome caused by the long-term use of computers, a mobile mouse pad is developed in this study, which can detect the amount of time people use the mouse. The air-pump motor in the mobile mouse pad can charge and release air regularly to repeat the up-down and left-right movements of the pad, thereby relieving and stretching the median nerve in the wrist. This product also initiates voice alarms periodically to remind users to stop operating the mouse and rest their hands appropriately. If a user continues to use the mouse, the voice reminder repeats. Consequently, this product can be used to prevent diseases and conditions related to an excess burden on the wrists.

REFERENCES

1. Horng, Y., S. Hsieh, Y. Horng, and M. C. Lin, "Occupational carpal tunnel syndrome," *Taiwan Journal of Public Health*, 85–92, 2009.
2. Lin, J., "Chinese new year syndromes: Beware of video-game and cell-phone elbows," *Consumer Reports of Taiwan*, Vol. 385, 21–23, 2011.

An ECG Signal Enhancement Based on Improved EMD

Mei-Lin Su[1] and Keh-Shih Chuang[2]

[1]Department of Communication Engineering
Oriental Institute of Technology, Taiwan
[2]Department of Biomedical Engineering & Environmental Sciences
National Tsing-Hua University, Taiwan

Abstract— Electrocardiogram (ECG) is an important biological signal to diagnose cardiac arrhythmia. The P wave is the combined result of the action potentials of the atrial muscle units, while the QRS and T waves are formed by the spatio-temporal summation of the action potentials of the ventricular muscle units. However, ECG signals are often corrupted by various noise, such as muscle noise, baselines wander and power-line interference. Therefore, ECG noise reduction is an important issue and has been studied for many years. A common encountered in ECG de-nosing systems is the removal of unwanted disturbances, i.e., a low-pass filter was designed to remove the high-frequency noise, and a high-pass filter was designed to remove the low-frequency noise. These filter banks based denoising process smooth the P and R amplitude of ECG signal and it is less robust to different levels of noise.

Comparatively, the empirical mode decomposition (EMD) based on the decomposition of data into a collection of intrinsic mode function (IMF) was investigated to improve the ECG signals. In this study, we proposed an adaptive method to select the IMF index for separating the noise components from the ECG signal. The performance of the proposed method is evaluated in terms of standard metrics by performing extensive simulations using the MIT-BIH arrhythmia database. The results show improvements of ECG signals at different levels of SNR. Moreover, the low frequency noise components are separated by a partial reconstruction from the IMFs and still preserve the QRS complex.

A Rehabilitation Device for the Patients of Carpal Tunnel Syndrome

Li-Lin Chen
Electronic Engineering Department
Oriental Institute of Technology, New Taipei City, Taiwan, R.O.C.

Abstract— People who move their wrist repetitively or under excessive force are prone to developing carpal tunnel syndrome (CTS). Cooks, pianists, and computer operators are among the people most likely to experience this condition. In modern society, people use computers not only for work but also for leisure and recreation activities. Thus, the incidence of CTS has risen, with the affected patients becoming increasingly younger. The primary symptom of carpal tunnel syndrome is numbness and paresthesia of the thumb, index, and third fingers [1, 2]. The impact of the condition for patients includes disturbed sleep because by severe wrist pain and to danger the future functions of their wrists. Thus, we have developed a rehabilitation device for the patients of CTS.

The CTS rehabilitation device developed in this study offers the following functions: (1) the patient's wrist is held at a fixed angle and then repeatedly rotated clockwise and counterclockwise for a specific period; (2) the lifted angles can be adjusted according to doctor recommendations and the situation of each patient; (3) the device rotation time and duration can be adjusted according to the specific stage of rehabilitation; (4) heat can be applied to the wrist to relieve pain; and (5) the small size of the device enable use at any time and place. Furthermore, the device can be employed for both the rehabilitation and prevention of CTS.

REFERENCES

1. Horng, Y., S. Hsieh, Y. Horng, and M. C. Lin, "Occupational carpal tunnel syndrome," *Taiwan Journal of Public Health*, 85–92, 2009.
2. Lin, J., "Chinese new year syndromes: Beware of video-game and cell-phone elbows," *Consumer Reports of Taiwan*, Vol. 385, 21–23, 2011.

Session 3P2b
RF, Microwave and Millimeter-wave Measurements

Estimation of Rain Attenuation at C, Ka, Ku and V Bands for Satellite Links in South Africa
Senzo Jerome Malinga, Pius Adewale Owolawi, Thomas Joachim Odhiambo Afullo, ... 560
Computation of Rain Attenuation through Scattering at Microwave and Millimeter Bands in South Africa
Senzo Jerome Malinga, Pius Adewale Owolawi, Thomas Joachim Odhiambo Afullo, ... 561
Six-port Based Wave Correlator with Application to Micro-displacement Measurement
Nobuaki Iwaki, Fengchao Xiao, Toshiyuki Yakabe, ... 562
Accuracy of Transmission Loss Measurements in W-band Antenna Gain Calibration System
Anton Widarta, Michitaka Ameya, ... 563
Uncertainty in Waveguide Vector Network Analyzer Measurements in the Frequency Range of D-band (110 GHz to 170 GHz)
Masahiro Horibe, Ryoko Kishikawa, ... 564
Applying Effective Medium Theory in Characterizing Dielectric Constant of Solids
Sucheng Li, Ruirui Chen, Shahzad Anwar, Weixin Lu, Yun Lai, Huanyang Chen, Bo Hou, Fengran Ren, Bangming Gu, ... 565
Downscaling of Passive Microwave Soil Moisture Using Radar and Visible near Infrared Data Sets
Venkat Lakshmi, ... 566

Estimation of Rain Attenuation at C, Ka, Ku and V Bands for Satellite Links in South Africa

S. J. Malinga[1], **P. A. Owolawi**[1], **and T. J. O. Afullo**[2]

[1]Department of Electrical Engineering, Mangosuthu University of Technology
Umlazi, KwaZulu-Natal, South Africa
[2]Department of Electrical, Computer and Electronics Engineering
University of KwaZulu-Natal, Durban, South Africa

Abstract— Despite the fact that over 20 fibre optic cable networks have been rolled out in Africa, satellite infrastructures continue to fulfil an important role in providing communication access to rural, remote and inland areas across the continent. The fast growth in telecommunications, increased demand for bandwidth, congestion in lower frequency bands and miniaturization of communication equipment have forced the designers to employ higher frequency bands such as the C (4 to 8 GHz), Ka (26.5 to 40 GHz), Ku (12 to 18 GHz) and V (40 to 75 GHz) bands. Rain is the most deleterious to signal propagation in these bands. The contribution of rain attenuation to the quality of signals in these bands, especially in the tropical and subtropical bands in which South Africa is located, need to be studied. The aims of this paper are to estimate the magnitude of rain attenuation using the ITU-R model, carry out link performance analysis, then propose reasonable, adequate fade margins that need to be applied for all provinces in South Africa.

Computation of Rain Attenuation through Scattering at Microwave and Millimeter Bands in South Africa

S. J. Malinga[1], **P. A. Owolawi**[1], **and T. J. O. Afullo**[2]

[1]Department of Electrical Engineering, Mangosuthu University of Technology
Umlazi, KwaZulu-Natal, South Africa
[2]Department of Electrical, Computer, and Electronics Engineering
University of KwaZulu-Natal, Durban, South Africa

Abstract— Attenuation due to rain at frequencies above 10 GHz in temperate climates and above 7 GHz in tropical, sub-tropical and equatorial climates is a critical factor for both terrestrial and satellite link system designers. This paper presents results of computed and measured attenuation due to rain, using the spherical method (Mie Scattering technique) and non-spherical method (Pruppacher and Pitter technique). The derived scattering amplitude coefficients are incorporated with available measured rain rate and droplet size distribution data to estimate specific and total attenuation for the region of South Africa. The results are then compared with the few existing rain attenuation models and one-year attenuation measurement campaign in Durban, South Africa. The results are further applied to the terrestrial radio links and satellite links at a chosen rain rate and specified frequencies. These results will serve as a good tool for radio planning engineers and technicians especially in the Southern African region where no comprehensive work has been carried out in the field of radio propagation through rain.

Six-port Based Wave Correlator with Application to Micro-displacement Measurement

N. Iwaki , F. Xiao, and T. Yakabe
The University of Electro-Communications, Japan

Abstract— As a remote sensing application of the six-port based wave-correlator (SPC), measuring the micro displacement of an object is discussed in this paper. One of the applications of this work is expected to predict landslide accidents by monitoring the micro displacement. The SPC is a two-channel wave receiver for determining the vector relation, both amplitude and phase difference, between the two input signals by measuring the power levels. A measurement system with a MMIC SPC is developed, which includes differential amplifiers, AD converters, control circuits, and microwave components such as isolators, a small type oscillator, a directional coupler and two horn antennas. The microwave generated in the internal small type oscillator is transmitted by a transmitter to irradiate the object. Then the reflected wave by the object is received by a receiver. The micro displacement is obtained from the phase difference between the two input signals: one is the microwave generated directly from the small type oscillator and the other is the microwave received by the receiver. The system parameters of the instrument describe the characteristics of the system, which include the signal loss, the wave leakage and any other factors. The micro displacement is determined if these system parameters are identified accurately. A novel calibration method uses an automatic positioning stage, a reflector and terminations. In the experimental, we verified the validity of the proposed calibration method by computing the micro displacement with the obtained system parameters. The computed results of the micro displacement exemplified the possibility of the developed measurement system in the practical application. The results have some discrepancy as compared with the reference values, and the improvement of the measurement accuracy will be further investigated.

Accuracy of Transmission Loss Measurements in W-band Antenna Gain Calibration System

Anton Widarta and Michitaka Ameya
National Metrology Institute of Japan (NMIJ)
National Institute of Advanced Industrial Science and Technology (AIST)
AIST Tsukuba Central, 1-1-1 Umezono, Tsukuba, Ibaraki 305-8563, Japan

Abstract— With recent developments in CMOS technologies, mm-wave has been applied in a lot of fields, such as radars for vehicular safety, security imaging systems at airport and high-speed wireless communications. Especially in radar applications, W-band (75 GHz to 110 GHz) mm-wave radar is already in practical use as an advanced emergency braking system for mitigating collision-damage. The advanced emergency braking system including mm-wave radars becomes mandatory for new type trucks from 2016 in the EU countries, as well as in Japan. For reliability assessment of the W-band radar and building a standard radar target in W-band, the antenna gain calibration in W-band is urgently required.

Accuracy of the antenna gain measurements is highly dependent on the transmission loss measurements carried out by the measuring receiver of the system. Therefore, it is required to evaluate precisely the fundamental characteristics of the receiver, i.e., linearity, before carrying out the measurements. In RF and microwave frequency range (10 MHz to 18 GHz), the linearity of a receiver is usually assessed by measuring a calibrated attenuation change of a step attenuator at different input power levels. However, in such this W-band high frequency range, standard laboratories that can provide attenuation calibration are still scarce and not available in Japan. On the other hand, our W-band antenna gain calibration system works based on the heterodyne detector technique, where the transmission loss occurs between the transmitting and receiving antennas is converted into low frequency ($f = 7.605$ MHz), and then is measured by the receiver. This condition allows us to assess the linearity of the receiving system using a calibrated step attenuator at 7.605 MHz.

This paper describes details of the linearity assessment procedure and the initial experiment results of our W-band antenna gain calibration system, performed with a calibrated step attenuator at 7.605 Hz. It is expected that the linearity of the system is better than 0.004 dB/dB.

Uncertainty in Waveguide Vector Network Analyzer Measurements in the Frequency Range of D-band (110 GHz to 170 GHz)

Masahiro Horibe and Ryoko Kishikawa
National Metrology Institute of Japan
National Institute of Advanced Industrial Science and Technology, Japan

Abstract— We have evaluated the measurement uncertainty for rectangular waveguide Vector Network Analyzer (VNA) measurements in the frequency range of D-band, 110 GHz–170 GHz. We developed a new waveguide flange design for precise connections and dimensional measurements to establish traceability to the SI for standard line as a calibration standard in VNA measurements. As the result of evaluation for VNA and its standard, we estimated VNA measurement uncertainty in the D-band.

Applying Effective Medium Theory in Characterizing Dielectric Constant of Solids

Sucheng Li[1], **Ruirui Chen**[1], **Shahzad Anwar**[1], **Weixin Lu**[1], **Yun Lai**[1], **Huanyang Chen**[1], **Bo Hou**[1], **Fengran Ren**[1], **and Bangming Gu**[2]

[1]School of Physical Science and Technology, Soochow University
1 Shizi Street, Suzhou 215006, China
[2]Institute of Applied Physics, Zhejiang Wanli University
8 Qianhu South Road, Ningbo 315101, China

Abstract— In this study, we present a simple approach to measure the permittivity of solid materials, based on the Maxwell-Garnett (MG) effective medium theory. In our method, the powder of the solids under investigation is mixed with silicone oil to form the composite fluid at certain volume fractions. From the measured permittivity of the oil and the composite, we can simply derive the permittivity of the inclusion, i.e., the solid, according to the MG formula. The proof demonstrations are performed on several materials including alumina, glucose, and pearl, and the results show the validity and the robustness of our method. Comparing with the conventional measuring configurations, our advantage is no requirements for solid shape and surface flatness in measurements and the broadband availability. Recently, the system of colloidal suspensions has paved a new way for realizing tunable metamterials and exotic electromagnetic properties like negative refraction. Here our method shows such system is also providing an alternative platform for implementing the material characterization on a level of single particle in an average sense. Finally, the capacity of our directly addressing the powder particles makes it very important to characterize the electromagnetic properties of some functional nanomaterials, such as ferroelectric nanoparticles.

Downscaling of Passive Microwave Soil Moisture Using Radar and Visible near Infrared Data Sets

Venkat Lakshmi
University of South Carolina, USA

Abstract— Soil moisture satellite estimates are available from a variety of passive microwave satellite missions, but their resolution is frequently too large for use by land managers and action agencies. In this paper we present and validate two different methodologies to downscale radiometer retrieved soil moisture. In the first method we use a change detection algorithm and radar data on consecutive days to downscale soil moisture retrieved from an aircraft based radiometer. This algorithm is tested in a field experiment SMEX02 in Ames Iowa. In the second method we use a soil moisture downscaling algorithm based on look-up curves between daily temperature change and daily average soil moisture is presented and developed to bridge the scale. The algorithm was derived from 1/8° spatial resolution North American Land Data Assimilation System (NLDAS-2) surface temperature and soil moisture data, and also used 5 km Advanced Very High Resolution Radiometer (AVHRR) and 1 km Moderate Resolution Imaging Spectroradiometer (MODIS) Normalized Difference Vegetation Index (NDVI) as look-up dataset for different vegetation and surface temperature conditions. The differences between 1 km MODIS temperature downscaled soil moisture values and Advanced Microwave Scanning Radiometer-EOS (AMSR-E) soil moisture values were used to modify AMSR-E soil moistures. These algorithms will be very important when SMAP (Soil Moisture Active Passive) mission is launched by NASA in 2015.

Session 3P3
SAR System and Signal Processing

The Progress of Unmanned Aerial Vehicle Synthetic Aperture Radar Development for Environmental Monitoring
Yee Kit Chan, Voon Chet Koo, Hean-Teik Chuah, ... 568
Development of an Integrated Velocity Compensation Timing and Control Unit for SAR
Huey Shen Boey, Tien Sze Lim, Chua Ming Yam, Voon Chet Koo, ... 569
Design and Development of a Sidelooking Microstrip Patch Antenna for Unmanned Aerial Vehicle Synthetic Aperture Antenna
Poi Ngee Tan, Yee Kit Chan, Tien Sze Lim, Gobi Vetharatnam, ... 570
Performance Evaluation of an Integrated IMU-GPS Motion Sensing System for UAVSAR
Wei Qiang Tan, Chot Chun Lim, Voon Chet Koo, Tien Sze Lim, ... 571
UAV SAR Signal Processing with Motion Error Compensation
Chee-Siong Lim, Voon Chet Koo, Yee Kit Chan, Chot Chun Lim, ... 572
High Speed AD DA for Synthetic Aperture Radar
Ming Yam Chua, Voon Chet Koo, Heng Siong Lim, Huey Shen Boey, Yee Kit Chan, Chot Hun Lim, Tien Sze Lim, Hean-Teik Chuah, ... 573
Realization of Interpolation-free Fast SAR Range-Doppler Algorithm Using Parallel Processing on GPU
Ozgur Altun, Selcuk Paker, Mesut Kartal, ... 574
Performance Analysis of DPCA Based SAR Moving Target Detection
Han Gao, Jingwen Li, Li Zhang, ... 575
A Three-component Model-based Target Decomposition for Compact Polarimetric SAR Data
Lei Xie, Hong Zhang, Chao Wang, Bo Zhang, ... 576

The Progress of Unmanned Aerial Vehicle Synthetic Aperture Radar Development for Environmental Monitoring

Yee Kit Chan, Voon Chet Koo, and Hean Teik Chuah
Faculty of Engineering & Technology, Multimedia University
Jalan Ayer Keroh Lama, Bukit Beruang, Melaka 75450, Malaysia

Abstract— The principle of synthetic aperture radar (SAR) was discovered nearly 40 years ago. It becomes a main tool of microwave remote sensing because of its capability to operate in nearly all weather condition and operates during day and night. As the radar platform flies over an observation area, the doppler spread of the echo signal can be processed using a digital signal processing method. This reduces the number of hardware components for doppler filtering as well as range gating.

Microwave remote sensing is one of the major research areas conducted by a research group in Multimedia University, Malaysia, for the past 10 years or so. Theoretical modelling and image processing technique on SAR images have been developed. However, the main limitation is the dependence on overseas institution to supply the measurement data and SAR images. For national monitoring and management of earth resources, limited number and timely supply of the required SAR images have been a major problem. Therefore, there is an urgent need to develop our own SAR sensor system.

In late 2007, the project to develop a UAVSAR system was initiated with joined collaboration with Agency Remote Sensing of Malaysia. The main objective of this project is to design and construct an imaging radar system with UAV as the platform. The SAR system is a C-band, single polarization, linear FM pulse radar system. This SAR system is designed to operate at low altitudes with low transmit power and small swath width in order to optimize the development cost and operating cost. The system will be used for monitoring and management of earth resources such as paddy fields, oil palm plantation and soil surface. A few flight missions have been conducted in Semprona and Mersing, Malaysia to verify the capability and performance of the sensor. This paper describes the development of the SAR sensor as well as the current status of the development.

Development of an Integrated Velocity Compensation Timing and Control Unit for SAR

Huey Shen Boey, **Tien Sze Lim**, **Chua Ming Yam**, **and Voon Chet Koo**
Faculty of Engineering and Technology, Multimedia University
Jalan Ayer Keroh Lama, Melaka 75450, Malaysia

Abstract— One of the main obstacles faced by SAR is motion error. Typically, a synthetic aperture radar (SAR) system modeling assumes that all flight path parameters are constants in generating SAR images. However, this is never true for real case. One of the most unavoidable motion errors is the variance in instantaneous velocity of the aircraft usually caused by wind turbulence, drag or limitations of the aircraft itself. A timing and control unit (TCU) integrated with velocity compensation has been developed to satisfy two main functions. Firstly, to supply consistent and accurate signals or pulses to necessary SAR modules that needs them. Secondly and most importantly, the TCU is capable of performing motion error compensation for instantaneous velocity error of the aircraft. A basic assumption of SAR is that the flight path is in a straight line moving with a constant velocity. Thus, the space in between each capturing point is also assumed to be of equal length. However, in real life conditions, these sample space are variables dependent on the instantaneous velocity of the aircraft. The developed TCU is capable of adjusting the Pulse Repetitive Frequency (PRF) of the SAR in real time in order to compensate with the velocity inconsistency of the aircraft during SAR measurement. This method is proven to increase final image quality and productivity of the TCU.

Design and Development of a Sidelooking Microstrip Patch Antenna for Unmanned Aerial Vehicle Synthetic Aperture Antenna

Poi Ngee Tan, Yee Kit Chan, Tien Sze Lim, and Gobi Vetharatnam
Faculty of Engineering and Technology, Multimedia University
Jalan Ayer Keroh Lama, Bukit Beruang, Melaka 75450, Malaysia

Abstract— In Multimedia University, Malaysia, an Unmanned Aerial Vehicle Synthetic Aperture Radar (UAVSAR) system has been developed which operates at C-Band (5.3 GHz). The SAR system requires bandwidth of 80 MHz and using dual antenna system. As the name tells, the SAR system will be installed and operate in an unmanned aerial vehicle and the UAVSAR antenna will installed underneath the UAV. Hence it places some limitation in the mechanical characteristics of the antenna of the SAR system. The weight, dimension and shape of the antenna must fulfill the actual flight condition such as the air resistance and landing force. To minimize the consumed space of the antenna, a microstrip patch array antenna with large amount of radiating elements is constructed. The antenna consists of 12 azimuth and 8 elevation radiation elements. Both transmit and receive antennas are installed on the same supporting structure which occupies 1 meter length and 30 cm width. To provide a greater swath width, the main lobe of the elevation radiation pattern is set to 25° away from the nadir line and the beamwidth is set to 40°. An onboard 3-way power divider is adopted in azimuth array to overcome asymmetrical issue of the parallel feeding network. To avoid spurious radiation from feeding network and making feeding network design easier, the feeding network is placed at the bottom layer of the antenna instead of same layer with radiating elements. The power is fed from feeding network to the radiating elements via a probe which penetrates through the ground plane at middle layer. The antenna prototype is simulated by using computer aided program to analyze its' performance.

Performance Evaluation of an Integrated IMU-GPS Motion Sensing System for UAVSAR

Wei Qiang Tan, Chot Chun Lim, Voon Chet Koo, and Tien Sze Lim
Multimedia University, Malaysia

Abstract— Motion error is one of the major challenges for Unmanned Aerial Vehicle Synthetic Aperture Radar (UAVSAR) system to obtain high quality SAR image. An integrated IMU-GPS motion sensing system has been developed in Multimedia University, Malaysia to provide accurate motion sensing measurement for UAVSAR application. This paper presents a series of laboratory conducted in on-ground and in-flight tests to evaluate the performance of the IMU-GPS motion sensing system. A practical calibration method is also proposed before conducting any experiment to compensate measurement in accuracy. The experimental results show that the developed motion sensing system is capable of providing accurate and stable motion data for SAR motion compensation.

UAV SAR Signal Processing with Motion Error Compensation

Chee-Siong Lim, Voon-Chet Koo, Yee-Kit Chan, and Chot-Hun Lim
Multimedia University, Malaysia

Abstract— SAR signal processing is an important process in any SAR system operation. However, most of the typical SAR processing algorithms were developed based on the assumption that the motion of the SAR platform is ideally straight at a constant speed. Unfortunately this assumption doesn't reflect the actual situation in real life. It is almost impossible for any airborne SAR platform to fly in a straight line at a constant speed because of the air turbulence especially when it comes to the lightweight UAV. In most cases, the result precision of the SAR signal processing could be deteriorated badly by the trajectory deviations due to the air turbulences. The key to motion compensation is to accurately predict the UAV's motion and dynamically correct the errors so that the output SAR image is well focused. These methods require accurate tracking of the antenna phase center, which greatly depends on the precision of the inertial measurement system. It is assumed that phase errors are *a priori* known by means of on-board instrumentation such as inertia navigation unit (INU) and global positioning system (GPS). The motion parameters associated with the sensor platform are used to estimate phase errors induced by motion instability (Kirk, 1975). The motion errors may then be compensated from the SAR data prior to image formation. This paper discusses how motion error compensation can be implemented in SAR signal processing algorithm and the accuracy of the proposed algorithm is examined on both simulated data and actual data from UAV SAR field measurement campaign.

High Speed AD DA for Synthetic Aperture Radar

Ming Yam Chua[1], **Voon Chet Koo**[1], **Heng Siong Lim**[1], **Huey Shen Boey**[1], **Yee Kit Chan**[1], **Chot Hun Lim**[1], **Tien Sze Lim**[1], **and Hean Teik Chuah**[2]

[1]Faculty of Engineering and Technology, Multimedia University, Malaysia
[2]University Tunku Abdul Rahman, Malaysia

Abstract— Multimedia University Malaysia has developed an C-band Synthetic Aperture Radar (SAR) in collaboration with Agency of Remote Sensing Malaysia (ARSM). The microwave sensor operates at center frequency of 5.3 GHz and 80 MHz of Linear Frequency Modulated (LFM) bandwidth with selectable pulse width. The sensor was mounted on an Unmanned Aerial Vehicle (UAV) and will be used for monitoring and management of earth resources such as paddy fields, oil palm plantation and soil surface in future. Apart of the radio frequency module, baseband SAR processor is an essential module, having the responsibility to synthesize the required baseband chirp pulse, perform front-end signal processing, and to digitize the down-converted backscattered signal for further processing. This paper discusses the design and development of high speed Digital-to-Analog (DA)and Analog-to-Digital (AD) hardware modulesin the baseband SAR processor. DA modules will be used radar baseband waveform synthesis while the AD module will be used for baseband backscattered signal digitization.The AD module is capable of delivering up to 500 MSPS total throughput rate while the DA module is capable of delivering upto 420 MSPS total throughput rate.Both the modules could be interfaced with Altera high performance Field Programmable Gate Array (FPGA) evaluation board through its High Speed Mezzanine Card (HSMC) interface. In the implementation, as for prototyping, the DA and AD modules were fabricated on 4-layers FR4 Printed Circuit Board (PCB) substrate. A series of in lab measurement were conducted to verify the performance of the DA and AD hardware modules.

Realization of Interpolation-free Fast SAR Range-Doppler Algorithm Using Parallel Processing on GPU

Ozgur Altun[1], **Selcuk Paker**[2], **and Mesut Kartal**[2]

[1]Informatics Institue, Satellite Communication and Remote Sensing, Istanbul Technical University, Turkey
[2]Electrical and Electronic Engineering, Istanbul Technical University, Turkey

Abstract— In this work, interpolation-free fast Range-Doppler (RD) Synthetic Aperture Radar (SAR) algorithm has been developed using parallel processing on Graphical Processing Unit (GPU). As known, the main steps of RD algorithm are range compression, transformation to Range-Doppler domain, Range Cell Migration Correction (RCMC), azimuth compression and transformation to spatial domain. In these steps, difference of RCMC process is having costly operation. One of the possible ways to realization of RCMC process is the interpolation on Range-Doppler domain. The 2-D complex valued interpolation on RCMC step produces some computation errors and also needs extra processing because of the search and calculation operations. Although this computational requirement could be realized by using parallel processing, interpolation error would still remain on the results. To minimize these errors, Discrete Fourier Transformation (DFT) technique can be applied at the expense of additional computation cost. In our work, Parallel-Discrete Fourier Transformation (P-DFT) and inverse FFT algorithms are used on RCMC step instead of classical interpolation algorithm. Usage of classical algorithms parallelization is not proper on CPU because of small number of processing units and its mathematical operation rate as compared with GPU. Implementation of the P-DFT algorithm on GPU also provides us fast implementation of processing step. To show the advantage of proposed method, we apply the P-DFT algorithm to a synthetic data obtained from a point scatterer model and a real ERS2 data. The results give us a more accurate image without sacrificing on processing time. We also obtain faster result as compared to classical method with our proposed parallelized interpolation-free method applied on the GPU platform.

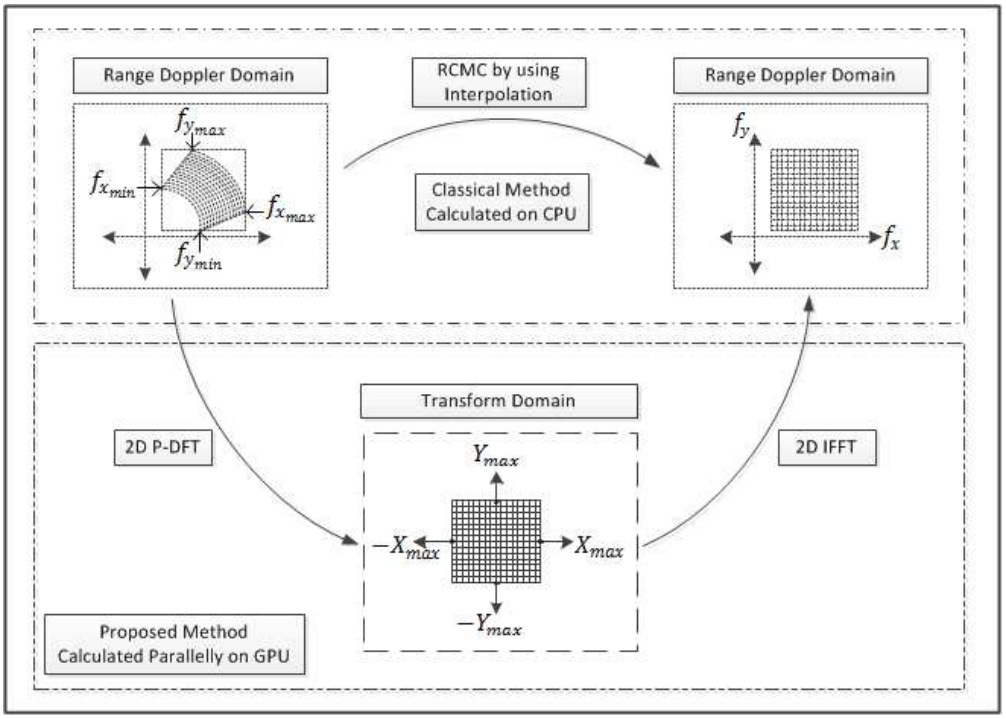

Figure 1: Block diagram of proposed method.

Performance Analysis of DPCA Based SAR Moving Target Detection

Han Gao, **Jingwen Li**, **and Li Zhang**
School of Electronics and Information Engineering, Beihang University, China

Abstract— Synthetic Aperture Radar (SAR) is an advanced instrument to achieve ground scene imaging, which also shows a lot of potential on moving target detection. To quantify the limits of performance and examine the capabilities of detection, performance analysis of SAR moving target detection under certain clutter suppression algorithm is demanded. Motivated by this demand, the performance of Displaced Phase Centre Antenna (DPCA) based SAR moving target detection is theoretically analyzed in this paper.

It is found that the performance of detection is related to the detection threshold directly, which is determined by the Probability Density Function (PDF) of detection metric [1]. Therefore, it is crucial for performance analysis to investigate on the PDFs under different statistical models. As multi-look process is commonly used for sparkle noise reduction after DPCA, it is taken into consideration in this paper, which increases the complexity but also practicability of the analysis.

The statistical models of multi-looked DPCA metric are established under hypothesis stationary clutter only case and the case that moving target signals are superimposed upon the stationary clutter. For simplicity, only homogeneous clutter is discussed here. The PDF under stationary clutter only hypothesis is given, which modifies the result from [2]. Under the alternative hypothesis, to represent more practical cases, several models of the metric dependent on the backscattering type (deterministic or random target signal) and spatial dimension (compared to the multi-look resolution cell size) of the moving target are proposed [3], and corresponding PDFs ground on these models are derived in closed-form. It is demonstrated that the backscattering type is the dominant factor that changes PDF in form, while the spatial dimension only alters parameters under deterministic target model but changes PDF in form under random target model.

Based on these derived PDFs, receiver operating curve and other measures are obtained to illustrate the performance for any set of system and target parameters, which plays a significant role in system parameter design and algorithm selection.

REFERENCES

1. Sikaneta, I., *Detection of Ground Moving Objects with Synthetic Aperture Radar*, University of Ottawa, 2004.
2. Liu, C. and G. Liao, "Canonical framework for multi-channel SAR-GMTI," *Journal of Systems Engineering and Electronics*, Vol. 19, No. 5, 923–928, 2008.
3. Gierull, C. H., "Moving target detection with along-track SAR interferometry," Technical Report TR 2002-084, Defence Research and Development, Canada, January 2002.

A Three-component Model-based Target Decomposition for Compact Polarimetric SAR Data

Lei Xie[1, 2], **Hong Zhang**[1], **Chao Wang**[1], **and Bo Zhang**[1]

[1]Key Laboratory of Digital Earth
Center for Earth Observation and Digital Earth, CAS, Beijing, China
[2]University of Chinese Academy of Sciences, Beijing, China

Abstract— The advent of high resolution SAR imagery, which has more rich spatial information, further provides opportunities to detect changes more accuracy. However, the traditional pixel-based change paradigm cannot adapt to the change detection of objects in different spatial scale, especially in build-up area, which has strong speckle noise. Recently, the image analysis based on multi-scale segmentation provides a feasible idea to solve it.

In this paper, we propose a segmentation algorithm based on mean shift [1], which combines the information of images acquired in multi-temporal. After segmentation, the labels of the segments in different images are corresponding. With different parameter setting, the segmentation map of different scale is generated. The difference map extraction is based on the segmentation blocks, and the cross entropy (KL) in information theory will be used. To ensure the KL measure independent from the statistical model, an edgeworth series expansion is applied to approximate the statistical model. Different scale will cause a different in difference map, and a fusion method based on Markov Random field [2] is utilized to derive the final binary change map.

To verify the effectiveness of the proposed method, we perform experiments on Beijing real SAR data sets. The study area focuses on Olympic park. Two TerraSAR-X images taken in different years by HH polarization from the descending path, are shown in Fig. 1. The first image was taken on May 23rd, 2008 with 33.12° incidence angle, and the second one on April 22nd, 2011 with 32.71° incidence angle at the center. Two images are Mutilook Ground Distance (MGD) product

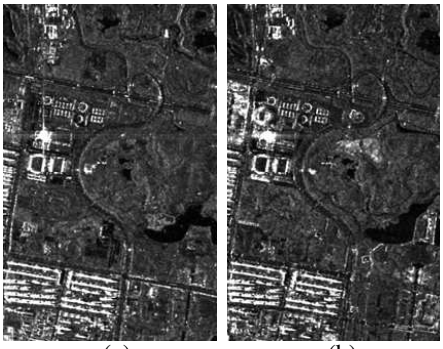

(a) (b)

Figure 1: TerraSAR-X images acquired (a) on May 4th, 2008 and (b) on April 22nd, 2011.

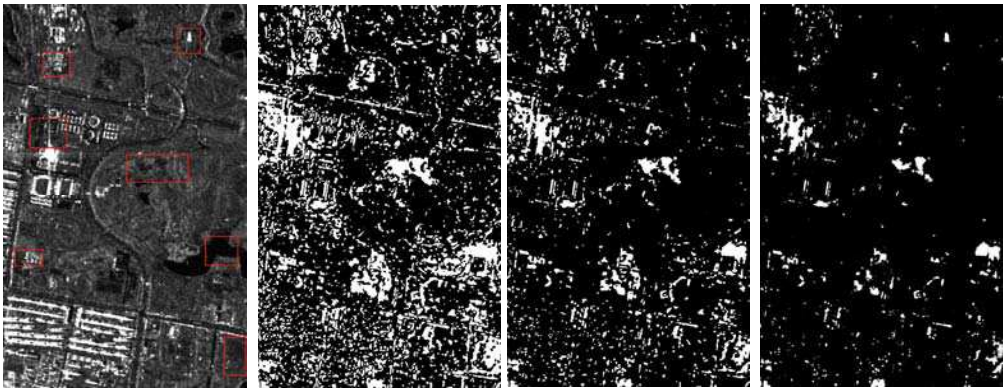

(a) (b) (c) (d)

Figure 2: The change maps in different scales.

and the resolution is 3 m/pixel. The preliminary results of the change detection in different scales is shown in Figs. 2(c) $\sim$ 2(d) and Original image with change area marked by red box (Fig. 2(a)).

REFERENCES

1. Jarabo-Amores, P., et al., "Spatial-range mean-shift filtering and segmentation applied to SAR images," *IEEE Transactions on Instrumentation and Measurement*, Vol. 60, No. 2, 584–597, 2011.
2. Melgani, F. and Y. Bazi, "Markovian fusion approach to robust unsupervised change detection in remotely sensed imagery," *IEEE Geoscience and Remote Sensing Letters*, Vol. 3, No. 4, 457–461, 2006.

Session 3P4a
Design and Simulation of Electromagnetic and Optical Devices 2

Frequency-dependent LOD-FDTD Simulation of THz Sensing
Jun Shibayama, Naoki Sasaki, Junji Yamauchi, Hisamatsu Nakano, ... 580
Microstrip Slot Antenna for Mobile Base Station
Mohamed S. El-Gendy, Haythem Hussein Abdullah, Esmat Abdel-Fattah Abdallah, ... 581
Analysis of Localized Circularly Polarized Light by Plasmonic Antennas for All-optical Magnetic Recording
Shinichiro Ohnuki, T. Kato, Yoshito Ashizawa, Katsuji Nakagawa, Weng Cho Chew, ... 582
Cavity Array Metamaterials
James Quach, Chun-Hsu Su, Andrew M. Martin, Andrew D. Greentree, Lloyd C. L. Hollenberg, ... 583

Frequency-dependent LOD-FDTD Simulation of THz Sensing

J. Shibayama, **N. Sasaki**, **J. Yamauchi**, **and H. Nakano**
Faculty of Science and Engineering, Hosei University, Tokyo 184-8584, Japan

Abstract— Recently, biomedical sensing has received much attention in an application using a THz wave [1]. As a basic research, numerical studies have been performed with the finite-difference time-domain (FDTD) method, in which dispersion properties of biomedical media are frequently taken into account using the Debye model [2, 3]. To treat the Debye model in the time-domain analysis, we often utilize the FDTD method based on the recursive convolution (RC), piecewise linear RC (PLRC), and trapezoidal RC (TRC) techniques [4, 5]. Among them, the TRC technique provides high accuracy comparable to the PLRC counterpart, while requiring only a single convolution integral as in the RC technique. However, the explicit FDTD analysis must satisfy the Courant-Friedrichs-Lewy (CFL) condition. This results in a quite small time step due to small spatial meshes for achieving sufficient accuracy.

To alleviate this problem and perform more efficient analysis, we utilize the locally one-dimensional (LOD) FDTD method that is free from the CFL condition [6]. First, the LOD-FDTD is extended to a frequency-dependent version for the analysis of the Debye model. We employ the TRC technique [4] and the fundamental scheme [7] in its formulation. Next, we simulate skin cancer detection to evaluate the performance of the frequency-dependent LOD-FDTD. As a result, the computational time is significantly reduced to 19%, due to the use of a time step 20 times as large as the explicit counterpart while maintaining the accuracy.

REFERENCES

1. Pickwell, E., A. J. Fitzgerald, B. E. Cole, P. F. Taday, R. J. Pye, T. Ha, M. Pepper, and V. P. Wallace, "Simulating the response of terahertz radiation to basal cell carcinoma using ex vivo spectroscopy measurements," *J. Biomed. Opt.*, Vol. 10, No. 064021, 2005.
2. Kashiwa, T. and I. Fukai, "A treatment by the FD-TD method of the dispersive characteristics associated with electronic polarization," *Microw. Opt. Technol. Lett.*, Vol. 3, No. 6, 203–205, 1990.
3. Luebbers, R. J., F. Hunsberger, K. Kunz, R. Stander, and M. Schneider, "A frequency-dependent finite-difference time-domain formuration for dispersive materials," *IEEE Trans. Electromag. Compat.*, Vol. 32, No. 3, 222–227, 1990.
4. Siushansian, R., and J. LoVetri, "A comparison of numerical techniques for modeling electromagnetic dispersive media," *IEEE Microw. Guided Wave Lett.*, Vol. 5, No. 12, 426–428, 1995.
5. Kelly, D. F., and R. J. Lubbers, "Piecewise linear recursive convolution for dispersive media using FDTD," *IEEE Trans. Antennas Propag.*, Vol. 44, No. 6, 792–797, 1996.
6. Shibayama, J., M. Muraki, J. Yamauchi, and H. Nakano, "Efficient implicit FDTD algorithm based on locally one-dimensional scheme," *Electron. Lett.*, Vol. 41, No. 19, 1046–1047, 2005.
7. Tan, E. L., "Fundamental schemes for efficient unconditionally stable implicit finite-difference time-domain methods," *IEEE Trans. Antennas Propag.*, Vol. 56, No. 1, 170–177, 2008.

Microstrip Slot Antenna for Mobile Base Station

Mohamed S. El-Gendy, **Haythem H. Abdullah**, **and Esmat A. Abdallah**
Electronics Research Institute, Dokki, Giza, Egypt

Abstract— A multi-band dual-polarized microstrip slot antenna for mobile base stations is proposed. The antenna is operating at the bands of GSM900 (0.87–0.96) GHz, DCS1800, PCS1900, and UMTS2100 (1.71–2.17) GHz used in mobile base stations. It is fabricated using the low cost FR4 dielectric substrate. The antenna is based on two orthogonal diamond cross slots etched on the ground plane and incorporates a two orthogonal microstrip feeding lines placed underneath the FR4 substrate material on the opposite side of the ground plane to achieve dual polarization. The measured isolation characteristics for the proposed antenna between the two ports do not exceed −30 dB within the operating bands. The front-to-back ratio is greater than 17 dB at GSM900, 20 dB at both DCS1800 and PCS1900 and 14 dB at UMTS2100. Average antenna gains about 7.9 dBi and 7.1 dBi have been obtained for lower and upper bands, respectively. The design is dedicated to the single array element which will be incorporated in an array in order to construct the base station antenna.

Analysis of Localized Circularly Polarized Light by Plasmonic Antennas for All-optical Magnetic Recording

S. Ohnuki[1], **T. Kato**[1], **Y. Ashizawa**[1], **K. Nakagawa**[1], **and W. C. Chew**[2]

[1]College of Science and Technology, Nihon University, Japan
[2]University of Illinois, USA

Abstract— All-optical magnetic recording with circularly polarized light has attracted attention for ultra-high speed magnetic recording [1, 2]. In the recording system, the magnetization reversal occurs by illuminating a single 40 fs circularly polarized laser pulse [1]. However, it is difficult to localize the circularly polarized light for realizing higher density magnetic recording. Therefore, we have proposed the combination of plasmonic antennas, which can generate the localized circularly polarized light in nano scale, and bit-patterned media for high speed and high density magnetic recording [3]. In this talk, we analyze the localized circularly polarized light radiated by the plasmonic antenna and the bit-patterned media for high density all-optical magnetic recording using the ADE-FDTD method [4]. The intensity and the generation time of the localized circularly polarized light are investigated in terms of the Stokes parameters [5].

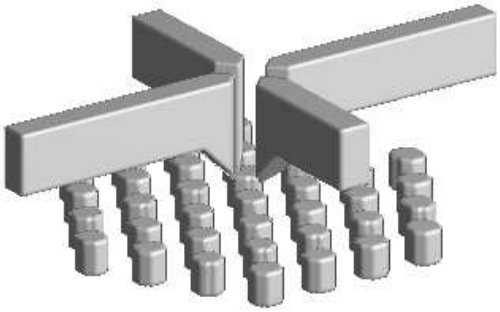

Figure 1: Plasmonic antenna and bit-patterned media.

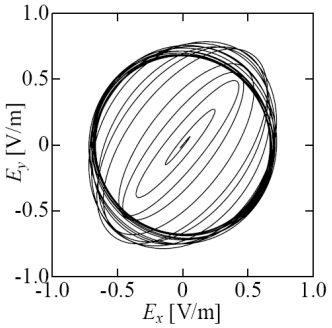

Figure 2: Clockwise circularly polarized light.

REFERENCES

1. Stanciu, C. D., F. Hansteen, A. V. Kimel, A. Kirilyuk, A. Tsukamoto, A. Itoh, and T. Rasing, "All-optical magnetic recording with circularly polarized light," *Phys. Rev. Lett.*, Vol. 99, No. 4, 047601-1–047601-4, 2007.
2. Nakagawa, K., Y. Ashizawa, S. Ohnuki, A. Itoh, and A. Tsukamato, "Confined circularly polarized light generated by nano-size aperture for high density all-optical magnetic recording," *J. Appl. Phys.*, Vol. 109, No. 7, 07B735-1–07B735-3, 2011.
3. Iwamatsu, H., T. Kato, S. Ohnuki, Y. Ashizawa, K. Nakagawa, and W. C. Chew, "Analysis of electromagnetic fields of a plasmonic cross antenna with bit-patterned media," *2012 IEEE International Symposium on Antennas and Propagation and USNC/URSI Radio Science Meeting*, Chicago, Illinois, USA, July 2012.
4. Yamaguchi, T. and T. Hinata, "Optical near-field analysis of spherical metals: Application of the FDTD method combined with the ADE method," *Opt. Express*, Vol. 15, No. 18, 11481–11491, 2007.
5. Biagioni, P., J. S. Huang, L. Duò, M. Finazzi, and B. Hecht, "Cross resonant optical antenna," *Phys. Rev. Lett.*, Vol. 102, No. 25, 256801-1–256801-4, 2009.

Cavity Array Metamaterials

James Quach[1], **Chun-Hsu Su**[2], **Andrew M. Martin**[1],
Andrew D. Greentree[3], **and Lloyd C. L. Hollenberg**[4]

[1]School of Physics, The University of Melbourne, Victoria 3010, Australia
[2]Department of Infrastructure Engineering, The University of Melbourne, Victoria 3010, Australia
[3]Applied Physics, School of Applied Sciences, RMIT University, Victoria 3001, Australia
[4]Centre for Quantum Computer Technology, School of Physics
The University of Melbourne, Victoria 3010, Australia

Abstract— We present a metamaterial design based on tight-binding properties of coupled optical-cavity arrays and quantum-mechanical atom-cavity arrays. Termed cavity array metamaterials (CAMs), we show that they can be used to create optical elements [1], cloaking effects, and through atom-cavity couplings, a reconfigurable quantum superlens [2]. Our work introduces a theoretical connection between quantum engineering/control in cavity quantum-electrodynamics platforms and classical metamaterials.

Coupled Cavity Array and Transformation Optics: We assume a uniform 2D periodic array of optical cavities coupled evanescently via field mode overlap, confined within a membrane in the xy-plane. We show that different regimes of the transmission band can be exploited for various optical applications. In particular, by tuning the transmission band we show that the system can give rise to negative refraction, collimation, and prism effects.

Transformation optics is an important methodology for the control of electromagnetic trajectories in metamaterials. However, since the size of the constituent elements of CAMs is commensurate with the operating wavelength, classical transformation optics cannot be applied on this platform. By directly transforming the internal geometry of the system whilst tuning intersite properties to ensure Hamiltonian invariance, we provide an alternative framework suitable for tight-binding implementation of metamaterials. We investigate CAM-based homeomorphic cloaking as a case study, as shown in Fig. 1(a).

Coupled Atom-cavity Array as Quantum Metamaterial: Embedding a two-level atomic or atom-like system at each site of the coupled-cavity array [Fig. 1(b)], creates a 2D lattice of Jaynes-Cummings systems, which is known as the Jaynes-Cummings-Hubbard model. By tuning dispersion and resonance relations through the control of the individual cavity atomic transition energy, we show that our system exhibits the superlens features of all-angle negative refraction and evanescent wave amplification for subwavelength imaging. The additional control of atomic

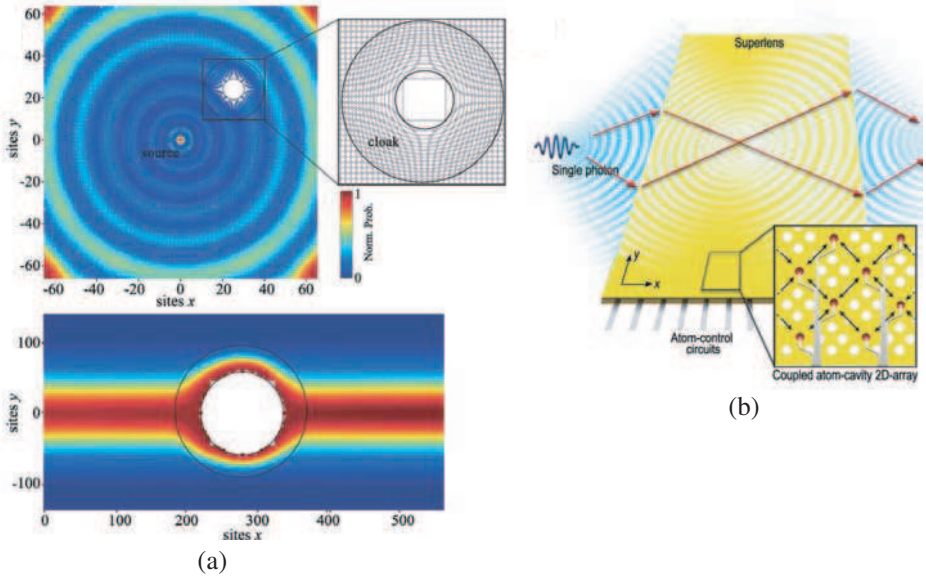

Figure 1: (a) Cloaking from a quasi-point source and in a continuous beam, using coupled cavity arries. (b) Ilustration of a reconfigurable quantum superlens built from a cavity-array metamaterial.

detuning also allows the superlens to be reconfigured after fabrication, enabling scanning of the resonant modes and allowing the focus of the lens to be adjusted. Furthermore, we also show that the atomic control also provides a mean to introduce an adiabatic spatial change of the dispersion properties across the cavity array, in effect producing a gradient-index structure.

REFERENCES

1. Su, C.-H., "Novel quantum technology based on atom-cavity physics," Ph.D. Thesis, University of Melbourne, 2010.
2. Quach, J. Q., C.-H. Su, A. M. Martin, A. D. Greentree, and L. C. L. Hollenberg, "Reconfigurable quantum metamaterials," *Optics Express*, Vol. 19, 11018, 2011.

Session 3P4b
Computational Electromagnetics

Computation of a Quasi-static Field Induced by Two Long Straight Parallel Wires in an Inhomogeneous Layered Conductor
François Caire, Denis Premel, Gérard Granet, ... 586
Finite Difference — Trefftz Schemes in Electromagnetics
Igor Tsukerman, ... 587
Special Difference Schemes for Singularity-free Boundary Methods
Osama Alkhateeb, Igor Tsukerman, ... 588
Distribution of Energy Flow by Dielectric Waveguide with Defects Composed of Air-hole Type Circular Cylinder Array
Ryosuke Ozaki, Tsuneki Yamasaki, ... 589
Resonance Absorption in Multilayered Bi-gratings
Yoichi Okuno, S. Bai, Taikei Suyama, Q. Zhao, X. Xu, ... 590
Applications of the High-order Method in Dielectric Material
Min Zhu, L. Zhao, Qunsheng Cao, ... 591
Application of the Eigenfunctions in Fast RCS Computing
You-Bao Wang, Xiao Zhu, Chao Shi, ... 592
Validating the Response of UHF Partial Discharge Sensor Using FDTD Method
Asnor Mazuan Ishak, Martin D. Judd, Wah Hoon Siew, ... 593

Computation of a Quasi-static Field Induced by Two Long Straight Parallel Wires in an Inhomogeneous Layered Conductor

François Caire[1], **Denis Prémel**[1], **and Gérard Granet**[2, 3]

[1]CEA LIST, DISC/LSME, Gif-sur-Yvette, Cedex 91191, France
[2]Clermont Universités, Université Blaise Pascal
Institut Pascal, BP10448, Clermont, Ferrand F-63000, France
[3]CNRS UMR 6602, Aubière F-63177, France

Abstract— The detection and characterization of subsurface anomalies in conducting structures are important problems for both geophysics and non-destructive evaluation. Eddy currents induced through an above-surface coil driven by a time-varying current are used successfully for probing such anomalies. Integral equation methods and finite elements methods are the most popular in studying the induced field response from any inhomogeneity. Recently an alternative approach has been investigated for the computation of the quasi-static electrical field induced by a 2D or 3D eddy current air core probe [1, 2]. Coming from grating theory, it is based on curvilinear coordinates and Maxwell's equations are written under a covariant form. In this presentation, following the very same ideas as in our initial work, we moreover use matched coordinates for investigating the effects of a gradient of conductivity in a conducting half plane. When scanning any conductive media of complex shape, a variation of the conductivity of the media with the depth of the work piece will be revealed by a variation of the coil impedance which is the quantity that we compute. The canonical configuration under study is displayed in Figure 1. It can highlight, in a first step of the developments, the key stones for understanding the novelty of the developed formalism. A two-dimensional long coil is constituted by two parallel straight lines current sources of infinite length. The two current sources are driven by harmonic currents of opposite signs. The current sources are separated by a distance $2x_0$. The lift-off of the 2D probe is denoted by l_0. The linear, isotropic, half-space is characterized by a magnetic relative permeability and the conductivity σ is assumed to be inhomogeneous. The half-space is divided into two regions separated by a surface parallel to the y axis and supported by a curve $z = a(x)$. Moreover, the conductivity is described by an analytic function $\sigma(x, z)$ and below it may considered as a constant. The essence of the method is to use a coordinate system which matches both the surface $(y, z = a(x))$ and the plane $(y, z = 0)$.

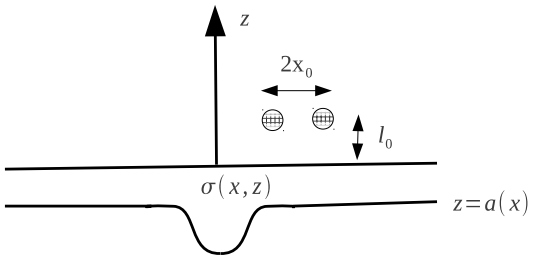

Figure 1: A long coil above an inhomogeneous layered conductor.

REFERENCES

1. Prémel, D., "Computation of a quasi-static field induced by two long straight parallel wires in a conductor with a rough surface," *J. Phys. D: Appl. Phys.*, Vol. 41, 245305, 2008.
2. Caire, F., D. Prémel, and G. Granet, "Semi-analytical computation of a quasi-static field induced by an eddy current probe in a conductor with an irregular surface," *Numélec*, 24–25, July 3–5, 2012, submitted to *European Physics Journal*.
3. Chandezon, J., D. Maystre, and G. Raoult, "A new theoretical method for diffraction and its numerical application," *J. Opt.*, Vol. 11, 23541, 1980.

Finite Difference — Trefftz Schemes in Electromagnetics

Igor Tsukerman
Department of Electrical and Computer Engineering
The University of Akron, OH 44325-3904, USA

Abstract— The Flexible Local Approximation MEthod (FLAME) qualitatively improves the accuracy of finite-difference analysis in electromagnetics by replacing the traditional Taylor expansions with much more accurate Trefftz approximations. Trefftz functions, by definition, satisfy the underlying differential equation and boundary conditions; examples of such functions are harmonic polynomials, plane waves, cylindrical or spherical harmonics. A suitably chosen local Trefftz basis around a given grid stencil defines a FLAME scheme.

Many traditional difference schemes (e.g., the five-point and seven-point schemes for the Laplace equation in 2D and 3D, respectively, as well as the Collatz "Mehrstellen" schemes) can be viewed as particular cases of FLAME. Moreover, a variety of special schemes can also be obtained directly from FLAME with a suitable choice of Trefftz bases: the exact schemes by Mickens, the Nehrbass and Lambe, et al. schemes for the Helmholtz equation, difference schemes developed by Hadley for electromagnetic wave propagation, the measured equation of invariance by Mei, et al.. Also closely related to FLAME are nonstandard high-order schemes proposed by Cole.

One particular manifestation of the high accuracy of FLAME is that the notorious "staircase" effect at curved and slanted interface boundaries is eliminated. FLAME schemes can be generated on regular, irregular and even quasi-random grid stencils; the number of stencil nodes may be greater than the number of approximating functions. In contrast with meshless methods and other similar techniques, the treatment of interface and exterior boundary conditions in FLAME is simple and natural. Since Trefftz-FLAME basis functions satisfy the underlying equation and the boundary conditions by construction, no additional constraints need to be imposed.

A variety of illustrative examples in 1D, 2D and 3D will be presented: electrostatic (magnetostatic) particle interactions, scattering of electromagnetic waves, plasmon resonances, wave propagation in photonic crystals, the computation of Bloch bands with 6–8 digits of accuracy on Cartesian grids of very modest size.

Special Difference Schemes for Singularity-free Boundary Methods

Osama Alkhateeb and Igor Tsukerman
Department of Electrical and Computer Engineering
The University of Akron, OH 44325-3904, USA

Abstract— The proposed boundary difference method (BDM) avoids the singularities inherent in traditional boundary integral methods. This is accomplished by reversing the sequence of stages in the numerical procedure. Traditionally, the differential equations are first reduced to boundary integrals with respect to equivalent sources on the boundary and then discretized; the kernels of the underlying integral equations are singular due to the infinite self-fields of concentrated sources. In BDM, the differential problem is first discretized on a regular grid to obtain a finite-difference approximation that is then reduced to a boundary difference equation with respect to auxiliary sources on the discrete boundary. The field of these sources can be expressed by convolution with the discrete Green function that, unlike its continuous counterpart, is finite at all points. Thus no singularities ever arise. The procedure involves nonsingular Green's functions on a lattice rather than their singular continuous counterparts.

The critical component of BDM is an accurate (high-order) difference scheme at the boundary of the scatterer. We use the Flexible Local Approximation MEthod (FLAME) that eliminates the notorious "staircase" effect and is capable of generating high-order schemes even at off-grid interface boundaries.

The validity of BDM has been demonstrated using 2D scattering from dielectric as well as perfectly conducting cylinders with smooth boundaries and with corners as a model problem. For smooth boundaries, the convergence rate is of the order ~ 2, commensurate with the order of the difference schemes employed. In the presence of corners, the rate of convergence is of the order ~ 1.5, due to field singularities at the corners.

Distribution of Energy Flow by Dielectric Waveguide with Defects Composed of Air-hole Type Circular Cylinder Array

Ryosuke Ozaki and Tsuneki Yamasaki
Department of Electrical Engineering, College of Science and Technology, Nihon University, Japan

Abstract— Optical wave propagation in periodic structure waveguide such as photonic crystal waveguide has been both theoretical and practical interest in many areas of physics and engineering. In periodic structures such as photonic crystals structure, it is known that a frequency stop band occurs. Also, in general, photonic crystals such as optical nanostructures with periodically permittivity distribution are known as technology which can be controlled the light in the periodic structure by interaction of both the wave nature of light and periodicity. They have expected the development in integrated optics circuit device. Therefore, in the design of photonic crystals structure with periodic constants same as optical wavelength, it is very important to investigate the stop band region or photonic band gaps. As these applications, for example, there are optical devices such as an optical branching filter, optical resonator, and optical coupler. But, it is not analyzed the stop band area in Bragg region in detailed, many numerical analysis are shown only distribution of electromagnetic fields by utilizing the FDTD method, TD-BPM method, and another numerical techniques.

In previous paper, we have analyzed the propagation characteristics of dielectric waveguide composed of dielectric circular cylinders array loaded with dielectric circular cylinders, dielectric triangular cylinders, and rhombic dielectric structure in the middle layer, and investigated the both complex propagation constants and distribution of energy flow by using the combination of improved Fourier series expansion method and multilayer method. As numerical results, it is shown that we can be obtained the confinement efficiency by loaded with rhombic dielectric structure in the middle layer for TM_0 mode.

In this paper, we have analyzed the distribution of energy flow for dielectric waveguide with defects composed of air-hole type circular cylinders array in all region as shown in Fig. 1(a), and investigated the influence of air-hole type dielectric waveguide compared with dielectric waveguide formed by dielectric circular cylinders array.

Numerical results are given for the complex propagation constants in the first stop band region and the distribution of energy flow by using the propagation constants at the guided area of dominant mode for the case of various permittivity and structures in the middle layer for TE_0 mode.

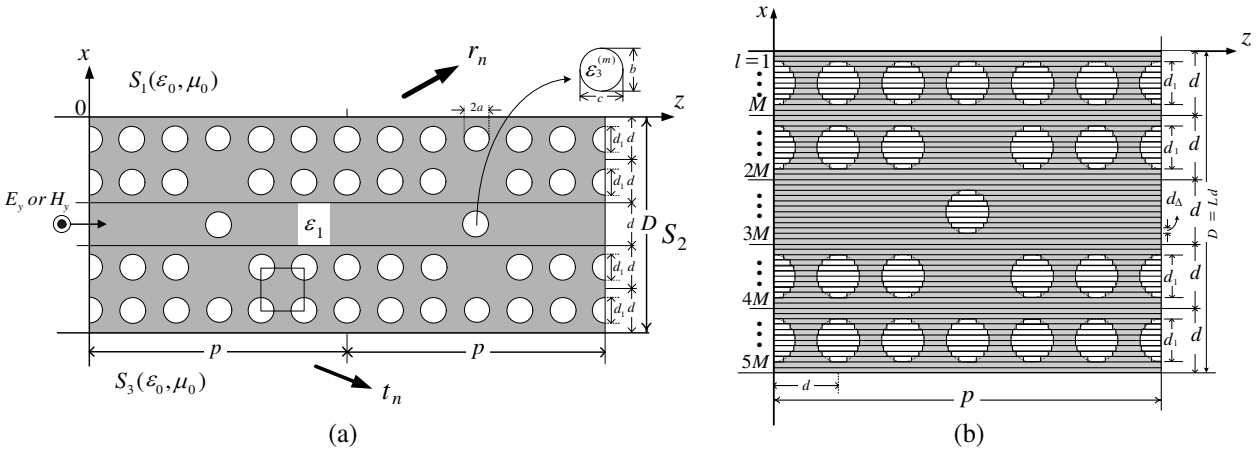

Figure 1: Structure of dielectric waveguides with defects composed of air-hole type circular cylinders array. (a) Coordinate system. (b) Approximated multilayer method.

Resonance Absorption in Multilayered Bi-gratings

Y. Okuno[1], **S. Bai**[1], **T. Suyama**[1], **Q. Zhao**[2], **and X. Xu**[3]

[1]Graduate School of Science and Technology, Kumamoto University, Kumamoto 860-8555, Japan
[2]School of Engineering, Kumamoto University, Kumamoto 860-8555, Japan
[3]School of Engineering, Kyushu Sangyo University, Fukuoka 813-0004, Japan

Abstract— We numerically investigate plane-wave diffraction by a multilayered bi-grating [1] consisting of thin films made of metal and dielectric whose surfaces are corrugated in two directions. A computational technique based on the mode-matching method was applied for solving the problems [2]. Taking a structure air/Ag/air for an example, we observe at a specific angle of incidence that: (1) excitation of single-interface surface plasmon (SISP) [3] for thick metal layer case; and (2) short-range and long-range surface plasmon (SRSP and LRSP) [4] excitation for thin enough metal layer case. Taking a structure air/Ag/SiO_2/Ag/air as another example, we find significant field enhancement in the dielectric layer between the metal layers for thin metal layer case.

REFERENCES

1. Suyama, T., Y. Zhang, Y. Okuno, Z. Q. Luo, and T. Matsuda, "Surface plasmon resonance absorption in a multilayered bigrating," *PIERS Online*, Vol. 6, No. 1, 76–80, 2010.
2. Okuno, Y., "Mode-matching method," *Analysis Methods for Electromagnetic Wave Problems*, 107–138, E. Yamashita, Ed., Artech House, Boston, 1990.
3. Suyama, T., Y. Okuno, and T. Matsuda, "Plasmon resonance-absorption in a metal grating and its application for refractive-index measurement," *Journal of Electromagnetic Waves and Applications*, Vol. 20, No. 2, 159–168, 2006.
4. Hibbins, A. P., W. A. Murray, J. Tyler, S. Wedge, W. L. Barnes, and J. R. Sambles, "Resonant absorption of electromagnetic fields by surface plasmons buried in a multilayered plasmonic nanostructure," *Phys. Rev. B*, Vol. 74, 073408, 2006.

Applications of the High-order Method in Dielectric Material

M. Zhu[1], **L. Zhao**[2], **and Q. S. Cao**[1]

[1]College of Electronic and Information Engineering
Nanjing University of Aeronautics and Astronautics, Nanjing 210016, China
[2]Nanjing ASSEN Environment Technology Co. Ltd., Nanjing 210042, China

Abstract— Recently, some important contributions have been made to the time domain scheme in computational electromagnetic field and much progress has been made to improve the finite-difference time-domain (FDTD) method. Among all these schemes, the high-order finite-difference time-domain (HO-FDTD) method has become an essential scheme for modern problem of moderately high frequency or a large domain in nature, especially the large computational involving complex geometries and dielectric material slab.

In this paper, we have introduced the HO-FDTD method which apply the Taylor series to instead the time and space derivatives and attach high accurate. The applications of the HO-FDTD scheme has been studied and discussed in dielectric material slab. Reflect coefficients can be obtained from the simulation of the material slab structure and used to measure the accurate of the method. The simulation results have been presented and compared with those of the classical FDTD and Multi-resolution time domain (MRTD) methods in a material slab geometric model. The comparison results show that the HO-FDTD method is well consistent with the analytical results and more accuracy than the other two methods. Further more, the comparisons of the HO-FDTD and MRTD method have been shown in this paper, and obtained that the HO-FDTD method presents the better accurate than MRTD method. Finally, we apply the different spatial stencil size of the HO-FDTD method in the same dielectric material layer simulation and observe that the large spatial stencil size present the better result. All these conclusions show that the HO-FDTD scheme is a powerful, efficient and precise to treat with the dielectric material problem.

Application of the Eigenfunctions in Fast RCS Computing

Y. B. Wang, X. Zhu, and C. Shi
Jiangsu Technology and Engineering Center for Meteorological Sensor Network
Nanjing University of Information Science & Technology, Nanjing, China

Abstract— The technique to integrate the composite hermitian operator eigenfunctions (CHOEs) with the general asymptotic waveform evaluation (GAWE) is proposed for computing the radar cross section (RCS) of a perfect electric conductor (PEC). In the analysis, the orthogonal and complete properties of the CHOEs are used to construct the solution space of a matrix equation. Hence, the solution of the equation can be obtained by combining the based-vectors of the solution space with a set of coefficients, which can be determined by the GAWE technique at a given frequency. The results of numerical examples prove that the novel technique is effective in computing RCS.

Validating the Response of UHF Partial Discharge Sensor Using FDTD Method

A. M. Ishak[1, 2], **M. D. Judd**[1], **and W. H. Siew**[1]

[1]University of Strathclyde, 204 George St., Glasgow G1 1XW, UK
[2]Universiti Pertahanan Nasional Malaysia (UPNM), Kuala Lumpur 57000, Malaysia

Abstract— The first application of UHF partial discharge (PD) sensors was to detect and locate defects in gas insulated substation (GIS). Then, the application of UHF sensors has been broadened to PD diagnosis of power transformers. Sensor technology is an important field since sensor can be installed at small spaces, continuous monitoring, and very sensitive to small changes. The sensor will measure the parameter conditions of a system and then transmit the relevant data to users for future maintenance activities. A lot of studies have been done to improve sensor application in terms of design, size, capability, accuracy, sensitivity and cost. Designing sensors for specific applications involves repetitive processes with the aim to achieve the desired target or output. These processes can be reduced or eliminated by modelling and testing the sensors using high performance software. This paper presents the validation of frequency response of UHF PD disc sensor using finite-difference time-domain (FDTD) simulation. The electrical sensitivities of UHF sensors are calculated by dividing the output voltage of the sensor in frequency domain (mV) by the input electric field in frequency domain (V/m). The UHF disc sensor has been manufactured based on the predicted average sensitivity using FDTD software. The simulated and measured results of the UHF sensor are compared. The influence of component designs and material properties in the simulation, to improve the sensitivity of the UHF sensor, will also been discussed.

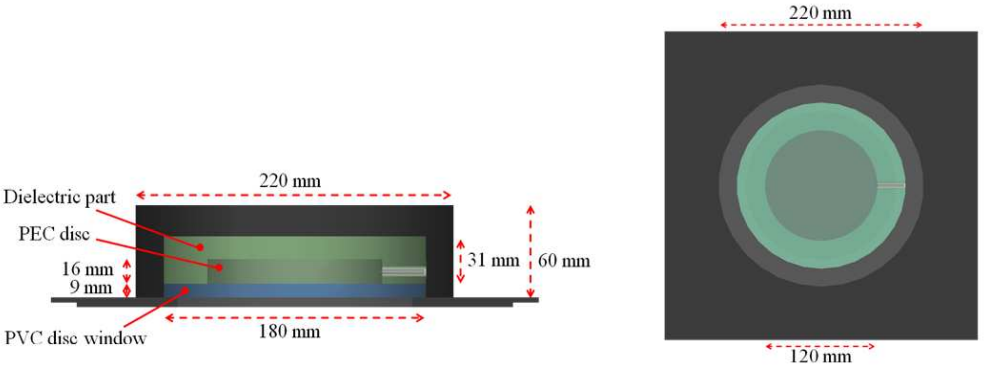

Figure 1: The dimensions of the simulated UHF PD disc sensor: (a) side view and (b) top view. Note that PEC and PVC refer to parts modelled as perfect electric conductors and polyvinyl chloride, respectively.

REFERENCES

1. Ishak, A. M., M. D. Judd, W. H. Siew, and P. C. Baker, "Evaluation of FDTD modelling as a tool for predicting the response of UHF partial discharge sensors," *IEEE International Symposium on Electrical Insulation (ISEI)*, San Juan, Puerto Rico, June 10–13, 2012.

Session 3P5
Antenna and EMC

An Improved Gain Log-periodic Dipole Array Design Using Swarm Optimization
Muhammad Aziz-ul-Haq, M. Tausif Afzal, M. Mansoor Ahmed, Qamar-ud-Din Memon, Umair Rafique, M. Arif Khan, ... 596
Assessment of Decoupling between MRI Array Elements at 300 MHz
Mikhail Kozlov, Robert Turner, ... 597
Circularly Polarized Patch Antenna Based on Chiral Metamaterial
Yahong Liu, Ying Qi, Kun Song, Shuai Gu, Xiao-Peng Zhao, ... 599
Simulation of the Noise Induced by Corona Discharges on a Ground VHF Antenna
Mingtian Wang, Alexandre Chabory, Jean-Pierre Boeuf, ... 600
Novel Design of Site Source for Radiation and Conduction Emission Test
Dau-Chyrh Chang, Chih-Hung Lee, Tsung-Yuan Yang, ... 601
Ultra-wideband Microstrip Patch Antenna for Microwave Communications
Syed Ahsan Ali, Umair Rafique, Umair Ahmad, M. Mansoor Ahmed, M. Arif Khan, ... 602
The Analysis of Antenna Performance due to PCB Grounding Effect from the EMC Bead Device
Hsiao-Bin Liang, Cheng-Wei Chen, Dau-Chyrh Chang, Ming-Ching Yen, Yu-Ling Chou, ... 603
Design, Analysis and Implementation of RF/MMW Passive Circuits for Combining Yagi Antennas Using Mixed-mode $\boldsymbol{S}$-parameters Concept
Hsiao-Bin Liang, Dau-Chyrh Chang, Cheng-Wei Chen, Chih-Ying Lin, ... 604
A Low Cost Elliptical Dipole Antenna Array for 60 GHz Applications
Jianjun Xu, Weidong Wang, ... 605
Reconfigurable Monopole Antenna for WLAN/WiMAX Applications
Hashimu Uledi Iddi, Muhammad Ramlee Bin Kamarudin, Tharek Bin Abdul Rahman, Raimi Dewan, 606
Performance Improvement of Broadband Double Ridged Horn Antenna
Dau-Chyrh Chang, Chih-Hung Lee, Tsung-Yuan Yang, ... 608
Upgrade the Traditional EMC Chamber for Avionic EMC Applications
Dau-Chyrh Chang, Chih-Hung Lee, Tsung-Yuan Yang, ... 609
EMS of AM/FM Car Radio
Dau-Chyrh Chang, Yao-Jyun Cai, Fong-Yi Lin, Bing-Hao Zeng, Jay Chen, ... 611

An Improved Gain Log-periodic Dipole Array Design Using Swarm Optimization

M. A. Haq[1], **M. T. Afzal**[1], **M. M. Ahmed**[1], **Q. D. Memon**[2], **U. Rafique**[1], **and M. A. Khan**[1]

[1]Department of Electronic Engineering
Mohammad Ali Jinnah University (MAJU), Islamabad, Pakistan
[2]Department of Electrical Engineering
University of Faisalabad, Faisalabad, Pakistan

Abstract— To accommodate large number of communication channels, a frequency independent antenna design is preferred. One of the powerful methods to address such type of requirements is the designing of a log periodic dipole array (LPDA). This paper presents an optimized design for log periodic dipole array (LPDA) for GSM phase (I and II), WiFi, WiMAX, 3G mobile communication and Bluetooth®. First, the LPDA is designed by evaluating length, diameter and spacing between dipole elements. The design is then optimized by using evolutionary technique called particle swarm optimization (PSO). It is observed that, the optimized design has improved gain and smaller size compared to the conventional LPDA design. Thus, the optimization technique provides a cost effective solution with improved characteristics for a broad band LPDA.

Assessment of Decoupling between MRI Array Elements at 300 MHz

M. Kozlov and R. Turner
Max Planck Institute for Human Cognitive and Brain Sciences, Leipzig, Germany

Abstract—

Purpose: The level of decoupling between the elements of an RF array coil at 7T is commonly assessed by examining the frequency sweep of each array element's reflection coefficient ($\mathbf{S_{xx}}$) with a network analyser. If this shows a single resonance, without splitting, it is usually considered that 7T head array elements are decoupled well enough. We investigated the consequences of coupling between array elements for RF transmit performance, in this condition such that the frequency sweep of $\mathbf{S_{xx}}$ for each array element is a single resonance.

Method: We investigated 7T arrays comprising 8 channels with identical rectangular loops of length 100 mm, mounted on a cylindrical acrylic former with diameter of 250 mm. The angular size of the loops was varied from 40 degrees (the closest element spacing) to 17.5 degrees (the largest gap between elements). The loads utilized were the Ansoft human body (head, shoulders, torso). The scanner gradient shield and magnet bore were included in the numerical domain. Using 3D EM and RF circuit co-simulation the arrays were optimized by a) minimization of $\mathbf{S_{xx}}$ without applying any dedicated decoupling network (8 optimization criteria); b) by minimization of $\mathbf{S_{xx}}$ and coupling between adjacent elements ($\mathbf{S_{xy}}$) using inductor based decoupling networks (16 optimization criteria). For obtaining performance measures the array elements were excited in CP mode, applying 1 W power to each port (array transmit power — $\mathbf{P}_{\mathrm{transmit}} = 8\,\mathrm{W}$), with a sequential phase increment. We analyzed $\mathbf{S_{xx}}$, $\mathbf{S_{xy}}$, the power balance, the current through each array element, and each element's Q factor, obtained from the current spectrum.

Results and Discussion: Circuit optimization results in a single resonance for $\mathbf{S_{xx}}$ (Fig. 1), with a minimum which is always below -40 dB at MRI operation frequency ($\mathbf{F}_{\mathrm{MRI}}$), for all array elements in all array geometries, and in all optimization conditions. The worst case $\mathbf{S_{xy}}$ (Fig. 2) was in the range of 14.7 dB to 16.9 dB with a decoupling network, and -5.4 dB to 6.4 dB without such a network. (For each of these cases the first value shown is for a loop of 40 degree angle and the second is for a 17.5 degree angle.) It should be noted that minimization of an error function, defined by both $\mathbf{S_{xx}}$ and $\mathbf{S_{xy}}$ optimization, unexpectedly resulted in $\mathbf{S_{xy}}$ having a non-zero phase, which could be as large as -16 degrees. With strong inter-coil coupling, excitation of a single coil element distributes power through several other elements, exciting a large sample volume. Thus for optimization condition "a", the Q factor was decreased, relative to that in condition "b", by a factor of about 2 for loops of angular size 17.5 degrees, and a factor of 4 for 40 degree loops.

Simulating a dual-element array with no decoupling network, we obtained a single resonance $\mathbf{S_{xx}}$ when this quantity was minimized. This optimization results in $\mathbf{S}_{21} = -2.3$ dB, and different values of tune and match capacitors for each loop element. Since the coupling between the corresponding elements for an 8 element cylindrical array with the same loop size and geometrical spacing is -5.6 dB, we can conclude that if there is asymmetrical tuning, or if coupling within the array has cylindrical symmetry so that coupling to left and right adjacent elements is equalized, the spectrum of $\mathbf{S_{xx}}$ can remain nonsplit, as it is for a single element or an ideally decoupled array. The reduction of the Q factor results, however, in broadening of the $\mathbf{S_{xx}}$ resonance spectrum.

The array properties that were most sensitive to element coupling were: the power absorbed by the load ($\mathbf{P}_{\mathrm{load}}$), the power reflected by the entire array ($\mathbf{P}_{\mathrm{array\_refl}}$) (Fig. 3) and the frequency at which the current $\mathbf{I}_{\mathrm{elem}}$ through a given array element approached its maximum ($\mathbf{F}_{\mathrm{Imax}}$). These properties are closely related to each other, such that $\mathbf{P}_{\mathrm{array\_refl}}$ approached its minimum (in the best case 0% of $\mathbf{P}_{\mathrm{transmit}}$) at $\mathbf{F}_{\mathrm{MRI}}$, $\mathbf{P}_{\mathrm{load}}$ approached its maximum at $\mathbf{P}_{\mathrm{MRI}}$, and $\mathbf{F}_{\mathrm{Imax}} = \mathbf{F}_{\mathrm{MRI}}$. This condition provided the best transmit performance for given array geometry and element material properties. $\mathbf{F}_{\mathrm{Imax}}$ values were not exactly the same for all array elements (Fig. 4) but the dependences on element coupling were very similar. The closest element spacing resulted in a large $\mathbf{P}_{\mathrm{array\_refl}}$, 48% of $\mathbf{P}_{\mathrm{transmit}}$ for non-decoupled arrays with loop angular size 17.5 degrees, and 71% of $\mathbf{P}_{\mathrm{transmit}}$ for a loop angle of 40 degrees. For the same array with a decoupling network, the value of $\mathbf{P}_{\mathrm{array\_refl}}$ was 3% and 5% of $\mathbf{P}_{\mathrm{transmit}}$ respectively. The closest element spacing resulted in a large value of $\mathbf{F}_{\mathrm{Imax}}$-$\mathbf{F}_{\mathrm{MRI}}$, which was 2.8 MHz and 18.8 MHz for non-decoupled array, with loop angular size 17.5 degrees and 40 degrees respectively. For estimation of array transmit performance, $\mathbf{F}_{\mathrm{Imax}}$-$\mathbf{F}_{\mathrm{MRI}}$ should be used together with the Q factor, because the larger the Q factor, the more severe the array transmit performance degradation, for a given $\mathbf{F}_{\mathrm{Imax}}$-$\mathbf{F}_{\mathrm{MRI}}$.

When on-bench or numerical array transmit performance optimization is performed, it can further be inferred, there is no need to measure or to calculate the combined 3-D EM fields, because the magnetic field generated by each coil element is defined by the current through it. The currents and the quantity $\mathbf{F}_{\mathrm{Imax}}$-$\mathbf{F}_{\mathrm{MRI}}$ for each array element can be monitored using current probes or pick-up loops, or calculated using an RF circuit simulator. On-bench there is only one drawback in the use of these quantities that are sensitive to coupling — all the array elements must be excited simultaneously with amplitudes and phases similar to those used in the actual MRI scan application. If only one element is excited, the spectrum (and $\mathbf{F}_{\mathrm{Imax}}$) of the current through the elements changes significantly, compared to simultaneous excitation (e.g., $\mathbf{F}_{\mathrm{Imax}}$ can shift by up to 27 MHz, 10% of $\mathbf{F}_{\mathrm{MRI}}$).

Although $\mathbf{B}_{1+}$, for single channel excitation, within the central transverse slice, differed significantly for arrays with and without a decoupling network, the values of $\mathbf{B}_{1+}$ within this slice had nearly the same profile when the entire array was excited in CP mode. In CP mode, $\mathbf{B}_{1+\mathrm{brain}}/\sqrt{\mathbf{P}_{\mathrm{brain}}}$ is also nearly the same for arrays with the same geometry, with or without a decoupling network. However, due to the large difference in $\mathbf{P}_{\mathrm{array\_refl}}$, there were significant differences in peak $\mathbf{B}_{1+\mathrm{brain}}$ and $\mathbf{B}_{1+\mathrm{brain}}/\sqrt{\mathbf{P}_{\mathrm{transmit}}}$.

Conclusion: Neither a single resonant $\mathbf{S_{xx}}$ spectrum, nor the profile of $\mathbf{B}_{1+}$ within the central transverse slice in CP mode, can be used as evidence of array element decoupling. The dependence of $\mathbf{S_{xx}}$ on coupling is not sensitive enough for precise evaluation of the influence of coupling on array transmit properties. Because direct measurement of $\mathbf{P}_{\mathrm{load}}$ is infeasible in human MRI scans, $\mathbf{P}_{\mathrm{array\_refl}}$, which can be obtained using available scanner SAR monitoring systems, is the best and most reliable figure of merit for checking 7T head array decoupling. Applying simultaneous all-element excitation, and using on-bench optimization current probes, couplers or pick-up loops, is effective if equipment to measure $\mathbf{P}_{\mathrm{array\_refl}}$ is not available.

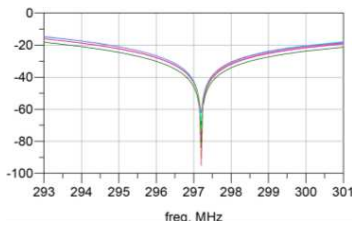

Figure 1: $\mathbf{S_{xx}}$.

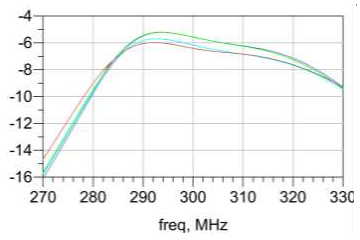

Figure 2: $\mathbf{S_{xy}}$.

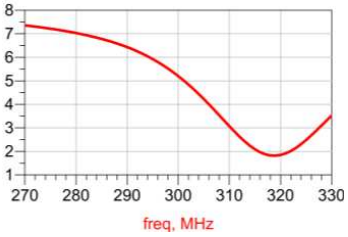

Figure 3: $\mathbf{P}_{\mathrm{array\_refl}}$.

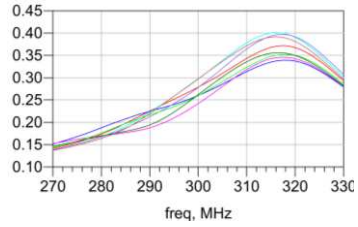

Figure 4: $\mathbf{I}_{\mathrm{elem}}$.

Circularly Polarized Patch Antenna Based on Chiral Metamaterial

Yahong Liu, Ying Qi, Kun Song, Shuai Gu, and Xiaopeng Zhao
Smart Materials Laboratory, Department of Applied Physics
Chang'an Campus, Northwestern Polytechnical University, Xi'an 710129, China

Abstract— In this paper, a circularly polarized patch antenna with chiral metamaterial cover based on wheel-like structure is proposed. The chiral metamaterial cover is consisted of arrays of wheel-like resonator pairs. The resonant properties of the chiral metamaterial have been studied. It is known that the left-handed circular polarized wave and right-handed circular polarized wave are the two eigen modes of the electromagnetic wave in the chiral metamaterial, and the corresponding transmission coefficients, which characterize the responses of the chiral metamaterial. The left-handed circular polarized transmission of the proposed chiral metamaterial which is used in the antenna is very high and the right-handed circular polarized transmission is very low at the resonant frequency. The designed patch antenna operates at the frequency where the chiral metamaterial exhibits circular dichroism. The antenna performances including as return loss, axis-ratio, and far-field radiation patterns have been studied. The study results show that the patch antenna can present left-handed circular polarized characteristics when the proposed chiral metamaterial cover is placed above the conventional linearly polarized rectangular patch antenna. Whereas, right-handed circular polarized patch antenna can be achieved when transmission property of the chiral metamaterial is changed where the right-handed circular polarized transmission of the chiral metamaterial is very high and the left-handed circular polarized transmission of the chiral metamaterial is low. It is regarded that the antenna polarized mode can be changed from linearly polarized mode to circularly polarized mode due to the introduction of the chiral metamaterial is significant. The proposed circularly polarized patch antenna has the advantages of simple structure, low weight, low-cost, and easy fabrication because of single-layer microstrip technology. Nowadays, with the technological development in wireless mobile communications, circularly polarized antennas have captured more and more attention. It can be expected that the proposed circularly polarized patch antenna has the potential application in the field of communications, radar detection, and among others.

Simulation of the Noise Induced by Corona Discharges on a Ground VHF Antenna

Mingtian Wang[1], **Alexandre Chabory**[1], **and Jean-Pierre Boeuf**[2]

[1]ENAC, TELECOM-EMA, 7 Avenue Edouard Belin, Toulouse F-31055, France
[2]LAPLACE, Paul Sabatier University, Toulouse, France

Abstract— A jamming phenomenon has been experienced by the french civil aviation authority (DGAC) on a ground station working in the VHF aeronautical frequency-band (118–134 MHz). This has yielded troubles in air-ground communications. This phenomenon appears in the presence of a strong natural electrostatic field, and is probably due to corona discharges located near the ground antennas. Indeed, corona discharges can be sources of VHF and HF noise. This type of noise is notably known for antennas onboard aircrafts and for antennas placed near high-voltage transmission lines [1, 2].

In this paper, we attest that the noise source is probably corona discharges by means of on-site measurements. Besides, we propose a model to predict the level of noise introduced by corona discharges at the output of VHF ground antennas.

The ground station is constituted by a metallic pylon with antennas that are either ground planes, or circular arrays of dipoles with reflectors. In order to find the origin of the noise, on-site measurements of the ambiant electrostatic field have been performed by means of an electric field mill. During several days, the antenna output signal and the electrostatic field have been recorded and compared. Results show that there exists a clear correlation between both measurements. The increase of the antenna noise appears simultaneously with a significant increase in the electrostatic field. Both phenomenon last the same time, and their levels are proportional. Thus, electrostatic discharges, and more particularly corona discharges may be the source of noise.

We now propose a model to predict the noise induced on a VHF ground antenna by nearby corona discharges. We consider antennas located on a pylon. We assume that the ambient electrostatic field is known. The model is divided into two parts: an electrostatic simulation to localize the place where corona discharges occur, and a simulation in the frequency domain to evaluate the noise induced by corona discharges at the output of the VHF antenna.

For the electrostatic simulation, we use the Laplace's equation to evaluate the potential and the electrostatic field in a domain around the pylon. For the boundary conditions, we define two electrodes, a sky electrode located above the pylon, and a ground electrode constituted by the pylon and the ground. The potential difference between electrodes is fixed by the ambient electrostatic field. Then lateral boundaries are placed far enough from the pylon, so that the horizontal component of the electrostatic field is zero, which corresponds to Neumann boundary conditions for the potential. The numerical simulation is based on the finite element method with Comsol. We then place corona discharges at the place where the electrostatic field is greater than a threshold.

The simulation in the VHF frequency domain are performed via Feko. We model the pylon and the VHF ground antennas so that to obtain realistic matching and radiation patterns. The corona discharges in the VHF band are represented by short electric dipoles [3]. Their dipolar moments are chosen accordingly with experimental results of [4]. To simulate the noise introduced by the corona discharges, we simulate the power at the antenna ports when they are excited by the short dipoles. The results of the simulations are in good agreement with the on-site measurements.

REFERENCES

1. Fu, H., Y. Xie, and J. Zhang, "Analysis of corona discharge interference on antennas on composite airplanes," *IEEE Trans. EMC*, Vol. 50, No. 4, Nov. 2008.
2. Olsen, R. and B. Stimson, "Predicting VHF/UHF electromagnetic noise from corona on power-line conductors," *IEEE Trans. EMC*, Vol. 30, No. 1, Feb. 1988
3. Chen, S., Y. Sun, and H. Xie, "Characteristics of electromagnetic wave radiated from corona discharge," *2001 IEEE International Symposium on Electromagnetic Compatibility, 2001 EMC*, Vol. 2, 1279–1282, 2001.
4. Boutlendj, M. and N. L. Allen, "Current-density distribution on a plane cathode in dc glow and streamer corona regimes in air," *IEEE Trans. on Electrical Insulation*, Vol. 28, No. 1, Feb. 1993.

Novel Design of Site Source for Radiation and Conduction Emission Test

Dau-Chyrh Chang[1], **Chih-Hung Lee**[2, 3], **and Tsung-Yuan Yang**[3]

[1]Oriental Institute of Technology, Taiwan
[2]Yuan Ze University, Taiwan
[3]Electronics Testing Center, Taiwan

Abstract— The electronic devices monitoring of electromagnetic interferences (EMI) has therefore emerged as a major issue for radiation emission (RE) and conduction emission (CE) test, while it must be performed under specialized conditions for EMI measurements. The standard EMI radiation sources will be generated from the harmonic generator in this paper. The oscillator sources used a 16 MHz crystal oscillator together with designed circuit integrate into Hex Inverter Buffer SN74AS04N to generate the fast transition speed of trapezoidal waveforms. The oscillator sources are combined a switching power supply of noise generation and without the LISN (Line Impedance Stabilization Network) for conducted emission test. The noise coupling to generated the AC power of the harmonics during 150 kHz to 30 MHz. A high performance dipole antenna has been implemented as the radiating structure for the signal source and the measurement has been performed in the frequency range 30 MHz to 1 GHz. For application of the novel site source for the monitor of daily test site RE and CE, repeated tests were carried out to check the frequency, power stability and polarization symmetrical of the site source.

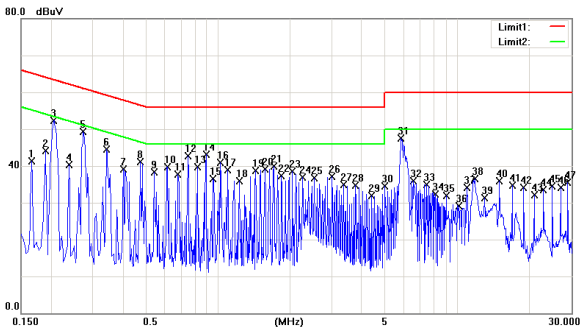

Figure 1: CE measurement result.

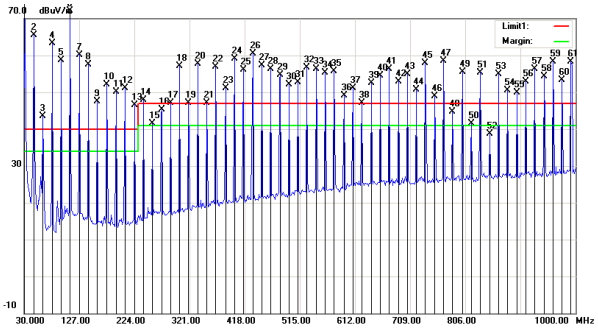

Figure 2: RE measurement result of 3 M radiation.

Ultra-wideband Microstrip Patch Antenna for Microwave Communications

S. A. Ali, U. Rafique, U. Ahmad, M. M. Ahmed, and M. A. Khan
Department of Electronic Engineering, Mohammad Ali Jinnah University (MAJU), Islamabad, Pakistan

Abstract— Wideband and ultra-wideband communication systems are becoming popular for short range and high bandwidth applications. With the increasing demand of the system, there is a need of such kind of antenna which provides largest bandwidth and high gain. In this paper, an ultra-wideband microstrip patch antenna is presented for microwave applications. The proposed design consists of two dielectric layers which consists of a rectangular patch elements. An air gap of 20 mm is used between the dielectric layers for better performance of a antenna [1]. An inverted configuration for upper patch element is used which is also helpful to increase the bandwidth of a patch antenna [1]. The lower and upper patch elements are connected through a coaxial pin. The upper patch is also get excited through a rectangular-loop slot which etched from the lower patch. From simulation results, it is noted that the proposed patch antenna is able to operate in the frequency range of 4.7–17 GHz (BW 113.3%) which covers most of the communication bands like wireless, radar and satellite communication. The average gain noted for the proposed patch antenna is 10 dBi. The proposed data is much efficient than [1–4].

REFERENCES

1. Islam, M. N., M. N. Shakib, and N. Misran, "High gain microstrip patch antenna," *European Journal of Scientific Research*, Vol. 32, No. 2, 187–193, 2009.
2. Neyestanak, A. A. L., "Ultra wideband rose leaf microstrip patch antenna," *Progress In Electromagnetics Research*, Vol. 86, 155–168, 2008.
3. Shakib, M. N., M. T. Islam, and N. Misran, "Stacked patch antenna with folded patch feed for ultra-wideband application," *IET Microwave, Antennas and Propagation*, Vol. 4, No. 10, 1456–1461, 2010.
4. Sarin, V. P., M. S. Nishamol, D. Tony, C. K. Aanandan, P. Mohanan, and K. Vasudevan, "A broadband L-strip fed printed microstrip antenna," *IEEE Transactions on Antennas and Propagation*, Vol. 59, No. 1, 281–284, 2011.

The Analysis of Antenna Performance due to PCB Grounding Effect from the EMC Bead Device

Hsiao-Bin Liang[1], **Cheng-Wei Chen**[1], **Dau-Chyrh Chang**[2]
Ming-Ching Yen[2], **and Yu-Ling Chou**[1]

[1]Climax Technology Co., Ltd, Taiwan
[2]Oriental Institute of Technology, Taiwan

Abstract— The effect of grounding separation, which is due to EMC consideration in a PCB, on the performances of on-board monopole antenna is analyzed. For improving the EMC property of PCB, keeping ground separate for sensitivity and noise portion of circuitry is one of the simplest and most effective methods of noise suppression. However, the bead, SMD device which is usually adopted for connecting different property of groundings and executing the function of noise suppression, has obviously influence on the monopole antenna in specific circumstance. In this paper, the simulated and measured results of an on-board PCB monopole antenna with and without bead are compared comprehensively. The return loss, efficiency, radiating pattern of the monopole antenna, and the current density of antenna's groundings under the condition of bead is attached or not will be presented and analyzed in this study. This analysis will give practical messages to the engineers who are engaging in EMC design-in/debug and antenna design for optimizing the performance of PCBs.

Design, Analysis and Implementation of RF/MMW Passive Circuits for Combining Yagi Antennas Using Mixed-mode *S*-parameters Concept

Hsiao-Bin Liang[1], **Dau-Chyrh Chang**[2], **Cheng-Wei Chen**[1], **and Chih-Ying Lin**[1]

[1]Climax Technology Co., Ltd, Taiwan
[2]Oriental Institute of Technology, Taiwan

Abstract— Two PCB Yagi Uda antennas are combined by power dividers and baluns (balance-to-unbalance) to enhance the radiation angle of a wireless communication system. The power divider and balun circuits are implemented by lumped (SMT device) and distributed (transmission line) architecture then analyzed/characterized by mixed-mode s-parameters. Also, the Yagi antenna, which is constructed by means of dipole structure, is also characterized by mix-mode *S*-parameter. Finally, the comprehensive performances of Yagi Uda antennas with those two type circuits are measured, compared and presented in this paper.

Introduction: For wireless communication system, the interface circuit design for antenna and RF front-end circuit is essential. Implementing antennas and passive RF/MMW circuits by PCB (printed circuit board) is the most simple and economic way to save BOM (bill-of-materials) then achieve cost-down consideration. However, due to insufficient PCB area and long wavelength of lower frequency band application (such as 868 MHz ISM band with 168 mm wavelength, respect to FR4 PCB with dielectric constant of 4.4), realizing passive RF/MMW circuits by distributed architecture is almost impossible for compact size wireless product design. To this end, the lumped RF/MMW circuits are the area-efficient way to be adopted for this condition. In this paper, the passive RF/MMW circuits, such as power divider and balun, are designed and implemented to combine two Yagi Uda antennas [1] for enhancing the radiation angle of wireless communication system. For convenience, the Yagi antennas combined with distributed and lumped RF/MMW circuits are noted as "Double Yagi" and "Double Yagi_sp" respectively. The performance of Yagi Uda antennas are measured by fast antenna measurement system, SATIMO. The *S*-parameters of passive RF/MMW circuits, balun and power divider, are measured by multi-port vector network analyzer, ZVB-4, then characterized and analyzed by mixed-mode *S*-parameters [2].

A Low Cost Elliptical Dipole Antenna Array for 60 GHz Applications

Jianjun Xu and Weidong Wang
Wireless Information Network Laboratory, University of Science and Technology of China, China

Abstract— As the demand of high speed data transmission increases, attention is transferred to the license free 60 GHz spectrum. The high oxygen absorb rate of signal and broad bandwidth both put forward new challenges for antenna design. Among all of the antenna solutions, microstrip antenna has attracted many attentions from researchers since it has so many advantages in wireless communication like low cost, compact, easy to manufacture and so on. To overcome the inherent disadvantages of narrow bandwidth of microstrip antenna and make it works well in 60 GHz band, many efforts have been taken like opening an air cavity in the substrate or stacked patch. However, these method of broadening the bandwidth always require complicated manufacture procedure like LTCC and result in high cost. In order to design a millimeter antenna with low complexity and cost and meanwhile has the bandwidth of over 7 GHz (from 58 GHz to 65 GHz) and an overall gain of more than 17 dBi to fulfill the link demand, an elliptical dipole microstrip antenna array is designed.

This antenna array comprises of three parts. The first part is a dielectric substrate with metal layer on both sides upon which will the antenna patten be etched. Although very low thickness dielectric substrate like 5 mil is available in manufacturing market, it's too thin to accomplish the task of this dielectric-support. Any deformation or distortion will greatly degrade the performance of the antenna, so an alternative solution-a 10 mil RT5880 dielectric substrate with copper foil of 17 um thickness on both sides is selected to hold the the dipole array firmly. The antenna pattern is fabricated on this dielectric substrate with the symmetrical radiating element of the elliptical dipole located on different sides of the the substrate for the convenience of the layout of feed network. As for the basic element dipole, an elliptical shape radiating model (long axis = 0.62 mm, short axis = 0.25 mm) is adopted. It has the advantage of broad bandwidth (20 GHz from 50 GHz to 70 GHz) and easy to tune since it has two parameters to adjust the tuning frequency and impedance matching compared with circular shape. In order to make the antenna be able to connect to coaxial cable, an exponentially tapered balun is designed to transfer the unbalance current of the coaxial cable to the balance current of the antenna array. This balun also undertakes the work of impedance matching. At one end of this balun, it's a microstrip line with 50 Ω port impedance, and on the other end, it's a balanced line with 75 Ω port impedance. The feed network consists of an equal power split T-junction where the 75 Ω line splits into two 150 Ω line since the port impedance of the elliptical dipole is 150 Ω. The distance of the radiating element is carefully chosen to achieve the largest gain and relative low sidelobe level. The overall size of this 16 element antenna array is 20×20 mm. The second part of this antenna is a reflect plane located $\lambda/4$ away from the substrate to increase the gain of the antenna, and the third part of this antenna is a ROHACELL foam with dielectric constant approximating 1 sandwiched between the substrate and the reflect plane.

The simulation of this antenna array is done with HFSS. The simulation results illustrate that the antenna achieves the performance requirement well.

Reconfigurable Monopole Antenna for WLAN/WiMAX Applications

Hashimu Uledi Iddi[1, 2], **M. R. Kamarudin**[1], **T. A. Rahman**[1], **and Raimi Dewan**[1]

[1]Wireless Communication Centre (WCC), Faculty of Electrical Engineering
Universiti Teknologi Malaysia, Malaysia
[2]College of Information and Communication Technologies
University of Dar es Salaam, P. O. Box 35131, Dar es Salaam, Tanzania

Abstract— With the current research trends which require more than one wireless application in one device, has increase the demand on the design of multiband and reconfigurable antenna for wireless applications. It is required for the multiband antenna to have low profile and simple in structure so as to be suitable for the miniaturized wireless devices [1]. In this paper, simple reconfigurable monopole antenna for WLAN/WiMAX application is presented. The antenna has been compared with the triple band antenna with three copper strips which operate at three frequency bands which are 2.45 GHz, 3.5 GHz and 5.8 GHz. In proposed antenna only strip $A \rightarrow B \rightarrow C$ of the triple band antenna has been used to design reconfigurable antenna which is connected by two switches. In simulation copper strip has been used as switch when it is on state and off state when the copper is removed. The antenna has been simulated using CST software studio and prototype has been fabricated using FR4 substrate.

It has been observed that the simulation of the proposed antenna is influenced by the copper strip length of the antenna. The final design of the antenna is small in size with overall dimension of $20 \times 35 \times 1.6\,\text{mm}^3$ for triple band antenna and $15 \times 33 \times 1.6\,\text{mm}^3$ for the reconfigurable antenna as shown on Figure 1. The triple band antenna provides the -10 dB bandwidth of 200 MHz from

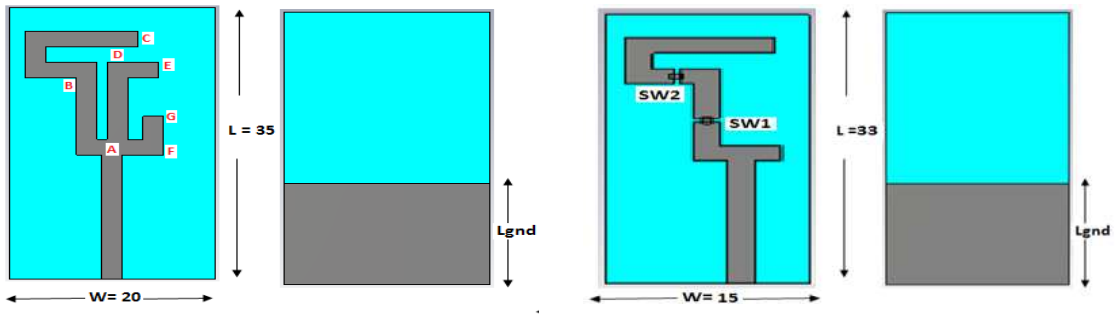

(a) Front view and back view (b) Front and back view

Figure 1: (a) Geometry of triple band monopole antenna and (b) reconfigurable monopole antenna.

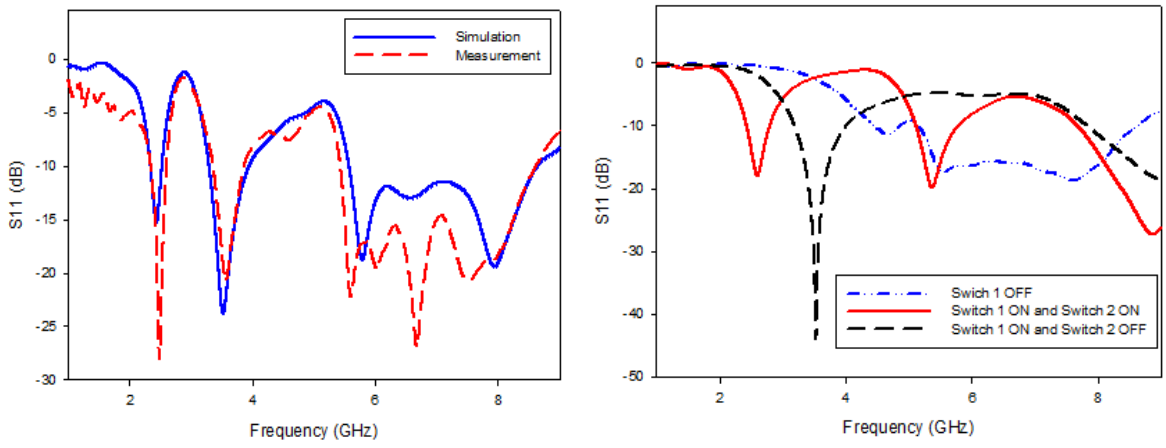

(a) (b)

Figure 2: Return loss (a) measured and simulated of triple band and (b) simulated of reconfigurable antenna.

2.33 GHz to 2.53 GHz, 640 MHz from 3.29 GHz to 3.93 GHz and a bandwidth of 3.04 GHz from 5.57 GHz to 8.61 GHz while the reconfigurable antenna provides −10 dB bandwidth of 367 MHz for 2.45 GHz, 799 MHz for 3.5 GHz and a bandwidth of 3.47 GHz for 5.8 GHz. Figure 2(a) shows the comparison between the simulated and measured return loss results of the triple band antenna and Figure 2(b) shows the simulated return loss for configurable antenna. The results show that the measured and simulated return loss characteristic of the optimized antenna satisfies the requirement of the 2.4/5.8 GHz WLAN and 3.5/5.8 GHz WiMAX antenna application. The antenna designed is low profile, compact and small in size and show good performance for WLAN/WiMAX bands. There is good agreement between the measurement and simulation results in terms of return loss.

REFERENCES

1. Li, W. M., et al., "A multi-band monopole antenna with two different slots for WLAN and WiMAX applications," *Progress In Electromagnetics Research Letters*, Vol. 28, 173–181, 2012.

Performance Improvement of Broadband Double Ridged Horn Antenna

Dau-Chyrh Chang[1], **Chih-Hung Lee**[2, 3], **and Tsung-Yuan Yang**[3]

[1]Oriental Institute of Technology, Taiwan
[2]Yuan Ze University, Taiwan
[3]Electronics Testing Center, Taiwan

Abstract— A 1 ∼ 18 GHz broadband double ridged horn antenna with coaxial feed section is investigated. This paper shows a comparatively method of feed cavity treatment in antenna for better sensitivity and spatial accuracy. A tapering shape of flared section and new feed coupling structure of this antenna are introduced to improve the radiation pattern and impedance characteristic in higher frequency. The antenna pattern is optimized by modification of the antenna structure and the main beam becomes more assemble. The matching problem of VSWR values can be resolved by adding coupling materials to the feed cavity of the antenna. The characteristics are in good agreement with the measurements over the 1 to 18 GHz operational bandwidth and indicate that the use of this type of double ridged horn antenna in EMC applications remains questionable.

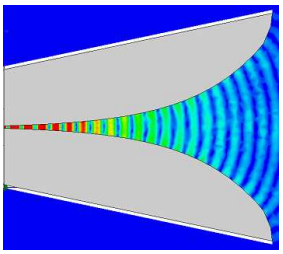

Figure 1: *E*-field distribution at 18 GHz.

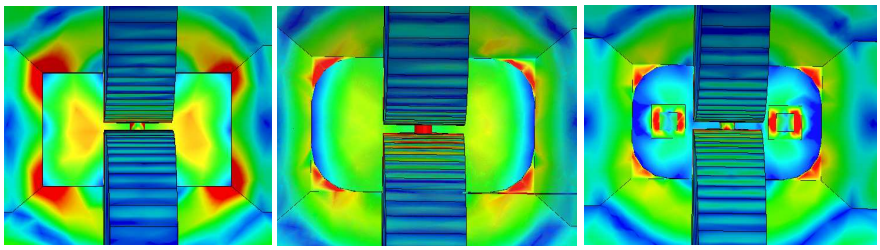

(a) (b) (c)

Figure 2: Current distribution at 18 GHz. (a) Traditional cavity. (b) U-shape cavity. (c) With du-ring cavity.

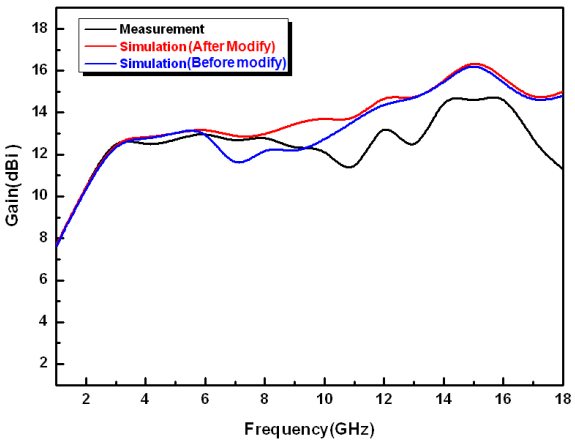

Figure 3: Comparisons of antenna gain.

Upgrade the Traditional EMC Chamber for Avionic EMC Applications

Dau-Chyrh Chang[1], **Chih-Hung Lee**[2, 3], **and Tsung-Yuan Yang**[3]

[1]Oriental Institute of Technology, Taiwan
[2]Yuan Ze University, Taiwan
[3]Electronics Testing Center, Taiwan

Abstract— In this paper, we describe electromagnetic interference (EMI) noise reduction in avionics of which uses the traditional EMC semi-anechoic chamber. The general noise suppressing technology for EMI measurement as below: EMI Source, Transmission or Coupling Medium, Susceptible Device. Follow the test method and test procedure of the international standard RTCA/DO-160E, the operation frequency range is 150 kHz to 6 GHz and the maximum deviation is less than 6 dB in identify proposed for the radiation emission test (e.g., the field intensity

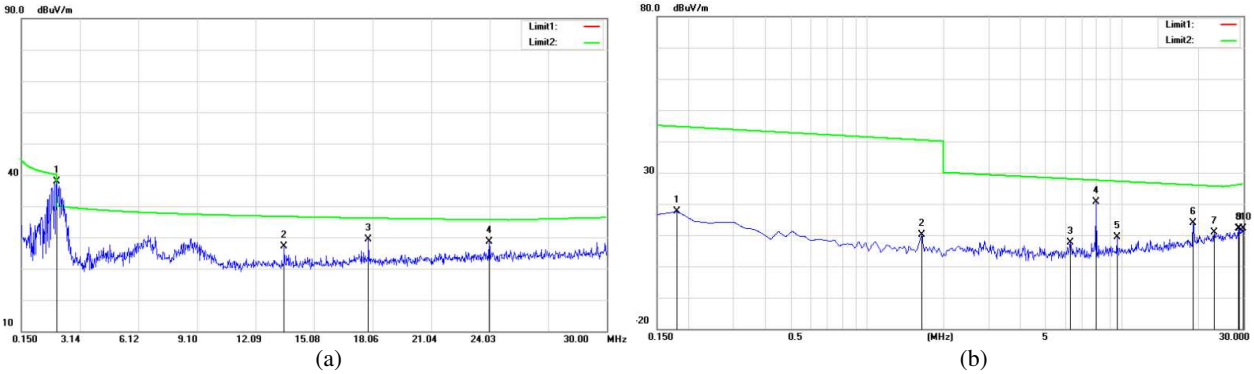

Figure 1: Ambient noise measurement from 150 kHz to 30 MHz. (a) Before modification. (b) After modification.

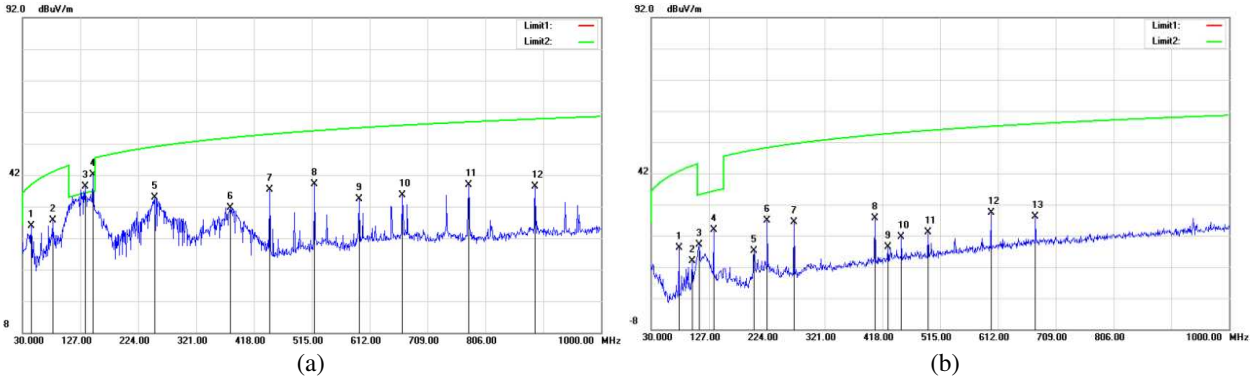

Figure 2: Ambient noise measurement from 30 MHz to 1000 MHz. (a) Before modification. (b) After modification.

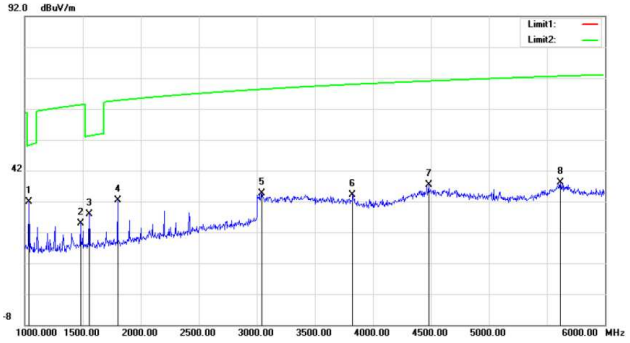

Figure 3: Ambient noise measurement from 1 GHz to 6 GHz.

should be 19 dBuV/m at 25 MHz). The difficult situation of ambient noise comes from 110/220 VAC power voltage regulator in EMI debugging. Combining the traditional EMC chamber technology together with adaptive filter techniques the presented system can perform lower emission measurements in the presence of ambient noise. After long-term, repeated and accuracy verifying, the results of the experiments confirmed the effectiveness of avionics on solving the problem of EMI noise in problem debugging process. Figures 1–3 show the ambient noise measurement results with and without modification for frequency from 150 KHs $\sim$ 6 GHz.

EMS of AM/FM Car Radio

Dau-Chyrh Chang[1], **Yao-Jyun Cai**[1], **Fong-Yi Lin**[1], **Bing-Hao Zeng**[2], **and Jay Chen**[2]

[1]Oriental Institute of Technology, Taiwan
[2]Lorom Industrial Co. Ltd, Taiwan

Abstract— There are many electric devices in cars, that's make cars exist in complicated electromagnetic environment, EMS (Electromagnetic susceptibility, EMS) of devices are different. There are many methods of EMS test, the BCI (Bulk current injection, BCI) is a item in CI (Conducted Immunity) of EMS, the Figure 1 is BCI test environment. We will introduce how to use BCI to test the AM/FM car radio and measurement results, the Figure 2 is the AM/FM Car Radio Antenna. To know the effects of BCI for AM/FM car radio.

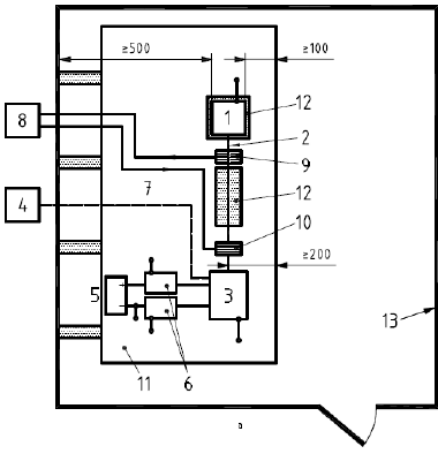

Figure 1: Test environment.

Figure 2: The AM/FM car radio antenna.

Session 3P6a
Biomedical Electromagnetic Instruments, EM Condensed Materials and Imaging and Education

RF Transmit Performance Comparison for Several MRI Head Arrays at 300 MHz
Mikhail Kozlov, Robert Turner, ... 614
Pulse Train Distributed Magnetic Field Generated from High Strength Concrete Using Magnetized Olivine Stone Aggregate
Kaneo Mohri, M. Sasaki, T. Uemura, Yoshiyuki Mohri, Muneo Yamada, Takeshi Kato, ... 616
Arousal Effect of Physiological Magnetic Stimulation on Car Driver's Pit of Stomach Evaluated with Electroencephalogram Using Driving Simulator
Yoshiyuki Mohri, Muneo Yamada, Kota Sakai, Wataru Kato, Kaneo Mohri, Tsuyoshi Uchiyama, . 617
Simulation of the Waveguide Earthquake by Using GL Geophysical Modeling
Ganquan Xie, Jianhua Li, Lee Xie, Qing Xie, Xianwei Zhou, Daxin Zuo, Feng Xie, Xuan Zhou, Mengji Xie, ... 618
GL EM Modeling for Entertainment
Jianhua Li, Ganquan Xie, Bihua Zhou, Xiangwu Xie, Ke Li, Chuan Xie, ... 619
GL EM Visualization for Electromagnetic Education
Jianhua Li, Hong Jun Li, Jian Sheng Liu, Ganquan Xie, Xiangqi Xie, ... 620

RF Transmit Performance Comparison for Several MRI Head Arrays at 300 MHz

M. Kozlov and R. Turner
Max Planck Institute for Human Cognitive and Brain Sciences, Leipzig, Germany

Abstract— **Purpose:** It is hard to compare transmit performance of published 7T head array coils because of the limited information provided. To fill this gap, using an established 3D-EM RF circuit co-simulation approach [1] we compared RF transmit performance data for several head array designs: loop [2] and strip line [3] based, and the locally shielded microstrip coil [4]. Considering this as the first step, we limited excitation of the array to a circular polarization mode, applying 1 or 0.5 W power to each port ($\mathbf{P}_{\mathrm{transmit}} = 8\,\mathrm{W}$), with a sequential 45 or 22.5 degree phase increment, for 8 and 16 channel arrays respectively. Using this excitation mode, we calculated the power balance and SAR.

Method: The realistic 3-D EM model of arrays included all coil construction details for the radiative elements, simulated with precise dimensions (length 150, 145, 190 mm for loop, strip based and locally shielded microstrip respectively) and material electrical properties. The load utilized was the Ansoft human body (head, shoulders, torso) with a scaling factor of 0.9, and the field of view (FOV) was the entire human brain. The scanner gradient shield (with diameter of 683 mm and length 1200 mm) and scanner bore (with diameter of 900 mm and length 3366 mm) were always included in the numerical domain for simulation of unshielded and shielded arrays. The strip-line array of Adriany was simulated in two modifications: the original design, and one with a local shield of diameter 325 mm and length 250 mm, to allow checking of the proposal for improvement of transmit performance of the strip line based array published by Wu [5].

Common-current suppression was assumed to be ideal. Neither RF cable traps nor coax cable interconnection wiring were included in the simulation domain.

For all geometries, the array was tune/match/decoupled using capacitive and inductive decoupling networks when suitable, or without any decoupling, tuned only by minimization of the power reflected by the entire array ($\mathbf{P}_{\mathrm{reflected}}$). For each array and tuning arrangement, the following power-balance related quantities were calculated: $\mathbf{P}_{\mathrm{reflected}}$, radiated power ($\mathbf{P}_{\mathrm{radiated}}$), power deposited in entire human model ($\mathbf{P}_{\mathrm{body}}$), power deposited in entire brain ($\mathbf{P}_{\mathrm{brain}}$), and inherent losses for the array ($\mathbf{P}_{\mathrm{array\_internal}}$). For the analysis of coil transmit performance over the entire brain, two transmit performance related quantities have been used: a) the ratio of mean $\mathbf{B}_1+$ over the entire brain ($\mathbf{B}_1+_{\mathbf{brain}}$) to the square root of $\mathbf{P}_{\mathrm{transmit}}$; b) the ratio $\mathbf{B}_1+_{\mathrm{brain}} / \sqrt{\mathbf{P}_{\mathrm{brain}}}$.

Results: The head model scaling factor of 0.9 ensures that the non-conservative electrical field dominates for all the arrays investigated (the coil is not a close fit). A summary of the results is presented in Table 1. For a stripline-based array, we provide data for a capacitive decoupling

Table 1: Simulation data for $\mathbf{P}_{\mathrm{transmit}} = 8\,\mathrm{W}$.

Design	microstrip coil retuned	microstrip coil original	16 element stripline	16 element stripline Shielded	8 element Loop "Pm"	8 element Loop "ID"	8 element loop shielded "Pm"	8 element loop shielded "ID"
$\mathbf{P}_{\mathrm{reflected}}$, W	0.05	3.8	0.6	0.39	0	0.56	0	0.25
$\mathbf{P}_{\mathrm{radiated}}$, W	0.25	0.12	2.33	0.44	0.63	0.82	0.07	0.08
$\mathbf{P}_{\mathrm{array\_internal}}$, W	2.06	1.12	1.39	1.49	0.21	0.25	0.34	0.42
$\mathbf{P}_{\mathrm{body}}$, W	5.64	2.96	3.68	5.67	7.16	6.37	7.59	7.25
$\mathbf{P}_{\mathrm{brain}}$, W	1.89	1.01	0.93	1.82	2.67	2.40	2.78	2.65
$\mathbf{B}_1+_{\mathrm{brain}}$, μT	1.29	0.93	0.96	1.29	1.57	1.48	1.62	1.58
$\mathbf{SAR}_{10g}$	2.84	1.70	1.64	3.3	4.07	4.09	4.54	4.44
$\mathbf{B}_1+_{\mathrm{brain}}/\sqrt{\mathbf{P}_{\mathrm{transmit}}}$, μT/√W	0.46	0.33	0.34	0.45	0.55	0.52	0.57	0.56
$\mathbf{B}_1+_{\mathrm{brain}}/\sqrt{\mathbf{P}_{\mathrm{brain}}}$, μT/√W	0.94	0.93	0.99	0.95	0.96	0.95	0.97	0.97
$\mathbf{B}_1+_{\mathrm{brain}}/\sqrt{\mathbf{SAR}_{10g}}$, μT/√(W/kg)	0.77	0.72	0.75	0.71	0.77	0.73	0.76	0.75

network, where coupling to the first neighbor is about −15 dB. For the loop array we show data for the minimized $\mathbf{P}_{\text{reflected}}$ condition ("Pm" — highly coupled configuration), and also for an inductive decoupling network, where "ID" coupling to the first neighbor is less than −16 dB. The "Pm" condition provides the best transmit performance in the CP excitation mode. Although the variation of the entire array performance (estimated as the ratio $\mathbf{B}_1{+}_{\text{brain}}/\sqrt{\mathbf{P}}_{\text{transmit}}$) is more than 72% (peak to peak) for all arrays analyzed, the ratio of $\mathbf{B}_1{+}_{\text{brain}}/\sqrt{\mathbf{P}}_{\text{brain}}$ is equal to $0.96\,\mu\text{T}/\sqrt{\text{W}}$, with only $+/-4\%$ variation. The ratio $\mathbf{B}_1{+}_{\text{brain}}/\sqrt{\mathbf{SAR}}_{10\text{g}}$ also varies only slightly. Assuming ideal common current suppression, the local shield improves strip based array performance mainly because it simultaneously reduces $\mathbf{P}_{\text{radiated}}$ significantly (from 29% to 6% of $\mathbf{P}_{\text{transmit}}$), and increases both $\mathbf{P}_{\text{body}}$ and the ratio $\mathbf{P}_{\text{brain}}/\mathbf{P}_{\text{body}}$ (from 25% to 32%). For a loop array the influence of the local shield on transmit performance is negligible for the "Pm" condition, because any reduction of the relatively small $\mathbf{P}_{\text{radiated}}$ (8% of $\mathbf{P}_{\text{transmit}}$) is accompanied by an increase of $\mathbf{P}_{\text{array\_internal}}$ and a slight decrease of the ratio $\mathbf{P}_{\text{brain}}/\mathbf{P}_{\text{body}}$ from 37.3% to 36.6%. Addition of the shield hardly affects $\mathbf{P}_{\text{brain}}$. For the "ID" arrangement, the shield improves $\mathbf{B}_1{+}_{\text{brain}}/\sqrt{\mathbf{P}}_{\text{transmit}}$ by 8% because use of the shield reduces not only $\mathbf{P}_{\text{radiated}}$ but also $\mathbf{P}_{\text{reflected}}$.

Conclusion: For excitation in CP mode of the entire brain, the dominance of non-conservative fields and delivery of the maximal fraction of transmit power to the brain ensure the best transmit performance, estimated as $\mathbf{B}_1{+}_{\text{brain}}/\sqrt{\mathbf{P}}_{\text{transmit}}$. If the non-conservative RF electric field is dominant, even major variations of the array's current distribution resulting from changes in array geometry and different tuning/matching/decoupling have a very weak influence on the integral ratios $\mathbf{B}_1{+}_{\text{brain}}/\sqrt{\mathbf{P}}_{\text{brain}}$ and $\mathbf{B}_1{+}_{\text{brain}}/\sqrt{\mathbf{SAR}}_{10\text{g}}$, although the $\mathbf{B}_1{+}_{\text{brain}}$ and SAR profile vary. For comparison of array transmit performance, which is obtained by numerical simulation, consideration of both $\mathbf{P}_{\text{reflected}}$ and $\mathbf{P}_{\text{array\_internal}}$ is very important, because $\mathbf{P}_{\text{reflected}}+\mathbf{P}_{\text{array\_internal}}$ can be as great as 37% of $\mathbf{P}_{\text{transmit}}$. Final decisions regarding coil design should include consideration of these factors.

REFERENCES

1. Kozlov, M. and R. Turner, *Journal of Magnetic Resonance*, Vol. 200, 147–152, 2009.
2. Kozlov, M. and R. Turner, *Proceedings of the 40th European Microwave Conference*, 328–331, 2010.
3. Adriany, G., et al., *Magn. Reson. Med.*, Vol. 59, No. 3, 590-7, Mar. 2008.
4. Weisser, A. and T. Lanz, "A volume head array with 8 transmit/receive channels for 7T," *Proc. ISMRM*, Vol. 14, 2591, 2006.
5. Wu, B., et al., *ISMRM*, Vol. 17, 107, 2009.

Pulse Train Distributed Magnetic Field Generated from High Strength Concrete Using Magnetized Olivine Stone Aggregate

K. Mohri[1, 4], **M. Sasaki**[2], **T. Uemura**[3], **Y. Mohri**[4], **M. Yamada**[5], **and T. Kato**[6]

[1]Nagoya Industrial Science Research Institute (NISRI), Nagoya 464-0819, Japan
[2]Shinchita Concrete Kogyo Corp., (NCC), Chita 478-0041, Japan
[3]Tsuruta Sekizai Corp., Nagoya 456-0024, Japan
[4]MI Institute, Nagoya 468-0028, Japan
[5]Faculty of Science and Technology, Meijo University, Nagoya 468-8502, Japan
[6]Graduate School of Engineering, Nagoya University, Nagoya 464-8603, Japan

Abstract— We have found a new effect in which the pressure strength of a concrete has increased using magnetized olivine crashed stones as the aggregate for development of the high-strength concrete technology. Increasing rate of around 14% in the pressure strength at 84 N/mm^2 was obtained at 91 days measurement for a concrete with the normal Portland cement, the mountain sand fine aggregate, and the magnetized olivine crashed stone coarse aggregate in place of the conventional non-magnetized olivine stone coarse aggregate. A tap water with dipped magnetized olivine crashed stones through one week was also used.

Alternatively pulse train distributed static magnetic field is generated on the surface of the reinforced high-strength concrete with around 200 mG in the pulse height and around 2 cm interval between adjacent pulses, which is considered to increase the number of free protons in the water to promote the hydration for concrete crystallization due to the protonics principle [1]. The bio activation and health recovery effects are expected on the magnetic concrete wall and floor due to the similar effect of the magnetized pipe stroking on the human body [2]. The electromagnetic micro wave absorption was measured for the magnetic concrete plate with around 1000 times higher than that of the non-magnetic concrete plate with the spin resonance energy losses.

REFERENCES

1. Mohri, K. and M. Fukushima, "Milligauss magnetic field triggering reliable self-organization of water with long range ordered proton transport through cyclotron resonance," *IEEE Trans. Magn.*, Vol. 38, No. 5, 3328–3330, 2003.
2. Mohri, K., Y. Inden, M. Yamada, and Y. Mohri, "Health recovery effect of physiological magnetic stimulation on elder person's immunity source area with transition of ECG and EEG," *PIERS Proceedings*, 240–244, Kuala Lumpur, Malaysia, Mar. 27–30, 2012.

Arousal Effect of Physiological Magnetic Stimulation on Car Driver's Pit of Stomach Evaluated with Electroencephalogram Using Driving Simulator

Y. Mohri[1], **M. Yamada**[2], **K. Sakai**[2], **W. Kato**[2], **K. Mohri**[3], **and T. Uchiyama**[4]

[1]MI Institute, Nagoya 468-0028, Japan
[2]Faculty of Science & Technology, Meijo University, Nagoya 468-8502, Japan
[3]Nagoya Industrial Science Research Institute (NISRI), Nagoya 464-0819, Japan
[4]Graduate School of Eng., Nagoya University, Nagoya 464-8603, Japan

Abstract— We report a new effective and safe method of arousal for car drivers with application of a physiological magnetic stimulation (PMS) on pit of the stomach with a magnetized olivine pendant, which is evaluated more widely applicable to car drivers of not only elderly persons [1, 2] but also younger persons. We focused a point for the PMS to pit of the stomach on the basis of the bio-magnetic detection using a pico-Tesla resolution MI sensor which shows relatively high bio-magnetic field time series changeable with the pulse train distributed static magnetic field PMS [1].

In the four-point Electroencephalogram (EEG) measurement just after 20-min night time highway driving with eyes closing state, five men subjects (21, 21, 23, 27, and 71 age men) showed higher value of the arousal index $(\alpha + \beta)/(\delta + \theta)$ (α: passive arousal, β: active arousal, δ: passive sleep, and θ: active sleep) with attachment of a magnetized sintered olivine stone pendant on pit of the stomach on the driving simulator than that with non-magnetic pendant case. Their driving behavior evaluated with the deflection from the car running reference line matched with the arousal index value level.

REFERENCES

1. Mohri, K., T. Uchiyama, M. Yamada, T. Watanabe, Y. Inden, T. Kato, and S. Iwata, "Arousal effect of physiological magnetic stimulation on elder person's spine for prevention of drowsiness during car driving," *IEEE Trans. Magn.*, Vol. 47, No. 10, 3066–3069, 2011.
2. Mohri, Y., M. Yamada, K. Endo, T. Suzuki, and K. Mohri, "Arousal effect of physiological magnetic stimulation on car driver's spine evaluated with electroencephalogram using driving simulator," *PIERS Proceedings*, 245–249, Kuala Lumpur, Malaysia, March 27–30, 2012.

Simulation of the Waveguide Earthquake by Using GL Geophysical Modeling

Ganquan Xie[1, 2], **Jianhua Li**[1, 2], **Lee Xie**[2], **Qing Xie**[1], **Xianwei Zhou**[3], **D. Zuo**[1], **F. Xie**[2], **Xuan Zhou**[1], **and Mengji Xie**[1]

[1]Hunan Super Computational Sciences Center, China
[2]GL Geophysical Laboratory, USA
[3]Beijing Scientific and Technology University, China

Abstract— There are many canyon in China and other countries in the world. The Earthquake happened in the canyon is waveguide type. It is named waveguide Earthquake. The main property of the waveguide Earthquake is that there are many strong aftershocks. These aftershocks are superimposed on each other that composes to cause danger collapse and stone rain etc. geological disasters. GL geophysical modeling is joint method that include Seismic, EM, Heat, Fluid, Earth pressures etc. simulation components. In this paper, we present simulation of the waveguide Earthquake by using GL geophysical modeling and obtained very good result that display the GL Geophysical Joint Modeling has advantages over than other approaches. The GL Geophysical modeling can be extended as GL Medical Diagnostic Modeling. The copyright and patents and all rights of this paper contents are reserved by authors in GL Geophysical Laboratory.

ACKNOWLEDGMENT

Authors thank Ms. Yuan Zhang in Ze Xing Group Company in China for her help.

GL EM Modeling for Entertainment

Jianhua Li[1, 2], **Ganquan Xie**[1, 2], **Bihua Zhou**[1, 3], **Xiangwu Xie**[1], **Ke Li**[1, 2], **and Chuan Xie**[1, 2]

[1]Hunan GL Super Computational Sciences Center, China
[2]GL Geophysical Laboratory, USA
[3]Xiangxiang First High School, China

Abstract— The electromagnetic (EM) entertainment is new and rapid development industry production. Recent year, we have been studying research and development of EM modeling for EM scenery. In this paper, we propose a GL EM modeling for entertainment. A group of sensors and GL EM modeling can be used to construct special devices for computational EM game, EM dance, EM psudo 2.5D and 3D movie and 3D mirages. Through 3D GL EM modeling simulation and scattering signal of the sensors adjustment, the best presentation of the EM entertainment is obtained. The copyright and patent are reserved by authors in GL Geophysical Laboratory in USA.

GL EM Visualization for Electromagnetic Education

Jianhua Li[1, 3], **Hong Jun Li**[2], **Jian Sheng Liu**[2], **Ganquan Xie**[3], **and Xiangqi Xie**[3]

[1]GL Geophysical Laboratory, USA
[2]Wang Cheng Second High School, Wang Cheng Area, Chang Sha City, China
[3]Hunan Super Computational Sciences Center, China

Abstract— In the high school and undergraduate study, the electromagnetic education is basic and important course content. There are several electric and magnetic and electromagnetic education experiments in high school and undergraduate university. However, the electromagnetic wave propagation intuition experiment is lacking. We propose GL electromagnetic wave propagation modeling simulation and sensor for visualization presentation of the electromagnetic wave propagation. Our GL electromagnetic visualization education has been get up student's interesting and understanding for electric, magnetic and electromagnetic conception, theory, and applications. For example, we proposed EM wave field around linear or nonlinear electric circuit by GL EM modeling. The GL EM education will be a powerful tool in mathematical vector equations and physical electromagnetic wave joint education and AP research courses.

Session 3P6b
Electromagnetic Modeling, Inversion and Applications

GL EM Modeling for an Industrial and Art Scenery Design Model
Jianhua Li, Ganquan Xie, Qing Xie, Lee Xie, Feng Xie, Y. J. Xie, Xinsheng Xie, Y. Zhang, ... 622
Electromagnetic, Seismic, Heating, and Fluid Modeling and Inversion for Social and Natural Earthquake Dynamic
Ganquan Xie, Jianhua Li, Qing Xie, Xianwei Zhou, ... 623
Three-dimensional Controlled-source Electromagnetic Finite Element Modeling Using A-Φ Method
Bo Han, Xiangyun Hu, Guiju Wu, ... 624
Temporal Orthogonal Projection Inversion Technique for EMI Sensing of UXO
Lin-Ping Song, Douglas W. Oldenburg, Leonard R. Pasion, Stephen D. Billings, Laurens Beran, ... 625
Speed-feedback, Direct-drive Control of a Low-speed Transverse Flux-type Motor with Large Number of Poles for Ship Propulsion
Yuta Yamamoto, Taichi Nakamura, Yasuhiro Takada, Takafumi Koseki, Yasuaki Aoyama, Yoshitaka Iwaji, ... 626

GL EM Modeling for an Industrial and Art Scenery Design Model

Jianhua Li[1, 2], **Ganquan Xie**[1], **Qing Xie**[1], **Lee Xie**[2], **Feng Xie**[2], **Y. J. Xie**[1], **Xinsheng Xie**[1], **and Y. Zhang**[1]

[1]Hunan Super Computational Sciences Center, China
[2]GL Geophysical Laboratoy, USA

Abstract— In the tradition theatrical stage scenery sets, many heave instruments devices and Manual body Labor were needed. If the stage scenery set is moved, the manual scenery Sets are needed to re installed. That is very inconvenience. In this paper, we propose a Global and Local (GL) new electromagnetic (EM) industrial and art scenery design model. Also, we use GL EM modeling to simulate the GL EM scenery in bridge and digit movies. The GL simulation present some advantages of the GL EM industrial and art scenery model over the traditional theatrical stage scenery.

Electromagnetic, Seismic, Heating, and Fluid Modeling and Inversion for Social and Natural Earthquake Dynamic

Ganquan Xie[1], **Jianhua Li**[1, 2], **Qing Xie**[1], **and Xianwei Zhou**[3]

[1]Hunan Super Computational Sciences Center, China
[2]GL Geophysical Laboratory, USA
[3]University of Sciences and Technology, China

Abstract— There is four kind of earthquakes that are natural earthquakes, artificial physics earthquakes, social earthquake, artificial social earthquake in social and natural dynamic. Natural earthquake is the uncontrollable natural earthquake on the Earth and the planet, likes Tangshan, Wenchuan and Yiliang earthquake. Artificial physical earthquakes are controllable local earthquake that is caused by the discharge, and underground nuclear explosions detonated, exciting, Artificial physical seismic is effective method for the geophysical exploration and oil exploration. MRI, EKG and ultrasound medical examination and nondestructive testing and physical to explore are artificial micro seismic method. Social earthquake includes foreign aggression, domestic revolution, unrest and coups. Germany Hitler and Japan launched the Second World War is the destruction social earthquake for all mankind social. The Chinese historical peasant uprising and the world revolution and coup are social earthquake of collapse, the social earthquake is not controllable. Analog controllable artificial physical earthquake, controllable artificial social earthquake is existence in logic and are actually there. National political reform, reform, improvement, constitutional monarchy, Japan Minzhi only new are controllable the artificial societies earthquake. However, a large-scale and intense artificial social earthquake with "rebel" slogan launched by the ruler himself are relatively rare in history. "Chairman Mao launched the Cultural Revolution" is a wide range of controllable artificial social earthquake. This unrest known as the "Cultural Revolution" in history there will be long-term impact. Earthquake includes felt earthquakes and No sense of the seismic and micro seismic. Felt earthquakes is divided into the destruction of the earthquake and no destruction of the earthquake. MRI, EKG and ultrasound micro without destruction of the earthquake. Tangshan, Wenchuan and Yiliang earthquake are uncontrollable destructive natural earthquake. The reform and opening up is harmonious and constructive controllable artificial social earthquake. The Cultural Revolution is controllable social earthquake, but it is social artificial earthquake with the destructive. Therefore, a new research project is a GL EM, Scismic, Heating, and Fluid joint inversion for natural earthquakes, artificial physical earthquakesocial earthquake, artificial social earthquake.

Three-dimensional Controlled-source Electromagnetic Finite Element Modeling Using A-Φ Method

Bo Han, Xiangyun Hu, and Guiju Wu
Institute of Geophysics and Geomatics, China University of Geosciences, Wuhan 430074, China

Abstract— During the last few decades, the numerical solutions of the controlled-source electromagnetic (CSEM) induction problems, which are widely applied in geophysical prospecting, have received a lot of attention. In this paper, we describe a finite element approach for 3D CSEM modeling in the frequency domain. The electric field **E** is decomposed into magnetic vector potential **A** and electric scalar potential **Φ** with a Coulomb gauge condition $\nabla \cdot A = 0$, and we solve the Maxwell's equations in terms of **A** and **Φ** based on nodal elements. In comparison with those methods which directly calculate electric field **E** and magnetic field **H**, the **A-Φ** method is much easier to guarantee the continuity of the tangential field components across material interfaces when nodal elements are employed. A Galerkin method is used to derive the system of equations for the Coulomb-gauged potentials. Since the resulting linear system is large, sparse and asymmetrical, the iterative quasi-minimal residual (QMR) algorithm is regarded as an adequate solver. We demonstrate the validity and efficiency of our method in several numerical experiments.

Temporal Orthogonal Projection Inversion Technique for EMI Sensing of UXO

Lin-Ping Song[1], **Douglas W. Oldenburg**[1], **Leonard R. Pasion**[2], **Stephen D. Billings**[2], **and Laurens Beran**[2]

[1]Department of Earth and Ocean Sciences, University of British Columbia, Canada
[2]Black Tusk Geophysics, Canada

Abstract— Electromagnetic induction (EMI) sensing has been a major protocol in environmental remediation of unexploded ordnance (UXO) contamination. Its effective use relies upon an inversion processing technique that is capable of extracting accurate target signatures (e.g., dipolar polarizabilities) from measured data for input to subsequent tasks of discriminating UXO from non-hazardous clutter.

This paper presents a new inversion method that is based upon the singular value decomposition (SVD) analysis of multiple-time channel responses. First, we use the multi-channel EMI sensor data to construct the spatial-temporal response matrix (STRM). The rows of the STRM correspond to measurements sampled at different time channels from one transmitter/receiver pair and the columns correspond to measurements sampled at the same time channel from different transmitter/receiver combinations. The SVD of the STRM gives that the left singular vectors are related to the sensor space and the right singular vectors form an orthonormal basis spanning the temporal space. If the effective rank of the STRM is r, then the first r left and right singular vectors span signal subspaces. The remaining singular vectors span the noise subspaces. Next, we do a one-sided projection by right multiplying the STRM with the temporal signal subspace matrix and obtain a transformed response matrix whose r columns are the signal subspace (SS) temporal channels. This allows us to carry out a temporal orthogonal projection inversion (TOPI) where the r SS projected temporal channels for source locations and the target polarizabilties are solved as a linear optimization problem in the original data domain.

The proposed approach is evaluated using the field data collected with different multi-chanel, mulit-static EMI sensor systems. The SVD of the STRM typically produce a rapid decay of singular values. This suggests that signals are compressible and can be represented with a low-rank approximation matrix. Our experiments show that an effective rank can be determined by finding the location of maximum curvature when plotting singular values versus their indices. Furthermore, we have found that the temporal projection generally leads to highly compressed signals whose significant components are concentrated around the first a few projected time channels. This suggests that the TOPI might be implemented by simply using the first projected temporal signals. In comparison with the usual method of using the original data, the TOPI approach demonstrates the potential for being more computationally efficient but producing more accurate results since a substantial portion of the noise in the data is winnowed from the analysis.

Speed-feedback, Direct-drive Control of a Low-speed Transverse Flux-type Motor with Large Number of Poles for Ship Propulsion

Y. Yamamoto[1], **T. Nakamura**[2], **Y. Takada**[1], **T. Koseki**[1], **Y. Aoyama**[3], **and Y. Iwaji**[3]

[1]The University of Tokyo, Japan
[2]West Japan Railway Company, Japan
[3]Hitachi Research Laboratory, Hitachi, Ltd., Japan

Abstract— We have designed and proposed direct-drive permanent magnet synchronous motor (PMSM) for ship main propulsion called for high torque at low speed [1]. It is necessary to increase the number of poles and decrease the pole pitch to achieve low-speed drive. So we focus on Transverse Flux-type motor which has flexibility adjusting pole pitch. On the other hand, if the number of poles in the motor is large and rated speed is low, it is difficult to obtain precise speed information due to insufficient speed information from the encoder. Thus, resolution of the speed is lost considerably in the lower speed region. As a result, stability of the system is remarkably worse as shown in Fig. 3(a). To resolve this issue, we applied Dual Sampling rate Observer (DSO) to the system [2]. The DSO is a discrete-time observer with two sampling rates. One is from encoder pulse T_1; the other is from control period T_2 of the system. The fundamental idea is to estimate the state variables of the system at every sampling period and correcting the error of estimation when an encoder pulse including real value is found. Estimation period is the same as control period so that the observer gives appropriate information to the controller at every control period. For example, when T_1 is shorter than T_2 ($T_1 < T_2$) means that it is operating at high speed, DSO is functioned as a usual discrete-time observer. The effectiveness of DSO, compared to the basic current controller and speed controller of cascade control composed

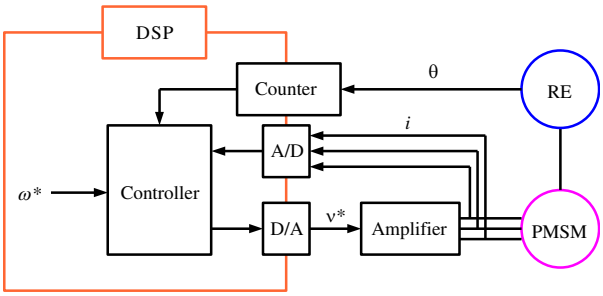

Figure 1: Configuration in motor-drive system for tests.

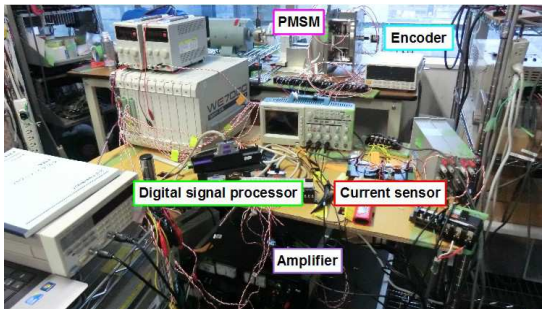

Figure 2: General view of the experiment.

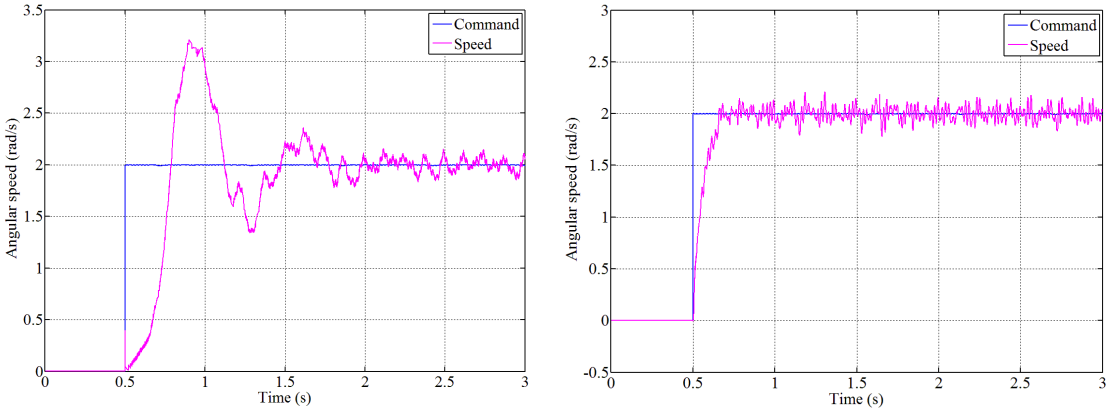

Figure 3: Comparison of the output signal for the speed in experiment with/without DSO (Reference of the angular velocity 2.0 rad/s). (a) Without DSO (Speed is calculated by inexact diffrential on position). (b) With DSO (Time constant of the observer 8.0 m/s).

of PI controllers, at low speed is confirmed through the simulations and experiments as shown in Figs. 1–3. Each gain of the controllers without DSO is decided by using Kessler method which is one of the Coefficient Diagram Methods (CDMs) to design uniformly [3]. In the full paper, the flow of decision on each gain and some experiments conducted by using another direct-drive motor such as no-load and load test will also be described in detail.

REFERENCES

1. Nakamura, T., T. Koseki, and Y. Aoyama, "A low-speed high-torque permanent magnet synchronous motor — Reducing cogging torque and eddy current loss," *The Japanese Society of Applied Electromagnetics and Mechanics*, Vol. 20, No. 2, 410–415, Jun. 2012.
2. Manabe, S., "The coefficient diagram method," *IFAC Symposium on Automatic Control in Aerospace*, 199–210, Aug. 1998.
3. Kovudhikulrungsri, L. and T. Koseki, "Precise speed estimation from a low-resolution encoder by dual-sampling-rate observer," *IEEE/ASME Transactions on Mechatronics*, Vol. 11, No. 6, Dec. 2006.

Session 3P8
Poster Session 4

A 2.4 GHz Array Combination High-power Amplifier
Chien-Hua Lai, Jeng-Rern Yang, ... 632
Design and Optimization of Carrier Suppression Circuit for UHF RFID Reader Applications
You Bin, Quliang Yu, Mingzhu Zhou, Xiao-Hong Zhang, ... 633
Planar Four-port Circulator Using Single Longitudinally Magnetized Ferrite Coupled Line Junction
Wojciech Marynowski, Adam Kusiek, J. Mazur, ... 634
Analysis of Magnetic Losses in Ferrite Coupled Lines Using SDA and Hybrid Root Finding Algorithm
Wojciech Marynowski, Piotr Kowalczyk, ... 635
A Novel Tunable Bandpass Filter Using Microstrip Open-loop Resonators and Varactor Diodes
Minoo Najafi, Alireza Malahzadeh, ... 636
Complex Permittivity Measurement for Thin Sample Using Rectangular Waveguide Filled with Supporting Materials
Tatsuya Suzuki, Sho Suzuki, Kyota Otsuka, Kota Kiyomi, Takanobu Ohno, Kouichi Ishii, ... 637
A Design for Ultra-wideband Bandpass Filter Using Parallel-coupled Line and Stepped Impedance Resonator by Genetic Algorithm
Kota Kiyomi, Tatsuya Suzuki, Kyota Otsuka, Sho Suzuki, Takanobu Ohno, Kouichi Ishii, ... 638
A Study on Thickness of High Loss Material for Determining Accurate Complex Permittivity in Transmission Line Method Using Rectangular Waveguide
Sho Suzuki, Tatsuya Suzuki, Kyota Otsuka, Kota Kiyomi, Takanobu Ohno, Kouichi Ishii, ... 639
Reasonable Estimations of Constituent Losses of Printed Circuit Board Interconnects
Kuen-Fwu Fuh, Pin Deng, Annie Liu, Eric Liao, ... 640
Implementation of a Compact RF Module by Analysis and Fabrication for Organic Substrate with Embedded Passives
Jongin Ryu, Jong Min Yook, Dongsu Kim, ... 641
Propagation Characteristics of the Meandered Defected Ground Structure
Wan-Ti Wang, Tzu-Hsiung Lin, Chien-Jen Wang, ... 642
Three-port De-embedding Methodology for GaAs pHEMT Characterization
Chie-In Lee, Wei-Cheng Lin, Yan-Ting Lin, ... 643
Wideband Leveling Amplifier Design Using 0.18 µm CMOS Process
Guan-Shian Li, Ching-Ying Huang, Robert (Shu-I) Hu, Chung-Ping Chen, ... 644
FPGA Implementation and Verification of Reed-Solomon Code in SDR System
Yi Hua Chen, Chang Lueng Chu, Chun Chun Yeh, ... 645
Design of a Bandwidth-enhanced Ultra Thin Metamaterial Absorber
Saptarshi Ghosh, Somak Bhattacharyya, Kumar Vaibhav Srivastava, ... 646
Investigation of Parasitic Effects Induced by the Ground on LTCC Passive Components
Runiu Fang, Min Miao, Yufeng Jin, ... 647
Microwave Optoelectronic Oscilator for Distribuited Receivers Operating Remotely
Larissa Aguiar Dantas de Britto, Débora Maria Souza Morais, Gefeson Mendes Pacheco, ... 649
LTE Mixer Array of 0.5 W High Output Power
Pang-Hsing Chen, Yen-Heng Chen, Jeng-Rern Yang, ... 650
Design of a Highly Linear Low-noise Amplifier with Noise and Distortion Cancelation
Pang-Hsing Chen, Jeng-Rern Yang, ... 651
Dual-band Bandpass Filer with a Tunable Upper Passband
Shun Fu Liao, Hsun-Hsiang Chen, Ching-Her Lee, ... 652
A Tunable Dual-band Bandpass Filter with Two Independently Tunable Passbands
Ding-Hong Jia, Quanyuan Feng, Xiao-Guo Huang, Qian-Yin Xiang, ... 653
A Constant Absolute Bandwidth Tunable Combline Bandpass Filter
Xiao-Guo Huang, Quanyuan Feng, Qian-Yin Xiang, Ding-Hong Jia, ... 654

Digital Predistortion for RF Power Amplifiers Based on Enhanced Orthonormal Hermite Polynomial Basis Neural Network
Xiao-Hui Yuan, Quanyuan Feng, Tiao Jun Zeng, Hongbo Ma, ... 655
The Investigation of the Effects of Electromagnetic Band Gap Structure and Configuration Size on Power Integrity of High Speed Circuit Board
Yun-Hsih Chou, Ming-Chang Tsai, ... 656
Closed Loop Cell Texture Thermodynamics
Karl F. Kaspareck, ... 657
Design of Parallel FFT Based on FPGA in the Field of Software Radio
Guochun Wan, Y. Q. Zhang, Mei Song Tong, ... 658
Dual Band Circuit Design Using Mixed Lumped Elements/Coupled Lines
Kuan-Yu Liao, Jan-Dong Tseng, ... 659
A Correction Term for Maxwell's Equations Transformed between Galilean Reference Systems (Part I)
Namik Yener, ... 660
A Correction Term for Maxwell's Equations Transformed between Galilean Reference Systems (Part II)
Namik Yener, ... 661
A Large Tuning Range Ring VCO in 180 nm CMOS
Xuemei Lei, Zhigong Wang, Lianfeng Shen, Keping Wang, ... 662
A Planar MIMO Antenna for Mobile Phones
Di Wu, Sing Wai Cheung, Tung Ip Yuk, Xiao Lei Sun, ... 663
CPW-coupled-fed Circular UWB Monopole Antenna
Jun Zhang, Sing Wai Cheung, Tung Ip Yuk, ... 664
A Compact Branch-line Directional Coupler Using Lumped-element CRLH TLs
Y. F. Wu, Jun Zhang, Sing Wai Cheung, ... 665
Direction of Arrival Estimation Based on Maximum Likelihood Criteria Using Gravitational Search Algorithm
Ahmed Magdy Mohamed, Korany Ragab Mahmoud, Samir G. Abdel Gawad, Ibrahim I. Ibrahim, ... 666
Experimental Studies on Microwave Gunn Oscillator Based Modulator-demodulator Systems with Chaotic Modulating Signals
Bishnu Charan Sarkar, T. Banerjee, Suvra Sarkar, Chaitali Koley, Arun K. Guin, ... 667
Effects of Nonlinear Bias Tuning of X-band Gunn Oscillator Based Frequency Modulators
Bishnu Charan Sarkar, T. Banerjee, Arun K. Guin, Chaitali Koley, ... 668
Experimental Studies on the Nonlinear Interaction between a Chaotic Signal and a Periodic Signal at Microwave Frequency Range
Bishnu Charan Sarkar, Suvra Sarkar, Chaitali Koley, Arun K. Guin, T. Banerjee, ... 670
A Contactless Inductive Charging Platform
Han-Chung Teng, Tsung-Lin Li, Guan-Pu Pan, Jwo-Shiun Sun, ... 672
FPGA Implementation of LDPC Encoder with Approximate Lower Triangular Matrix
Yi Hua Chen, Jheng Shyuan He, ... 673
A Novel Function Tuner with Microstrip Circuit for Slot Patch Antenna
Chia-Ching Chu, Lih-Shan Chen, Hsien-Chiao Teng, Shen Cherng, ... 674
An Emergency Medical Service Support System
Li-Lin Chen, ... 675
A Novel Design of Reconfigurable Annular Slot Active Patch Antenna
Yu-Ming Lee, Shen Cherng, Hsien-Chiao Teng, Shuming T. Wang, ... 676
A Surface-potential Based Compact Model of Gate Capacitance in GaN HEMTs
Jie Wang, Lingling Sun, Jun Liu, Mingzhu Zhou, ... 677
Design of the Envelope Modulator for High Efficiency RF Envelope Tracking Power Amplifier (ET-PA)
C. A. Schecht, Donald Y. C. Lie, J. Lopez, ... 678
Design of a Multi-band Dielectric Resonator Antenna
Hsin-Chih Tsai, Tsung-Lin Li, Hung-Wen Liu, Jwo-Shiun Sun, ... 679
Design of a Circularly Polarized Rectenna for Wireless Power Transmission
Si-Jyun Hung, Tsung-Lin Li, Yi-Ching Huang, Jwo-Shiun Sun, ... 680
High-peak Power, Low-average Power RF Pulses, Bioeffects and Standards: Recent Developments
Michael R. Murphy, ... 681
Electromagnetic Forces in the Curved Octonion Spaces

Zi-Hua Weng, ... 682
The Effect of Exposure to ELF-EMFs on Learning and Memory Ability Changes in Rats
Jian Feng Guo, Dong Wang, Lingfeng Kong, ... 683
Electron Energy Loss and Second-harmonic Emission of Nonlinear Nanoparticles
Jinying Xu, Xiangdong Zhang, ... 684
3D CFDTD PIC Simulation Study on Low-frequency Oscillations in a Gyrotron
Ming-Chieh Lin, David N. Smithe, ... 685
A Prototype Design of Dental Microwave Imaging Equipment
Chun-Sen Wu, Hsien-Nan Kuo, Tsung-Chih Yu, ... 686
Research of Improved Matching Doherty Solid State Power Amplifier
Zheng-Qin Li, Wei Wei Cheng, Yuan-Yuan Wu, ... 687
Research of Doherty Solid State Power Amplifier with Improved Bias Matching
Ming-Hai Xu, Wei Wei Cheng, ... 688
Analysis and Design of the Microstrip Matching for Doherty Amplifier
Ming-Hai Xu, Shengyun Luo, ... 689
A Novel Oscillator Based on Film Bulk Acoustic Resonator
Wei Wei Cheng, Shu Rong Dong, Shengyun Luo, ... 690
Analysis and Optimization of the Linearity and Efficiency for Doherty Amplifier
Zheng-Qin Li, Wei Wei Cheng, Mei-Yi Xiang, ... 691
Design and Implementation of Low Phase Noise Oscillator Based on Film Bulk Acoustic Resonator
Wei Wei Cheng, Shu Rong Dong, Shengyun Luo, ... 692

A 2.4 GHz Array Combination High-power Amplifier

Chien-Hua Lai and Jeng-Rern Yang
Microwave Laboratory, Department of Communication Engineering
Yuan Ze University, Jhongli City, Taoyuan Country 320, Taiwan

Abstract— The purpose of this study was to design a 2.4 GHz class-A RF power amplifier following the TSMC CMOS 0.18 μm Process. The circuit was designed for fully integrated power amplifiers. To prevent the problems of an excessively large area created in the past when excessive inductance of power transmitter circuits was used to achieve the desired watt level, this study employed a side-by-side array, combining the electrical currents gathered in the amplifiers, and using the positive and negative signal conversion between the n-channel metal-oxide semiconductors (NMOS) and p-channel metal-oxide semiconductors (PMOS) to save driver area. For the output matching circuit, the optimal resistance point of a central tap inductor under a 2.4 GHz band was adopted, this inductor used Metal 6 and Metal 4 layers as the signal and current paths. A wire of 30 μm in width, with a 30 μm coil radius, was wrapped three times using the center point as radius to produce the inductance required for this circuit. The final output was transformed from a dual-end to a single-end signal. With this method, the entire area used is smaller than the combined area of traditional power amplifiers. A high-pass filter was employed for front-end matching, and a load-pull method was used for back-end matching. Matching design was conducted for a 2.4 GHz band. The output power of this power amplifier design was about 26 dBm. The P1 dB compression point was about 16 dBm, the power-added efficiency (PAE) was about 18.4%, and the power-gain was 11 dB. For an overall supply voltage of 3.1 V, the overall power consumption was approximately 1.8 mW. The area of the chip was approximately 0.63 mm × 1.3 mm, this power amplifier achieving high power front-end and back-end matching by the output power combining transfer.

Design and Optimization of Carrier Suppression Circuit for UHF RFID Reader Applications

You Bin, Quliang Yu, Mingzhu Zhou, and Xiaohong Zhang
Key Laboratory of RF Circuits and Systems, Ministry of Education
Hangzhou Dianzi University, Hangzhou 310018, China

Abstract— In this paper, a new design is proposed to optimize 902M–928 MHz UHF RFID reader systems. With coupler RCP890A05, captured TX Signal after being attenuated and Reversed-Phase, is superimposed on leakage signal, at best, two LO signals will offset each other. When only using a circulator or directional coupler, isolation is always insufficient, then TX-to-RX leakage signal lead to saturation of the low noise amplifier or demodulator. This scheme adopts relatively simple circuit design; on one hand it will not increase the cost and circuit complexity, on the other hand, reader performance is significantly improved, measurement show that more than 60–70 dB isolation is acquired.

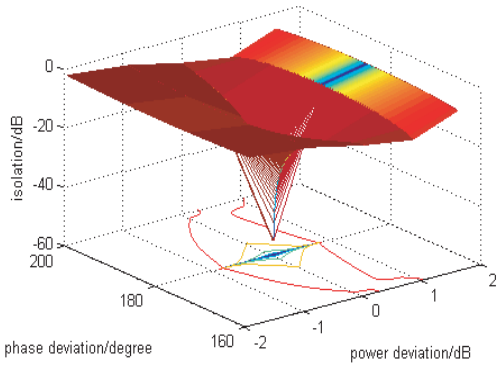

Figure 1: Signal simulation results.

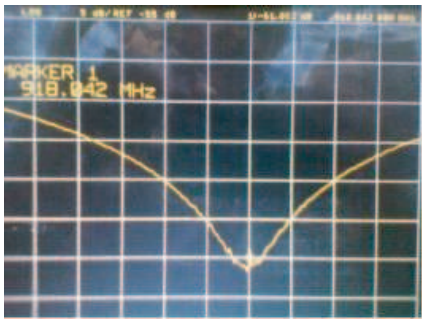

Figure 2: Measured isolation with CLS front-end.

REFERENCES

1. Bai, P., Y. Yin, and X. Yang, "A novel RX-TX front-ends for passive RFID reader with high isolation," *International Symposium on Microwave, Antenna, Propagation and EMC Technologies for Wireless Communications*, 332–335, 2007.
2. Brauner, T. and X. Zhao, "A novel carrier suppression method for RFID," *IEEE Microw. Wireless Compon. Lett.*, Vol. 19, No. 3, 128–130, Mar. 2009.
3. Jung, S.-C., M.-S. Kim, and Y. Yang, "A reconfigurable carrier leakagecanceller for UHF RFID reader front-ends," *IEEE Circuits Syst. I, Reg. Papers*, Vol. 58, No. 1, 70–76, Jan. 2011.
4. Jung, J.-Y., C.-W. Park, and K.-W. Yeom, "A novel carrier leakage suppression front-end for UHF RFID reader," *IEEE Transactions on Microwave Theory and Techniques*, Vol. 60, No. 5, May 2012.

Planar Four-port Circulator Using Single Longitudinally Magnetized Ferrite Coupled Line Junction

W. Marynowski, A. Kusiek, and J. Mazur

Gdansk University of Technology, Poland

Abstract— Recently, different configurations of integrated nonreciprocal devices using longitudinally magnetized ferrite coupled lines (FCL) are developed [1–6]. The most important advantages of such structures are wide operation bandwidth and weak biasing magnetic field needed for their nonreciprocal operation. However, the significant disadvantage of this class of devices are high insertion losses, which mainly result from the magnetic losses of the FCL section [4]. Hence, the recent research is focused on the reduction of insertion losses occurring in such devices.

In FCL devices the length of the ferrite section is determined by $\pi/4$ Faraday rotation angle which ensures nonreciprocal operation of the section. This effect can be utilized to build four-port circulators. These devices can be designed in two ways: as a cascade of two FCL sections and the even or odd T-junctions [1–4] or as a single FCL section in cascade with an even-odd four-port structure, i.e., hybrid coupler [5] or magic-T junction [6]. Since, the second configuration uses only a single FCL section, such structure offers lower insertion losses than the first arrangement, however, the complex even-odd four-port structure has to be designed. The four-port circulator using single FCL section is presented in [6], and low insertion losses are obtained. However, the circulator operates only in a narrow frequency band, which is limited by operation band of the used cylindrical FCL junction.

In this paper, the integrated planar four-port circulator is designed. The proposed structure is obtained as a cascade connection of planar four-port magic-T junction [7], planar ferrite coupled line section and transformer from coupled to uncoupled microstrip lines. The main advantage of the proposed configuration is usage of planar FCL section offering wider operation band than cylindrical one. The FCL section ensuring $\pi/4$ Faraday rotation angle is designed using own software based on spectral domain approach and mode matching technique (SDA/MM). Using commercial software HFSS the validation of the results obtained from SDA/MM and design planar reciprocal circuits of the structure are performed. The overall scattering parameters of the four-port circulator are obtained by cascading the scattering parameters of the planar circuits and FCL junction. Predicted performance of the designed device was verified experimentally.

ACKNOWLEDGMENT

This work was supported in part by Polish Ministry of Science and Higher Education from sources for science in the years 2012–2013 under Contract No. 0340/IP2/2011/71.

REFERENCES

1. Queck, C. K. and L. E. Davis, "Broad-band three-port and four-port stripline ferrite coupled line circulators," *IEEE Transactions on MTT*, Vol. 52, No. 2, 625–632, Feb. 2004.
2. Marynowski, W., A. Kusiek, and J. Mazur, "Microstrip ferrite coupled line isolators," *International Conference MIKON*, Vol. 1, 342–345, Krakow, Poland, May 2006.
3. Marynowski, W., A. Kusiek, and J. Mazur, "Microstrip four-port circulator using a ferrite coupled line section," *AEU — Int. Journal of Electronics and Communications*, Vol. 63, No. 9, 801–808, Jul. 2008.
4. Marynowski, W. and J. Mazur, "Study of nonreciprocal devices using three-strip ferrite coupled line," *Progress In Electromagnetics Research*, Vol. 118, 487–504, 2011.
5. Queck, C. K. and L. E. Davis, "Microstrip and stripline ferrite-coupled-lines (FCL) circulators," *IEEE Transactions on MTT*, Vol. 50, No. 12, 2910–2917, Dec. 2002.
6. Kusiek, A., W. Marynowski, and J. Mazur, "Investigations of cylindrical ferrite coupled line junction using hybrid technique," *Progress In Electromagnetics Research*, Vol. 120, 143–164, 2011.
7. Marynowski, W. and J. Mazur, "Investigation of multilayer magic-T configurations using novel microstrip-slotline transitions," *Progress In Electromagnetics Research*, Vol. 129, 98–108, 2012.

Analysis of Magnetic Losses in Ferrite Coupled Lines Using SDA and Hybrid Root Finding Algorithm

W. Marynowski and P. Kowalczyk
Gdansk University of Technology, Poland

Abstract— Ferrite coupled lines (FCL) are applied in a wide class of nonreciprocal devices [1] since 80's of 20th century, however the idea of FCL is still being developed and modified [2–5]. One of the main disadvantage of this structures is the high level of insertion losses. The significant part of losses is caused by the magnetic losses [2], therefore a detailed analysis of this phenomenon is required. A commercial software [6] can be successfully applied for such investigations, however universal and flexible tools are not efficient for optimization process because of a long calculation time. In such a case dedicated software is much more useful and effective. One of the methods of FCL analysis is spectral domain approach (SDA), where the calculation domain is not discretized. The propagation problem in SDA is reduced to searching zeros of a real function. In SDA the magnetic losses can be introduced replacing real permeability tensor by complex values. Such a modification implies complex values of the final function. Hence, a different algorithm for zero searching must be used.

In this paper, a hybrid complex root-finding algorithm is introduced. The problem can be particularly difficult if the number of roots and its multiplicity is unknown. Numerous algorithms of searching zero of a complex function are well described and successfully applied. However most of them require a starting point (Muller's method) or evaluation of the function in many points (splitting circle method [7]). In the presented method the function is sampled in adaptive mesh which is based on Delaunay triangulation. After the initial verification of the subregions (triangles) by Muller's method or splitting circle method the new points are added to the mesh. In the following steps subregions in the suspected area become smaller and the root can be found with high precision.

In order to present the validity of the algorithm two FCL structures were investigated and the results were compared with the ones obtained using commercial software.

ACKNOWLEDGMENT

This work was supported in part by Polish Ministry of Science and Higher Education from sources for science in the years 2012–2013 under Contract No. 0340/IP2/2011/71.

REFERENCES

1. Davis, L. E. and D. B. Sillars, "Millimetric nonreciprocal coupled slot finline components," *IEEE Transactions on Microwave Theory and Techniques*, Vol. 34, No. 7, 804–808, Jul. 1986.
2. Marynowski, W. and J. Mazur, "Study of nonreciprocal devices using three-strip ferrite coupled line," *Progress In Electromagnetics Research*, Vol. 118, 487–504, 2011.
3. Kusiek, A., W. Marynowski, and J. Mazur, "Investigations of cylindrical ferrite coupled line junction using hybrid technique," *Progress In Electromagnetics Research*, Vol. 120, 143–164, 2011.
4. Abdalla, M. A. and Z. Hu, "Compact novel CPW ferrite coupled line circulator with left-handed power divider/combiner," *2011 41st European Microwave Conference (EuMC)*, 794–797, Oct. 2011.
5. Kusiek, A., W. Marynowski, and J. Mazur, "Investigations of nonreciprocal devices employing cylindrical ferrite coupled line junction," *Journal of Electromagnetic Waves and Applications*, Vol. 26, No. 13, 1685–1693, 2012.
6. High Frequency Structure Simulator (HFSS), http://www.ansoft.com/.
7. Rodrguez-Berral, R., F. Mesa, and F. Medina, "Systematic and efficient root finder for computing the modal spectrum of planar layered waveguides," *International Journal of RF and Microwave Computer-aided Engineering*, Vol. 1, No. 14, 73–83, Jan. 2004.

A Novel Tunable Bandpass Filter Using Microstrip Open-loop Resonators and Varactor Diodes

Minoo Najafi and Alireza Malahzadeh
Islamic Azad University, Bushehr Branch, Bushehr, Iran

Abstract— A novel tunable narrow-band bandpass filter (NB BPF) is designed and developed in this paper. The proposed filter comprises of four microstrip open-loop resonators including electrical, magnetic and mixed couplings and and varactor diodes realizing a tunable NB BPF for personal communication systems. It is shown that by changing the capacitance of the varactor diodes, the resonant frequency of the filter can be tuned. By taking the advantage of the transmission zeros of this kind of resonators, a novel narrow-band tunable bandpass filter is designed and simulated and then the performance is verified by measurement. The measured results demonstrate the priority of this design in comparison with the conventional filters with higher frequency range of tunibility with improved insertion loss. Figure 1 shows the simulated and the measured performance of the proposed filter.

The proposed tunable BPF is then fabricated on a 31-mil-thickness 5880 substrate with dielectric constant 2.2 and measured its performance using an Agilent 8722D network analyzer. As provided here, by changing the bias voltage of varactor diode, we can simply tune the resonant frequency of the filter.

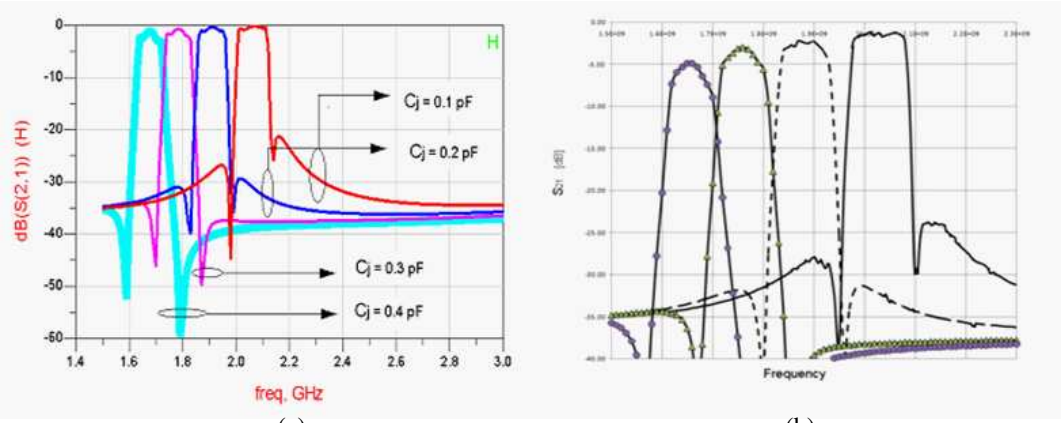

(a) (b)

Figure 1: Shows (a) the simulated and (b) the measured performance of the proposed filter.

REFERENCES

1. Schwindt, R. and C. Nguyen, "A new compact band-pass filter employing three parallel-coupled lines," *IEEE MTT-S Digest*, 1994.
2. Nguyen, C., "Miniaturized multi-octave band-pass filters," *Antennas and Propagation Society International Symposium*, 1995.
3. Genc, A. and R. Baktur, "A tunable bandpass filter based on varactor loaded split-ring resonators," *Microw. Opt. Tech. Lett.*, Vol. 51, No. 10, Oct. 2009.
4. Leuzzi, G., V. Stornelli, S. Del Re, and L. Pantoli, "High quality factor integrable bandpass filter by using tunable active inductor," *IEEE Microwave Conf.*, 2011.
5. Chiou, Y.-C. and G. M. Rebeiz, "A tunable three-pole 1.5-2.2-GHz bandpass filter with bandwidth and transmission zero control," *IEEE Trans. Microwave Theory Tech.*, Vol. 59, No. 11, 2872–2887, Nov. 2011.
6. Li, S. and F. Liu, "The design of a novel tunable filter," *IEEE Microwave Sym.*, 2011.

Complex Permittivity Measurement for Thin Sample Using Rectangular Waveguide Filled with Supporting Materials

T. Suzuki, S. Suzuki, K. Otsuka, K. Kiyomi, T. Ohno, and K. Ishii
Kisarazu National College of Technology, Japan

Abstract— This paper presents a transmission line method for determining complex permittivity of a thin sample in an X-band rectangular waveguide. PTFE are located on both sides of a thin sample to support it, and suitable thickness of PTFE for determining complex permittivity of a sample is examined by the transmission line theory and FDTD simulation.

Figure 1 shows a model of a transmission line method using rectangular waveguide for determining complex permittivity of a thin sample. The complex permittivity of a measurement sample shown in Fig. 1 is $10.0-j3.0$ assuming epoxy resin, and sample thickness (d) is 0.5 mm or 1.0 mm. Fig. 2 shows the calculated results of $|S_{11}|$ varying thickness of PTFE (d_0) based on transmission line theory. In Fig. 2, thickness of PTFE that indicates reflection less than -10 dB is from 5 mm to 11 mm in $d = 0.5$ [mm], and is from 6 mm to 9 mm in $d = 1.0$ [mm]. Figs. 3 and 4 show simulated results of complex permittivity for various PTFE thickness at 10 GHz using FDTD method. PTFE thickness which is from 7 mm to 10 mm in Fig. 3 and is from 6 mm to 9 mm in Fig. 4 can determine complex permittivity of a sample precisely. As a result, thickness of PTFE achieving low reflection condition obtains a good result of complex permittivity of a thin sample.

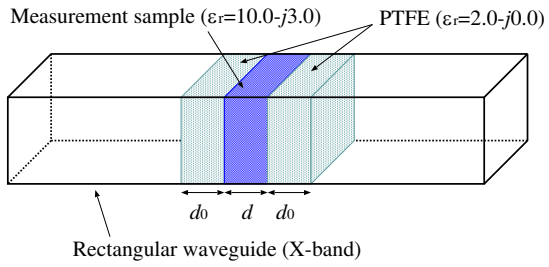

Figure 1: Model of transmission line method using rectangular waveguide.

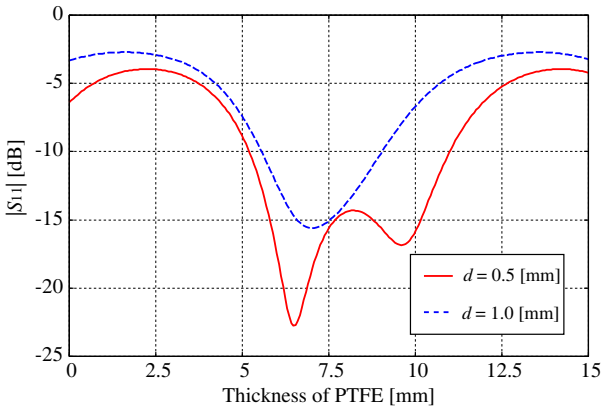

Figure 2: Calculated results of $|S_{11}|$ versus thickness of PTFE by transmission line theory.

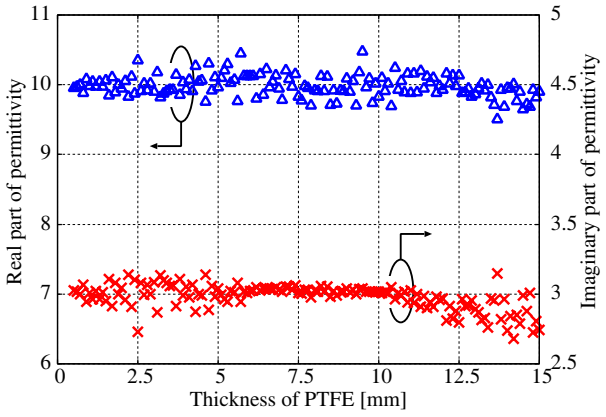

Figure 3: Simulated results of complex permittivity versus thickness of PTFE ($d = 0.5$ [mm]).

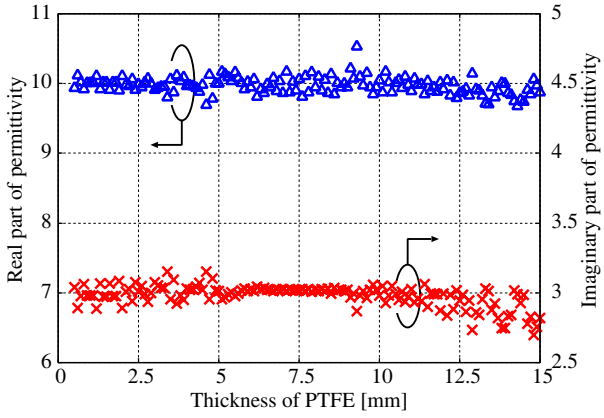

Figure 4: Simulated results of complex permittivity versus thickness of PTFE ($d = 1.0$ [mm]).

A Design for Ultra-wideband Bandpass Filter Using Parallel-coupled Line and Stepped Impedance Resonator by Genetic Algorithm

K. Kiyomi, T. Suzuki, K. Otsuka, S. Suzuki, T. Ohno, and K. Ishii
Kisarazu National College of Technology, Japan

Abstract— This paper presents a design method for a ultra-wideband (UWB) bandpass filter (BPF) by genetic algorithm (GA). The circuit structure consists of stepped impedance resonators (SIR) and parallel-coupled lines. The transmission characteristic of the BPF designed by GA is simulated and measured.

Figure 1 shows a schematic circuit of a BPF using parallel-coupled lines and SIRs. As shown in Fig. 1, l and Z are length and characteristic impedance of transmission line, and l_c, w and s are length, width and gap of parallel coupled line. The simulated result of the BPF which is designed by GA is shown in Fig. 2. As a result, the BPF obtains the bandwidth from 3.22 to 10.34 GHz. Moreover, out-band characteristic is satisfied FCC (Federal Communications Commission) indoor limit.

Figure 3 shows a photograph of the fabricated BPF. The measured result of the BPF is shown in Fig. 4. As a consequence, it is confirmed that wide passband from 3.45 to 10.1 GHz is obtained. Moreover, the result indicates similar transmission characteristic with the simulated result in Fig. 2. Therefore, the above results show that GA is useful for designing UWB filter.

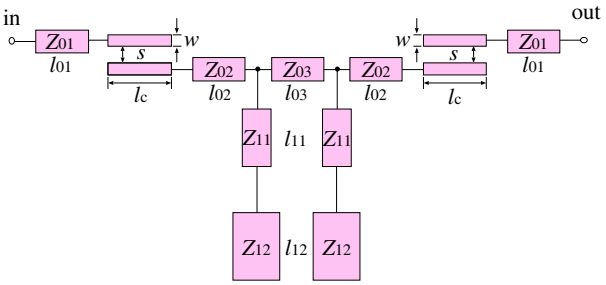

Figure 1: Schematic circuit of BPF using parallel coupled lines and SIRs.

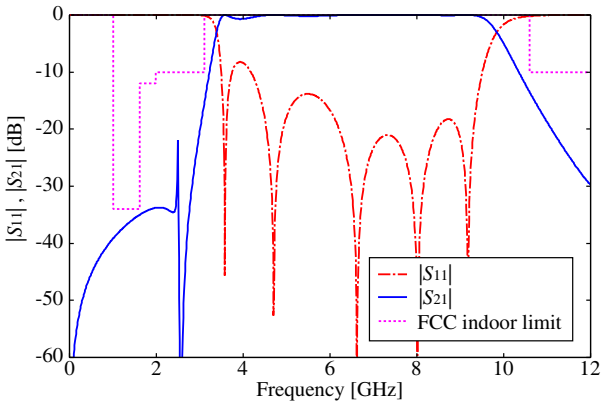

Figure 2: Simulated results of BPF shown in Fig. 1.

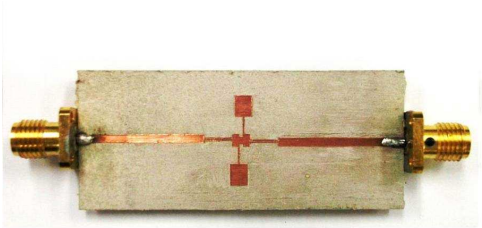

Figure 3: Photographs of BPF using parallel coupled lines and SIRs.

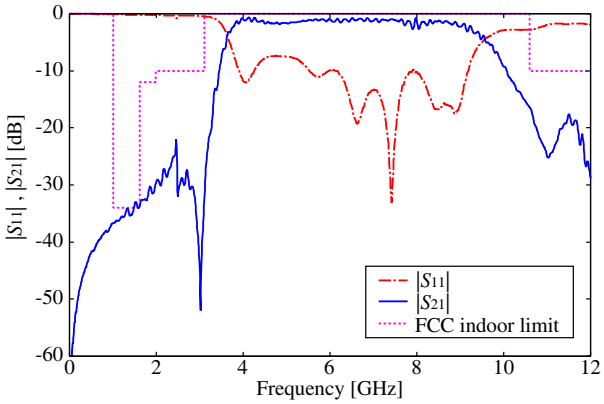

Figure 4: Measured results of the BPF shown in Fig. 3.

A Study on Thickness of High Loss Material for Determining Accurate Complex Permittivity in Transmission Line Method Using Rectangular Waveguide

S. Suzuki, T. Suzuki, K. Otsuka, K. Kiyomi, T. Ohno, and K. Ishii
Kisarazu National College of Technology, Japan

Abstract— In this paper, a permittivity of a high-loss sample is calculated by using the results of FDTD simulation. The relationship between the thickness of a high-loss sample and accuracy of calculated complex permittivity is examined.

Figure 1 shows an FDTD model of an X-band rectangular waveguide loaded with a high-loss sample. Table 1 shows complex permittivity of sample assuming high-loss material. In Fig. 1, TE_{10} mode at a frequency of 10 GHz is excited at $z = 10$, and a sample shown in Table 1 is loaded in the center of the waveguide. The complex permittivity of a sample is determined from complex transmission coefficient ($\dot{S}_{21}$) obtained by electric field at the observed point. Fig. 2 shows simulated results in the case of $\dot{\varepsilon}_r = 12 - j3.6$ ($\tan\delta = 0.3$) in FDTD, as an example. As shown in Fig. 2, the calculated complex permittivity approaches to the value of complex permittivity set in FDTD as a function of incleasing thickness of sample. Therefore, sample thickness greater than 15 mm is required to determine the complex permittivity with an accurate of less than 1%.

Table 1: Permittivity of samples.

Real part of complex permittivity	Imaginary part of complex permittivity		
	$\tan\delta = 0.1$	$\tan\delta = 0.3$	$\tan\delta = 0.5$
3	0.3	0.9	1.5
5	0.5	1.5	2.5
7	0.7	2.1	3.5
10	1.0	3.0	5.0
12	1.2	3.6	6.0
16	1.6	4.8	8.0

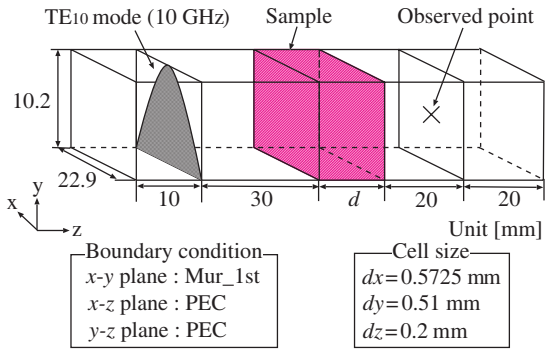

Figure 1: Model of transmission line method using rectangular waveguide.

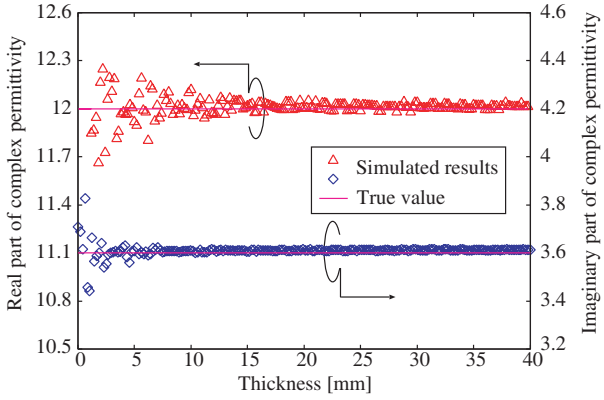

Figure 2: Simulated results of complex permittivity ($\dot{\varepsilon}_r = 12 - j3.6$) versus sample thickness.

Reasonable Estimations of Constituent Losses of Printed Circuit Board Interconnects

K. F. Fuh[1], **P. Deng**[1], **A. Liu**[2], **and E. Liao**[2]

[1]Department of Electronic Engineering, National United University, Taiwan
[2]Taiwan Union Technology Corporation, Taiwan

Abstract— The reasonableness of conventional procedure for estimating conductor and dielectric losses of printed circuit board (PCB) interconnects is investigated in this paper. There are several well-developed methodologies that can efficiently extract wideband propagation constant γ of a PCB interconnect; the real par of γ, phase constant β, reflects the dispersion property of dielectric constant of PCB material and the imaginary part, attenuation constant α, accounts for the total loss of dielectric and conductor. If the characteristic impedance Zc was directly measurable, conductor and dielectric losses of a interconnect can be definitely separated. Practically, Zc of a PCB interconnect is now estimated based on certain algorithm of separation or assignment of dielectric and conductor losses; and the accuracy of Zc is dependent on the reasonableness of the separation algorithm. The conductor loss is generally estimated by Hammerstad's model with a root-mean-square (RMS) value of copper foil roughness. In addition to RMS roughness, Fig. 1 illustrates the estimated tan based on different values of roughness. The assumption of well-shaped (0.0 µm) conductor profile is extremely unreasonable and it results in overestimated loss tangent ($\tan\delta$). The zero-slope curve corresponds to a roughness value that causes most flat loss tangent at higher-frequency range; and curves corresponding to RMS and average value (Ra) are located slightly above the zero-slope curve and they slowly decay as frequency increases. However the measured $\tan\delta$ of bare PCB substrate, measured with split-post cavity, exhibits increasing trend as frequency increases. Although the scenario of multilayer PCB is different from bare substrate, it is reasonable to assume that loss tangent will have a positive slope with frequency and near the value of bare substrate. When the value of conductor roughness approaches 1.5 µm the assumption is mostly matched. Additionally, the fast rising of $\tan\delta$ at lower frequency end indicates that Hammerstad's model is not suitable for conductor-loss estimation in the low-frequency range.

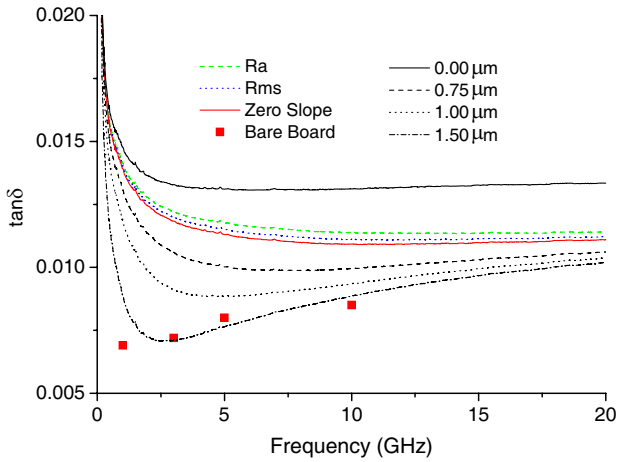

Figure 1: Estimation of dispersive $\tan\delta$ based on different roughness or conductor-loss assumptions.

Implementation of a Compact RF Module by Analysis and Fabrication for Organic Substrate with Embedded Passives

Jong-In Ryu, Jong Min Yook, and Dongsu Kim
Package Research Center, Korea Electronics Technology Institute, South Korea

Abstract— This paper presents embedded passives in organic substrate. By using this technology, a compact module for a Bluetooth and GPS are implemented in this paper.

The organic substrate is composed of epoxy and Ajimoto-bonding films (ABFs) and is called printed-circuit-board (PCB). Three times lamination and 6 copper layers are proposed in PCB. Each dimension of embedded capacitor is 0.6 mm × 0.3 mm × 0.3 mm. Capacitors are positioned in epoxy core and located in exact position by Surface Mounting Technology (SMT) Various capacitors as 2.2 µF, 1 µF, 470 nF, 100 nF, 22 pF, 1 pF, so on are embedded in PCB and total number of embedded capacitors is 17.

In order to obtain the effect of embedded capacitors, embedded capacitors and surface mounted capacitors are simulated and compared by Sonnet program. The results are analyzed in view of Z-parameter and S-parameter. Embedded capacitor is better than surfaced mounted capacitor in insertion loss.

A compact module for a Bluetooth and GPS by using embedded passives as system-on-package (SoP) technology. In order to implement a compact module, interposer with fine line/pitch and embedding technology are proposed. Capacitors are embedded in printed-circuit-board (PCB). A Bluetooth IC and a GPS IC are mounted in interposer. In side view, ICs, interposer substrate, and a PCB with capacitors are sequentially located from top and bottom as shown in Fig. 1. This module is composed of a Bluetooth IC, a GPS IC, interposer with 30 µm line width, and 17 shunt capacitors.

In order to check the performance and size for embedded modules, two representative modules for Bluetooth/GPS with SMT and with SoP are designed and compared. The size of module with SMT and SoP are as 15 mm × 10 mm and 12 mm × 7 mm, respectively. Almost 50% size reduction is obtained by SoP.

A presented module for Bluetooth/GPS was measured by using Agilent's N5230 oscilloscope, spectrum analyser, Bluetooth test program, and GPS signal of field. In order to perform Bluetooth, two test devices are communicated with each other to measure sensitivity by adopting non-signalling method. Two devices are connected through attenuator as air interface. The value of attenuator is raised as if distance is increased because distance means the RF loss between antennas in view of RF system. Tx power and Rx sensitivity are given as 6 dBm and −72 dBm, respectively. The received signal strength of GPS is −155.7 dBm/Hz, respectively. Actually, Bluetooth and GPS are well performed in commercial field. GPS mode will be more improved until final due date.

A presented module for Bluetooth/GPS was designed and implemented by lamination process with polymer material. Various capacitors were embedded in PCB in this paper. Fine line was realized in interposer substrate. Implemented modules with SMT and with SoP were compared in size. This paper presented that SoP technology was better than SMT technology in a view of size. Implemented module had good performance and slim size.

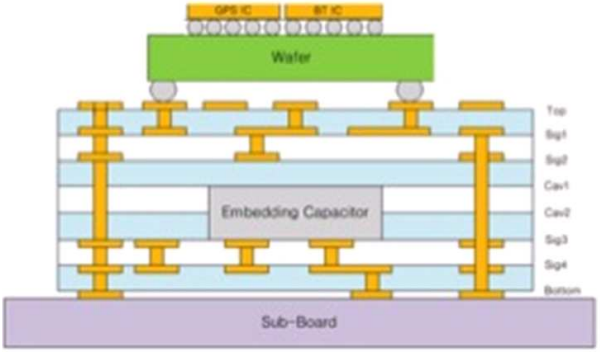

Figure 1: The cross-section of a proposed module.

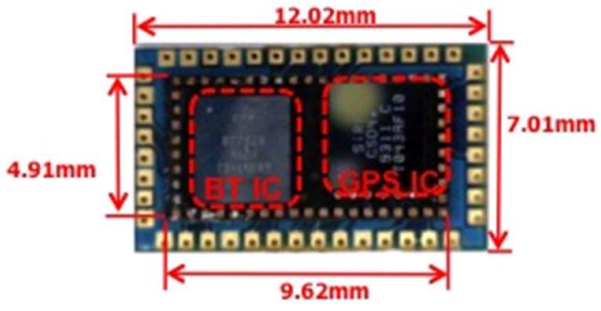

Figure 2: Implemented module.

Propagation Characteristics of the Meandered Defected Ground Structure

Wan-Ti Wang, Tzu-Hsiung Lin, and Chien-Jen Wang
Department of Electrical Engineering, National University of Tainan, Tainan, Taiwan

Abstract— In this paper, a compact meander-shaped slotted-ground-plane resonator disturbs the surface current distribution in a ground plane and the impedance characteristics of a transmission line are changed has been demonstrated. The meandered slot provides a wideband resonator with low insertion loss and very sharp cutoff frequency response. Unlike a conventional slot in a ground plane acting a bandstop resonator, a meander slot possesses multi-band frequency-rejection characteristics with a shape transition knee. The phenomenon the rejection bands are theoretically analyzed by utilizing magnetic field distribution. Detailed discussions for important dimensional parameters are determined.

Three-port De-embedding Methodology for GaAs pHEMT Characterization

C. I. Lee[1, 2], **W. C. Lin**[1], **and Y. T. Lin**[1]

[1]Department of Electrical Engineering, National Sun Yat-Sen University, Taiwan
[2]Institute of Communications Engineering, National Sun Yat-Sen University, Taiwan

Abstract— A three-port de-embedding procedure without the lumped equivalent circuits is utilized to accurately remove the parasitics of the dangling leg for pseudomorphic High Electron Mobility Transistors (pHEMTs) for the first time. Due to the low-loss gallium-arsenide (GaAs) substrate, the de-embedding method is carried out without a ground shield. The de-embedded reflection coefficients at each port are acquired by neglecting the coupling effects. Based on the cascaded methodology, the distributed nature of the interconnect line including the source dangling leg is taken into account. Three dummy structures including one simple open and two thru are employed. The length of the thru lines is equal to the length of the input and output interconnect and the source dangling leg so that the interconnect parasitics are totally removed. Because the forward port to port coupling is negligible, the simple open structure can be used to eliminate the ground-signal-ground (GSG) pad parasitics of the three ports. The presented de-embedding method for extracting the small-signal equivalent circuit parameters is performed. Compared with the conventional two-port cascaded de-embedding procedure, the parasitics induced from the dangling leg are removed from the test structure by using the three-port de-embedding methodology. Excellent agreement between de-embedded and simulated data of the intrinsic pHEMT Y-parameters demonstrates the parasitic effect of the source dangling leg can be removed by this three-port de-embedding method. Therefore, the equivalent circuit model of the pHEMT at different biases can be constructed accurately through the presented three-port de-embedding method for the circuit designers.

Wideband Leveling Amplifier Design Using 0.18 μm CMOS Process

Guan-Shian Li[1], **Chin-Ying Huang**[2], **Robert Hu**[2], **and Chung-Ping Chen**[2]

[1]College of Electrical Engineering and Computer Science, NTU, Taiwan
[2]College of Electrical and Computer Engineering, NCTU, Taiwan

Abstract— This manuscript reports the development of leveling amplifier, or known as active gain equalizer, designed using commercial 0.18 μm CMOS process. Similar to a distributed amplifier, this circuit uses artificial transmission lines to achieve broadband input and output matching; each of the gain cells utilizes two cascode amplification stages to sustain wideband gain performance. Allowing attenuation of the input transmission line to be frequency-dependent, where the shunt admittance G comes from a resistor in series with a capacitor, this equalizer's gain slope can be adjusted. On the other hand, the output transmission line will be altered by the capacitors attached to the gate nodes of the output common-gate transistors, and that in turn shifts the equalizer's cutoff frequency. In the simulation, the high-frequency gain can be lifted from 15 dB up to 30 dB in small steps, while the cutoff frequency can be finessed within 1 GHz. Small input and output reflection coefficients are also observed, and the port isolation is better than 40 dB across the bandwidth.

FPGA Implementation and Verification of Reed-Solomon Code in SDR System

Yi Hua Chen, Chang Lueng Chu, and Chun Chun Yeh
Institute of Information and Communication Engineering
Oriental Institute of Technology, New Taipei City, Taiwan

Abstract— This study used the LabView FPGA to implement two Reed-Solomon codes (R-S code), R-S (31, 15, 8) and R-S (63, 47, 8) using $m = 8$, on the NI SDR PXIe-5641R FPGA module. Besides providing a detailed discussion on the encoding and decoding mechanism of R-S code, this study completed software simulation and hardware verification of R-S code. When the error probability is 10^{-4}, the coding gain of R-S (31, 15, 17) [10] using $m = 5$ can be up to 2 dB, R-S (31, 15, 8) using $m = 8$ can be up to 2.5 dB, R-S (63, 47) [11] can be up to 1.5 dB and R-S (63, 47, 8) using $m = 8$ can be up to 3.5 dB. The result indicates that the R-S (63, 47, 8) implemented in this study has the best power-saving capacity. Comparing the error performance, when the E_b/N_0 is fixed at 5 dB, the error probability of R-S (31, 15, 17) [10] is 10^{-2}; the error probability of R-S (63, 47) [11] is much greater than 10^{-1}; the error probability of R-S (31, 15, 8) code is small greater than 10^{-3}; and the error probability of R-S (63, 47, 8) code is small less than 10^{-4}, indicating that the R-S (63, 47, 8) implemented in this study has the best correction capacity.

Design of a Bandwidth-enhanced Ultra Thin Metamaterial Absorber

Saptarshi Ghosh, Somak Bhattacharyya, and Kumar Vaibhav Srivastava
Department of Electrical Engineering, Indian Institute of Technology, Kanpur, India

Abstract— Metamaterial (MTM) structures can be used as Electromagnetic (EM) absorbers due to some attractive properties, where the effective permittivity and permeability can be modified to minimize both transmittance and reflectance at the absorption frequency. Electric field driven LC (ELC) resonating structures [1] are extensively used for this purpose as incident electromagnetic (EM) wave travels lesser distance compared to conventional split ring resonator (SRR) based MTM absorber [2]. This paper proposes a low-profile (single layer) circular MTM absorber structure which gives almost unity absorption (99.92%) at 11.22 GHz (X-band). The structure is made up with two copper layers separated by a 1 mm thick FR4-epoxy substrate [3]. The bottom layer is completely copper laminated and the top layer is shown in Fig. 1(a). The proposed structure also shows high (94%) absorbance for angular incidence up to 50°.

Further a 2×2 array has been studied using two different variants of the same resonating structure (different number of concentric rings), which shows two different absorption peaks. When these peaks are brought closer by optimizing its dimensions [4], the structure exhibits a bandwidth of 0.86 GHz (11.74–12.60 GHz) above 70% absorbance with two absorbance peaks at 12 and 12.5 GHz (95% and 93% absorbance respectively) and with minimum absorbance at 12.3 GHz (72% absorbance) as shown in Fig. 1(b). This proposed bandwidth-enhanced MTM absorbance structure can be used in stealth technology for both X and Ku band.

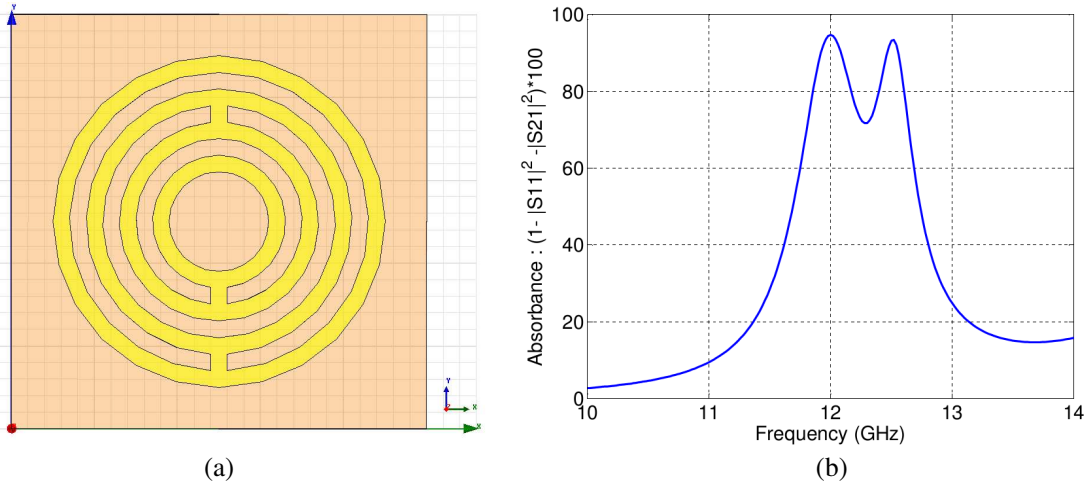

Figure 1: (a) Proposed structure. (b) Absorbance plot for the proposed 2 × 2 array MTM structure.

REFERENCES

1. Landy, N. I., S. Sajuyigbe, J. J. Mock, D. R. Smith, and W. J. Padilla, "Perfect metamaterial absorber," *Physical Review Letters*, Vol. 23, 207402, May 2008.
2. Bilotti, F., L. Nucci, and L. Vegni, "An SRR-based microwave absorber," *Microwave and Optical Technology Letters*, Vol. 48, No. 11, 2171–2175, Nov. 2006.
3. Li, M. H., L. H. Yang, B. Zhou, X. P. Shen, Q. Cheng, and T. J. Cui, "Ultrathin multiband gigahertz metamaterial absorbers," *Journal of Applied Physics*, Vol. 110, 014909, 2011.
4. Lee, J. and S. Lim, "Bandwidth-enhanced and polarization-insensitive metamaterial absorber using double resonance," *Electronics Letters*, Vol. 47, 8–9, 2011.

Investigation of Parasitic Effects Induced by the Ground on LTCC Passive Components

Runiu Fang[1], **Min Miao**[1,2], **and Yufeng Jin**[1]

[1]National Key Laboratory of Science and Technology on Micro/Nano Fabrication
Peking University, Beijing, China
[2]Institute of Information Microsystem, Beijing Information Science and Technology University, China

Abstract— In a highly competitive market like consumer electronics, size, power consumption and cost efficiency of electronic components are the determining factors of a product. Therefore, many efforts have been devoted to improving or balancing these factors. For RF applications, the LTCC (Low Temperature Co-fired Ceramic) material is considered as an alternative for the traditional silicon-based RF module, achieving lower cost and higher quality factor. As one major advantage of LTCC technology, passive components can be embedded in the LTCC substrate, thereby eliminating the need for discrete passives. Multilayer LTCC integrated passive have been demonstrated as a favorable option to realize both high inductance or capacitance and high Q passives. The increasing operation frequency and demand of high density integration of RF modules cause severe coupling and crosstalk problems between components, which can be dissipated to a great extent by inserting ground planes. Therefore, effects of ground planes on LTCC passives, mainly capacitors and inductors, need to be investigated.

In this paper, the parasitic effects of ground plane on LTCC capacitors and inductors are discussed respectively. In terms of capacitors, the ground-induced effects cause the discrepancy between effective capacitance seen at different ports. The coupling between ground and the lower plane of the capacitor increases the effective capacitance, and the discrepancy increases while the distance between ground plane and capacitor decreases. For LTCC inductors, the simplified π circuit mode is applied to extract parameters of the circuit and figure out the effects of ground plane on LTCC inductors. The results of extraction indicate that a closer distance between ground and inductor lead to both a lower effective inductance and quality factor, and the Self Resonant Frequency (SRF) slightly increases. By scrutinizing every impact of equivalent circuit components

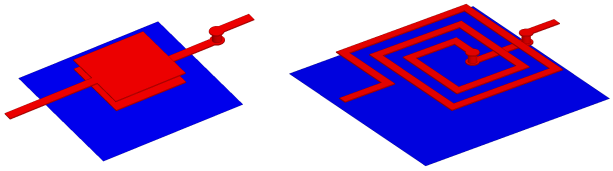

Figure 1: Three-dimensional view of the LTCC capacitor and inductor.

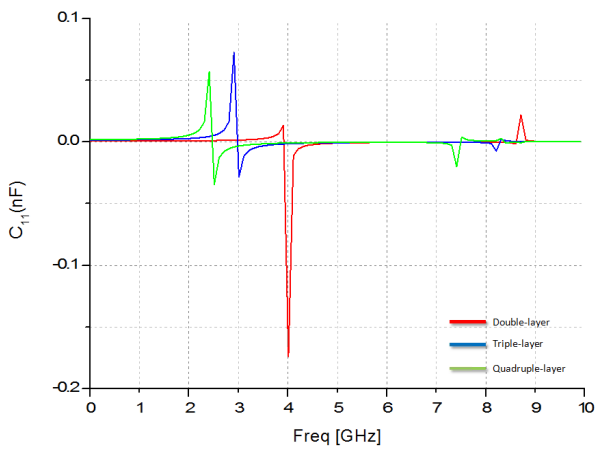

Figure 2: The extracted effective capacitance of the capacitor.

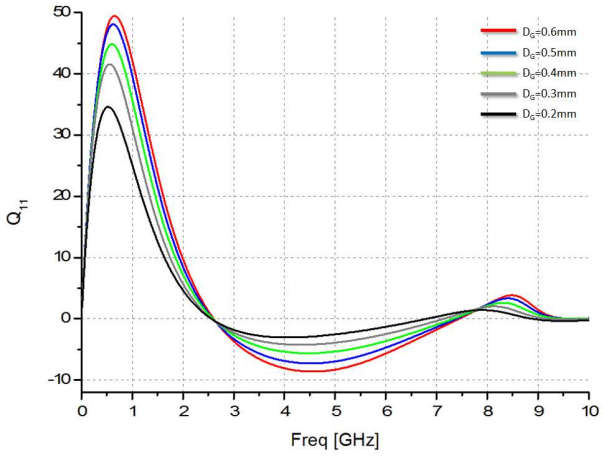

Figure 3: The extracted quality factor of the inductor.

on effective inductance, the decreasing of effective inductance with distance between ground and inductors is explained. The nearer ground results a higher coupling capacitance, but the negative mutual inductance cause by image current on ground plane is more dominant in terms of contributing to the effective inductance.

REFERENCES

1. Brown, R. L. and P. W. Polinski, "The integration of passive components into MCMs using advanced low-temperature cofired ceramics," *International Journal of Microcircuit and Electronic Packaging*, Vol. 16, No. 4, 328–338, 1993.

Microwave Optoelectronic Oscilator for Distribuited Receivers Operating Remotely

Larissa Aguiar Dantas de Britto,
Débora Maria Souza Morais, and Gefeson Mendes Pacheco
Microwave and Opto-Electronic Department, Aeronautics Technical Institute
Avenida Brigadeiro Eduardo Gomes, São José dos Campos, São Paulo, Brazil

Abstract— This paper describes the first results related to the implementation of a system combining microwave and photonic technologies in Brazil. Such combination comes from an circuit for radio frequency signals generation known as Optoelectronic Oscillator. Starting from a configuration previously presented in the literature, a small and innovative change in the oscillator feedback loop was proposed. The characterization of the photonic circuit reveals output signal amplitude of −27 dBm, line width less than 30 kHz and the phase noise better than −90 dBc/Hz for 1 MHz deviation. The obtained results are discussed in the spite of the previous theoretical analysis of the OEO and prospective applications for remote signal receivers.

LTE Mixer Array of 0.5 W High Output Power

Pang-Hsing Chen, Yen-Heng Chen, and Jeng-Rern Yang
Microwave Laboratory, Department of Communication Engineering
Yuan Ze University, Jhongli City, Taoyuan Country 320, Taiwan

Abstract— The paper presents the design of 1.7 GHz LTE system power amplifier by using mixer array, compile the output current of mixer and use transform balun to convert its signal from double-ended to single-ended. Using this schematic to construct a power amplifier application, and to realize CMOS Fully Integrated 0.5 W output power of the transmitter front-end circuit differ from the known PA topologies applied. The conventional design of the mixer and the power amplifier can be directly replaced two mixer unit without using the inductor to reduce the chip area.

Usually power amplifier and upconverter separately designed two parts on a CMOS process RF transmitter front-end circuit design. With the advances in process technology, the CMOS amplifier process has progressed from 0.18 µm to 0.13 µm, 90 nm and even 35 nm, the advantages of size is getting smaller and smaller. With low-cost advantages of CMOS process will be able to use the very large number of transistors to solve the problems encountered in the conventional design, and achieve a higher output power even reach the watt-level output power. In addition, the supply voltage, for example, GSM and GPRS requires a peak-to-peak voltage value of approximately 20 V, but the breakdown voltage of 0.18 µm transistor is too low, the maximum drain voltage only 2 V and offers about 10 mW, must using conversion impedance to change its output voltage and current relations.

The following simulation results are the simulation results of the 16-unit number. The output power was 27 dBm, the power-added efficiency (PAE) was 19%. For an overall supply voltage of 3 V, The area of the chip was approximately 1.512 mm × 1.285 mm.

Design of a Highly Linear Low-noise Amplifier with Noise and Distortion Cancelation

Pang-Hsing Chen and Jeng-Rern Yang
Microwave Laboratory, Department of Communication Engineering
Yuan Ze University, Jhongli City, Taoyuan Country 320, Taiwan, R.O.C.

Abstract— This study presents a highly linear low-noise amplifier with noise and distortion canceling. The circuit design of this amplifier focuses on the realization of high linearity and low-noise amplification. An operation within LTE frequency bands (0.7–2.6 GHz) produces a noise level of 2.3–3.1 dB; IIP3 was +8 dBm at a center frequency of 1.7 GHz, and P1 dB was −10 dBm at 1.7 GHz, with an operating voltage of 1.3 V. However, enhancement of linearity in an NMOS design may result in additional power consumption. Therefore, this design involved using a PMOS and an NMOS that could cancel second-order harmonic distortion, and the supply of single current could reduce power consumption. The circuit area is $0.86 \times 0.63\,\mathrm{mm}^2$.

Low-noise amplifier (LNA), which is the first-stage active amplifier circuit in a receiver front-end circuit, is used to receive and amplify weak signals while reducing potential noise. According to the definition of the noise figure in an overall circuit, the noise of an LNA can directly influence the noise level and sensibility of a receiver, and a higher gain in an LNA can further restrain the gain of a back-end circuit.

Based on this description, the primary goal of an LNA design is to reduce the noise figure as much as possible, and to reduce back-end noise. However, the gain of an LNA design must not be too low, and an increase of the gain causes a decrease of linearity and an increase in power consumption. Power consumption and circuit area must be minimized to reduce the cost of mainstream circuit designs. Satisfying all of the demands is a challenge; therefore, a trade-off must be made.

Dual-band Bandpass Filer with a Tunable Upper Passband

Shun Fu Liao[1], **Hsun-Hsiang Chen**[1], **and Ching-Her Lee**[2]

[1]Graduate Institute of Electronic Engineering
National Changhua University of Education, Changhua, Taiwan
[2]Graduate Institute of Communication Engineering
National Changhua University of Education, Changhua, Taiwan

Abstract— This paper presents a dual-band bandpass filter designed using TSMC 0.18-µm CMOS technology. The upper passband can be varied by tuning the position of a transmission zero occurring near the upper edge of the upper passband. This transmission zero can be shifted by changing the DC-biased voltage across the varactors in the BPF circuit. Simulated results show that the designed BPF can achieve a lower passband of 3.3–6.5 GHz with a minimum insertion loss of 2.7 dB and a maximum return loss of 22.65 dB. The varactor-induced transmission zero can be varied from 41.4 to 44.5 GHz, leading to a tunable upper passband of 20–28.83 GHz to 20–31.93 GHz with a minimum insertion loss of around 3.41 dB and a maximum return loss of 44.31 dB.

A Tunable Dual-band Bandpass Filter with Two Independently Tunable Passbands

D.-H. Jia, Q.-Y. Feng, X.-G. Huang, and Q.-Y. Xiang
School of Information Science and Technology
Southwest Jiaotong University, Chengdu, Sichuan 610031, China

Abstract— In this paper, a novel tunable dual-band bandpass filter is proposed. Based on two quarter-wavelength resonators and one half-wavelength resonator, dual-band character is designed by introducing two independent coupling paths. Therefore, the whole filter structure can be divided into two parts and designed respectively. The tuning results of the two parts are also shown in this paper. Two chip capacitors C_g are adopted to enhance the tuning range and return loss. The Transmission Zeros (TZs) and passbands are derived through simulation. The first passband and TZ1 are generated by the input/output and the two quarter-wavelength resonators, meanwhile, the second passband and TZ2 are generated by the input/output, the half-length resonator and cross coupling, respectively. The SPICE mode of the varactor diodes and DC bias are adopted in the simulation. By varying the reverse bias voltage applied to the varactor diodes connected to the resonators respectively, each passband can be tuned independently. All simulations are done in SONNET and ADS tools. Finally, the simulation results of the dual-band tunable filter shows a first tunable passband constant fractional-bandwidth range of $4.35 \pm 0.35\%$, a center frequency of 1.25–1.75 GHz, a insertion loss of 4.25–2.16 dB, and a second passband absolute-bandwith of 80 ± 5 MHZ, a center frequency of 1.83–2.27 GHz, a insertion loss of 2.75–1.97 dB. During the tuning of one passband, the other passband shows a very small variation.

A Constant Absolute Bandwidth Tunable Combline Bandpass Filter

X.-G. Huang, Q.-Y. Feng, Q.-Y. Xiang, and D.-H. Jia
School of Information Science and Technology
Southwest Jiaotong University, Chengdu, Sichuan 610031, China

Abstract— This paper presents a novel two-pole constant absolute bandwidth tunable combline bandpass filter with controllable coupling coefficient. The combline bandpass filter can be divided two parts: coupling section and non-coupling section. By controlling the length ratio of the coupling section and non-coupling section while maintaining the total length unchanged, the external quality Q_{ext} maintains stationary and the coupling coefficient k can be tuned to desirable values to meet the requirement of a constant absolute bandwidth. Detailed design equations for the combline resonators are given and the realization of the constant absolute bandwidth tunable filter using these equations is discussed. The simulated results show the the proposed structure have a small bandwidth variation. The filter is designed on F4b-2 substrate with $\varepsilon_r = 2.65$ and 0.5 mm. The measured results show that the frequency can be tuned from 1.13 to 1.53 GHz with a 3-dB absolute bandwidth 80 ± 4 MHz. The tested results show good agreement with the simulated results.

Digital Predistortion for RF Power Amplifiers Based on Enhanced Orthonormal Hermite Polynomial Basis Neural Network

X. H. Yuan, Q. Y. Feng, T. J. Zeng, and H. B. Ma
School of Information Science and Technology
Southwest Jiaotong University, Chengdu, Sichuan 610031, China

Abstract— In this paper, a digital baseband predistorter for RF power amplifiers (PAs) based on enhanced orthonormal Hermite polynomial basis neural network (EOHPBNN) is proposed. Digital predistortion technique based on neural network has been a hot topic in recent years, but the commonly used neural network predistorters employs feedforward neural networks (FNNs) with sigmoid functions as the hidden neurons' activation functions, which have limited linearization performance. The new proposed predistorter utilizes an orthonormal Hermite polynomial basis neural network where the orthonormal Hermite polynomial terms are chosen as the hidden neurons' activation functions. Taking advantage of the universal approximation capability of Hermite polynomial, the EOHPBNN predistorter shows superior linearization performance to the traditional NN-based predistorter. Also, the design of the EOHPBNN predistorter is combined with the AM/AM and AM/PM distortion characteristics, showing an improved linearization performance. The experimental results on a class-AB power amplifiers using wideband CMMB test signal demonstrate the excellent linearization performance.

The Investigation of the Effects of Electromagnetic Band Gap Structure and Configuration Size on Power Integrity of High Speed Circuit Board

Yun-Hsih Chou and Ming-Chang Tsai
Department of Electronic Engineering, St. John's University
499, Sec. 4, Tam King Road, Tamsui, Taipei 251, Taiwan, R.O.C.

Abstract— In this paper, it is mainly to use three different kinds of Electromagnetic Band Gap (EBG) structure and various configuration size of Uniplanar Compact (UC), L-bridged and L-Bridged + Slits (LBS) to explore the benefits of noise interference reduction of high speed PCB power supply. In the lab test it uses FR4 double-side circuit board with copper foil thickness 0.036 mm, circuit board height 0.72 mm and the dielectric constant $\varepsilon_r = 4.5$. In the fixed size 12 cm × 12 cm circuit board it considers three different size configurations with unit size of 4 cm × 4 cm, 3 cm × 3 cm and 2 cm × 2 cm respectively and then through HFSS simulation software and the circuit board measurement to study and compare the variation of power noise interference reduction with different unit size structure. It appears that with different Electromagnetic Band Gap (EBG) structure it surely has the benefits in the reduction of power noise interference in different frequency bands and it also shows that when the unit configuration size of Electromagnetic Band Gap becomes smaller the bandwidth in the reduction of power noise interference becomes wider but its reduction magnitude becomes worse.

Closed Loop Cell Texture Thermodynamics

K. F. Kaspareck
CTE, Italy

Abstract— Analysis of nuclear resonance image (NMR) through integration and derivation techniques can lead to quantitative diagnosis of cell texture properties.

Cellular bound and unbound hydrogen vibrational moment attenuation is closely linked to cells' water textural thermodynamics. After allowing for instrumental uncertainties flammated cellular texture is described clearly by the first derivative of attenuation with minimum ambiguity and quantitatively. The spectral ends of attenuation's derivatives identify unbound and bound hydrogen with a much-improved dynamic range in comparison to standard and intensity images High values coincide with flammated texture, where hydrogen tends to bind and binds (and this to a certain extent can also be seen as less water).

Plasmatic oxygen is interconnected to intracellular water, thus bound state. Furthermore, hemoglobin becomes paramagnetic in presence of an oxygen deficit, thus of water. The change in magnetic field allows for differential free water content measure, a key control parameter in cellular thermodynamics.

A hypothesis arises from these instances, where cellular texture may naturally initiate a differential reduction process by acquiring hydrogens adiabatically. The adiabatic phase, given the specific phase's inertia, would link to the speed(s) of thermodynamic reaction(s). This reaction and its feedback would then be relevant to several other cellular processes including apoptosis. Differentiating between bound and free water in a flammated texture becomes therefore very critical.

Monitoring over time will allow reconstruction of attenuation gradients and information on the speed of intracellular thermodynamic changes, thus also an assessment of immunity and its evolution.

Design of Parallel FFT Based on FPGA in the Field of Software Radio

G. C. Wan, Y. Q. Zhang, and M. S. Tong
Department of Electronic Science and Technology, Tongji University
4800 Cao'an Road, Shanghai 201804, China

Abstract— There are two key ideas of software radio: making A/D/A (analog to digital/digital to analog) converters as close to the antenna as possible and achieving as many radio functions as possible by software. One of the main techniques is the high-speed signal processing including baseband processing, modulation, demodulation, coding, decoding, and some other functions. Most of these functions are used to realize the transformation of signal between time domain and frequency domain by Discrete Fourier Transform (DFT) first. However, the calculation of DFT is very time-consuming in practice and the Fast Fourier Transform (FFT) is desirable. The FFT can reduce the computational costs by resolving a long sequence DFT into short sequences. The field programmable gate array (FPGA) is a good hardware choice to process the signal exported by the high-speed A/D because of its high efficiency based on the application specific integrated circuit (ASIC) and its flexibility for system realization. Meanwhile, the FFT-IP (intellectual property) core on FPGA provided by Xilinx is widely used to accomplish the FFT calculation. It seems very convenient for the users to call the FFT-IP core by setting some parameters. However, the FFT-IP core only supports serial input rather than parallel input. This disadvantage makes it inappropriate for high-speed signals. Also, the design of distributing memory cell to every radix-2 butterflies occupies too much resource of FPGA in the field of software radio.

In this work, we develop a design of parallel FFT in which the data exported by every butterfly processing element flow to the next level directly without storage in order to avoid data stack. If the synchronous sequential circuit is adopted, a set of calculation results will be exported at every clock tick that can greatly improve the speed of computation. When fixed-point operation is taken by FPGA, such as complex-multiply, the bit-wide of the data will double each time, so the data should be truncated to avoid the occupation of much resource of the devices. The method we use is to obtain the high 16 bits of the data exported by every multiplier and to halve the calculation results of butterfly elements at each level. In this process, how the errors caused by data reduction will impact on the final results will be addressed. Then the Signal Noise Ratio (SNR) in completing FFT in FPGA will be analyzed and the results compared with the simulation data by Matlab will also be presented.

Dual Band Circuit Design Using Mixed Lumped Elements/Coupled Lines

Kuan-Yu Liao and Jan-Dong Tseng
Department of Electronic Engineering, National Chin-Yi University of Technology
Taichung 411, Taiwan, R.O.C.

Abstract— This paper proposes a circuit structure by combining lumped elements and coupled-line to achieve dual band response. The structure uses lumped elements and coupled lines to create low pass and band pass functions respectively. The circuit analysis applied $ABCD$ matrix for cascade and parallel circuit configurations and transferred to scattering parameters at the final stage. The dual band circuit has been designed to branch line coupler and Wilkinson power divider. The circuit simulation used electromagnetic simulation software (IE3D), two center frequencies are set at 13.56 and 925 MHz especially for RFID applications. The circuit was fabricated on 1.6 mm FR-4 substrate. Both the simulation and the measurement show good agreement in the frequency of interest.

Figure 1 shows the mixed lumped elements/coupled lines circuit and Figure 2 shows the dual band Wilkinson power divider capable using in 13.56 and 915 MHz dual band RFID applications.

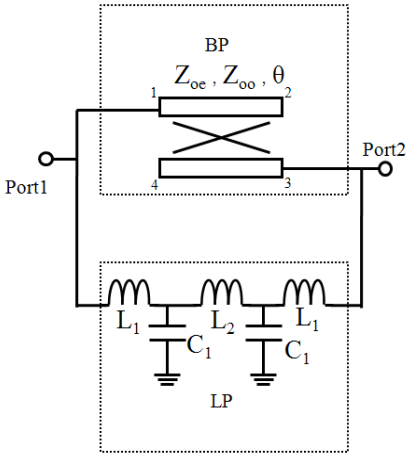

Figure 1: The mixed lumped elements/coupled lines circuit.

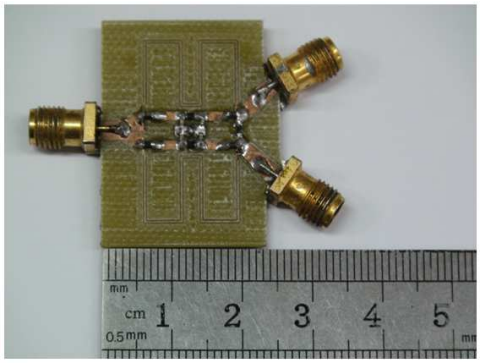

Figure 2: Dual band Wilkinson power divider.

A Correction Term for Maxwell's Equations Transformed between Galilean Reference Systems (Part I)

Namık Yener
Biomedical Engineering Department, Technology Faculty
Umuttepe Campus, Kocaeli University, Izmit, Kocaeli 41380, Turkey

Abstract— Two electromagnetic problems are solved in which Maxwell's equations are shown to need a correction term when their Lorentz transformation is taken between two Galilean reference systems. In the examples two relations exist between the wave number k' and frequency ω' in K' which is in uniform rectilinear motion with respect to K. One of these relations dictates the law by which k' and ω' abide on their path to zero. The other one which is the representation of Maxwell's second equation yields the unbalance between the two sides of this equation when the limit $\omega' \to 0$ and $k' \to 0$ is taken. This constitutes the first part of the two papers describing the work.

A Correction Term for Maxwell's Equations Transformed between Galilean Reference Systems (Part II)

Namık Yener
Biomedical Engineering Department, Technology Faculty
Kocaeli University, Umuttepe Campus, Izmit, Kocaeli 41380, Turkey

Abstract— Two electromagnetic problems are solved in which Maxwell's equations are shown to need a correction term when their Lorentz transformation is taken between two Galilean reference systems. In the examples two relations exist between the wave number k' and frequency ω' in K' which is in uniform rectilinear motion with respect to K. One of these relations dictates the law by which k' and ω' abide on their path to zero. The other one which is the representation of Maxwell's second equation yields the unbalance between the two sides of this equation when the limit $\omega' \to 0$ and $k' \to 0$ is taken. This constitutes the second part of the two papers describing the work.

A Large Tuning Range Ring VCO in 180 nm CMOS

Xuemei Lei[1, 2], **Zhigong Wang**[1], **Lianfeng Shen**[1], **and Keping Wang**[3]

[1]School of Information Science and Engineer, Southeast University
Sipailou 2, Nanjing 210096, China
[2]College of Electronic Information Engineering, Inner Mongolia University
Daxuexilu, Hohhot 010010, China
[3]University of Washington, USA

Abstract— The phase noise requirements are decreased in some applications of short-range communication, the data rates are low, and the channel spacing is wide. This makes a voltage-controlled ring oscillator is widely applied which needs a smaller chip area but a larger tuning range. On the other hand, the low supply voltage is trend of the electronic communications. Thus, a large tuning range ring VCO based on a different cascade voltage logic delay cell is presented, which is suitable for low supply voltage. The delay cell is composed of a differential pair of NMOS transistors with two cross coupled load PMOS transistors, along with two PMOS transistors which change the current of output node. A new typical structure is suit for low supply voltage with large tuning range and less transistors. In SMIC 180-nm CMOS process, simulation results show that the maximum oscillator frequency of the ring VCO is 6.9 GHz and the tuning range is from 75 MHz to 6.9 GHz with a worse phase noise level of 101.1 dBc/Hz at an offset of 10 MHz. Its maximum average power consumption is 5.18 mA from 1.2 V power supply and the minimum average power consumption is 0.10 mA from 0.7 V power supply. The core area is 50 µm × 35 µm in a 180-nm CMOS process.

Figure 1 is the circuit implementation of the proposal ring VCO, and the layout is shown in Figure 2.

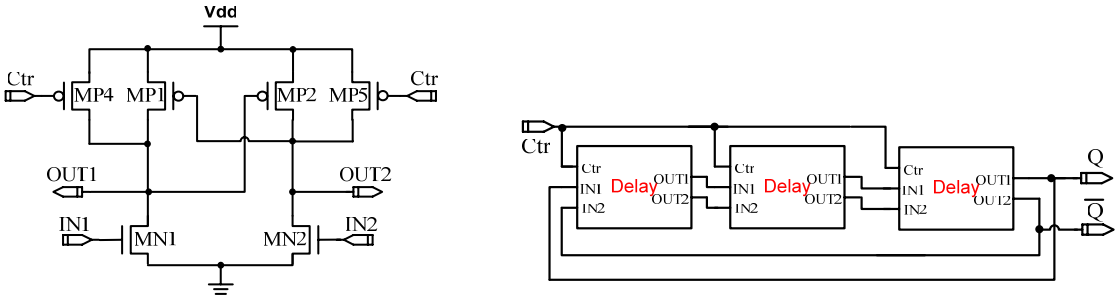

(a) delay cell (b) ring oscillator

Figure 1: Circuit implementation of the proposal ring VCO: (a) delay cell and (b) ring oscillator.

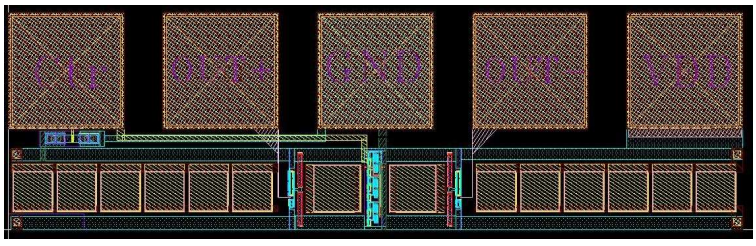

Figure 2: The layout of the ring VCO.

A Planar MIMO Antenna for Mobile Phones

Di Wu[1], S. W. Cheung[2], T. I. Yuk[2], and X. L. Sun[2]

[1]City University of Hong Kong, Hong Kong, China
[2]The University of Hong Kong, Hong Kong, China

Abstract— This paper presents a multiband MIMO antenna using planar technology for the next generation mobile phone applications. The multiband MIMO antenna is composed of two identical monopoles which are orthogonally printed at the adjacent edges of the ground plane of the mobile phone. Each monopole consists of two radiating branches to generate two frequency bands. A parasitic element is used in each antenna to increase the operating bandwidth. An impedance network implemented using lumped elements is used to optimize impedance matching at port 1 port 2. Simulation results show that these two frequency bands can cover the LTE (lower band), DCS1800, PCS1900, UMTS-2100, Wibro Band, 2.4G-WLAN, and Wimax (upper band). By cutting a slit on the PCB ground, isolation between the two monopoles can be greatly enhanced for the frequency bands designed for the MIMO antenna. The MIMO antenna has a planar structure and can be printed on the same PCB, so it is low profile with low cost for mobile phone applications.

Introduction: Multiple-input multiple-output (MIMO) system that utilizes multiple antennas to increase channel capacity without sacrificing additional spectrum or transmitted power has received a growing amount of interest in recent years. MIMO antenna technology can provide higher receiver gain, increased data rates, larger network throughput, and improved reliability through antenna diversity. However, to achieve these advantages, the MIMO antenna is required to have low mutual coupling between closely packed antenna elements, which is quite difficult to realize using the limited spaces of the handsets. Recently, there have been efforts on research in attempts to reduce the mutual coupling between elements in MIMO antennas [1–5]. Most of these MIMO antennas could only work in a single band, about 2.4 GHz and above. The lower band LTE700 operation (which needs a larger antenna size) for the next generation of communication system was missed out in the studies.

In this paper, a MIMO antenna designed using planar technology for use in mobile phones is presented. The MIMO antenna is composed of two identical monopoles printed orthogonally at the adjacent edges of the mobile-phone ground plane. A specific shape of slit is cut on the PCB ground to reduce the mutual coupling and increase the isolation between the two elements. The EM simulation tool, CST, is used to study and design the MIMO antenna. Simulation results illustrate that the proposed planar MIMO antenna can generate two frequency bands which can cover the LTE (lower band) DCS1800, PCS1900, UMTS-2100, Wibro Band (2.3–2.4 GHz), 2.4-GHz WLAN, and WiMAX (upper band) systems, simultaneously.

REFERENCES

1. Ou Yang, J., F. Yang, and Z. M. Wang, "Reducing mutual coupling of closely spaced microstrip MIMO antennas for WLAN application," *IEEE Antennas and Wireless Propagation Letters*, Vol. 10, 2011.
2. Chung, K. and J. H. Yoon, "Integrated MIMO antenna with high isolation characteristic," *Electronics Letters*, Vol. 43, No. 4, 199–201, 2007.
3. Chiu, C. Y., C. H. Cheng, R. D. Murch, and C. R. Rowell, "Re-duction of mutual coupling between closely-packed antenna elements," *IEEE Transactions on Antennas and Propagation*, Vol. 55, No. 6, 1732–1738, 2007.
4. Minz, L. and R. Garg, "Reduction of mutual coupling between closely spaced PIFAs," *Electronics Letters*, Vol. 46, No. 6, 392–394, Mar. 2010.
5. Diallo, A., C. Luxey, P. Le Thuc, R. Staraj, and G. Kossiavas, "Study and reduction of the mutual coupling between two mobile phone PIFAs operating in the DCS1800 and UMTS bands," *IEEE Transactions on Antennas and Propagation*, Vol. 54, No. 11, 3063–3074, Nov. 2006.

CPW-coupled-fed Circular UWB Monopole Antenna

J. Zhang, S. W. Cheung, and T. I. Yuk
Department of Electrical and Electronic Engineering
The University of Hong Kong, Hong Kong, China

Abstract— In this paper, a co-planar-waveguide (CPW) coupled-fed monopole antenna is proposed for UWB applications. The antenna is composed of a CPW feed line terminated with a trapezium patch on one side of the substrate and a radiator with a circular segment shape on the other side. With such configuration, there are many parameters such as the dimensions in the radiator, patch and feed line which can be used to optimize the design. Computer simulation is used to study the antenna and results show that the antenna has a large impedance bandwidth covering the frequency band from 2.7 to 11.4 GHz with return loss larger than 10 dB. The return loss, radiation pattern, peak gain and efficiency of the antenna are studied using computer simulation. The results show that the proposed antenna is a good candidate for UWB applications.

A Compact Branch-line Directional Coupler Using Lumped-element CRLH TLs

Y. F. Wu, J. Zhang, and S. W. Cheung
Department of Electrical and Electronic Engineering
The University of Hong Kong, Hong Kong, China

Abstract— In this paper, a compact directional branch-line coupler designed using lumped-element CRLH TLs is presented. The compactness is achieved by replacing the $-90°$ right-handed transmission lines (RH TL) branch lines in a conventional directional branch-line coupler with a $+90°$ composite right/left-handed transmission lines (CRLH TLs) which is implemented using lumped elements. Computer simulation is used to study the performance of the coupler and results show that the coupler has a bandwidth from 0.96 to 0.99 GHz, with $|S_{11}|$ and $|S_{41}|$ lower than -15 dB, $|S_{21}|$ and $|S_{31}|$ close to -3 dB, and a phase difference of $90°$ between ports 2 and 3. For comparison, a conventional branch-line coupler implemented using the RH TL and working at the same center frequency is also designed. Simulation results show that the proposed coupler can achieve a size reduction of 82.8% compared with the conventional RH TL branch line coupler.

Direction of Arrival Estimation Based on Maximum Likelihood Criteria Using Gravitational Search Algorithm

Ahmed Magdy, K. R. Mahmoud, S. G. Abdel-Gawad, and I. I. Ibrahim
Department of Electronics, Communications and Computers
Faculty of Engineering, Helwan University, Cairo, Egypt

Abstract— DOA estimation is an important problem in many fields such as radar, sonar, radio, astronomy, under water surveillance and seismology to estimate the source location. One of the simplest versions of this problem is the estimation of the directions-of-arrival (DOAs) of narrow-band sources where the sources are located in the far field of the sensor array. There are different optimization techniques are considered in the previous literature to optimize the ML function such as genetic algorithm (GA), Alternating Projection (AP)ML optimization, Particle swarm optimization (PSO), Ant colony optimization (ACO), and Bacteria Foraging Optimization (BFO).

Recently GSA algorithm has been successfully applied in different applications and showing better performance compared to other algorithms. In the DOA estimation, due to multimodal, nonlinear, and high-dimensional nature of the parameter space, the problem seems to be a good application area for GSA, by which the excellent performance of ML criteria can be fully explored. In this paper, the GSA optimization technique applied to ML criterion functions for accurate DOA estimation in Gaussian noise for a Uniform Circular Array (UCA) is considered A minimum square error comparison between MUSIC, PSO and GSA algorithm in addition to the resolution with SNR are considered. Also, the relation between actual and estimated DOA in case of adjacent incoming signals from multiple sources is studied. It is found that, the MSE for GSA is better than both other techniques and shows accurate results even for a big set of simultaneously incident signals. The proposed technique is simple and appropriate for real time applications.

Experimental Studies on Microwave Gunn Oscillator Based Modulator-demodulator Systems with Chaotic Modulating Signals

B. C. Sarkar[1], **T. Banerjee**[1], **S. Sarkar**[2], **C. Koley**[1], **and A. K. Guin**[1]

[1]Department of Physics, Burdwan University, India
[2]Electronics Department, Burdwan Raj College, India

Abstract— The application of Gunn Oscillators (GOs) as FM/PM modulators is well documented in the literature [1]. The frequency of oscillation of a waveguide mounted GO depends on the dimension of the cavity and the bias voltage applied to the Gunn diode. A GO based modulator can be designed using the bias modulation technique, where the modulating signal is superimposed on the dc bias voltage of the GO. In a chaos based communication system, the information bits are masked with or mapped into chaotic signals which are used as modulating signals in transmitter modulators. That information is retrieved by synchronizing the demodulator oscillator with the received signal. In the present paper, we report two schemes for transmission and reception of RF chaos through a microwave guided channel. In first scheme, a free running GO is angle modulated with the RF chaos, and in the second scheme, an injection synchronized GO is employed to recover the RF chaos by using a suitable phase comparator circuit. When the modulating chaotic signal is superimposed on the dc bias of a free running GO, one gets a frequency modulation (FM) type modulator. However, the free running GOs suffer from frequency instability due to temperature variations, dc bias fluctuations etc. To have the stability of oscillation often an external signal is used to synchronize the GO by injection locking technique. The chaotic modulating signal is then superimposed on the dc bias of the injection synchronized GO to have a phase modulation (PM) type modulator The obtained results can be summarized as follows

1. In an FM type angle modulator with free running GO, the demodulated chaotic signal is nearly equivalent to the modulating signal with an overall phase difference. Also due to the inherent nonlinearity in the FM modulator type GO some distortions in the demodulated chaotic signal are observed.
2. In a PM type angle modulator with synchronized GO, the demodulated chaos is almost same as the modulating chaos signal with a constant phase shift. As the inherent nonlinearity in PM type modulator is small compared to the FM type modulator, the distortion in the demodulated chaotic signal is negligible.

In the experiment, a chaos signal of 190 KHz generated by a Single amplifier biquad (SAB) based chaotic oscillator [2] is added with the dc bias of the modulator GO (MGO). The free running frequency of MGO is set at 10.300 GHz. The frequency of the synchronizing signal (fr) is same as the free running frequency of the MGO. The demodulator GO (DGO) at the receiver end is synchronized with the modulated output of the MGO. The amplitude of the modulating signal is varied to get different values of modulation index. It is evident from the obtained results that the demodulated output is similar to the input chaotic signal in both FM and PM schemes. Some additional signal components are seen at the output spectrum for the FM scheme. With the increased of amplitude of the modulating chaotic signal, the demodulated signal from the FM signal is distorted much compared to that from the PM signal. The experimental study reported in the work establishes the possibility of using bias tuned GOs in chaotic communication at microwave frequency range. Also it is observed that a free running GO used as a modulator would provide FM signals with higher modulation index and more distortion, but an synchronized GO could be used as a phase modulator with lower modulation index and less distortion. RF chaotic signals could well be used as information bearing modulating signal on X-band MW carrier signals.

REFERENCES

1. Wei, C. T. and F. J. Rosenbaum, "Amplitude and frequency modulation of a waveguide cavity CW Gunn oscillator," *IEEE Trans. on Microwave Theory and Techniques*, Vol. 18, No. 11, November 1970.
2. Tanmoy, B., B. Karmakar, and B. C. Sarka, "Single amplifier biquad based autonomous electronic oscillators for chaos generation," *Nonlinear Dynamics*, Vol. 62, 859–869, 2010.

Effects of Nonlinear Bias Tuning of X-band Gunn Oscillator Based Frequency Modulators

B. C. Sarkar, **T. Banerjee**, **A. K. Guin**, **and C. Koleye**
Department of Physics, Burdwan University, India

Abstract— The instantaneous frequency of an ideal frequency modulator should be a linear function of the modulating signal [1]. As such, X-band bias tuned Gunn Oscillators (GO) used as frequency modulators [2, 3] would have desired response if its oscillation frequency changes linearly with the applied dc bias voltage. However, the experimental measurement of the variation of a GO frequency with the GO dc bias voltage above the threshold voltage shows a nonlinear characteristics as shown in Fig. 1(a). The present paper aims to study the effect of this nonlinearity on the response of a GO based FM modulator (FMM) both analytically and experimentally.

First, the experimentally obtained dependance of the GO frequency (f_r) on the applied dc bias voltage V_B has been expressed by a power series about a suitable operating dc bias point. The coefficients used in the power series expression have been determined by the curve fitting technique. Then considering a sinusoidal type modulating signal applied along with the dc bias, the amplitude of the component signals of the resultant FM signal have been obtained. Thus in the analytical consideration, the applied bias to the GO is a sinusoidal function of time above a fixed dc value which results in the time variation of the GO frequency as a nonlinear function of time. The spectrum of the GO output would be given by a complicated expression involving different orders of Bessel functions of the modulation parameters. This quasi-analytical relation has been numerically examined to find the strengths and frequencies of the component signals obtained at the modulated GO output. The results indicate that

1. The average frequency of the modulated signal is shifted from the free running frequency of the GO.
2. The amplitudes of identical order side bands on the higher and lower sides of average frequency are different due to the nonlinear modulation.
3. The asymmetry in the property of side bands is more pronounced when the operating dc bias is close to and much away from the threshold bias required for negative differential resistance of the Gunn diode.

These predictions obtained in the analysis of the nonlinear modulation condition suggest that the operating dc bias should be optimally chosen and the modulating signal amplitude should be of moderate level so that the operation in the linear region is ensured. The experimental studies carrier out with an X-band Gunn oscillator confirm the above observation satisfactorily in the qualitative sense. Fig. 1(b) depicts some experimental results indicating difference in the side band powers.

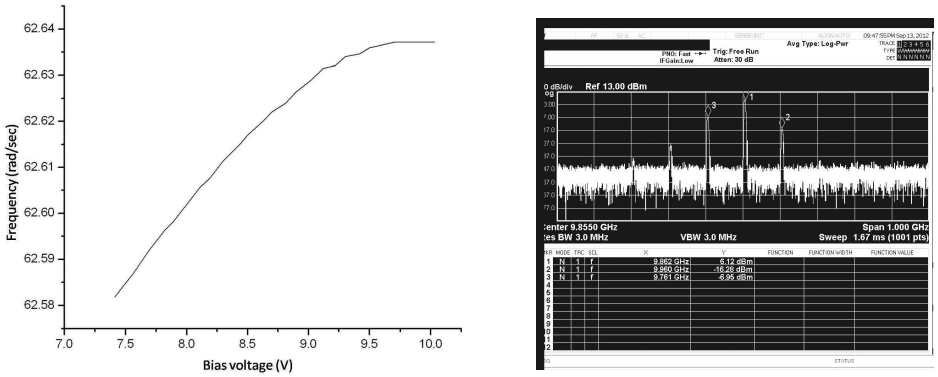

(a) (b)

Figure 1: (a) Variation of oscillation frequency with dc bias voltage when other circuit parameters are kept fixed. (b) Experimentally obtained spectrum indicating difference in the side band powers.

REFERENCES

1. Lathi, B. P., *Modern Digital and Analog Communication System*, 3rd Edition, Oxford University Press.
2. Bestwick, P. R, P. S Drinan, G. S. Hobson, P. N. Robson, M. Thomas, and R. Tozer, "Direct frequency modulation of wave guide cavity CW Gunn oscillator," *IEEE Journal of Solid state Circuits*, Vol. 8, No. 1, 37–43, 1973.
3. Sarkar, B. C., C. Koley, A. K. Guin, and S. Sarkar, "Some numerical and experimental observation on the growth of oscillation in an X-band Gunn oscillator," *Progress In Electromagnetic Research B*, Vol. 40, 325–341, 2012.
4. Sarkar, B. C., C. Koley, A. K. Guin, and S. Sarkar, "Studies on the dynamics of a system of Bilaterally coupled chaotic Gunn Oscillators," *Progress In Electromagnetic Research B*, Vol. 42, 93–113, 2012.
5. Consolo, G., et al., "Combined frequency-amplitude nonlinear modulation theory and application," *IEEE Transaction on Magnetics*, Vol. 8, No. 1, 37–43, 1973.

Experimental Studies on the Nonlinear Interaction between a Chaotic Signal and a Periodic Signal at Microwave Frequency Range

B. C. Sarkar[1], **S. Sarkar**[2], **C. Koley**[1], **A. K. Guin**[1], **and T. Banerjee**[1]

[1]Department of Physics, Burdwan University, India
[2]Electronics Department, Burdwan Raj College, India

Abstract— The generation of broad band Microwave chaotic signals has become an important technological challenge in the context of chaotic communication systems [1, 2]. X-band Gunn Oscillators (GOs) using waveguide type cavity resonators operating in chaotic mode are potential sources of microwave chaos. There are several techniques for producing chaotic oscillations in a GO, like, driving a periodic GO (PGO) with one or more external RF signals or bilateral coupling of two PGOs etc. [3–5]. Recently, a novel technique using a so called under-biased GO has been reported in the literature [6]. Here, the Gunn diode is biased below the threshold dc voltage needed for the appearance of negative differential resistance (NDR) of the device in the presence of a weak external RF signal in the oscillator cavity. Depending on the magnitude of the applied dc bias and the frequency of the injected RF field, one gets chaotic signals of different power and bandwidth.

In the present paper, some experimental methods of enhancing bandwidth as well as power of the microwave chaos have been discussed. The basic physics behind this technique is the nonlinear interaction between the chaotic signal obtained from an under-biased GO with a PGO oscillating at some adjacent frequency. The chaotic signal is injected into the PGO and the output of the latter one is examined. For different values of the detuning between the frequency (f_0) of the PGO and that of the external signal (f_r) used in the chaotic GO, one gets different types of signals at the GO output. The obtained results can be qualitatively summarized as follows:

1. When the magnitude of Δf ($= |f_r - f_0|$) is large compared to the bandwidth of the chaotic signal, the bandwidth of the chaos remains almost unaffected but the spectral characteristics of the PGO becomes slightly broadened. This indicates a feeble interaction between two interacting signals.
2. With the gradual reduction of $|\Delta f|$, the interaction becomes more prominent resulting in the broadening of the continuous broadband spectrum of the chaotic signal. The spectrum of the PGO losses its identity and becomes a part of the resultant broad spectrum.

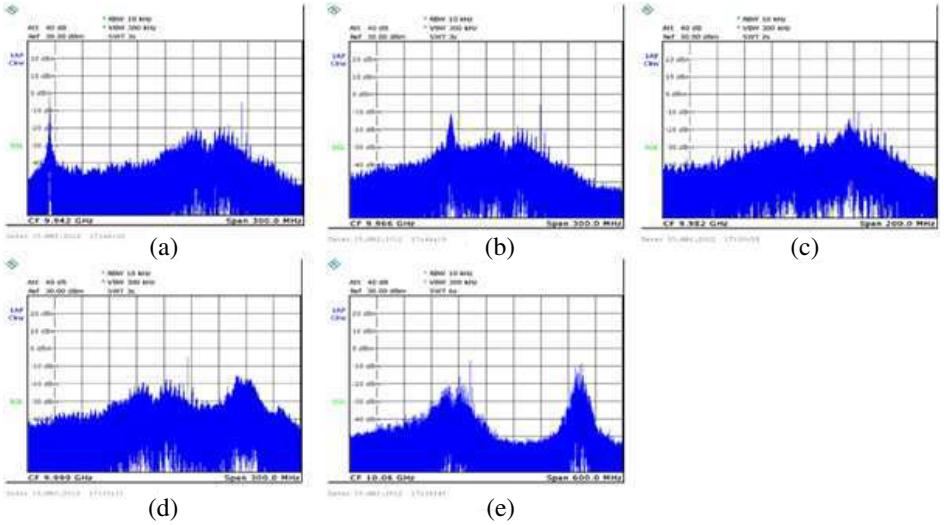

Figure 1: The nature of output spectra of the PGO subject to a chaotic signal for different detuning between f_0 and f_r: (a) $|\Delta f|$=0.209 GHz (BW=130 MHz). (b) $|\Delta f|$=0.1 GHz (BW =170 MHz). (c) $|\Delta f|$=0.006 GHz (BW =140 MHz). (d) $|\Delta f|$=0.064 GHz (BW =200 MHz). (e) $|\Delta f|$=0.236 GHz (BW =130 MHz).

3. When $|\Delta f|$ is small, i.e., f_r and f_0 are comparable, the bandwidth of the PGO output signal becomes of the same order of the original chaotic signal. This may be a case of synchronized state of the PGO with the injected chaotic signal.
4. The observations are qualitatively similar for positive and negative values of $|\Delta f|$. However, there is a quantitative asymmetry in the nature of the output spectra of the PGO on the two sides of f_r in terms of the amount of enhancement in the bandwidth and the power of the resultant chaos.

In the experiment, the values of f_r (10.025 GHz) and the applied dc bias (4.77 Volt) in the chaotic GO have been kept fixed. The frequency of the PGO is varied by mechanical tuning of the GO cavity. A few pictures of the output spectra of the PGO subject to a chaotic RF signal are shown in Fig. 1 for specific values of f_r and f_0 mentioned in the corresponding captions and 20 dBm bandwidth (BW) for different detuning are measured. In brief, the outcomes of the study reported in the paper are (i) A PGO can be synchronized to a chaotic signal of proper bandwidth and power. (ii) Due to nonlinear interaction, in the non-synchronized state between a chaotic and periodic RF signals, the bandwidth of the chaotic signal is broadened.

REFERENCES

1. Kennedy, M. P., R. Rovatli, and G. Setli, *Chaotic Electronics in Telecommunications*, Taylor and Fracis, 2000.
2. Elarson, L., L. S. Tsimring, and J. M. Lih, *Digital Communications Using Chaos and Nonlinear Dynamics*, Springer, 2006.
3. Mosekilde, E., et al., "Mode locking and spatio-temporal chaos in periodically driven Gunn diode," *Physical Rev. B*, Vol. 41, 2298–2306, 1990.
4. Sarkar, B. C., D. Sarkar, S. Sarkar, and J. Chakraborty, "Studies on the dynamics of bilaterally coupled X-band Gunn oscillators," *Progress In Electromagnetics Research B*, Vol. 32, 149–167, 2011.
5. Chakravorty, J., T. Banerjee, R. Ghatak, A. Bose, and B. C. Sarkar, "Generating chaos in injection-synchronized Gunn oscillator: An experimental approach," *IETE Journal of Research*, Vol. 55, 106–111, 2009.
6. Sarkar, B. C., C. Koley, A. K. Guin, and S. Sarkar, "Some numerical and experimental observations on the growth of oscillations in an X-band Gunn Oscillator," *Progress In Electromagnetics Research B*, Vol. 40, 325–341, 2012.

A Contactless Inductive Charging Platform

Han-Chung Teng, Tsung-Lin Li, Guan-Pu Pan, and Jwo-Shiun Sun
Institute of Computer and Communication Engineering
National Taipei University of Technology, Taipei, Taiwan

Abstract— This paper proposes a contactless inductive charging platform (CICP), which allowed cell-phone or other mobile devices placed and charged. By wound-wire structure and magnetic coupling, wireless power transmission could be achieved between platform and mobile device.

This paper started from the parameters of induction coil for the magnetic field distribution, and optimize the design principal. With this principle, the coil could be designed as an unit array coil, and extended it to compose array structure. The experimental results show that maximum power output is 1.6 W and a maximum transmission efficiency of 41%. The transmission efficiency maintained above 40%, when the secondary coil displacement less than 6 mm. By designing appropriate secondary-side circuits to meet the charging requirements of different types of mobile device.

FPGA Implementation of LDPC Encoder with Approximate Lower Triangular Matrix

Yi Hua Chen and Jheng Shyuan He
Institute of Information and Communication Engineering
Oriental Institute of Technology, New Taipei City, Taiwan

Abstract— This study used the weight (3, 6) approximate lower triangular regular parity check matrix to implement the LDPC encoding on the 5641R FPGA of the Software Define Radio system developed by National Instruments (NI) [1]. This study provided a detailed introduction to the encoding mechanism of the approximate lower triangular LDPC, and completed the implementation and verification of FPGA hardware.

REFERENCES

1. SDR Forum website: Hhttp://www.sdrforum.orgH.

A Novel Function Tuner with Microstrip Circuit for Slot Patch Antenna

Chia-Ching Chu[1], **Lih-Shan Chen**[1], **Hsien-Chiao Teng**[3], **and Shen Cherng**[2]

[1]Department of Electronic Engineering, I-Shou University, Taiwan, R.O.C.
[2]Computer Science and information Engineering, Chengshiu University, Taiwan, R.O.C.
[3]Department of Electrical Engineering, ROC Military Academy, Taiwan, R.O.C.

Abstract— This paper presents a design of microstrip functional tuner for slot patch antenna. It consists of a SMA-connector and an adjustable microstrip circuit. The implemented antenna was excited through a T-shape feed line being coupled to the rectangular patch. The operation frequency is designed at 2.6 GHz. The connector is embedded to the rectangular patch being connected to the function tuner to control the impedance bandwidth of the proposed antenna. In this study, the impedance bandwidth of the proposed antenna can be simply controlled by adding resister on to the microstrip circuit. The impedance bandwidth of the proposed antenna without circuit loading was designed at 3.4%. If the circuit loading of 75 Ω was added, the impedance bandwidth of the proposed antenna would increase to 11.4%. If the circuit loading is changed to 50Ω and 25 Ω, the impedance bandwidth of the proposed antenna would be shifted to 14.3% and 20.8% respectively. The equivalent circuit simulated by ADS for our designed functional tuner is demonstrated. The calculated and experimental results confirmed that our proposed functional tuner embedded onto the implemented antenna has good performance.

An Emergency Medical Service Support System

Li-Lin Chen
Electronic Engineering Department, Oriental Institute of Technology, New Taipei, Taiwan, R.O.C.

Abstract— Taiwan has lots of steep landforms. In addition to the aborigines, forest workers, and farmers who live and work in mountainous areas, tourists often visit these areas during the weekend and holidays. People have experienced injury or sudden health conditions in mountainous areas; however, because of inconvenient transport or traffic controls, some of the injured people could not reach hospitals promptly, thus eventually dying. To reduce the time required for people in rural areas to reach emergency care services and prevent the above tragedies, an "Emergency Medical Service Support System" was developed. This system is aimed at support both the current emergency and rescue command center, also named as 119 units. During emergencies in rural areas, the rescue command center can authorize nearby vehicles with the rights to perform as an ambulance to transport emergency patients to hospitals promptly. With this additional function, the rescue operation can effectively prevent treatment delays caused by waiting for an ambulance to arrive from a distant location. Additionally, the emergency and rescue command center can coordinate with the units responsible for the sections of road under construction to assist emergency vehicles in traveling through these areas smoothly. Finally, an ambulance can be sent to a relay station to transport patients to a hospital rapidly. This support system effectively transports emergency patients in rural areas to hospitals promptly to receive appropriate medical treatment.

A Novel Design of Reconfigurable Annular Slot Active Patch Antenna

Yu-Ming Lee[1], **Shen Cherng**[2], **Hsien-Chiao Teng**[3], **and Shuming T. Wang**[1]

[1]Department of Electrical Engineering, I-Shou University, Taiwan, R.O.C.
[2]Computer Science and Information Engineering, Chengshiu University, Taiwan, R.O.C.
[3]Department of Electrical Engineering, ROC Military Academy, Taiwan, R.O.C.

Abstract— This paper presents a novel reconfigurable annular slot structure. The proposed antenna has a functional dual branch microstrip line components being coupled with annular slot to create circular polarized radiation. Two PIN diodes are embedded to the dual branch microstrip line and excited by $V_{dc} = 3\,\mathrm{V}$ and $I_{dc} = 150\,\mathrm{mA}$. Reconfigurable circular polarizations can be simply shifted back and forth with linear, right-handed and left-handed polarization by modifying the modes of pin-diode. Simulation and experimental results have shown the good impedance bandwidth for return loss and antenna gains in circularly polarized states.

A Surface-potential Based Compact Model of Gate Capacitance in GaN HEMTs

Jie Wang[1,2], **Lingling Sun**[1,2], **Jun Liu**[1], **and Mingzhu Zhou**[1]

[1]Key Laboratory of RF Circuits and Systems, Ministry of Education, Hangzhou Dianzi University, China
[2]Department of Electrical Engineering, Zhejiang University, China

Abstract— In this paper, a new surface-potential based compact model of the gate capacitance C_{gg} in AlGaN/GaN HEMTs is presented. Considering the density of the two dimensional electron gas (2DEG) is very high on the AlGaN/GaN interface, We first integral of the quasi-Fermi potential effect to the source equation of the surface-potential and use new analytic approximation for quasi-Fermi potential which is accurate for any carrier density evaluated [1]. The proposed surface potential provides the accurate descriptions of accumulation ($V_{gs} - V_{fs} < 0$) and transitional region between the sub-threshold and inversion region, develops consistent and higher order differential current and charge equations. The resulted C-V expressions are given explicitly in close form [2, 3], which will highly improve the simulation continuity and accuracy. The explicit model is valid in all regions of device operation and verified by comparing with the Pao Sah implicit model numerical solutions and TCAD simulations. The model not only leads to a more clear understanding of GaN HEMTs device behavior but also provides a better platform for the next generation of GaN HEMTs compact models.

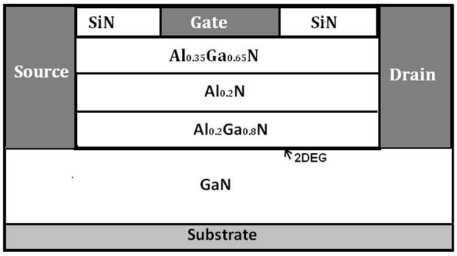

Figure 1: The structure of the $Al_{0.2}Ga_{0.8}N$/GaN HEMT.

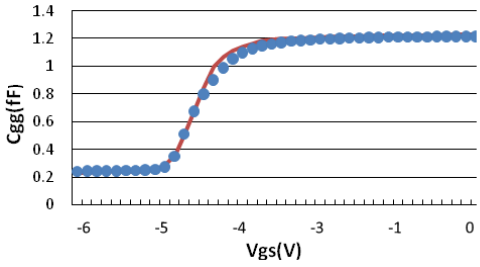

Figure 2: (line) Simulated and (dot) TCAD C_{gg} for an $Al_{0.2}Ga_{0.8}N$/GaN HEMT for $V_{ds} = 1$ V.

REFERENCES

1. John, D. L., F. Allerstam, et al., "A surface-potential based model for GaN HEMTs in RF power amplifier applications," *2010 IEEE International Electron Devices Meeting (IEDM)*, 8.3.1–8.3.4, 2010.
2. Cheng, X. and Y. Wang, "A surface-potential-based compact model for AlGaN/GaN MODFETs [J]," *IEEE Transactions Electron Devices*, Vol. 58, No. 2, 448–454, 2011.
3. Khandelwal, S. and T. A. Fjeldly, "A physics based compact model of gate capacitance in AlGaN/GaN HEMT devices," *2012 8th International Caribbean Conference on Devices, Circuits and Systems (ICCDCS)*, 1–4, 2012.

Design of the Envelope Modulator for High Efficiency RF Envelope Tracking Power Amplifier (ET-PA)

C. A. Schecht, D. Y. C. Lie, and J. Lopez
Department of Electrical and Computer Engineering, Texas Tech University (TTU)
Lubbock, TX 79409-3102, USA

Abstract— With the popular trend in consumer technology moving further towards battery powered portable handheld devices, more and more focus has been placed on optimizing the efficiency of individual components to maximize the battery life. One of the most power consuming elements in these battery powered devices is the radio-frequency power amplifier (RF-PA). Current state-of-the-art RF communications systems rely on high bandwidth, high peak-to-average ratio (PAR) signals with a non-constant amplitude to maintain the high data rates that consumers demand in their portable devices. To meet the stringent linearity requirements of these systems, the RF-PA is often forced to be operated in the linear output-back-off (OBO) region which greatly reduces the efficiency of the overall transmitter (TX) system. Thus, it is exceedingly desirable to design TX systems with very linear and highly efficient RF-PAs. Techniques such as Envelope Elimination and Restoration (EER) and Envelope Tracking (ET) have been investigated for decades as methods for improving both the linearity and efficiency of TX systems [1, 2]. For modern high bandwidth and high PAR OFDM-like (Orthogonal Frequency-Division Multiplexing) signals, an ET-PA system is found to improve not only the efficiency of the TX system but the linearity as well. The focus of this paper, therefore, will be on the design of highly efficient and linear *envelope modulators* (both discrete and monolithic versions) for their effective use in ET-PA TX systems. There are many design challenges for realizing a highly efficient envelope modulator (EM). A typical linear-assisted switching amplifier-based EM is discussed throughout this work as shown in Fig. 1 [3]. An overview of each section of the EM design will be shown, as well as insights into how to optimize the overall ET-PA system performances.

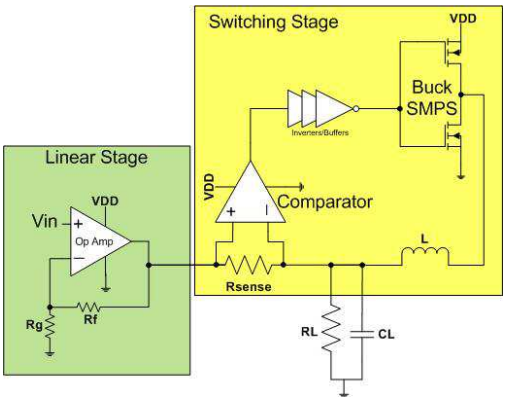

Figure 1: Block diagram for a linear-assisted switching amplifier based envelope modulator (EM).

REFERENCES

1. Kahn, L., "Single-sideband transmission by envelope elimination and restoration," *Proc. IRE*, 803–806, Jul. 1952.
2. Sahu, B. and G. Rincon-Mora, "A High-efficiency linear RF power amplifier with power-tracking dynamically adaptive buck-boost supply," *IEEE Trans. Microw. Theory Tech.*, Vol. 52, 112–120, Jan. 2004.
3. Li, Y., J. Lopez, D. Y. Lie, K. Chen, S. Wu, T.-Y. Yang, and G.-K. Ma, "Circuits and system design of RF polar transmitters using envelope-tracking and sige power amplifiers for mobile WiMAX," *IEEE Transactions on Circuit and Systems I*, Vol. 58, No. 5, 893–901, May 2011.

Design of a Multi-band Dielectric Resonator Antenna

Hsin-Chih Tsai, Tsung-Lin Li, Hung-Wen Liu, and Jwo-Shiun Sun
Institute of Computer and Communication Engineering
National Taipei University of Technology, Taipei, Taiwan

Abstract— In this paper, a hybrid structure multi-band rectangular dielectric resonator antenna (DRA) that combined a rectangular and parasitic slot was proposed. By optimizing the structure parameters, the hybrid structure allows not only the parasitic slot to resonate at one band but also the DR to resonate at another band, and multi-band can be independently designed. The simulated and measured results verify the validation of the proposed design.

This paper has proposed a novel hybrid structure multi-band antenna that combines a rectangular dielectric resonator and a parasitic slot are present. With these features, this antenna is useful for multi-band operation of PCS, UMTS, WiMax-2.4, WLAN-802.11b, WLAN-802.11a wireless communication system.

Design of a Circularly Polarized Rectenna for Wireless Power Transmission

Si-Jyun Hung, Tsung-Lin Li, Yi-Ching Huang, and Jwo-Shiun Sun
Institute of Computer and Communication Engineering
National Taipei University of Technology, Taipei, Taiwan

Abstract— A circularly polarized (CP) rectenna (rectifying antenna) for the applications of wireless power transmission has been studied. This study includes: 1. Design of a circularly polarized wide-slot antenna which can reduce the multi-path fading efficiently and solve the depolarization effect of random polarization in free space and complicate environment. 2. Design of the balun (balance to unbalance) and matching network by using the chip components. 3. Design of the double voltage rectifying circuit.

The proposed design of circularly polarized slot antenna exhibit antenna gain of is about $2.2 \sim 3.2$ dBi. Design circularly polarized rectenna show of a maximum voltage of 8.15 V and a conversion efficiency of 81% could be attainable.

High-peak Power, Low-average Power RF Pulses, Bioeffects and Standards: Recent Developments

Michael R. Murphy
Bioeffects Division, 711th Human Performance Wing
Air Force Research Laboratory, Ft Sam Houston, Texas, USA

Abstract— With the ever increasing use of Radio Frequency (RF) energy, there is also an increase in the opportunity, even certainty, for increased human exposure to RF emissions. Also, the nature of the exposures are entering new regimes, with possible exposure to RF pulses of nanosecond and picosecond duration and with extremely high-peak electric fields becoming more common Scientifically based human exposure standards are needed to both protect humans from the real hazards of exposure to RF pulses and to provide a relatively stable base for maximal safe exploitation of RF pulse-based technologies. Two widely used international RF exposure standards, one produced by the IEEE International Committee on Electromangetic Safety (ICES) [1], and the other by the International Commission for Non-Ioniing Radiation Protection (ICNIRP) [2], are similar in the total RF energy allowed within a specified averaging time, but differ greatly in their guidelines for limiting exposure to single RF pulses. IEEE ICES basic restrictions limit the Specific Absorption (SA) in any one pulse to 28.6 J/kg and limit the peak e-field for any single pulse to 100 kV/m. ICNIRP basic restrictions limit the energy per pulse to 0.01 J/kg (occupational exposure) or 0.002 J/kg (public exposure) for any exposure that includes the head, but has no specific basic restriction for peak e-field. The current IEEE ICES limit on peak e-field is based on the possibility of air breakdown and subsequent spark discharge, whereas the ICNIRP limit on SA (J/kg) is based on a concern to avoid the microwave hearing phrnomrnon. Thus, the basic restricions for these two standards differ by as much as 14,300 times for the SA of a pulse. Recent standards activity and research findings bearing on the safety of high-peak power, low-average power RF pulses will be discussed.

REFERENCES

1. IEEE International Committee on Electromangetic Safety (ICES), "C95.1: IEEE standard for safety levels with respect to human exposure to RF electromagnetic fields 3 kHz to 300 GHz," 2005, http://www.ices-emfsafety.org.
2. International Commission for Non-Ioniing Radiaiton Protection (ICNIRP), "Guidelines for limiting exposure to time-varying electric, magnetic, and electromagnetic fields (up to 300 GHz)," 1998, http://www.icnirp.de.

Electromagnetic Forces in the Curved Octonion Spaces

Zi-Hua Weng
School of Physics and Mechanical & Electrical Engineering
Xiamen University, Xiamen 361005, China

Abstract— J. C. Maxwell was the first scholar to depict the classical electromagnetic theory with the vector terminology as well as the algebra of quaternions. This method galvanizes the subsequent scholars to study the electromagnetic theory and the gravitational theory with the curved octonion space.

By means of the orthogonality definition of two octonions, the paper applies the parallel transport and the covariant derivative to describe simultaneously the features of gravitational and electromagnetic fields in the curved octonion space.

In the curved octonion spaces for the gravitational and electromagnetic fields, it can be deliberated the field equations, momentum, angular momentum, energy, torque, power, force, and the continuity equations etc..

The results affirm that the connection coefficient and the curvature of the curved octonion space can impact directly the gravitational and electromagnetic forces etc in the electromagnetic and gravitational fields.

ACKNOWLEDGMENT

The authors are grateful for the financial support from the National Natural Science Foundation of China under grant number 60677039.

The Effect of Exposure to ELF-EMFs on Learning and Memory Ability Changes in Rats

Jianfeng Guo[1], **Dong Wang**[1], **and Lingfeng Kong**[2]

[1]Shenzhen Environmental Monitoring Centre
No. 8 Meiao Road, Shangmeilin, Futian, Shenzhen 518049, China
[2]Environmental Protection of Guangdong Province
No. 213 Longkou Road, Tianhe, Guangzhou 510630, China

Abstract— Exposures to extremely low-frequency electric and magnetic fields (ELF-EMFs) emanating from the generation, transmission, and use of electricity are a ubiquitous part of modern life. At present stage of ELF-EMFs bioeffects research, most of ELF simulation models didn't give the stimulation of electric and magnetic fields simultaneously. And these couldn't get ELF-EMFs health effects exactly.

To explore the effect of exposure to extremely low frequency electromagnetic fields (ELF-EMFs) of working environment on learning and memory in rats, and changes of hippocampus neuron. Designed an 50 Hz EMFs exposure system. 40 Wistar rats were exposed 8 hours per day and 5 days per week for 8 consecutive weeks. Then, learning and memory ability of rats and hippocampus pathological changes were studied to find the changes. The neuron apoptosis in hippocampus were studied. In addition, the changes among exposed and the sham exposed rats were tested. In this simulation, 20 rats were exposed to an electric field of approximately 5 kV/m and a magnetic field of approximately 78 μT simultaneously, other 20 rats were exposed to an electric field of approximately 5 kV/m and a magnetic field of approximately 100 μT simultaneously. The learning and memory ability of the sham exposed rats is better than the exposed rats ($P < 0.05$). Besides, there were no significant changes of the pathological change in hippocampus and the neuron apoptosis in hippocampus. The results show that exposure to 50 Hz EMFs for a period could injure central nervous system. And the neurobehavioral dysfunction is in juried before histopathological damage and hippocampus neuron cell injuryIn particular, the magnetic field have greater impact.

Electron Energy Loss and Second-harmonic Emission of Nonlinear Nanoparticles

Jinying Xu and Xiangdong Zhang
Beijing Computational Science Research Center, Beijing, China

Abstract— In this work we present a fast and general technique to investigate the interaction between a fast electron and the nonlinear material consisting of centrosymmetric spheres and explore the relativistic Electron-energy-loss spectroscopy (EELS) and radiation emission in the nonlinear materials. In contrast to the fundamental frequency (FF) case, negative loss probabilities are observed in the secondharmonic (SH) spectra although the photon emission probabilities are always positive. This means that the SH field cannot only cause the energy loss of moving electrons, but also it can increase the energy of the moving electron at some frequencies. Such a phenomenon originates from various excitations of the SH field when a fast electron moves along a straight-line trajectory passing near the nonlinear materials. When a fast electron moves with velocity v and passes near the object, it may engender the radiation with wide frequency spectrum. The energy loss suffered by the fast electron is related to the force exerted by the radiation electric field acting on it. The interaction between the radiation field and the object consisting of the nonlinear materials can cause the generation of the SH field. In contrast to the FF field, the change of the SH field is more abundant. The direction of the SH electric field may be identical with or opposite to the moving direction of the electron beam, which depends on the characteristic of the nonlinear object and the frequency. When the direction of the SH electric field is identical with the moving direction of the electron beam, the radiation electric field acting on the electron beam results in positive energy loss. However, we would like to point out that the energy conservation still be preserved for such a case. This is similar to the case of the generation of the SH field from the nonlinear materials, which the energy conservation is preserved. The magnitude of the negative energy loss depends on features of the nonlinear object. At the same time, strong SH emissions can also be obtained by the moving the electron beam. We find that the SH emissions exhibit different dependence of the angle in comparison with those of the FF. For the case of the FF, the Smith-Purcell radiations produced by interaction of fast electron beams with finite and infinite strings of sphere have been discussed very well in the previous works. Our present results are agreement with them. However, the nonlinear Smith-Purcell radiation caused by the SH field has never been observed before. Our calculated results demonstrate such an effect and show the possibility of using this effect to produce tunable SH emissions.

3D CFDTD PIC Simulation Study on Low-frequency Oscillations in a Gyrotron

M. C. Lin and D. N. Smithe
Tech-X Corporation, Boulder, CO 80303, United States

Abstract— Low-frequency oscillations (LFOs) have been observed in a high average power gyrotron and the trapped electron population contributing to the oscillation has been measured. As high average power gyrotrons are the most promising millimeter wave source for thermonuclear fusion research, it is important to get a better understanding of this parasitic phenomenon to avoid any deterioration of the electron beam quality thus reducing the gyrotron efficiency. However, understanding of the LFOs remains incomplete and a full picture of this parasitic phenomenon has not been seen yet. In this work, we use a 3D conformal finite-difference time-domain (CFDTD) particle-in-cell (PIC) method to accurately and efficiently study the LFOs in a magnetron injection gun (MIG) of a high average power gyrotron. Employing a highly parallelized computation, the model can be simulated in time domain more realistically. LFOs have been obtained in a 3D time domain simulation for the first time. From our preliminary simulation studies, it is found that not only magnetic compression profile but initial velocity or velocity ratio play an important role in the operation of a MIG electron gun. In addition, the secondary emission effects on the LFOs are also studied. Detailed results will be presented.

ACKNOWLEDGMENT

This work is supported by the U.S. Department of Energy under Grant No. DE-SC0004436. Also the authors would like to thank the VORPAL Team.

REFERENCES

1. Cerfon, A. J., E. Choi, C. D. Marchewka, I. Mastovsky, M. A. Shapiro, J. R. Sirigiri, and R. J. Temkin, "Observation and study of low-frequency oscillations in a 1.5-MW 110-GHz Gyrotron," *IEEE Trans. Plasma Sci.*, Vol. 37, No. 7, 1219–1224, 2009.
2. Nieter, C. and J. R. Cary, "VORPAL: A versatile plasma simulation code," *J. Comput. Phys.*, Vol. 196, 448–473, 2004.
3. Dey, S., R. Mittra, and S. Chebolu, "A technique for implementing the FDTD algorithm on a nonorthogonal grid," *Microwave and Opt. Technol. Lett.*, Vol. 14, 213–215, 1997.
4. Dey, S. and R. Mittra, "A locally conformal finite-difference time-domain (FDTD) algorithm for modeling three-dimensional perfectly conducting objects," *IEEE Microwave and Guided Wave Lett.*, Vol. 7, 273–275, 1997.
5. Chen, F. F., *Introduction to Plasma Physics and Controlled Fusion*, 2nd Edition, Springer, 1984.

A Prototype Design of Dental Microwave Imaging Equipment

Chun-Sen Wu, Hsien-Nan Kuo, and Tsung-Chih Yu
Metal Industries Research & Development Centre, Taiwan

Abstract— In this paper, a prototype of microwave imaging equipment is designed for dental clinic application. Considerations in both microwave imaging technique and clinical dental treatment are studied. Equipment design planning includes system operation flow, structure design, mechanical layout, specification of hardware requirements and software functions, database design, integration of information system, system stability and security. The benefit and economic effect of this system were also analyzed.

Research of Improved Matching Doherty Solid State Power Amplifier

Zheng-Qin Li[1], **Wei-Wei Cheng**[2], **and Yuan-Yuan Wu**[3]

[1]Electronic Engineering Department, School of Information
City College of Wenzhou University, Wenzhou, Zhejiang 325025, China
[2]Institute of Microelectronics and Optoelectronics
Zhejiang University, Hangzhou, Zhejiang 310027, China
[3]College of Information Engineering, Guizhou Minzu University
Guiyang, Guizhou 550025, China

Abstract— This paper makes a detail analysis of the several important parameters of Doherty solid state power amplifier, which focus on the gain flatness, efficiency, power additional efficiency, matching impedance and so on. Then it proposed a method to optimize the matching technology to improve the linearity to balance the amplifiers, and the linearity increases by 5% with the general gain flatness.

Research of Doherty Solid State Power Amplifier with Improved Bias Matching

Ming-Hai Xu[1] **and Wei-Wei Cheng**[2]

[1]Electronic Engineering Department, School of Information
City College of Wenzhou University, Wenzhou, Zhejiang 325025, China
[2]Institute of Microelectronics and Optoelectronics
Zhejiang University, Hangzhou, Zhejiang 310027, China

Abstract— This paper makes a detail analysis of the several important ways to improve the efficiency of solid state radio frequency power amplifier, which focus on the power gain, efficiency, power additional efficiency, gate bias matching and so on. Then it proposed a method to optimize the bias technology to improve the linearity to balance the amplifiers, and the linearity increases by 6% with the general gain.

Analysis and Design of the Microstrip Matching for Doherty Amplifier

Ming-Hai Xu[1] **and Sheng-Yun Luo**[2]

[1]Electronic Engineering Department, School of Information
City College of Wenzhou University, Wenzhou, Zhejiang 325025, China
[2]Physical Electronics Lab, Department of Materials Science
Fudan University, Shanghai 200433, China

Abstract— This paper makes a detail analysis of the several important ways to improve the efficiency of RF power amplifier, and analyze the main structure and mechanism of Doherty amplifier, and proposes a microstrip matching way to improve the efficiency and linearity of radio frequency amplifier.

A Novel Oscillator Based on Film Bulk Acoustic Resonator

Wei-Wei Cheng[1], **Shu-Rong Dong**[1], **and Sheng-Yun Luo**[2]

[1]Institute of Microelectronics and Optoelectronics
Zhejiang University, Hangzhou, Zhejiang 310027, China
[2]Physical Electronics Lab, Department of Materials Science
Fudan University, Shanghai 200433, China

Abstract— A novel low phase noise oscillator with film bulk acoustic resonator (FBAR) technology is presented. The longitudinal mode FBAR and shear mode FBAR are fabricated. The High Q FBAR also obtained from cutting AVAGO's FBAR produce. The Clapp oscillator based on FBAR at 1881 MHz is designed and fabricated on printed circuit board. The testing results show that the output power of this FBAR oscillator is −3.5 dBm.

Analysis and Optimization of the Linearity and Efficiency for Doherty Amplifier

Zheng-Qin Li[1], **Wei-Wei Cheng**[2], **and Mei-Yi Xiang**[3]

[1]Electronic Engineering Department, School of Information
City College of Wenzhou University, Wenzhou, Zhejiang 325035, China
[2]Institute of Microelectronics and Optoelectronics
Zhejiang University, Hangzhou, Zhejiang 310027, China
[3]College of Information Science Technology
East China Normal University, Shanghai 200062, China

Abstract— This paper makes a detail analysis of the second-order product, the third order product, power back-off and 1 dB compression point, then makes adjustment for the matching to improve the linearity of amplifier, and proposes an optimization for the out power at $P_{1\,\mathrm{dB}}$ point to increase the efficiency.

Design and Implementation of Low Phase Noise Oscillator Based on Film Bulk Acoustic Resonator

Wei-Wei Cheng[1], **Shu-Rong Dong**[1], **and Sheng-Yun Luo**[2]

[1]Institute of Microelectronics and Optoelectronics
Zhejiang University, Hangzhou, Zhejiang 310027, China
[2]Physical Electronics Lab, Department of Materials Science
Fudan University, Shanghai 200433, China

Abstract— A novel low phase noise oscillator with film bulk acoustic resonator (FBAR) technology is presented. The longitudinal mode FBAR and shear mode FBAR are fabricated. The High Q FBAR also obtained from cutting AVAGO's FBAR produce. The Clapp oscillator based on FBAR at 1881 MHz is designed with PMBVD model and fabricated on printed circuit board. The testing results show that the output power of this FBAR oscillator is −3.5 dBm, while the phase noise is −130 dBc/Hz at 1 MHz.

Author Index

Abdallah Esmat Abdel-Fattah, 454, 581
Abdulaziz Mahdi B., 296
Abdullah Haythem Hussein, 454, 581
Abdulrahman Amuda Yusuf, 339
Aberra-Guebrou S., 79
Abrishamian Mohammad Sadegh, 521
Abuelma'atti Muhammad Taher, 516, 517
Abuelmaatti Ali M. T., 516, 517
Adekola Sulaiman Adeniyi, 464, 501
Afullo Thomas Joachim Odhiambo, 174, 401, 402, 560, 561
Afzal M. Tausif, 596
Agafontsev Dmitry, 17
Ahmad Umair, 602
Ahmed Istiaque, 250
Ahmed M. Mansoor, 486, 596, 602
Alabidi Ebrahim Sailan, 342
Albinet Clément, 169
Alhammadi Abdulraqeeb, 115
Ali Syed Ahsan, 602
Alias Mohamad Yusoff, 112, 114, 115
Aliyazicioglu Zekeriya, 325
Alkhateeb Osama, 588
Alkina Gulnar K., 320
Alkoot Essa M., 296
Alkoot Fuad M., 296
Alsuhaim Hamad Suliman, 407
Altun Ozgur, 574
Amano Tomohiro, 137
Ameya Michitaka, 189, 190, 563
Anwar Shahzad, 565
Aoyama R., 453
Aoyama Yasuaki, 626
Arai Hiroyuki, 188, 193
Arora P., 237, 550
Ashizawa Yoshito, 121, 448, 582
Asiyo Mike Omondi, 401
Astafiev Oleg, 75
Atai Javid, 15
Atamaniuk Barbara, 299
Ayorinde Ayotunde Abimbola, 464
Azim Rezaul, 343
Azini A. S., 532
Aziz-ul-Haq Muhammad, 596

Bai Kai-Hao, 66
Bai S., 590
Bai Xue, 405
Balzano Quirino, 161
Banerjee T., 667, 668, 670
Bao Taojie, 157
Barbastathis George, 149
Bartal G., 154
Bartušek Karel, 25, 28, 30, 31, 84, 248
Bashir Muhammad Adil, 486
Battu Serge, 289
Bau Nguyen Quang, 257, 258, 360
Bauer Jan, 426
Bednar Miroslav, 425
Bellessa Joel, 79
Beran Laurens, 625
Berezin M., 73
Berg Matthew J., 434
Berginc Gerard, 362
Bernard Erwan, 168
Bessaudou Annie, 289
Bhattacharyya Somak, 646
Billings Stephen D., 625
Bin You, 633
Biscans Beatrice, 434
Biswas Anjan, 14, 319
Bit-Babik Giorgi, 161
Blondy Pierre, 289
Bobrovs Vjaceslavs, 224, 225
Bodemann Ralf, 284
Boeuf Jean-Pierre, 600
Boey Huey Shen, 569, 573
Borderies Pierre, 169, 439
Brooks Daniel, 191
Buisson Olivier, 74

Cai Yao-Jyun, 611
Caire François, 586
Can Wang, 531
Cao Qunsheng, 173, 513, 591
Cao Y. R., 104
Cap Martin, 29, 30, 88, 247
Carney P. Scott, 273
Castanie Aurore, 81
Caulliez Guillemette, 439
Ceolato Romain, 168, 434
Chabory Alexandre, 600
Chai Guowei, 222
Chan Che Ting, 264, 265
Chan H. B., 264
Chan Yee Kit, 568, 570, 572, 573
Chane-Ming Fabrice, 391
Chang Chia Min, 105
Chang Chih-Wei, 242, 540
Chang Dau-Chyrh, 62, 63, 139, 293, 538, 601, 603, 604, 608, 609, 611
Chang Fang-Jui, 203
Chang Hong-Hsiang, 430
Chang Hsuan-Hao, 100
Chang Hun-Pin, 446
Chang Hung-Chun, 354
Chang Hung-Wen, 198–200, 205–207
Chang Kao-Der, 540
Chang Li-Han, 484
Chang Liann-Be, 241
Chang Wen-Teng, 530
Chang Yen-Kai, 242, 540
Chang Yu-Peng, 356, 417
Chang Yun-Chorng, 421
Chao Yuan-Chun, 100
Chau Lai-Kwan, 102
Chau Yuan-Fong, 226, 524, 525
Chen Cheng-Wei, 603, 604
Chen Chi-Xian, 472
Chen Chia-Hsiang, 350
Chen Chih-Min, 549
Chen Ching-Hui, 456
Chen Chung-Ping, 644
Chen Deyuan, 533
Chen Fu-Chiarng, 142
Chen Fu-Sung, 428
Chen Guorong, 223
Chen Hongsheng, 267
Chen Hsing-Yi, 118, 162
Chen Hsun-Hsiang, 652
Chen Huanyang, 565
Chen I-Fong, 509, 510
Chen I-Hong, 16
Chen Jay, 139, 611
Chen Jie, 235, 403
Chen Jing-Yen, 129
Chen Ku Chieh, 359
Chen Kuan-Ren, 548
Chen L., 18
Chen Li-Lin, 555, 557, 675
Chen Lifeng, 443
Chen Lih-Shan, 674
Chen Ming Hui, 67, 459
Chen Mou-Ray, 16
Chen Pang-Hsing, 650, 651
Chen Po-Chou, 429
Chen Ruirui, 565
Chen Shiuan-Yeh, 546
Chen Sung-Lin, 506
Chen Teng-Kai, 465

Chen Tungyang, 151
Chen Wei Ting, 542
Chen Wei-Sheng, 385–387
Chen Wei-Yu, 419
Chen Wen-Shan, 128, 129, 503
Chen Xi, 12
Chen Xudong, 527, 528
Chen Xuewen, 418
Chen Yen-Heng, 650
Chen Yi Fan, 483
Chen Yi Hua, 645, 673
Chen Yi-Lin, 240
Chen Ying, 215
Chen Yu, 100
Chen Yu Lim, 105
Chen Yu-Hsuan, 100
Chen Yu-Liang, 201
Chen Zhi, 410
Cheng Bo Han, 103
Cheng Chien-Min, 128, 129
Cheng George G., 291, 292
Cheng Li-Yuan, 142
Cheng Wei Wei, 687, 688, 690–692
Cheng Wei-Ming, 548
Cheng Yueh-Hung, 105
Cherng Shen, 674, 676
Cheung Sing Wai, 333, 335, 337, 338, 507, 663–665
Chew Weng Cho, 121, 122, 181, 316, 448, 471, 582
Chiang Hai-Pang, 105, 544
Chiang Jung-Sheng, 201–203
Chiang Po-Jui, 204
Chieh Shao-Wei, 429
Chim-Oye T., 409
Chin Albert, 214
Chiou Yu-Zung, 128
Chiu Hsien-Chin, 217
Chiu Shih-Chiang, 129
Chiueh Her-Lih, 470
Choi Se-Hwan, 505
Choo Yong Huat, 35
Chou Chung-Kwang, 159, 280, 284
Chou Hsi-Tseng, 66, 176, 456
Chou Yu-Ling, 603
Chou Yun-Hsih, 656
Chou Yung-Hsiang, 177
Chowdhury S. A. M. S., 15
Choy Sue-Lynn, 391
Choy Wallace C. H., 181, 471
Christ Andreas, 163
Chu Chang Lueng, 645
Chu Cheng Hung, 105
Chu Chia-Ching, 674
Chu Chia-Wei, 410
Chu Fang-Dar, 385–387
Chu Yi, 226, 524, 525
Chua Ming Yam, 573
Chuah Hean-Teik, 433, 568, 573
Chuang Keh-Shih, 556
Chung W. H., 151
Ciarkowski Adam, 438
Clune Thomas L., 435
Colin Elizabeth, 111
Conway John Thomas, 321
Correia Américo, 42, 44
Cortés A. Lizbeth Cortés, 52
Csaki Andrea, 415

Dalmay Claire, 289
Daniel Luca, 119
Danner Aaron J., 475
Dashti Ahmad A., 296
Datta Biplab Kumar, 19
De Britto Larissa Aguiar Dantas, 649
De Silva Pasan, 38
Decker M., 78
Dedková Jarmila, 89, 90
Deng Pin, 640
Deng Zi-Lan, 153
Derevyanchuk Ekaterina D., 59
Dewan Raimi, 606
Dhont Jan K. G., 22
Ding Chaoliang, 252, 393, 535
Dinis Rui, 42, 47
Ditchi Thierry, 150, 482
Dohnal Premysl, 32
Dong Jian-Wen, 153
Dong Shu Rong, 690, 692
Dovan Thanh, 284
Dowlet Darell, 150
Drexler Petr, 29, 404
Du Yang, 123, 436
Du Yu, 231
Du Yu-Lei, 489
Duan Yubo, 410
Dumur Etienne, 74
Dungkanya K., 409
Dutta Prasanta Kumar, 19
Dutta-Gupta Shourya, 412

Eaipresertsak K., 409
Ebihara Tadashi, 49
Eichelkraut T., 270
El-Gendy Mohamed S., 581
Elamin Nassrin Ibrahim Mohamed, 339
Emoto Akira, 228
Endo Yuta, 164
Esslinger M., 275
Everitt Mark J., 72
Ewe Hong Tat, 433

Fahmy Eman Ahmed, 499
Fang Nicholas X., 265
Fang Ning, 382, 529
Fang Runiu, 647
Fang Xiao Sheng, 132, 136
Fang Yuming, 533
Fatras Christophe, 439
Fayed Zaki Taha, 499
Felbacq Didier, 81
Feng Quanyuan, 372, 384, 511, 653–655
Feng Shengfei, 468
Feofanov Alexey K., 74
Fiala Pavel, 26, 27, 29, 32, 379
Fickenscher Thomas Heinrich, 300, 437
Filter R., 270
Fischer S., 270
Fjørtoft Roger, 439
Fligl Stanislav, 426
Foong Shaohui, 286, 287
Friedl Martin, 32, 87, 88
Fritzsche Wolfgang, 415
Frohlich Lubomír, 88
Fu Erjiang, 391
Fuangfoong Manu, 409
Fuh Kuen-Fwu, 640
Fujimoto Takafumi, 140
Fukusako Takeshi, 130, 141
Fung Kin Hung, 265
Futatsumori Shunichi, 46

Gallinet Benjamin, 271
Gao Han, 575
Gao Hanhong, 149
Garcia Martin Lopez, 443
Garwe Frank, 415
Gawad Samir G. Abdel, 666
Ge Yuehe, 531
Georgiev Georgi Nikolov, 323
Georgieva-Grosse Mariana Nikolova, 323
Geran F., 495
Geron Emmanuel, 150, 482
Gescheidtová Eva, 24, 28, 30, 248, 249, 253
Gettman Ken, 284
Gevorkyan Eduard A., 318
Ghosh Saptarshi, 646
Gialich Matthew, 325
Gilbert Cedric, 491
Gilles Thierry E., 57
Goldschmidt J. C., 270
Golovach Vitaly N., 74
Goto Nobuo, 449
Govyadinov Alexander A., 273
Granet Gérard, 56, 586
Grebennikov Alexandre, 52–54

Greentree Andrew D., 583
Grzesik Jan Alexander, 291, 292
Gu Bangming, 565
Gu Shuai, 599
Guan D., 264
Guichard Wiebke, 74
Guin Arun K., 667, 668, 670
Guizal Brahim, 81
Guo Gaofeng, 508
Guo Jian Feng, 683
Guo Wen-Yu, 241
Guo Xiao Dan, 408
Guo Yufeng, 533
Gupta A., 300
Guu George Chang-Lin, 478
Guzatov Dmitry V., 547

Hakonen Pertti J., 77
Hamad Safwat Helmy, 499
Hamadi Alia, 169
Hamazaki Junichi, 312
Han Bo, 624
Han Pin, 395
Han Yin-Yi, 100
Hang Zhi Hong, 264
Hanzelka Michael, 26, 32
Hao Li, 370, 371
Hao Yue, 214
Hashish Essam Abdel Haleem, 454
Hassel J., 77
Hayakawa Junki, 187
He Cui Juan, 489
He Dong Feng, 172
He Jheng Shyuan, 673
He Tsum-Yen, 202
He Wen Wei, 518
He Xiang, 513
Hein Yemin, 505
Hekking Frank W. J., 74
Hempel Jochen, 210
Herschel Reinhold, 355
Heshmati Abrahim, 495
Hespel Laurent, 168
Hietanen Maila, 283
Hieu Nguyen Van, 257, 258, 360
Hikita Mitsutaka, 171
Hillenbrand Rainer, 273
Hirano Tomoyuki, 447
Hirayama Hiroshi, 137, 192
Hirose Haruka, 146
Hirose Masanobu, 189, 190
Ho Wen-Hsien, 429
Ho Wen-Jeng, 356, 417
Ho Ying-Lung Daniel, 443
Ho You Zhe, 103
Hoi Bui Dinh, 258
Holé Stephane, 482
Hollenberg Lloyd C. L., 583
Hones Jesse, 191
Hong Jian-Shiung, 548
Hong Minghui, 543
Hong Weiwen, 36
Honore Randriamihaja Manjakavola, 56
Horibe Masahiro, 564
Horng Jing-Shyang, 353
Horng Tzyy-Sheng, 211
Hosaka Jun, 171
Hosako Iwao, 312
Hou Bo, 147, 313, 565
Hou Da Jun, 470
Hou Longfei, 287
Hou Qiang, 302
Hou Shang-Lin, 230–232
Houdali Nabil, 482
Hsiao Hui-Hsin, 354
Hsiao Yu-Chung, 119
Hsu Chun-Hao, 515
Hsu Haiyin, 348
Hsu Heng-Tung, 236
Hsu Jui-Ming, 446
Hsu Ko-Wen, 515
Hu Cheng-Nan, 504
Hu Chi-Jing, 400
Hu Chia-Ming, 202–204
Hu Dan, 468
Hu Jie, 251
Hu Jun, 179
Hu Robert (Shu-I), 215, 644
Hu Xiangyun, 624
Huang Boren, 241
Huang Chia-Ping, 538
Huang Chien-Chang, 478
Huang Ching-Ying, 644
Huang Chiu-Yueh, 457
Huang Chua-Zu, 546
Huang Dingwei, 105
Huang Guo-Wei, 216
Huang Hsiang-Lin, 544
Huang Huanting, 166
Huang Hui-Hsiang, 211
Huang Jer-Shing, 416
Huang Kuan-Yan, 350
Huang Lin, 310
Huang Shao Ying, 121, 286, 287, 487
Huang Wei-Hua, 519
Huang Xiao-Guo, 653, 654
Huang Yao-Wei, 105
Huang Yen-Chieh, 350
Huang Yi-Ching, 680
Huang Yu-Chien, 214
Huang Zhonglai, 396, 397
Huff Gregory H., 465
Huh Joo Young, 394
Hui Hon Tat, 131
Hung Ching-Chih, 509
Hung Si-Jyun, 680
Hung Wei Che, 506
Hung Yu-Han, 357
Huth F., 273
Hutová Eliska, 31
Hwang H. K., 325
Hwang I-Shyan, 358, 359
Hwang Mou-Chuan, 246
Hwang Sheng-Kwang, 357
Hwang Wei-Min, 246

Ibrahim Ibrahim I., 666
Ibrahim Imran Mohd, 332
Iddi Hashimu Uledi, 342, 606
Ikegami Tomoaki, 244
Im Andrew, 325
Imai Suguru, 453
Ishak Asnor Mazuan, 593
Ishii Kouichi, 514, 637–639
Ishii Nozomu, 187, 188
Islam Mohammad Tariqul, 65, 343
Islam Mohd Rafiqul, 110
Isota Yoji, 186
Isozaki Eiju, 46
Istivan Taghrid, 250, 534
Ito Koichi, 164
Ivanovs Girts, 225, 233
Ivans Veronica, 280
Iwaji Yoshitaka, 626
Iwaki Nobuaki, 562
Iwasaki Kazuya, 108
Iwasaki Yoichiro, 244

Jagadish C., 78
Jahr Norbert, 415
Jainal Siti Fatimah, 458
Jamlos Mohd Faizal, 340
Jandieri Vakhtang, 442
Jauberteau Marie-Odile, 289
Jayaram Anoop, 461
Jen Yi-Jun, 414
Jeng C. C., 18
Jeng Ming-Jer, 241
Jeong Hoon, 238
Jheng Ci-Yao, 525
Jheng Kai-Hong, 504
Jheng Kai-Teng, 554
Jheng San-Cai, 525
Jia Ding-Hong, 511, 653, 654
Jiang Lijun, 272, 274, 316
Jiang Ling, 310
Jiang Ming, 179
Jiao Dan, 125

Jin Yufeng, 647
Joffe Roman, 156
Joh Young Deuk, 394
Judd Martin D., 593
Juillerat-Jeanneret Lucienne, 412
Jung Wen-Shiang, 400

Kadlec Radim, 379
Kakiuchida Hiroshi, 228
Kamarudin Muhammad Ramlee Bin, 340, 342, 532, 606
Kamenetskii Eugene O., 73, 156
Kanada Naoki, 46
Kang Kyongok, 22
Kao Hsuan-Ling, 217
Kao Tsung Sheng, 543
Kao Yao-Huang, 470, 473
Kartal Mesut, 574
Kashiwa Tatsuya, 453
Kaspareck Karl F., 657
Kato T., 582
Kato Takeshi, 616
Kato Wataru, 617
Kavet R., 284
Kesavan Ulaganathen, 110, 332
Keshvari Jafar, 163
Khan M. Arif, 596, 602
Khemiri Mehdi, 392
Khosravi Mahdie, 521
Kiang Jean-Fu, 69, 177
Kikuma Nobuyoshi, 137, 192
Kim Dongsu, 641
Kim Mi Joung, 238
Kim Seongsin Margaret, 148, 311
Kim Seung-Bum, 166
Kishikawa Ryoko, 564
Kishimoto Seiya, 121
Kitatani Kazuhiro, 512
Kivshar Yuri S., 78
Kiyomi Kota, 514, 637–639
Klauenberg Bertram J., 284
Klimov Vasily V., 152, 547
Kobayashi Takehiko, 108
Kohmura Akiko, 46
Koleck Thierry, 169
Koley Chaitali, 667, 668, 670
Komatsu S., 453
Komiyama Akira, 317
Konas Petr, 32
Kondo Toshiaki, 422
Kong Lingfeng, 683
Koo Voon Chet, 568, 569, 571–573
Koseki Takafumi, 626
Kowalczyk Piotr, 635
Kozlov Mikhail, 278, 597, 614
Krankowski A., 304
Kravchenko Oleg V., 85
Krishnan Ananth, 237, 550
Kriz Tomáš, 27
Kriz Tomas, 89, 90, 247, 404
Krolikowski Wieslaw, 18
Kroutilová Eva, 379
Kubasek Radek, 248
Kuga Nobuhiro, 194
Kuleshov Yuriy, 391, 399
Kung Bruno, 74
Kung Patrick, 148, 311
Kuo Hsien-Nan, 291, 686
Kuo Kwo-Sen, 435
Kuo Wen-Kai, 472
Kuribayashi H., 453
Kurokawa Satoru, 189, 190
Kusiek Adam, 368, 496, 498, 502, 634
Kutishchev Stanislav Nikolaevich, 328
Kwon Young Mi, 394

Lacroix Aurelie, 289
Lahteenmäki Pasi, 77
Lai Chien-Hua, 632
Lai Wei-Jr, 519
Lai Yun, 565
Laio Allen, 520
Lakshmi Venkat, 566
Lalaurie Jean-Claude, 439
Lalloué Fabrice, 289
Lan Yung-Chiang, 103, 421, 548, 549
Landoulsi Alaeddine, 289
Lautrette Christophe, 289
Le Toan Thuy, 169
Lech Rafal, 368, 496
Lederer Falk, 270
Lee Bau-Yi, 129
Lee Cheng-Ling, 353, 446
Lee Chie-In, 643
Lee Chieh-Sen, 213
Lee Chien-Chih, 385–387
Lee Chien-Nan, 554
Lee Chih-Hung, 293, 538, 601, 608, 609
Lee Ching-Her, 652
Lee Dongjoo, 238
Lee Esther, 504
Lee Heng-Ming, 162
Lee Jae-Young, 505
Lee Jiayou, 490, 492
Lee Jin-Fa, 178, 183
Lee John, 191
Lee Min-Chin, 400
Lee R.-K., 18
Lee Ray-Kuang, 16
Lee Tao-Yi, 484
Lee Yee Hui, 288, 487
Lee Yi-Ying, 490
Lee Yi-Yu, 417
Lee Yong-Gu, 545
Lee Yu Jen, 433
Lee Yu-Ming, 676
Lei Jingli, 230–232
Lei Shih-Cing, 202
Lei Xuemei, 662
Lekner John, 326, 329
Lemaitre A., 79
Lertsakwimarn Kittima, 138
Lettl Jiri, 424–426
Leung Kwok Wa, 132, 136
Li (Lee) Renzhi (Imshik), 157
Li Bin, 215
Li Chai-Ming, 353, 446
Li Chuanrong, 351
Li Chun, 310
Li Chun-Fang, 11
Li Clark, 473
Li En, 508
Li Fang-Chi, 204
Li Guan-Shian, 644
Li Hong Jun, 620
Li Hsin-Chi, 62, 63
Li Hui, 235
Li Jensen, 153
Li Jianhua, 469, 618–620, 622, 623
Li Jing-Hong, 160
Li Jingwen, 575
Li Jun, 235
Li Kang-Ling, 510
Li Ke, 619
Li Kun-Jhe, 203
Li Lingyun, 365
Li Mingjian, 133
Li Pei-Kuen, 118
Li Q. F., 451
Li Shuang, 383
Li Sucheng, 147, 565
Li Suo-Ping, 230–232
Li Tsung-Lin, 672, 679, 680
Li Wei, 533
Li Yan, 263
Li Zheng-Qin, 687, 691
Lian Wei-Nan, 100
Liang Hsiao-Bin, 603, 604
Liang Yiong, 408
Liao Chia-Shu, 386
Liao Chun Yen, 542
Liao Eric, 640
Liao Ke-Fei, 381
Liao Kuan-Yu, 659

Liao Kun, 64
Liao Shun Fu, 652
Liao Si Pei, 302
Liao Tien-Hao, 166
Liaw Shien-Kuei, 347, 348
Lie Donald Y. C., 678
Liem Andrew Tanny, 359
Lim Chee-Siong, 572
Lim Chot Chun, 571, 572
Lim Chot Hun, 573
Lim Heng Siong, 573
Lim Soon Pheng, 34
Lim Tien Sze, 569–571, 573
Lin Chang-Tsun, 506
Lin Chi-He, 417
Lin Chi-Hung, 100
Lin Chih-Ying, 604
Lin En-Hong, 420
Lin Fong-Yi, 139, 538, 611
Lin G. C., 239
Lin G. Z., 240
Lin Han-Nien, 519, 520
Lin Heh-Nan, 419
Lin Huai-Yu, 509
Lin Huang-Tien, 386
Lin Hung Erh, 473
Lin Hung-Ying, 129
Lin I. C., 358
Lin Jhe-Min, 356
Lin Ji-Shing, 281
Lin Jiun-Hwa, 536
Lin Ke-Ming, 128, 503
Lin Li-Huei, 246
Lin Meng-Jie, 414
Lin Ming-Chieh, 685
Lin Ming-Shan, 520
Lin Tzu-Hsiung, 642
Lin Wei-Cheng, 643
Lin Y.-Y., 18
Lin Yan-Ting, 643
Lin Yi-Peng, 427
Lin Yuan-Yao, 16
Lin Yuyi, 371
Liou Jheng-Jie, 417
Liou Yuei-An, 391, 399
Liu Ai Qun, 542
Liu Annie, 640
Liu Chi-Chung, 236
Liu Hui, 144, 264
Liu Hung-Wen, 679
Liu Jia, 382, 529
Liu Jian Sheng, 620
Liu Jingui, 109
Liu Jun, 677
Liu Leilei, 533
Liu Li, 333
Liu Meng, 170
Liu Q. S., 122
Liu Qing Huo, 64, 101, 126, 158
Liu R. Y., 347, 348
Liu Szu-Ling, 214
Liu Ting-Yu, 100
Liu Wei-Chih, 541
Liu Ya'nan, 173
Liu Yahong, 599
Liu Yan-Jun, 230–232
Liu Yan-Tian, 492
Liu Yang G., 471
Liu Yanhui, 64
Liu Yinyao, 223
Liu Yunfei, 310
Liu Zhili, 256
Lo Sheng-Yung, 419
Loete Florent, 491
Lopes Silvania, 367
Lopez J., 678
Lou Zong-Xing, 540
Lu H. H., 239
Lu Hai-Han, 240, 356
Lu Weixin, 313, 565
Lu Ying-Hua, 489
Lu Yun, 234
Luan Pi-Gang, 103
Lucas Jerome, 150, 482
Luk Kwai Man, 133
Lum K. M., 34–37
Lunot Vincent, 212
Luo Ma, 126
Luo Shengyun, 689, 690, 692
Luo Yuan, 410
Lv Rui, 230–232

Ma Hongbo, 372, 384, 655
Maeda Hiroshi, 442
Mahanta D., 237
Mahmoud Korany Ragab, 499, 666
Malahzadeh Alireza, 636
Malinga Senzo Jerome, 174, 560, 561
Mansor Mohd Fais, 65
Marcet Z., 264
Marcon Petr, 25, 28, 30, 379
Markel Vadim A., 272, 274
Martin Andrew M., 583
Martin Olivier J. F., 271, 412
Maruyama Sotaro, 130
Marynowski Wojciech, 496, 498, 502, 634, 635
Masuda Hideki, 422
Mazur J., 634
Mazur Jerzy, 368
Mazur Mateusz, 497, 498, 502
Mei Jun, 263
Mei Shengtao, 376
Memon Qamar-ud-Din, 486, 596
Meng Guixian, 157
Meng Ling Ling, 221
Meng Qiao, 408, 518
Mi Siya, 288
Miao Min, 647
Michishita Naobumi, 193
Mikulka Jan, 23, 24, 26–28, 31, 249
Minovich Alexander, 78
Miroshnichenko Andrey E., 78
Misran Norbahiah, 65
Mitsugi Fumiaki, 244
Miyazaki Yasumitsu, 55, 449
Mobashsher Ahmed Toaha, 343
Mohamed Ahmed Magdy, 666
Mohri Kaneo, 616, 617
Mohri Yoshiyuki, 616, 617
Molotkov I. A., 299
Morais Débora Maria Souza, 649
Moretto Alain, 111
Moriwaki Retsu, 229
Moriya S., 172
Mowete Alex Ike, 464, 501
Mu Sin-Yuan, 198, 199, 207
Muhammed Hisham Abubakar, 501
Muhlig S., 270
Mukherjee Shouvik, 19
Mukhopadhyay Sourabh, 19
Mulangu Chrispin Tshikomb., 174
Murphy Michael R., 681
Myška Radek, 29, 404

Najafi Minoo, 636
Nakagawa Katsuji, 121, 448, 582
Nakaiwa Koichi, 380
Nakamiya Toshiyuki, 243, 244
Nakamura Shigehisa, 388–390
Nakamura Taichi, 626
Nakano Hisamatsu, 447, 580
Nakatake Yoshimasa, 445
Nasswettrová A., 32
Nepa Paolo, 66
Neshev Dragomir N., 78
Nghia Nguyen Van, 257, 258, 360
Nhan Nguyen Vu, 257
Nicol Stuart, 191
Nie Zai-Ping, 64, 179
Nieto David Esteban Ardila, 182
Niino K., 120

Nikoukar Ali Akbar, 359
Nishimura Naoshi, 120
Nishio Kazuyuki, 422
Niu Hongbing, 167
Numai Takahiro, 222
Numrich Robert W., 435
Nyete Abraham M., 402

Ochiyama Keita, 193
Ogiwara Akifumi, 228, 229
Oh Kien Keng, 37
Ohno Takanobu, 514, 637–639
Ohnuki Shinichiro, 121, 448, 582
Ohtera Yasuo, 146
Okamura Yasuyuki, 512
Okuno Yoichi, 590
Oldenburg Douglas W., 625
Ono Hiroshi, 228
Orenstein Meir, 154, 266
Osepchuk John Moses, 159
Osorio Jimmy Alexander Cortes, 182, 398
Otsuka Kyota, 514, 637–639
Ou Shengyuan, 427–430
Ouyang Guangzhou, 167
Owolawi Pius Adewale, 560, 561
Ozaki Ryosuke, 589

Pacheco Gefeson Mendes, 649
Paker Selcuk, 574
Pan Guan-Pu, 672
Pan He Ping, 302
Pan Leiting, 157
Pan Li, 528
Pan Liuzhan, 252, 535
Pan Ming-Yang, 420
Pan Na, 369
Pan Tianhong, 405
Pang Yi-Hsin, 483
Parajuli Hum Nath, 355
Paraoanu Gheorghe Sorin, 77
Park Won-Kwang, 394
Parkinson P., 78
Parts Rolands, 224, 225
Pasion Leonard R., 625
Pavelyev Alexander G., 391, 399
Pavelyev Alexey A., 399
Peidaee Pantea, 534
Peng Chia-Mei, 509, 510
Peng Peng-Chun, 356
Peng Weimin, 393
Peng Zhen, 178, 183
Peter Thomas, 335, 338
Petersen R. C., 284
Phongcharoenpanich Chuwong, 138
Pioch Sébastien, 439
Pirogova Elena, 250, 251, 407, 534
Plhak Ondrej, 424
Pokludová Michaela, 249, 253
Popov Alexei, 299
Porins Jurgis, 233
Potekhin Alexander P., 298
Pothier Arnaud, 289
Pourova Marika, 92
Premel Denis, 586
Proulx Pierre, 367
Przepiórka D., 304
Pu Shi, 131
Puch Christophe Bounaix Morand Du, 289
Purnamirza T., 332

Qi Ying, 599
Qing Xutang, 234
Quach James, 583

Rafique Umair, 486, 596, 602
Raghavan Singaravelu, 245, 406, 461
Rahim Mohamad Kamal Abd, 458
Rahim Sharul Kamal Bin Abdul, 335, 338, 532
Rahman Tharek Bin Abdul, 110, 332, 335, 338, 339, 342, 532, 606
Rahmani Mohsen, 543
Rajeshkumar V., 245
Rambaud Patrick, 367
Ramirez Ivan Dario Arellano, 398
Rani Mohd Subri Bin Abdul, 338, 532
Raniriharinosy Karyl, 56
Rao B. Prabhakara, 526
Rao V. Madhusudana, 526
Rarity John G., 443
Rastelli Gianluca, 74
Ratovsky K. G., 298
Raza Muhammad Bilal, 437
Reilly J. Patrick, 284
Reindl Leonhard M., 210
Reis Carlos, 44
Ren Fengran, 565
Ren Jing, 223
Renaudat Mathieu, 168
Riviere Nicolas, 168, 434
Rocca Fabio, 169
Rockstuhl Carsten, 270
Rodriguez-Lara Blas Manuel, 10
Rogerie G., 305
Romanova E. B., 298
Rosenblatt Gilad, 154, 266
Rothkaehl Hanna, 304
Roubal Zdeněk, 84
Rowley Jack, 282
Ryu Jongin, 641

Sabran Mursyidul Idzam bin, 332, 340
Sadeghzadeh Ramezan Ali, 495, 521
Saito Kazuyuki, 164
Saito Shingo, 312
Sakai Kota, 617
Sakakibara Kunio, 137, 192
Sako T., 448
Salazar Edwin Andres Quintero, 398
Samatsu Takashi, 243
Samson J. H., 72
Samusev K. B., 78
Sandoghdar Vahid, 418
Santschi Christian, 412
Sapumohotti Chamal, 112, 114
Sarkar Bishnu Charan, 667, 668, 670
Sarkar Debdeep, 500
Sarkar Suvra, 667, 670
Sasaki M., 616
Sasaki Naoki, 580
Sasamori Takayuki, 186
Sassi Imed, 392
Saurav Kushmanda, 500
Sautbekov Seil S., 320, 327
Sautbekova Merey S., 320, 327
Savel'ev S. E., 72
Savinov Vitaly, 547
Schäffer C. G., 355
Schecht C. A., 678
Schiffmann Bob, 159
Schneider Thomas, 415
Schnell Martin, 273
Schwarz Stefan, 355
Sedlácek Jirí, 87, 88
Sekine Norihiko, 312
Selamat Arshad, 65
Seman Norhudah, 340
Senellart Pascale, 79
Seow Chee Kiat, 38, 39
Sha Wei E. I., 181, 221, 471
Shao Hsiang-Yun, 239
Shao Yang, 178
Shavit Reuven, 73, 156
Shbat Modar Safir, 109
Shen Hung-Yu, 490, 492

Shen Jian Qi, 376
Shen Lianfeng, 662
Shen Linfang, 470
Shen Ming, 18
Shen Zejun, 369–371
Sheng C., 144
Sheng W. T., 124
Sheppard Asher R., 161
Shestopalov Yury V., 59
Shi Chao, 592
Shi Jiankui, 298
Shi Jun, 381
Shiao Yu-Shao Jerry, 216
Shibayama Jun, 447, 580
Shichi Hiromu, 228
Shimabukuro F. I., 346, 474
Shin C. S., 348
Shishkin I., 78
Shiu Ruei-Cheng, 548
Shiwa Mitsuharu, 172
Shu Lei, 489
Shu Yao-Te, 536
Shukla Ravi, 534
Shyu Zen-Der, 358
Siegfried Thomas, 271
Siew Wah Hoon, 593
Sigg Hans, 271
Silva Jo ao Carlos, 47
Silva Mario Marques da, 42, 44, 47
Sjoland Henrik, 405
Smíra P., 32
Smirnov Yury G., 59
Smithe David N., 685
Song Kun, 599
Song Lin-Ping, 625
Song Rencheng, 527, 528
Song Yanlin, 260
Sonoda Yoshito, 243, 244
Sorokosz Lukasz, 497
Souto Nuno, 44, 47
Spiller T. P., 72
Spolitis Sandis, 225
Sprlakova Andrea, 28
Sreenivasan V. K. A., 78
Srivastava Kumar Vaibhav, 500, 646
Staude I., 78
Stepanov A., 298
Steshkin V. I., 318
Stranik O., 415
Su Chun-Hsu, 583
Su Hsin-Lung, 506
Su Mei-Lin, 556
Su Min, 382, 529
Su Yu-Ching, 128
Suárez Guillaume, 412
Subbarao Akkala, 406
Sultan Kamel Salah, 454
Sumiya Yasuto, 46
Sun Greg, 105, 542
Sun Haiying, 157
Sun Handong, 267, 268
Sun Jwo-Shiun, 672, 679, 680
Sun Lingling, 677
Sun Nai-Hsiang, 201–204
Sun Sheng, 122
Sun Wenfeng, 468
Sun Xiao Lei, 337, 663
Sun Xiao-Wei, 365
Supe Andis, 233
Suwalak Rattapong, 138
Suyama Taikei, 590
Suzuki Sho, 514, 637–639
Suzuki Tatsuya, 514, 637–639
Symonds Clementine, 79
Szabó Zoltán, 84, 87
Słomińska E., 304

Taguchi Kenji, 453
Takada Kohei, 194
Takada Yasuhiro, 626
Takahara Junichi, 413
Takahashi Koichi, 449
Takahashi Masaharu, 164
Takeuchi Takashi, 448
Talhi Rachid, 305
Tan Poi Ngee, 570
Tan Soon Yim, 39
Tan Su Wei, 112, 114, 115
Tan Wei Qiang, 571
Tanaka Akinori, 140
Tanaka K., 452
Tanaka Masahiro, 448, 452
Tanaka Toshiyasu, 193
Tang Lingli, 167, 351
Tang Lingling, 546
Tang Ross Chin Hang, 265
Tao Wei, 298
Taverne Mike P. C., 443
Tebaldini Stefano, 169
Tell R. A., 284
Teng Han-Chung, 672
Teng Hsien-Chiao, 674, 676
Thansandote Art, 284
Tian Xin-Cheng, 214
Tobana Teruo, 186
Tong Mei Song, 104, 124, 180, 432, 451, 658
Tong Penger, 264
Tong Yu, 223
Tormanen Markus, 405
Trifonovs Ilja, 224
Tsai Bo-Yuan, 336
Tsai Chi-Lin, 457
Tsai Chihming, 212
Tsai Chung-Bo, 429
Tsai Churng-Jou, 336
Tsai Din Ping, 103, 105, 542, 544
Tsai Hsin-Chih, 679
Tsai Kun-Tong, 100
Tsai Ming-Chang, 656
Tsai Po-Hung, 417
Tsai Shou-Feng, 202
Tsai W. S., 240
Tsai Wan-Shao, 106
Tsai Wen-Shing, 239
Tsai Yau-Jyun, 538
Tsang Leung, 166
Tseng Jan-Dong, 659
Tseng Kuei-Jie, 530
Tseng Ming Lun, 105
Tseng W. H., 386
Tseng Yen-Lin, 520
Tsuda Ryoichi, 244
Tsukerman Igor, 272, 274, 587, 588
Tu Wen-Hua, 515
Tuan Shih-Chung, 66, 176, 456
Turner Robert, 278, 597, 614
Tuzlukov Vyacheslav, 109
Tyc Tomas, 475
Tyrovolas Ilias J., 374

Uchiyama Tsuyoshi, 617
Udalcovs Aleksejs, 224
Uemura T., 616
Underhill Michael James, 254, 306, 462
Urban Robert, 26, 27, 247

Van Den Brink Alec Maassen, 80
Vargas Jairo Alberto Mendoza, 182
Vesely Alessandro Alberto, 377
Vesely Sara Liyuba, 377
Vetharatnam Gobi, 570
Villard L., 169
Vlcek Martin, 425
Vogelgesang Ralf, 275
Vojisavljevic Vuk, 251, 407
Vrba David, 95, 96, 98
Vrba Jan, 92–94
Vrba, Jr. Jan, 95, 96, 98

Wada Masahiro, 512
Wakabayashi Toshio, 458
Wakabayashi Y., 447
Wakiwaka Hiroyuki, 380
Wan G. C., 124
Wan Guochun, 451, 658
Wang Bao Fa, 382, 529
Wang Chao, 170, 508, 533, 576

Wang Chien-Jen, 642
Wang Chun-Kai, 128
Wang Dong, 683
Wang Guo Hong, 302
Wang Guojun, 298
Wang H., 348
Wang Haixia, 393
Wang Huai-Hsien, 100
Wang Jie, 256, 677
Wang Jin, 265
Wang Jue, 183
Wang Juen-Kai, 100, 354
Wang Jui-Chien, 427
Wang Kai-Te, 66
Wang Keping, 662
Wang Ly-Yun, 419
Wang Mingtian, 600
Wang Pengbo, 403
Wang Rui-Sheng, 201
Wang S. B., 264
Wang S. M., 144
Wang Shinn-Fwu, 226, 524, 525
Wang Shu-Na, 365
Wang Shuming T., 676
Wang Ting-Hao, 546
Wang Wan-Ti, 642
Wang Wei, 365
Wang Weidong, 605
Wang Wensong, 513
Wang X., 298
Wang Xiaoxu, 157
Wang Xinhong, 167, 351
Wang Xinke, 468
Wang Y., 144
Wang Y. C., 347
Wang Y. Q., 104, 180
Wang Yao-Ting, 103
Wang Yi, 173
Wang Yinhui, 123, 436
Wang You-Bao, 592
Wang Yu-Jiu, 484
Wang Yuh-Lin, 100
Wang Zhigong, 662
Watanabe Koki, 445
Watanabe Minoru, 229
Watanabe Soichi, 164
Wei Jeng-Hua, 226
Wei M. H., 104, 180, 432
Wei Miao-Hsu, 227
Wei Pei-Kuen, 106, 420
Wei Sheng-Jun, 511
Wei Xiang, 179
Weissl Thomas, 74
Wen Jincai, 256
Wen Kai, 39
Weng Chung-Ning, 151
Weng Zi-Hua, 373, 523, 682
Widarta Anton, 563
Wilde Jürgen, 210
Wilson R., 72
Wirth J., 415
Wu Chien-Jang, 236, 470, 472, 473
Wu Chun-Sen, 291, 686
Wu Di, 663
Wu Guiju, 624
Wu Huang-Ming, 414
Wu Jieh-Chian, 227
Wu Jin-Jei, 236, 470, 473
Wu Jiu Hui, 287
Wu Kun-Long, 215
Wu Liang, 365
Wu Ming-Hsiung, 350
Wu Pin Chieh, 542, 544
Wu W. F., 347
Wu Y. F., 665
Wu Ying, 262, 263
Wu Yuan-Yuan, 687
Wu Yumao, 316

Xiang Mei-Yi, 691
Xiang Qian-Yin, 653, 654
Xiao Fengchao, 562
Xie Chuan, 619
Xie Feng, 469, 618, 622
Xie Ganquan, 469, 618–620, 622, 623
Xie Lee, 469, 618, 622
Xie Lei, 576
Xie Mengji, 618
Xie Qing, 618, 622, 623
Xie Xiangqi, 620
Xie Xiangwu, 619
Xie Xinsheng, 622
Xie Y. J., 622
Xin Yu-Ling, 160
Xin Zi-Hua, 11
Xiong Xiaoyan, 272
Xiong Xiaoyan Y. Z., 274
Xu Hongyi, 267, 268
Xu Huaping, 383
Xu Jianjun, 605
Xu Jinying, 684
Xu Leijun, 405
Xu Ming-Hai, 688, 689
Xu Sanyuan, 381
Xu Su, 267
Xu X., 590
Xu Xiaolan, 166

Yahya Roshayati, 340
Yakabe Toshiyuki, 562
Yam Chua Ming, 569
Yamada Hirohito, 146
Yamada Muneo, 616, 617
Yamada Yoshihide, 193
Yamamoto Yuta, 626
Yamasaki Tsuneki, 589
Yamauchi Junji, 447, 580
Yams Lu-I, 510
Yanagishita Takashi, 422
Yang Chih-Kai, 549
Yang Chin-Lung, 213, 457, 480
Yang Jeng-Rern, 632, 650, 651
Yang K., 432, 451
Yang Kuang Yu, 542, 544
Yang Shuang-Yan, 11
Yang Song-Han, 69
Yang Tsung-Yuan, 293, 601, 608, 609
Yang Tzong-Jer, 470, 473
Yang Wayne, 226, 524, 525
Yang Wei, 403
Yang X. J., 333
Yasumoto Kiyotoshi, 442
Ye Jia-Sheng, 468
Ye Xi, 170
Ye Xiuzhu, 527
Ye Yu, 365
Yeh Cavour, 346, 474
Yeh Chih-Sheng, 217
Yeh Chun Chun, 645
Yen Chia-Yi, 241
Yen Hsuan-Der, 216
Yen Ming-Ching, 538, 603
Yen Ta-Jen (David), 544
Yener Namik, 660, 661
Yeo Swee Ping, 528
Yonemoto Naruto, 46
Yook Jong Min, 641
Yu Chien-Te, 66
Yu Quliang, 633
Yu Shao-Ping, 480
Yu Tsung-Chih, 686
Yu Yi-Lin, 347
Yuan Hong, 351
Yuan Jiansheng, 369–371
Yuan Xiao, 173
Yuan Xiao-Hui, 372, 384, 655
Yue Xiaoxiao, 234
Yuk Tung Ip, 337, 507, 663, 664

Zagoskin Alexandre M., 72, 76
Zeng Bing-Hao, 139, 611
Zeng Heping, 235
Zeng Hongcheng, 403
Zeng Tiao Jun, 372, 384, 655
Zhang Baile, 149, 267, 268
Zhang Bo, 576
Zhang Changchun, 533
Zhang Cunlin, 310
Zhang Hong, 170, 576
Zhang Jianhua, 158

Zhang Jianzhong, 396, 397
Zhang Jin-Ling, 489
Zhang Jun, 664, 665
Zhang Keifei, 399
Zhang Li, 575
Zhang Ling Yan, 289
Zhang Nan, 489
Zhang Xiangdong, 684
Zhang Xianmin, 473
Zhang Xiao-Hong, 633
Zhang Xiao-Ling, 381
Zhang Y., 622
Zhang Y. Q., 104, 180, 432, 658
Zhang Yan, 468
Zhang Ye, 141
Zhang Zhenwei, 310
Zhao H., 18
Zhao Hang, 376
Zhao L., 591
Zhao Q., 590
Zhao Ran, 179
Zhao Xiao-Peng, 599
Zhao Xiaowei, 158
Zheludev Nikolay I., 542
Zheng Xu, 443
Zheng Y. J., 144
Zheng Zhi-Zong, 353
Zherebtsov G. A., 298
Zhou Bihua, 619
Zhou Feng, 302
Zhou Mingzhu, 256, 633, 677
Zhou Xianwei, 618, 623
Zhou Xuan, 618
Zhu Bo, 167, 351
Zhu Cong, 144
Zhu Hailiang, 507
Zhu Jinfeng, 101
Zhu Min, 591
Zhu S. N., 144
Zhu Xiao, 592
Zhu Yong, 291, 292
Zhu Z. Y., 124
Zieniutycz Wlodzimierz, 497, 498
Ziskin Marvin C., 284
Zou Jun, 371
Zuo Daxin, 618
Zuo Peng, 369, 370
Zvyagin Andrei V., 78